# Femtosecond and attosecond chiral dynamics investigated by velocity map imaging and photoelectron photoion coincidence spectroscopy

Etienne Bloch

université de BORDEAUX

École doctorale des Sciences Physiques et de l'Ingénieur

# Femtosecond and Attosecond Chiral Dynamics Investigated by Velocity Map Imaging and Photoelectron-Photoion Coincidence Spectroscopy

## THÈSE

présentée et soutenue publiquement le

**16/10/2020**

pour l'obtention du

**Doctorat de l'université de Bordeaux**

Spécialité lasers, matière et nanosciences

*par*

**Etienne BLOCH**

Directeur : Yann MAIRESSE

Composition du Jury :

| | | |
|---|---|---|
| **Thierry RUCHON** | Chercheur au CEA, LIDYL | Rapporteur, Président |
| **Gustavo GARCIA-MACIAS** | Scientifique de Ligne de Lumière au synchrotron SOLEIL | Rapporteur |
| **Danielle DOWEK** | Directrice de Recherche au CNRS, ISMO | Examinatrice |
| **Maria-Novella PIANCASTELLI** | Professeure à Sorbonne Université, LCPMR | Examinatrice |
| **Till JAHNKE** | Professeur à la Goethe-Universität, Institut für Kernphysik | Examinateur |
| **Stefan HAACKE** | Professeur à l'Université de Strasbourg, IPCMS | Examinateur |
| **Yann MAIRESSE** | Directeur de Recherche au CNRS, CELIA | Directeur de thèse |

**Centre Lasers Intenses et Applications, UMR 5107**
**Université de Bordeaux, CNRS, CEA**
43 rue Pierre Noailles, 33400, Talence, France

# Contents

# Acknowledgements

First and foremost, I would like to warmly acknowledge the members of my jury, Thierry Ruchon, Gustavo Garcia, Danielle Dowek, Maria-Novella Piancastelli, Till Jahnke and Stefan Haacke, for reviewing my PhD thesis and attending my defence. Even if their fields of research cover a broader range than the questions addressed in this thesis, and that the reading of such a document can be tedious, they all have enthusiastically accepted this task and I am sincerely grateful for it.

Of course, I would also like to thank my PhD supervisor, Yann Mairesse, for these three years. Firstly, you have set the bar quite high in the lab by managing to put together this amazing experimental setup. It is a beamline on which everybody would love to do a PhD, and you provided me this chance. Secondly, you have been there for substantially steering the researches and developments towards really refreshing and exciting directions. This ability you have has always impressed me, along with your capacity to make complicated things simple. And thirdly, you unite this wonderful team in which it has been a great pleasure to be. I know you absolutely hate being described as a group leader (because it is all about teamplay, right?), so in Dota terms, let us just say that you play carry.

I also thank Valérie Blanchet, my unofficial second supervisor. We have spent quite a lot of time in the lab struggling on painful and burdensome developments, and you have always been there for support. So, even if every time I thank you for your help, you just answer "don't thank me, it's my job", still, thank you.

I think the very best side of these three years was the team and the lab I was part of, and they all deserve to be acknowledged. Let us begin with the theoreticians, who cheerfully burnt my left leg with their endless days of calculations. Bernard, the king of the croco, for patiently teaching me theory so many times, and showing me how to be twice as young while being twice as aged. Baptiste, who I far too little interacted with because he can not help doing so many thing, and doing it well. Fabrice, for all these discussions, randomly jumping from quantum mechanics to economy. But life is not only made of $H_4^{3+}$. I can not count how many times I asked stupid laser questions to Dominique during the "pauses clopes" (often the same question several times in a row, in fact). I hope I am Descamps-approved now (gold standard, above peer-review). I would also like to thank all the other people I have closely interacted with : Stéphane, for your endless support when the laser goes reaaally bad, Jérôme, for your refreshing not-pessimistic-at-all vision of things (only challenged

by our Vin-ké du 37 haha), Nikita, my Russian master in terms of random-idea-why-not-to-make-a-windmill-with-a-beer-tank, along with Romain and Anatoly for your advice for my absurd Arduino and Raspberry projects. I also warmly thank the administrative staff, Céline, Sonia and Sophie, whose kindness makes paperwork almost pleasant. The mechanics, Laurent and more recently Franck, also deserve a special thank for patiently showing me how to drill and cut like a pro (it's crazy how satisfying this can be), but also helping me fixing my daaamn bike so many times. And of course a few words for the IT, Richard and Gaëtan, that I bothered sooo many times and who saved my life at least as many times. I can not cite every single person of the lab for all the good moments spent together, but let me guarantee here that I have really enjoyed being in the nice atmosphere you all contributed to.

The collaborations were also a very enriching part of my thesis. For this reason, I thank Francesca for welcoming me in her so, so nice team and lab in Hamburg. And also Nirit, for sending us her coolest students. I also really appreciated to work with Jason, Caoihme, Nadia and Marie-Catherine. Even if this was before my thesis, some people have greatly impacted my present work. I must acknowledge Steve and his ultrafast team, in particular Ashley and Erika, for this wonderful semester I spent in Berkeley, and Reinhard and his ultimate-COLTRIMS-guru team in Frankfurt, especially my two lost Mexikaner Giammarco and Isabel, and of course all the others.

That's also the place for a big big thank to all the PhD students of the group, for these endless hours of work that you have turned into a lot of fun, and also beyond the lab. Antoine, the talented experimenter that has no control over its wandering hands (AKA the tac-tac-bin-pouf guy), and Alex, the talented theoretician that has no control over its computer (just kidding, I don't either). Split between the phalanx-crushing, knuckle-grinding, tendon-wrecking sessions (in other words, bouldering, just in case we don't have enough tryhard all day long already), countless beers (I actually believe we should have had more of them, I can't wait for the end of the lockdown) and much more. Bitching-Bouldering-Beers, it's like the perfect trinity of a PhD, thanks to you guys. Alex, I keep your recipe for beer brewing and motherboard cooking. Let us not forget Sandra and Sylvain, my cell mates. I'm so sorry for inflicting you my obsessive-compulsory disorder of tidily insulting my computer on a quarter-hour basis. With these random conversations ranging from K-pop to parking lot multilevel progressive hostile takeover, I really enjoyed being locked with you two. I don't know if you know, but you contributed to change my vision about PhD. But we will discuss this again next year (have fun with the manuscript, ha-ha-ha). And Debobrata, always using your poker face to distill so much fun. I hope you enjoy yourself here in France, and in the lab with my painful legacy. It's probably time to mention the ones gone too early (in postdoc, i mean). A little nostalgia for the pastis de trop with Sam, our official Quebecois never-resting war machine (no idea how you do, man, let me know one day). And also for Quentin and Geoffrey, the definitions of power-to-mass ratio. And finally let me thank the other PhD students that I had fun with during terribly painful experiments in collaboration. Shaked, never give up your convulsion-inducing colorbars, they are perfect. We'll also have to figure out this High-Phone startup at

some point, but never without hula-hoop ! And Vincent, our official Quebecois never-resting kebab machine, the chillest dude I have ever met in a lab, and yet, with a weirdly acute sense of mobility (more seriously, I would also rent luggage vans for only 9 cents per minute if I could).

There are also some other people who deserve some credit for this thesis. The ones I wish I could have seen so much more often.

Firstly, my scattered mates from the ENS in Paris. You are all insane in your own manner (like, for real, we have mental conditions). That's a lot of fun, but more importantly, you are all so inspirational to me. Marius-S.l.C. (I won't tell the meaning), crazy enough to s'en balek of everything (I could acknowledge you much further, but we all know you balekouyfrerr). Thomas, the exact opposite, always wondering what is the sense of life even if his life makes more sense than any other (and by the way, about the surfer lifestyle, we will have to discuss again, because -no offense-, I don't have any memory of you actually standing on a board hehe). Aurélien, The Chaeef, I think you deserve the trophy of insanity here. Seriously man, I don't know how you managed to stay alive so far. But your homeless-businessman-Gypsy-kite-instructor-scam-professor model is worth a try. Note that my life won't be complete before I witness the retour de bâton, I look forward to it. Not to forget, Guillaume (the nightmare is over... or has just begun haha), Seb-the-fdp (#norage #pumpiron), Pierre-the-Camarade-fdp (you were right, I'll just boil booze for the rest of my life), Hugo-the-fdp (#norage #tesconcestfacile), the whole Couscousbangbang team (#yallahyallah), Grosnico, Faussexx...

Secondly, the originalz, the realz, the homies from Nancy. I don't know where to start. It's not that I just missed you, in fact, it was a real misery to see you so sparsely for such a long time. Seriously, what's the point of it all if at the end of the day you can't hang out with your friends. Getting a PhD I guess, but from now on, we might operate a few adjustments of the targets. The good news is that even if we don't see each others for a long time, I know you will still be there. The acknowledgements are already getting too long, and if I start explaining why I owe you all so much, it will never end. So let met just thank you all : Chloü, AlmaXgros, Repier-the-Pastavorus, Charlot-Chucky-Chuck-the-Cheezy-Fromagist, Lobo El-Chien-Loup-dla-Sseca, Cheddar-Fiemax, Socrate-the-Chillum-Mastah, Raton-sur-Roussette, Djodjo, Paula, Babat's, Maud, the whole gang-of-Huberts, Sylvia, Binouz, Nitnelav (the only one who could actually be there for the defence haha)... and so many more that I have lost on the way. I hope to find you all again just where I left you, we'll have time to catch up the missing pints.

And finally, I think my family deserves the biggest thank of all. You have all loved me unconditionally, and that's be basis of everything else. In particular, my parents have gave me so much that I can't even describe it. They have always let me do whatever I wanted to do, but always supported me. Well, at the end, I'm still alive and I did a PhD. I've always wanted to make you proud of me, not because you wanted it, but because you deserve it. You are just the best. Everybody says this about their parents, but in my case, it's just an objective fact.

Even when you are not there and even when what I do is completely unrelated to you, it's thank to you. It's no coincidence if all of my friends want to see Patou et Gégé even when I'm not there. You are my model of art and science, literature and general knowledge, sociability and grumpiness. And my brother, Nino, you're the least stupid lawyer I've ever seen. On paper we are so different, and yet we're quite the same. That's what I like with you, you bring me refreshing perspectives that I can find in no other place. I know I can have blind trust in you, and it's always so much fun to hang out together. A final word for my grandparents. Even if we can't discuss my thesis too much in details for reasons of different orders, you have greatly influenced me, and I'm proud of you four.

Last but not least, these three years of my life have not only corresponded to my PhD. They have also been three years alongside Laurie. You were here to bring me back to reality so many times, to prevent me from working all night so many times. To remind me that life is also about discovering new countries for pleasure and not for beamtimes, reading books which are not about quantum mechanics, to meet people who have no idea what a Fourier-limited laser pulse is, and to have all these little pleasures that are not productive and that's exactly the point. And don't worry, I don't mind at all if your friends and family don't study chirality, that's exactly why I like them !

Thank you all ! And call me doctor haha

# Personal Journey

I have had a hard time choosing between chemistry and physics during my studies, which is why I more or less picked both. I had the opportunity in bachelor to study Density Functional Theory with Gilles Frison in a laboratory of the Ecole Polytechnique. I enjoyed it a lot, but I wanted to dig deeper into the foundations of chemistry. In this respect, I think that Richard Taïeb and Jérémie Caillait from the LCPMR, who taught me spectroscopy, quantum mechanics and light-matter interaction at the Ecole Normale Supérieure of Paris, played a decisive role. I found a good balance between theory and applications in their courses. I had the chance, in their laboratory, to approach numerical resolution of the Schrödinger equation, applied to the generation of high-order harmonics (HHG). A this moment, I knew that ultrafast spectroscopy was what I was looking for. I also wanted to experience the experimental side of research, which I did with Amelle Zaïr at the Imperial College of London, again on HHG and non-linear optics. At the time, we had a collaboration with the CELIA in Bordeaux, where I found an interesting place for my next internship. I studied there transient emission spectroscopy with Yann Mairesse and all the team I know much better now. I also learned the field of research of the group about chiral molecules, which I found particularly interesting, from its basis of physics and laser science to its stakes in organic chemistry and biology. We thus set up a plan for a PhD project, but not directly at the time. In the meantime, between my Master's degree and my PhD, I had the chance to have an funded year of additional scientific experience, which I again enjoyed a lot. I took this opportunity to improve my knowledge in both optical and photoelectron spectroscopy, in particular towards ultrafast techniques that can be extended to molecular systems. I could spend a semester in the group of Stephen Leone in Berkeley, focusing on attosecond four-wave mixing. My other semester was dedicated to learn photoelectron-photoion coincidence spectrometry in the laboratory of Reinhard Dörner in Frankfurt, which has been a decisive asset for my PhD. Back in Bordeaux, I could import my (modest) experience to this new activity of the group, right in time for the development of the new apparatus and the new high-repetition rate beamline. The rest of this manuscript will take up from here.

Looking back at my initial quandary : Physics or chemistry? I could find a field where there is no such distinction. Optical or photoelectron spectroscopy? Both are cool! Theory or experiment? Well, there are only 24 hours in a day... And at the end of the day, what is this all about? Having fun doing research with nice people, I think.

(For the record, it actually started when I was 5-years-old when my chemist grandpa used to show me explosive, fragrant and colorful chemical reactions in his basement to make me laugh. It undoubtedly made me laugh, but perhaps not only.)

# Résumé

Cette thèse rend compte de l'étude expérimentale de dynamiques chirales dans des systèmes moléculaires en phase gazeuse. Elle a pour but de sonder ces propriétés à leur échelle ultrarapide naturelle, par l'utilisation d'impulsions laser ultracourtes et d'une observable très sensible, le dichroïsme circulaire de photoélectrons. Ces avancées dans la compréhension des interactions lumière-matière chirales peuvent aussi être replacées dans un contexte plus général de résolution des mécanismes de la reconnaissance chirale.

**Chapitre 1 : Introduction Générale**

Un objet est dit *chiral* lorsqu'il n'est pas superposable à son image miroir. Comme nous le verrons dans la section 1.I, cette propriété géométrique peut se retrouver à l'échelle moléculaire, et est d'importance fondamentale dans un large champs de domaines, de la biologie à la chimie, jusqu'à la synthèse de médicaments et la physique. Néanmoins, son étude est principalement basée sur des mesures statiques, en particulier en phase gaz où des composés isolés peuvent être étudiés. Comme introduit dans 1.II, nous utiliserons des impulsions laser ultracourtes pour résoudre les aspects dynamiques de la chiralité à son échelle de temps naturelle, de la femtoseconde ($10^{-15}$ s) à l'attoseconde (($10^{-18}$ s). L'accès à la chiralité moléculaire n'est pas direct, car la sonde doit être elle même chirale pour des raisons de symétrie. La lumière polarisée circulairement peut jouer ce rôle. Une observable de choix, le dichroïsme circulaire de photoélectrons (PECD), se manifeste comme une forte asymétrie chirosensible dans la distribution angulaire de photoélectrons produite lorqu'une cible chirale gazeuse est photoionisée. Initialement établie dans le régime d'ionisation à un photon, elle dispose d'une grande gamme de sensibilités, comme présentées dans 1.III. La mesure des distributions de photoélectrons nécessite un appareillage particulier. Une partie conséquente de cette thèse a été consacrée au développement d'un des systèmes de détection les plus complets pour les processus de photoionisation, un spectromètre de photoélectrons-photoions en coïncidence, globalement présenté dans 1.IV. Il permet de lever les ambiguïtés qui pèsent quant aux différentes voies d'ionisation qui peuvent se superposer dans les spectres complexes, pour séparer les processus d'ionisation de différentes espèces, ou encore pour retrouver les informations d'orientation dans des échantillons orientés aléatoirement.

**Chapitre 2 : Développement Expérimental**

Le second chapitre 2 présente les développements expérimentaux mis en œuvre.

Notre source laser à haute cadence de nouvelle génération sera tout d'abord présentée dans 2.I. Ses capacités de vitesse d'acquisition sans précédent constituent une avancée significative

par rapport aux technologies laser existantes, bien que de nouveaux défis se présentent. Nous verrons ensuite comment la ligne de lumière a été conçue pour être aussi adaptable que possible, et d'accéder à une grande gamme de régime d'interaction lumière-matière. Cela est réalisé en particulier par la conversion de fréquence de la longueur d'onde fondamentale, la génération de hautes harmoniques (HHG) pour la production de photons de plus haute énergie, et l'amplification paramétrique optique pour l'obtention d'une accordabilité continue en longueur d'onde. La question de la durée des impulsions sera discutée avec une brève présentation de la technique de postcompression.

Notre spectromètre imageur de vecteur vitesse (VMI) sera décrit dans 2.II. C'est un appareil relativement simple, couramment employé pour la détection de distributions angulaires de photoélectrons. Nous verrons ensuite comment les distributions complètes peuvent être retrouvées à partir des projections mesurées, avec l'inversion d'image pour les distributions présentant une symétrie cylindrique ou en utilisant la reconstruction tomographique pour les distributions arbitraires.

Dans la section suivante 2.III, nous verrons comment les limites du VMI peuvent être dépassées, en particulier comment la mesure directe des distributions angulaires de photoélectrons en 3D peuvent être effectuées et comment les différentes voies d'ionisation peuvent être différenciées, en utilisant la détection de photoélectrons-photoions en coïncidence. Dans cette optique, le développement d'un COLTRIMS, ou microscope réactionnel, sera présentée. Après un bref historique de la détection en coïncidence, nous détaillerons le principe de fonctionnement des détecteurs. Nous discuterons ensuite de la conception du spectromètre qui est adapté à notre objectif, à savoir la détection des parties chirosensibles dans les distributions angulaires de photoélectrons en coïncidence avec le spectre de masses correspondant. La détection requiert une interaction lumière-matière en phase gazeuse dans des conditions particulières. Une description de la configuration du jet, du vide et du faisceau sera alors proposée. Enfin, l'algorithme de reconstruction, utilisé pour assigner les coïncidences et reconstituer les distributions, sera présenté.

Ce type d'appareil nécessite une attention particulière pour fonctionner à ses pleines capacités en termes de taux d'acquisition et de résolution, comme nous le discuterons dans la section 2.IV. La caractérisation du COLTRIMS sera effectuée, puis nous identifierons les différentes contraintes de la détection en coïncidence, tels que le filtrage du bruit et le taux de comptage, qui sont des questions centrales pour obtenir une détection efficace. Nous verrons que la résolution et la vitesse d'acquisition nécessitent de faire des compromis. Des efforts importants ont aussi été dédiés dans l'optimisation du taux d'acquisition, et nous discuterons des perspectives d'améliorations dans le but de réaliser des expériences pompe-sonde en coïncidence, l'un des schémas les plus exigeants. Enfin, la calibration et la résolution de notre nouveau spectromètre seront présentées.

**Chapitre 3 : Régime Multiphotonique**

Ce chapitre 3 présentera l'étude de la chiralité moléculaire dans le régime d'ionisation multiphotonique.

Nous introduirons tout d'abord dans 3.I les aspects intéressants de l'ionisation multipho-

tonique augmentée par les résonances (REMPI), en particulier sa grande sensibilité à de multiples processus moléculaires, mais aussi comment elle peut être utilisée pour découpler l'excitation et l'ionisation. Nous verrons ensuite comment des effects dichroïques au delà des polarisations purement circulaires peuvent fournir de bonnes perspectives dans ce contexte. En comparaison de l'ionisation à un photon, ce régime présente aussi l'avantage d'être adapté aux expériences pompe-sonde résolues en temps.

La seconde section 3.II présentera une nouvelle technique analytique de détermination d'excès énantiomériques et de contenu isomérique en temps réel. Un nouvel effet chiroptique sera introduit, le dichroïsme elliptique de photoélectrons (PEELD), qui consiste en l'extension du PECD à des champs polarisés elliptiquement. Nous verrons comment cela enrichit la sensibilité aux processus moléculaires, en particulier en terme d'anisotropie d'excitation créée dans le paquet d'onde excité. Les résultats sont obtenus dans le VMI, et nous verrons que la source à haute cadence permet une acquisition très rapide. En particulier, un schéma de détection synchrone permettant un filtrage du bruit particulièrement efficace sera présenté. Nous verrons ensuite comment cela peut être utilisé pour effectuer des mesures d'excès énantiomérique avec une grande justesse, ainsi que des mesures continues d'excès énantiomérique. Cet effet étant hautement spécifique à chaque molécule, nous verrons que des 'empreintes digitales' moléculaires peuvent être déterminées et utilisées pour la caractérisation de mélanges à composants multiples. Cela rend la technique particulièrement compétitive par rapport aux solutions industrielles existantes.

L'étude du dichroïsme elliptique de photoélectrons sera ensuite étendue au COLTRIMS dans la section 3.III. Cela constitue aussi la première mise en œvre expérimentale du spectromètre. Pour commencer, la capacité de détection directe en 3D de notre nouveau COLTRIMS sera comparée à la reconstruction tomographique depuis des images VMI, dans le but d'évaluer les avantages et les inconvénients de chaque méthode. Nous étenderons ensuite l'étude du PEELD à deux nouveaux systèmes chiraux, l'Ethyl- et le Méthyl-Lactate. Ces molécules ont été choisies pour leur grande propension à former des dimères mais doivent être caractérisées de zéro. La détection en coïncidence sera aussi utilisée pour étudier la dépendance à la fragmentation des spectres de photoélectrons, ainsi que les mécanismes de fragmentation en jeu. Cela constituera aussi une bonne base de discussion pour montrer les capacités du COLTRIMS et les défis qui restent à résoudre dans le but de combiner toutes ses capacités en une même expérience, ce qui nécessite des ordres de grandeur supplémentaires de temps d'acquisition. Enfin, nous présenterons des calculs de théorie de la fonctionnelle de la densité dépendants du temps (TDDFT), qui représentent un excellent support pour des études plus approfondies. En particulier, les pespectives en terme de résolution des voies d'ionisation, et de fragmentation lors de processus complexes, seront soulignées.

Dans une dernière section 3.IV, une étude du PECD résolue en temps à l'échelle de la femtoseconde, reposant sur un schéma pompe-sonde dans le Méthyl-Lactate, sera présentée. Ce travail a été effectué en collaboration, sur une source externe IR-UV de quelques cycles optiques, qui est complémentaire de la nôtre. Elle a en effet une plus faible cadence mais une meilleure résolution temporelle. La ligne de lumière sera présentée, ainsi que sa caractérisation et le schéma d'analyse utilisé. Le rapport signal sur bruit fût en effet un enjeu sensible et

doit être caractérisé attentivement. De plus, le large support spectral des impulsions courtes mélange de nombreux processus. Les résultats expérimentaux et leur interprétation seront discutés, avec l'aide de modélisations numériques. En particulier, l'évolution transitoire du PECD à l'échelle femtoseconde pourrait révéler des dynamiques électroniques ou nucléaires ultrarapides.

**Chapitre 4 : Régime Champs Forts**

Le chapitre 4 de ce manuscrit explorera la chiralité dans le régime d'interaction lumière-matière en champs forts.

Nous commencerons par introduire les spécificités du cadre champs-forts dans la première section 4.I. De manière intéressante, lorsque le potentiel d'un champ laser devient comparable avec le potentiel moléculaire, une description semi-classique simplifiée des processus peut être faite. Nous présenterons une approximation largement utilisée : l'approximation des champs forts (SFA), ainsi que ses conséquences. En particulier, la génération d'harmoniques d'ordre élevé et la spectroscopie de photoélectrons en champs forts seront détaillées. L'effet de la chiralité moléculaire n'est ici pas trivial, car le potentiel moléculaire joue un rôle de moindre importance. Nous verrons comment les processus chiroptiques peuvent néanmoins apparaître dans le régime des champs forts.

La section 4.II sera basée sur une nouvelle technique que nous avons développé, appelée Enantioselective Sub-Cycle Antisymmetric response Gated by electric-field rOTation (ESCARGOT). Elle est basée sur l'utilisation de champs orthogonaux à deux couleurs (OTC), un champs optique vectoriel dont la chiralité instantanée alterne à l'intérieur même du cycle optique. Nous verrons qu'une telle quantité, qui va au delà de la définition habituelle de l'ellipticité, basée sur une vision moyennée sur les cycles optiques, est pertinente et peut être utilisée pour accéder aux dynamiques sous-cycle optique des processus chiroptiques. L'étude est basée sur des mesures VMI et sur la résolution numérique de l'équation de Schrödinger dépendante du temps (TDSE). L'interprétation en terme de trajectoires semi-classiques de photoélectrons sera ensuite discutée.

Dans une troisième section 4.III, l'extension de la technique ESCARGOT en trois dimensions sera étudiée. Elle donne la possibilité d'accéder aux phénomènes en jeu par l'utilisation de l'interférométrie de photoélectrons, augmentée ici par la signature sensible à la chiralité. Nous introduirons la cartographie du vecteur potentiel sur l'impulsion des photoélectrons, un effet typique des champs forts, qui peut être utilisé pour résoudre plus en profondeur les dynamiques intra-cycle optique à l'œuvre dans les champs OTC. Nous verrons ensuite comment la chiralité peut être finement encodée dans l'interférométrie de photoélectrons, à l'aide de calculs TDSE et de mesures COLTRIMS. Différents types de trajectoires de photoélectrons seront identifiées, et nous verrons qu'elle peuvent être affectées différemment par le potentiel moléculaire chiral. Une description explicite des trajectoires sera proposée avec un modèle SFA étendu, et nous verrons en particulier comment le Coulomb focusing peut jouer un rôle. Des potentiels écrantés de Yukawa seront aussi utilisés dans des calculs TDSE dans le but de distinguer les effets de courte et de longue portée du potentiel moléculaire chiral.

Enfin, une autre configuration de champs exotique, les champs bicirculaires bichromatiques contrarotatifs, sera brièvement discutée dans une dernière section 4.IV. Ce champ vectoriel en forme de trèfle sera utilisé pour voir les processus chiraux de photoélectrons sous un autre point

de vue. Notamment, des familles de trajectoires seront identifiées et leur sensibilités respectives à la chiralité seront dévoilées. L'observable la plus frappante sera un effet d'attoclock chiral. Il est habituellement appliqué aux cibles achirales de manière à lire, à travers des décalages angulaires des distributions de photoélectrons, de fins délais dans la photoionisation. Son extension aux systèmes chiraux permet de spécifiquement encoder l'interaction chirale avec le cœur ionique de manière quantitative.

**Chapitre 5 : Conclusions Générales et Perspectives**

Le chapitre 5 sera consacré au résumé des résultats obtenus tout au long de cette thèse et à la discussion des perspectives d'études à venir. En particulier, la ligne de lumière laser à haute candence est un pas en avant significatif en terme de taux d'acquisition de signal, et elle peut être utilisée dans un vaste champ de régimes d'interaction. Néanmoins, des défis de stabilité à long terme et de durée d'impulsions restent à résoudre. L'adaptation du spectromètre de photoélectrons-photoions en coïncidence à cette nouvelle source compacte présente de vastes perspectives pour la résolution complète de processus moléculaires de photofragmentation et photoionisation, quand bien même une grande marge de progression reste disponible pour son optimisation. Nous soulignerons aussi le fait que le PECD multiphotonique est hautement sensible à l'anisotropie d'excitation. Cette propriété peut être, entre autre, utilisée très efficacement dans des applications analytiques. L'étude résolue en temps du PECD, utilisant un schéma pompe-sonde, ouvre aussi la voie à la résolution femtoseconde de processus moléculaires chiraux, c'est-à-dire l'échelle à laquelle les réactions chimiques se déroulent. Pour finir, la vision en profondeur dans les interactions chirales sous-cycle optique fournie dans le régime d'ionisation en champs forts est d'intérêt fondamental pour comprendre la nature de notre observable de choix de la chiralité. Cela ajoute aussi un angle de vue supplémentaire très prometteur dans la boîte à outils des champs forts, qui présente de nos jours un grand intérêt pour saisir l'essence de l'interaction lumière-matière aux échelles de temps attosecondes.

# Abstract

This thesis reports on the experimental investigation of chiral dynamics in molecular systems in the gas phase. It aims at probing these properties at their natural ultrafast timescale, with the use of ultrashort lases pulses and a very sensitive observable, photoelectron circular dichroism. These advances in the understanding of chiral light-matter interaction can be also related to the global context of resolving the mechanism of molecular chiral recognition.

**Chapter 1 : General Introduction**

A object is *chiral* when it is not superimposable with its mirror image. As will be introduced in Section 1.I, this geometrical property can arise at the molecular scale, and is of fundamental importance in a broad range of fields, from biology, chemistry, to drug synthesis, and physics. However, most of its studies are based on static measurements, in particular in the gas phase, where isolated compounds can be studied. As introduced in 1.II, we will use ultrashort laser pulses to resolve the dynamical aspects of chirality at its natural timescale, from femtosecond ($10^{-15}$ s) to attosecond ($10^{-18}$ s). Accessing molecular chirality is not straightforward, since the probe used must be chiral itself for symmetry reasons. Circularly polarized light can play this role. An observable of choice, photoelectron circular dichroism (PECD), arises as a strong chirosensitive asymmetry in the photoelectron angular distribution produced when a gaseous chiral target is photoionized. Firstly established in the one-photon ionization regime, it has a great range of sensitivities, as presented in 1.III. The measurement of the photoelectron distributions requires particular apparatus. A significant part of this thesis was dedicated to developing one of the most complete detection system for photoionization processes, a photoelectron-photoion coincidence spectrometer, broadly presented in 1.IV. It enables one to lift ambiguities on the ionization channels overlapping in complex spectra, to disentangle ionization from different species, and to retrieve orientation-dependent information from a randomly oriented sample.

**Chapter 2 : Experimental Development**

The second Chapter 2 presents the experimental developments implemented.

Our new generation high-repetition rate laser source will be firstly presented in 2.I. Its capacities of unprecedented signal acquisition rate constitute a significant breakthrough compared to the previous laser technologies, even if new challenges arise. We will then see how the beamline has been designed to be as versatile as possible, and access a broad range of light-matter interaction regimes. This is achieved in particular by using frequency conversion of the fundamental wavelength, high-order harmonic generation to produce high-energy photons, and optical

parametric amplification to get a continuous tunability of the wavelength. The question of the pulse duration will be addressed with the brief presentation of the postcompression technique.

Our velocity map imaging (VMI) spectrometer will be described in 2.II. It is a relatively simple device, commonly employed for the detection of photoelectron angular distributions. We will then see how the complete distributions can be retrieved from the measured projections, with the inversion of the images for the distributions having a cylindrical symmetry or by using tomographic reconstruction for any arbitrary distribution.

In the next Section 2.III, we will see how the limitations of a VMI can be overcome, in particular how the direct measurement of the photoelectron angular distributions in 3D can be performed and how the different ionization channels can be distinguished using a photoelectron-photoion coincidence detection. For this purpose, the development of a COLTRIMS, or reaction microscope, will be presented. After a brief history of the coincidence detection, we will detail the operation principle of the detectors. We will then discuss the design of the spectrometer, which is adapted to our purpose, *i.e.* the detection of chirosensitive parts in the photoelectron angular distributions in coincidence with the corresponding mass spectrum. The detection requires the light-matter interaction to happen in the gas phase in particular conditions. The jet, vacuum and beam configuration will then be described. Finally, the reconstruction algorithm, used to assign the coincidence and reconstitute the distributions, will be introduced.

Such a device requires particular attention to operate at its full acquisition rate and resolution capacities, as will be discussed in Section 2.IV. The characterization of the COLTRIMS will be performed, and we will discuss the different constraints of the coincidence detection, such as noise filtering and counting rate, which are central questions to get an efficient detection. We will see that the resolution and the acquisition rate result from compromises. Important efforts have also been put into the optimization of the acquisition rate, and the perspective to further increase it in order to perform pump-probe experiments in coincidence, one of the most challenging scheme, will be discussed. Finally, the calibration and the resolution or our new spectrometer will be presented.

**Chapter 3 : Multiphoton Regime**

This Chapter 3 will present the study of molecular chirality in the multiphoton ionization regime.

We will firstly introduce in 3.I the interesting aspects of resonance-enhanced multiphoton ionization (REMPI), in particular its great sensitivity to multiple molecular processes, and also discuss discuss how it can be used to decouple the excitation and the ionization. We will then see how dichroic effects beyond purely circular polarizations can provide good perspectives in this context. Compared to the single-photon ionization, this regime has also the advantage of being suited for time-resolved pump-probe experiments.

The second Section 3.II will present a new analytical technique of real-time determination of enantiomeric and isomeric content. A new chiroptical effect, photoelectron elliptical dichroism (PEELD), consisting in extending PECD to elliptically polarized fields, will be introduced. We will see how this enriches the sensitivity to molecular processes, in particular in terms of anisotropy of excitation created in the excited wavepacket. The results are obtained in the

VMI, and we will see that the high repetition rate source enables for a very fast acquisition. In particular, a lock-in detection scheme, providing a particularly efficient noise filtering will be presented. We will then introduce how this can be used to perform accurate measurements of enantiomeric excess as well as continuous enantiomeric excess measurements. We will see that this effect being highly molecule-specific, molecular fingerprints can be determined and used for the characterization of multicomponent mixtures. This renders the technique particularly competitive to the current solutions existing at an industrial grade.

The study of the photoelectron elliptical dichroism will then be extended in Section 3.III in the COLTRIMS. This also constitutes the first experimental implementation of the spectrometer. At first, the direct 3D detection capacity of our new detection device will be compared to the tomographic reconstruction from VMI images, in order to assess the pros and cons of each methods. We will then extend the PEELD study to two chiral systems, Ethyl- and Methyl-Lactate. These molecules have been chosen for their great tendency to form dimers but have to be characterized from scratch. Coincidence detection will also be used to study the fragmentation-dependent photoelectron spectra, as well as the fragmentation mechanisms at play. This will also constitute a good basis of discussion to show the capability of the COLTRIMS and the challenges that remain to be solved in order to use all its capabilities at the same time, which requires orders of magnitude more acquisition time. Finally, time-dependent density functional theory (TDDFT) calculations, providing an excellent support for further investigations, will be presented. In particular, the perspectives provided in term of resolution of the ionization and fragmentation channels in intricate processes will be highlighted.

In a last Section 3.IV, a time-resolved study of the PECD at the femtosecond scale using a pump-probe scheme in Methyl-Lactate will be presented. This work has been performed in collaboration on an external few-optical cycles IR-UV beamline, which is complementary to ours. It has indeed a lower repetition rate, but a greater temporal resolution. The beamline will be presented, as well as its characterization and the analysis scheme used. The signal-to-noise ratio was indeed a challenge and has to be characterized carefully. In addition, the broad spectral support of the short pulses mixed numerous processes. Experimental results and their interpretation will be discussed, with the help of numerical modeling. In particular, the transient evolution of the PECD at the femtosecond timescale might reveal electronic or nuclear ultrafast chiral dynamics.

**Chapter 4 : Strong Field Regime**

The last Chapter 4 of this manuscript will explore chirality in the strong-field light-matter interaction regime.

We will start by introducing the specificity of the strong-field framework in the first Section 4.I. Interestingly when the laser field potential becomes comparable with the molecular potential, a simplified semi-classical description of the processes can be made. We will present this widely used strong field approximation (SFA), and its consequences. In particular, high-order harmonic generation and strong field photoelectron spectroscopy will also be detailed. The effect of molecular chirality is not trivial here, since the fine details of the molecular potential should not matter in this framework. We will discuss how chiroptical processes can nevertheless arise

in the strong field regime.

The second Section 4.II will be based on a new technique we have developed, named the Enantioselective Sub-Cycle Antisymmetric Response Gated by electric-field rOTation (ESCARGOT). It is based on the use of orthogonal two-color (OTC) fields, a vectorial optical field whose instantaneous chirality alternates within the optical cycle. We will see that such a quantity, which goes beyond the usual cycle-averaged definition of the ellipticity, is relevant and can be used to access the sub-optical cycle dynamics of chiroptical processes. The study is based on VMI measurements and time-dependent Schrödinger equation (TDSE) calculations. The interpretation in terms of semi-classical electron trajectories will then be discussed.

In a third Section 4.III, the extension of the ESCARGOT technique in three dimensions will be studied. It provides the possibility to access the phenomena at play by using photoelectron interferometry, enhanced here with the chiral-sensitive signature. We will introduce the mapping of the vector potential on the photoelectron momentum, a typical strong-field effect, which can be used to further resolve the sub-optical cycle dynamics at play in OTC fields. We will then see how chirality can be finely encoded in photoelectron interferometry, with TDSE calculations and COLTRIMS measurements. Different types of photoelectron trajectories will be identified, and we will see that they can be affected differently by the chiral molecular potential. An explicit description of the trajectories will be proposed with an extended SFA model, and in particular we will investigate how Coulomb focusing can play a role. Yukawa screened potentials will also be used in TDSE calculations in order to disentangle the short- and long-range effects of the chiral molecular potential.

Finally, another exotic field configuration, the counter-rotating bicircular bichromatic fields, will be more briefly discussed in the last Section 4.IV. This clover-shaped vectorial field will be used to obtain an other angle of view on chiral photoelectron processes. In particular, families of trajectories will be identified, and their respective sensitivity to chirality will be unveiled. The most striking observable will be a chiral attoclock effect. It is usually applied in achiral targets to read fine delays in the photoionization as angular offsets in the photoelectron distributions. Its extension to chiral systems enables specific encoding of the chiral interaction with the ionic core in a quantitative manner.

**Chapter 5 : General Conclusion and Perspectives**

Chapter 5 will summarize the results obtained during this thesis and discuss the perspectives of future studies. In particular, the high repetition rate laser beamline is a major step forward in terms of signal acquisition rate, and can be used in a broad range of interaction regimes. However, challenges regarding long term stability and pulse duration remain to be tackled. The adaptation of the photoelectron-photoion coincidence spectrometer to this new table-top source presents great perspectives for the complete resolution of molecular processes in photofragmentation and photoionization, even if a great margin remains for its optimization. We will also underline the fact that multiphoton PECD is indeed highly sensitive to anisotropy of excitation. This property can, among others, be used for analytical purposes very efficiently. The study of time-resolved PECD using a pump-probe scheme also paves the way to resolving femtosecond chiral molecular processes, *i.e.* the scale at which chemical reactions occur. Finally, the deep insight

into the sub-optical cycle chiral interaction provided in the strong field ionization regime is of fundamental interest for understanding the nature of our observable of choice of chirality. This also adds a very promising angle of view to the strong field tools, which are nowadays of high interest to grasp the essence of light-matter interaction at the attosecond timescale.

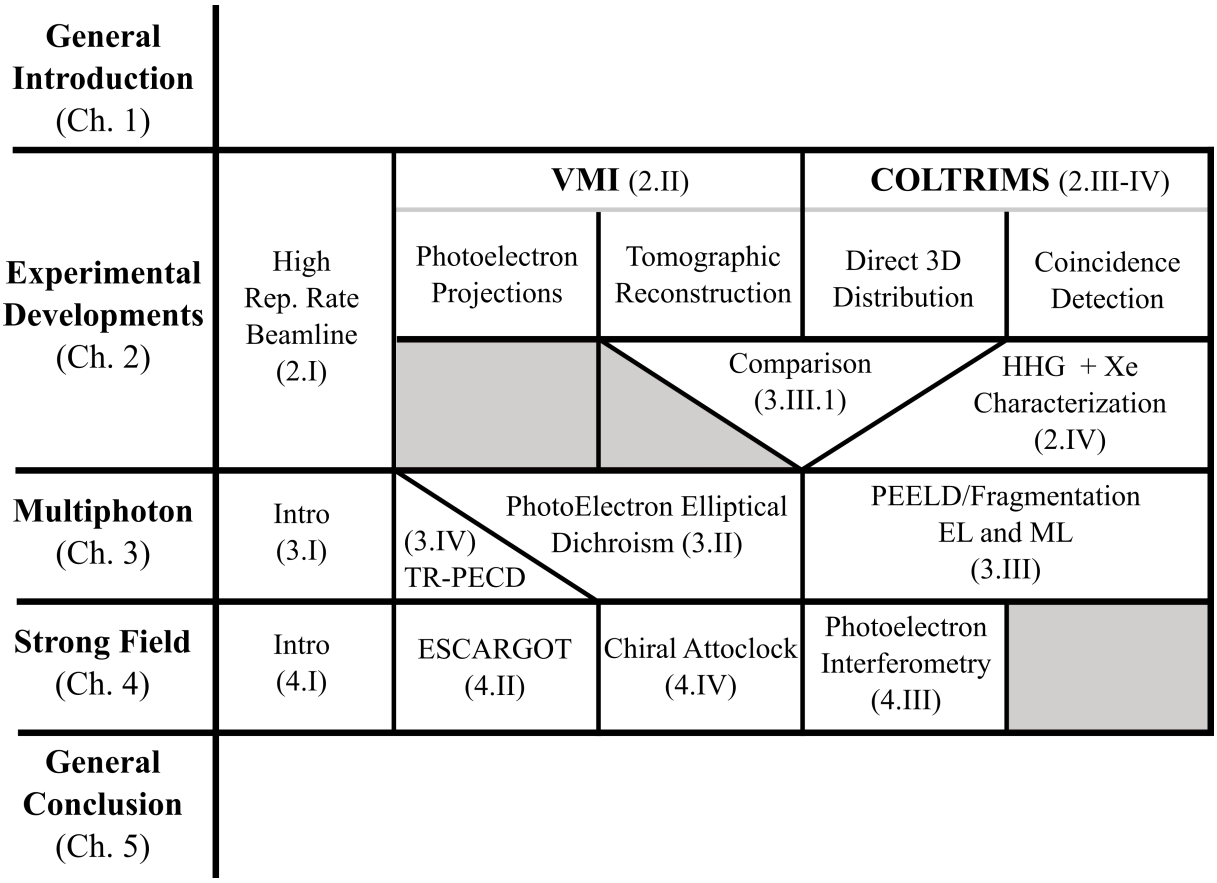


**Figure 1** – *Table of content of this thesis manuscript.*

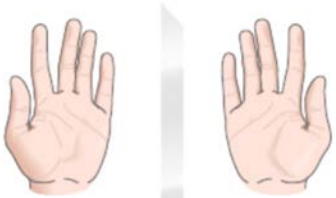

# Chapter 1

# General Introduction

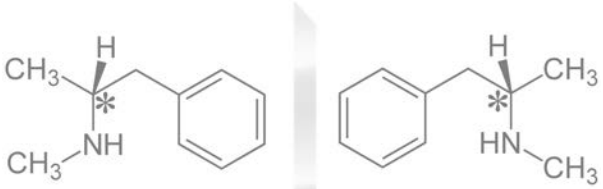


This thesis aims at investigating chiral molecular systems in the gas phase, in particular the chiral ultrafast dynamics by the use of ultrashort laser pulses and photoelectron/photoion spectroscopy. The central concepts which will be used throughout this manuscript are presented in this introduction chapter.

## I Chirality

**Concept**

Chirality is a general geometric property of asymmetry. An object is chiral if it is not superimposable onto its mirror image, or in other words if it does not have a mirror symmetry. The best illustration is perhaps given by hands ($\chi\epsilon\iota\rho$, or *kheir* in Greek), as the mirror image of a right hand is a left hand, and are of course distinct (Fig. 1.1 (a)). Many everyday life objects are chiral, such as gloves, scissors, guitars and so on, and all of them can exist in two forms, the 'left' or 'right' handedness to keep the example of the hands. A central property associated is that chiral objects do not interact the same way with other chiral objects depending on their handedness. For instance, a right hand fits in a right glove, but does not in a left glove. Oppositely, they interact the same way with achiral objects (for instance, a pen, which has a mirror symmetry, can be held on both hands).

It turns out that chirality can also take place at the microscopic scale. Organic molecules, among others, can be achiral or chiral, depending on their structures. The latter case often (but not always) involves asymmetric carbons (bound to four different groups) denoted with a star in the example in Fig. 1.1 (b). Like macroscopic objects, chiral molecules can be found in two forms called *enantiomers*, labeled *dextro* (+) or *levo* (-). Enantiomers have exactly the same chemical and physical properties (melting point, density, vibrational spectrum, ionization potential...), except in one specific case : chiral molecules do not interact or react with each other the same way depending on their handedness. Chemical reactions can thus be *enantiospecific*, meaning that depending on the handedness of the enantiomers involved, the reaction can occur, differ or even be forbidden. A intuitive parallel can be drawn with handshakes, where two right hands can fit in each other, two left hands can fit in each other but a right hand can not shake

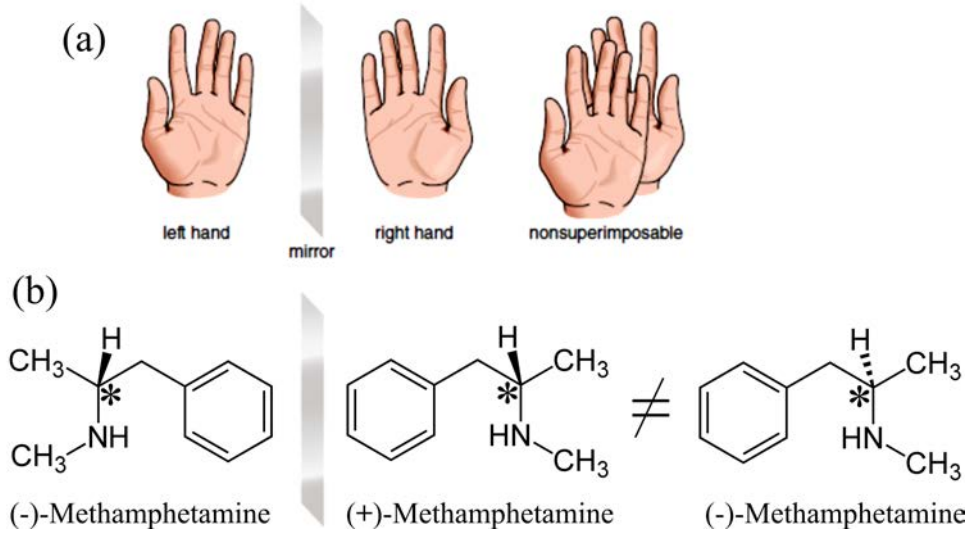


**Figure 1.1** – *Concept of chirality, illustrated at the macroscopic scale (a) and molecular scale (b).*

a left hand. Similarly, molecules can fit the same way, fit differently or not fit in each other depending on their symmetry.

Note that in the cases where the molecule contains several asymmetric carbons, enantiomerism occurs with the inversion of all the chiral centers (global mirror imaging) while diastereoisomerism arises when the configuration reversal is not applied to all the centers (local mirroring). Since this latter modifies the whole structure of the molecule, and not only its global symmetry, diastereoisomers have different chemical and physical properties. They can thus be simply considered as different chiral molecules. This type of isomerism is then excluded from this study.

**Homochirality of Life**

The concept of chirality is particularly visible at the macroscopic scale since many items are designed for right-handers (have you ever tried to use a corkscrew with your left hand?). However, a chemical reaction of achiral reagents can only yield an equal mixture of enantiomers (*racemic*). At first sight, enantiomers should thus be found in equal abundance in nature and the story could have ended there, but a fascinating property at the molecular scale changes everything, namely *homochirality of life*. It happens that most of the chiral molecules found in living systems only occur naturally under one enantiomer. This is the case for the vast majority of the elementary components of life : sugars, amino acids (and thus proteins), nucleotide basis (and thus DNA) and so on. For instance, every single DNA helix in physiological condition, whether found in a human body, an elephant, a bacteria or a potato, rotates towards the right (note that a few counter-examples can be found in very isolated environments, such as abysses). This property has been conserved since the origin of life, as it transmits by descendancy. However, its origin remains an open question, and a wide variety of scenarios have been considered. Two main families of hypothesis exists : the deterministic and the random ones. To cite a few examples, they range from spontaneous separation (random), parity violation in the weak interaction (deterministic), to asymmetric interstellar photoreactions [Hadidi 18] (deterministic,

see reviews in [Jorissen 02, Evans 12]). At some point, an excess of a compounds' enantiomer had to occur to break the symmetry of the chemical reaction from achiral bricks. Even a small excess could have led to a complete homochirality, by chiroselective amplification [Soai 00].

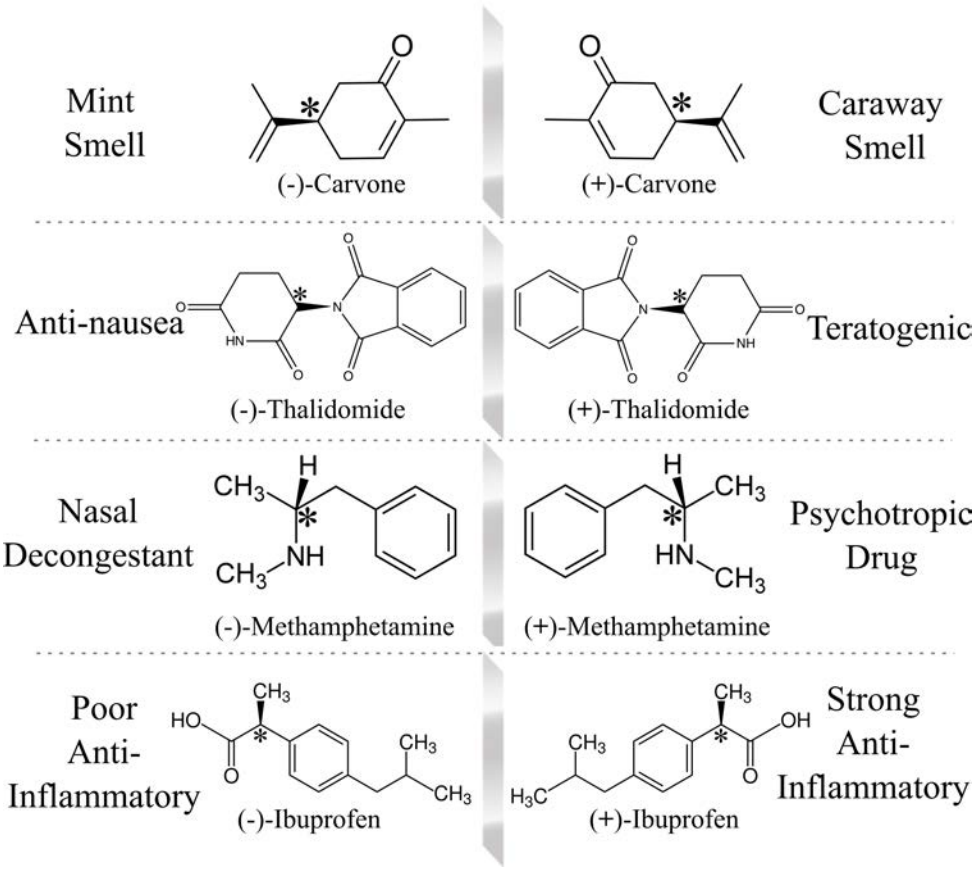


**Figure 1.2** – *Examples of chiral organic molecules, whose effect on the human body differs depending on the enantiomer.*

Because of the enantiospecificity of a wide variety of reactions, living systems do not necessarily interact the same way with the two enantiomers of a molecule. For instance, neuronal receptors can be chiral and found in only one handedness (say 'right glove'), which can only be activated by the adequate drug enantiomer (corresponding 'right hand'). A great variety of examples can be found, as depicted in Fig. 1.2. For instance, (-)-Carvone has a minty smell, while (+)-Carvone smells like caraway. Perhaps more importantly, some drugs can have different effects depending on their handedness. Thalidomide was used in the 1960s' as an anti-nausea medicine for pregnant women. However, while its (-) form was actually beneficial, it could racemize in the human body in its (+) form which induces teratogenic effects, and caused a medical scandal. (+)-Methamphetamine is a strong psychotropic synthetic drug while (-)-Methamphetamine is an over-the-counter nasal decongestant. Intermediate situations also exist, such as the (-)-Ibuprofen which has the same anti-inflammatory properties as the (+) enantiomer, but is simply 3 times less effective. Nevertheless, using a enantiopure compound is even beneficial in this case, in particular to minimize side effects which can be of equal impact

for both forms.

For these reasons, the ability to produce pure enantiopure compounds (asymmetric synthesis) and to characterize such compounds is of crucial importance for biology, chemistry, and physics, and is worth billions of dollars in the pharmaceutical industry.

**Asymmetric Chemistry**

Molecular chirality is particular in the sense that, conversely to conformational isomerism for instance, the transformation of an enantiomer to the opposite one requires to break chemical bounds, and no exchange between the two forms can occur without chemical reaction. In this sense, an enantiomer is very rarely obtained from the opposite one.

Several ways exist to produce enantiopure compounds, or at least an excess of enantiomers in a mixture. It is for example possible to derive a compound from a plant or animal extract, already naturally enantiopure because of the homochirality of life. In this case, the chiral centers can be conserved upon chemical reaction to the products. Interestingly, compounds directly derived from naturally abundant precursors are often much less costly than the opposite enantiomer, which has to be obtained another way. A widely used technique to obtain a pure enantiomer from achiral reagents is asymmetric catalysis, awarded by the 2001 Chemistry Nobel Prize, which consists in using a chiral catalyst to kinetically foster a given symmetry. This is used at an industrial scale despite the need for expensive chiral catalysts, since these latter are not consumed upon reaction. Biocatalysis can also be highly enantioselective, and plays a central role in living systems. As mentioned above, enzymes are only naturally found in one symmetry, and like the hand and the glove, they are usually effective at producing one enantiomer only. This is perhaps one of the most important mechanism involved in the conservation of life homochirality.

An alternative solution to produce enantiopure compounds is to perform enantiomer separation from racemic mixtures. This method is not straightforward, since enantiomers have exactly the same chemical and physical properties. The only way to separate them is, again, by making them interact with an external chiral reference. For instance in chiral chromatography, a chiral substrate can be used and interacts differently with the two enantiomers of a chiral molecule. As a consequence, these latter can have a different migration time in the column, and be separated.

Broadly speaking, despite being powerful, no technique is universally applicable. Their use is defined on a case-by-case basis, and constitutes a fascinating field of chemistry. Interestingly, they all dwell on the use of an already asymmetric (and pure) external reference. This makes the origin of life homochirality even more puzzling.

**First Observation and Characterization**

As previously mentioned, enantiomers only differ by a mirror symmetry, and thus have exactly the same chemical and physical properties (except when interacting with other chiral objects). As a consequence, characterizing the enantiomeric content of a sample can be a challenging task.

Molecular chirality was initially discovered by Louis Pasteur in 1848 [Pasteur 48], when he noticed that synthesized tartaric acid crystals could be faceted with two opposite symmetries

(see Fig. 1.3 (a)). The crystallization indeed brought to the macroscopic scale a microscopic property. He also observed by the way that tartaric acid derived from living things only crystallized under one form. Beyond this particular case, molecular chirality was historically studied with the *optical activity*, *i.e.* the fact that chiral molecules can rotate the polarization plane of linearly polarized light upon transmission (Fig. 1.3 (b)). Opposite enantiomers rotate it in opposite directions, with a magnitude defined by the compound-specific optical rotation. This effect, discovered before chirality in 1815 by Jean-Baptiste Biot, has yielded the *dextro* (+) and *levo* (-) designation.

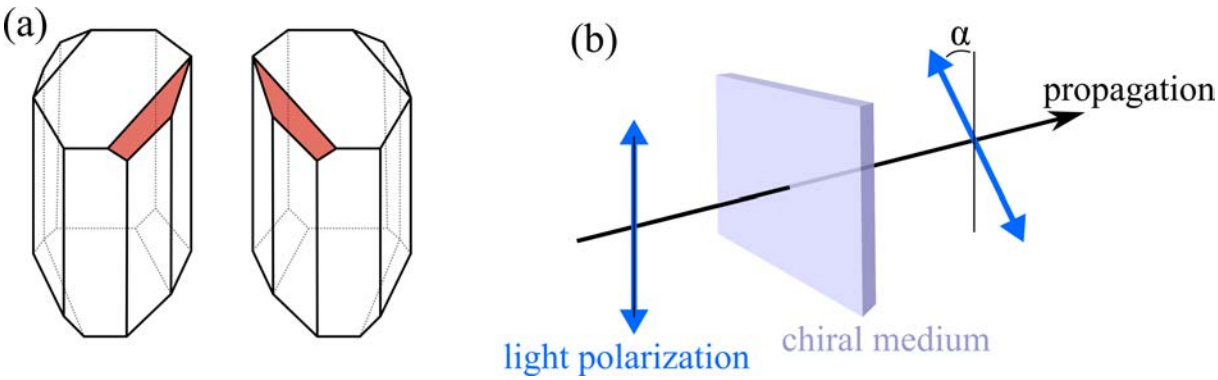


**Figure 1.3** – *(a) Representation of enantiopure crystals obtained with opposite enantiomers. (b) Illustration of the optical activity.*

**Chiroptical Processes**

The asymmetric interaction of light with chiral compounds paved the way to what is nowadays referred to as *chiroptical processes*. Molecular chirality can only be probed by chiral objects, but molecules are not the only chiral tool available : light can also be chiral. A left-circularly polarized (LCP) electromagnetic field is indeed the mirror image or a right-circularly polarized (RCP) one. As a result, light can interact differently with an enantiomer depending on its polarization and the molecule's handedness. For symmetry reasons, RCP interacts with (+) enantiomers the same way that LCP does with (-) ones, but differently than RCP with (-) and LCP with (+). These processes are called *dichroic effects*, and will be the bedrock of this manuscript.

The most common chiroptical process is absorption circular dichroism (CD), which is a difference of absorption of the enantiomers depending on the rotation of circularly polarized light. Since absorption and dispersion are linked, the physical origin of this process is common to the optical activity mentioned above. Depending on the wavelength, different types of transitions can be addressed with various sensitivities. Rotational transitions can be probed in the microwave range, but the dichroism is weak as the wavelength is much longer than the size of the molecule. Infrared wavelengths can be used to access vibrational circular dichroism. One of its advantage is that the vibrational spectra can be quantitatively calculated with standard quantum chemistry packages. Finally, electronic circular dichroism can also arise with visible/ultraviolet light. A more exhaustive description of widely used modern chiroptical processes is proposed in Section 3.II. Unfortunately, these effects are relatively weak (absorption

CD of the other of $10^{-4}$). This is due to the fact that they originate from magnetic dipolar transitions, electric quadrupolar, or higher perturbative orders.

**Chiral Recognition**

The understanding of the processes involved in chiroselective and chirosensitive chemical reactions is of crucial importance, but can be difficult to access. Typically, this issue is in fact often completely dodged. For instance, one can test many reagents or catalysts in an systematic manner to determine the most suited ones. While this can be a practical solution, this is of course fundamentally unsatisfactory. Different intermolecular interactions can play a role in chemical reactions, with different ranges and different strengths [Berthod 06], as summarized in Table 1.1. A few examples are depicted in Fig. 1.4.

| Type of Interaction | Strength | Direction | Range |
|---|---|---|---|
| Steric Hindrance | Very strong | Repulsive | Very Short |
| Coulomb | Very strong | Attractive/repulsive | Medium ($1/d^2$) |
| Hydrogen Bond | Very strong | Attractive | Long |
| $\pi$-$\pi$ | Strong | Attractive/repulsive | Medium |
| Ion - Dipole | Strong | Attractive | Short |
| Dipole - Dipole | Intermediate | Attractive | Short ($1/d^3$) |
| Dipole - Induced Dipole | Weak | Attractive | Very short ($1/d^6$) |
| Induced Dipole - Induced Dipole | Very weak | Attractive | Very short ($1/d^6$) |

**Table 1.1** – *Characteristics of intermolecular interactions. Adapted from [Berthod 06].*

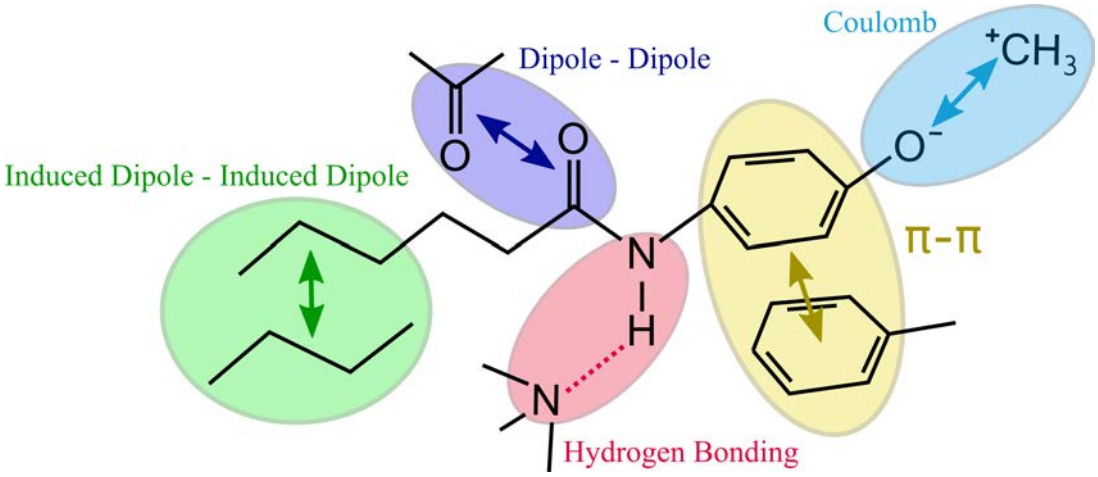


**Figure 1.4** – *Illustration of various types of intermolecular interactions.*

The way these intermolecular processes induce an enantiomer-specific interaction is referred to as *chiral recognition* mechanisms. They are typically studied statically using various static spectroscopic techniques combined with theoretical modeling, such as fluorescence or infrared spectra, in order to determine the structures and the bindings during chemical reactions between different enantiomers [Zehnacker 08, Scuderi 11] (see for instance Fig. 1.5). The structures are then obtained with different combinations of enantiomers, and the chiral selection mechanisms are deduced. The effects can be very diverse depending on the

molecules involved [Berthod 06], and constitute a wide field of exploration. For instance, $\pi$-$\pi$ interaction can be a chiral selector in $\pi$-complexes, while Coulomb or ion-dipole interaction typically play this role in ligand exchange. Natural chiral selectors can be, for example in polysaccharides, hydrogen bonds, dipolar interaction or steric hindrance. These interactions can typically lead to chirosensitive reaction mechanisms with an asymmetric configuration of multiple binding sites, a key-and-lock association or for instance the insertion into a helical structure.

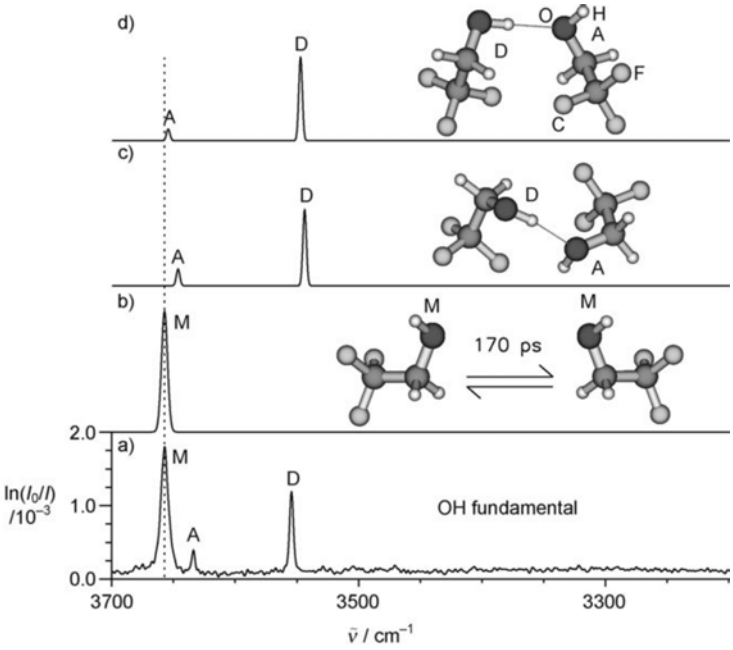


**Figure 1.5** – *(a) Experimental Fourier-transform infrared (FTIR) spectrum of the OH stretching frequency in hydrogen-bonded Trifluoroethanol dimers. (b-d) Simulated spectra of the monomer (M), hydrogen bound donor (D) and acceptor (A), for different bonding geometries. Reproduced from [Zehnacker 08], adapted from [Scharge 07].*

Yet, these studies remain static and rely mostly on structural informations. In this context, the perspective to directly access the temporal dynamics of chirosensitive processes is of high interest. Can we use time-resolved spectroscopy to experimentally resolve the reaction mechanisms and obtain the interaction types and ranges? Can we track the evolution of molecular chirality upon chemical reaction?

The timescale at which such dynamics occur sets a strong constraint on the techniques at our disposal. In other words, how can we investigate molecular chirality at its natural timescale, which is orders of magnitude faster than what any detector can reach?

## II Ultrafast Dynamics and Observable

**Timescale**

We will here briefly discuss the tools used for time-resolved investigations of dynamics. A historical timeline of time-resolved Physics is proposed in Fig. 1.6. The foundation of this field is attributed to Eadweard Muybridge, who decomposed in 1878 the motion of a running horse in

several photographs using a mechanical shutter. By doing so, he demonstrated that a galloping horse does not always have a hoof in contact with the ground. This was the first time something too fast for the naked eye was resolved, in this case of the order of milliseconds. Going further in the timescales, stroboscopes can be used down to microsecond processes. At this stage, the development of electronics took the lead, and has nowadays a $\sim$ 100 ps resolution.

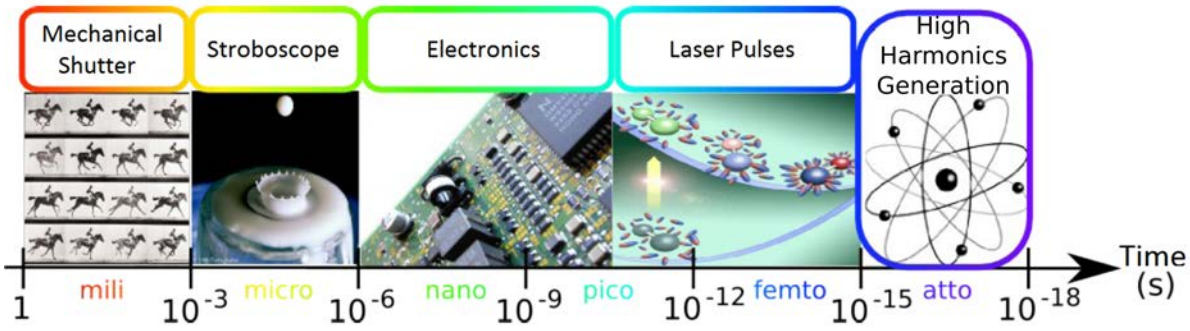


**Figure 1.6** – *Timescales at which different dynamics occur, and typical technologies able to resolve them.*

Nevertheless, the molecular dynamics we are interested in occurs at a much faster level. Molecular rotation happens in the picosecond timescale, vibration at the dozens of femtoseconds timescale and electron motion in few femtoseconds or hundreds of attoseconds ranges. An incredibly useful tool that has revolutionized the time-resolved studies of such dynamics is pulsed laser. Similarly to the exposure time of a camera, or the duration of a stroboscope flash, the duration of the laser pulse determines the thickness of the slices of time that can be resolved. Pulsed lasers are a whole field of Physics by themselves and are beyond the scope of this manuscript. Let us simply mention that such pulses can be obtained by phase-locking the modes of a laser cavity, which periodically add up constructively. Since the early 2000s', lasers able to deliver $\sim$ 30 fs-long light pulses have become widely available. The short pulse duration comes along with a breakthrough in the peak intensities the laser field can reach, while maintaining the average power manageable. In particular, this became possible thanks to the chirped pulse amplification (CPA) technique, initiated in the 1980s', and honored by the Nobel prize of Physics in 2018. Since then, more advanced technologies, which will be mentioned in this thesis, enable the generation of few-femtosecond pulses in the visible range (postcompression), or sub-femtosecond, down to dozens of attoseconds in the XUV range (high-order harmonic generation). At this level, the wavelength becomes a limitation, since at least a few optical cycles (2.7 fs at 800 nm) are necessary to define an optical pulse. Even if such short pulses are available, they can not be used like a stroboscope, and the question of the observables that can carry the information becomes central.

**Observable : Light or Matter**

Since in any case, no detection device can have a sub-100 fs resolution, the observation of ultrafast dynamics can not be direct. Instead, a scheme commonly used is pump-probe experiment, in which two laser shots are employed. The first one (pump) initiates a molecular

dynamics, while the second one (probe) probes the state of the system at a variable ulterior delay. By repeating the measurement several times with a varying delay, the temporal evolution can be reconstructed. This delay can be finely tuned by changing the relative optical path of the two pulses. The only limitation of the temporal resolution is thus the pulse duration. This paved the way to the resolution of molecular processes at the femtosecond timescale, namely femtochemistry, that was awarded with the Nobel prize of Chemistry of Ahmed Zewail, in 1999. We will see in this manuscript that other spectroscopic techniques can provide sub-optical cycle resolution without the need of a pump-probe configuration.

Two types of observables can be used : light or matter. In the first case, the absorption or the emission of photons can be used to probe the system at a given delay. In the context of chirality we are interested in here, this can for instance arise as circular absorption dichroism. However, pump-probe experiments typically require an additional order of magnitude of sensitivity compared to the static case. As mentioned previously, most of the chiroptical processes are already weak, requiring liquid-phase samples involving interaction between molecules and with a solvent. Even if this scheme is challenging, it is worth mentioning that the first experimental demonstration of time-resolved absorption circular dichroism was very recently published [Oppermann 19]. Other fully optical techniques will be mentioned along this document.

Conversely, the information can be accessed by detecting particles, in particular if the chiral molecules get ionized. This thesis will dwell on photoelectron/photoion spectroscopy produced by multiphoton ionization or tunnel ionization. We will see that the chirosensitive information can be encoded specifically in the photoelectron distributions with a very high sensitivity, as presented in the next paragraph.

## III Photoelectron Circular Dichroism

**Effect and Interpretation**

Photoelectron circular dichroism (PECD) is a forward/backward asymmetry in the photoelectron angular distribution along the laser propagation axis, that arises when a chiral molecule is ionized by a circularly polarized electromagnetic field. This asymmetry reverses with the light helicity or the enantiomer handedness. Conversely to asymmetries that can be observed in oriented or aligned molecules, namely where the medium is anisotropic, PECD takes place for a sample of randomly aligned chiral molecules, and is thus experimentally simple to access. Unlike other chiroptical processes, this one is described under the electric dipole approximation, and is thus much greater, up to dozens of percents of the total signal. With such an amplitude, this effect can be used to study chiral molecules in the gas phase, where the systems are free from solvatation effects. Higher electromagnetic orders, such as electric quadrupolar and magnetic dipolar effects, can also induce asymmetries in the photoelectron angular distributions [Hemmers 04]. However, these phenomena are not inevitably related with the chirality of the sample. They do not necessarily reverse with the light helicity and can arise with achiral targets. In any case, they remain weak compared to the PECD we are interested in, at least in the dipole-allowed transitions we will investigate in this manuscript.

The information about the chirality is encoded angularly here, but where does it come from? When ionized, the photoelectrons scatter into the (chiral) molecular potential under the influence of the (chiral) circularly polarized field. The scattering process is very sensitive to this potential in general, but for symmetry reasons, the interplay of the asymmetry of the potential with the asymmetry of the field will arise as an asymmetry in the final photoelectron distribution. Note that with a linearly polarized or unpolarized field or an achiral target, such distributions are necessarily forward/backward symmetric. This observable thus isolates specifically the chiral part of the interaction. We will see that this provides a very high sensitivity to molecular properties.

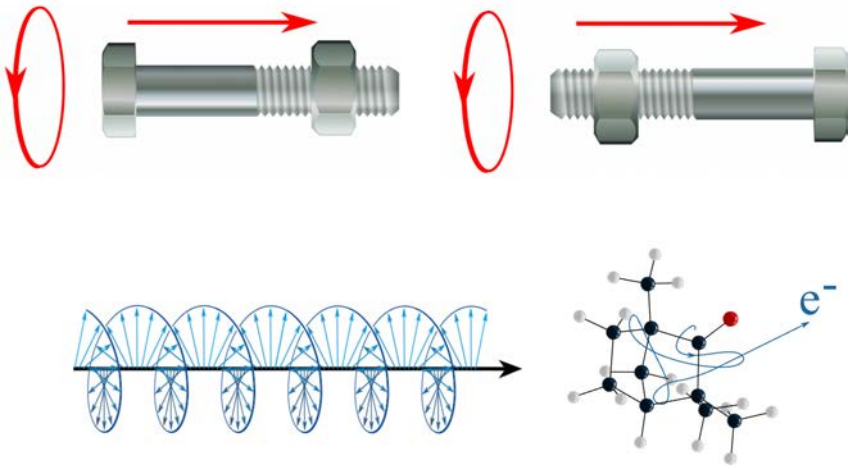


**Figure 1.7** – *Schematized interpretation of the photoelectron circular dichroism. In this parallel, the rotation is imposed by the electric field, the nut is the electron and the bolt is the molecule (or the molecular potential). The effect reverses only if one reverses the rotation (the field helicity), or the threads (the enantiomer).*

The physics underlying this effect will be extensively discussed in this manuscript. A schematized interpretation, introduced by Ivan Powis [Powis 08], is illustrated in Fig. 1.7. When ones rotates a nut on a bolt, the threads convert a rotational motion into a translational motion. Remarkably, for a given rotation and a given handedness of the threads, the nut will always go the same direction, regardless of the orientation of the bolt. In this parallel, the rotation is imposed by the electric field, the nut is the electron and the bolt is the molecule (or the molecular potential). The effect reverses only if one reverses the rotation (the field helicity), or the threads (the enantiomer). Of course, this is just an image. The molecule does not have to be helically-shaped for PECD to take place, and the photoelectrons are not always, but simply preferentially in average ($< 30\%$), ejected forward or backward along the laser propagation axis.

**Single-Photon Ionization**

PECD was first theoretically predicted in 1976 [Ritchie 76], but only more recently accurately modeled in 2000 [Powis 00] and experimentally demonstrated in 2001 [Böwering 01]. In the following decade, many interesting properties were demonstrated in the one-photon ionization regime. Most of the organic molecules have an ionization potential of the order of 10 eV, and XUV photons are thus used to ionize. In this case, the PECD has a simple angular struc-

ture, as shown in Fig. 1.8 (1) in Camphor ionized at $\hbar\omega = 10.3$ eV. Obtained by subtracting the photoelectron angular distributions measured with left circular polarization and right circular polarization (1-b), it clearly appears as a forward/backward asymmetry along the laser propagation axis (vertical here), and reverses with the enantiomer handedness (1-c). Since its angular structure is simple, the PAD and PECD are often represented as angularly-integrated quantities, where the radius is the photoelectron kinetic energy, as depicted in Fig. 1.8 (2). Importantly, single-photon PECD is known to be remarkably sensitive to the whole dynamics of the photoionization process, and strongly depends on several factors :

(i) Ionized orbital : The initial orbital from which the electron is emitted plays an important role [Turchini 04, Nahon 06]. For instance in Fig. 1.8 reproduced from [Nahon 06], the photoelectron kinetic energy spectrum of Camphor can be split into four regions (labeled I-IV in panel (2)). These regions can be assigned to different ionized orbitals. In particular, the regions I and II can be associated respectively with the HOMO and HOMO-1. Fig. 1.8 (3) shows the PECD as a function of the photon energy for the different regions. It appears clear, in particular, that the sign of the PECD from the HOMO and HOMO-1 has an opposite sign. The calculated electron densities obtained with two types of calculations is depicted in panel (4) for comparison, and are clearly not localized at the same part of the molecule. Interestingly, one-photon ionization from inner-shell, atomic-like spherically symmetric orbitals still shows a significant PECD [Hergenhahn 04]. This means that the ionized photoelectron is not only sensitive to the localization of its initial density : it explores the molecular potential before being ejected, and is thus sensitive to its global chirality.

(ii) Molecular structure : For this reason, single-photon PECD is very sensitive to the whole structure of the ionized molecule. For instance, [Nahon 16] compares (+)-Camphor and (-)-Fenchone, two similarly-structured isomers with the same asymmetric carbon configuration, *i.e.* the same chiral skeleton (see Fig. 1.9 (a)). The only difference between the two compounds is the substitution of two methyl groups that are not bonded to asymmetric carbons. While the photoelectron spectrum is relatively similar for the two molecules (panel (b), where only an offset can be noted), their PECD has an opposite sign (Fig. 1.9 (c)). Note that the HOMO from which the ionization is performed here is not even mainly located on the substituted groups (Fig. 1.8 (4)) and are very similar to each other. This underlines even more the sensitivity of PECD to the global molecular structure.

The substitution- and orbital-dependency of PECD has also been demonstrated [Stener 04]. An example of this property, adapted from [Garcia 04], comparing (-)-Methyloxirane and (+)-Trifluoromethyloxirane is depicted respectively in Fig. 1.9 (d) and (e). The effect is even more spectacular here, as these two molecules only differ by the substitution of terminal hydrogen atoms by fluorine. In particular, the PECD from the HOMO is drastically affected, even if its density is completely away from the substituted group.

Because of this effect, single-photon PECD is furthermore sensitive to the conformational geometry of the chiral target [Turchini 09, Turchini 13]. For instance in Fig. 1.10 adapted from [Turchini 13], the experimental PECD (right) of the two dominating conformations (left) has been shown to have opposite signs. Despite being an interesting property, this can significantly complicate the observation of PECD in samples at room temperature. In addition, this con-

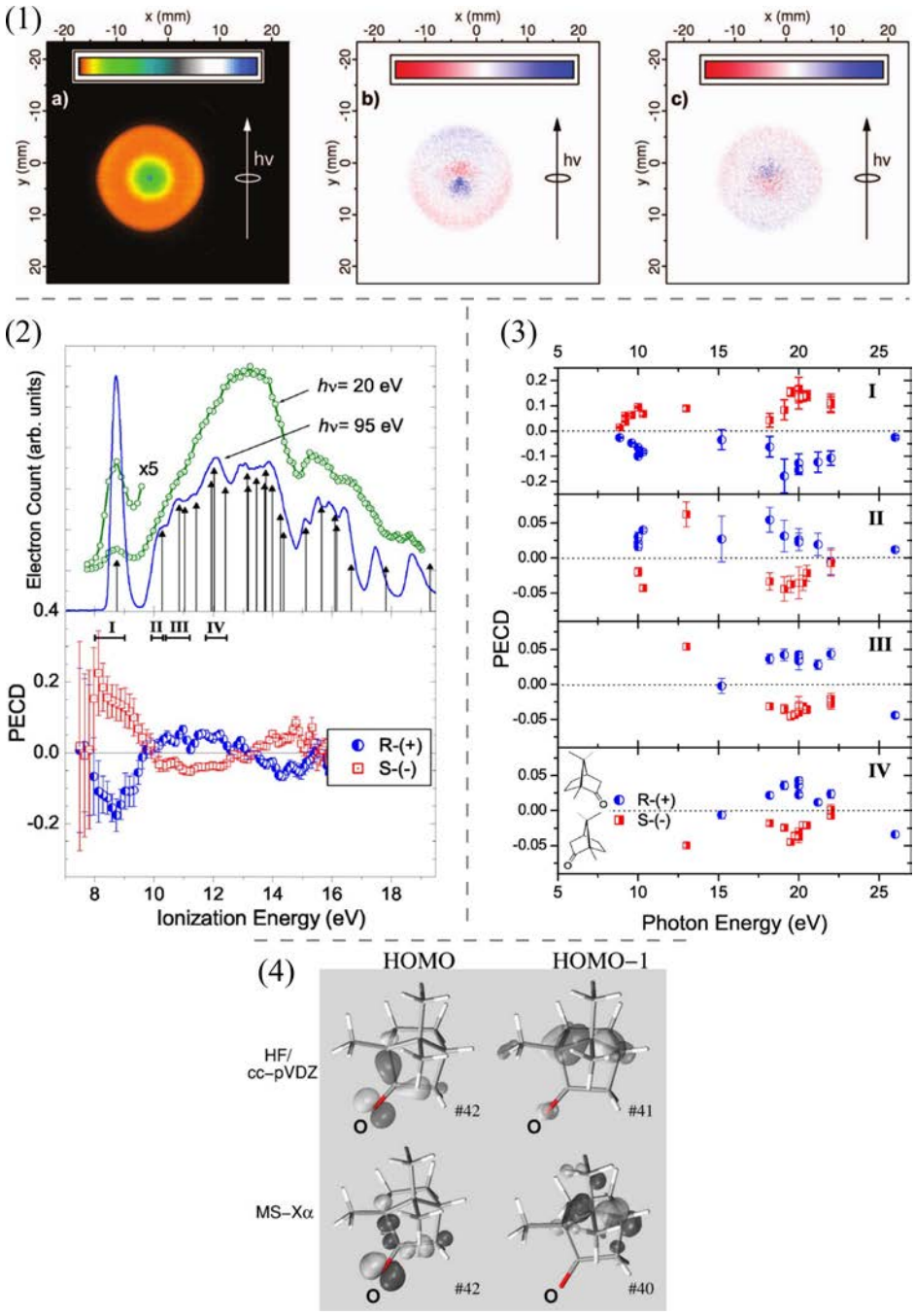


**Figure 1.8** – *(1) (a) Raw photoelectron angular distribution (PAD) produced in one-photon ionization of Camphor at $\hbar\omega = 10.3$ eV. (b) Corresponding subtraction between the signals obtained with left circular polarization and right circular polarization, in the (+) enantiomer. The PECD clearly appears as a forward/backward asymmetry along the laser propagation axis. (c) Same as (b) in the (-) enantiomer. The asymmetry clearly reverses. (2) Angularly-integrated photoelectron spectrum (PES) and PECD as a function of the photoelectron kinetic energy in Camphor. (Top) PES obtained at $\hbar\omega = 95$ eV (blue line), compared to a reference at 20 eV (green line). (Bottom) Corresponding PECD measured for the two enantiomers. The spectrum can be cut into four regions, assigned to different orbitals ionized. (3) PECD of the four labeled regions as a function of the photon energy. Region I is assigned to the ionization from the HOMO, region II to the HOMO-1 and region III to the HOMO-2 and HOMO-3. (4) Electron density of the HOMO and HOMO-1 obtained using two types of calculation. Reproduced from [Nahon 06].*

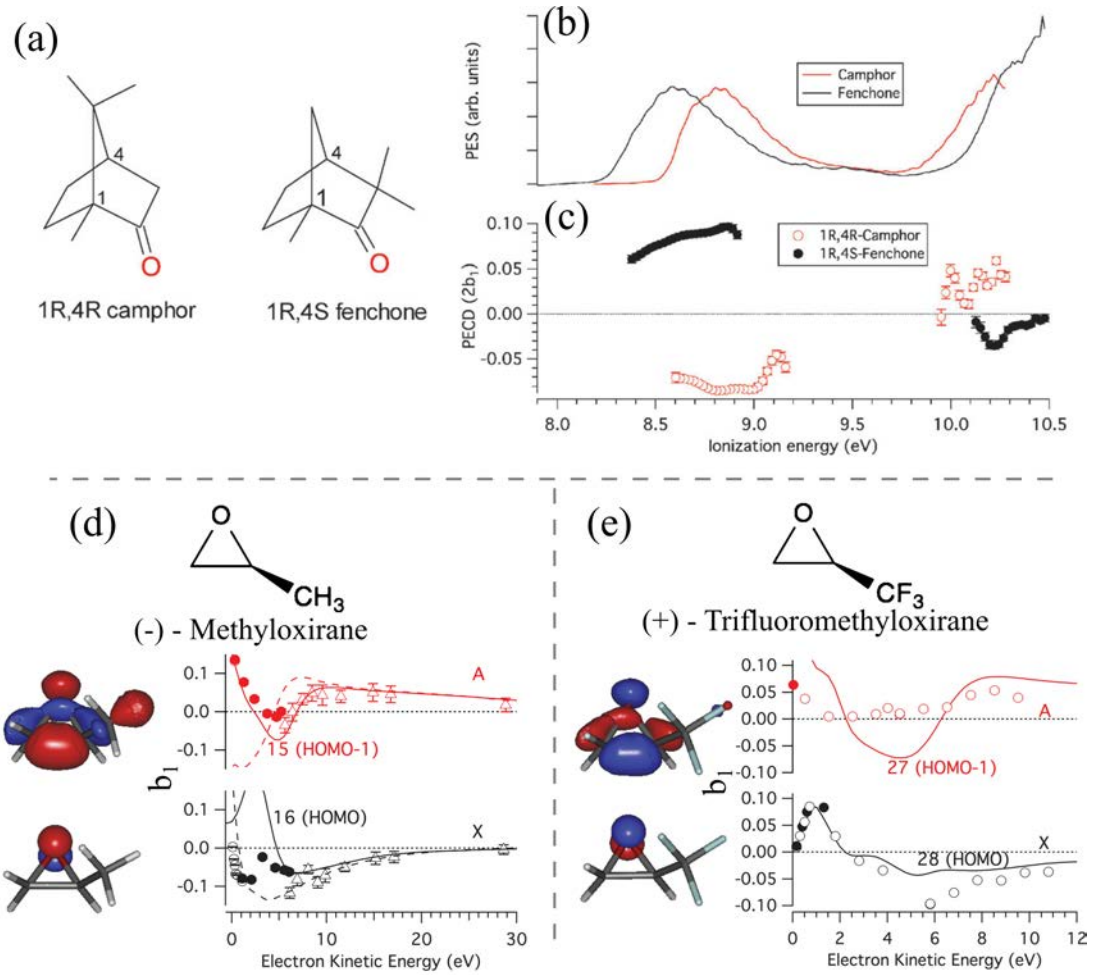


**Figure 1.9** – *(a) Structure of (+)-Camphor and (-)-Fenchone, two similarly-structured isomers with the same asymmetric carbon configuration (labeled 1 and 4 here). (b) PES of Camphor and Fenchone, recorded respectively at $\hbar\omega = 10.3$ eV and 10.5 eV. (c) Corresponding measurement of the PECD of (+)-Camphor and (-)-Fenchone. Adapted from [Nahon 16]. (d) Structure, densities of the HOMO and HOMO-1 and associated PECD of (-)-Methyloxirane. The datapoints are indicated with the circles and the lines correspond to calculations. (e) Same as (d) with (+)-Trifluoromethyloxirane. Adapted from [Garcia 14].*

stitutes a major additional computational cost for quantitative calculations of PECD. The use of constrained structures, such as the bicyclic ketones previously mentioned, can remove this parameter.

(iii) Kinetic energy : PECD is also a function of the kinetic energy with which the photoelectron is ejected. Electrons emitted from the same orbital and differing only by a few eV can show opposite dichroic signals [Powis 08]. Futhermore, PECD tends to vanish at high photoelectron kinetic energy (above a few dozens of eV). This can be understood as the electrons escape the molecular potential too quickly to be imprinted with its chirality. Note that PECD can be recovered at high kinetic energies in particular cases, for instance involving an autoionizing state at severals hundreds of eV [Hartmann 19]. The influence of the photoelectron kinetic energy on PECD can be decoupled from other effects and properly identified as in [Ganjitabar 20].

(iv) Vibrational excitation : The Born-Oppenheimer approximation consists in the factor-

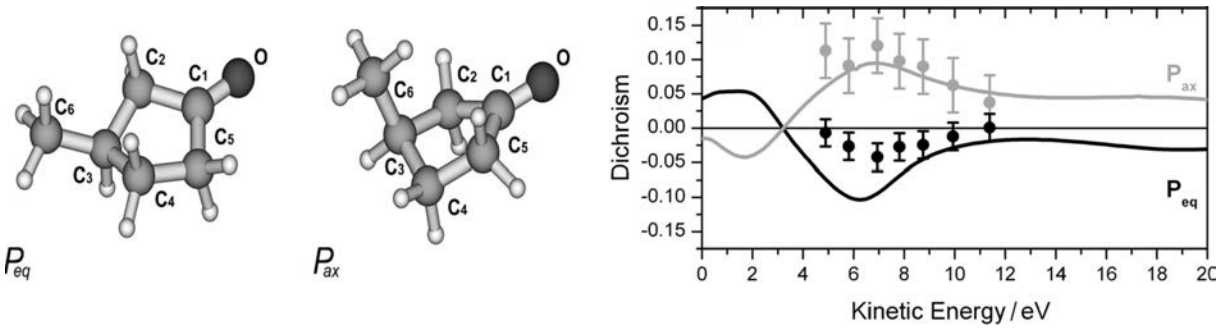


**Figure 1.10** – *(Left) Calculated structure of the two conformers $P_{eq}$ and $P_{ax}$ of the (+)-3-Methylcyclopentanone. (Right) Experimental dichroism $D_{eq}$ (black dots) and $D_{ax}$ (grey dots) for the HOMO state, together with the theoretical dispersions for $P_{eq}$ and $P_{ax}$ (black and grey solid curves, respectively). Adapted from [Turchini 13].*

ization of the molecular wavefunction into an electronic and a nuclear part. It is justified by the fact that the nuclei are much heavier than the electrons, in such a way that the dynamics of the nuclei is effectively frozen at the timescale of the electronic motion. The electronic part thus only depends parametrically on the nuclear geometry. Furthermore, under the Franck-Condon approximation, the electronic transition matrix elements are assumed to vary negligibly with the nuclear coordinate. In other words, it does not depend on the nuclear geometry sampled during vibrational motion. As a result, the electronic and nuclear motions are effectively decoupled. Since this approximation is widely used in molecular physics, one might expect PECD, which results from an electronic transition, to be insensitive to the vibrational dynamics.

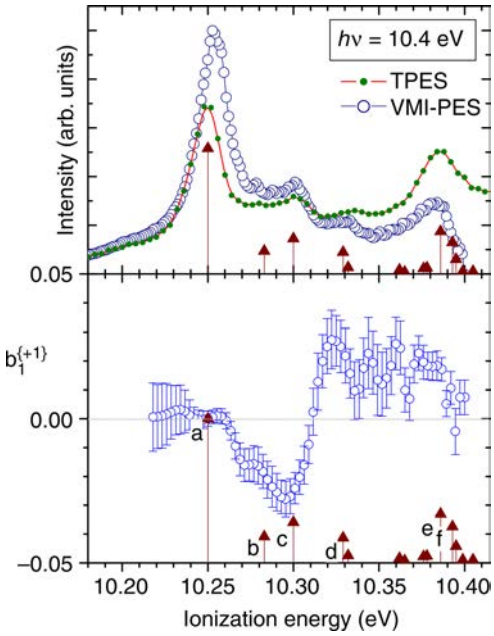


**Figure 1.11** – *(Top) PES associated with the HOMO of (-)-Methyloxirane measured at $\hbar\omega$ = 10.4 eV. The red arrows correspond to the calculated vibrational spectrum. (Bottom) Corresponding PECD. Adapted from [Garcia 13].*

However, it has been shown that PECD was actually sensitive to the vibrational excitation [Garcia 13, Powis 14], as shown in Fig. 1.11 adapted from [Garcia 13]. The PES associated with

the ionization from the HOMO of (-)-Methyloxirane at $\hbar\omega = 10.4$ eV is shown in the top panel. The calculated vibrational spectrum is indicated by the red vertical arrows. The bottom panel presents the corresponding PECD. It appears that a sign change of the dichroism associated with two consecutive vibrational states can be observed. This property was later observed in other chiral compounds [Ganjitabar 18, Ganjitabar 20].

This is a clear breakdown of the Franck-Condon approximation. It is remarkable since the effect is general. In particular, shape resonances, which can typically break this approximation [Piancastelli 99], are not involved here. This shows again an interesting sensitivity of PECD.

(v) Molecular orientation : PECD is generally measured in samples of randomly oriented molecules. The nut/bolt analogy qualitatively explains how it can survive molecular orientation averaging. However, PECD is of course expected to depend on molecular orientation. More generally, the photoelectron angular distribution obtained for instance with aligned diatomic (achiral) molecules molecules are known to be anisotropic, as shown in Fig. 1.12 (1-a) and (1-b), adapted from [Tia 17]. However, they still conserve a mirror symmetry corresponding to the polarization plane. Effects of circular dichroism in oriented achiral samples [Westphal 89] or in their molecular frame [Dowek 07] are indeed well-known. The corresponding asymmetries maximize in the light polarization plane, and are then different from circular dichroism in randomly aligned chiral molecules. The two effects can thus be combined. In the case of an oriented chiral molecule, the target has lost any symmetry, in such a way that the distribution also has no symmetry anymore (1-c). The inversion of the field helicity does not even reverse the distribution, but globally modifies it (1-d). The experimental measurement of the evolution of PECD as a function of the molecular alignment is show in panel (2), for the two enantiomers of Methyloxirane. It appears clear here that the PECD reverses with the enantiomer, greatly evolves with the molecular alignment, and can even change sign. The randomly-aligned PECD is simply what survives the summation over all the molecular orientations. This simple observable has thus a good sensitivity to anisotropies of the sample.

Single-photon PECD is thus a powerful probe of many aspects of molecular chirality, and is still of high interest nowadays for fundamental and analytical purposes. In addition to this, such process can occur naturally in interstellar environment, and has astrophysical implications [Hadidi 18]. Indeed, partially circularly polarized radiation can be found in the interstellar merdium (particularly at the Lyman $\alpha$ radiation) and could induce a chiral bias, which might be at the origin of the homochirality of life. This hypothesis is supported by the observation of enantiomer-enriched amino acids in carbonaceous meteorites.

The XUV photons required to ionize the systems are most of the time obtained from a synchrotron source. It has great advantages, among others high flux, high stability, full wavelength tunability, polarization tunability, and a very high repetition rate, up to hundreds of MHz. However, it not always suited for time-resolved experiments since their pulse duration is typically of tens of picoseconds. Alternatively, particular schemes of high-order harmonics generation can yield attosecond pulses of circularly polarized XUV photons [Ferré 15b], as will be discussed later. Nevertheless in any case, a simple single-photon ionization scheme does not allow for pump-probe experiments.

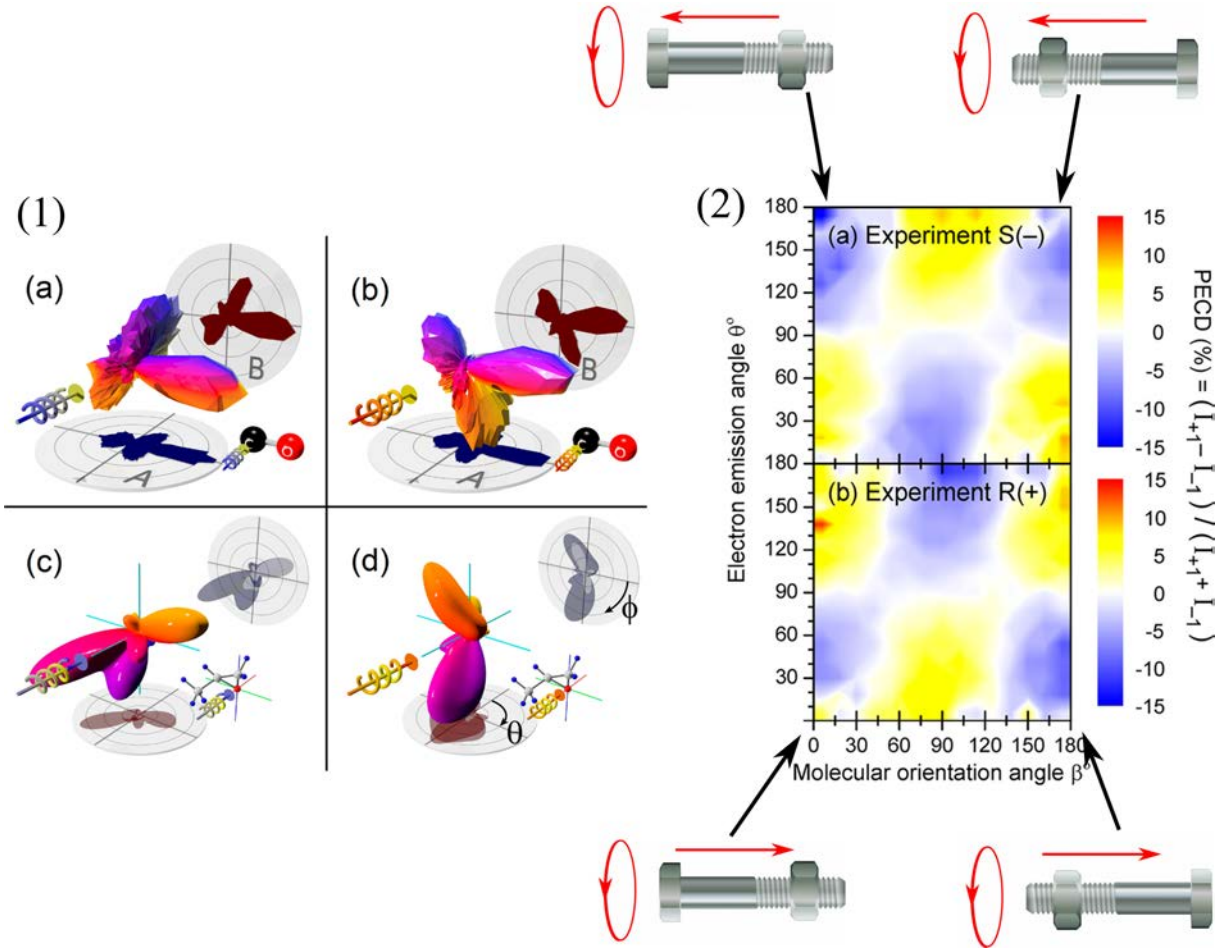


**Figure 1.12** – *(1) 3D molecular frame photoelectron angular distributions from (a-b) the C 1s-electrons emitted from CO for left (a) and right (b) circularly polarized light. (c-d) Theoretical distributions computed here for the O 1s-ionization of (+)-Methyloxirane by left (c) and right (d) circularly polarized light. The molecules are oriented as depicted in the insets. (2) PECD as a function of the photoelectron emission angle $\theta$ and the molecular orientation angle $\beta$ after O 1s-photoionization of (-) (a) and (+) (b) Methyloxirane. Adapted from [Tia 17]. The two situations where the molecule is aligned along the field propagation axis are depicted with the nut and bolt parallel.*

We will see how changing the interaction regime can provide a new angle of vision into molecular chirality. It has been demonstrated in the 2010s' that PECD could also take place in other ionization regimes. How does replacing the ionizing XUV radiation by an intense ultrashort infrared or visible laser pulse affect the PECD? As we will see, one-photon PECD has a simple angular structure, where the information is only encoded in the forward/backward asymmetry. By increasing the number of photons absorbed, the photoelectron angular distribution gets sharper along the polarization of the field, and PECD can become much more structured. Can we use these structures to enhance the sensitivity of the observable and gain a new insight into chiral molecular processes?

**Multiphoton Ionization**

The pioneering works of the Kassel [Lux 12] and the Amsterdam/Nottingham groups [Lehmann 13] in the early 2010s' established the existence of multiphoton-PECD. Using three-

photon absorption of circularly polarized 400 nm femtosecond laser pulses to ionize chiral molecules, they observed strong forward/backward asymmetries, as shown in Fig. 1.13

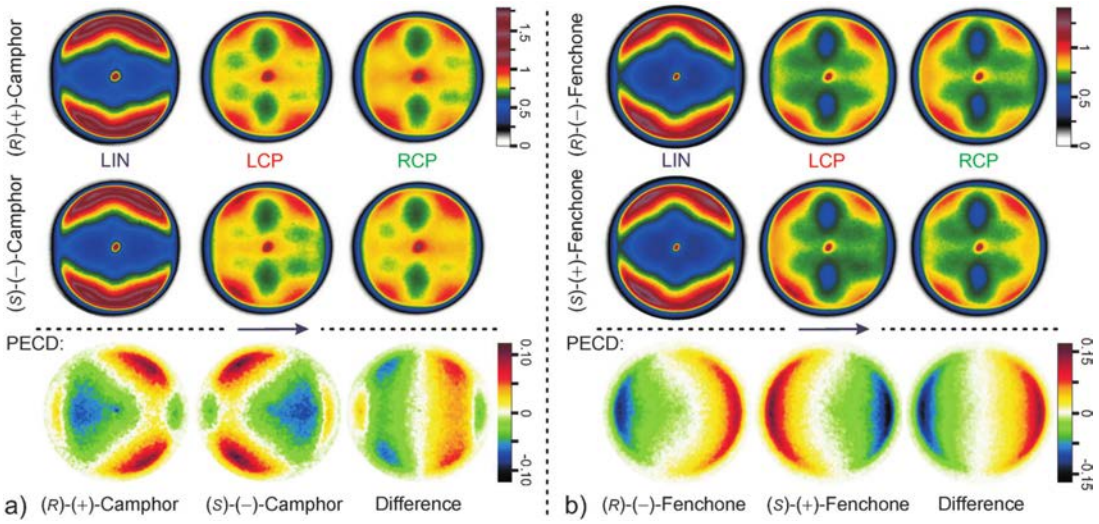


**Figure 1.13** – *(Top rows) Photoelectron angular distributions measured in the 3-photon ionization of the two enantiomers of Camphor (a) and Fenchone (b) at 400 nm, for linear (LIN), left circular polarization (LCP) and right circular polarization (RCP). (Bottom row) PECD signal obtained with the two enantiomers and their subtraction. Reproduced from [Lux 12].*

Since then, most of the single-photon properties presented above were also extended to this regime. Essentially, the sensitivity of multiphoton PECD to the molecular structure [Lux 12, Lux 15] the orbital ionized [Rafiee Fanood 14] and the excited vibrational state [Beaulieu 16a] is also established. In addition, intermediate excited states can be reached during a multiphoton ionization process. PECD can be very sensitive to them [Beaulieu 16a, Kastner 17], and constitutes an additional sensitivity to molecular chiraly. These characteristics will be presented more thoroughly in the introduction of Section 3.I.

While PECD occurs for randomly aligned samples, the creation of a wavepacket by a laser field can break the isotropy of the excited medium. Does it have consequences in multiphoton PECD? Conversely, can PECD be used to access such anisotropy of excitation? We will see that this complexification of the light-matter interaction will be encoded in particular in the angular structures of the photoelectron distributions. Since PECD is enantiomer-specific, it has already been used for analytical purposes, in particular to determine the enantiomeric excess of samples [Rafiee Fanood 15, Kastner 16, Miles 17]. Can we use the additional sensitivity that the anisotropy of excitation could bring to enhance the accuracy of the technique?

On the other hand, one might think that by being sensitive to too many parameters, multiphoton PECD can end up being unusable. Indeed, interpretation of experimental results can be challenging, and as will be presented, theoretical support can be of great importance.

Finally, resonance-enhanced multiphoton ionization (REMPI) processes present a massive advantage : the excitation and the ionization from the excited states can be decoupled. The use of pump-probe scheme with ultrashort laser pulses enables one to access the dynamics at the molecular timescale. While this type of scheme has already been used to resolve chiral dynamics at the hundreds of femtoseconds timescale [Comby 16], the characteristics of PECD at a shorter

scale remains unexplored. Can we access chiral molecular dynamics in the femtosecond range, which is the timescale of the electronic and vibrational processes? Can the sensitivities of PECD be used to have an additional insight into these dynamics, compared to achiral photoelectron spectroscopy?

These questions will be addressed in Chapter 3.

**Strong Field Ionization**

Ionization can also be performed beyond the perturbative regimes discussed so far, by using higher laser intensities and longer wavelengths. One can expect that increasing the number of photons absorbed will even further complicate the interaction. Paradoxically, it turns out that the latter is actually simplified. In strong field conditions, the electric potential of the laser indeed dominates the molecular potential, and the photoionization can be described semi-classically without paying so much attention to the exact molecular structure. This description and its wide consequences will be discussed in the introduction of Section 4.I.

This might seem like a bad omen for the investigation of molecular chiraly with PECD. If the molecular potential is dominated, can it still be imprinted to the photoelectrons? It has been shown that PECD still takes place in the strong field ionization regime [Beaulieu 16a], as shown in Fig. 1.14. It is weaker, in the few percents range, but still remains much greater than many other chiroptical processes. Can the simplification of the description of photoionization be used in order to get a simple picture of the scattering process? Strong field physics is known to be very sensitive to the vectorial properties of the field applied, since this latter dominates. This domain has been recently of high interest for the resolution of dynamical processes at an unprecedented timescale, namely at the sub-optical cycle scale. Can these achievements be extended to chirality and in particular, is PECD defined at such a timescale? In other words, for how long should light be circular to produce a PECD? Chapter 4 will tackle these questions.

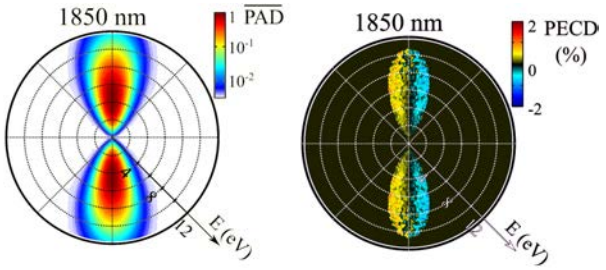


**Figure 1.14** – *Photoelectron angular distribution (left) and corresponding PECD (right) obtained in strong field ionization of (+)-Fenchone with 1850 nm pulses at $I \sim 4 \times 10^{13}$ $W.cm^{-2}$. Extracted from [Beaulieu 16a].*

## IV COLTRIMS or Reaction Microscope

In order to collect the photoelectron produced by the photoionization of chiral molecules in the gas phase by ultrashort laser pulses, a particle detection device is required. In particular, it has to resolve the angular dependence of such distributions to access PECD, our observable of choice. Our group in CELIA has been using a velocity map imaging (VMI) spectrometer since

2013, presented in Section 2.II, which can either detect photoions or photoelectrons. In this latter case, 2D projections of the photoelectron momentum distributions can be measured. One dimension resolved being the laser propagation axis, PECD can be accessed. The VMI is a relatively simple apparatus, and a significant part of the results obtained during this thesis were obtained with it.

However, while the photoelectron spectra tend to be relatively simple for atomic targets, their complexity dramatically increases in large molecular systems. Indeed, many ionization channels can overlap, and since PECD is highly sensitive to many parameters, their relative contributions can be hard to disentangle in the final distributions. In order to overcome this limitation, the construction and characterization of a new spectrometer, a COLTRIMS (or reaction microscope), was decided and constituted a significant part of this thesis. Such a device is capable of measuring both the photoelectrons and photoions distributions in coincidence, meaning that each photoelectron is associated with its photoion counterpart. Furthermore, the distributions are measured directly in 3D. A thorough presentation of the device is proposed in Section 2.III.

**Range of Applications**

The knowledge of both the photoelectron and photoion momenta, or kinetic energies, enables one to fully reconstruct photoionization processes. This capacity makes such a spectrometer extremely powerful and used in a broad range of studies, ranging way beyond the scope of this thesis. To give a few examples, multiple fragmentation pathways can be disentangled by monitoring the fragment-dependent photoelectron spectra, for instance from Auger photoemission subsequent to core excitation with high energy photons [Miron 08]. Since several photoelectrons can be detected, this tool is also particularly suited for the study of electron-electron correlation [Zhang 14b]. Interestingly, since the vectorial recoil of the ions acquired during photofragmentation processes can be measured, the orientation or alignment of the molecule at the moment of ionization can be obtained in small systems. As a result, the photoelectron angular distribution can be retrieved in the molecular frame [Dowek 09, Billaud 12, Menssen 16] (see Fig. 1.15 (a)). The access to the ion recoil can also be used in Coulomb explosion imaging, which consists in performing multiple ionization leading to an explosion of the molecule because of the Coulomb repulsion. This can be for instance used to retrieve the molecular orientation [Jahnke 04], or the absolute configuration of a chiral molecule [Pitzer 13], which is not a trivial task. Other strong field processes can also be studied with this device. Laser-induced electron diffraction (consisting in ionizing an electron and scatter it back on the ionic core within an optical cycle) can, for instance, provide structural information about the molecular skeleton and orbitals [Meckel 08] (see Fig. 1.15 (b)). COLTRIMS are thus tools of choice to investigate matter at the molecular scale, and are sometimes called Reaction Microscopes.

Pump-probe schemes can of course be applied to investigate dynamical evolutions [Sturm 17]. Temporal resolution can alternatively be retrieved from static measurements thanks to their high level of completeness. Typically, the fragmentation coordinate of a dissociative state can be encoded energetically if this state decays to a lower state whose potential energy surface is not parallel. As a result, the photoelectron kinetic energy can map the fragmentation coordi-

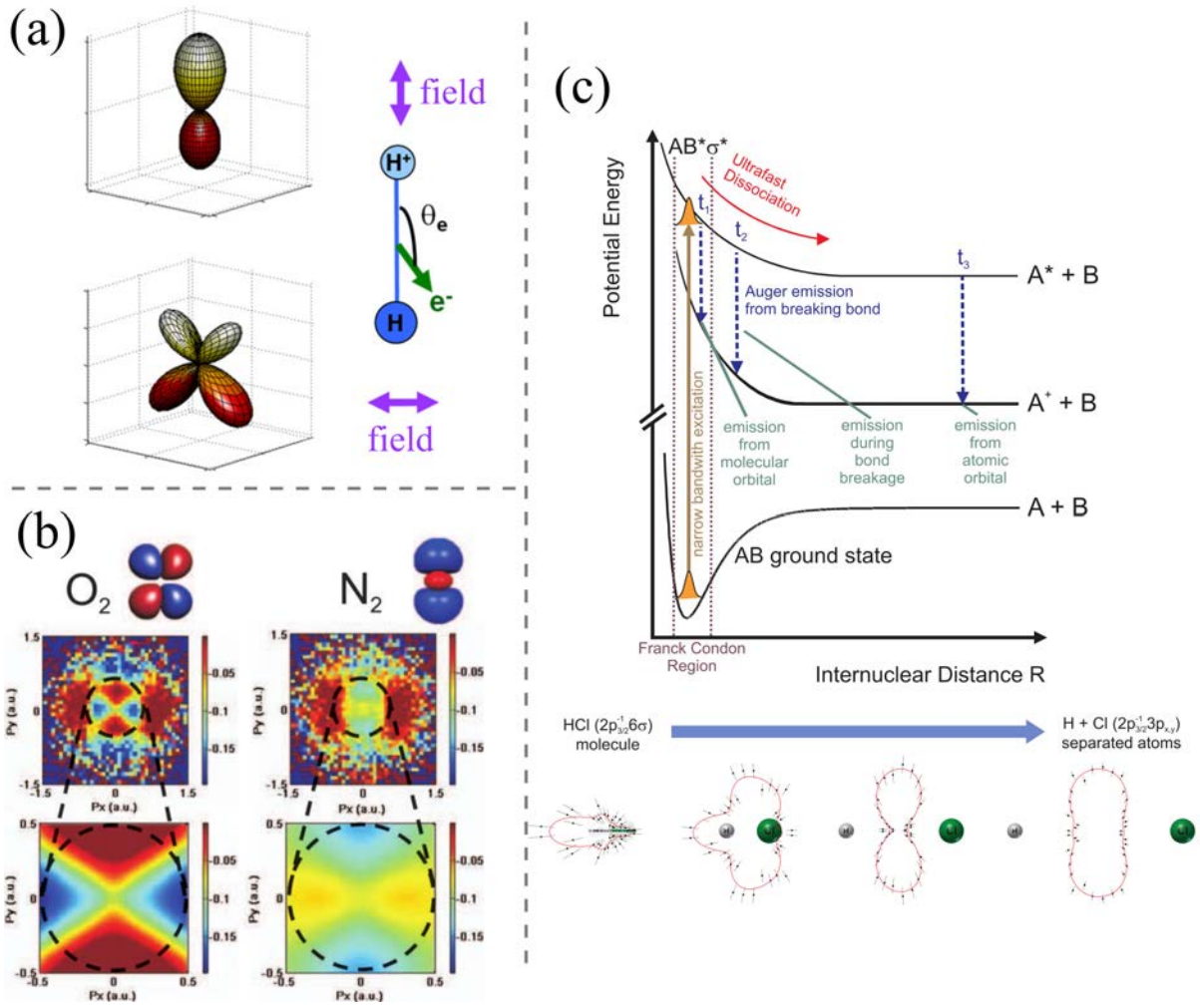


**Figure 1.15** – *(a) Examples of molecular-frame photoelectron angular distributions (MFPAD) measured in $H_2$. Adapted from [Billaud 12]. (b) Photoelectron holographic patterns obtained by laser-induced electron diffraction from $O_2$ and $N_2$, whose HOMO is depicted above. Reproduced from [Meckel 08]. (c) (Top) Sketch of the mapping between fragmentation coordinate and Auger photoelectron kinetic energy, during single-photon induced ultrafast dissociation. (Bottom) Corresponding measurement of the evolution of the molecular orbital during the fragmentation of HCl. Adapted from [Sann 16].*

nate, which is somehow equivalent to time. This has been used for instance to dynamically study interatomic Coulombic decay, which is the long-range energy transfer that can occur in loosely bound matter (Van der Waals or hydrogen bounded complexes) [Trinter 13]. Similarly employed with Auger decay, the spatial evolution of molecular orbitals during the ultrafast dissociation of HCl have been retrieved [Sann 16] (depicted in Fig. 1.15 (c)). Finally, temporal information can be encoded by the mapping between the vector potential at the ionization time with the final photoelectron momentum, which stands in the strong field regime. This has been used for instance to resolve the sub-optical cycle delays in nonsequential double ionization [Eckart 16].

Not all these types of studies can be carried out with a single spectrometer. In our case, we are particularly interested in resolving the asymmetries in the photoelectron angular

distributions, tagged with the corresponding ion or fragment mass. A few similar studies have also been performed in other teams, for instance in the single-photon [Garcia 14], multiphoton [Lehmann 13, Rafiee Fanood 14] or strong field ionization regimes [Fehre 19], but the surface of this growing field has only begun to be scratched.

**Challenges**

To associate the photoelectrons with their respective photoions, a strong limitation stands : at most one event must occur per light pulse. As a consequence, the light source must have a high enough repetition rate in order to have a good statistics in an reasonable time. For this reason, COLTRIMS have been primarily used with synchrotron sources. Despite being very powerful and versatile sources, their accessibility is often limited. In addition, their long pulse duration usually prevents pump-probe experiments, in such a way that the aforementioned more complex ways around are required to access dynamical informations.

The recent advances in high repetition rate laser sources is significantly extending the scope of the coincidence spectrometers. The development of a COLTRIMS, coupled to a new generation high repetition rate fiber laser system will be presented in Chapter 2. Such a table-top beamline not only allows for more routinely accessible coincidence measurements, it also brings the perspective of applying the tools of time-resolved pump-probe studies. New challenges in terms of source stability, implementation and temporal resolution will be addressed. The versatility of the beamline is of course a significant goal, in order to access the different interaction regimes at which PECD takes place. We will see how frequency conversion is used to perform studies in the multiphoton regime, tailored laser fields are employed for strong field interaction and high-order harmonic generation is implemented to obtain high-energy photons. We will also see that the new high-repetition rate beamline does not only enable for a fundamental breakthrough in coincidence detection, but also provides a unprecedented signal acquisition rate in more standard photoelectron detection, which can then be pushed to another level.

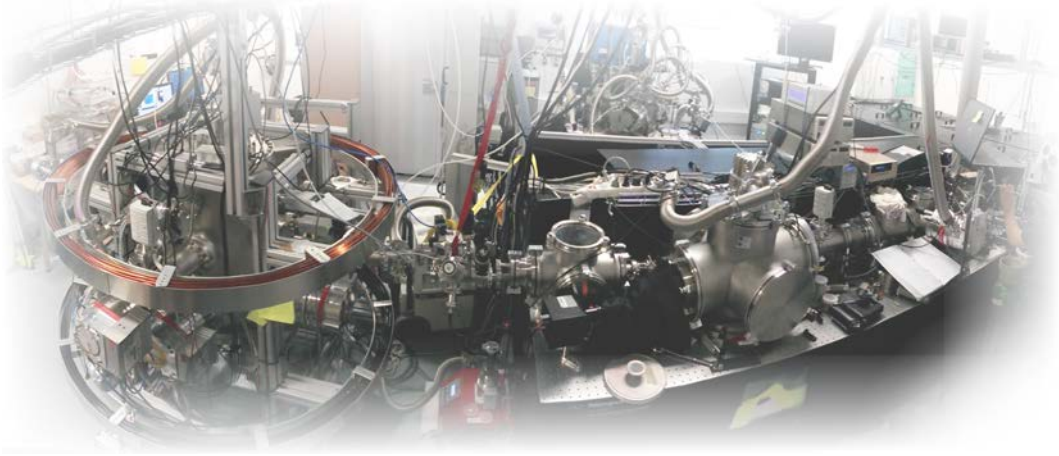

# Chapter 2

# Experimental Development

The development and implementation of experimental setups have been at the core of the presented thesis, such that about half of the timespan of my PhD was dedicated to it. This was motivated by the scientific challenges presented in the introduction chapter, and can be split into two major lines : the laser source and the detection apparatus. The first one started with the delivery of the new generation Yb-doped fiber laser system, a few month before the beginning of my project. Despite being a commercial system, its implementation in academic research was very recent, and a lot of effort has been put in adapting it for state-of-the-art experiment and make it as versatile as possible to study single-photon, multiphoton and strong field processes. Unless mentioned otherwise, I have been personally involved in the presented developments. The other end of the beamline was initially constituted of an XUV spectrometer, for high-order harmonic spectroscopy, and a Velocity Map Imaging spectrometer, that will be presented, for photoelectron studies. To go beyond the capacities of this apparatus, I have been in charge of building and implementing the photoelectron-photoion coincidence detection device, also discussed in this chapter.

These challenges are motivated by the broad range of physical processes we could access. They will be discussed throughout this manuscript, but we can already cite a few important ones. The high repetition rate table-top source not only delivers a high photon flux, providing cutting-edge signal-to-noise ratio, but also breaks through the fundamental limitations of the coincidence detection. The wavelength accordability is of high importance for the possibility of controlling the excitation scheme in resonance-enhanced multiphoton ionization. In particular, aiming or avoiding some resonances of interest, or being able to change the number of photons involved or the interaction regime is an interesting degree of freedom. The continuous wavelength tunability is also attractive to finely select and scan across the resonances. Broadly speaking, we are interested in resolving the ultrafast molecular processes by using the photoionization as an observable. Being able to use either a strong laser field or high energy photons, using high-order harmonic generation, is thus valuable. The information provided is not only contained in the photoelectron kinetic energy spectrum, but is also encoded in the angular distributions. In particular, the forward/backward asymmetry along the laser propagation axis, namely photoelectron circular dichroism, reveals the asymmetric interaction between circularly

polarized light and chiral molecules. One must thus have the adequate detection devices to resolve this information. In addition, the photoion mass spectrum completes the picture, for example by unraveling the associated fragmentations, and its detection in coincidence with the photoelectron angular distributions is a major step forward.

# I High-Repetition Rate Laser Beamline

## I. 1 Fiber Laser Source

Titanium-Sapphire (Ti:Sa) laser systems have become a reference in the generation of femtosecond pulses [Keller 03], in particular for ultrafast spectroscopy. Thanks to their large gain spectral range, they are able to deliver typically 20 fs pulses, around 800 nm, with nowadays energies of 30 J at a repetition rate of 0.01 Hz, or an average power up to 30 W at 1-10 kHz or 1 W at 100-250 kHz. This technology has been optimized for decades and has reached its inherent limitations, especially in terms of average power and repetition rate without damaging the crystal. This is mainly due to the short upper state lifetime and the large quantum defect of the Ti:Sa, requiring an intense pumping, typically from frequency-doubled Nd:YAG around 530 nm.

A more recent technology has been holding great promises to address this issue, by using ytterbium-doped optical fibers instead of crystals as the gain medium. By doing so, the thermal load can be spread on meters of material and handled more efficiently. Nevertheless, since the damage threshold of the optical fibers is also limited, this technology has primarily gone towards the high repetition rates, with a limited energy per pulse. Additionally, fibers are self-guiding elements and can be wrapped, such that they can be implemented into intrinsically stable and compact sources. For these reasons, this technology has gone beyond the academic research and is nowadays commercially available. Note that for different applications, bulk ytterbium sources can be interesting because of their low quantum defect (three-level system, 980 nm pumping, 1030 nm lasing) but have a longer pulse duration ($\sim$ 1 ps). Thin disk geometries can also be of interest, providing a good handling of the thermal load at the cost of a less efficient amplification.

The source used throughout this thesis, the BlastBeat system at CELIA, is a commercial Yb-doped rod-type fiber laser system, made of two Tangerine SP (Short Pulse) amplifiers seeded by a common fully fiber-integrated oscillator (Amplitude Systemes). Each amplifier can deliver 50 W at a central wavelength of 1030 nm (FWHM = 18.5 nm), with a pulse duration of 135 fs. The repetition rate can be tuned from 166 kHz to 2 MHz, providing energies between 300 $\mu$J and 25 $\mu$J with a constant average power. The lower bound of the repetition rate is imposed by the energy acceptance of the fiber, while the upper one can be in principle higher. The output beam has a diameter of 2.7 mm and its quality is specified with a $M^2 = 1.2$. Phase distortions induced by non-linear effects in the fiber are corrected with a liquid crystal phase mask in the amplifier cavity. A set of predefined corrections is optimized for a 50 W output power and for various repetition rate ranges. For this reason, the amplifiers are always operated at full power and the power modulation is performed using a half waveplate and a polarizer, as

depicted in Fig. 2.1. The seeding oscillator is boxed in a rack and connected to the amplifiers on the optical table with fibers. The two amplifiers can be operated independently, except for the repetition rate that is controlled with a common pulse picker. Along with the reliability and a convenient daily operation, the best attribute of such a laser is the high repetition rate, breaking the barriers in terms of signal acquisition time and average flux. It is also beneficial for applications requiring high flux but low energy such as coincidence detection. On the other hand, it goes with a high average power that has to be dealt with, a longer pulse duration and a different wavelength compared to the standard Ti:Sa lasers, that very often serves as a reference. Notably, all the reflective optics have to be highly reflective ($R > 99.9$ %) to avoid absorption, the optical mounts are specifically designed against thermal drift, the transmittive optics and the coatings have to be chosen with care. An overview of the beamline has been published in [Comby 20a].

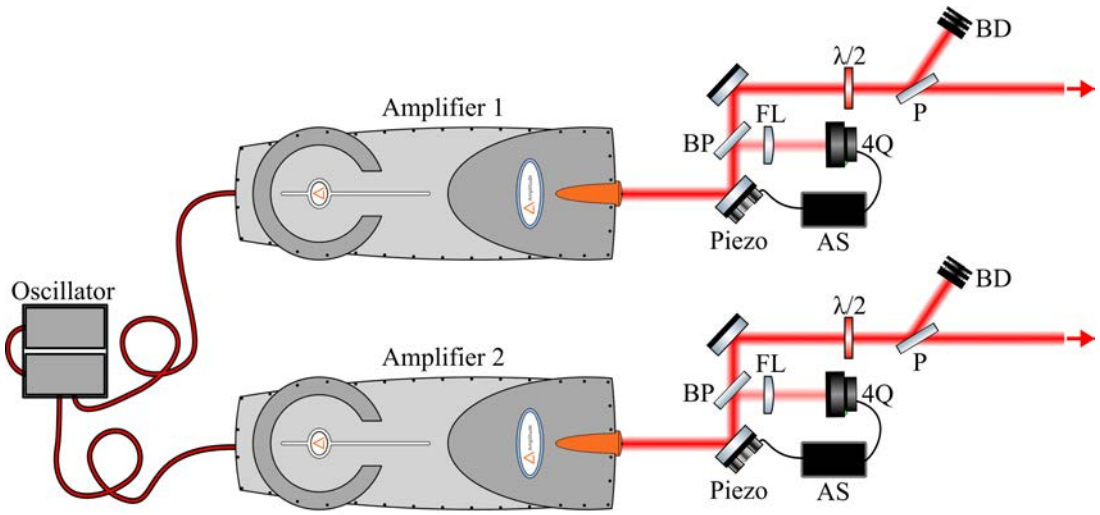


**Figure 2.1** – *Fiber laser source, with the active pointing stabilization and the power modulation setup, see text for details. BP = Brewster plate, 4Q = 4-quadrants, AS = active stabilization feedback, P = polarizer, BD = beam dump.*

**Stability Tests**

The commercial specifications for the stability of the laser are 1.2 % RMS shot-to-shot and a long term stability of 0.1 %. This long-term stability is essential for long acquisition time experiments. As the output of the amplifiers are mostly used for highly non-linear processes, such as high harmonics generation or multiphoton/strong field ionization, even small fluctuations are magnified and can affect the signal. A stability test has been performed to monitor the slow drifts and fluctuations. The results, starting from a cold amplifier, are displayed in Fig. 2.2 and are slightly different for the first and second amplifier (respectively left and right columns).

The stability of the first amplifier is the best. Globally, the laser stabilizes after a $\sim 30$ mn transient, corresponding to the warm-up. The output power (Fig. 2.2 (a)) is relatively constant around the $51.45 \pm 0.5$ W. The intermediate field pointing evolution along the horizontal and vertical axis are shown respectively in panels (b) and (c), and have the same converging tendency. The measurements presented here were monitored $\sim 50$ cm away from the amplifier, and a f = -7.5 cm lens was placed before the pointing-sensitive powermeter to magnify the fluctuations.

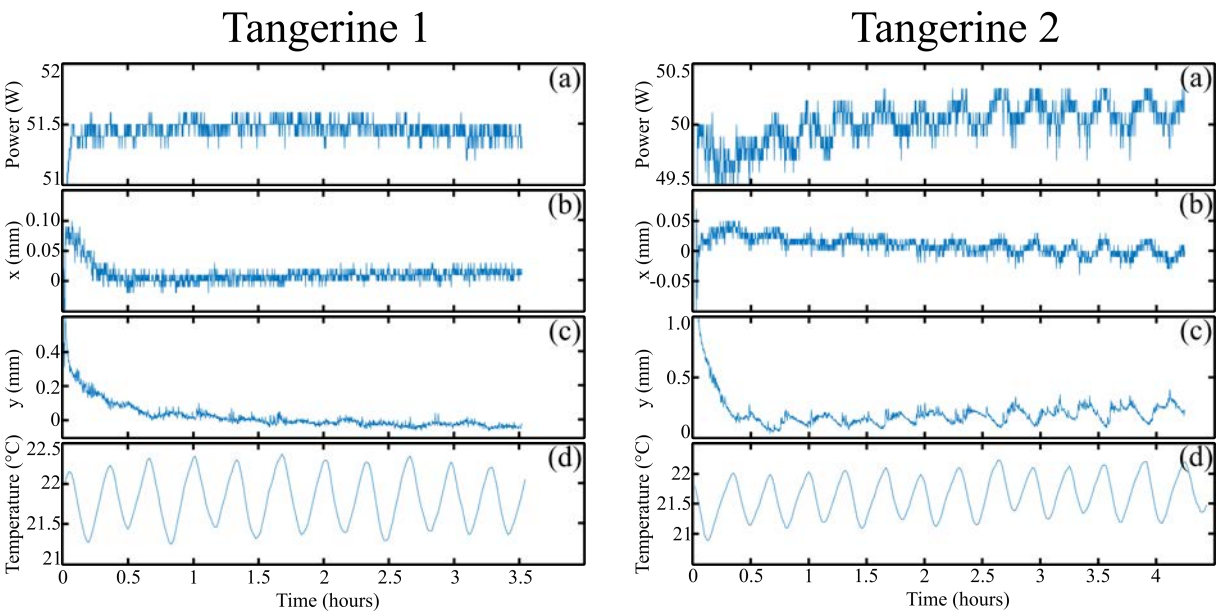


**Figure 2.2** – *Stability test on the first (left column) and second (right column) amplifiers, ran over a few hours. (a) Output power, (b) horizontal pointing, (c) vertical pointing and (d) temperature near the amplifiers. The pointing was acquired ∼ 50 cm away from the amplifier, and a f = -7.5 cm lens was placed before the detector to magnify the fluctuations.*

The second amplifier shows an additional behavior (Fig. 2.2, right column). While the warm-up duration seems to be longer, especially up to 1h30 in the power evolution, the power and pointing oscillate at a ∼ 20 mn period. The output power oscillation amplitude is about ±0.15 W and the pointing one up to 0.2 mm peak-to-peak. We found out that these oscillations were in phase with the room temperature in the vicinity of the amplifiers, which is about $21.5 \pm 0.5$°C for the second one. The ±0.5°C oscillation of the room temperature is caused by a defect in the air conditioning stabilization setting. The problem should thus be solvable. Such a behavior is not found in the first amplifier, despite being affected by the same room temperature fluctuations. This is probably due to a slightly different internal alignment in the two Tangerines that induces a different dynamics of the internal temperature regulation.

In order to contain the pointing oscillations, an active pointing stabilization has been implemented directly at the output of the two amplifiers (see Fig. 2.1). Each one is corrected with a mirror steered by a piezoelectric mount controlled by a 4-quadrant detector. A focusing lens is placed before the 4-quadrant so that this latter images the far field. We assumed that a single mirror correction was sufficient since the experiments and sensitive optical elements are at least a few meters away from the source. This setup reduced the peak-to-peak fluctuations of the beam pointing by a factor ∼ 2.7.

Note that a slight effect of the air conditioning fluctuations has also been noticed in the laser pulse duration. After a relatively long investigation, we found out that it was due to the fact that the active thermal stabilization of the oscillator breadboard was utilizing the same power supply as the pumping diodes. As a result, when some current was used to keep the temperature at the setting point, the diodes were not inducing exactly the same nonlinearities in the amplification medium, effectively moving the optimal compression point. This effect was

not visible in the output power as the pumping is saturated anyway. We have solved the issue recently by simply decoupling the power supplies. Before this upgrade, the slight fluctuations of the compression were not a crucial issue, as the acquisitions were either much shorter (VMI) or much longer (COLTRIMS) than the typical oscillation period. We can now avoid the averaging of the fluctuations in the COLTRIMS acquisitions, which is a significant improvement for the very long acquisitions we aim at performing.

More recent measurements of the stability of the second amplifier, where all the improvements mentioned above are implemented, are shown in Fig. 2.3. The configuration is close to an actual experiment : the 1030 nm fundamental beam is split in two, and one arm is frequency-doubled in a BBO crystal. The power and pointing of both beams are monitored 5.5 m away from the amplifier, corresponding to the entrance of the COLTRIMS. Even if the measurement is not directly comparable with the one presented in Fig. 2.2, one can see that the oscillations of the power, compression (visible trough the 515 nm power) and pointing have been mainly eradicated. The only notable issue is a slow horizontal pointing drift of the 515 nm beam only (e). It was due to a defective mirror mounting, and has been fixed since then. Perhaps most interestingly, the short-term pointing stability at the entrance of the COLTRIMS is then of the order of tens of micrometers, as resolved for the 515 nm beam in the panels (e) and (f). Such deviations should be negligible for the apparatus resolution, as will be discussed in Section 2.IV. The implementation of a second active pointing stabilization just before the spectrometer is currently ongoing, so that possible slow, larger drifts are avoided during very long acquisitions.

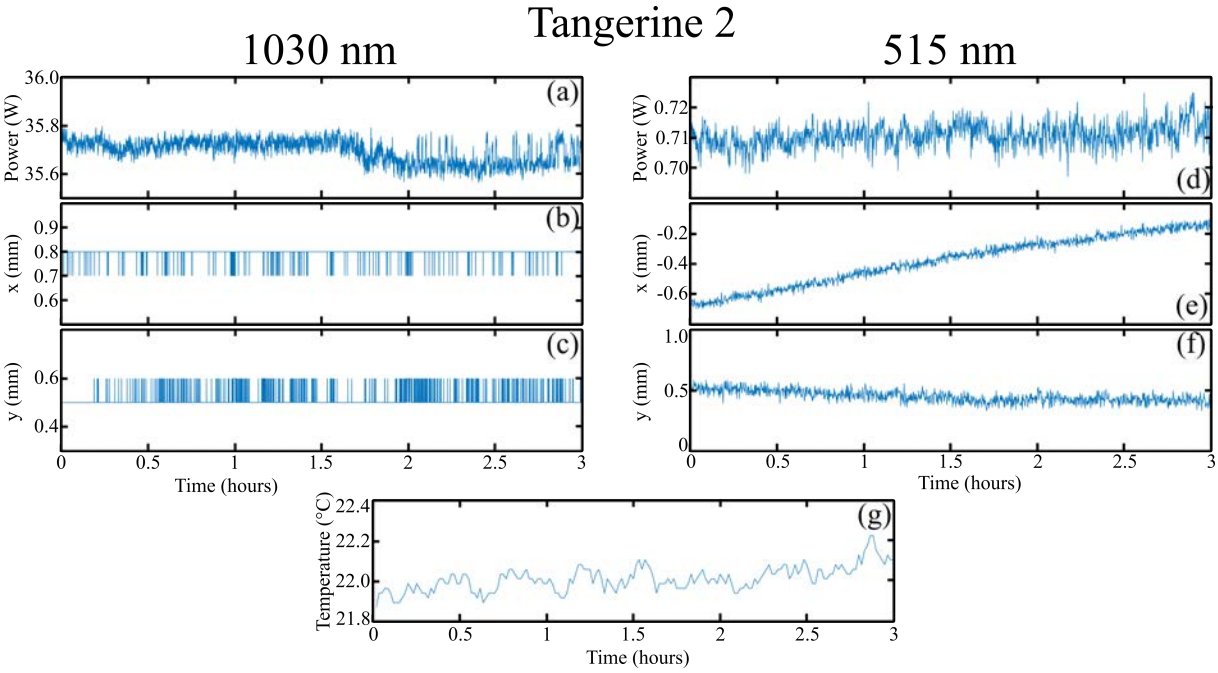


**Figure 2.3** – *Stability test performed on the fundamental and second harmonic of the second amplifiers. (a) Power, (b) horizontal pointing and (c) vertical pointing of the unused part of the 1030 nm beam. Note that the position resolution is of 0.1 mm here. (d), (e), (f) are the same, with a much higher spatial resolution, for the 515 nm beam obtained by second harmonic generation in a BBO crystal. Both pointings were monitored without lens 5.5 m away from the amplifier, corresponding to the entrance of the COLTRIMS. (g) Room temperature near the amplifier.*

## I. 2 Frequency conversion : $2\omega$, $3\omega$, $4\omega$

The primary use of the source is the study of ultrafast molecular dynamics. In this context, laser wavelength tunability is an important degree of freedom, which enables resonant excitation or changing the light-matter interaction regime. However, the central wavelength of a fiber laser source is of course fixed, hence the various solutions presented here that have been implemented.

Second, third and fourth harmonics generation of the fundamental frequency of the laser $\omega_L$ ($\lambda - L = 1030$ nm) are performed at 166 kHz, as the non-linear frequency conversion efficiency scales with the pulse energy. The optimization has primarily been performed by Antoine Comby, Stéphane Petit and the team of Amplitude Systemes.

The second harmonic generation (SHG), at 515 nm, is simply obtained through a 1 mm thick type-I BBO crystal, and a pair of dichroic mirrors are used to isolate it. The power of $2\omega_L$ obtained was 19 W, corresponding to a 36% conversion efficiency and a pulse energy of 114 $\mu$J. The second harmonic pulse duration has been measured to be 130 fs FWHM with a home-made SHG-FROG.

The third harmonic generation (THG), at 343 nm, is slightly more complicated and has been implemented with an in-line frequency conversion setup. A first 1 mm thick type-I BBO crystal ($\theta = 23°$) is used to partially convert the fundamental beam in $2\omega_L$ radiation, collinearly to the $\omega_L$ one, with orthogonal polarization. A 1 mm thick calcite plate in inserted to adjust the relative delay between the two frequencies. A second type-I 0.75 mm thick BBO crystal is then placed to generate the $3\omega_L$. The $3\omega_L$ frequency is then isolated with 3 dichroic mirrors and measured at 12 W of average power (72 $\mu$J, 24% conversion efficiency). We noticed, however, that thermal effects can occur in the setup beyond 9.5 W, particularly in the second BBO, appearing as pointing drifts. The pulse duration has been calculated with the SNLO software, and has been estimated around 140 fs.

The fourth harmonic generation, at 257 nm, consists in a two-stage SHG setup mounted on a compact breadboard for convenience. The first one is the same as described above, and the generated $2\omega_L$ is sent into a second 200 $\mu$m thick type-I BBO crystal. A thin crystal is required here to minimize the dispersion caused by the large difference in the group velocities of the $2\omega_L$ and $4\omega_L$, that limits the phase matching. Thermal effects once again had to be handled, in particular the two-photon absorption in the second BBO. For this reason, the $2\omega_L$ beam was magnified with a -150/250 mm telescope before the second BBO, which did not induce losses in the efficiency. The final power at $4\omega_L$ reached 2 W (12 $\mu$J, 4% efficiency from the fundamental). Once again the duration of the 257 nm pulses was calculated with SNLO and estimated to be 135 fs. At this wavelength, only high quality $CaF_2$ transmittive optics can be used in the rest of the setup without thermally inducing wavefront distortion and colored centers.

A summary of the frequency conversion performances obtained is presented in Table 2.1. Note that the frequency conversions were saturated, in such a way that the pulse durations of the harmonics are similar to the fundamental, as well as the energy widths.

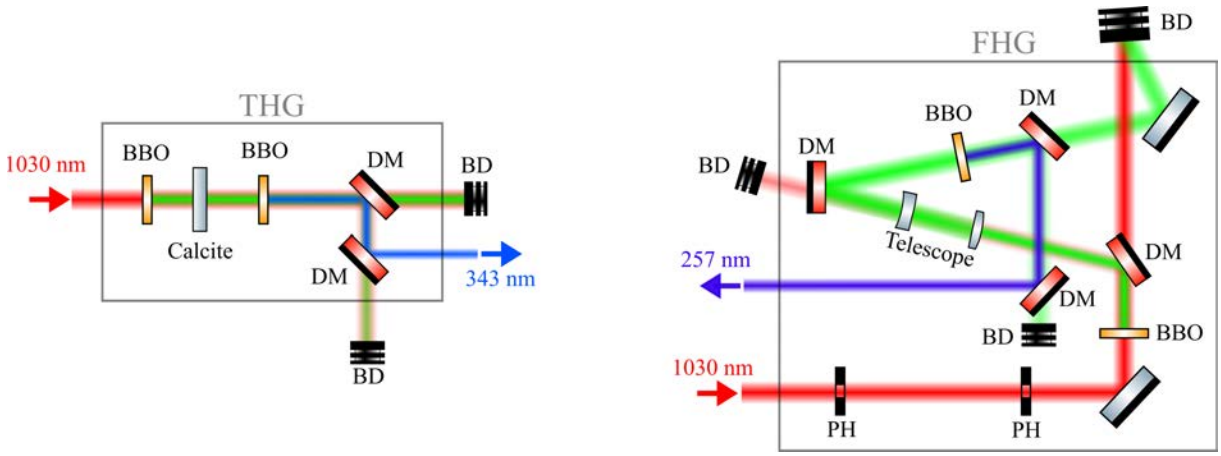


**Figure 2.4** – *Third harmonic generation (THG) and Fourth harmonic generation (FHG) breadboards, see text for more details. BBO = beta barium borate, DM = dichroic mirror, BD = beam dump, PH = pinhole.*

| Harmonic | 1 | 2 | 3 | 4 |
|---|---|---|---|---|
| Frequency | $\omega_L$ | $2\omega_L$ | $3\omega_L$ | $4\omega_L$ |
| Wavelength (nm) | 1030 | 515 | 343 | 257 |
| Photon Energy (eV) | 1.2 | 2.4 | 3.6 | 4.8 |
| Average Power (W) | 50 | 19 | 9.5 | 2 |
| Energy ($\mu$J/pulse) | 300 | 115 | 57 | 12 |
| Conversion Efficiency | - | 38% | 19 % | 4% |
| Pulse Duration (fs) | 135 (m) | 130 (m) | 140 (e) | 135 (e) |
| Bandwidth (meV) | 22 | 22 | 22 | 22 |

**Table 2.1** – *Summary of the frequency conversion performances obtained with the setup presented in the text, from the output of one amplifier, at 166 kHz. The pulse durations are either measured (m) or estimated with SNLO software (e).*

## I. 3 High-Order Harmonic Generation

### Fundamental Aspects

When a gas target, made of rare gas or small molecules, is irradiated at an intensity of about $10^{14}$ $W.cm^{-2}$, high harmonics of the laser field can be produced. The frequencies generated are much higher than what the perturbation theory could predict, and is referred to as high-order harmonics generation (HHG). Initially discovered in Saclay [Ferray 88] and Chicago [McPherson 87] in the 1980s, this process has raised a great interest primarily for three reasons.

Firstly, HHG enables the generation of coherent radiation at very short wavelength ranging from the extreme ultra-violet (XUV) to the x-rays domain [Popmintchev 12], being nowadays able to reach hundreds of eV photons, in particular in the water window (282-533 eV) [Chen 10, Ren 18, Cousin 17, Johnson 18, Barreau 20] which is of great interest for biological studies. This property is for example central in coherent imaging applications, such as high-quality diffraction on periodic samples [Gardner 17].

Secondly, HHG was shown to generate extremely short pulses [Paul 01, Hentschel 01], down to only a few dozens of attoseconds long [Li 17, Gaumnitz 17, Zhao 20]. This is of particular interest for pump-probe time-resolved experiment, where the pulse duration limits the tempo-

ral resolution. It initiated major advances in atomic, molecular and solid state physics, with unprecedented temporal resolution [L'Huillier 03, Krausz 09, Lépine 14, Nisoli 17]. HHG-based sources are routinely being used to measure or instance attosecond electronic dynamics in atoms [Goulielmakis 10], molecules [Calegari 16, Warrick 17], and solids [Tao 16], through photoionization or transient absorption spectroscopy. Remarkably, this has been used for instance to observe the real-time evolution of valence electrons in rare gas [Goulielmakis 10], or to track the dynamics of chemical reactions [Pertot 17].

Thirdly, the HHG process can be used to probe the structure and dynamics of the generating medium itself, in a scheme referred to as high-harmonics spectroscopy [Itatani 05, Baker 06]. This technique was initially restricted to diatomic and triatomic molecules, but was recently extended to polyatomic organic molecules [Marangos 16]. The sensitivity of the HHG process to the generating medium is a direct consequence of its strong-field nature of the interaction, and can be understood within the three-steps model, based on the SFA description.

The underlying strong field process is presented in Section 4.I of this manuscript.

**Technological Aspects**

The discovery of the HHG process was primarily performed using 36 ps pulses at 1060 nm from a Nd:YAG laser [Ferray 88] and sub-ps pulses at 248 nm from a dye laser [McPherson 87]. Later on, HHG was pushed to a higher level by the advent of Ti:Sa lasers, which can provide in a reliable manner intensities about $10^{14}$ $W.cm^{-2}$ at visible or near-infrared (NIR) wavelengths. The short and energetic pulses produced by the Ti:Sa technology is valuable for the production of short (single attosecond pulses) or intense XUV pulses (up to the $\mu$J/pulse [Hergott 02, Takahashi 02, Nayak 18], enough for non-linear XUV interaction [Tzallas 03, Takahashi 13, Senfftleben 20]). Note that high energy photons, up to the water window, are preferentially generated from long wavelengths, mainly obtained from parametric sources [Ren 18, Barreau 20]. The latter will not be extensively discussed in this manuscript, but can present interesting characteristics.

In any case, the relatively low repetition rate of the Ti:Sa technology and the limited conversion efficiency of the HHG essentially caps the average flux of XUV photons available at low pulse energy. This is deleterious in numerous applications, such as for instance photoelectron coincidence detection (due to the coincidence condition, discussed in Section 2.IV and angle-resolved photoemission spectroscopy from surfaces (where space charge has to be avoided).

More recent Yb fiber-based lasers, able to operate at a higher repetition rate, give appealing perspectives to circumvent these issues. While high XUV fluxes were restricted to synchrotron sources for a long time, the HHG process is starting to be an interesting table-top alternative.

**Setup Implementation**

The design, implementation and optimization of the high-order harmonic generation (HHG) chamber has also been essentially performed by Antoine Comby, and constitutes a central element in the beamline in terms of high-energy photon production. Its performances are presented

and discussed in [Comby 19].

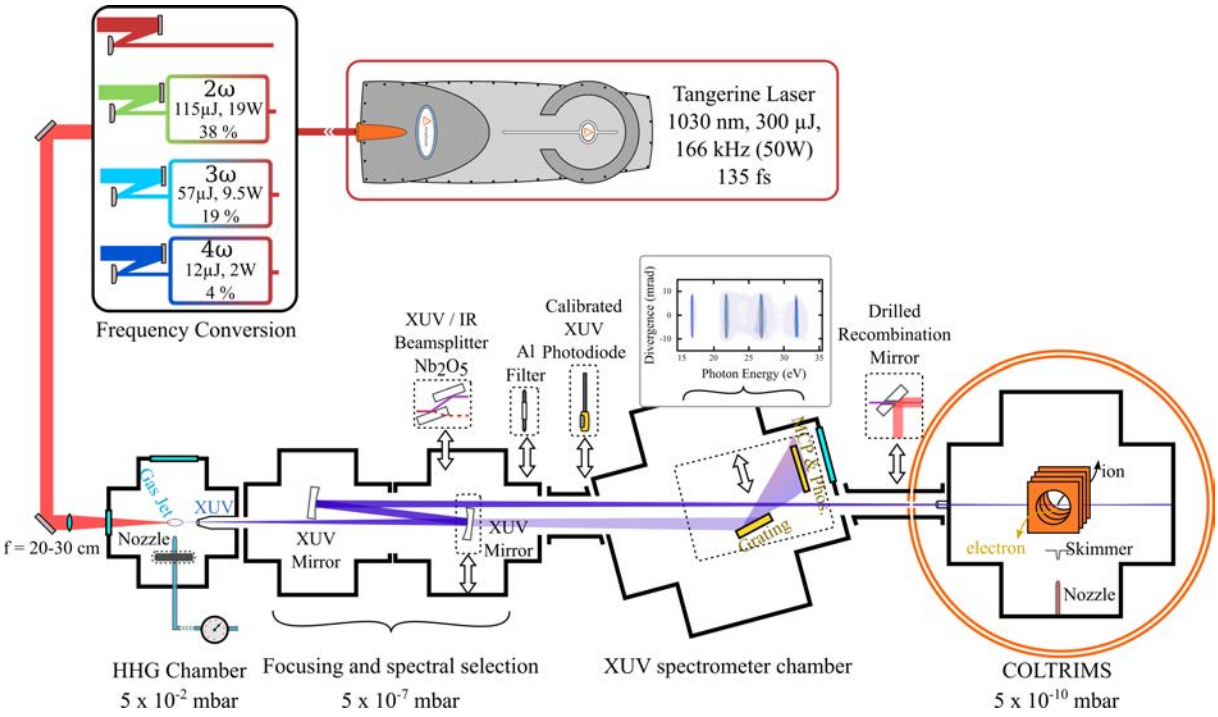


**Figure 2.5** – *Overview of the high-order harmonics generation beamline. The beam from an ytterbium-doped fiber amplifier is frequency upconverted before being focused into a vacuum chamber to produce HHG. A telescope made of two spherical XUV mirrors can be inserted to spectrally select some harmonics, and refocus them 3 m away into the interaction chamber of a COLTRIMS . Adapted from [Comby 20a].*

The table-top HHG setup developed for the BlastBeat beamline is presented in Fig. 2.5. The driving beam is initially magnified with a telescope (x3) and focused (f = 20-30 cm, depending on the wavelength) onto a motorized gas jet placed in a vacuum chamber to perform the non-linear generation process. A camera monitoring the plasma created in the jet enables a convenient optimization of the generation conditions, as well as an absolute gas density profiling (more details in [Comby 18]). This interaction chamber is directly pumped with a 600 $m^3/h$ root pump to $\sim 5 \times 10^{-2}$ mbar and connected to the rest of the line with a differential pumping hole, of diameter gradually increasing from 0.5 mm to 5 mm over 8 cm, placed at 3 mm of the laser focus. Turbomolecular pumps keep a low pressure in the chambers downstream ($\sim 5 \times 10^{-7}$ mbar) to ensure a low reabsorption of the harmonics. The beam can be then guided and collimated by two motorized XUV mirrors (f = 60 cm and f = 300 cm) into the photoelectron detection part, with a typical $\sim 50$ $\mu m$ spot size. Despite showing a lower reflectivity, the normal incidence reflective optics do not affect the polarization state, compared to e.g. grazing incidence toroidal mirrors. This matter of high importance for the generation of circularly or elliptically polarized harmonics to study chiral molecules. The beamline has been designed for versatility. Monochromatization of the harmonics comb and removal of the driving beam can be performed in three different manners, either using multilayer XUV mirrors, fused silica plates coated with $Nb_2O_5$ under 20° grazing incidence or thin metallic foils (Al, In). In practice, the foils cannot hold the full power of the incident beam without the couple of fused

silica plates. These latter respectively reflect 42% and 0.7% of the s and p polarizations at 1030 nm and 60% and 0.7% at 515 nm, while in the 20-45 eV range, they reflect 20-50% in s and 10-30% in p polarization. The characterization of the high harmonics generated can be performed with an XUV spectrometer, made of a gold-coated grating with variable groove spacing (1200 $mm^{-1}$ average). It images the spectrum spatially on a set of chevron-stacked MicroChannel Plates (MCP) coupled with a phosphor (P46) screen and a CCD camera. The decay time of the screen is fast enough (10% of the signal reached in 500 ns) to avoid memory effect between each pulses (6 $\mu$s at 166 kHz). The grating is placed on a translation stage to be removed easily, to let the beam reach the photoelectron device. A calibrated XUV photodiode can also be inserted for precise flux measurements, after two metallic filters whose transmission can thus be calibrated independently. Finally, a drilled recombination mirror can be placed at the end of the beamline to perform pump-probe experiments.

**Cascaded HHG**

Depending on the application, the most adapted driving wavelength can vary. A systematic study of the HHG from our high-repetition rate system as a function of the frequency used has thus been performed [Comby 19]. It turns out that the high-order harmonics generation from the harmonic of the laser field, namely cascaded HHG, shows great performances. Typical harmonics comb, generated in argon with a driving beam frequency $\omega_L$, $2\omega_L$, $3\omega_L$ and $4\omega_L$, measured with the XUV spectrometer, is shown in Fig. 2.6. Using higher generating frequencies presents advantages and drawbacks. On the one hand, it increases the conversion efficiency ($d_{HHG} \propto \omega^{\alpha}$, $\alpha \in [4:8]$) and reduces the required laser power, which is especially interesting with such a high-repetition rate source. Moreover, it increases the spectral separation between the harmonics ($= 2\hbar\omega$), which helps a lot for the monochromatization and the reduction of the complexity of the photoelectron spectra obtained. On the other hand, cascaded HHG shows a lower cutoff (scaling as $\propto \lambda^2$), and adequate transmittive UV optics have to be found. On our case, the only entrance window material that could resist more than 8 hours at 2 W of 257 nm radiation without showing colored centers was high quality $CaF_2$ (Crystran Ltd.).

The photon flux for several harmonics in the XUV generated from the wavelength presented in Table 2.1, measured with the calibrated photodiode, are shown in Table 2.2. Essentially, doubling the driving wavelength increases the HHG fluxes by two orders of magnitude. Using the third harmonic increases it even further, so that the source reaches the mW range at 18 eV. Using the fourth harmonic seems to be detrimental, because the cutoff energy is very low (expected at 17 eV here), such that the generation regime is not really HHG.

Our results can be compared to the state of the art. Comparable fluxes have been reached, for example generated after a postcompression stage (0.83 mW at 21.3 eV) [Klas 16] or in a cavity (2 mW at 12.7 eV and 0.9 mW at 19.7 eV) [Porat 18b] in krypton, showing respectively a conversion efficiency of $7 \times 10^{-6}$ and $2.5 \times 10^{-5}$. These results are of course remarkable, but they rely on highly complex and costly setups. Conversely, the cascaded high-harmonics generation scheme presented here remains relatively simple, and presents benefits in terms of efficiency, up to $(3.8 \pm 0.8) \times 10^{-5}$. It also shows that our relatively long laser pulse duration and low energy per pulse are not detrimental for the HHG yield, as far as tight focusing conditions are used.

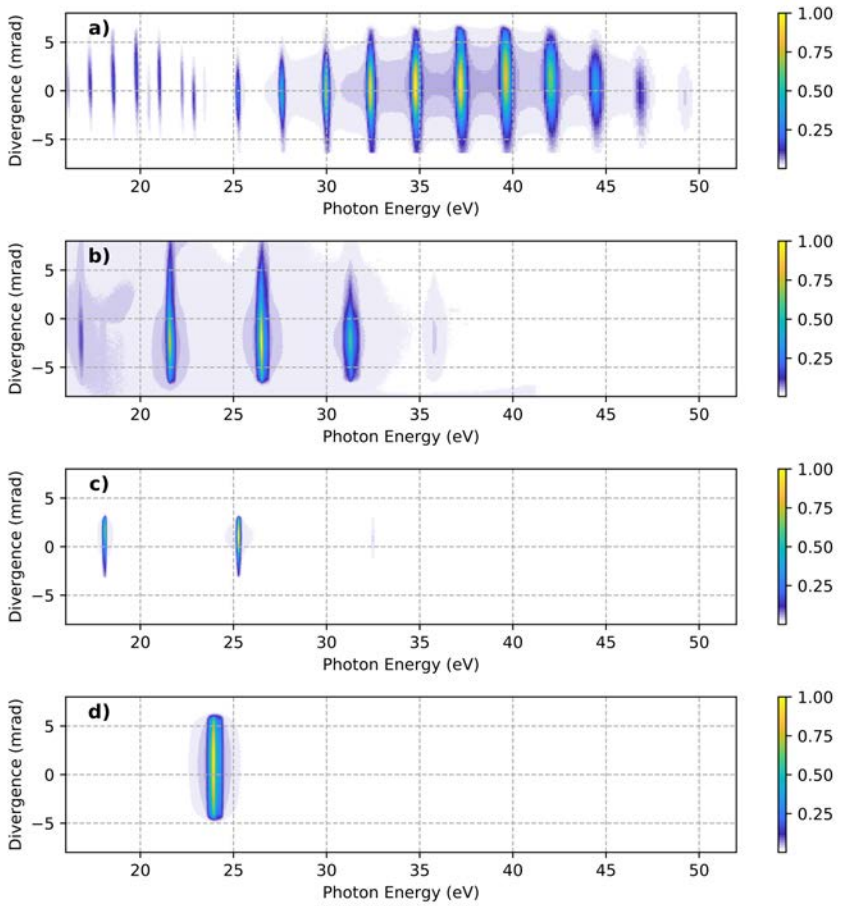


**Figure 2.6** – *(a)-(d) Spatially resolved high-harmonic spectra generated in argon using a driving laser at 1,2,3 and 4$\omega_L$, with respective intensities of 1.5, 2.8, 3.4 and 1.6 × $10^{14}$ W.cm$^{-2}$. The peak density in the generating medium is 4.5 × $10^{18}$ at./cm$^3$ at $\omega_L$ and 3.5 × $10^{18}$ at./cm$^3$ at 2,3 and 4$\omega_L$. The spectra at 1 and 2 $\omega_L$ are recorded after reflection on two $Nb_2O_5$ plates. The spectra at 3 and 4 $\omega_L$ are recorded after transmission through an Al filter. Note that the edges of the harmonics can be spatially cut by apertures here, and that the energy resolution is limited by the spectrometer. Adapted from [Comby 19].*

**Stability**

High-order harmonics generation is a highly non-linear process. As a result, it magnifies the fluctuations of the driving laser. The harmonic signal presents two kinds of instabilities. The first one is the fast fluctuations, which are primarily caused by jet fluctuations and laser fluctuations, for example because of the propagation in air. If their amplitude remains small (say $\sim 10$ % range), they are not such an issue since they are used in one-photon ionization processes, and only induce a fluctuation of the signal of the same magnitude. The second instability is the slow decay of the signal. This one can be more problematic for experiments requiring long acquisitions, such as in the COLTRIMS. We identified in particular a transient corresponding to the thermalisation of the XUV optics specifically under vacuum, which take more time than in the air as it can only efficiently occur through the heat conduction of the mounts (typically dozens of minutes). As mentioned previously, cascaded HHG helps minimizing this effect. In principle, alignment drifts can be iteratively corrected until the thermalisation is completed.

| Driving Field | Generated Harmonics | | | |
|---|---|---|---|---|
| $\omega_L$ | Photon Energy (eV) | 25.2 (H21) | 39.6 (H33) | 44.4 (H37) |
| 1030 nm | Photon Flux ($\times 10^{10}$ photons/s) | 1.2 ± 0.2 | 8.2 ± 1.5 | 1.4 ± 0.3 |
| 45 W | Power (nW) | 50 ± 10 | 520 ± 100 | 100 ± 20 |
| $2\omega_L$ | Photon Energy (eV) | 21.6 (H9) | 26.4 (H11) | 31.2 (H13) |
| 515 nm | Photon Flux ($\times 10^{13}$ photons/s) | 2.3 ± 0.4 | 2.1 ± 0.4 | 0.3 ± 0.05 |
| 19 W | Power ($\mu$W) | 80 ± 15 | 90 ± 20 | 15 ± 3 |
| $3\omega_L$ | Photon Energy (eV) | 18.0 (H5) | 25.2 (H7) | - |
| 343 nm | Photon Flux ($\times 10^{14}$ photons/s) | 6.6 ± 1.3 | 0.5 ± 0.1 | - |
| 7.3 W | Power (mW) | 1.9 ± 0.4 | 0.20 ± 0.04 | - |
| $4\omega_L$ | Photon Energy (eV) | 14.4 (H3) | 24.0 (H5) | - |
| 257 nm | Photon Flux ($\times 10^{12}$ photons/s) | 9 ± 2 | 0.8 ± 0.2 | - |
| 2 W | Power ($\mu$W) | 21 ± 4 | 3 ± 1 | - |

**Table 2.2** – *Measured XUV photon flux in optimized conditions obtained by cascaded HHG from a fundamental at 1,2,3 and 4$\omega_L$. Adapted from [Comby 20a].*

However, the alignment in the HHG chamber is usually very tight, for example through the differential pumping holes, and over long distances (typical angular acceptance of $10^{-3}$ rad). We have for instance observed that slight pointing drifts before the generation could result in ablating the tip of the harmonic generation jet nozzle, depositing matter on the surrounding optics and irreversibly damaging them. An ongoing project to prevent it is the active stabilization of the pointing both before and throughout the HHG chambers. Other sources of drifts can be various and are not necessarily specific to high repetition rate beamlines. Let us simply mention that they can be usually compensated from time to time during an acquisition, for example by correcting the jet density accordingly. For the same reason as the fast fluctuations, this usually does not affect the experiments validity in our case. Finally, a last issue specific to the high driving field flux have been noticed in some cases. In an experiment where a solid organic sample was used, carbon impurities were released and deposited on the optics under vacuum, inducing an irreversible darkening. With gaseous targets, the purity of our vacuum is however good enough to avoid this issue.

The high flux and stability of our source has been already used in recent experiments. For instance, the third harmonic of the $4\omega$ has been used successfully as an irradiation EUV source to investigate the photochemical processes of Titan's Atmosphere. By exposing a reactor for more than 6 hours, the formation of species twice as heavy as previously detected with a similar HHG-EUV-monochromatized source at 1 kHz has been observed [Bourgalais 20].

**Generation of Circular or Elliptical Harmonics**

The capacity to generate circular, or at least highly elliptical high energy radiation is pivotal for many applications such as magnetic circular dichroism or photoelectron circular dichroism. This has been a challenge in HHG, as the efficiency of the process quickly diminishes with the driving field ellipticity (the process is discussed in Section 4.I), but several ways around have emerged. We have tested, on our high-repetition rate beamline, the use of bicircular bichromatic driving field where the clover-shaped electric fields enables to generate high-harmonics, which is

impossible using a simple circular polarization [Fleischer 14, Kfir 15]. The comb of harmonics generated presents a particular structure due to the momentum conservation. Instead of being constituted only by odd orders, it consists in a consecutive threefold sequence of harmonic at a given helicity, followed by the opposite helicity and a forbidden harmonic, as shown in Fig. 2.7. The spectral selection capacity previously mentioned can thus be of great interest here to select a single harmonic of given ellipticity sign. The optical setup used to generate the driving field was in-line for a better stability, namely using the Mazel-Tov technique [Kfir 16].

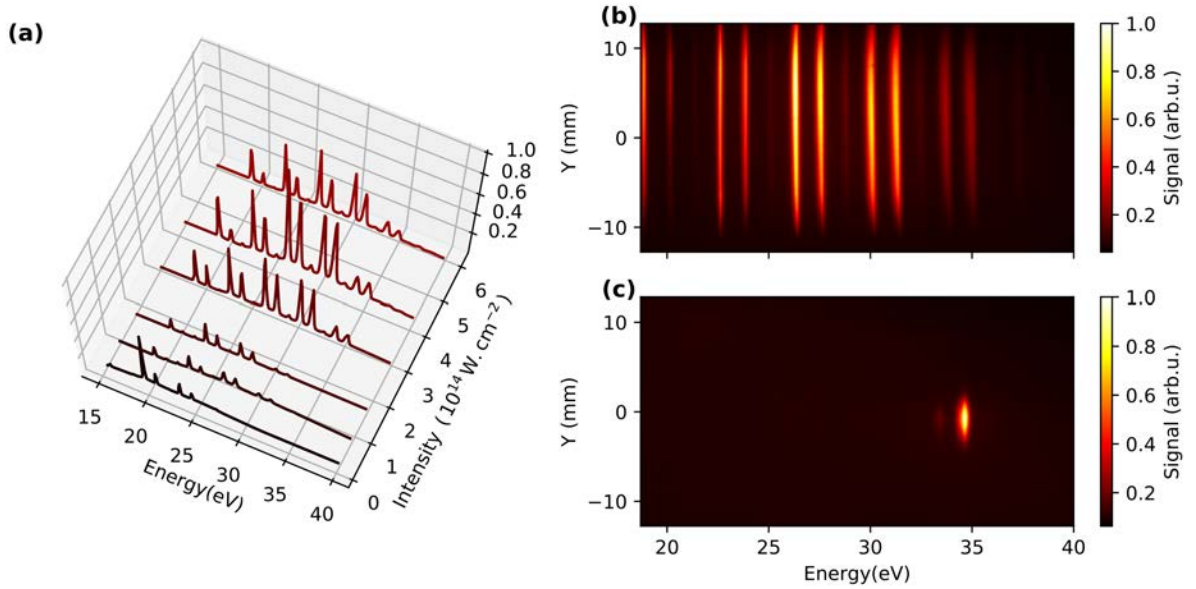


**Figure 2.7** – *Bichromatic bicircular HHG. (a) Intensity dependency of the HHG spectrum. Spatially resolved bichromatic bicircular HHG spectrum before (b) and after (c) multilayer mirrors at 35 eV, showing both the spectral selection and refocusing. Extracted from [Comby 20a].*

Another possibility to generate elliptically polarized harmonics is the use of intermediate resonances in the target. It has been demonstrated that this effect could lead to 80 % ellipticity from only 20 % ellipticity of the driving elliptical field in $SF_6$ molecules with Ti:Sa sources [Ferré 15b]. However, this target was not suited to the ytterbium source since the photons do not match the resonance energies. This process has thus been tested in argon, where it worked in this case only if the pulses are short enough (using the postcompression described in the next paragraph), reaching up to 50 % ellipticity in the harmonics with 30 % ellipticity of the fundamental field.

The characterization of the ellipticity of the harmonics can also be challenging. For this purpose, Antoine Comby has build a grazing-incidence reflective XUV polarizer, based on four mirrors, that has an extinction ratio of more than 20 at least in the 15-30 eV range. It can be rotated under vacuum for the measurement of Malus' law curves. Note that, however, this method can not distinguish the unpolarized light from the circular one. For the complete characterization of the XUV polarization state, other techniques based on complex optical detection [Koide 91, Schäfers 99, Nahon 04] or coincidence imaging [Veyrinas 13, Barreau 18] can be employed.

## I. 4 Postcompression

The 135 fs duration of the pulses delivered by our fiber laser can be a critical issue in terms of temporal resolution on the molecular dynamics compared to the Ti:Sa sources. Techniques to reduce the pulse duration exist, such as the postcompression demonstrated in the late 1990's [Nisoli 96], which is nowadays routinely used on Ti:Sa lasers to produce few-cycles pulses. Its applicability to high-repetition rate Yb-doped fiber lasers has been more recently demonstrated, for example compressing a source with a duration similar to ours (130 fs) down to 14 fs [Lavenu 17]. A double-stage postcompression can even be used in this case to reach sub-6 fs from an initial 340 fs duration [Hädrich 16].

The pulse duration $\Delta t$ is limited by its spectral bandwidth $\Delta\nu$ through the Fourier limit, which can been seen as an Heisenberg uncertainty principle. For Gaussian profiles, it writes $\Delta\nu\Delta t \geq 0.441$. This implies that a spectral broadening is necessary to shorten the pulses. This is performed in postcompression by using the self-phase modulation process, which is a third-order polarizability response $P^{(3)} = \epsilon_0\chi^{(3)ijk}E_iE_jE_k$, that can be expressed, for a single laser field, as an intensity-dependent optical index : $n = n_0 + n_2I(t)$. The result is a symmetric broadening of the spectrum. Since this specific order cannot be isolated from others, this process is always associated with lower order ones, such as dispersion, and higher order ones, for instance self-steepening, inducing an asymmetry in the spectrum. While this latter can be minimized by tempering the field intensity, the linear dispersion must be compensated, typically using chirped mirrors. Note that recent alternatives have been developed, for example solitonic self-compression, where the dispersion is finely balanced within the optical fiber itself [Travers 19]. The postcompression is a spatio-spectral coupling that can become very complex. Simply put, it is most of the time performed in hollow-core capillary filled with rare gas on the TEM00 Gaussian mode. This way, the beam is focused on a long distance, rendering the process efficient, and spatially homogeneous. Note that other recent alternatives also display nice perspectives, especially at high average power, such as multipath cells [Lavenu 18].

In our case, Dominique Descamps has implemented a hollow-core capillary module developed by Amplitude Systemes, in a collaborative work with this company. The details will not be discussed extensively in this manuscript. Briefly, the setup has been optimized, at 166 kHz, on the SHG at 515 nm. As we have seen above, the $2\omega$ shows indeed a good balance between the HHG generation efficiency and the energy spacing of the harmonics. This wavelength is also relevant for us in the context of time-resolved pump-probe experiments in the multiphoton regime, while the fundamental 1030 nm tends more to the strong field ionization regime. We will see in Chapter 4 that in this latter regime, one can use another way to overcome the temporal resolution of the pulse duration. 19 W of the second harmonic were focused on a 150 $\mu$m spot, corresponding to an intensity of $\sim 9\times10^{12}$ $W.cm^{-2}$ in a 1.1 m long, 250 $\mu$m diameter hollow-core capillary. The capillary was placed in a chamber filled with krypton, as its non-linear optical index $n_2$ is relatively high. About 1200 $fs^2$ of second-order dispersion were compressed at the output using chirped mirrors specifically designed for this wavelength, which were challenging to find. The final duration was measured with a home-made SHG-FROG. An example of measurements done with an initial 18.2 W of SHG is presented in Fig. 2.8. The output power was

12.3 W (74 $\mu$J/pulse), corresponding to 67% transmission before compression, and 7.8 W (47 $\mu$J, 43%) after. A 50 nm spectral broadening has been obtained with 1 bar of krypton. The corresponding temporal profile retrieved is shown on Fig. 2.8 (b), with a 18.7 pulse duration FWHM.

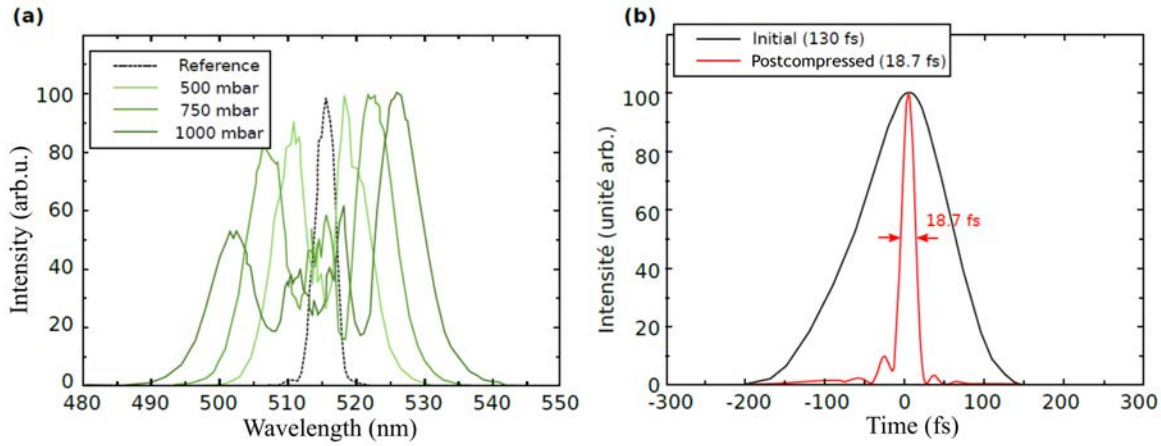


**Figure 2.8** – *Result of the postcompression of the $2\omega_L$ frequency, using krypton in a hollow-core capillary. (a) Spectrum broadening for various gas pressures. (b) Best duration obtained, measured with a SHG-FROG.*

High-order harmonics generation has been performed with the postcompressed pulses but is beyond the scope of this thesis. Simply put, the shorter duration allows a higher intensity, yielding an extended cutoff energy (*e.g.* from 25 eV to 35 eV in argon in the same conditions, but partially tempered by some spatial chirp from the focusing lens). It also enables a better conversion efficiency, but does not provide an overall higher XUV flux.

## I. 5 Optical Parametric Amplifier

Continuous wavelength tunability is an important asset in molecular spectroscopy, as it provides the possibility to compare or select on-resonance and off-resonance processes, but this parameter of freedom remains challenging in the multi-kHz domain. Historically, dye lasers have provided such a accordability but most of the time bounded to picosecond pulses. While they remain sometimes used for their fine spectral resolution [Kastner 20], a much more widespread alternative can be found in parametric sources. In this latter, the tunability originates from the generation of a light supercontinuum from femtosecond filamentation in a bulk material [Dubietis 17]. A fraction of the broad spectrum generated can be amplified in a crystal with a second laser pulse (in practice, the two pulses come from the same source). The supercontinuum produced is chirped, in such a way that the spectral selection practically appears by setting the temporal delay between the two pulses.

We had the opportunity to implement and characterize such an Optical Parametric Amplifier (OPA) in a 6 weeks collaboration with Amplitude and APE. This product, the MANGO SP, was adapted to fit our Tangerine SP source. A schematic view of the setup is depicted in

Fig. 2.9.

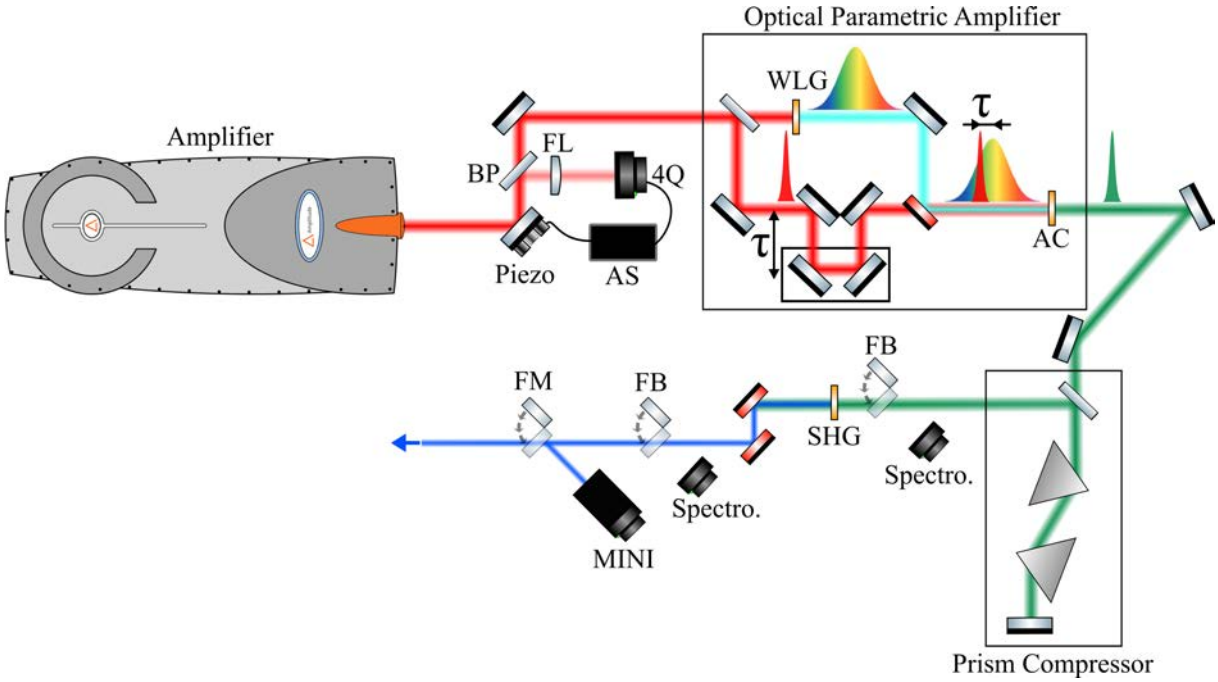


**Figure 2.9** – *Setup of the optical parametric amplification. The principle of the OPA is schematized and dwells on the generation of chirped white light. A fraction of the fundamental beam is used to amplify a narrow part of the spectrum, which can be chosen by tuning the relative delay $\tau$. The tunable pulses are then compressed in a prism compressor and undergo second harmonic generation. The pulses can be characterized both in spectrum and duration by a spectrometer and the MINI autocorrelator module. BP = Brewster plate, FL = focusing lens, 4Q = 4-quadrants, AS = active stabilization feedback, WLG = white light generation, AC = amplification crystal, FB = foldable blocker, FM = foldable mirror.*

The OPA is set to work with a 50 W, 135 fs pulses at 1030 nm input beam, at a repetition rate of 166 kHz. Typical spectrum of the OPA signal are presented in Fig. 2.10.

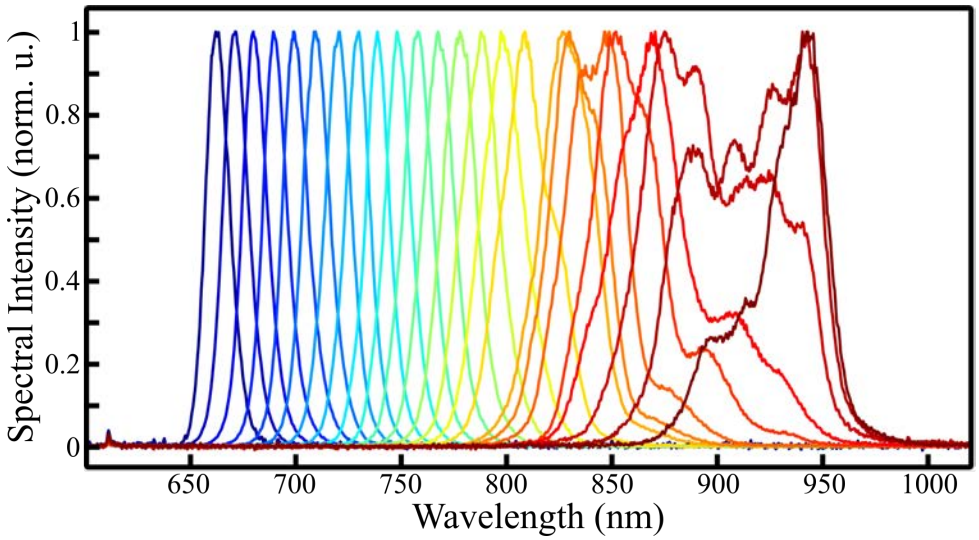


**Figure 2.10** – *Normalized spectrum of the OPA signal, at different central wavelengths.*

One can notice that the spectra obtained present a relatively Gaussian shape between 660

nm and 840 nm and become more structured between 840 nm and 950 nm. These modulations typically come from the properties of the amplification crystal. A major challenge in a commercial OPA is the capacity to be a turn-key system. In particular, the central wavelength is always coupled with other parameters, such as the amplification efficiency, the pointing, the divergence, the beam shape and quality and the pulse dispersion. The value (and cost) of such a system lies in the calibration and automatic compensation of all these variations. In the best case scenario, the wavelength constitutes an independent degree of freedom in the experiment. Otherwise, the source is rather used at one wavelength at a time, and requires a re-optimization at every wavelength modification. The second case applied here, but further time investment could have been largely beneficial. Firstly, the output spatial mode could deteriorate at certain wavelengths. Moreover, the output of the module was compressed with an external prism compressor that had to be tuned manually. Obviously, this implies a specific alignment for every photon energy, but this could ultimately be automated. The restricted duration of the experiment did not enable a full optimization of the NOPA geometry, since we preferred to use it as is for photoionization experiments.

Our main interest was the generation of UV photons with a tunable wavelength, which is more relevant for our molecular studies. The ionization potentials of our chiral molecules of interest are typically above 8 eV, and a two-photon absorption in the UV range reaches the Rydberg state manifold in most of the cases. For this reason, we doubled the compressed output with a second harmonic generation module (based on a BBO crystal). The final pulses were characterized with a spectrometer (HR2000, Ocean Optics) and the pulse duration was measured with a two-photon absorption photodiode autocorrelator (MINI TPA, APE). This module could retrieve durations down to 50 fs, at wavelengths ranging from the infrared down to 250 nm depending on the photodiode head mounted.

From the spectrally clean $\sim$ 690-850 nm range, the central wavelength obtained from the SHG module ranged from 427 nm to 343 nm, with a energy in the 0.72-3.2 $\mu$J/pulse range, and pulse durations between 63 fs and 110 fs. The efficiency of the whole frequency conversion process, from the output of the laser, is comprised between 1.1 % and 0.24 %. A difficulty was that not all the parameters were optimized at best at the same time. For instance, strong filamentation conditions in the continuum generation usually yielded the strongest output, at the cost of a poor spectrum and poor spatial profile. Similarly in the second harmonic generation module, the strongest frequency conversion efficiency was not necessarily the one yielding the shortest pulses. The values indicated have been obtained from a compromise, having at least a decent beam quality, spectrum and pulse duration.

The evolution of the performances with respect to the wavelength is presented in Table 2.3. One can see that the pulse duration increases with the photon energy, but remains remarkably shorter than the initial 135 fs. Conversely, the yield does not present a monotonous behavior. This is partly due to the manual re-optimization that has to be performed at every wavelength, but also reflects an intrinsic challenge of the parametric sources. This implies that in a systematic study of the wavelength-dependence of a process, the power has to be carefully leveled to keep a constant intensity. The intensities obtained were not sufficient to detect signal in our COLTRIMS detector (see further parts in this chapter for details). Nevertheless, we could

| OPA Output | | Second Harmonic | | | | |
|---|---|---|---|---|---|---|
| Wavelength (nm) (eV) | Power (W) | Wavelength (nm) (eV) | Power (W) | Energy ($\mu$J/pulse) | Yield (‰) | Duration (fs) |
| 853 (1.45) | 1.65 | 427 (2.90) | 0.37 | 2.2 | 7.4 | 63 |
| 840 (1.48) | 1.55 | 420 (2.95) | 0.53 | 3.2 | 11 | 72 |
| 828 (1.50) | 1.36 | 414 (2.99) | 0.48 | 2.9 | 9.6 | 73 |
| 799 (1.55) | 0.43 | 399 (3.11) | 0.12 | 0.72 | 2.4 | 70 |
| 735 (1.69) | 0.71 | 367 (3.38) | 0.29 | 1.7 | 5.8 | 100 |
| 701 (1.77) | 1.11 | 350 (3.54) | 0.34 | 2.0 | 6.8 | 110 |
| 686 (1.81) | 1.02 | 343 (3.61) | 0.34 | 2.0 | 6.8 | 110 |

**Table 2.3** – *Overview of the measurements of the OPA signal after compression and after the SHG module, at a repetition rate of 166 kHz, from the initial 50 W at 1030 nm. The wavelength indicated are the central values.*

perform acquisitions in the VMI, which has a much denser molecular jet and accepts tighter focusing conditions (f = 300 mm can be used with the VMI while and only f = 400 mm in the COLTRIMS). A few photoelectron distributions measured with the VMI, produced at different wavelengths, are shown in Fig. 2.11.

These images were recorded during 20 minutes each. The ionization is a 3-photon process for all the wavelengths presented here. Conveniently, the tunability range covers 400 nm, which corresponds to the second harmonic of a Ti:Sa source, and 343 nm, which is the third harmonic of our Yb-fiber laser, two energies at which we have extensively investigated the photoionization of chiral molecules. The first influence of the photon energy is of course the kinetic energy at which the electrons are emitted, corresponding here to the radius ($E_{kin} \propto R^2$). The REMPI process at play, discussed more extensively in Chapter 3, appears to evolve with the wavelength (as expected at less than 2 eV below the ionization threshold, where the density of vibronic states is very high). In particular, the relative importance of different rings varies, with each one having an opposite dichroic signal. This is in nice agreement with similar studies [Kastner 17], where the process is more extensively discussed.

The last point to address is the OPA stability. The repeatability was good, since the conditions obtained one day could be retrieved the day after. This is important for the perspective of automation. Note that it required the complete thermalization of the amplifier, then the thermalization of the OPA, which typically took in total $\sim$ 3 hours. Note that this thermalization time of the amplifier was later reduced by increasing the setting point of the thermalized bench in the laser head. While the pointing stability was more or less the one of the amplifier (see Fig. 2.2), the spectrum stability greatly depended on the output wavelength. Some wavelength often failed to provide stable spatial mode and energy, in particular in the range around 400 nm. At some others, typically when the spectrum had a double peak structure, we could observe a slow ($\sim$ 10 min) oscillation between the two spectral components, uncorrelated to the air conditioning. Still, we managed to reach situations where the parameters were stable for several hours. Unfortunately, we did not have enough time to perform a systematic study of the long term stability. To summarize our observations, let us simply say that a nicely Gaussian OPA signal spectrum is usually a basis for good stability. Conversely, the wavelengths at which such

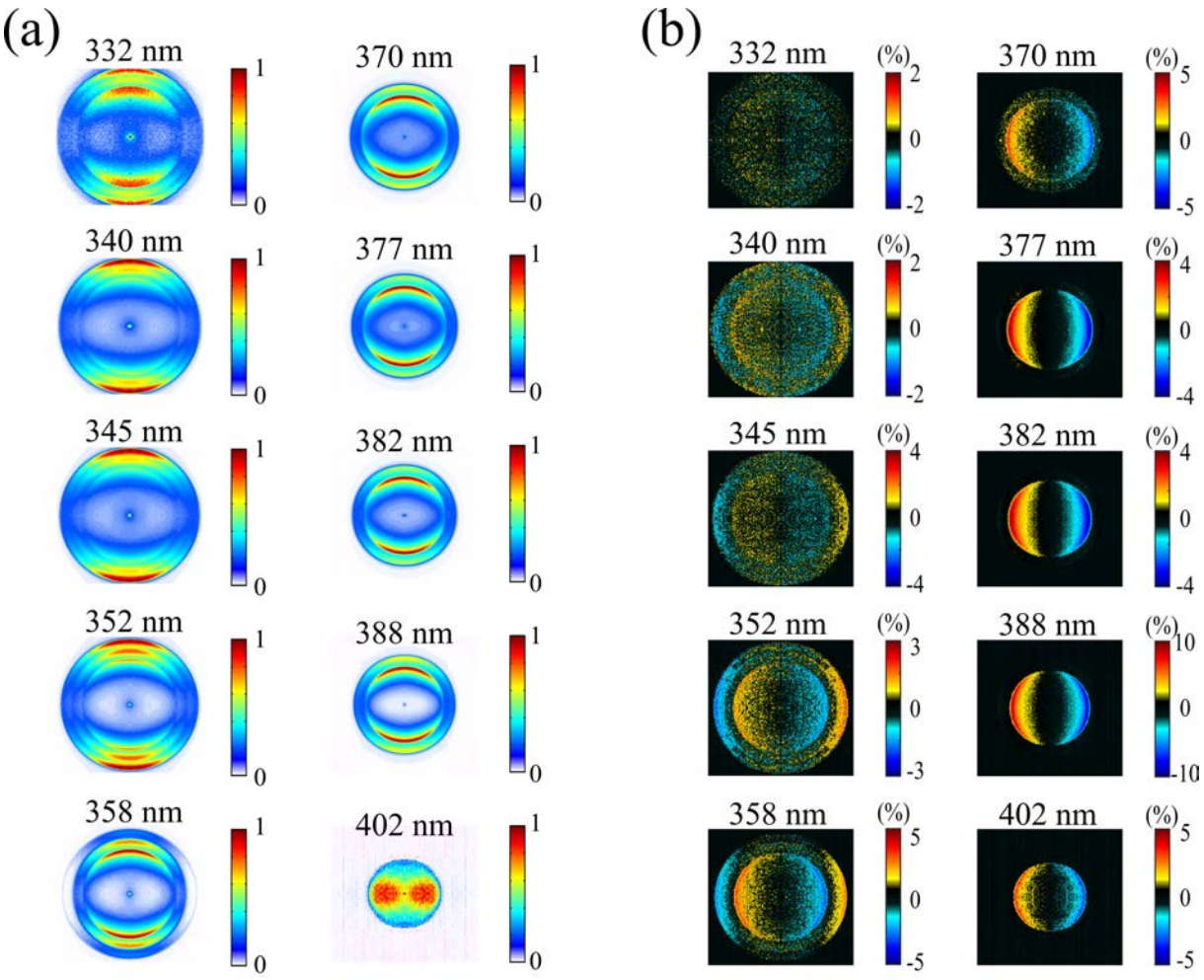


**Figure 2.11** – *Photoelectron angular distributions (a) and corresponding forward/backward antisymmetric parts (b), at different wavelengths generated in the OPA, obtained with (+)-Fenchone in the VMI using the PEELD technique (see Chapter III.II for details of the analysis).*

a spectrum could not be obtained were often associated with difficulties to control all the other parameters.

# II Velocity Map Imaging Spectrometer

## II. 1 Device

### Principle

The Velocity Map Imaging (VMI) device is one of the most widely used photoelectron imaging technique for gaseous targets, due to its $4\pi$ collection angle. While some other detectors manipulate the charged species with magnetic field or a combination of magnetic and electric fields, the VMI uses only electric fields, which are most of the time static. It consists of an array of plates at different voltages, imposing an electric field that extracts the charged particles created by the interaction between a matter jet and a radiation beam, and directed towards a detector, as depicted in Fig. 2.12. A homogeneous field configuration is

the most simple, but suffers from the spatial extension of the source and the initial velocity of the particles. The modern designs thus result from several practical improvements that have become the norm. The first milestone, reached in the 1950's, is the Wiley-McLaren geometry [Wiley 55], which consists in splitting the spectrometer into three homogeneous field regions. A first field is applied in the ionization region to extract the species, then a second one accelerates them towards the third one, which is a field-free drift tube, ending on the detector. With a carefully chosen set of fields and region lengths, the time-of-flight (TOF) resolution can be significantly improved. This can be understood as the particles emitted further away from the detector are more accelerated in the field regions and "catch-up" the others in the field-free region. Another major step forward initiated in the 1980's is the use of spatially-resolved detectors [Chandler 87]. Such a detector, still widely used today, is made of a microchannel plates (MCP) which multiply the particle signal in a cascade of electrons, and a phosphor screen which converts the electrons into visible light recorded with a camera (instead of the simple cathode of the Wiley-McLaren TOF). This paved the way toward particle imaging, in particular photoelectron imaging [Helm 93, Bordas 96, Whitaker 03, Ashfold 06]. A final important improvement is the use of electrostatic lens, introduced in the late 1990's [Eppink 97]. Instead of using metallic meshes which clearly define homogeneous and isotropic electric field regions, imposing the potentials with centrally hollowed plates (such as in Fig. 2.12) creates a gradient of electric field. The corresponding potential isolines, depicted in blue in Fig. 2.12, act like the refraction index gradient of an optical lens, and focus the particles on the detector. In the correct field conditions, corresponding to the correct "focal length", the source is imaged on the detector and the measured particle position is proportional to the initial momentum in the detection plane. The detected distribution is then a 2D projection of the 3D particle momentum distribution. In good imaging conditions, it is neither sensitive to the spatial extension of the source nor to the momentum along the axis of the spectrometer (as far as the source volume is contained typically below 2-3 $mm^3$). Note that the gravitational force is completely negligible, but that the geomagnetic field must be compensated with Helmholtz coils, or more conveniently shielded by enclosing the spectrometer in a $\mu$-metal tube (heat-treated Ni-Fe-Mo alloy with high magnetic permeability).

**Implemented Apparatus**

The VMI used in our group has been developed during the PhD of Charles Handschin in 2010-2013. Its plan is displayed in Fig. 2.13. The continuous molecular jet is created from a 200 $\mu$m capillary at 6 cm of the interaction spot, and mounted on a positioning system for alignment. It is supplied by a manifold of flasks containing chiral molecules that can be heated in a bath to increase the vapor pressure, and connected by a gradually heated pipe to avoid condensation. The jet is sprayed in an expansion chamber, pumped by 600 L/s capacity of turbomolecular pumps, and its central part goes to the interaction chamber through a 1 mm skimmer placed at 6-10 mm from the nozzle. The gas jet density is estimated to be $\sim 10^{11}$ molecules.$cm^{-3}$ in the interaction region. The total pumping capacity of the interaction chamber is 2000 L/s, providing a pressure below $10^{-6}$ mbar with the jet, which is necessary to operate the MCP. The MCPs and phosphor screen, of radius 80 mm, can be isolated with a valve. The images are recorded

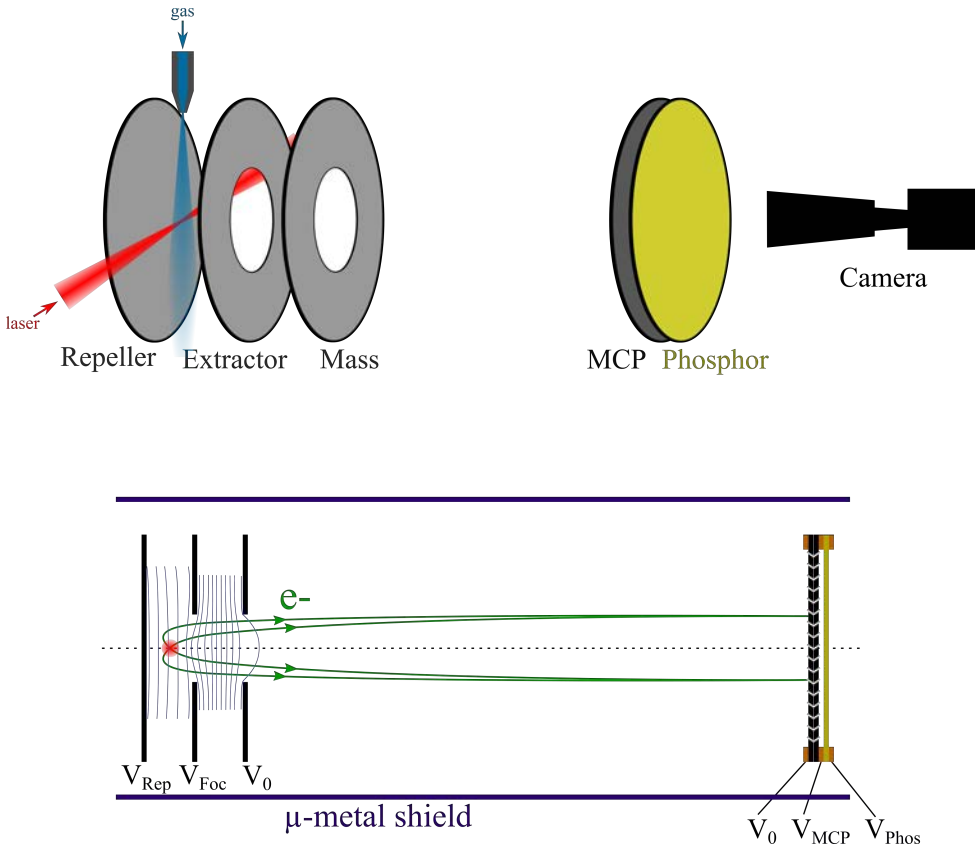


**Figure 2.12** – *Principle of a Velocity Map Imaging spectrometer (VMI). With the correct voltages, the array of plates forms an electrostatic lens which images the photoelectron momentum onto the 2D spatially-resolved detector. Typical voltages used on the VMI at CELIA are $V_{Rep}$ = 1.5-3 kV and $V_{Foc}/V_{Rep}$ = 0.714.*

with a scientific CMOS camera (Orca Flash 4.0, Hamamatsu) with no deadtime between images. The jet and laser can enter through 10 mm holes in the $\mu$-metal shield. The repeller and extractors are separated by 23 mm and the extractor and mass plate by 34 mm. The plates diameter is 11 cm and the drilled ones have a 2.5 cm hole at their centers. The drift region is 500 mm long. This geometry was decided to minimize the aberrations of the electrostatic lens, and be able to detect typical kinetic energies up to 9 eV using $V_{Rep}$ = 2 kV (up to 35 eV with $V_{Rep}$ = 8 kV, at the cost of a lower resolution). The imaging conditions are fulfilled if the potential ratio between the repeller and the extractor is $\frac{V_{Ext}}{V_{Rep}} = 0.714$. The voltages can then be scaled accordingly to get the desired compromise between the resolution and the detection range.

### Ion Detection Mode

A VMI can be operated in two ways, the ion mode or the electron mode, depending on the voltages polarity. In ion mode, the first information of interest is the mass spectrum. It is obtained by measuring the time-of-flight (TOF) on an oscilloscope, by connecting a high pass filter and an amplifier to the MCPs. An important relationship links the TOF and the mass spectrum. In a typical VMI configuration, the acceleration length can be considered as small compared to the one of the drift region $L_d$, and yields the relationship :

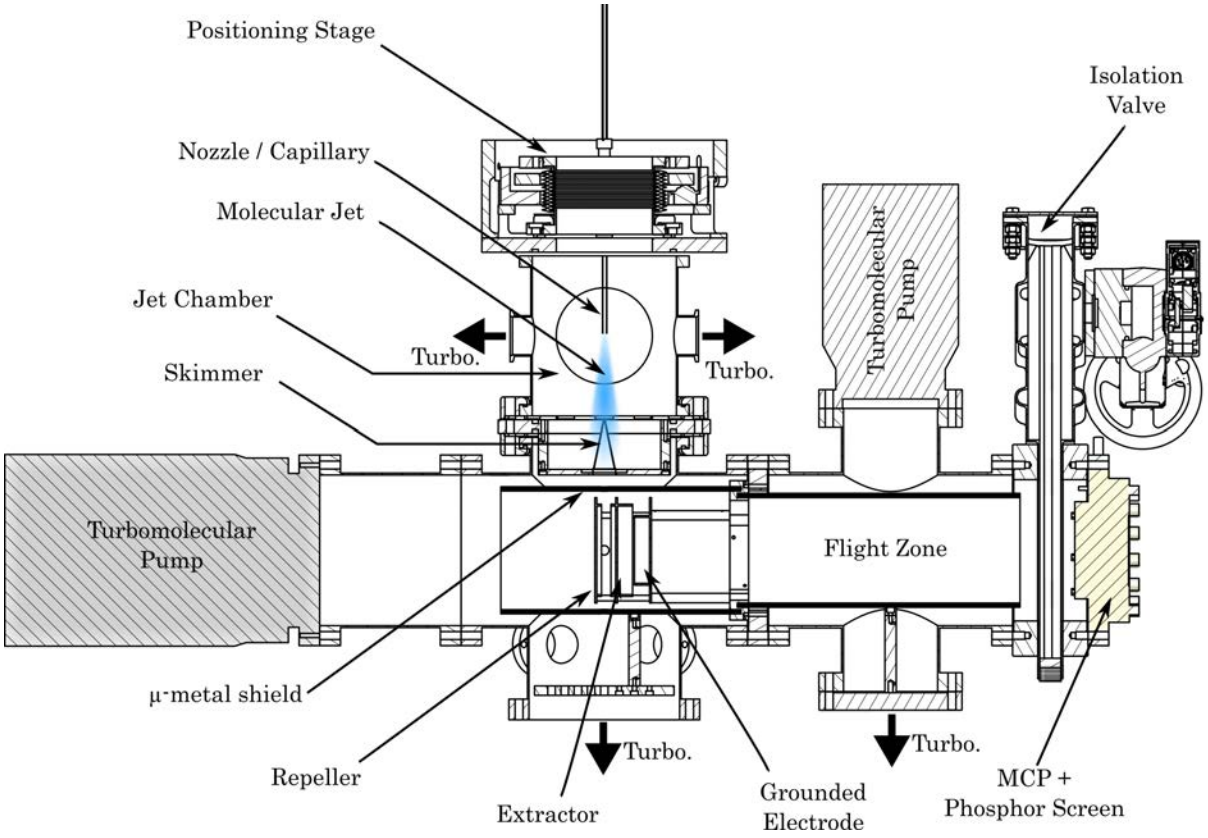


**Figure 2.13** – *Plan of the velocity map imaging spectrometer used. Additional turbomolecular pumps are indicated with the arrows. Extracted from Charles Handschin PhD thesis.*

$$TOF = L_d \sqrt{\frac{m}{2qV_{Rep}}} \propto \sqrt{\frac{m}{q}} \tag{2.1}$$

where $L_d$ is the drift region length, $q$ and $m$ are respectively the charge and the mass of the species and $V_{Rep}$ is the repeller voltage. The mass resolution $\Delta m$ can be derived from this equation to :

$$\frac{\Delta m}{m} = 2\frac{\Delta T}{TOF} \tag{2.2}$$

where $\Delta T$ is the time resolution, driven by the MCP and high pass filter response time and the resolution of the electronics ($\leq$ 15 ns). With a typical $V_{Rep} = 2$ kV, the resolution is about $\Delta m \leq 1$ amu up to 75 amu and $\Delta m \leq 2$ amu up to 300 amu.

Furthermore, the spatial resolution of the detection provides information about the momentum of the ions. We will not extensively discuss this question is the case of the VMI detection, but a similar approach will be presented in the COLTRIMS further in this chapter. Let us simply give a point of reference in the present configuration, where the theoretical resolution is about $\Delta E/E = 3.9 \times 10^{-3}$ (135 meV at 35 eV, $V_{Rep} = 8$ kV), even if this number varies with the energy. In particular, the ion momentum can be interesting to access its recoil energy in the case of photofragmentation processes, and even the axis of fragmentation. Another property of the spatially-resolved detection is the ability to visualize the mass spectrum spatially along

the jet axis. Indeed, the different masses are encoded as spots along this axis as their initial velocity distribution in the jet is fixed by the carrier gas pressure and by the nozzle conductance whatever the species contained in the jet.

Finally, the momentum imaging conditions can be detuned to get a sensitivity to the location of the source. This can be done in order to precisely adjust the focus position of the laser to place it at the center of the VMI. Overall, the ion mode is the more sensitive and is usually the one used for optimization of the laser and jet alignment, and the beam overlap in case of pump-probe studies.

## II. 2 Inversion of the Photoelectron Distributions

The electron mode is the more useful one for us as we are mainly interested in the photoelectron angular asymmetries induced by dichroic light-matter interaction. In this case, the electrons are ejected with a kinetic energy given by the conservation law $E_{kin}^{elec} = n\hbar\omega - E_i$, where $n$ is the number of photons absorbed, $\omega$ their frequency and $E_i$ the transition energy between the molecular orbital ionized and the final ionic state, potentially vibrationally excited. The 3D photoelectron momentum distributions are thus made of concentric spheres or radius $r \propto \sqrt{E_{kin}}$, for the different transitions involved and the different number of photons absorbed, projected on the 2D detector. These spheres are not isotropic and information is contained in their angular dependency, for instance depending on the symmetry of the orbital ionized, the number of photons, the polarization of the field and the chirality of the field and target. The point is thus to recover this angular information partially lost along the projection axis. To illustrate the concepts, we will start by considering unphysical isotropic distributions. The projection of such spheres is schematically represented in Fig. 2.14 (a), for three spheres of different radii and different relative weights. A typical cut of the 2D signal (purple rectangle) is shown in panel (b).

The raw data carries information, such as the maximal ejection momentum materialized by the outer edge of each ring indicating the levels ionized, or qualitative information about the angular structure (missing in the example of isotropic spheres presented here). However, most of the quantitative information can only be accessed by processing the raw signal. Several methods exist, and rely on the cylindrical symmetry of the distributions to retrieve the corresponding 3D distributions. Note that the cylindrical symmetry axis can be either the polarization axis for linearly polarized light or the light propagation axis for circular polarizations. This cylindrical symmetry results from the fact that the molecules are randomly oriented in the jet. One condition must be fulfilled to retrieve the 3D distributions : the symmetry axis must be contained in the detector plane. A first method, called onion peeling [Manzhos 03], consists in angularly integrating the 2D signal, fitting and "peeling" each "layer", from the external to the internal ones, as schematized in Fig. 2.14 (c). This typically can, however, introduce artifacts towards the center by oversubstracting the outer features. Another method is based on the inverse Abel transform [Heck 95], which corresponds to the inverse Hankel transform of the Fourier transform of the projection, and is usually less sensitive to the noise than the onion peeling [Dasch 92]. An improvement in the reliability was achieved with the BASEX method (BAsis Set Extension)

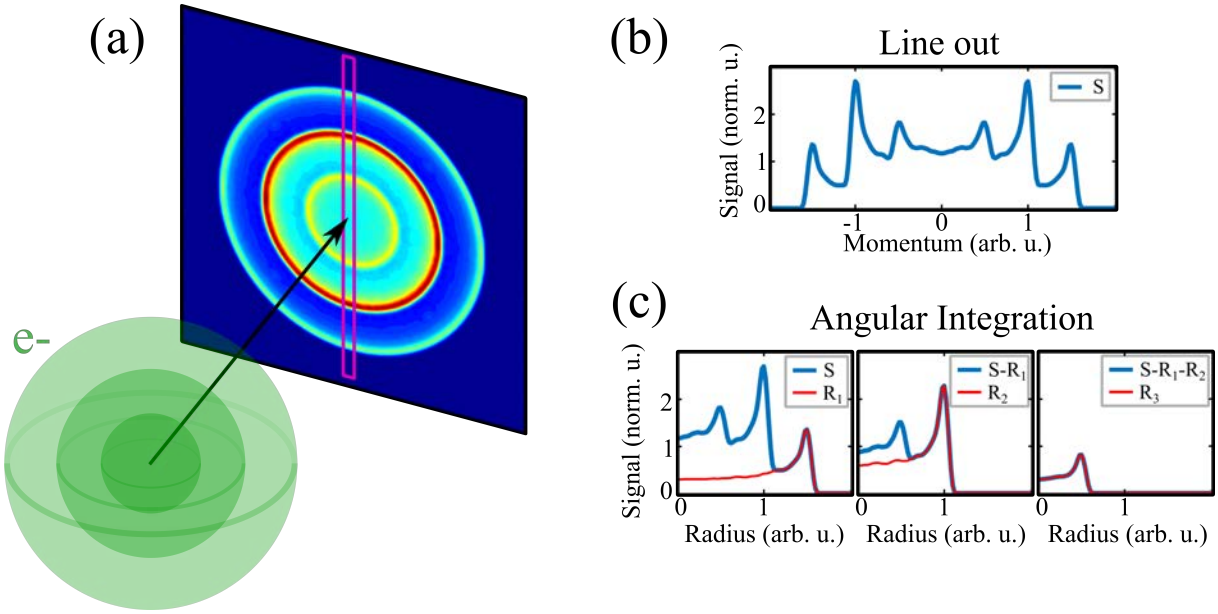


**Figure 2.14** – *Principle of the VMI projection of a 3D photoelectron momentum distribution. Ideal isotropic spheres are schemed here for illustration. (a) 2D projection of three isotropic spheres of different radius, that would correspond to different electron kinetic energies. (b) 1D lineout of the distribution. (c) Principle of the onion peeling, where the peak are fitted and subtracted from great to small radius.*

[Dribinski 02]. It is performed by expanding the projections on a basis of known Gaussian-like functions and fitting the relative contributions. Finally, the BASEX method has been implemented in polar coordinates, namely pBASEX, and is more adapted to the symmetry of the distributions, requiring less functions and less computational power to correctly fit [Garcia 04]. In particular, the pBASEX technique allows on the one hand to directly fit the angular structures in terms of Legendre polynomials $P_i^0$, and on the other hand the radial structures in terms of Gaussian functions :

$$S(r,\theta) = \sum_k \sum_i c_{k,i} e^{\frac{-(r-r_k)^2}{\sigma^2}} P_i^0(cos(\theta)) \tag{2.3}$$

where $k$ are the initial spheres of radius $r_k$, $i$ the order of the polynomials and $c_{k,i}$ a weight coefficient. The angle $\theta$ is defined according to the axis of cylindrical symmetry, *i.e.* the laser propagation axis for circularly polarized fields (or unpolarized light) or the polarization axis for linear polarizations. Indeed, in the electric dipole approximation, the field is homogeneous at the scale of the molecule, in such a way that the polarization effectively describes a circle circle or a line, respectively.

Indeed, while the quantitative retrieval of the radial structures indicates the relative weight of the contributions, the observable we are the most interested in is, as mentioned, the angular structure. Firstly, the angular distributions are never isotropic and are maximized along the light polarization axis, for linear polarizations, or polarization plane for circular ones. Secondly, the photoelectron circular dichroism, extensively discussed in this manuscript, is the forward/backward asymmetry along the laser propagation axis. Essentially, the angular struc-

tured can be naturally described on a basis of Legendre polynomials. More details about their interpretation is given in Chapter 3.

The reconstruction algorithm used in Section 3.IV was developed in our group by Baptiste Fabre and is based on the pBASEX method. The results are usually presented as 2D cuts passing trough the center of the reconstructed distribution and containing the cylindrical symmetry axis, or simply in terms of retrieved coefficients $b_i$ for each radius $r$ on the basis :

$$S(r,\theta) = \sum_i b_i(r) P_i^0(cos(\theta)) \tag{2.4}$$

where $S$ is the signal in the VMI plane, $\theta$ is the electron ejection angle relatively to the cylindrical symmetry axis and $P_i^0$ are the Legendre polynomials of order $i$.

An example of processing on quite noisy PECD data is presented in Fig. 2.15. The horizontal axis corresponds the laser propagation and is the cylindrical symmetry axis here. The pBASEX algorithm is applied to the raw distribution (far left), and the best fit found is presented as 'Rec'. The corresponding central cut 'Inv' reveals features of opposite sign along the horizontal axis that were hidden under the dominant features, but retrieved from the modulation of this latter. Finally, the difference between the raw and reconstructed distributions is depicted on the far right, and has angular symmetries that were not included in the Legendre polynomial basis used (up to the third order here).

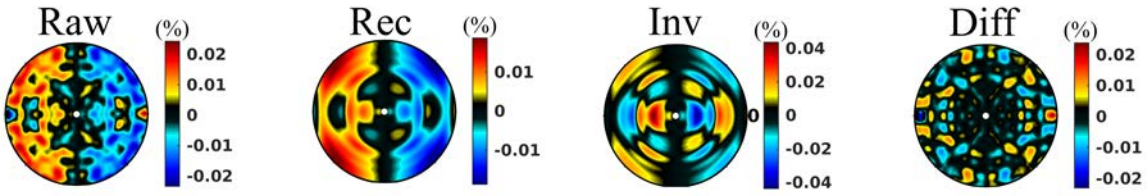


**Figure 2.15** – *Abel inversion of a noisy dataset, recorded using Methyl-Lactate in a [2x400 nm + 800 nm] REMPI process, using Legendre polynomials up to the 5th order. (Raw) raw PECD image, (Rec) reconstructed image, (Inv) Inverted image, (Diff) difference between the reconstructed image and the raw data, which presents contributions of symmetries that can not be fitted with the basis used.*

## II. 3 Tomographic Reconstruction

Unfortunately, all the reconstruction techniques presented above are only valid if the photoelectron angular distribution has a cylindrical symmetry. They can still be applied with any arbitrary distributions, but the result can lose some of its meaning. In several experiments presented in this manuscript, this cylindrical symmetry is broken : the ionizing radiation can be elliptically polarized (Sections 3.II-3.III), a combination of linearly and circularly polarized pulses can be used in a pump-probe configuration (Section 3.IV) or a tailored vectorial laser field can be employed (Chapter 4). While a VMI projection already provides some information on the process and can be used for a first analysis in some of these cases, retrieving the 3D distribution would be interesting. This can be achieved by tomographic reconstruction [Wollenhaupt 09, Smeenk 09].

For doing so, one needs to record $n$ 2D-projections $P_{\theta_i}(p'_x, p_z)$ of the 3D distribution along

different axis $p'_y$ perpendicularly to the laser propagation $p_z$, for angles $\theta_i = i \times \Delta\theta$ with an angular spacing $\Delta\theta = \pi/n$ (see Fig. 2.16). In practice, this is done by rotating the ionizing field along the axis $z$. A discrete inverse Radon transform is then performed on the measured projections $P_{\theta_i}(p'_x, p_z)$ to retrieve the 3D distribution $S$ as :

$$S(p_x, p_y, p_z) = \frac{\pi}{n} \sum_{i=0}^{n} P_{\theta_i}(p_x \cdot cos(\theta_i) - p_y \cdot sin(\theta_i), p_z) \tag{2.5}$$

Note that despite having the same name, this technique is completely distinct from medical tomography for example, in which the measurements are actually performed in spatial slices of the samples.

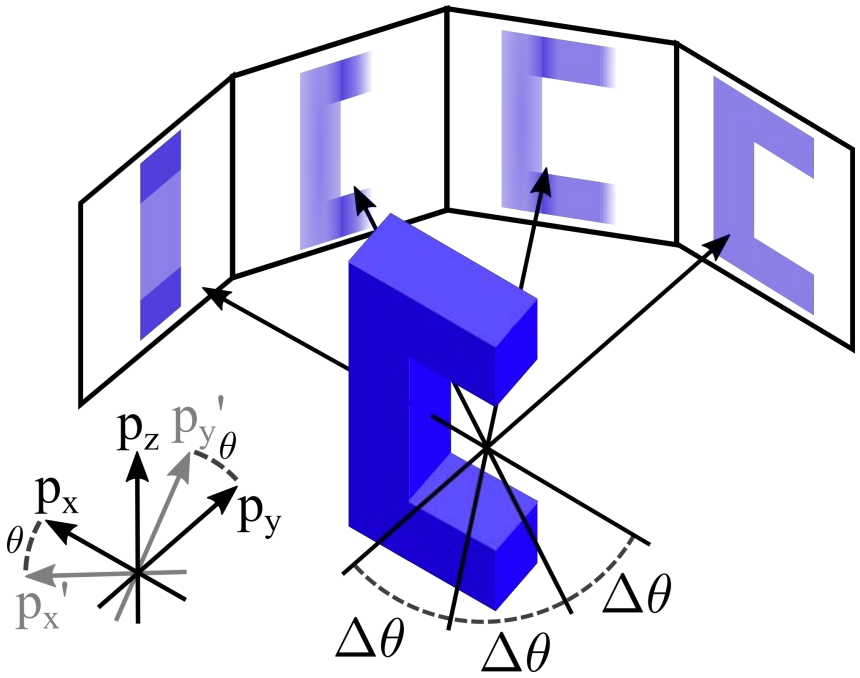


**Figure 2.16** – *Schematic principle of the tomographic reconstruction of an arbitrary 3D object from 2D projections along several axis $y'$ in the polarization plane $(x, y)$. $z$ is the laser propagation axis.*

The tomographic reconstruction takes significantly more acquisition time than the cylindrical symmetry inversion, since it requires $n$ VMI acquisitions for every distribution. Moreover, one can understand from simple sampling considerations that structures finer than $\Delta\theta$ can not be correctly retrieved. This means that complex distributions will require a large number of projections, increasing even more the acquisition time. Nevertheless, the great reduction of the acquisition time provided by our high repetition rate source helps overcoming this issue.

We will see in the next section that we have implemented another photoelectron detector, using delay lines, that is capable of directly access the 3D distributions in a single measurement, at the cost of a slower acquisition rate. Without prior knowledge, determining which technique is the fastest and provides the best resolution is not trivial. A comparison is proposed in Section 3.III of this manuscript.

# III Development of the COLTRIMS

I have been the main person in charge of designing, developing, implementing and testing the COLTRIMS in our group. This was a major task of my PhD and took approximately the entire first year. The unmounted parts, software and technical support were provided by Roentdek GmbH.

After introducing the context, we will see in this section the subtleties of the apparatus, presented in a bottom up progression since the entire setup is designed relatively to the particular detection capacity. Firstly, we will detail the functional principle of the single-particle time-of-flight- and position-sensitive detectors, which is at the core of the device. Secondly, the associated spectrometer bringing the photoions and photoelectrons to their respective detectors will be presented. The ensemble requires a particular arrangement of the interacting molecular target and ionizing radiation, which will be discussed in a third part. Finally, the algorithm used to fully reconstruct the events from the raw data will be detailed.

## III. 1 Brief History

Broadly speaking, the complete investigation of the quantum dynamics of fragmentation processes in the gas phase requires, for each event, the measurement of both the ions and the electrons momenta. A tool, the COLd Target Recoil Ion Momentum Spectrometer (COLTRIMS), or reaction microscope (REMI), has become a staple of this experimentally challenging task. Historically initiated from the Recoil Ion Momentum Spectrometers (RIMS) in particle collisions in Frankfurt in the late 1980's [Ullrich 87, Ullrich 88], continuous improvements have been added by a few groups, mainly at the University of Frankfurt, the Max-Planck Institute of Heidelberg, the Kansas State University and the GANIL in Caen [Dörner 00]. With the advances in light sources, the technique has gradually been adapted to the "photon-matter" collisions, as the kinematic framework remains essentially the same [Ullrich 03], with an unprecedented temporal resolution. Since the 1990's, these detectors are capable of resolving the vectorial momenta of several particles (photoelectrons, photoions, photofragments) with a complete $4\pi$ angle of collection [Moshammer 94, Ullrich 95, Moshammer 96]. Importantly, the technique enables to determine which particles come from the same event, the so-called coincidence. The target can be carried by cold jets, yielding an unprecedented resolution of the order of magnitude of 1 meV for slow photoelectrons and 1 $\mu$eV for the ions, corresponding to few mK temperatures. The ground-breaking completeness of the accessible observables has led to major advances in many light-matter processes, which were discussed in the introduction chapter of this manuscript.

Depending on the particle energies and the resolution required, not all the capacities are necessarily desired. To cite the most common schemes employed, PhotoElectron-PhotoElectron COincidence (PEPECO) can be used to study electron correlations, PhotoElectron-PhotoIon COincidence (PEPICO) resolves the energy distribution between the electrons and ions or the ion- or fragment-dependent photoelectron momenta, and the PhotoIon-PhotoIon COincidence (PIPICO) gives an insight into multifragmentation processes. In particular, if the fragments

are ejected under the axial recoil approximation, the angular distributions can be retrieved in the molecular frame (Molecular-Frame Photoelectron Angular Distribution, MFPAD) without actual orientation or alignment of the molecules.

## III. 2 Detectors

The core of the COLTRIMS capacity lies in the particle detectors (ions and electrons). The signal is firstly amplified by a pair of two microchannel plates (MCPs) (Photonis for the ions, Hamamatsu for the electrons) of diameter 80 mm, stacked in chevron and contacted by a shim (Fig. 2.17). This configuration, where the two plates are relatively rotated by $\sim 180°$ with respect to each other, is commonly used to have a more uniform amplification efficiency with respect to the angle of incidence of the particles. This latter, whether it is an ion or an electron, initiates a cascade of electrons in the channel that exit at the back. Since the detection has to be single-particle sensitive, the bias voltage of the MCP is quite high, +2400 V in our case (+1200 V for each plate). The multiplied signal can then be detected by the delay lines, placed at 7-10 mm from the back of the MCPs. A slight voltage difference is applied here (+260 V) to make sure the electrons reach the delay lines.

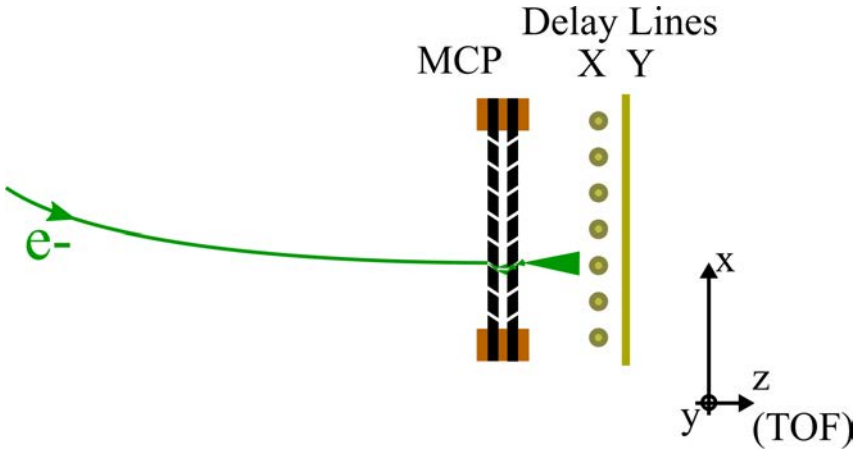


**Figure 2.17** – *Principle of the COLTRIMS ion and electron detector. The microchannel plates (MCP) multiply the particle signal and the stack of delay lines detect the time-of-flight and position, each one along one dimension.*

### Delay Lines

The delay lines are, properly speaking, the detectors and are made of a grid of conductive copper wires. Each layer of the grid is made of a single wire, wrapped in a way that each winding of the wire is parallel to the previous one, with a slight spatial offset, as depicted on Fig. 2.18 (a). When an electron burst comes from a channel, it is partially captured by the wire at one spot. These captured electrons induce a bell-shaped transient signal that propagates in both directions in the wire. The two resulting pulses are detected electronically, and their timings constitute the observable. Each layer provides two timings, say $t_1$ and $t_2$, one for each end of the wire. The position and time of detection of the electron burst can then be calculated, using :

$$\begin{aligned} x_{hit} &= (t_1 - t_2)/2 \\ t_{hit} &= t_1 + t_2 \end{aligned} \tag{2.6}$$

Importantly, the expression of $x_{hit}$ does not depend on the absolute time of detection $t_{hit}$. Moreover, the expression of $t_{hit}$ does not depend on the position of detection $x_{hit}$ and simply corresponds to the sum of the (known) time of travel along the entire wire from a (known) timing reference and the time of travel of the particle, which is the observable. These formulas voluntarily omit the calibration factors, which will be discussed more extensively in the last part of this section. Note that the $t_{1,2}$ timing resolution ($\sim$ 100 ps) is not fine enough to resolve the spatial dimension parallel to the winding. Each layer thus gives a one-dimensional spatial resolution perpendicularly to the winding (see Fig. 2.18 (a)), denoted $x_{hit}$ here, and the time of detection $t_{hit}$. Note that the spatial resolution can look limited here by grid grooving (1 mm). Nevertheless, in practice, the cloud of electrons ejected from the MCP shines across several windings of the wire. The pulses smear out into a single peak during the signal propagation, in such a way that the position is reconstructed from their center of mass [Jagutzki 02]. This means that the spatially discrete collection is actually not encoded in the final signal, and the spatial resolutions are ultimately given by the timing resolution, equivalent to 100 $\mu$m.

In order to get the complete spatial information, for instance along $y$, one needs additional lines. Two solutions exist. The first and simpler one consists in adding a second similar layer orthogonally to the first one (Fig. 2.18 (b)). The front one has enough transmittance to let some signal reach the second one, that then gives from its two timings $t_3$ and $t_4$ :

$$\begin{aligned} y_{hit} &= (t_3 - t_4)/2 \\ t_{hit} &= t_3 + t_4 \end{aligned} \tag{2.7}$$

that provide the wanted set $(x_{hit}, y_{hit}, t_{hit})$ of the particle. The $t_{hit}$ measurement is redundant here. An additional redundancy, for timing but also position, can be achieved by using three delay lines layers in a hexagonal configuration (Fig. 2.18 (c)). This configuration enables a greater detection efficiency, since an event can be retrieved even if one layer missed the electron burst, and has a better multi-hit capacity because two concomitant hits can be more efficiently disentangled. In the hexagonal geometry, the redundancy of the measurement reads :

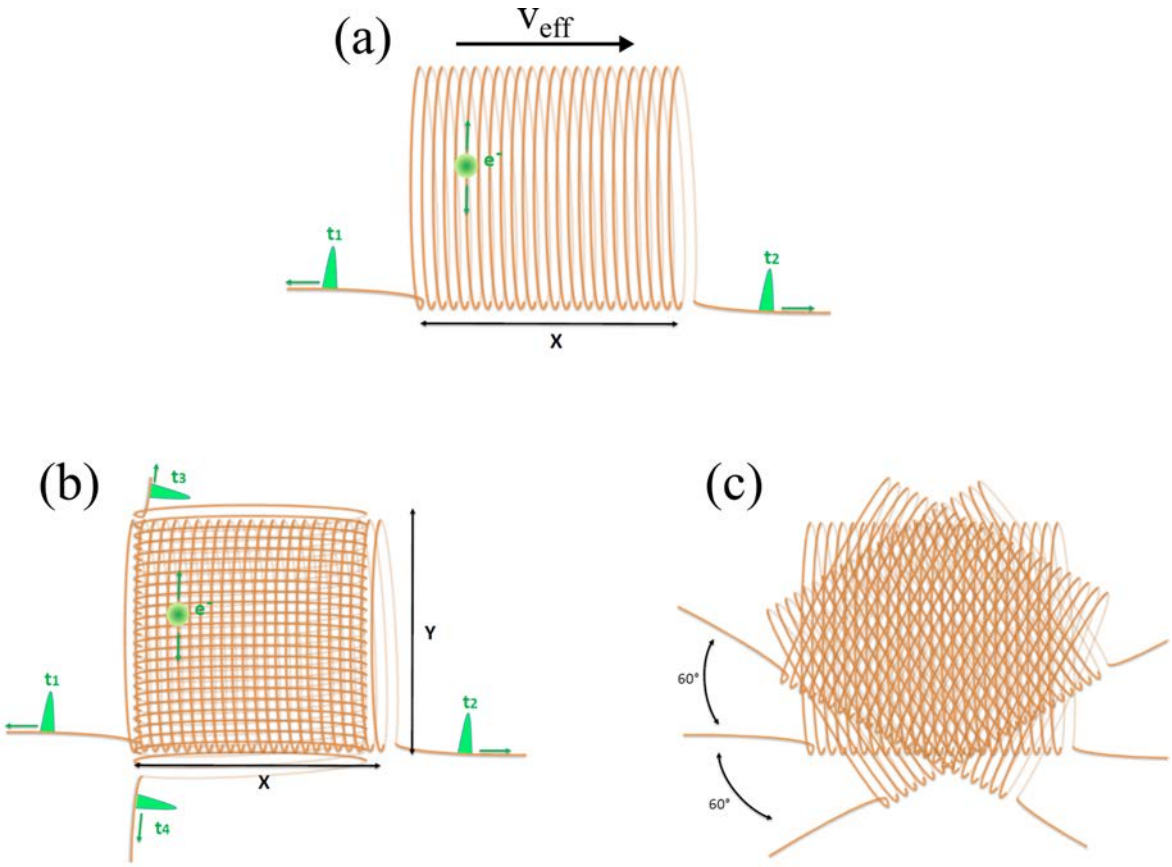


**Figure 2.18** – *Front view of the delay lines. (a) Each line captures some electrons from the MCP that generates a signal that propagates in both directions in the line. The position and time-of-flight are calculated from the timings of these signals. $v_{eff}$ is the effective transverse velocity of the signal in the line. (b) Square delay line configuration, in order to resolve the position in 2D. (c) Hexagonal configuration, to have redundancy of the detection.*

$$\begin{aligned} x_{hit} &= (t_1 - t_2)/2 \\ &= (t_3 - t_4)/2 + (t_5 - t_6)/2 \\ y_{hit} &= ((t_1 - t_2) - 2(t_3 - t_4))/2\sqrt{3} \\ &= (2(t_5 - t_6) - (t_1 - t_2))/2\sqrt{3} \\ &= ((t_5 - t_6) - (t_3 - t_4))/2\sqrt{3} \\ t_{hit} &= t_1 + t_2 \\ &= t_3 + t_4 \\ &= t_5 + t_6 \end{aligned} \tag{2.8}$$

In our case, the ion detector is made of two layers (DLD80, Roentdek GmbH) and the electron detector has the hexagonal configuration (HEX75, Roentdek GmbH), shown in Fig. 2.19.

Note that in practice, each wire is doubled, with a spacing of 0.5 mm. The first wire (SIG for signal) has a $V_{SIG} = +260$ V bias compared to the back MCP to collect the electron burst

**Figure 2.19** – *Picture of the electron hexagonal delay lines with the MCP, mounted on the chamber flange.*

as explained so far. The second one (REF for reference) has a voltage $V_{REF} = V_{SIG} - 36$ V. This way, the REF does not collect the electrons but is as sensitive to the local electromagnetic noise as the SIG. Each end $i = 1, 2$ of each line $j = 1, 2$ or $j = 1, 2, 3$ is made of the difference

$$S_{i,j} = S_{i,j,SIG} - S_{i,j,REF} \tag{2.9}$$

to remove the noise. Additionally, the timings of the voltage variation of the back MCPs caused by the electron multiplication on both the ion and electron side, $t_{MCP_i}$ and $t_{MCP_e}$, are used, as we will see in the last part of this section discussing the reconstruction algorithm. Finally, the timing from the pulse picker of the oscillator of the laser $t_{pulse}$ is also recorded to get a reference. At the end, one ionization event made of potentially several ions $m$ and several electrons $n$ is completely described by the set of timing :

$$event = \{t_{m,i,j}, t_{n,i',j'}, t_{MCP_i}, t_{MCP_e}, t_{pulse}\} \tag{2.10}$$

in our case, 4+6+3 = 13 timing threads.

Contrarily to the phosphor screen used in the VMI, this detector is position- and time-sensitive. Nevertheless, it is not capable of measuring more than a few events at a time (*i.e.* per laser shot), setting a severe restriction in term of acquisition time, even without coincidence. A high repetition rate laser source is thus largely beneficial, even in this latter case. Note that multianode detectors also exist [Gethyn Timothy 16], consisting of an array of anodes which encode directly the spatial information into independent pixels. This type of devices has a better spatial resolution, but is much more complex, and is typically used in space telescopes.

**Electronics**

The entire detection apparatus relies on the measurement of the timings. To do so, the signals are extracted from the DC voltage of the different sources with high pass filters. These filters, as well as the SIG-REF subtracters are contained in two modules (FT12-TP, Roentdek GmbH). The electron MCP signal was isolated with an external decoupler (HFSD). The signals are then carried with shielded wires to the electronics rack to undergo several processing steps, as shown in Fig. 2.20.

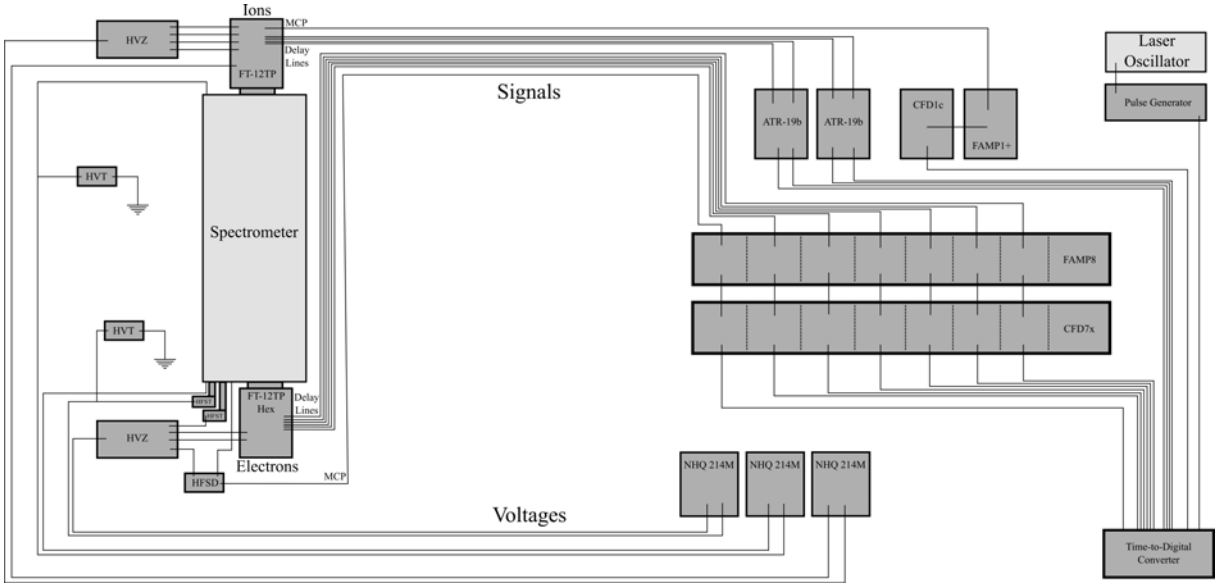


**Figure 2.20** – *Scheme of the cabling of the COLTRIMS spectrometer, with the associated electronics. See text for description.*

Each signal thread is amplified from 0.2-2 mV to about 1 V in fast timing amplifier units (FAMP8 for the electron lines and back MCP, two ATR19-2 and FAMP1+ for the ion lines and back MCP). However, the timings can not be readily measured here. If they were obtained for instance from a simple voltage threshold, they would be sensitive to the amplitude fluctuations (see Fig. 2.21 (a)). Indeed, one hit means one particle and the exact amplitude only depends on the distribution of the MCP gain and the delay lines collection fluctuations, which are completely irrelevant. To avoid this issue, Constant Fraction Discrimination (CFD) modules are used (CFD7x for the electron lines and MCP, FAMP1+ and CFD1c for the ions lines and MCP, Roentdek GmbH).

The principle of the CFD is depicted on Fig. 2.21 (b). The first step consists in splitting the signal $S(t)$ in two with a ratio $R$. One arm is delayed by a time $\tau$ and the other one is inverted. They are finally summed. The resulting signal $S_{CFD} = R \cdot S(t-\tau) - (1-R) \cdot S(t)$ has a temporal profile that starts in the negative values, and goes to the positives. Since an amplitude modulation of the initial signal $S(t)$ would equally affect the terms $R \cdot S(T-\tau)$ and $-(1-R) \cdot S(T)$, the $S_{CFD} = 0$ line is crossed at one given time $T$ that does not depend on the initial amplitude. The amplitude-free timings are thus recorded as the zero crossing point. In most cases, a ratio R=0.5 and a delay $\tau = FWHM/2$ (typically a few ns) is used so that this point is crossed with the steepest slope. In some cases, for example for very noisy or saturated

signal, different settings can be used. The CFD modules have a few additional settings that have to be finely tuned. In particular, the zero crossing trigger has to be enabled from preceding threshold trigger to prevent it from activating from the noise in the early rising edge, as shown in Fig. 2.21 (c). This latter trigger must be tuned for each specific noise and signal level of each line. This also means that the settings are defined for one given MCP gain. Fortunately, each line behavior can be checked on the software and it is pretty straightforward to see if one of them is not enough or too sensitive, as discussed at the end of the section, or if one of the modules failed.

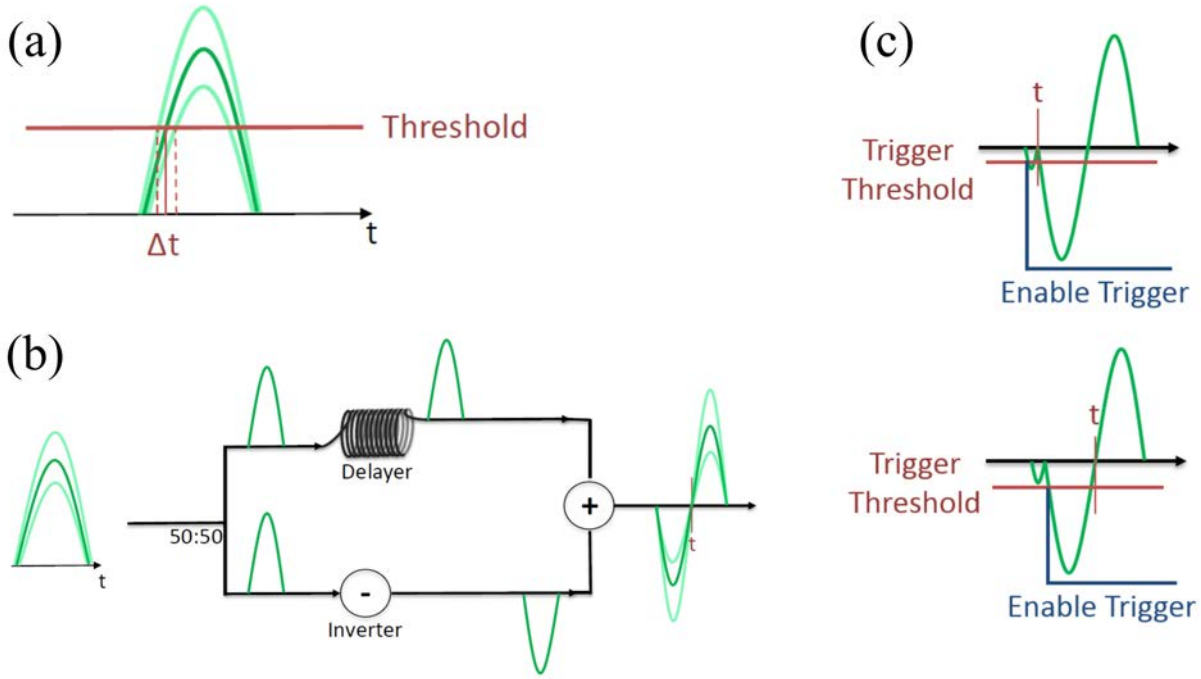


**Figure 2.21** – *Principle of the timing measurement. (a) Simple threshold, giving a dependency to the signal amplitude. (b) Principle of the constant fraction discriminator (CFD). The timing is defined where the signal crosses 0 V, which is in principle not sensitive to the signal amplitude. (c) Tuning of the CFD. The trigger threshold depicted enables the measurement of the timing, and must be high enough to avoid the noise in the leading edge but low enough to not miss an actual count.*

The output of the CFD modules, as well as the clock signal from the laser (conditioned with a Digital Pulse Generator, DG535, SRS), are delivered to a time-to-digital converter (TDC8HP, $<$ 35 ps resolution). The global resolution of the timings is estimated to be about 100 ps in good conditions, and is actually determined by the electronic noise level, whatever its origin.

## III. 3 Design of the Spectrometer

**Purpose**

A lot can be done with COLTRIMSs, but not everything with the same COLTRIMS. Indeed, the capacities of such a device result from a rather subtle interplay between parameters in the spectrometer design, with constraints and compromises, that will be discussed in this section. As a result, each setup is purpose-oriented. In our case, we are mainly interested in the mass spectrum resolution of the ions for typical organic chiral species (about 150 amu for

fenchone, up to a few hundreds of amu for the dimers or trimers), and not really in the vectorial momentum resolution. For example, the measurement of the ions recoil or multi-ions processes are quite secondary. Also, recoil-frame and molecular-frame photoelectron angular distributions (RFPAD and MFPAD) are likely to be inaccessible anyway since the axial recoil approximation (assuming that fragmentation is fast enough compared to the rotation and vibration of the ion) is hardly applicable for these large polyatomic molecules with our quite low energy photons ($\leq$ 100 eV). We aim at resolving the photoelectron angular distributions for low kinetic energies, within $\sim$ 0-10 eV, as the photoelectron circular dichroism quickly vanishes at higher energy. Double ionization processes are not the main goal, but can be of interest. Moreover, we want the first implementation to be rather simple and robust. A simple field configuration is thus preferred. Finally, the chiral molecules have to be carried in the supersonic gas jet, involving a high backing pressure, with a decent density. With that in mind, we converged to the following design.

**Spectrometer Configuration**

Conversely to the VMI, this spectrometer does not require spatial imaging of the momentum on the detectors. Indeed, as we have seen in the previous section, the detectors are position and time-of-flight sensitive, so that the electron trajectories can be explicitly reconstructed, in our case with the commercially available Cobold softwave (Roentdek, GmbH). The entire spectrometer thus consists in an array of plates, spaced by 5.2 mm, imposing a unidirectional gradient of voltage. This generates a homogeneous, constant and isotropic electric field along the spectrometer axis as shown on Fig. 2.22.

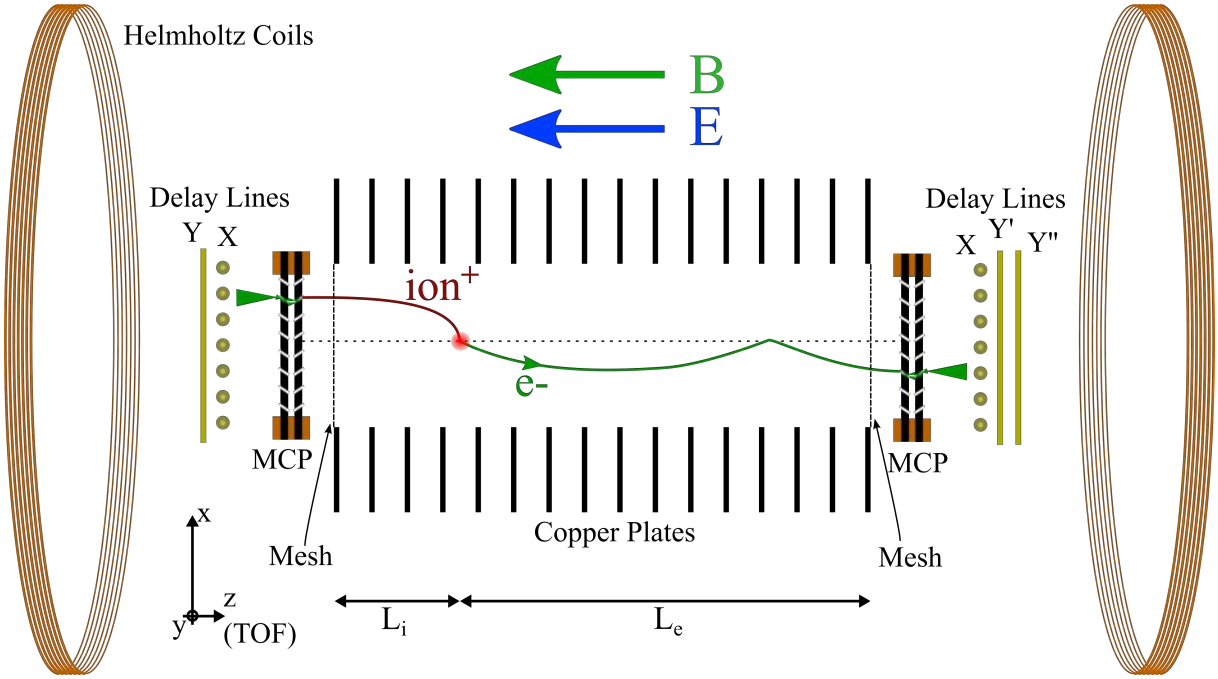


**Figure 2.22** – *Scheme of the spectrometer and detectors of the COLTRIMS.*

The plates are connected in series with resistors (R = 100 $k\Omega$), so that only two voltage supplies are required to polarize the spectrometer. In our case, we maximized the distance of the electron side (55 spacers, $L_e$ = 28.6 cm) to get the best resolution and we have chosen a small

one in the ion side (8 spacers, $L_i = 4.16$ cm) to keep the time-of-flight short. The electric field generated is in general relatively weak in COLTRIMS, of the order of 10 V.cm$^{-1}$, in order to have a decent resolution. However, the MCP efficiency drops significantly for low kinetic energy ions and electrons, as shown in the MCP specifications in Fig. 2.23. For this reason, each side of the spectrometer ends with a short acceleration zone, separated with a metallic mesh placed at 6 mm from the front MCPs. The meshes' transmission is about 80 %. Note that with such a short distance between the interaction spot and the ion mesh, the electric field must be greater than 4.9 V.cm$^{-1}$ to prevent the electrons up to 20 eV to hit the ion mesh, which would cut the electron collection angle and create unwanted signal on the ion detector.

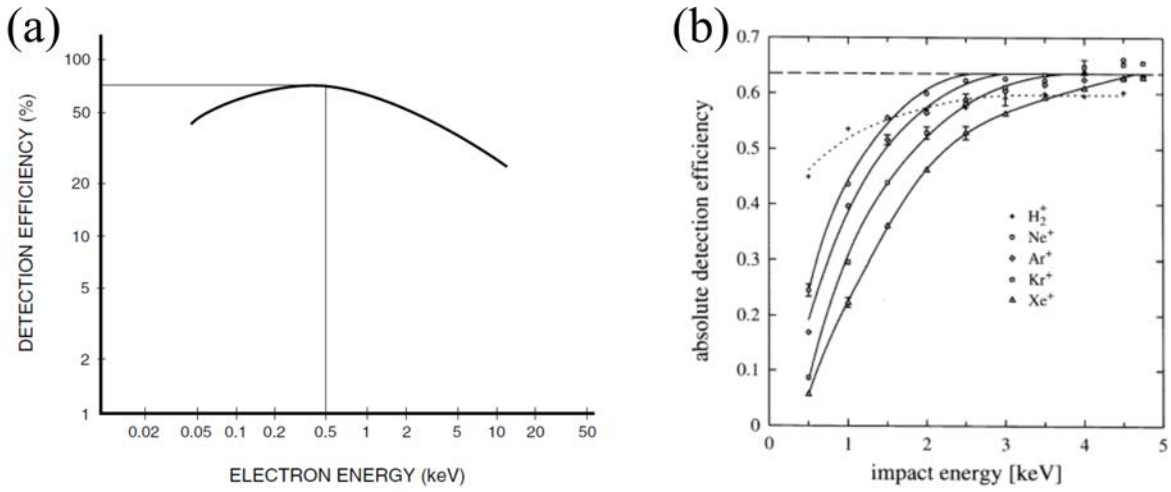


**Figure 2.23** – *Microchannel plates detection efficiency as a function of the particle kinetic energy for electrons (a) and ions (b). The efficiency of the electrons maximizes at 500 eV. The one of the ions requires at least 1 kV and increases with the kinetic energy until saturation around 64 %, more or less quickly depending on the ion mass. We have mostly used total accelerations of +340 V and -2160 V, respectively for the electrons and the ions. Figures adapted from the Hamamatsu MCP manual and [Oberheide 97].*

The entire spectrometer and the ion detector are held on ceramic rods from the vacuum flange, and the electron detector is fixed to the opposite flange. The assembly is shown on Fig. 2.24.

The complete voltage configuration that we have mainly used is displayed in Fig. 2.25. It uses in total only six voltage supplies (HV2/4, Roentdek GmbH), as the detectors voltages are distributed with passive adjustment boxes (HVZ-BA3). The homogeneous electric field generated in the spectrometer is $E \approx 8$ V.cm$^{-1}$. We have noticed that the holes in the electrodes that let the laser and the jet enter the spectrometer can create distortions of the electric field. This imposes that in the area of the interaction volume, the voltages must be about 0 V. This condition and the voltage limitations without creating sparks (especially between the meshes and the MCPs and between the high voltage of the electron detector and the ground), we converged to mesh-front MCP acceleration potentials of -2127 V for the ions and +111 V for the electrons. Including the spectrometer, a total of respectively -2160 V and +340 V are applied. An issue can occur when a low voltage supply is "pulled up" by a higher

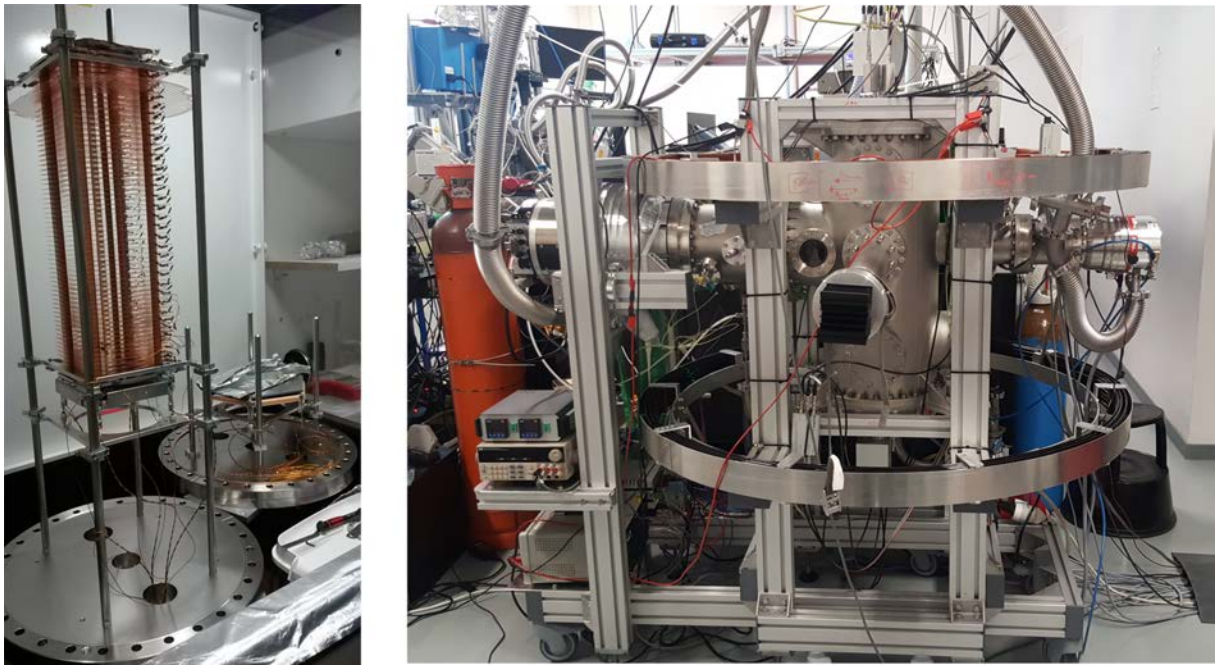

**Figure 2.24** – *(left) Picture of the spectrometer, made of 64 copper electrodes, mounted with the ion detector on a vacuum flange. The electron detector is build on the opposite flange. (right) Vacuum chamber containing the spectrometer. The main Helmholtz coils (120 cm diameter) defining the magnetic field along the spectrometer (vertical) are visible. With this point of view, the laser beam is horizontal and points towards us, while the jet goes from left to right.*

one, though the MCPs or the spectrometer for example. This is circumvented by using load resistors (1 MΩ) connected to the ground (HVT in Fig. 2.20).

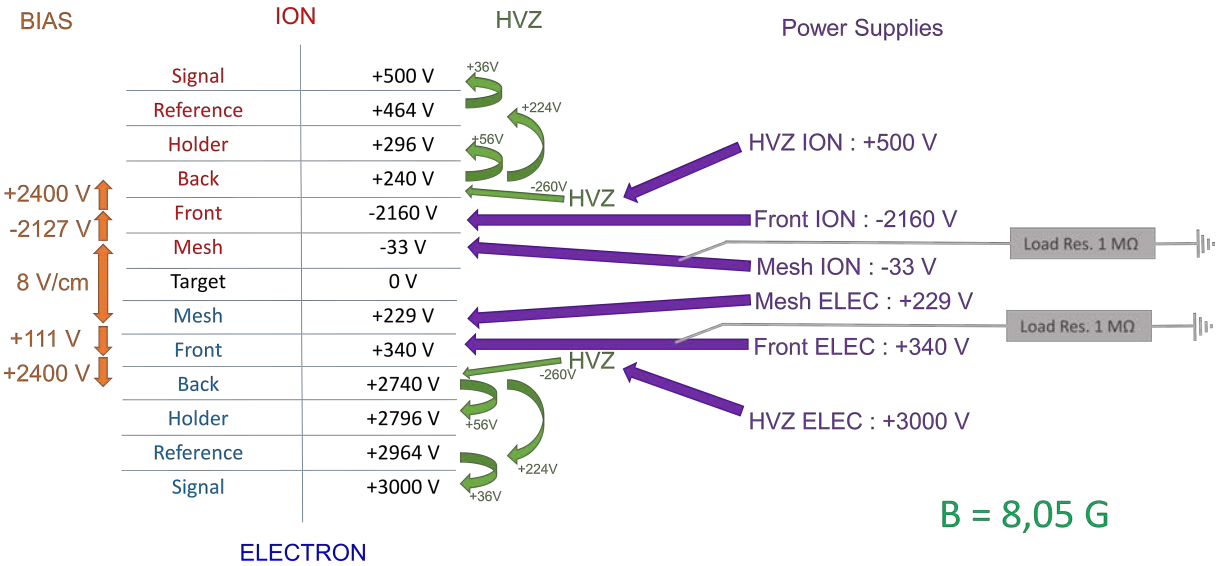


**Figure 2.25** – *Field and voltage configuration of the spectrometer. Only six power supplies are used, thanks to the HVZ (passive adjustment modules).*

### Magnetic Field

With this electric field and spectrometer geometry, the solid angle of collection of the

electrons is lower than $4\pi$ at a few eV of kinetic energy (Fig. 2.26 (a)). This could be avoided with a stronger field, but it would severely affect the temporal resolution, translated into the ion mass spectrum and the component of the electron momentum along the spectrometer. The solution thus consists in confining the electrons in the spectrometer by applying a homogeneous magnetic field along the spectrometer axis (typically of the order of 10 Gauss). This is done using external Helmholtz coils (60 cm radius, 60 cm spacing, 60 windings, horizontal on the Fig. 2.24, right), while smaller ones are used orthogonally to cancel the geomagnetic field. Let us parametrize the space as $(x, y, z) = (r, \theta, z)$, where $z$ is the spectrometer axis and $(x, y) = (r, \theta)$ the detection plane. The trajectories of the photoelectrons will follow a helical motion in the plane of the detectors while their velocity component along the spectrometer (and especially their TOF) is unaffected, as depicted in Fig. 2.26 (b) and (c). The radius of the helix $R_{helix}$ and its angular velocity $\omega_{helix}$ are given by :

$$\begin{aligned} R_{helix} &= \frac{p_r}{qB} \\ \omega_{helix} &= \frac{qB}{m} \end{aligned} \tag{2.11}$$

where $p_r$ is the initial photoelectron momentum component in the $(r, \theta)$ plane, $B$ is the magnetic field amplitude and $m$ and $q$ are the electron mass and charge. This formula also applies for the ions, but their much higher mass/charge ratio renders the helical motion negligible ($R_{helix} \to +\infty$).

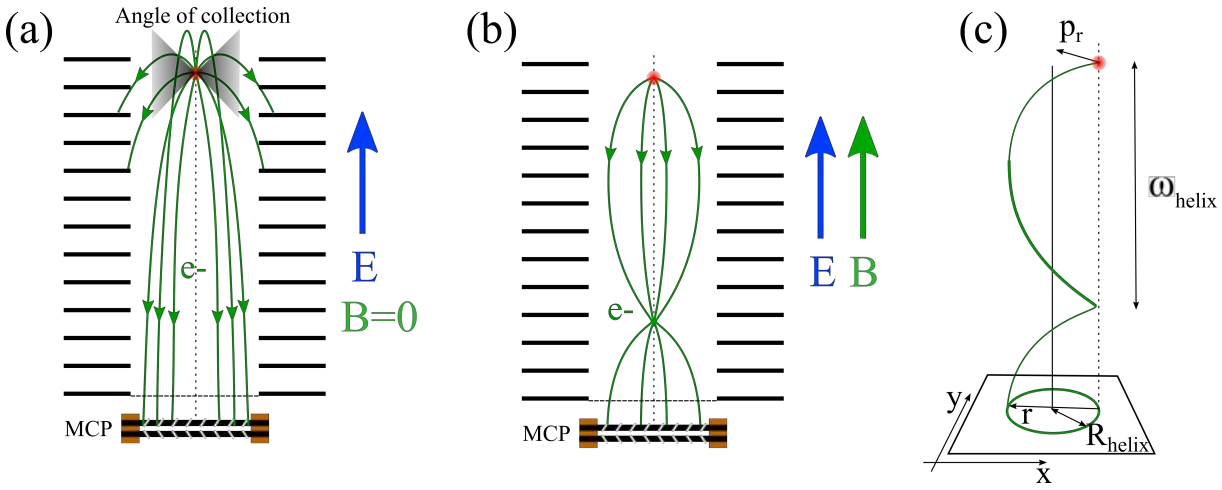


**Figure 2.26** – *(a) Typical photoelectron trajectories in the spectrometer without magnetic field. Only a fraction of the solid angle of emission is collected. (b) Typical photoelectron trajectories in the spectrometer in the presence of the magnetic field. The helical motion keeps the electron in the spectrometer. (b) Parametrization of the helical motion.*

Importantly, the radius of the photoelectrons from the center of the detector $r_{wiggle}$ will oscillate, or wiggle, according to the formula :

$$r_{wiggle} = 2R_{helix}|sin(\omega_{helix} \cdot TOF/2)| \tag{2.12}$$

This means that all the electrons whose TOF is a multiple of $2/\omega_{helix}$ end up at the center of the detector, regardless of their initial momentum in this plane $p_r$. This completely erases the momentum resolution and must be avoided as much as possible. In practice, $B$ has to be set such that the electrons ejected with zero momentum along the spectrometer axis reach the detector at the maximum $r_{wiggle}$ and make sure that the rest of the electrons, within a certain kinetic energy range, does not spread too much in TOF from this value.

**Choice of Parameters**

The optimization of the geometry and fields used has multiple factors. With an electric field of E=8 V.cm$^{-1}$, the time-of-flight of the zero kinetic energy electrons is expected to be 63.8 ns. We chose a magnetic field of B=8.05 Gauss so that the first wiggle ($r_{wiggle} = 0$) occurs at 44.4 ns and the second one at 88.8 ns. For the electrons with kinetic energy of 20 eV, the TOF of the ones ejected towards the electron detector is 47.6 ns (3.2 ns after the first wiggle) and the ones ejected oppositely to the detector is 85.3 ns (3.5 ns before the second wiggle). The spatial resolution is thus significantly reduced for the electrons that have a strong momentum component along the spectrometer axis. With these fields, the maximum radius $2R_{helix}$, which is reached for a 20 eV kinetic energy with $p_z = 0$, is 37.5 mm, meaning we should approximately use the full surface of the detector. The TOF of the ions at 152 amu (Fenchone) is expected to be 12.8 $\mu$s, and 12.75 $\mu$s at 151 amu, which should be largely sufficient to resolve the species with a precision above 1 amu with the $\sim$ 100 ps resolution of the electronics.

We have originally calculated a few other configurations, such as a magnetic field-free one with E=17.5 V.cm$^{-1}$ and a shorter spectrometer length $L_e$. This latter configuration optimized the electron spatial resolution up to 5 eV but diminished too much their TOF resolution, as it was in the 24-32 ns range. We have also tried E=3 V.cm$^{-1}$ and B=5 Gauss, which is close to the finally chosen parameters. The detector radius used by the 5 eV electrons was 30 mm and the TOF spread in the 82-132 ns range. However, for reason discussed in the next section, the ion TOF at 152 amu (20.9 $\mu$s) was limiting the counting rate because it was too long compared to the maximum time separating two consecutive laser pulses (6 $\mu$s at 166 kHz). A summary of the parameters used is given in Table 2.4.

| Spectro. Length | E and B fields | Ion TOF | Electron Max Radius | Electron TOF |
|---|---|---|---|---|
| $L_i = 6.24$ mm<br>$L_e = 11.96$ mm | 17.5 V.cm$^{-1}$<br>0 Gauss | 10.6 $\mu$s (152 amu)<br>10.56 $\mu$s (151 amu) | 37.4 mm (5 eV)<br>5.22 mm (0.1 eV) | 24-32 ns (5 eV)<br>27.3-28.5 ns (0.1 eV) |
| $L_i = 4.16$ mm<br>$L_e = 28.6$ mm | 3 V.cm$^{-1}$<br>5 Gauss | 20.9 $\mu$s (152 amu)<br>20.83 $\mu$s (151 amu) | 30.0 mm (5 eV)<br>4.2 mm (0.1 eV) | 82-132 ns (5 eV)<br>100-108 ns (0.1 eV) |
| $L_i = 4.16$ mm<br>$L_e = 28.6$ mm | 8 V.cm$^{-1}$<br>8.05 Gauss | 12.8 $\mu$s (152 amu)<br>12.75 $\mu$s (151 amu) | 37.5 mm (20 eV)<br>2.54 mm (0.1 eV) | 47.6-85.3 ns (20 eV)<br>62-65 ns (0.1 eV) |

**Table 2.4** – *Examples of parameter set used in the COLTRIMS spectrometer. The first line is magnetic field-free but does not provide enough electron TOF resolution. The second line was originally designed to optimize the electron resolution up to 5 eV, but resulted in a too long ion TOF. The last line has been found to be a good compromise for a first utilization of the COLTRIMS.*

To summarize, in our simple spectrometer configuration, the degrees of freedom are the

spectrometer length of the ion $L_i$ and electron $L_e$ side, the electric field E and the magnetic field B. The goal is to get a short ion TOF, with a decent 1 amu resolution, which is always the case here. One also needs to optimize the electron TOF resolution (with E and $L_e$) and the electron spatial resolution (from B and the electron TOF), for the desired kinetic energy range. The constrains are the radius of the detector, the size of the vacuum chamber, and the voltage limitations previously mentioned.

The actual momentum resolution is hard to get directly from these parameters and will be discussed in Section 2.IV.

## III. 4 Interaction : Jet, Vacuum, Photons

**Supersonic Jet**

The target atoms or molecules are brought in the spectrometer in a supersonic gas jet. In such a jet, the high translational velocity acquired during the expansion translates in a cooling of the internal degrees of freedom (rotation and vibration [Scoles 88]). It is produced with a 30 $\mu$m diameter nozzle connected to a 3/2 mm gas tube with a high backing pressure of carrier gas, typically 2 bars of nitrogen or helium. With a low enough residual pressure (typically $10^{-4} - 10^{-5}$ mbar), the jet expands in a supersonic regime, following the profile depicted in Fig. 2.27. The exact hydrodynamics of the jet is beyond the scope of this manuscript. In brief, the center of the zone of silence is selected with a 200 $\mu$m skimmer placed at 9 mm from the nozzle, in order to get a clean jet profile. A two-skimmers configuration could have been used to have a very narrow translation distribution, but we prefer in our case keeping the distance between the nozzle and the laser short (10 cm) to leave a high target density since one goal is to create Van der Waals complexes. For instance, a helium jet velocity with a backing pressure of 1 bar has been measured from the ion distribution to be 1500 m.s$^{-1}$ in our apparatus.

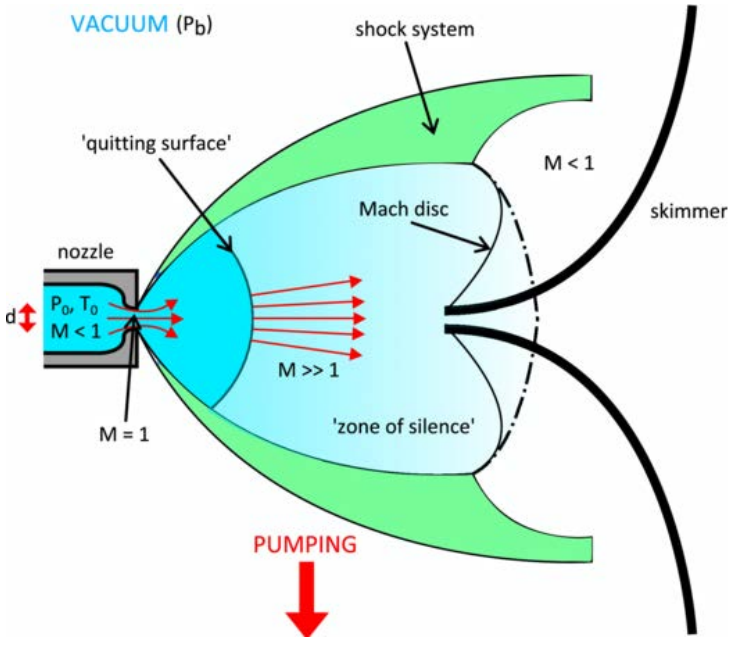


**Figure 2.27** – *Profile of the supersonic flow produced at the nozzle, extracted from [Scoles 88]. The goal is to select the central part of the zone of silence with the skimmer.*

The nozzle is supplied by a line of carrier gas that goes into a bubbler containing the liquid chiral molecules, as shown in Fig. 2.28 (a). This configuration has been chosen since the saturation vapor pressure of the chiral organic compounds is too low to obtain a supersonic expansion (see Fig. 2.28 (b)). The bubbler can be heated in the 20-100°C range to modulate the partial pressure of the chiral molecules. The lines between the bubbler are gradually heated (80-110°C) to avoid condensation. The nozzle is also heated for the same reason, up to 120°C. We expect the jet to have a composition of the order of 1 % of chiral compounds.

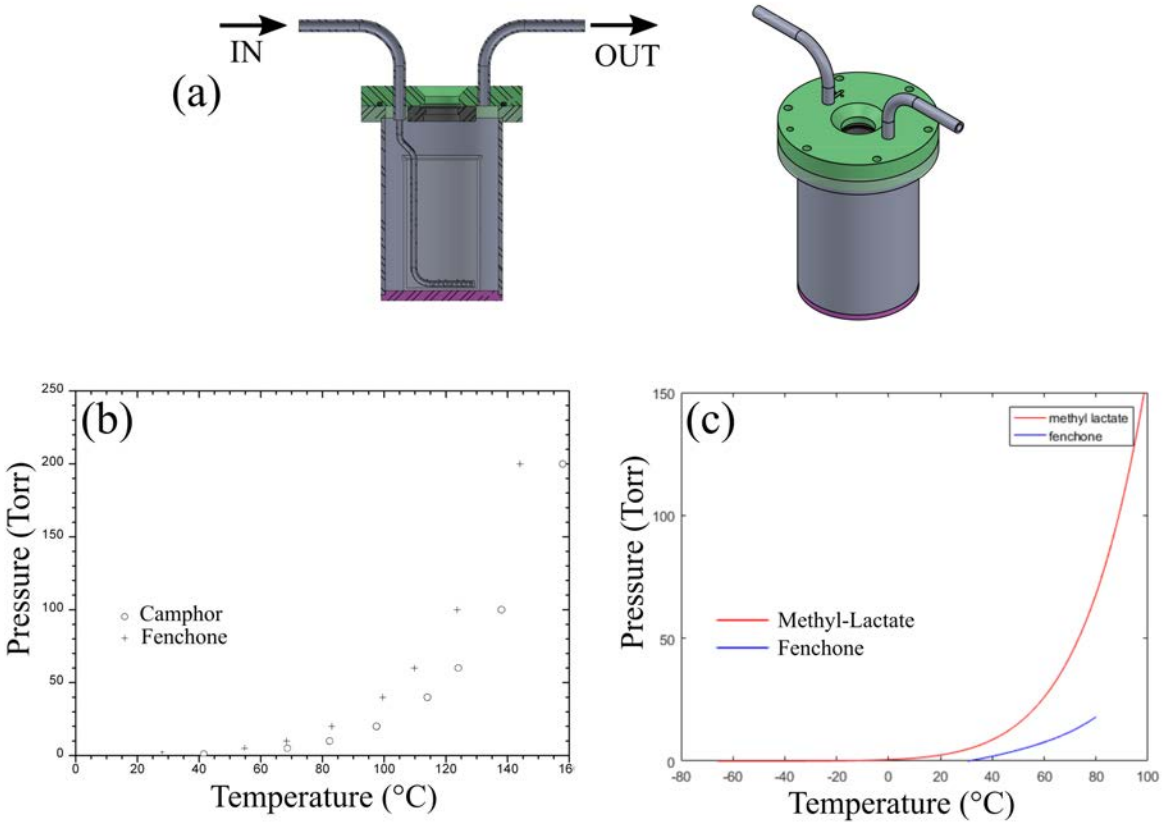


**Figure 2.28** – *(a) Drawings of the bubbler used to evaporate chiral compounds in the carrier gas. (b) Vapor pressure curves of Fenchone and Camphor. These compounds are volatile, but not enough to produce a supersonic expansion. The carrier gas is thus required.*

At the end, the diameter of the jet at the interaction spot with the laser is about 2.5 mm and its density in chiral molecules is estimated around $10^{10}$ molecules.$cm^{-3}$. It must be finely directed in the spectrometer to overlap with the laser beam at its center. In principle, they should all be perfectly centered respectively to the vacuum chamber, and in particular with respect to the optical windows. However in practice, since the spectrometer is fixed from the upper flange, we have noticed that this latter was positioned 1 mm below the expected value. The jet nozzle, skimmer, dump (presented just below) and the laser were thus redefined accordingly.

**Vacuum System**

The vacuum in the spectrometer must be kept at least below $10^{-6}$ mbar for normal operation

of the MCPs and high voltages. In practice a much lower value is required to avoid events coming from the interaction between the laser and the residual pressure, especially with XUV photons. For this reason, the COLTRIMS is split into three chambers, as depicted in Fig. 2.29 (a). The first one is the jet expansion chamber. The gas skimmed out from the jet remains in this part and must be pumped with a high capacity turbomolecular pump (1800 L.s$^{-1}$), for a residual pressure of the order of $10^{-4}$ mbar. The spectrometer and the detectors are in the interaction chamber at the center of the apparatus. It is pumped with two 700 L.s$^{-1}$ turbomolecular pumps for a vaccum reaching a few $10^{-10}$ mbar after two weeks of pumping without jet and about 5 $\times 10^{-8}$ mbar with jet. The molecular beam goes from the skimmer, through the spectrometer and ends in the dual-stage jet dump (see Fig. 2.29 (e)). It is made of two consecutive tubes of respective diameters 10 mm and 15 mm, and of 80 mm lengths that end in two separate chambers. The tubes are designed so that the jet can go though but minimizes the backflow diffusion of the pressure. The first dump is pumped with a 300 L.s$^{-1}$ pump and the second one with a 80 L.s$^{-1}$ one. Each jet dump stage provides an improvement of the pressure of one order of magnitude. With the jet, the typical pressure in the second dump is about $10^{-6}$ mbar.

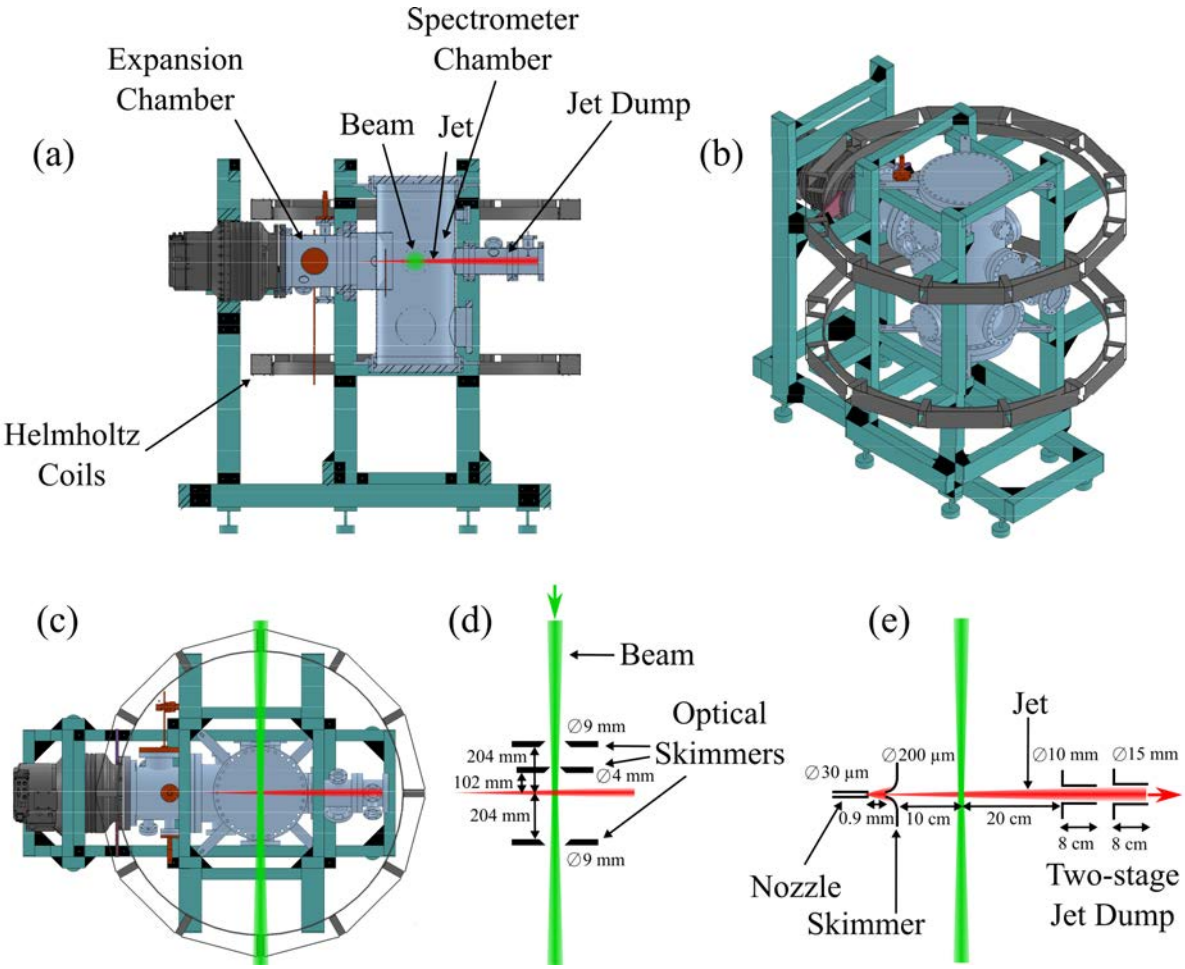


**Figure 2.29** – *Side (a), tilted (b) and upper (c) view of the COLTRIMS apparatus. (d) Details of the optical elements, from upper view. (e) Details of the jet elements, from upper view. See text for details.*

The expansion (or source) chamber and the jet dumps handle high pressure fluxes and

require a good pumping capacity. They are directly backed with a 120 $m^3$/h primary pump. Conversely, the interaction chamber necessitates a good limit vacuum. For this reason, the corresponding turbomolecular pumps backed with a secondary pumping station made of a turbomolecular pump (33 $L.s^{-1}$) connected to a diaphragm pump (HiCube, Pfeiffer Vacuum).

**Laser or HHG Handling**

The photons directly obtained from the laser (1.2 eV) or its second (2.4 eV), third (3.6 eV) or fourth (4.8 eV) harmonic are focused on the jet with a lens placed outside the chamber and enter it through a EUV-grade fused silica window, perpendicularly to the molecular jet (Fig. 2.29 (c)). Due to the size of the chamber, the focal length must be of at least 400 mm. With the $\sim$ 1 mm beam diameter, the focal spot is about 100 $\mu$m for the $\omega_L$ wavelength, 50 $\mu$m for $2\omega_L$, 34 $\mu$m for $3\omega_L$ and , 25 $\mu$m for $4\omega_L$, with a Rayleigh length of respectively 8.4 mm, 4.2 mm, 2.8 mm and 2.1 mm (see Table 2.7). Up to the third harmonic, the photon energy is lower than the work function of copper (4.65 eV) or stainless steel (4.4 eV) and the scattering light does not raise any issue. In this case, the beam directly exits the chamber with an exit window and is sent into a beam dump. However, using the fourth harmonic to interact with the target constituted a big challenge that we have not managed to solve so far. Two types of noise have been identified at $4\omega$. The first one came from scattering light directly hitting the ion MCP, as this latter is 5 cm away from the laser beam, generating fake ion counts and creating electrons that traveled to the electron detector. In principle, these counts could be filtered out since the false ion TOF are instantaneous and the electron noise comes with a longer TOF that the one from the jet. A second source of electron noise came from the photoelectric effect of the scattering light on the copper plates of the spectrometer of the stainless steel walls of the chamber. This one was harder to distinguish from the actual signal. In any case, the sources of noise must be minimized to optimize the useful counting rate since the absolute counting rate is caped by the coincidence condition, as discussed in the next section.

We have found two efficient ways to temper them (see Fig. 2.29 (d)). Firstly, two optical skimmers have been placed before the target (9 mm diameter at 204 mm of the jet and 4 mm diameter at 102 mm) to get rid of the potential halo around the entering beam. This halo can caused by the imperfections of the mirrors and the scattering processes in the lens (even high quality $CaF_2$) and the vacuum window. Secondly, an exit optical skimmer has been placed after the target (9 mm diameter at 204 mm) to avoid backscattering or backreflections. Moreover, the window on this side has been placed 1 m away to minimize the solid angle able to go back into the skimmer. Finally, an XUV mirror has been placed at 45° downwards to direct the beam into a dump that does not have direct vision to the skimmer.

These implementations have also been important for the use of the high order harmonics. The problem was less critical in this case, because the HHG beam is less divergent and can be skimmed more efficiently and because the ionization of the target was performed in a one-photon process, requiring a much lower flux. When using the high harmonics, the COLTRIMS was connected to the HHG line with a differential pumping hole of 5 mm diameter and 47.5 mm length, mounted on a frame that could be tilted from outside. With the beamline shown in Fig. 2.5, the focal length of the HHG beam is of 300 cm resulting in a $\sim$ 55 $\mu$m spot with a much

longer 34 mm Rayleigh length. The implications of this will be discussed in the next section.

## III. 5 Reconstruction Algorithm

The COLTRIMS system described so far is built to detect photoionization of species at a punctual interaction spot in the center of the spectrometer, and measure the momenta of the resulting electrons and mass spectrum of the ions, with a single-particle sensitivity. The measurement of the spatial and temporal detection coordinates are retrieved from the delay lines timings, and are used to reconstruct the photoelectron momentum distribution. This section focuses on the complete reconstruction algorithm, mostly based on the Cobold software (Roentdek GmbH).

**Detector Calibration**

One can start the calibration with noise from an ionization gauge, which is a continuous source of electrons, for example. For now, one "event" is defined with a hit detected on the MCP. The first step is to make sure that all the delay lines work properly. This can be done by plotting the histogram, for each line, of the number of counts detected per MCP hit. An example is given in Fig. 2.30. In the best case, each MCP hit gives one line hit, on each line. In practice, some shots are always missing, meaning the signal captured by the line was not sufficient to trigger the Constant Fraction Discriminator module. To solve this, one could be tempted to increase the sensitivity of this trigger, but this could also induce false counts from the noise. The sensitivity is thus adjusted such that the histogram bars of zero and two counts per MCP hit are close, as shown on the figure. Afterwards, these histograms can be used to easily identify defective lines or electronics.

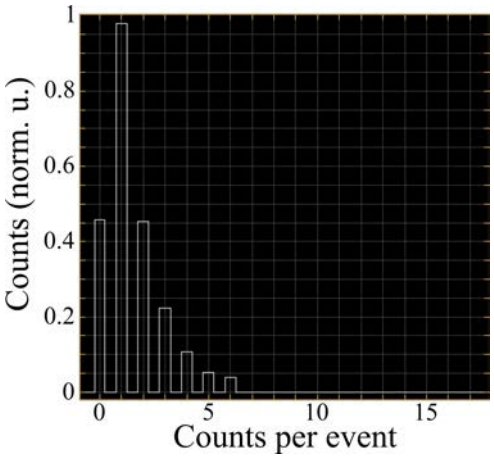


**Figure 2.30** – *Histogram of the number of counts detected per event, for one electron delay line end. In the ideal case, one count should be detected per event. The bar at 0 represents the missing events, and the ones at 2 and higher are mainly due to noise counting. The sensitivity threshold of the electronics is set to balance the lines at 0 and 2.*

Secondly, one must perform at least once the detector calibration, which is specific to the delay lines geometry used. The effective velocity of the pulse though the lines (across the resolved spatial dimension, not along the wire) is calibrated for each line $i$. This is done so that the spatial distribution of the signal matches the MCP radius, and is about $v_{s_i} = 1$

mm/ns. This relates the 100 $\mu$m resolution to the 100 ps timing precision. The distribution is also centered with a parameter $\Delta x_i$, which is proportional to the relative offset between the two ends of each line. Secondly, the delay offset $\Delta t_i$ between the different lines $i$ is determined so that the time sum between the two ends of each line $t_i + t'_i$ are the same. This correction $\Delta t_i$ accounts for the difference in the total length of the lines and cables to the electronics, and is only set relatively between each lines $i$. From there, one needs to get signal from the laser source. The last parameter that must be found to get the actual TOF is the absolute time offset $\Delta t_0$ from the reference, given by the laser clock $t_{pulse}$. It depends on the optical pathway of the beam, and has to be found for each detector since they are not synchronous so far. At this point, $t_0$ can be set roughly, and will be refine further in the process. The position and time-of-flight is thus obtained for each line timings $t_i$ and $t'_i$ measured :

$$\begin{aligned} x_i &= \frac{t_i - t'_i}{2v_{s_i}} - \Delta x_i \\ TOF_i &= t_i + t'_i - \Delta t_i - \Delta t_0 - t_{pulse} \end{aligned} \tag{2.13}$$

**Physical Observable Reconstruction**

The detection capacity is in principle the same for the photoelectrons and the photoions. However, in our case, the ions side will be primarily used as a mass spectrometer. In this case, the ion TOF spectrum simply has to be calibrated with the ion TOF reference $\Delta t_0^{ion}$ in Eq. 2.13 and a square scaling. This can be done explicitly from the spectrometer configuration characterized by the electric field $E$ and the length of the ion side $L_i$, as :

$$\frac{m}{q} = \frac{E}{2L_i}(TOF^{ion})^2 \tag{2.14}$$

but in most cases, it is eventually done with a few known species of mass $m_{ref}$, following :

$$\frac{m}{q} = \frac{m_{ref}}{q_{ref}} \cdot \left(\frac{TOF^{ion}}{TOF^{ion}_{ref}}\right)^2 \tag{2.15}$$

Most of the complexity lies in the reconstruction of the 3D photoelectron momentum distributions (at the target). In our simple field configuration, it can be calculated explicitly from the detected quantities. All the axis are not equivalent, and one must start with the one along the spectrometer, denoted $z$, as it is not affected by the magnetic field. From the electron acceleration length $L_e$ and the electric field $E$, $p_z^{elec}$ can be retrieved from the measurement only of the electron TOF as :

$$p_z^{elec} = m_e \cdot v_z^{elec} = m_e \frac{L_e}{TOF^{elec}} - \frac{eE}{2} TOF^{elec} \tag{2.16}$$

The electron detector global offset $\Delta t_0^{elec}$ in Eq. 2.13 can be precisely adjusted here to get the zero kinetic energy electrons time-of-flight by centering the $p_z$ on zero, as shown in Fig. 2.31.

After this calibration, the photoelectron momentum in the detector plane $(x, y)$ can be cal-

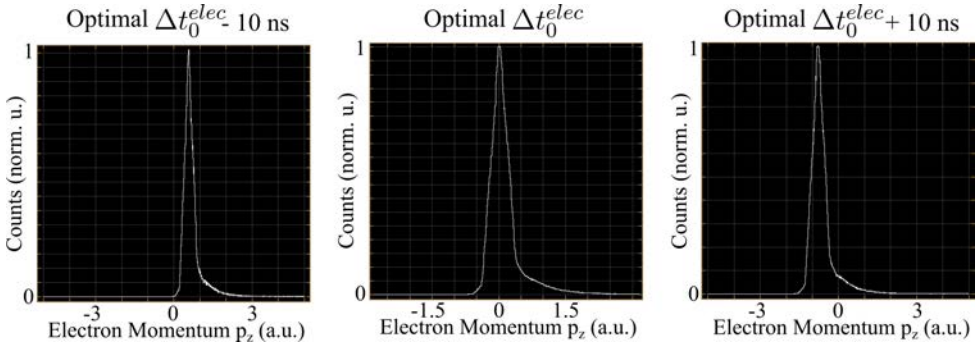


**Figure 2.31** – *Reconstructed distributions of the photoelectron momentum along the spectrometer axis, for different timings references. The central panel is retrieved with optimal parameters, while the panel on the left (right) shows the deviation with a -10 ns (+10 ns) error. Note that a ± 1 mm drift of the laser pointing, which is of the order of the aperture of the COLTRIMS, only induces a ± 0.1 ns deviation.*

culated. Primarily, the geomagnetic field must be compensated with small correction Helmholz coils, placed along the laser axis and along the jet axis. The currents are tuned so that the electron distribution is centered on the detector, as shown in Fig. 2.32 (a). This can also be used to shift the distribution, to avoid damage on the detector for example. As this magnetic field is relatively weak, one can consider the deflection as almost linear, but non-linearity corrections can be implemented in the software. A stronger magnetic field $B$ along the spectrometer axis is generated with the main Helmholtz coils. It imposes a helical motion in the detector plane, as depicted in Fig. 2.32. The angular frequency only depends on the magnetic field as $\omega_{helix} = \frac{eB}{m_e}$, and with a polar parametrization ($r = \sqrt{x^2+y^2}, \theta = arctan(\frac{y}{x})$), the radius of the helix is can be written $R_{helix} = \frac{p_r}{eB} = \frac{r}{2}|sin(\omega_{helix} \cdot TOF/2)|$. The projection on the $(x, y)$ plane of the emission momentum $p_r$ and its angle $\varphi$ can be found from the detected $r$, $\theta$ and $TOF$ as :

$$\begin{aligned} p_r &= \frac{e \cdot B \cdot r}{2}|sin(\omega_{helix} \cdot TOF/2)| \\ \varphi &= \theta - \frac{\omega_{helix} \cdot TOF}{2} \end{aligned} \tag{2.17}$$

or, in Cartesian coordinates :

$$\begin{aligned} p_x &= p_r \cdot cos(\varphi) \\ p_y &= p_r \cdot sin(\varphi) \end{aligned} \tag{2.18}$$

A relevant plot to tune the physical value of the magnetic field is $x = f(TOF)$ (or $y = f(TOF)$, $r = f(TOF)$), shown in Fig. 2.32 (c), in logarithmic color scale. The electron wiggles are perceptible in the spread, weak signal baseline here in the tail of the distribution of hits, highlighted with the while lines. This graph enables to make sure that the TOF of the zero kinetic energy electrons (65 ns) matches the maximum radius of the wiggle, *i.e.* has the best spatial resolution. In addition, this also illustrates the fact that the electrons in the range of interest in the experiments (around 65 ns) with a strong momentum component $p_z$ (*i.e.* with

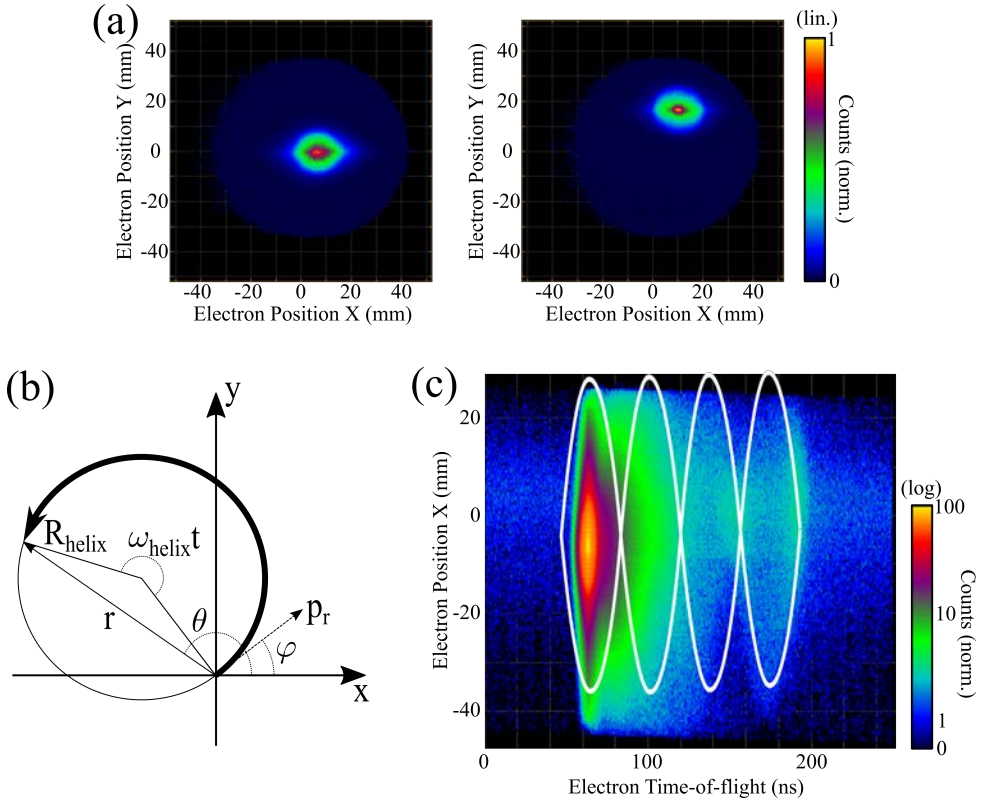


**Figure 2.32** – *(a) Photoelectron $(x, y)$ spatial distributions with and without the compensation of the geomagnetic field, (b) Parametrization in the detector plane of the helical motion (wiggles) of the photoelectron trajectories, for an initial momentum component $p_r$ in the detection plane $(x, y)$ at an angle $\varphi$ and a detected radius $r$ and angle $\theta$, (c) Photoelectron spatial detection coordinate as a function of the time-of-flight, in logarithmic color scale. The spread, weak baseline distribution follows the radius oscillation with the time-of-flight, highlighted with the white lines. The magnetic field is set so that the resolution of the signal, in the first wiggle, is maximized.*

a TOF much greater or smaller than the central value) have a lower spatial resolution as they come closer to the wiggle nodes.

A schematic representation of the reconstruction algorithm is presented in Fig. 2.33. In principle, all the parameters result directly from the spectrometer configuration, and have been chosen with the simulations based on the desired resolution and range of detection. However, their actual values in the physical setup can slightly vary compared to the prediction (for instance $E = 8.2$ V.cm$^{-1}$ instead of 8.0 V.cm$^{-1}$, or $B = 8.25$ Gauss instead of 8.05 Gauss). While this does not really affect the spectrometer capacity, the reconstruction parameters used in the algorithm must be precisely adjusted. This is based on physically relevant observations, for example a wrong magnetic field parameter induces an elliptical shape of the distributions. Most of the time, each parameter adjustment have multiple effects, in such a way that their optimization is done iteratively and can be fastidious. Importantly, they can be a source of loss of resolution, which can be non trivial to quantify. This question will be discussed in the section of this chapter dealing with the characterization of the resolution of our setup.

**Coincident Events**

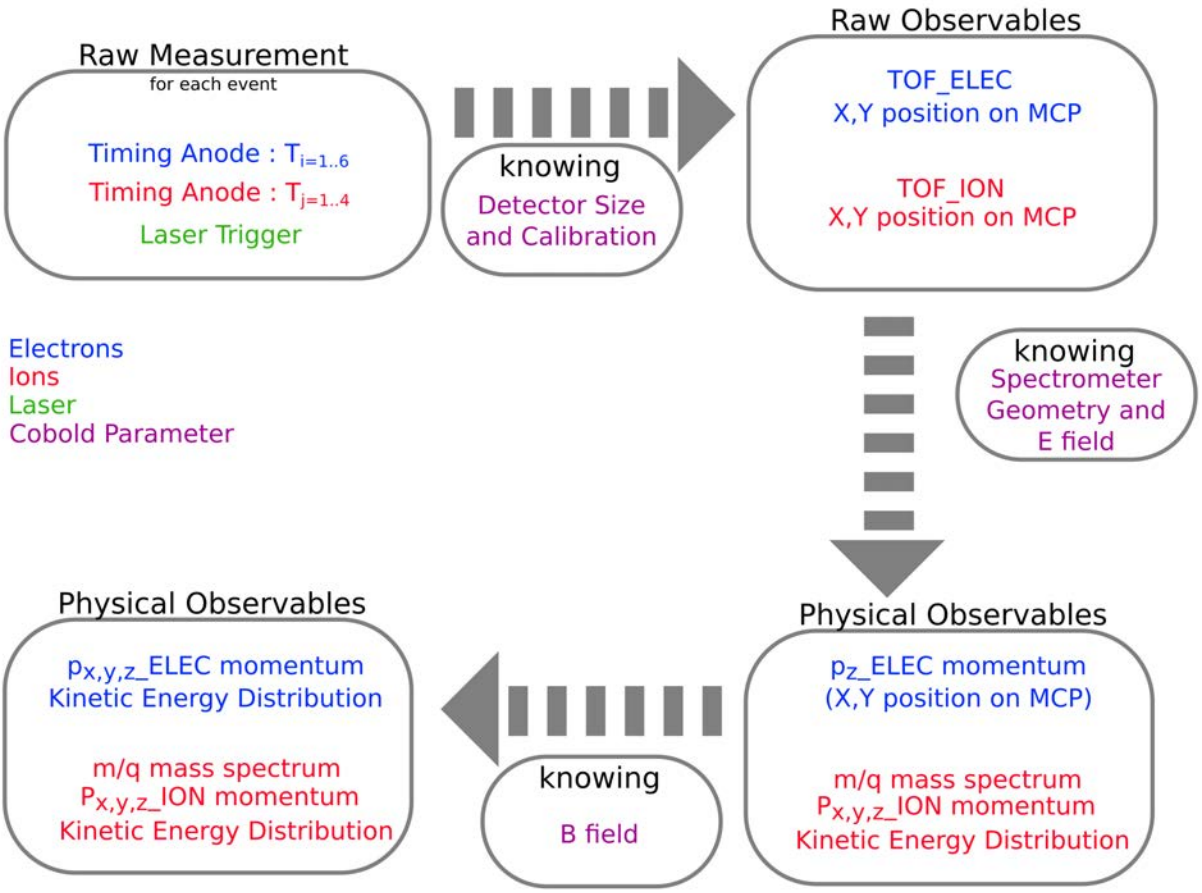


**Figure 2.33** – *Scheme of the reconstruction algorithm described in the text. The raw data only consists in timings, from which the physical observables are reconstructed knowing the spectrometer configuration and fields.*

Once the software is set to reconstruct the detected ion and electron counts, an important task is to assign the coincident events, meaning grouping the particles that came from the same ionization event. To do so, no more than one ionization must be done per laser shot, otherwise it is almost impossible to know which electron came from which ion. This is achieved by adjusting the energy per pulse (tuning the laser intensity and repetition rate). Ultimately if the laser conditions are fixed it is possible to modulate the rate of ionization per shot with the gas jet density (with the backing pressure, by heating the bubbler or with a different skimmer configuration). Practically, the number of ionization per shot is set to be statistically about 1/10, namely the coincidence condition. This, of course, limits the counting rate (∼16 kHz at a repetition rate of 166 kHz), and does not completely exclude the double events. For this purpose, filters can be applied, as developed in the next section.

The events assignment can be done in two ways, in a window mode or in continuous mode. In window mode, which is the mode that we have used throughout this thesis, a trigger is defined on one channel event (electron, ion or laser short). A time window is then open for a given duration, and any detected event in the window is labeled as coming from the same ionization event. In our case, the trigger was set on the electron detector. The window is

opened 500 ns backward in time (with a buffer) to detect the preceding laser timing, and a few dozens of $\mu$s forward in time to collect the ions (see Fig. 2.34 (a)). In this configuration, the trigger could be activated from a background electron that does not come from the jet. To avoid this, the window is not triggered if no laser shot was found just before the electron (meaning if the electron TOF is not consistent with a regular kinetic energy). The advantage here is that the reference shot is found easily. Different configurations have been tested, for example using the ion as the trigger and using a longer backward window to collect the corresponding electron (Fig. 2.34 (b)). This could be an advantage as the ion detection efficiency is usually lower than the one of the electrons. It is thus less likely to open a window for nothing from an ion with a missing electron than from an electron with a missing ion. However with the trigger on the ions, the electron could be wrongly assigned to the previous window, meaning a window would be opened for nothing (Fig. 2.34 (c)). Additional issues can occur with ion trigger, in such a way that we prefer triggering on the electrons. For instance, if several electrons and ions are ionized from different laser shots but are recorded in the same window, a filter can be straighforwardly applied to recover at least the event that has opened the window if this latter is triggered by an electron, while this is much more complex if it is triggered by an ion.

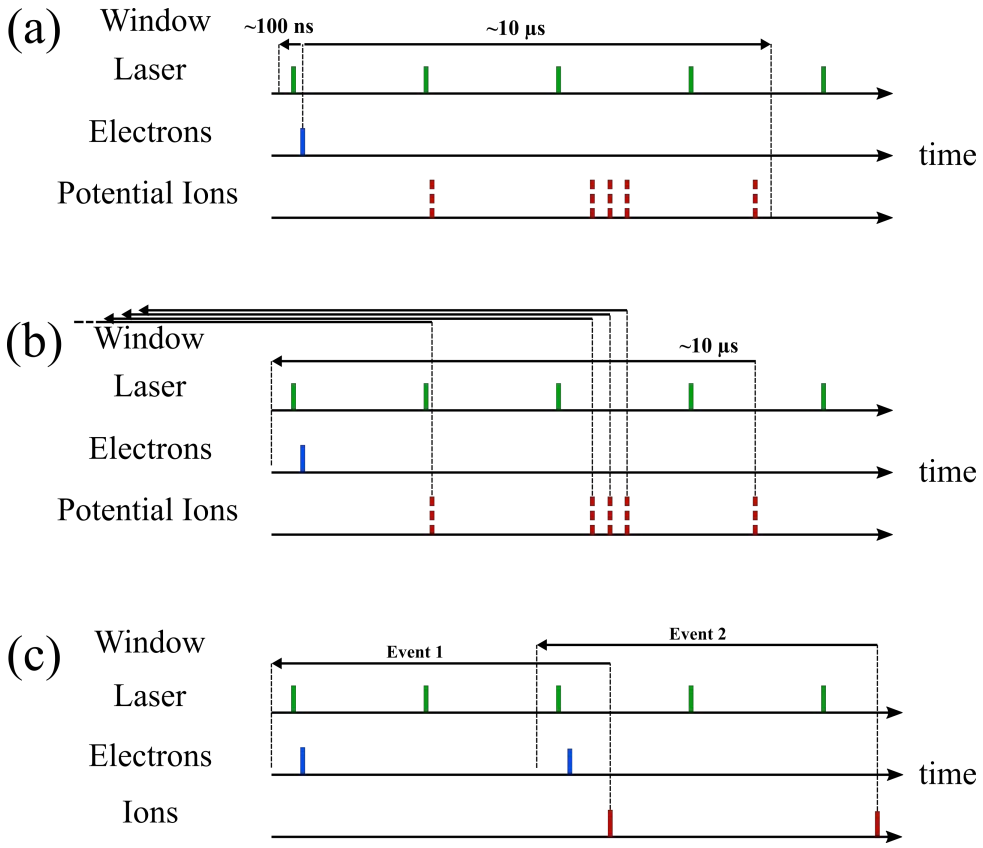


**Figure 2.34** – *Timeline of the window acquisition mode. (a) Trigger on the electrons. The window is open backward in time in a buffer to get the laser shot reference and forward to get the coincident ion, up to the heavier mass. (b) Trigger on the ions. The window is open backward to get the electron and laser short. Note that in principle only one of the potential ions depicted in (a) and (b) is produced for one electron. (c) Example of issue encountered with the trigger on the ions, where the coincident electrons is counted in the previous window.*

In any case, the window scheme is robust but suffers from several limitations. Firstly, only one window can be open at a time. This limits the counting rate at best to $1/T_{window}$ where $T_{window}$ is the total window duration, completely independently of the coincidence condition. $T_{window}$ must be at least the TOF of the heavier ion to be able to count it, and can become problematic for heavy species. Indeed, the TOF of the Fenchone (152 amu was about 21 $\mu$s in the first electric field configuration used, giving at best a counting rate of 48 kHz for the monomers, 34 kHz if we want to be able to detect the dimers, and so on. For this reason, we moved to a higher electric field value at the cost of resolution, so that the TOF of the Fenchone was of 12.8 $\mu$s. Depending on the ion species of interest, it can be worth to cut the window just after its TOF, especially for light fragments. This does not prevent the windows from opening for nothing, but at least they open for a shorter duration and the next event can be more quickly detectable. Indeed, a second issue comes from the fact that the minimum repetition rate of our laser source is 166 kHz. While the high repetition rate is absolutely necessary with COLTRIMS because of the coincidence condition, the maximum duration between two laser pulses is 6 $\mu$s, *i.e.* less than the typical ion time-of-flight. If a first event opens a window and a second event happens from the next laser shot, the second one is unusable (as in Fig. 2.34 (c)). Worse, the ion mass spectrum of the first event can be mixed with the one of the second event. We will see in the next section a way to filter this out, but it still means that a count that is in principle usable is lost. Also, this issue worsens with the laser repetition rate, and limits the use of the full tunability of the source, up to 2 MHz.

This concern has already been encountered with the synchrotron sources, historically used with COLTRIMS. One way to overcome it is to do the acquisition in continuous mode. Instead of triggering windows, all the events are recorded and the assignment is performed afterwards (Fig. 2.35). This requires, however, that the mass spectrum is not too congested so that the assignment is unambiguous.

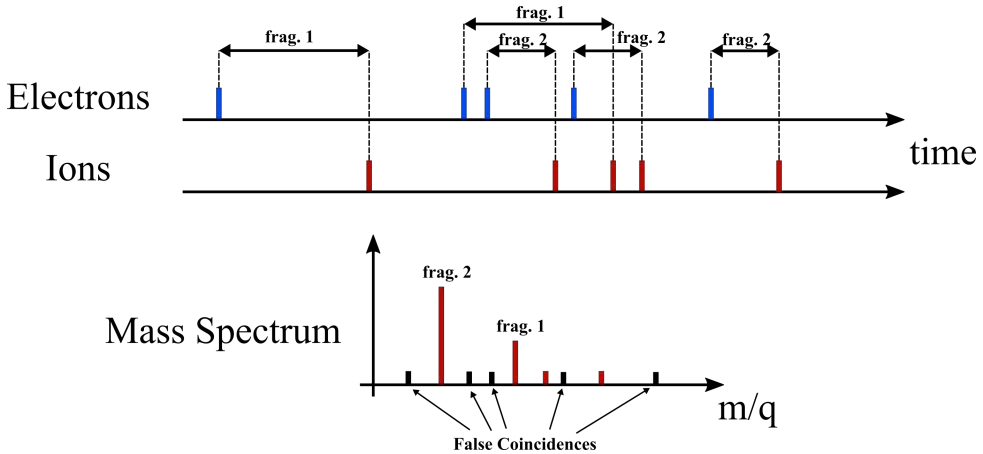


**Figure 2.35** – *Principle of the continuous acquisition mode, where the coincidence is determined in post-analysis based on the known mass spectrum. False coincidences appear as unreasonable masses.*

The spatial resolution of the ion detector can be used to get an additional time reference. An example was recently demonstrated, and consists in adding ion deflection plates in the

spectrometer [Osborn 16]. Supplied with varying voltages, the deflection, *i.e.* the detected ion position, depends on the time at which the ionization was performed. Combined with the time-of-flight, one can retrieve the original laser shot without the electron informations. The electrons and ions can thus be unambiguously assigned, regardless of the mass spectrum complexity. We will see in the next section that we also use the ion spatial information in a similar fashion.

Up to this date, the Cobold software we are using is based on the window mode. Implementing a continuous acquisition mode is an appealing perspective that is currently being investigated, in order to increase the repetition rate limitation. Note that in the studies where we were only interested in the photoelectron angular distribution, the window mode could be used with a much shorter window duration. Without this limitation and the coincidence condition, the electron counting rate could be easily increased up to 100 kHz. This was very useful to quickly measure 3D distributions with good statistics. Beyond this counting rate, the recovery time of the individual channels of the MCPs becomes comparable to the time between two hits ($\sim$ 1 ms). This diminishes the multiplication efficiency and the hits can not trigger the CFD modules anymore. This is typically indicated by a depleted signal at the location where it is supposed to be maximized and must be avoided.

Note that with a decent CPU, the Cobold software is able to reconstruct the events at about 100 kHz, and that several instances can be launched in parallel for offline analysis. Nevertheless, the acquisition of the raw timings can be performed at a much higher rate, which has never limited us.

# IV Characterization of the COLTRIMS

The development of the COLTRIMS has been presented in the previous section. The present one will focus on its characterization. Indeed, the great dimensionality of the measurement enables to filter the noise from the signal. As we will see, this is to be balanced with the acquisition rate and compromises have to be made. Additionally, the accuracy and resolution of the apparatus depend on several factors that will be discussed. Lastly, a typical example of 3D photoelectron angular distribution reconstruction will be given.

## IV. 1 Constraints : Noise Filtering and Acquisition Rate

### Detection Efficiency

The particle detection efficiency is of great importance in coincidence measurements, as an incomplete event can not be used but still counts in the ionization per shot ratio. Additionally, it can lead to wrong coincidence particle coincidence assignment. The global detection efficiency depends on three factors.

The first one is the number of particles that actually reach the detector. Thanks to the magnetic field, the collection angle of the photoelectrons up to 20 eV of kinetic energy is $4\pi$. However, the metallic meshes used in the spectrometer to define homogeneous electric field

regions have a certain transmission, which depends on the distance between the strands and their thickness. The greater the distance between the strands, the higher the transmission, but a small electrostatic lens effect can start to appear within the grid if they are too much spaced. The particle transmission of the meshes is thus generally about $\sim$ 80 %. For this reason, spectrometer configurations requiring many meshes can be problematic. In our case, we only use one on each detector side to impose a short acceleration just before the MCPs.

This is related to the second factor affecting the detection efficiency, namely the MCP efficiency. It depends on various parameters, such as the particle type, its velocity and angle of incidence, and the MCP characteristics such as the cross section of the microchannels. A typical curve of the ion detection efficiency, as a function of kinetic energy and species, is given in Fig. 2.23. In our case, the ions are accelerated at 2160 eV which corresponds to 45-55% of MCP efficiency depending on the ion mass, up to 150 amu. The electrons reach the detector with about 340 eV, corresponding to a 80% MCP detection efficiency.

The final limitation to particle counting efficiency is the ability of the delay lines and electronics to detect a retrievable signal. This is a function of the delay line collection efficiency and the CFD modules sensitivity, considering that one needs at least four delay lines timings to reconstruct a particle hit (out of four for the ions, out of six for the electrons). This factor can be globally determined by comparing the number of hits counted on the MCP back and the one actually reconstructed in the momentum space for the photoelectrons, or in the detector space for the ions. We have estimated it to be $\sim$ 77 % for the electrons and $\sim$ 54 % for the ions. This number is probably better for the electrons because of the redundant hexagonal delay lines.

At the end, the global electron detection efficiency is about 50 % and the one of the ions around 22 %. Combining these two numbers gives, for the one-electron one-ion events we are interested in, a 11 % probability to fully retrieve an event that occurred. This number can look poor at first sight, but is typically of the order of magnitude for this dual single-particle spectrometer. Improvements could be made by, for instance, using a hexagonal delay line detection on both sides, accelerating the ions closer to the efficiency saturation (about 64 %) or moving to a spectrometer geometry which does not use metallic meshes. Conversely, the electron MCP detection efficiency is around a maximum. Note that the detection efficiency of the MCPs could be potentially increased by using funnel type microchannels, for instance. Overall, this 11 % factor adds up to the coincidence condition, since this latter stands for the actual ionization events. To this regard, the use of a high repetition rate source is even more justified.

**Laser Shot Reference**

As we have seen in the previous section, a window event is triggered by an electron count (see Fig 2.34 (a)). To avoid it to be on an fake count, from the MCP noise or from an electron that does not come from a laser shot, the window is only activated if a laser shot was detected about 100 ns before the electron (the order of magnitude of the electron TOF). The coincidence assignation works straightforwardly if two consecutive events are well separated in time, namely by more than the window duration and in principle only one ion should be measured in the

window. But since the ion time-of-flight (up to 21 $\mu$s at 450 amu, Fenchone trimers) is greater than the duration between two laser shots (at most 6 $\mu$s, at 166 kHz), there is a probability to collect other events generated by other lasers pulses detected in the same window. With a 1/10 ionization per shot ratio, this probability is thus of at least 20% at 166 kHz, and increases a lot with the laser repetition rate. The electrons that have not triggered the window are easily discarded. However, the corresponding ions can be more problematic. Indeed, they appear in the time-of-flight spectrum, and thus in the mass spectrum, as replicas of the actual spectrum shifted in time by n times 1/(repetition rate), as displayed in Fig. 2.36. In practice, the replicas often overlap with actual TOF peaks, even if this can be sometimes avoided by fine-tuning the laser repetition rate. If the actual spectrum is very simple, the irrelevant TOFs can be discarded, but this is not a general solution and it worsens with a higher laser repetition rate.

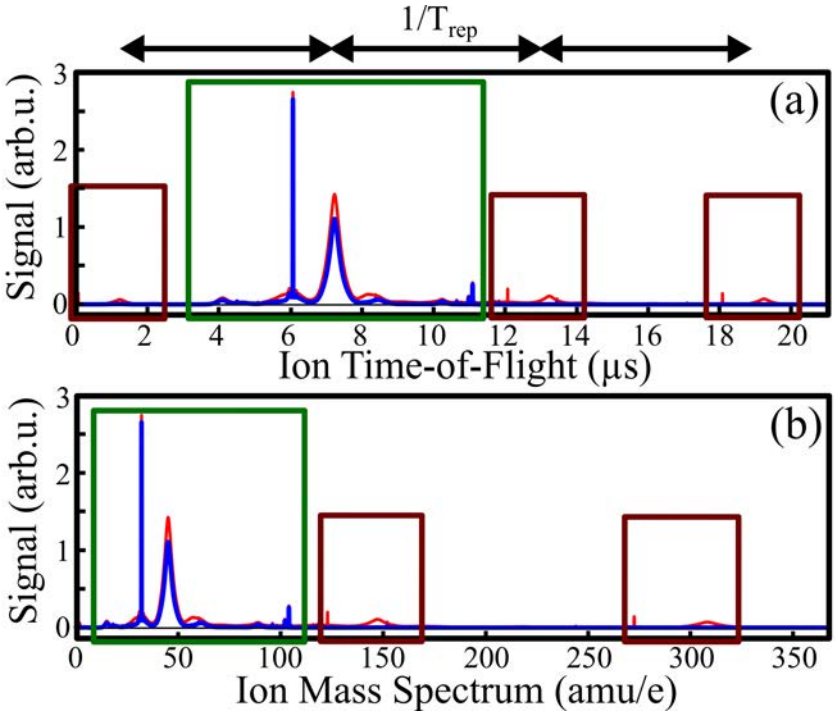


**Figure 2.36** – *Ion time-of-flight (a) and mass spectrum (b) of Methyl-Lactate, with 515 nm laser field. Complete (red) and filtered (blue) are displayed. In addition to the parent ion (104 amu) and a few fragments in the 35-50 amu range, fake masses appear in the unfiltered case, coming from events from the next or previous laser shots.*

A rough solution could consist in simply discarding all the events containing more than one ion in the window. Besides significantly affecting the usable events counting rate, the imperfect ion detection efficiency would lead to a very high fraction of wrong assignations, as the actual ion of interest is not always detected, without possibility to discriminate them.

The solution chosen uses the spatial resolution of the ion detector. The ions are spread along the detector axis corresponding to the molecular jet axis, as shown in Fig. 2.37 (a). Since the species carried in the jet have approximately the same velocity, this position is proportional to their time-of-flight. A relevant representation is $Y = f(TOF)$, displayed in Fig. 2.37 (b), where the slope $\alpha$ corresponding to the jet velocity clearly appears. This is a precise manner to determine the velocity, that depends on the carrier gas and the backing pressure (1500 m/s in

the example given, with 1 bar of helium). Importantly in this plot, the position is proportional to the actual TOF, while the abscissa is the reconstructed TOF. These two quantities match along the $TOF = \alpha \cdot Y$ line, meaning that any count along this axis are ions with a good TOF reference (within a certain margin to account for the velocity dispersion and the recoil of the fragments). On the contrary, any count outside of this range has a wrong reference and can be discarded. One can identify the features due to the previous or next laser shots along the $TOF = \alpha \cdot Y + nT$ where T=1/(rep. rate) and $n \in \mathbb{Z}$, as highlighted in Fig. 2.37 (c).

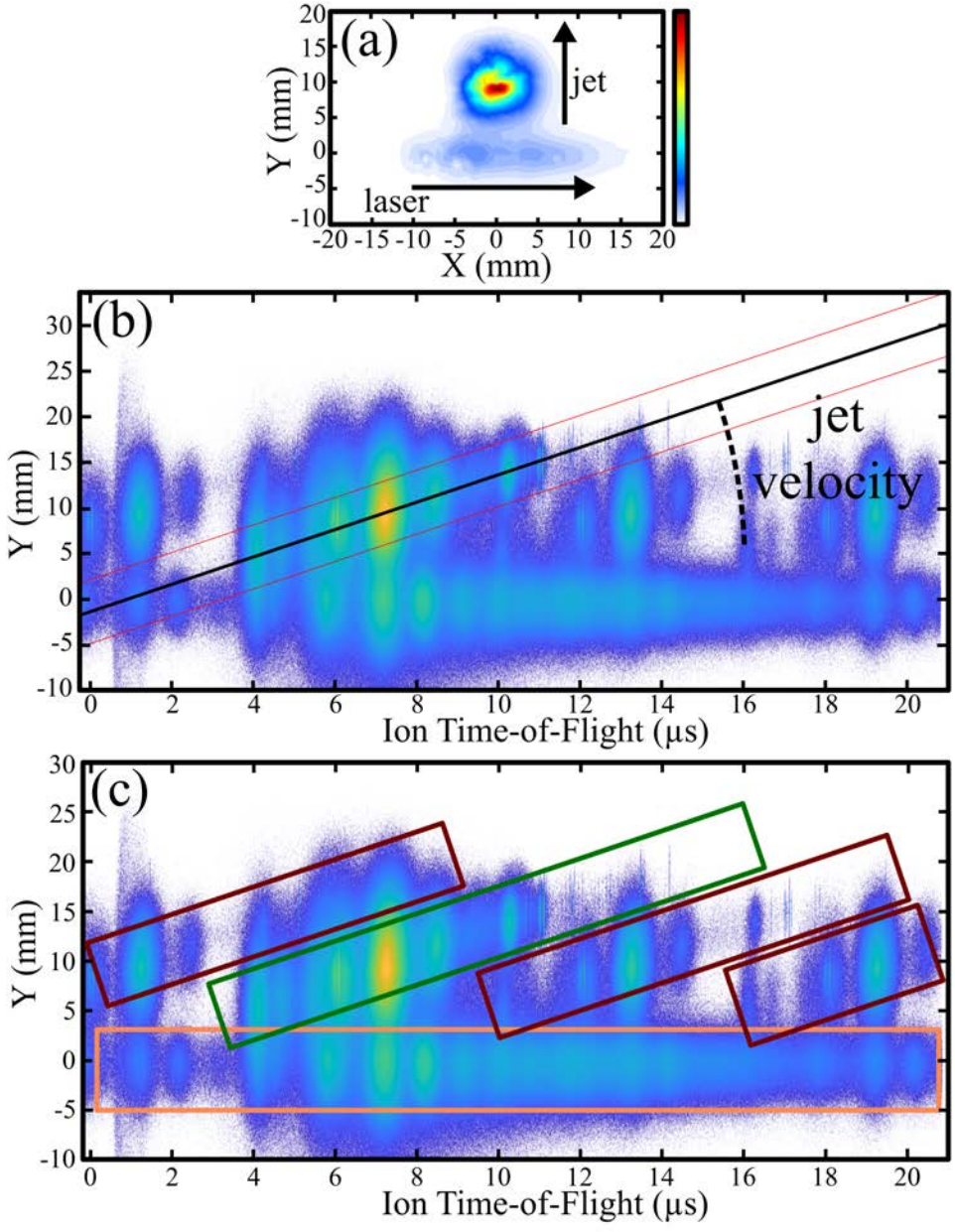


**Figure 2.37** – *(a) Spatial ion distribution, from the same dataset as Fig. 2.36. The signal along the laser axis comes from the residual pressure while the one along the jet axis comes from it. (b) Corresponding spatially-resolved time-of-flight spectrum, along the jet axis. The jet velocity is visible in the slope indicated. (c) Same as (b) where areas of interest are indicated. The signal that comes from the jet and the right laser shot is in the green box, while the signal that has a wrong laser shot reference is highlighted in red and the signal from the residual pressure is in orange.*

By selecting the green area only, the cleaned mass spectrum can be safely obtained. So far, this multidimensional filtering is performed offline. We have planned to implement it in the online analysis in the perspective of using a continuous acquisition scheme, in order to be able to directly get the ion laser shot reference and electron, without need of triggered window. However, this requires the assistance of Roentdek since we can only implement minor custom modifications to the C++ code of the software by ourselves.

**Residual Pressure and Interaction Volume**

Another feature identified in Fig. 2.37 (c) are ions detected with a zero mean momentum, *i.e.* along $Y = 0$. They corresponds to molecules that were not in the supersonic jet, but in the residual pressure in the interaction chamber (about $10^{-8}$ mbar). They can not be distinguished from the bare mass spectrum and could contribute to the usable signal. However, their TOF replicas can not be filtered as they do not spatially spread on the detector, and must thus be entirely discarded with the spatial filtering discussed above (orange box in Fig. 2.37 (c)). These ionization events thus constitute a limitation to the usable counting rate and must be minimized. This can be achieved by increasing the pumping capacity, which we have done, using a multiple jet skimmers configuration or adding a jet dump stage (if this latter is limiting the vacuum). One can also magnify the incident beam to have a shorter Rayleigh length, up to the maximum angular acceptance (40 mrad here with the optical skimmers).

More specifically, the relative importance of the residual pressure counts compared to the jet counts depends on the photon wavelength and the beam focusing conditions. The size of the interaction volume and its consequences on the spectrometer resolution will be discussed in this section. Let us simply mention here that loose focus conditions, *i.e.* long Rayleigh range, deteriorates this ratio. A highly nonlinear ionization (with a large number of photons involved) tends to be localized only at the focus, while a one-photon ionization has a probability to occur all along the laser path. This can be seen in Fig. 2.38 which shows typical spatial distributions of the ions produced in the conditions given in Table 2.5. At $2\omega_L$ with Methyl-Lactate (a), a significant fraction of the signal comes from the jet. At $4\omega_L$ (b), the majority of the signal comes from the residual pressure and the diffuse background from the scattered light. When using XUV radiation (16.9 eV) to ionize xenon (c), the ratio between the jet and the residual pressure is relatively balanced as the focus is much more spread, from the one-photon process. When higher photon energy (35 eV) are used in helium and Fenchone (d), the carrier gas can be ionized and prevails, both in the jet and along the beam. This illustrates the relative ease to study strong field and multiphoton studies, compared to the more challenging XUV experiments.

The ratio between the counts originating from the jet and from the residual pressure can be accurately determined with these figures, and is summarized in Table 2.5, for the focusing conditions presented in Table 2.7. Note that these plots are also used to finely center the beam waist (along the laser) on the jet, and adjust the pointing (along the spectrometer) by maximizing the signal from the jet.

At $2\omega_L$, the part of the beam in which the intensity is high enough to ionize is mainly in the jet, giving a quite low count loss due to the residual pressure along the laser (23 %). At $4\omega_L$, it constitutes more of an issue, at 47 %. A solution could consist in using tighter focusing,

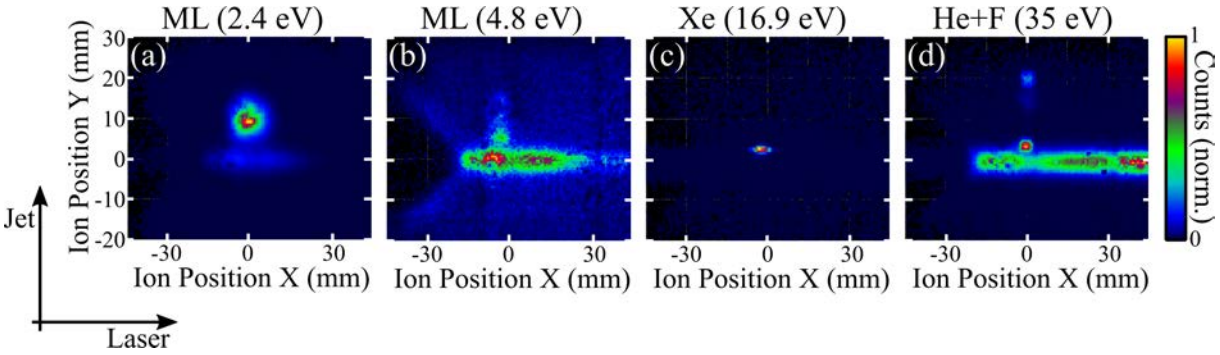


**Figure 2.38** – *Ion spatial distribution for several field wavelengths an targets, indicated in Table 2.5 and 2.7. The signal along the horizontal line comes from the residual pressure while the signal along the vertical axis comes from the jet. Note that the left side of the detector is damaged. ML = Methyl-Lactate, F = Fenchone*

| Harmonic Order | Target Molecule | Number of Photons | Jet Counts | Residual Pressure | Background Noise |
|---|---|---|---|---|---|
| $2\omega_L$ | ML | 5 | 69 % | 23 % | 8 % |
| $4\omega_L$ | ML | 3 | 5 % | 47 % | 48 % |
| $14\omega_L$ | Xe | 1 | 53 % | 40 % | 7 % |
| $29\omega_L$ | He + F | 1 | 23 % + 14 % | 50 % | 13 % |

**Table 2.5** – *Counts ratio between events originating from the jet, from the residual pressure and background counts (which consists of the rest of the counts spatially spread on the detector). In any case, the noise counting rate without laser is very low, typically a few dozens of Hz. ML = Methyl-Lactate, F = Fenchone*

but this goes against another issue already mentioned at this wavelength, which is the scattered light producing a high level of background from the metallic surfaces. This quandary has not been solved so far despite several attempts, in such a way that we have not used this wavelength efficiently.

In the case of high-order harmonics, the ionization is a one-photon process (the ionization yield is directly proportional to the intensity) and the jet/residual ratio does not benefit from the focusing, since the intensity flux is constant along the beam propagation. For this reason, the pumping capacity has been increased to the values mentioned in the description of the apparatus (we added a 700 L.s$^{-1}$ turbomolecular pump). The next step would be to increase the distance between the nozzle and the skimmer to introduce a second skimmer as previously discussed.

#### Balancing Noise and Acquisition Rate

The optimization of the usable counting rate merges all the parameters presented so far and can be quite complex. Let us consider the following simplified model, to get a hint of the interacting parameters. We will assume here that the setup is already optimized, so the ion detection efficiency $\alpha$, the ratio of signal from the residual gas $\beta$ and the event window duration $T_{win}$ are fixed. The degrees of freedom are the ionization probability $P$ per laser shot and the laser repetition rate. The probability of detection of a single event is $\alpha P$. The probability to

get two ionization events per shot is $P^2$, in which either the two ions are detected ($\alpha^2 P^2$), one is detected ($2\alpha(1-\alpha)P^2$) or none is detected ($(1-\alpha)^2 P^2$). The first case can be discarded, the second one can not be identified as such and causes a non-filtrable background (false coincidence), and the last one is simply undetected. Additionally, the probability to get an event from the residual pressure is $\beta\alpha P$. Finally, the probability that an event (already counted) is discarded as a replica is $k\alpha^2 P^2(1+\beta)$, where $k = round(rep.rate \cdot T_{win})$ is the number of additional laser shots contained in the event window. This corresponds to the red boxes in Fig. 2.36. For simplicity, we omit the high order terms as $\beta$ and $P$ are relatively small.

The total number of ionization events per shot $R_{event}$ is thus :

$$R_{event} = P + P^2 + \beta P \tag{2.19}$$

The total counting rate per shot $R_{count}$ is :

$$R_{count} = \alpha P + (\alpha^2 + 2\alpha(1-\alpha))P^2 + \beta\alpha P - k\alpha^2 P^2(1+\beta) \tag{2.20}$$

in which the usable rate $R_{use}$, the discarded rate $R_{disc}$ and the fake coincidence $R_{fake}$ are respectively :

$$\begin{aligned} R_{count} &= R_{use} + R_{disc} + R_{fake} \\ R_{use} &= \alpha P - k\alpha^2 P^2 \\ R_{disc} &= \alpha^2 P^2 + \beta\alpha P - k\alpha^2 P^2 \beta \\ R_{fake} &= 2\alpha(1-\alpha)P^2 \end{aligned} \tag{2.21}$$

Note that the undetected events $R_{und}$ and the replica rate $R_{repl}$ are respectively :

$$\begin{aligned} R_{event} &= R_{count} + R_{und} + R_{repl} \\ R_{und} &= (1-\alpha)P + (1-\alpha)^2 P^2 + (1-\alpha)\beta P \\ R_{repl} &= k\alpha^2 P^2(1+\beta) \end{aligned} \tag{2.22}$$

The evolution of these quantities for a good detection efficiency $\alpha = 0.9$ is depicted in Fig. 2.39 (1). Panel (a) show the evolution of $R_{use}$, $R_{fake}$ and $R_{disc}$, which sum accounts for the detected counting rate, and $R_{repl}$ and $R_{und}$ as a function of the ionization probability $P$, at a repetition rate of 166 kHz. One can see that a very low $P$ does not give a good signal acquisition rate. Conversely, a high $P$, a lot of the acquired signal is discarded, which diminishes the usable counting rate. In between, a maximum of $R_{use}$ can be found around $P \sim 0.28$. At this probability, about 30 % of the total counting is usable and $\sim$ 10 % of the usable signal actually comes from fake coincidences (panel (b)). From there, one can be tempted to increase the laser repetition rate. The evolution of the usable counting $R_{use} \times (rep.rate)$ as a function of $P$ and the repetition rate is shown in Fig. 2.39 (1-c). Lineout of this map, depicted by the black lines, are plotted in panels (d) and (e). The saw teeth pattern originates from the fact

that the number of replica suddenly increases when an additional laser shot comes in the event window. The increase within each teeth is due to the increase of the global acquisition rate with the repetition rate. The effect of the replicas appears very detrimental, in such a way that in this case the only optimization consists in increasing the repetition rate from 166 kHz to 230 kHz, yielding about 29 kHz of usable events. This number must be tempered, since 10 % of fake coincidences is quite high. In practice, one uses a lower value of $P$, about 1/10.

The result of the same procedure for a lower detection efficiency ($\alpha = 0.5$) is shown on Fig. 2.39 (2). Of course, the first effect is the larger fraction of undetected counts. Also, the curve of $R_{use}$ is more spread across $P$, and the number of fake coincidences drastically increases as they correspond to two events from the same laser shot with only one ion detected. For this reason, the optimal value of $R_{use}$ can not be chosen and a much lower $P$ is required to have 10 % of fake coincidences, in this case $P \sim 0.10$. This shifts the optimal repetition rate up to 840 kHz before the replicas become problematic, for a final $\sim$ 21 kHz of usable events. However, this does not take into account several other factors. Firstly, panels (a) and (b) also evolve with the repetition rate, meaning that the procedure must be done iteratively as 840 kHz is far from the initial 166 kHz, pushing it to an even higher value. Secondly, the laser average power is limited, and the choice of $P$ can be constrained by the repetition rate. Thirdly, beyond the lenient fake coincidence acceptance, increasing $P$ as much as possible increases a lot the signal on the detectors, and especially the unusable and the undetected one. This induces a quicker aging of the MCPs, and more problematically the dynamical limit of the detectors can be reached (about 100-150 kHz). In the same trend, increasing the repetition rate linearly increases the fraction of unusable signal (replicas), thus quadratically increases counting rate of unusable events, while it only increases the usable rate linearly, quickly leading to the saturation of the detectors for a minor increase of the usable counting rate. Finally, independently of all this reasoning, the acquisition mode limits the total acquisition rate at $1/T_{window}$ because only one window can be open at a time. This number is usually between 40 and 75 kHz depending on the mass of the species of interest, and puts a much higher cost on the unusable detected events.

The statistical model discussed here underlines and illustrates the effect of the different parameters at play but is approximate. At the end, we have determined the best usable counting rate empirically. Discrepancies with the model can be noted, in particular due to the fact that this latter does not take into account the deadtime of the detectors. This implies that some events can not be correctly reconstructed, decreasing the effective $\alpha$ depending on the counting rate. By varying the laser repetition rate and the energy per shot, we have experimentally determined that the best usable counting rate was reached when the total acquisition rate was about 10-15 kHz, and that increasing the repetition rate did not help significantly. This is in contradiction with the model presented, and we have been investigating the causes of this effect in order to verify if it is an intrinsic limitation or not, but the multiple parameters at play render the task tedious. Nevertheless, various factors of loss of counts can be retrieved from the analysis of recorded sets of data. Table 2.6 shows these numbers obtained in two cases. One uses two high-order harmonics at 12.0 and 16.85 eV generated from a 515 nm wavelength shot on Xe, at an event counting rate of 13-15 kHz. The other one was recorded in Methyl-Lactate directly

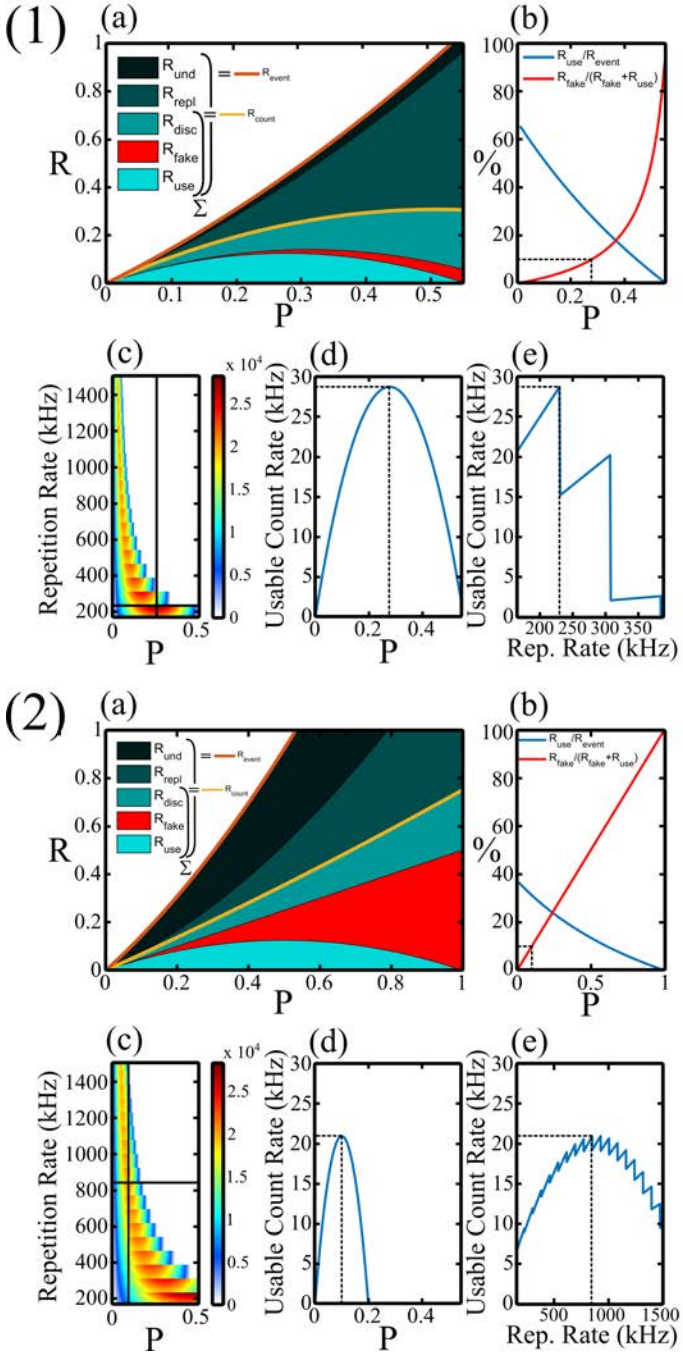


**Figure 2.39** – *Evolution of the usable counting rate with the ionization probability and repetition rate, calculated with the simplified statistical model presented, for a detection efficiency of 0.9 (1) and 0.5 (2), and $T_{win}$ = 13 µs. (a) Evolution of the different types of rate per shot composing the total counting rate and total ionization rate, as a function of the ionization per shot probability at a repetition rate of 166 kHz. (b) Fraction of usable counts and false coincidence counts, as a function of the ionization per shot probability, at 166 kHz. (c) Map of the final usable counting rate, as a function of the ionization per shot probability and of the repetition rate. The black lines indicate the optimal value. (d) Lineout of (c) along the ionization per shot probability for the optimal repetition rate of 230 kHz (1) and 840 kHz (2). (e) Lineout of (c) along the repetition for the optimal ionization per shot value of 0.28 (1) and 0.10 (2).*

ionized by the 515 nm beam, at a counting rate of 10-12 kHz. Note that the ion MCP efficiency was deteriorated by a factor 4 in the first case due to a damage. One has to keep in mind that the electron detection efficiency indicated in this table only accounts for the electronics efficiency, as these values are retrieved from measurements and not from the actual, unknown event probability.

| Photons & Target | Detection Efficiency Electron/Ion (%) | False Coincidence Filter (%) | Fraction from the Jet (%) | Replica Filter (%) | Total (%) | Event Counting Rate (kHz) |
|---|---|---|---|---|---|---|
| HHG 12.0-16.9 eV in Xe | 78/6.2 | 94 | 53 | 67 | 1.6 | 13-15 |
| 515 nm 2.4 eV in ML | 76/24 | 92 | 69 | 82 | 9.5 | 10-12 |

**Table 2.6** – *Summary of the factors of loss of usable counting rate, experimentally measured in two typical conditions given in the first column, at a repetition rate of 166 kHz. These numbers are deducted from the different quantities accessible in the analysis software, and by filtering the events of interest.*

The comparison between these two cases shows two characteristic trends. The first one is that the signal from the residual pressure represents about half of the signal in one-photon ionization while it decreases about one third in multiphoton ionization, as previously explained. The second one is that more events are lost in the replica in the first case, as the probability $P$ was slightly higher than in the second one. This usable counting rate loss is, however, almost exactly counterbalanced by the higher acquisition rate.

Finally one must add a last factor in the HHG case that is not comprised in this table, which is the size of the interaction volume in the jet. Due to its extension along the radiation beam axis, only the central part of the ion distribution (about two thirds) yielded a decent reconstructed photoelectron distribution. This is more related to the calibration of the detector, and is presented in the next section.

## IV. 2 Calibration and Resolution

The determination of the resolution of the COLTRIMS depends on several elements, and can be quite indirect since the physical quantities are reconstructed from timings. We will address in this section the different factors.

**Physical Resolution**

The first key element defining the resolution is the precision of the measured quantities, which are the delay lines timings. The temporal resolution of the detectors is $\sim$ 100 ps in good conditions, *i.e.* with a very low electronic noise. From Eq. 2.13, one can estimate the time-of-flight resolution to $\Delta TOF$ = 200 ps, assuming a good detector calibration. The ion mass spectrum resolution $\Delta(m/q)$ and relative resolution $\frac{\Delta(m/q)}{(m/q)}$ can be derived from Eq. 2.14, reading :

$$\begin{aligned}\Delta(m/q) &= \sqrt{\frac{2E}{L_i}}\Delta TOF\sqrt{m/q} \\ \frac{\Delta(m/q)}{m/q} &= \sqrt{\frac{2E}{L_i}}\Delta TOF\sqrt{m/q}^{-1}\end{aligned} \tag{2.23}$$

Fig. 2.40 shows the evolution of these two quantities for the spectrometer configuration mainly used ($E$ = 8 V.cm$^{-1}$, $B$ = 8.05 Gauss, $L_i$ = 4.16 cm, last line in Table 2.4). The theoretical $\Delta(m/q)$ is much lower than 1 for the masses we are interested in ($\sim$ 150 amu for monomers and fragments, up to 450 amu for trimers of fenchone), but other factors will play a role here, such as the size of the interaction volume discussed in a further paragraph.

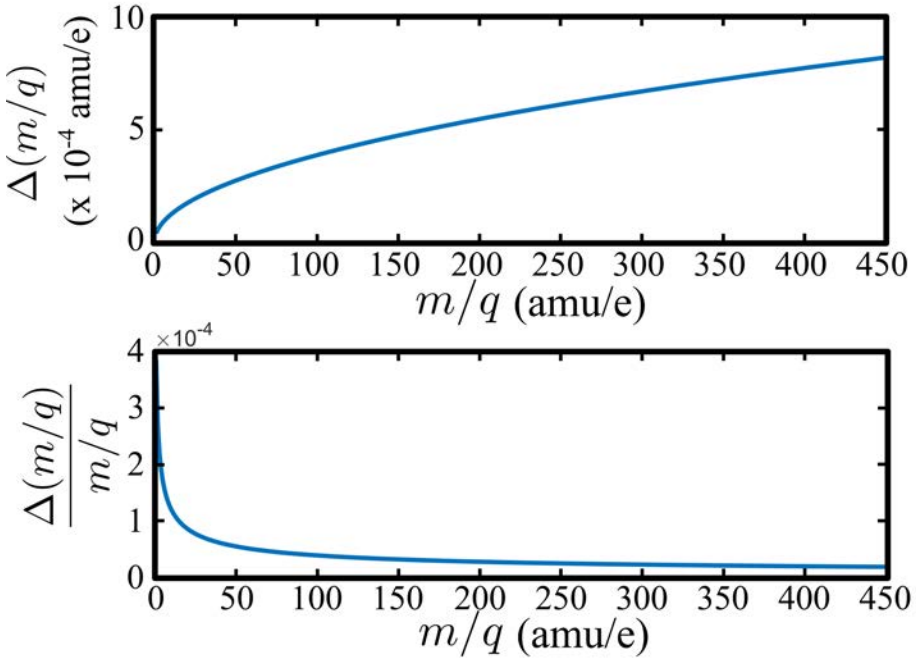


**Figure 2.40** – *Evolution of the ion mass spectrum physical resolution of the spectrometer* $\Delta(m/q)$ *and* $\frac{\Delta(m/q)}{(m/q)}$*, as a function of* $(m/q)$ *in our range of interest.*

For the electrons, the calculation is a bit more complex since the quantities of interest are the momenta, that are reconstructed from the equations 2.16 and 2.17. The momentum along the spectrometer $p_z$ is simpler as it only depends on the time-of-flight. From Eq. 2.16, the resolution $\Delta p_z$ can be derived as :

$$\Delta p_z = \left( \frac{2m_e L_e e^2 E^2}{(-p_z + \sqrt{p_z^2 + 2eEm_e L_e})^2} + eE/2 \right) \Delta TOF \tag{2.24}$$

Fig. 2.41 shows the evolution of $\Delta p_z$ for values of $p_z$ between -1.2 and 1.2 a.u., corresponding to kinetic energies within 20 eV. The resolution is between 0.020 and 0.036 a.u., *i.e.* between 5 and 18 meV in energy (in comparison the laser energy width up to $4\omega$ is a bout 22 meV FWHM).

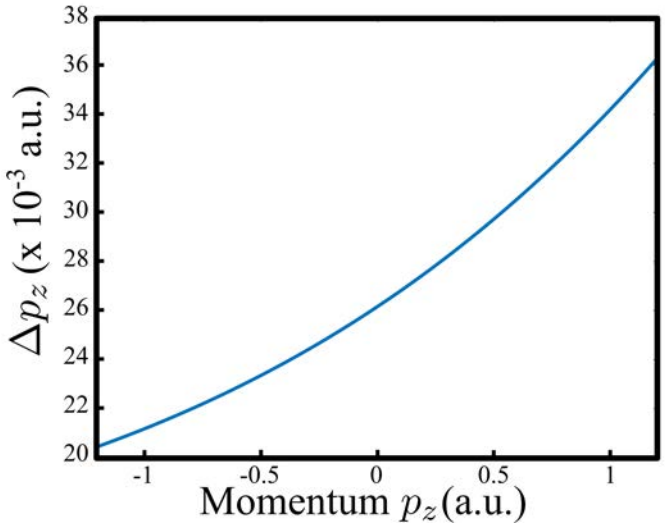


**Figure 2.41** – *Evolution of the physical photoelectron momentum resolution $\Delta p_z$ as a function of $p_z$.*

The assessment of the photoelectron momentum resolution in the detector plane $\Delta p_x$ and $\Delta p_y$ (or $p_r$, $\varphi$ in radial coordinates) requires the spatially-resolved detection. The spatial resolution of $\Delta X = \Delta Y = 200$ $\mu$m is related to the timing resolution, as previously explained. Note that the diameter and the pitch of the holes of the microchannel plates are respectively of 25 $\mu$m and 32 $\mu$m for both the ions and the electrons, and thus do not limit the spatial resolution. In addition, the resolution will also depend on the time-of-flight, or $p_z$, because of the helical trajectories caused by the magnetic field. Indeed, the spatial resolution is maximized at the tip of the wiggle, set at $p_z = 0$, and reduces with $|p_z|$. From Eq. 2.17, one can obtain :

$$\begin{aligned}\Delta p_r &= \frac{eB}{2} sin\left(\frac{\omega}{2eE}(-p_z + \sqrt{p_z^2 + 2eEm_eL_e})\right)\Delta r + |p_r|\frac{\omega}{2}tan^{-1}\left(\frac{\omega}{2eE}(-p_z + \sqrt{p_z^2 + 2eEm_eL_e})\right)\Delta TOF \\ \Delta\varphi &= \frac{X\Delta Y + Y\Delta X}{X^2 + Y^2} + \frac{\omega}{2}\Delta TOF\end{aligned} \tag{2.25}$$

$\Delta p_r$ can here be reduced to be a function of $p_r$ and $p_z$, and is plotted in Fig. 2.42 (a), in logarithmic scale. The black circles represent the momentum spheres of the 20 eV, 5 eV, 1 eV and 0.1 eV electrons. This figure underlines a crucial property of the wiggles : the resolution in $p_r$ is maximized when the time-of-flight is close to a half-integer value of $\omega_{helix}$ and is seriously affected close to a integer value of $\omega_{helix}$. Moreover, is also reduced with $|p_r|$. Combining these two effects, $\Delta p_r$ is the best for $p_r = 0$ and $p_z = 0$ at a given photoelectron energy. This can be an issue for our main goal which is resolving the angular asymmetries in the distribution, as we will see further in this section. The evolution of $\Delta p_r$ as a function of $p_r$ and $p_z$ are respectively plotted in panels (b) and (c), for kinetic energies respectively along $z$ and $r$ of 0, 0.1, 1, 5 and 20 eV. Overall, $\Delta p_r$ is within 0.010 a.u. for photoelectrons with a total kinetic energy up to 5 eV, corresponding to 1.6 meV. Once again, this will not be the only factor.

The evolution of $\Delta\varphi$ explicitly depends on the detected position $(X, Y)$ and can not be

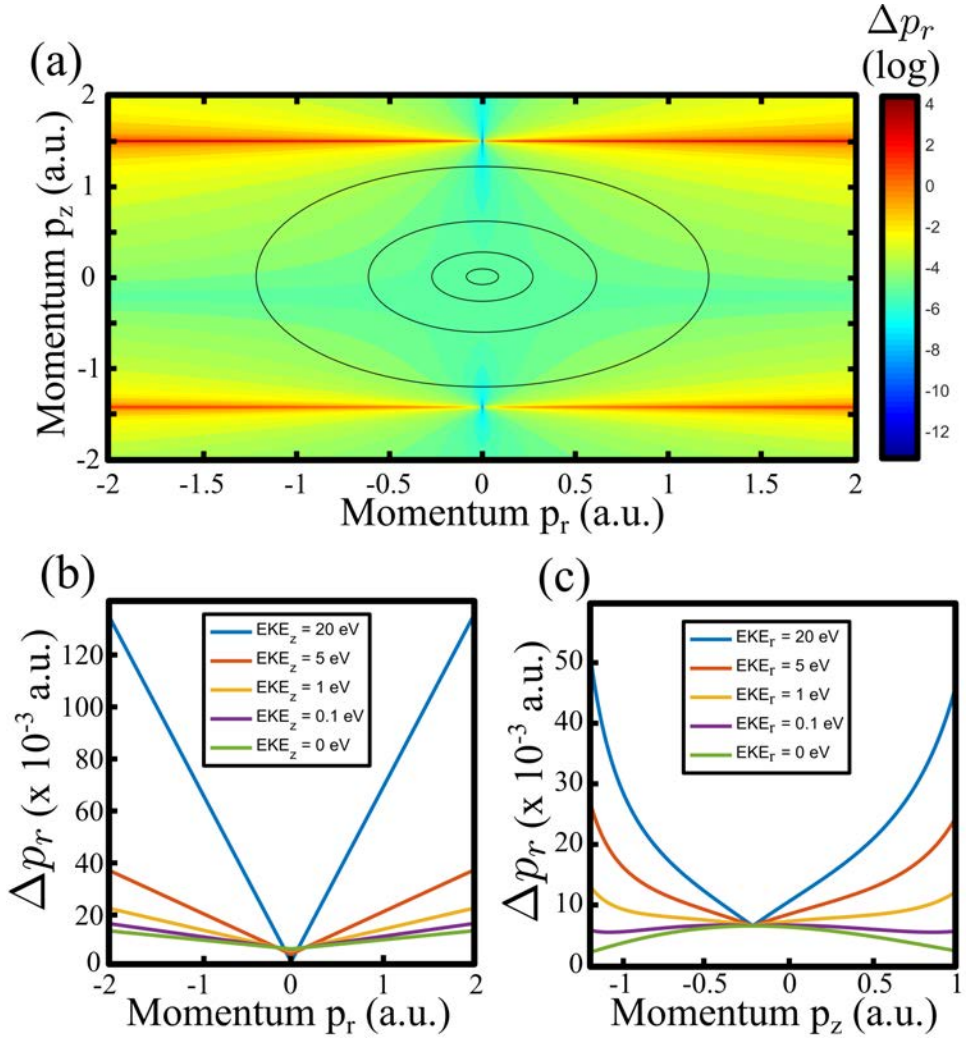


**Figure 2.42** – *(a) Evolution of the physical radial photoelectron momentum resolution $\Delta p_r$ as a function of $p_r$ and $p_z$, in logarithmic scale. The black circles indicate the momentum sphere of kinetic energies of 20 eV, 5 eV, 1 eV and 0.1 eV. (b) Evolution of $\Delta p_r$ with $p_r$, at fixed $EKE_z$. (c) Evolution of $\Delta p_r$ with $p_z$, at fixed $EKE_r$.*

reduced to the physical momenta. Let us simply mention that the error decreases with the radius of detection $r$, as the angular resolution increases at high radius.

**Reconstruction Parameters**

The equations presented above do not take into account the error that could originate from the reconstruction parameters. Some physical quantities, such as the electric and magnetic fields or the delay offsets are roughly known from the voltage or the current generators. However, their actual values have to be much more precisely defined in the reconstruction algorithm. The best way to refine them is to minimize some typical defaults in the reconstructed events. This specifically applies to the electron momentum distributions, since the mass spectrum is ultimately calibrated on known species. From Eq. 2.16 and 2.17, one can see that $p_z$ depends on the spectrometer length $L_e$ and the electric field $E$ and the timing reference. Practically, they all have the same effect, which is shifting the $p_z$ distribution, *i.e.* the zero kinetic energy

time-of-flight. The evolution of the kinetic energy spectrum (*i.e.* the angular integration of the distributions) are shown in Fig. 2.43 (a), for $E$ field parameters of 98 %, 99 %, 100 %, 101 % and 102 % of the optimal value found. They are all calculated from the same raw data set of $75 \times 10^6$ events generated in Methyl-Lactate at 515 nm, that is used in Section 3.III. This shows that variations of 1 % of the parameter used can induce significant loss of resolution.

$p_x$ and $p_y$ additionally depend on the magnetic field $B$ parameter. Reconstructions with variations of $\pm 10\%$ from the optimal value are presented in Fig. 2.43 (b). Errors on $B$ induce a asymmetric distortion of the distribution. Of course, the deviation can be mainly corrected by correcting the parameter to get a rounder distribution, but the precision of this procedure is hard to assess. Importantly, these asymmetries can be in competition with the actual asymmetries we are interested in. In principle, they can be partially canceled out by subtracting distributions obtained with opposite laser helicities, but still remains hard to quantify. Note that this effect is amplified at high photoelectron kinetic energy.

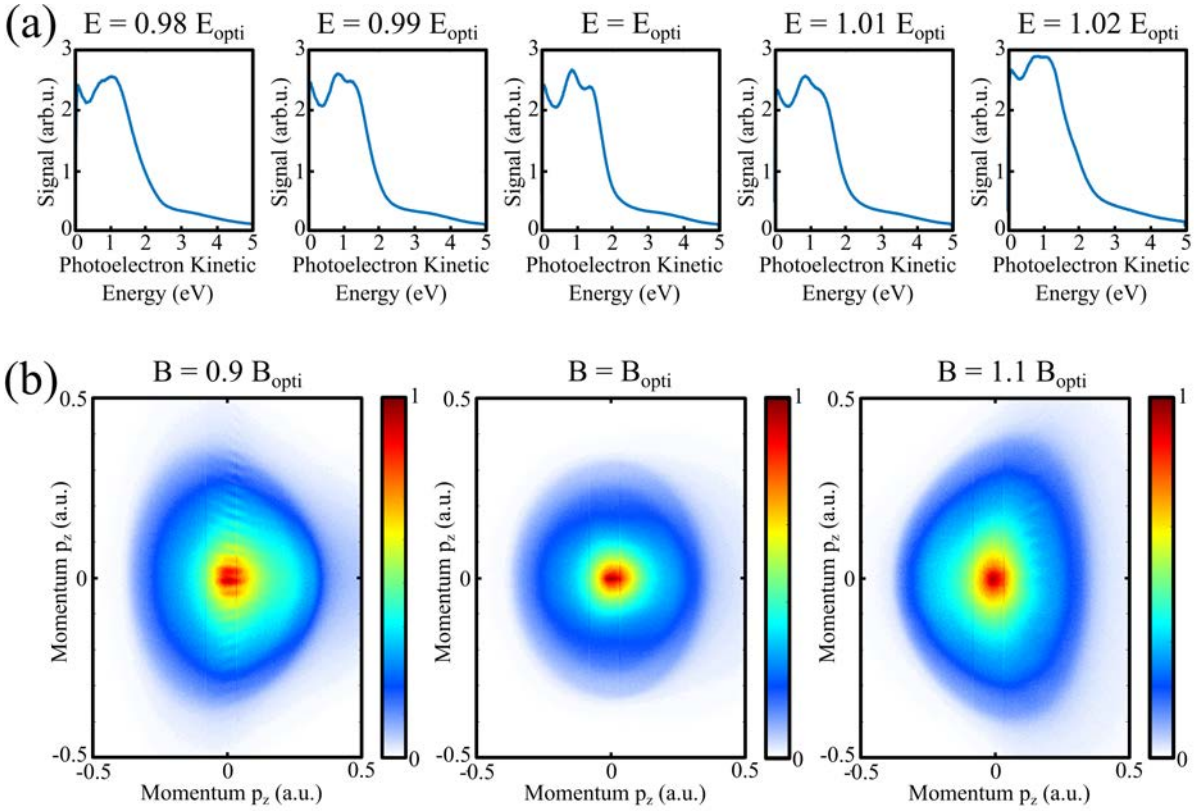


**Figure 2.43** – *Evolution of (a) reconstructed photoelectron kinetic energy and (b) $(p_x, p_z)$ reconstructed momentum distributions, as a function of the reconstruction parameters, for the same set of raw data (7.5 M events recorded by ionizing Methyl-Lacate with a circularly polarized field at 515 nm). $E_{opti}$ and $B_{opti}$ are the optimal values found, respectively being 8.2 $V.cm^{-1}$ and 8.25 Gauss.*

Finally, the drifts of the laser pointing can introduce a time dependency to the reconstruction parameters, in particular the distances between the target and the detectors $L_i$ and $L_e$. Nevertheless, two solutions can be found. The first one consists in splitting the data into subsets, and adapt the reconstruction parameters to each subset. This can be tedious and is only satisfactory if a sudden pointing offsets occur only a few times. The other possibility

consists in actively stabilizing the pointing. We aim at implementing such a stabilization with a precision of a few dozens of $\mu$m, so that this effect becomes negligible in terms of reconstruction parameters (the question of the interaction volume is discussed in the next paragraph). Note also that the laser temporal jitter is in the femtosecond range and is completely marginal.

**Interaction Volume**

As already mentioned, the reconstruction of the mass spectrum and photoelectron momentum distribution is performed assuming a punctual source. Taking into account the size of the interaction volume can lead to a broadening of the spectra. Assuming a Gaussian beam shape, the intensity profile is given by :

$$I(r,z) = I_0 \left(\frac{w_0}{w(z)}\right) exp\left(\frac{-2r^2}{w(z)^2}\right) \tag{2.26}$$

where $w_0 = \frac{\lambda}{\pi\theta}$ is the beam waist, $z_R = \frac{\pi w_0^2}{\lambda}$ is the Rayleigh range, $w(z) = w_0\sqrt{1+\left(\frac{z}{z_R}\right)^2}$ and $I_0$ is the intensity at the waist, as parametrized on Fig. 2.44.

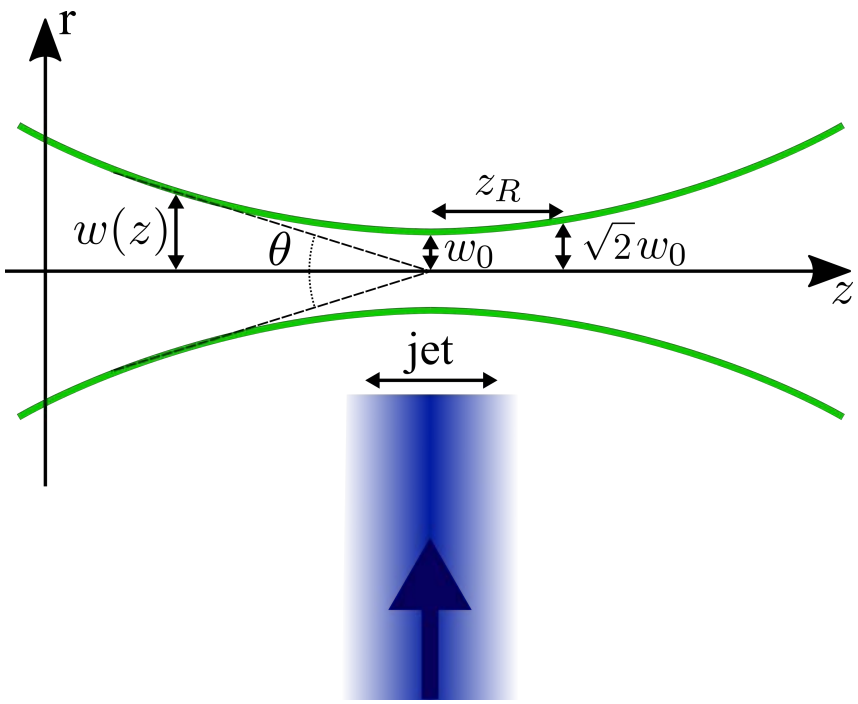


**Figure 2.44** – *Parametrization of a Gaussian beam profile.*

The interaction volume is defined along the spectrometer and the jet axis (both orthogonal to the laser) by the waist $w_0$, and along the laser axis by the Rayleigh range $z_R$ and the width of the jet. A table of these parameters in the typical condition used with the laser fundamental $\omega_L$ and $2\omega_L$, $3\omega_L$, $4\omega_L$ and high-order harmonics $14\omega_L$ is shown on Table 2.7. The focal lengths $f$ indicated are the shortest one that can be used in the current beamline configuration.

The more nonlinear the ionization is (*i.e.* the longer the wavelength), the more localized is the ionization area. In the perturbative ionization regime (single photon or multiphoton), the ionization probability scales with $I^n$ where n is the number of photon involved. We will

| Harmonic Order | Photon Energy (eV) | Wavelength (nm) | f (mm) | Divergence (mrad) | $w_0$ ($\mu$m) | $z_R$ (mm) |
|---|---|---|---|---|---|---|
| $\omega_L$ | 1.2 | 1030 | 400 | 6.2 | 52 | 8.4 |
| $2\omega_L$ | 2.4 | 515 | 400 | 6.2 | 26 | 4.2 |
| $3\omega_L$ | 3.6 | 343 | 400 | 6.2 | 17 | 2.8 |
| $4\omega_L$ | 4.8 | 257 | 400 | 6.2 | 13 | 2.1 |
| $14\omega_L$ | 16.85 | 74 | 3000 | 0.84 | 28 | 34 |

**Table 2.7** – *Typical focusing conditions used, for a beam diameter of 10 mm.*

simply assume that the effective interaction volume (in which $I^2 > 0.1I_0^2$) extends on a cylinder of diameter $\sqrt{2ln(10)}w_0/\sqrt{n}$ and of length $2z_R\sqrt{^n\sqrt{10}-1}$. Note that this last value can be limited by the jet width ($\sim$ 10 mm for a quite high assumption).

The mass spectrum is only affected by the extension of the interaction volume along the time-of-flight axis, corresponding to the spectrometer axis. It will appear as a distribution $\Delta L_i \sim \sqrt{2ln(10)}w_0/\sqrt{n}$ of $L_i$ in Eq. 2.14. The corresponding broadening in $m/q$ can be obtained with :

$$\Delta(m/q) = \frac{E}{2L_i^2} TOF_{ion}^2 \Delta L_i \tag{2.27}$$

The extension of the beam waist also appears as a distribution $\Delta L_e = \Delta L_i$ in Eq. 2.16. The broadening in the photoelectron momentum $p_z$ due to this uncertainty can be obtained with :

$$\Delta p_z = \frac{m_e}{TOF} \Delta L_e \tag{2.28}$$

Once again the situation is much more complex for the distributions in the polarization plane. Its resolution is both affected by the broadening in $p_z$ (or in time-of-flight) and by the spatial broadening of the detection. Especially, the spatial distributions are broadened by $\sim \sqrt{2ln(10)}w_0/\sqrt{n}$ along the jet axis and by $\sim 2z_R\sqrt{^n\sqrt{10}-1}$ or the jet width along the laser axis. This last term always dominates, so assuming $\Delta r = 2z_R\sqrt{^n\sqrt{10}-1}$ (up to 10 mm), the resolution $\Delta p_r$ and $\Delta\theta$ can be derived from Eq. 2.17 as :

$$\begin{aligned} \Delta p_r &= \frac{eB}{2} |sin\left(\frac{\omega}{2}TOF\right)| \Delta r + \frac{e^2B^2r}{4m_e} |cos\left(\frac{\omega}{2}TOF\right)| \Delta TOF \\ \Delta\varphi &= \Delta\theta + \frac{\omega}{2}\Delta TOF \end{aligned} \tag{2.29}$$

These equations have multiple implicit dependencies and do not take into account the anisotropy of $\Delta r$. Let us just calculate the order of magnitude of the broadening :

$$\Delta p_r \approx \frac{1}{2}\frac{eB}{2}\Delta r + \frac{1}{2}\frac{e^2B^2r_0}{4m_e}\Delta TOF \tag{2.30}$$

where $\Delta TOF \approx \sqrt{\frac{2m_e}{eE}}\frac{\Delta L_e}{L_e}$ and $r_0 = 10$ mm is the typical distribution radius.

| Harmonic Order | Number of Photons n | $\Delta L_i = \Delta L_e$ (mm) | $\Delta r$ (mm) | $\Delta(m/q)$ (amu/e) | $\Delta p_z$ (a.u.) | $\Delta p_z$ (eV) | $\Delta p_r$ (a.u.) | $\Delta p_r$ (eV) |
|---|---|---|---|---|---|---|---|---|
| $\omega_L$ | 8 | 0.039 | 9.7 | 0.15 | $3\times10^{-4}$ | $1\times10^{-6}$ | 0.16 | 0.34 |
| $2\omega_L$ | 4 | 0.028 | 7.4 | 0.10 | $2\times10^{-4}$ | $5\times10^{-7}$ | 0.12 | 0.20 |
| $3\omega_L$ | 3 | 0.021 | 6.0 | 0.08 | $1.5\times10^{-4}$ | $3\times10^{-7}$ | 0.10 | 0.13 |
| $4\omega_L$ | 2 | 0.020 | 6.2 | 0.073 | $1.4\times10^{-4}$ | $3\times10^{-7}$ | 0.10 | 0.14 |
| $14\omega_L$ | 1 | 0.060 | $\sim 10$ | 0.22 | $4\times10^{-4}$ | $2.5\times10^{-6}$ | 0.16 | 0.36 |

**Table 2.8** – *Overview of the different factors of broadening due to the spatial extension of the interaction volume, from the simplified model presented in the text, at the wavelengths and focusing conditions given in Table 2.7. The number of photons involved and masses are given for m = 152 amu and Ip=8.6 eV, corresponding to Fenchone.*

A summary of the broadening induced by the extension of the interaction volume is presented in Table 2.8, with the laser conditions given in Table 2.7. Overall, this effect of the ionization volume is more critical than the intrinsic resolution of the spectrometer. Regarding the photoelectron momentum resolution, the spatial extension of the source along the laser axis dominates in such a way that the pointing fluctuations of the laser should be negligible. In the worst case, corresponding to the $\sim 1$ mm acceptancy of the optical skimmers, $\Delta p_z$ remains below 1 meV and $\Delta p_r$ only increases by 3 %. Nevertheless, it would induce a $\frac{\Delta(m/q)}{(m/q)} \approx 3\%$ which is problematic. For this reason and the global continuity of the acquisitions, we are currently working on implementing a pointing stabilization with a precision close to the beam waist, which will be largely sufficient to keep the mass resolution well below 1 amu in our range of interest (up to 450 amu), at least regarding the ionization volume.

Generally speaking, the dominant effect on the photoelectron momentum resolution (the extension of the source along the laser axis) could be tempered by using very tight focusing conditions, highly nonlinear ionization or a narrower jet, by using a double skimmer configuration.

**Experimental Measurements**

We can compare the experimental width of the mass spectra and the electron kinetic energy spectra in two typical cases, the first one using a 515 nm wavelength to ionize Methyl-Lactate molecules ($I_p = 10.3$ eV) and the second one where we ionized xenon ($I_p = 12.1$ eV) with the 7th harmonic of a 515 nm driving field.

The mass spectrum around the species of interest are shown in Fig. 2.45. In panel (a), the Methyl-Lactate has a mass of 104 amu and one can observe, in addition to a fragment at 102 amu, small peaks at 103 and 105 amu due to $^{13}C$ isotopes. The mass resolution is clearly below 1 amu/e, as the main peak is fitted with a Gaussian profile of $\sigma = 0.06$ amu/e. The mass spectrum of xenon in panel (b) is a bit more congested because of its natural isotopic composition. The fit is thus performed over all the atomic masses with a fixed relative weight, shown in black lines. The fit does not manage to reproduce the experimental data very well, but still gives a reasonable $\sigma = 0.77$ amu/e. This is enough to distinguish the isotopes, but here the large volume

of interaction (due to the EUV ionization wavelength) significantly reduces the mass resolution. In the case of the multiphoton ionization of Methyl-Lactate, the mass spectrum resolution is in good agreement with the predictions. Nevertheless, the theoretical values of the resolution seem underestimated in the HHG case. This could be attributed to additional processes, such as the photodissociation of xenon dimers during the flight in the spectrometer, inducing a recoil that broadens the distributions. A perspective to avoid this situation can be to use a mixture of xenon and helium, or by heating the nozzle.

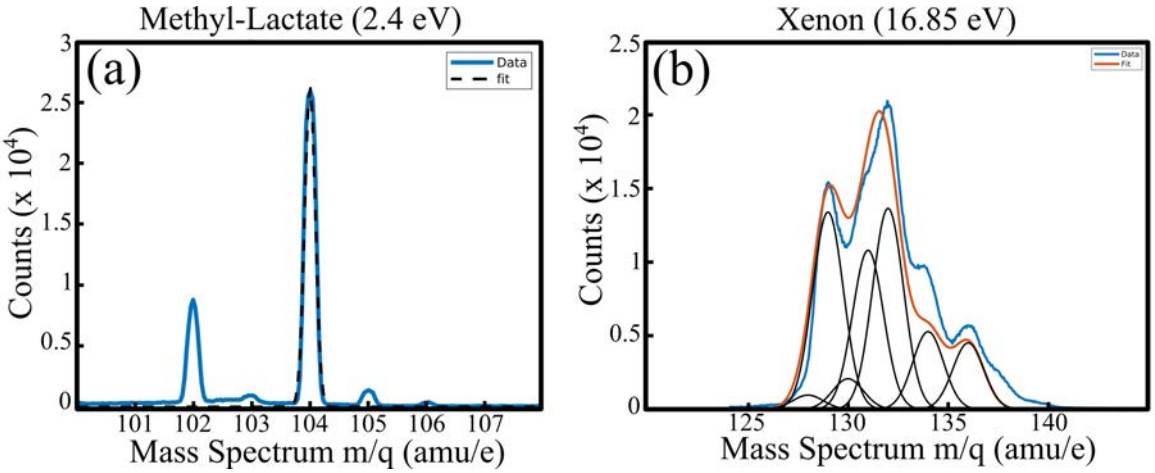


**Figure 2.45** – *Measured ion mass spectrum of (a) Methyl-Lactate and (b) Xenon, respectively produced by a 5-photon ionization at 515 nm and one-photon ionization by the 7th harmonics of a 515 nm field (16.85 eV).*

The corresponding photoelectron spectra are shown in Fig. 2.46, in coincidence with the Methyl-Lactate parent ion (a) and the xenon monomers (b). In the first case, a single photoelectron peak appears and is fitted with $\sigma = 0.27$ eV. The value at which the peak arises can not be compared to any reference of ionization potential since this latter has not been measured elsewhere. The center of the line, found at 1.75 eV, corresponds to a 5-photon ionization at 515 nm (2.401 eV), resulting in a 10.29 eV estimation of the vertical ionization energy. Conversely, xenon is suited for calibration as its energy levels are well known. The kinetic energy spectrum of the xenon shows two lines that are fitted independently. They correspond to the ionization to the $5s^2 5p^5\ ^2P^0_{\frac{1}{2}}$ and $5s^2 5p^5\ ^2P^0_{\frac{3}{2}}$ of respective ionization thresholds of 13.44 eV and 12.13 eV, by the 7th harmonic (16.85 eV). They are respectively fitted with $\sigma = 0.33$ eV and $\sigma = 0.49$ eV. The kinetic energies at which the lines are located are measured at 3.10 eV and 4.35 eV, where values found in the NIST database were respectively 3.41 eV and 4.72 eV.

It thus seems like our detector systematically overestimates the electron kinetic energies. In practice, such a measurement on a known target enables one to apply a scaling correction on the kinetic energy range, which would be in our case about x1.1. The spin-orbit coupling measured here is of 1.25 eV, while the expected value is 1.31 eV, confirming the importance of the empirical calibration to obtain such a precision.

Regarding the energy resolution, the values found experimentally are always above the one predicted from the theoretical uncertainties, but are of the same order of magnitude. Part of the additional error could be attributed to imperfect reconstruction parameters, inhomogeneity

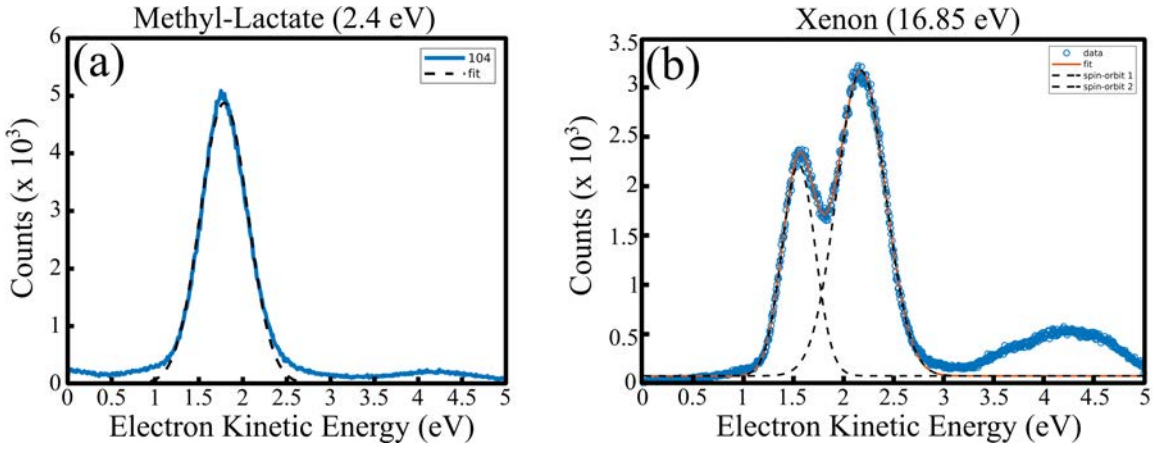


**Figure 2.46** – *Measured photoelectron kinetic energy spectrum of (a) Methyl-Lactate in coincidence with the unfragmented molecule and (b) Xenon in coincidence with the monomer, respectively ionized in multiphoton by 515 nm radiation and one-photon by the 7th harmonics of a 515 nm field.*

in the electric or magnetic fields, especially since the resolution reduces quite quickly with the photoelectron kinetic energy, and also due to the energy width of the photons. Note that this latter is not accessible in our case, since the resolution of our XUV spectrometer is too great (of the order of 100 meV).

## V Conclusions and Outlook

This chapter has mentioned some of the advances of the group on the new generation high repetition rate beamline. Great efforts have been put to characterize and enhance the capacities of the laser source in order to make it as versatile as possible. In particular, frequency conversion setups have been implemented and optical parametric amplification have been tested. One of the original activity of the group, high-harmonics generation, has been adapted to the new source (mostly by other group members). The generation of circular or highly elliptical high-order harmonics remains challenging, and several techniques have been tested, such as using bicircular bichromatic driving fields or resonant HHG. Even if this Yb-doped fiber laser provides a unprecedented signal acquisition rate, its main drawback is its pulse duration (135 fs) which is longer than the widely used Ti:Sa lasers. We have achieved so far postcompression below 20 fs, and expect great advances in this way as new technologies become available. We look forward to further improvements in the global stability of the beamline in order to run experiments that require very long acquisitions, over several days in a row. In addition, we aim at implementing continuous wavelength tunability.

Regarding the photoionization experiments, the new source has pushed the velocity map imaging spectrometer, which has been used for a long time on crystal lasers, to a new level of sensitivity. Moreover, the tunability of the repetition rate between 166 kHz and 2 MHz introduces a revolutionary concept for the study of resonant multiphoton processes : the energy per pulse can be widely modulated without affecting the acquisition time. The high and tunable repetition rate of the source is also crucial for the new detection apparatus. An important

part of this thesis consisted in building and characterizing a coincidence spectrometer, which enables the direct measurement of the 3D photoelectron momentum distributions in coincidence with the corresponding mass spectra. It has been fruitfully used so far, but remains dependent on very long acquisitions. Indeed, even if a decent 3D distribution can be measured in a few minutes, the acquisitions increases by an order of magnitude when the coincidence is required. Moreover, the measurements of the photoelectron circular dichroism, our chiral observable of choice, requires an additional order of magnitude, up to dozens of hours. This step has been reached recently, but we are willing to carry out time-resolved pump-probe experiments, that require even more runtime. Beyond the stability of the laser source (in particular related to the thermal drifts over several days), this could be achieved by enhancing the window coincidence scheme to a continuous acquisition scheme.

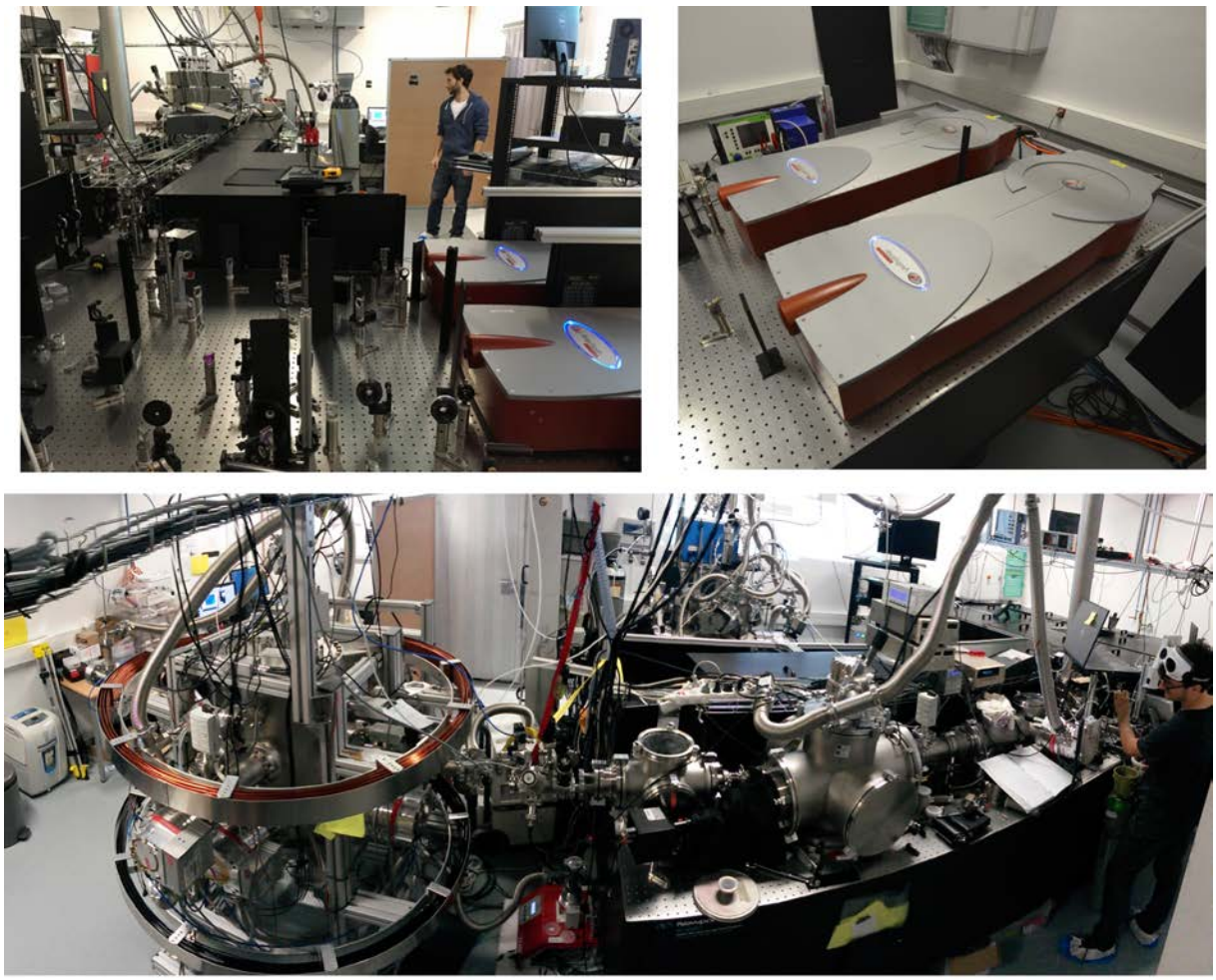

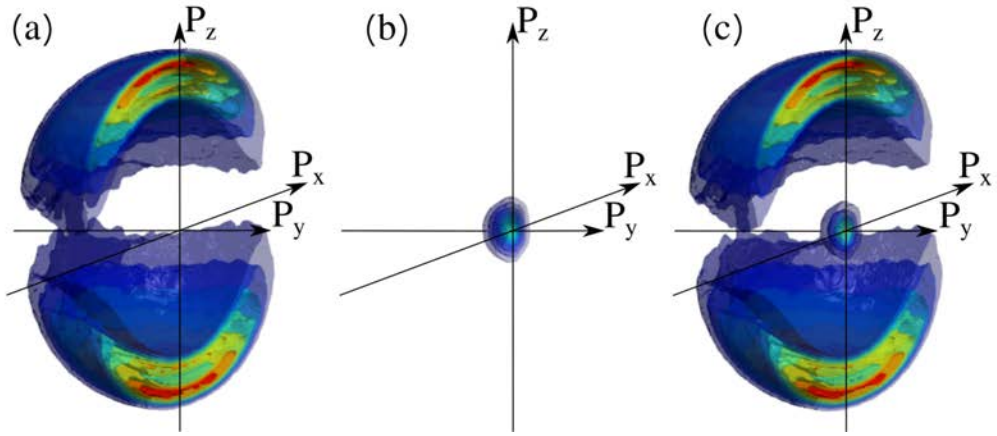


**Figure 2.47** – *Pictures of the high repetition rate beamline. (Up, right) Dual fiber amplifiers on the optical table, (Up, left) Optical setup, (Middle) HHG beamline coupled to the COLTRIMS, with the VMI and the laser in the background. (Bottom) Example of photoelectron angular distributions produced with HHG beam and measured in coincidence with xenon monomers (a), xenon dimers (b) and without coincidence (c).*

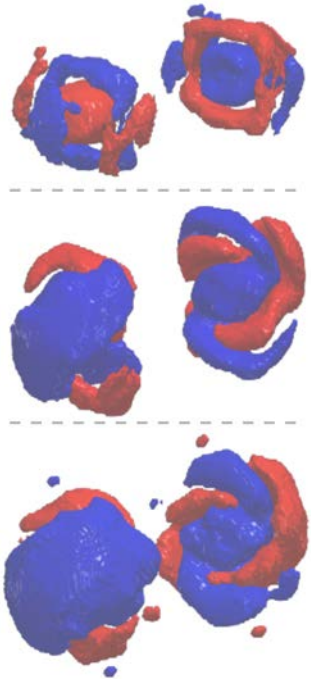

# Chapter 3

# Multiphoton Regime - Molecular Sensitivity

As we see throughout this manuscript, Photoelectron Circular Dichroism is a powerful tool to investigate molecular chirality in a wide variety of ionization regimes [Beaulieu 16b], ranging from the single-photon, the multiphoton to the ATI and tunnel ionization regimes. In this chapter, we will focus on the multiphoton regime and more specifically on the opportunity it provides in terms of sensitivity to the excited molecular states and dynamics.

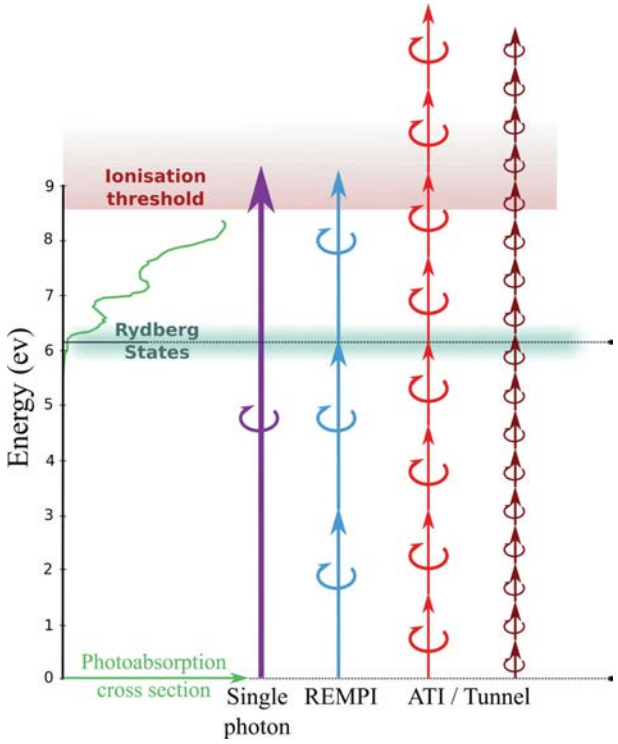


**Figure 3.1** – *Illustration of the different ionization regimes at which the PECD arises. In particular in the resonance-enhanced multiphoton ionization, the intermediate excited states can play an important role, in this chapter mainly through the anisotropy of excitation that they induce. The Rydberg states density of Fenchone is depicted here as an example. Extracted from [Beaulieu 16b].*

# I Introduction

## I. 1 Resonance-Enhanced MultiPhoton Ionization (REMPI)

**Properties of the Single-Photon PECD**

As we have seen in the introduction chapter, the sensitivity of the PECD was initially demonstrated in the single-photon ionization regime. In this case, PECD is known to be remarkably sensitive to the whole dynamics of the photoionization process, and strongly depends on several factors. Firstly, the initial orbital from which the electron is ionized plays a role, for instance the PECD associated to the HOMO or HOMO-1 can have an opposite sign [Turchini 04, Nahon 06]. Secondly, it depends on the whole structure of the ionized molecule. Substituting a group far away from the ionized orbital can lead to an inversion of the PECD [Nahon 16]. This reflects the non-local character of this observable, the chiral response being imprinted during the electron scattering onto the whole molecular potential. As a result, it is also sensitive to the conformational geometry [Turchini 09, Turchini 13]. Thirdly, PECD is a function of the kinetic energy with which the photoelectron is ejected [Powis 08]. Electrons emitted from the same orbital and differing only by a few eV can show opposite dichroic signals. Fourthly, it is affected by the vibrational excitation. Sign change of the dichroism associated with two consecutive vibrational states of the Methyloxyrane ion were observed [Garcia 13], and this property was later observed in other chiral compounds [Ganjitabar 18, Ganjitabar 20]. Finally, single-photon PECD depends on the molecular orientation of the target [Tia 17], even if it survives the averaging over all the orientations in randomly aligned samples.

**Extension to the Multiphoton Ionization Regime**

Replacing the XUV radiation by a femtosecond laser pulse affects the structure of the PECD as we will see in the next paragraph, but most of the aforementioned properties still apply. In addition to them, a new element will play an important role. When performing multiphoton ionization of an atomic or molecular systems, intermediate excited states can indeed be reached (see Fig. 3.1) and drastically affect the process. Generally, transitions to the excited states enhance the ionization yield compared to the non-resonant case, leading to the so-called Resonance-Enhanced MultiPhoton Ionization (REMPI). This situation is very common, including when chiral molecules are ionized with femtosecond laser pulses. The ionization potential of these molecules is typically below 10 eV, with a high density of states above 6-7 eV (the typical threshold of the Rydberg series), in a range that can easily be reached by absorption of a few photons of the fundamental laser (1030 $nm$ *i.e.* 1.20 $eV$ with our Yb fiber laser, 800 $nm$ *i.e.* 1.55 $eV$ with a Ti:Sa laser) or its harmonics. These processes are usually denoted as [n+m] REMPI, where n is the number of photons required to reach the resonance and m is the number of photons from this resonance to the continuum.

The observation of the PECD in the multiphoton regime (MP-PECD) was first established by the Kassel [Lux 12] and the Amsterdam/Nottingham groups [Lehmann 13]. In [Lux 12] in 2012, multiphoton PECD was measured in Fenchone and Camphor, two bicyclic ketones

isomers. Comparing the signal from these two isomers and from Norcamphor revealed significant differences, even though these molecules have relatively similar structures, close electronic densities and ionization thresholds (respectively 8.6 , 8.7 $eV$ and 9.2 $eV$ vertical $I_p$) [Lux 15]. This demonstrated a high sensitivity of MP-PECD to the precise molecular structure. Since then, REMPI-PECD has also been measured in a few other chiral compounds such as Limonene [Rafiee Fanood 15, Beaulieu 18a], Iboprofen [Comby 20b], Ethyl-Lactate, Methyl-Lactate and thus happens to be a general effect.

Studies have shown for example in [2+1] ionization of Fenchone with a wavelength ranging from 359 $nm$ to 431 $nm$ that the sign of the PECD can be inverted if the intermediate resonant state was the $3s$ (6.10 $eV$) or one of the three $3p$ (6.58 $eV$) [Kastner 17]. This effect has been reproduced with nanosecond pulses [Kastner 19], even if the mechanism is more sequential than with femtosecond pulses. More generally, it turns out that the PECD is also sensitive to the orbital excited (for example HOMO or HOMO-1 of Limonene [Beaulieu 18a] or HOMO-(0-2) of Fenchone [Beaulieu 16a]) and to the vibrational state. Fine resolution of the vibrational levels has been performed with nanosecond dye lasers, but this study, made only in Fenchone, suggested that the PECD was not drastically sensitive to it under these conditions [Kastner 20]. The generality of this latter observation remains to be confirmed, however. At the end, the signal very often comes from a manifold of excited states and calculations typically based on Density Functional Theory (DFT) [Rafiee Fanood 15, Beaulieu 16a, Beaulieu 16b] method helps assigning the excited state density, but is quite challenging in the Rydberg states manifold. As a result, the process depends also on the precise laser wavelength and [n+m] REMPI scheme [Lehmann 13, Beaulieu 16a, Beaulieu 16b, Demekhin 18]. Quantitative numerical simulations of the PECD itself in the multiphoton regime can be possible using for example Time-Dependent Single Center (TDSC) method [Demekhin 18]. It can also be calculated by using or a combination of *ab initio* calculation (to get the transition dipoles) and perturbative theory for the description of the excitation and a single-center description of the ionization step [Goetz 17, Goetz 19]. Multi-center basis set can also be employed [Turchini 13]. Finally, it seems credible that MP-PECD can be sensitive to the conformational state of the molecules, even if this effect has only been described in single-photon ionization. This layer of complexity can be avoided, typically in strained molecules such as the bicyclic ketones previously mentioned.

As a result, the MP-PECD is a double-edged sword. On one hand, it is a very rich observable to investigate the chiral response of molecular system. It is experimentally handy, as it survives molecular orientation averaging, and provides a remarkably high signal (1-10% range) with a relatively simple setup. On the other hand, the high sensitivity of MP-PECD to many parameters (initial orbital, intermediate state, vibrational ionic state, electron kinetic energy...) makes the physical interpretation quite indirect, and it can be challenging to disentangle the molecular effects involved.

**Quantifying the MP-PECD**

The structure itself of the MP-PECD differs from the single-photon case. The higher number

of photons involved leads to sharper structures in the photoelectron angular distributions. These angular features contain information which can be quantified. Typically when the measurements are performed with a Velocity Map Imaging spectrometer, the photoelectron angular distribution $S_p(E,\theta)$ can be expressed on a basis of Legendre polynomials $P_i^0$ :

$$S_p(E,\theta) = \sum_{i=0}^{2N} b_i^p(E) P_i^0(cos(\theta)) \tag{3.1}$$

where $E$ is the photoelectron kinetic energy, $p = \pm 1$ is the light helicity, $\theta$ is the ejection angle and $i$ is the order of the polynomial. Note that the even order ones are symmetric along the laser propagation axis and the odd ones are antisymmetric. In the simple case where the field is circularly polarized, or more generally when the field has a cylindrical symmetry (and that the symmetry axis in contained in the VMI projection), the maximal order of polynomial $2N$ corresponds to twice the number of photons $N$ involved in the ionization [Reid 12]. This can be understood as a consequence of angular momentum conservation. The distribution yielded by a single photon ionization is thus necessarily simply described by $P_0^0$ and $P_2^0$, grasping the non-chiral part, and $P_1^0$, expressing the chiral-specific response. In the multiphoton regime however, the distribution can be significantly more complex, and the different orders of polynomial can be associated with specific physical interpretation as we will see in this chapter. In any case, the odd orders vanish when using linearly polarized fields or achiral targets, and their sign reverses with the light helicity otherwise, unlike the even orders.

With such a decomposition, it becomes possible to define an angularly integrated quantity which gives the overall asymmetry, the MPPECD. It quantifies the excess of electrons emitted forward compared to backward along the field propagation axis, which can be normalized and expressed at the third order as :

$$MPPECD(E) = (2b_1(E) - \frac{1}{2}b_3(E))/b_0(E) \tag{3.2}$$

where $b_0$ is the total number of photoelectrons and $E$ is their kinetic energy. This expression is valid as far as the cylindrical symmetry in maintained in the ionization process, which is not the case for instance when the sample is not randomly oriented.

Note that the normalization of the PECD found in the literature can differ depending on the authors, and can be either with respect to the total number of photoelectrons [Kastner 17], as presented above, or relatively to the number of electrons emitted by hemisphere [Rafiee Fanood 15]. The first case will apply throughout this manuscript, except in the fast enantiomeric excess measurements presented in this chapter. In any case, the quantities are defined in every corresponding sections.

Finally, using a REMPI scheme in PECD experiments provides an additional degree of freedom as the exciting and ionizing fields can be independently manipulated in a pump-probe experiment fashion. This can, of course, be used to get temporal resolution on the processes. This aspect will be discussed in the last section of this chapter. This can also be used in order to disentangle the respective influence of the excitation and the ionization steps, as we will see

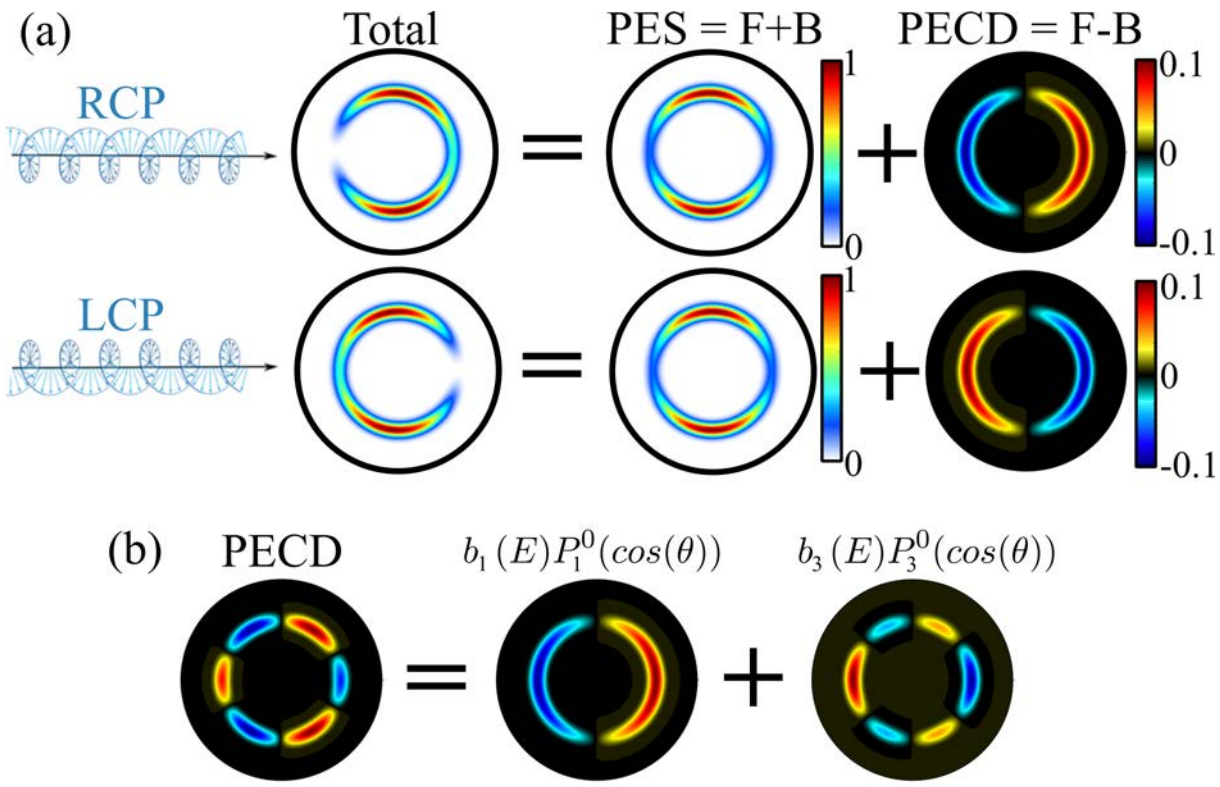


**Figure 3.2** – *(a) Schematic of the decomposition of the photoelectron angular distributions on a basis of Legendre polynomial. The total distribution has a symmetric and antisymmetric part along the laser propagation axis (horizontal). The antisymmetric part reverses with the light helicity while the symmetric one remains unchainged. Note that the distribution is fully symmetric if the light is linearly polarized of if the molecule is achiral. The PECD depicted is typical of a one-photon ionization, where the first order Legendre polynomial fully described the antisymmetric part. (b) Decomposition of a typical multiphoton PECD, where higher Legendre polynomial orders are reached (here for a two-photon ionization).*

in the next paragraph.

## I. 2 Disentangling the Excitation and the Ionization

### Bound-Bound and Bound-Continuum Transitions

An important question in MP-PECD is the role of the bound-bound and bound-continuum transitions in the emergence of the dichroic signal. A previous study was carried out in our team [Beaulieu 18a] to investigate this question in the REMPI-PECD in Limonene ($I_p$ = 8.5 $eV$). Firstly, they compared [2+1] (396 nm) with [2+2'] (396 nm + 800 nm) and [1+1'] (199 nm + 402 nm) REMPI schemes, where the intermediate states lie in the same $3s$ and $3p$ Rydberg states manifold around 6 $eV$, and the final energy was about 9.3−9.4 $eV$ in all cases (Fig. 3.3 (a)). Interestingly, the PECD was sensitive to the number of photons involved in the excitation. This was interpreted as the consequence of a different anisotropy of excitation. Indeed, the PECD is a quantity that arises as an average over randomly aligned molecules, but it is known that the dichroic response of aligned molecules can be very strong and not necessarily similar to the PECD for all orientations [Tia 17]. The stronger the bound-bound transition is compared to the non-resonant ionization, the more this transition selects the subset of molecules whose transition

dipole matches the laser polarization plane. In the most dramatic cases of photoexcitation anisotropy, the sign of the PECD can even be inverted. Generally speaking, a higher number of photon involved leads to a higher maximal order of Legendre polynomials, and the anisotropy of excitation tends to appear in the high-order terms ($b_{(2k+1)}$, $(2k+1) \geq 3$).

A two-color REMPI scheme allows an independent control of the polarization state of the fields performing either the excitation or the ionization (Fig. 3.3 (b)). Firstly, it appears that a circularly polarized ionizing field with a linearly polarized exciting field are sufficient to produce significant PECD, as also theoretically predicted in [Goetz 17]. It can even yield greater MP-PECD values compared to the fully circular case. This is due to the significant anisotropy of excitation induced, as the linear polarization not only preferentially selects a plane, but an axis of molecular orientations. Secondly, when comparing the distributions yielded by circularly polarized fields for both the excitation and ionization, measurements indicate that PECD hardly varies when switching the handedness of the excitation field. This indicates that the pump does not dominate the dichroic response of the light-matter interaction in the photoionization. This is confirmed by the fact that the asymmetries in the photoelectron angular distributions are strongly reduced when using a circular pump and a linear probe (see also [Beaulieu 18b]).

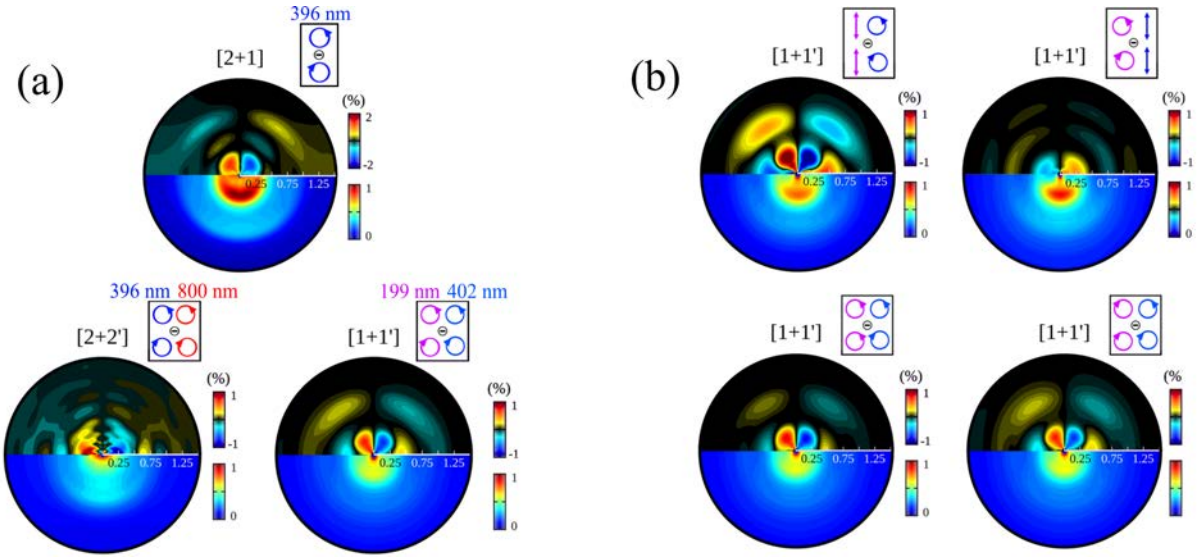


**Figure 3.3** – *Photoelectron angular distributions in (+)-Limonene in different REMPI schemes. The PECD and the PES are depicted respectively in the upper half and the lower half of each panel. (a) Wavelength dependency of the distributions. (b) Pump and probe polarization dependency of the distributions. Adapted from [Beaulieu 18a].*

Indeed, PECD is not expected to occur with linearly polarized ionizing fields. However, experiments have shown that non-zero forward/backward asymmetries could exist in such a case, meaning that the bound-bound transitions can induce a chiroptical effect, as we will see in the next paragraph.

**PhotoeXcitation Circular Dichroism (PXCD)**

A recent study previously performed in our team demonstrated that a chiroptical interaction leading to strong forward/backward asymmetries can also be induced in neutral chiral molecules, without the need of the photoionization step [Beaulieu 18b]. This effect, called PhotoeXcitation Circular Dichroism (PXCD), occurs if the photoexcitation is performed with circularly polarized light and coherently excites at least two excited states of a chiral target. The dipole transitions to these two states must be non-collinear. An orientation-averaged dipole $\vec{d}$ can then start oscillating, describing a helical motion. The component of the dipole in the polarization plane oscillates at the frequencies corresponding to the energies of the excited states, *e.g.* $\Delta E_{01}$ and $\Delta E_{02}$ if we consider only two excited states $|1>$ and $|2>$ . The created dipole vector describes a beating helix, rotating at the laser frequency, as depicted in Fig. 3.4 (a). Interestingly, the component of the dipole along the laser propagation axis $z$ can be written as :

$$d_z^{PXCD} \propto \sigma[\vec{d}_{01} \times \vec{d}_{02}] \cdot \vec{d}_{12} sin(\Delta E_{12} t) \tag{3.3}$$

where $\vec{d}_{01}$ and $\vec{d}_{02}$ are the transition dipole matrix elements from the ground state to the excited states $|1>$ and $|2>$, $\vec{d}_{12}$ is the one between the two excited states (linked to the coherence between these two states) and $\Delta E_{12}$ is the energy difference between them. This equation can be generalized for any number of excited states with all the corresponding cross-terms. This dipole oscillation can be expressed as an oscillating electronic current :

$$j_z^{PXCD} \propto \sigma[\vec{d}_{01} \times \vec{d}_{02}] \cdot \vec{d}_{12} \Delta E_{12} cos(\Delta E_{12} t) \tag{3.4}$$

Importantly, these two quantities along the laser propagation axis vanish if the target is not chiral or if the field is linearly polarized, and they change sign with $\sigma = \pm 1$ the helicity of the field. It is thus a proper chiroptical effect, that appears under the electric dipole approximation, similarly to PECD. These two effects are however totally distinct since the PECD results from an asymmetric scattering of the photoelectrons. It is also fundamentally different from the anisotropy of excitation mentioned in the previous paragraph as it requires at least two coherently excited states and is chirosensitive.

This effect has been calculated theoretically, but also detected experimentally by ionizing the excited molecules with a probe pulse. This latter one was linearly polarized to avoid adding standard PECD effect from the bound-continuum transition, as sketched in Fig. 3.4 (b). This scheme, called PhotoeXcitation-induced photoElectron Circular Dichroism (PXECD), has been performed in Fenchone and Camphor molecules. In the first one, the excitation coherently populated the $3s$ and $3p$ Rydberg states manifold and yielded PXECD signal. Interestingly, in the second target, only the $3s$ manifold was excited but still yielded some dichroic signal. This means that both coherences between electronic or vibronic states can lead to this effect. Due to the limitations encountered in the pump pulse duration ($\geq$ 50 fs), the PXCD fast oscillations were only directly accessible theoretically, and have been calculated to reach up to 35%. The experimental observable, PXECD, has been measured in the few % range due to the time-averaging over the pulse duration, which is again significantly stronger that magnetic or quadrupolar-based chiroptical processes. The temporal aspect of the process is mentioned in the last section of this chapter.

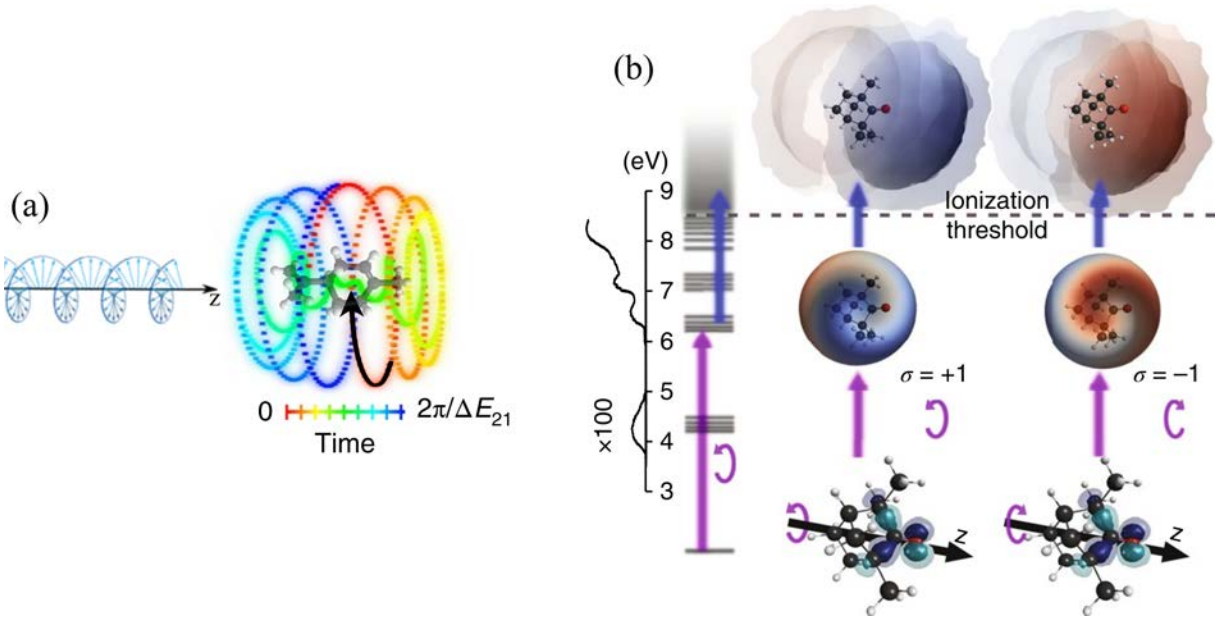


**Figure 3.4** – *(a) Representation of the induced excited states dipole $\vec{d}_{01} \times \vec{d}_{02}$, describing a helical motion. If the wavepacket is created in a chiral molecule, there is also a directional preference (initial phase) imposed on this helical rotation along the laser propagation axis that starts oscillating. The phase of this forward/backward oscillation depends on the enantiomer handedness (PXCD). (b) PEXCD REMPI scheme used in Limonene (similar in Fenchone). Adapted from [Beaulieu 18b].*

## I. 3 Beyond Circular Field Polarization

The recent development in laser science has brought the opportunity to tailor exotic laser fields, as also discussed in the Strong Field chapter of this manuscript. Several implementations have recently emerged in the multiphoton interaction with chiral systems. A scenario of coherent control between a direct ionization with a [1+1] REMPI process using two circularly polarized fields, based on the individual control of all the possible intermediate states, has for example led to a predicted 68% asymmetry in [Goetz 19]. Differently, bilinear Orthogonal Two-Color (OTC) fields, where the field can describe a chiral "8" or "C" shape depending on the two-color phase, have for instance been theoretically studied in [Demekhin 18]. In this case, the interference between the one-photon ionization from the second harmonic with the two-photon process from the fundamental frequency (both linearly polarized) can be balanced to foster the asymmetry in the photoelectron angular distribution up to 25%.

In a much simpler fashion, the ellipticity of the light can also be a control parameter. In the one-photon ionization regime, it is established that PECD obtained with elliptical polarization is simply proportional to the amount of circularly polarized photons, quantified by the Stokes parameter $S_3$ [Nahon 06]. In this case, there is thus no clear interest in using elliptical polarization. However, in a REMPI-PECD scheme, the intermediate resonances will once again significantly modify the chiral response. Several studies that can be found in the literature reported a deviation from the linear response to $S_3$ in the multiphoton regime, ranging from an increasing slope at high ellipticities [Lux 15] to a sharp slope change at $|S_3| = 0.4$ [Miles 17]

(Fig. 3.5). This naturally raises interesting questions : can we use this non-trivial behavior to enrich the chiroptical response of a chiral molecule? Modulating the field ellipticity is a much more easy-going degree of freedom than pump-probe schemes, for example. Can we thus use it to get a novel, experimentally robust, insight into the chiral molecular systems? These questions are all considered in the following part.

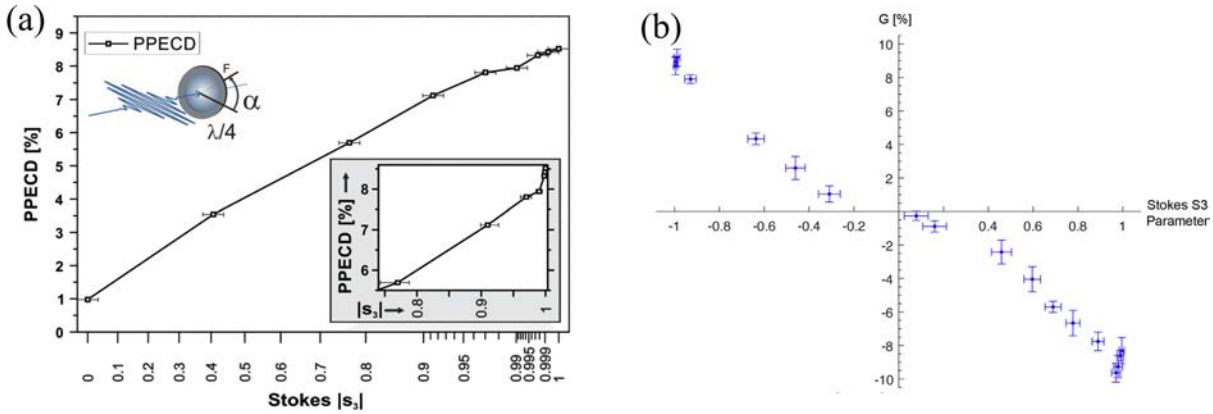


**Figure 3.5** – *Non-linear scaling of the PECD with respect to the Stokes parameter $S_3$ in the multiphoton ionization of chiral molecule, found in the literature. (a) Extracted from [Lux 15] and (b) from [Miles 17]. Both examples are in (-)-Camphor, and the wavelength used were respectively 398 nm and 394 nm. Note that the quantities depicted are slightly different but that the sign of the PECD is actually the same.*

# II Real-Time Determination of Enantiomeric and Isomeric Content

Molecular chirality plays a central role in a wide range of scientific fields and applications, such a in organic chemistry, biology, drug design and asymmetric catalysis as presented in the introduction of this manuscript, and could also have implications in astrophysics [Hadidi 18]. Characterizing the enantiomeric composition of a sample is thus of crucial importance, fundamentally and practically. The determination of the absolute configuration from scratch can be challenging, but methods such as X-ray scattering in crystallized matrices [Inokuma 13], molecular frame coulomb explosion using COLTRIMS [Pitzer 13] (illustrated in Fig. 3.6 (a)), or vibrational circular dichroism (VCD) compared with *ab initio* calculations [Batista Jr. 15] have been demonstrated as possible techniques. On the other hand, most of the techniques used are only able to discriminate two enantiomers and are simply compared to known samples. The most commonly used analytical characterization is the chromatography through a chiral substrate, where two enantiomers of a sample have different migration times in a column depending on their handedness. Such technique can be implemented in the gas phase, for example in two-dimentional gas chromatography - time-of-flight mass spectrometry (GCxGC-TOFMS) [Vetter 97] that reaches a state-of-the-art 0.1% precision in the enantiomeric excess determination. However, this method has drawbacks, such as the lack of a universal substrate, a cumbersome preparation and the inherent long time required for the migration (typically hours).

Chiroptical processes have emerged as a competitive alternative as their natural timescales are much faster. The aforementioned VCD is nowadays reaching $\sim 1\%$ sensitivity in commer-

cial instruments, able to monitor the enantiomeric excess in real time [Guo 04, Mower 18] by simply recording the variation of vibrational absorption depending on the light helicity. This technique, however, relies on electric quadrupolar and magnetic dipolar effects, and is thus only implementable in liquid samples, requiring a significant amount of molecules and introducing difficulties related to the solvatation effects. This is the case more generally for the historical absorption circular dichroism and optical rotation experiments (linked together with the Kramers-Kronig relation). In the gas phase, microwave three-wave mixing, based on a combination of two fields to selectively excite rotational transitions, inducing a chiral-sensitive free induction decay, yields a $\sim 1\%$ precision [Patterson 13a, Patterson 13b, Shubert 14] (depicted in Fig. 3.6 (b)). High-order harmonic generation has also been proved to be chiral-sensitive [Cireasa 15, Baykusheva 19] but still remains a weak effect, even if recent theoretical developments on locally and globally chiral fields hold the promise of strongly increasing this sensitivity [Ayuso 19].

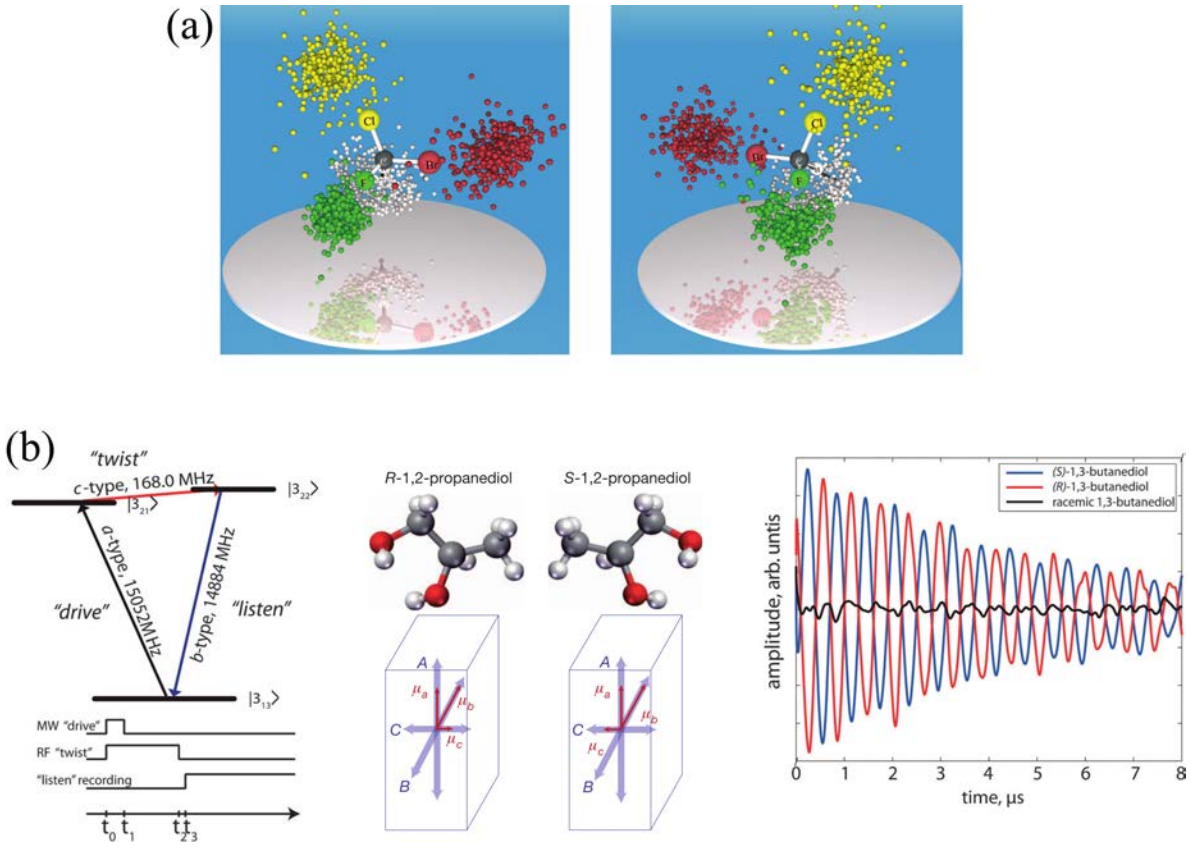


**Figure 3.6** – *Illustrations found in the literature of chirality-sensitive observables. (a) Coulomb explosion imaging of the two enantiomers of the CHBrClF molecule, extracted from [Pitzer 13]. (b) (left) Microwave three-wave mixing scheme, in which the initial phase of the emitting dipole depends on the handedness of the enantiomer and thus the enantiomeric excess. (middle) Orientation of the transition dipoles involved. The last one reverses with the enantiomer handedness. (right) Resulting rotational free induction decay, measured in the two enantiomers of 1,3-butanediol (right). Extracted from [Patterson 13a].*

Finally, photoelectron circular dichroism, discussed at length in this manuscript, has been applied to retrieve the enantiomeric purity of various samples in the gas phase. Precision of

$\leq$ 1% has been reached in a few hours in single-photon ionization using XUV synchrotron radiation [Nahon 16]. Similar precision was achieved in REMPI-PECD in about 10 mn with a 1 $kHz$ repetition rate laser [Kastner 16] and 5% in 1 min at higher repetition rate [Miles 17]. Interestingly, multi-component enantiomeric determination was demonstrated using PECD and photoelectron-photoion coincidence detection, distinguishing compounds and yielding $\sim$ 20% accuracy in the enantiomeric excess in 18 h [Rafiee Fanood 15]. We will see in this section how these performances can be significantly improved by employing elliptical polarizations in REMPI processes, combined with a high repetition rate table-top laser. It can provide a better precision, within a shorter acquisition time, and even resolve multicomponent mixtures without the need of mass spectrometry.

## II. 1 Photoelectron ELliptical Dichroism (PEELD)

This experiment has been done in Bordeaux in collaboration with Jason Greenwood and Caiomhe Bond from the Queen's University of Belfast. As mentioned in the introduction of this chapter, the photoelectron angular distribution does not have a cylindrical symmetry if the polarization of the laser field is neither linear nor circular. In particular, this is the case with elliptical polarizations. Consequently, a typical VMI projection does not contain all the information encoded in the distribution in this case. Two methods can be used to access the full 3D distribution : either tomographic reconstruction from several VMI images projected along different axis, or direct 3D measurement using delay lines detector, as discussed in the previous chapter. These two possibilities will be compared in the next section.

Fig. 3.7 illustrates the 3D photoelectron distribution retrieved using tomographic technique, for several chiral molecules (left column) with several field ellipticities (top row) measured in a [3+1] REMPI scheme at 515 $nm$. The field intensity used was 5 $\times 10^{13}$ $W.cm^{-2}$ and the repetition rate of the laser was set to 2 MHz. For each molecular target (row), 36 VMI projections were recorded. For each projection, the ellipticity of the field was continuously varied and the axis of the field ellipse were kept fixed. The ellipse was rotated by steps of 10 degrees between the projections in order to perform the tomographic reconstruction. Thanks to the high repetition rate of the laser source, each projection took about 200 s to record, for a total of 120 min for each row. The analysis method will be more extensively presented in the next section. Essentially, a lock-in detection technique enabled an efficient filtering of the noise. The distributions presented above in each panel are the 3D reconstructed photoelectron distributions at a given ellipticity. The lower distributions in each panel are the corresponding dichroic signals, corresponding to the part of the distribution that reverses with the handedness of the field (at the same ellipticity). They can also be obtained by selecting the forward/backward antisymmetric part along the laser propagation axis for a given polarization, or by subtracting the signal obtained between the two enantiomers. These three methods are in principle redundant for PECD. In practice, the two first ones were applied to the data in order to cancel experimental artifacts, and the comparison with the opposite enantiomer is only used for sanity check, as it is more cumbersome to change the sample handedness than the light helicity. We will see that this turns out to be more subtle than PECD in the present case.

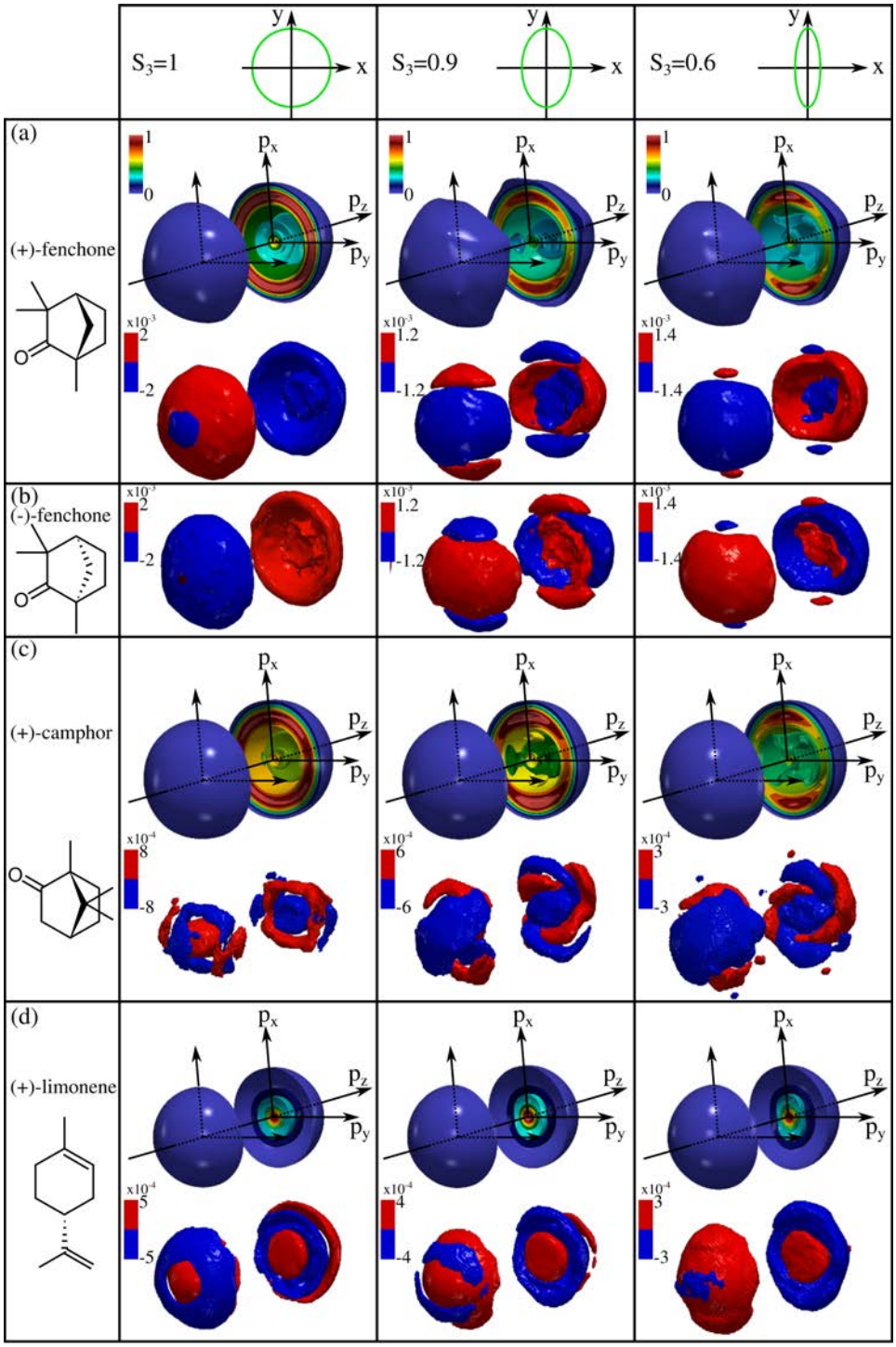


**Figure 3.7** – *3D photoelectron momentum distributions retrieved using tomographic reconstruction from VMI projections in (+)-Fenchone (a), (-)-Fenchone (b), (+)-Camphor (c) and (+)-Limonene (d). The laser field used was at a wavelength of 515 nm ([3+1] REMPI in all the cases) at 5* $\times 10^{13}$ *W.cm*$^{-2}$*, and the columns correspond to a Stokes parameter* $S_3 = 1$ *(left), 0.9 (center) and 0.6 (right). In each caption, the total distribution is depicted above and the corresponding dichroic part (defined in the text) is depicted below. z is the laser propagation axis (towards positive values), and also the axis around which the projections are rotated for the tomographic reconstruction, in order to reconstruct the 'blind' y axis. 36 projections were recorded for each row, with 10° steps, for a total of 120 min of acquisition per row.*

Each panel displays isosurface contours of the complete and dichroic part of the measured distributions, and several important features are visible. At first sight, one can notice that both the total and the chiral-specific distributions are very sensitive to the target. One can see that the distributions obtained with the circularly polarized field ($S_3 = 1$) do have a cylindrical symmetry around $z$, corresponding to the PECD. But when introducing ellipticity ($S_3 = 0.9$ and 0.6), the symmetry is broken, the distribution starts to be peaked along the main axis of the field ellipse and finer structures in the dichroic signal appear. The more ellipticity is introduced, the more prominent this effect is, especially in Camphor (c). We named this effect Photoelectron ELliptical Dichroism (PEELD). This typically reveals the anisotropy of excitation induced by the non-circular field, preferentially exciting the molecules transition dipole along the main axis of the field. As the excited state manifold involved greatly depends on the molecular structure, the PEELD signal is intrinsically very sensitive to it. Especially, Fenchone and Camphor have very distinguishable distributions even if these two molecules are isomers that can not be resolved in a mass spectrum. Even with a small ellitpicity ($S_3 = 0.9$), the dichroic signal globally changes sign in Fenchone for example. Finally, the comparison between (+) and (-)-Fenchone confirms the enantiomeric sensitivity of the experimental measurements.

Note that an intriguing whirl shape is visible in the dichroic parts with elliptical polarizations, in particular in Camphor (c) at $S_3 = 0.9$. This reflects an additional symmetry breaking : while the inversion of the $S_3$ parameter only inverts the signs of the features, the inversion of the enantiomer handedness also reverses the rotation of the whirl. This is confirmed by the comparison of the central features in Fenchone (a) and (b), at $S_3 = 0.9$ and 0.6. In the strong field ionization regime, this could be understood as a chiral attoclock effect, but in the present multiphoton regime, the interpretation is more indirect and not fully understood so far. In any case, this indicates that elliptical fields break the cylindrical symmetry by introducing preferential axis. As a consequence, one must be careful with the quantities defined. In the present case, the dichroic signal is forward/backward antisymmetric and reverses sign with the ellipticity, but sustains a spatial inversion with the reversal of the enantiomer handedness. This is the reason why the dichroic signal can not be directly obtained from the subtraction of the signal obtained with the two enantiomers in this case. Interestingly, the photoelectron angular distributions are thus defined absolutely by the set of field and enantiomer here, and not only relatively. This type of effects will also be described with strong tailored laser fields in the last chapter of this manuscript.

**Asymmetry Factor G**

Despite containing all the accessible information, the complete distribution is not necessarily the best observable. Primarily because acquiring enough statistics for a 3D measurement necessarily takes time. Furthermore, it makes the estimation of the overall forward/backward asymmetry quite difficult. For this purpose, similarly to the PECD, we define an asymmetry factor G as :

$$G = \frac{4(F-B)}{(F+B)} \tag{3.5}$$

where F and B are respectively the integrated signal on the forward and backward hemispheres. The evolution of G with respect to the Stokes parameter $S_3$ measured in (+)-Fenchone, (+)-Camphor and (+)-Limonene measured at a field intensity of $I_{515nm} = 5 \cdot 10^{12}\ W.cm^{-2}$ is presented in Fig. 3.8. Interesting features appear more clearly here. Firstly, the asymmetry factor G has a linear dependency with $S_3$ at low ellipticity, depicted with the dotted lines. Secondly, one can observe a drastic nonlinear behavior for $|S_3| \geq 0.6$, even leading to a sign change of G around $|S_3| = 0.9$. Thirdly, the observable shows a strong molecular dependency, especially between Fenchone and Camphor/Limonene, as G is maximized in the first case in circular polarization while it almost vanishes for the other ones. Note that reducing the whole evolution with respect to a single factor can be a little bit too simplistic : one can see here that Camphor and Limonene are hardly distinguishable with G only. We will address this issue in the next sections.

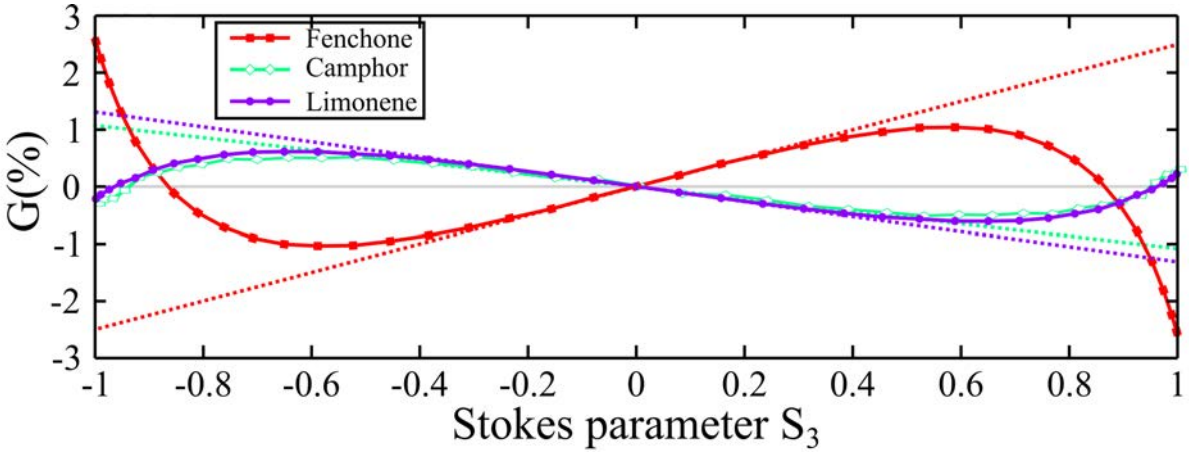


**Figure 3.8** – *Evolution of the the forward/backward asymmetry G as a function of $S_3$, in (+)-Fenchone (red squares), (+)-Camphor (green diamonds) and (+)-Limonene (purple circles), at $5{\times}10^{12}$ $W.cm^{-2}$. The dotted lines are a linear extrapolation of the low-$S_3$ behavior.*

**Interpretation**

With the 515 *nm* laser wavelength used here, the ionization occurs in a [3+1] REMPI scheme, where the intermediate states lie in the Rydberg state manifold at $3 \times 2.41 = 7.22$ *eV*, just below the ionization threshold as depicted in Fig. 3.9 for Fenchone, whose $I_p = 8.72$ *eV* (HOMO). When circular polarization is used, the excitation preferentially occurs in the randomly aligned sample for the molecules whose transition dipole moment is in the polarization plane (right panel). If lower ellipticity is introduced, the excitation will start to be also due to the linear polarization component of the field. In this case, the excitation will preferentially occur along the polarization axis (left panel). The key point here is that this multiphoton excitation is more efficient for the linear photons than for the circular ones. Indeed, within a perturbative approach, the efficiency of a three-photon process scales with the cube of the laser electric field, and for a given beam energy flux, a linear field has a greater amplitude than a circular one (by a factor $\sqrt{2}$). This non-linearity makes the anisotropy of excitation very

sensitive even to a small linear component. On the other hand, it is thus not very sensitive to the circular component at low $S_3$ parameters. This competition between circular and linear components does not take place in the ionization step as we mainly focus on the dichroic part of the photoelectron distribution : only the circular ones will produce PEELD signal. This part can thus be considered as a single-photon ionization process from the excited states, that scales linearly with $S_3$. Overall, despite the fact that the "pump" and the "probe" are not independently controlled here, the whole enrichment of the PEELD is related to this preferential excitation. It yields a sharp evolution of the asymmetry at high $S_3$, and can be considered as linearly evolving with $S_3$ at low ellipticities, when the linear component completely dominates the excitation.

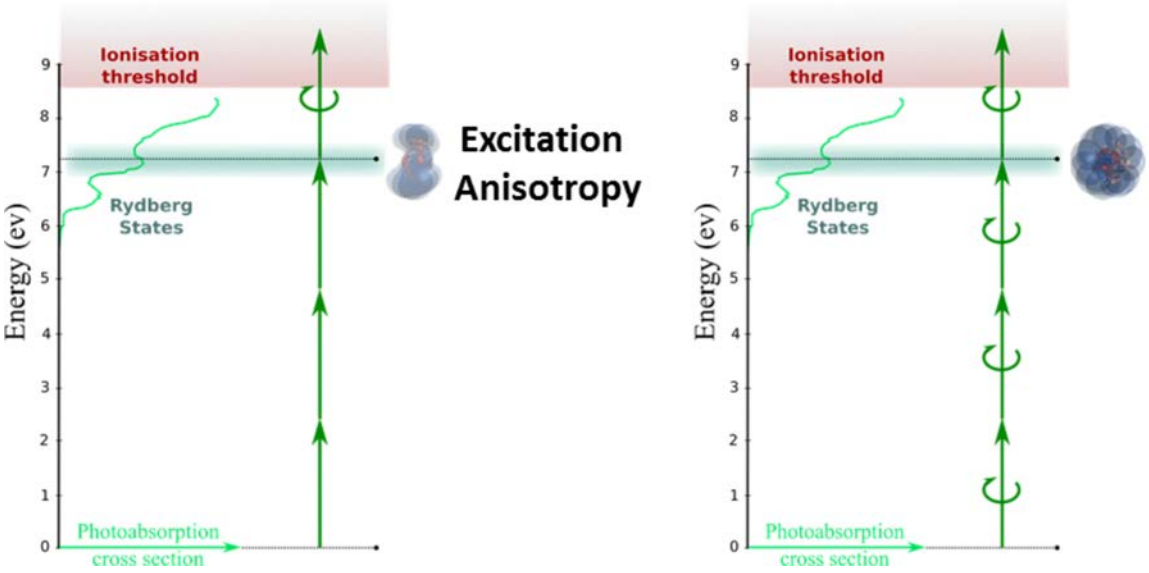


**Figure 3.9** – *PEELD effect in the REMPI scheme of the Fenchone at a wavelength of 515 nm. (left) At low field ellipticity, the excitation to the intermediate states is preferentially performed by the linearly polarized photons. This induces an anisotropy of excitation in the randomly aligned sample, as the molecules having a transition dipole along the polarization axis are preferentially excited. The dichroic response only comes from the part ionized from the excited states with circularly polarized photons. (right) At high ellipticity, the excitation is performed mainly by circularly polarized photons, selecting all the molecules in the polarization plane.*

**Evolution with the Field Intensity**

From the comparison of the two studies of the evolution of the asymmetry in the photoelectron distributions carried in Camphor, at 398 nm [Lux 15] and 394 nm [Miles 17], presented in the Fig. 3.5 in the introduction of this chapter, an intriguing discrepancy appears. Even if the evolution of the asymmetry with $S_3$ is monotonous in both cases, their exact evolution slightly differ. This might be either caused by a slightly different central wavelength, or by a different intensity used. In both cases, this indicates that the nonlinearity can be very sensitive to the exact levels at play.

In order to gain an additional hint into the role of the intermediate resonances, we have investigated the evolution of the PEELD with the laser intensity. Fig. 3.10 (a) and (b) show the 3D-PEELD projection in the VMI plane $(p_x, p_z)$, where $x$ corresponds to the

linear polarization axis and $z$ is the laser propagation axis, respectively using laser intensities of $I_{515nm} = 5 \times 10^{12}$ $W.cm^{-2}$ and $I_{515nm} = 1.7 \times 10^{13}$ $W.cm^{-2}$, for several $S_3$ values, in (+)-Fenchone. The $p_y$-integrations are normalized to the maximum of the symmetric signal value as 2(L-R)/max(L+R), where L and R and respectively the signal of the left and right hemispheres (forward/backward). Since the resonances at play in the REMPI process lie in the Rydberg manifold close to the ionization threshold, they are likely to be subject to Stark-shift from the laser field. Consequently, increasing the intensity will shift the energy levels resonant with the excitation, modifying the PEELD response. This is consistent with the data recorded with the OPA presented in Section 2.I, where the tunability of the source enables to scan across the resonances. Indeed, we have seen that consecutive excited states can have an opposite sign of PECD. One can thus expect a similar behavior on the PEELD response in the present case where the levels are shifted, for a fixed wavelength. However, the resonant energy shift range was quite great with the tunable source, but the ionization was performed in a [2+1] REMPI scheme while it is at [3+1] in the current study. The excited states involved are thus closer to the continuum and are more sensitive to Stark shift. In addition, we have seen that the nonlinearity of the PEELD could have a higher sensitivity than PECD to the intermediate levels. The analysis of the data recorded with the tunable source is still ongoing, but we can already expect that the Stark shift of the intermediate states could strongly affect the PEELD response in the present case, for a fixed wavelength. The intensity-dependent evolution of the PEELD presented in Fig. 3.10 (a) and (b) is mostly visible for the low energy structures, corresponding to the [3+1] ionization. The relative weight of the outer ring, corresponding to the 5-photons process, also increases but remains quite independent on the ellipticity. This suggests that this latter feature does not build on the resonances. The reduction of the global evolution to the G factor is displayed on Fig. 3.10 (c). At low intensity, the asymmetry maximizes at $|S_3| \sim 0.6$, while it is dominated in circular polarization between a few $10^{12} - 10^{13}$ $W.cm^{-2}$. The process will tend to the strong field regime when further increasing the intensity, in which case the chiral molecular potential plays a less prominent role in the scattering process, yielding a weaker dichroic response.

In summary, the nonlinear dependency on $S_3$ appears even more drastically here than in the previously mentioned literature. Varying this Stokes parameter significantly expands the molecular and enantiomeric specificity of the photoelectron distribution. The PEELD effect seems to be a universal effect of REMPI schemes in chiral molecules and brings the perspective to use its non-monotonic behavior to enrich the molecular signatures for analytical purposes.

### II. 2 Lock-in Detection : Continuous Modulation of $S_3$

The most straightforward manner to measure a PEELD experimentally is to simply set a polarization, then record the signal, then fix a new polarization and so on. However, this type of incremental recording is very exposed to fluctuations (laser power, alignment, target density...). The longer the acquisition, the more at risk it is. A common but fastidious manner to mitigate the fluctuations is to repeat the experiment several times in a row and average the result. Addi-

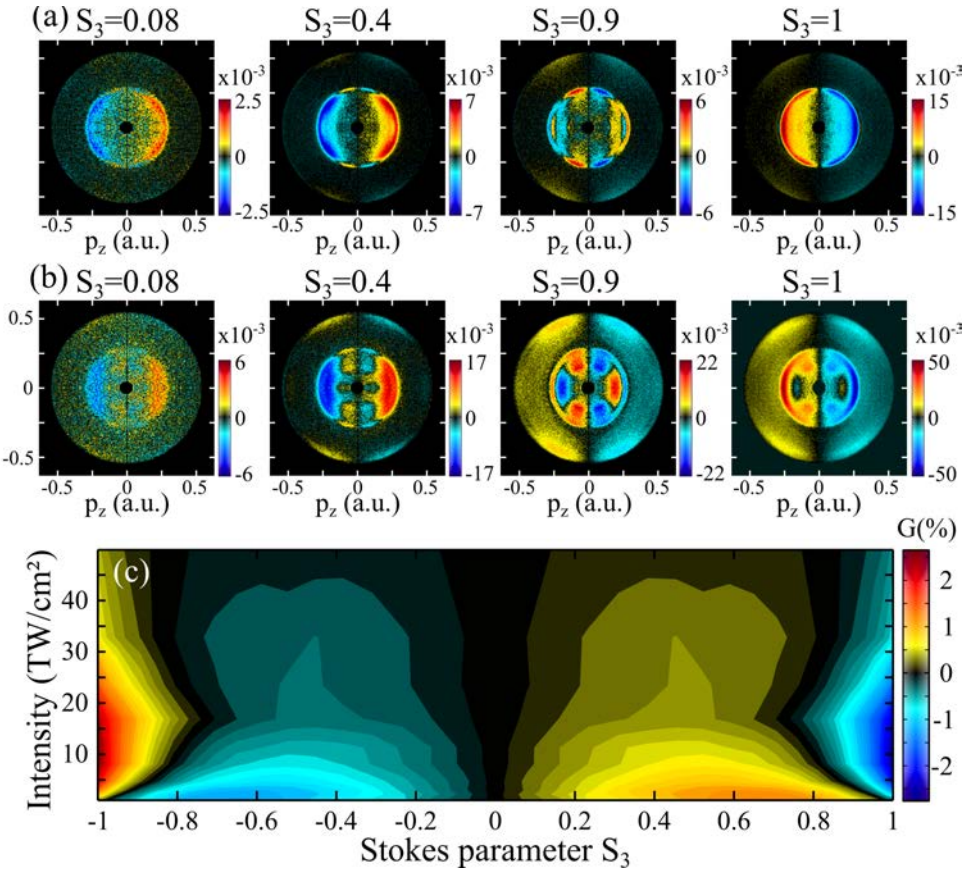


**Figure 3.10** – *(a-b) Projections of the 3D-PEELD from (+)-Fenchone in the (x,z) plane, at $5\times10^{12}$ $W.cm^{-2}$ (a) and $1.7\times10^{13}$ $W.cm^{-2}$ (b). The z axis is the laser propagation direction (towards positive values) and the x axis is the main axis of the laser ellipse, and the VMI detector lies in the (x,z) plane. The (x,z) projection are integration over the time-of-flight (y) axis of the VMI. (c) Evolution of the ellipticity dependence of the forward/backward asymmetry G with laser intensity in (+)-Fenchone. The measurements took about 10 minutes at each intensity, with a laser repetition rate of 2 MHz, by rotating a quarter waveplate at 45°/s in front of the VMI and using the lock-in detection presented in the next paragraph.*

tionally in our case, the use of a high repetition rate laser renders the exposure time necessary to record a decent VMI image very short (down to 50 ms). It means that even with an advanced motorized stage, the acquisition duty cycle is severely limited by the time it takes to rotate the waveplate to the next ellipticity. It is not necessarily related to its angular velocity, but more to the acceleration/deceleration and the inherent deadtimes of the softwave synchronizing the camera and the stage.

In order to overcome these two inconveniences, we implemented a continuous ellipticity modulation scheme. A quarter-waveplate is rotated at a constant angular velocity, so that the $S_3$ parameter of the laser beam is continuously and periodically modulated, combined with a continuous acquisition of the PEELD (c-PEELD) in the VMI device. The temporal evolution of the polarization state is depicted on Fig. 3.11. The polarization goes from a given circular to the opposite one every 90°, from circular to linear or conversely every 45° and the whole evolution has a 180° periodicity. In between, the polarization continuously evolves through all the elliptical intermediates. Note that the axis of the ellipse also rotates, so the projection

angle relatively to the ellipse varies with the ellipticity. This can be circumvented by rotating a half-waveplate in front of a fixed quarter-waveplate, which was necessary in the tomographic reconstruction presented in Fig. 3.7. However, the rotation of the ellipse does not affect the implementation that will be presented in the rest of the section. Since the VMI records projections and is insensitive to the momentum along the spectrometer axis $p_y$, the only difference that could happen would be a slight displacement of the features along the $p_x$ axis (the main axis of the polarization ellipse) and would not induce any significant change. The goal here is to Fourier-transform the periodically modulated signal to isolate every frequency of the total signal and the antisymmetric part, as we will see. The Fourier transform acts as a lock-in detection, filtering out the experimental fluctuations that are very unlikely to match the relevant frequencies. Additionally, the fluctuations of the signal level are also canceled by the normalization of the asymmetry parameter.

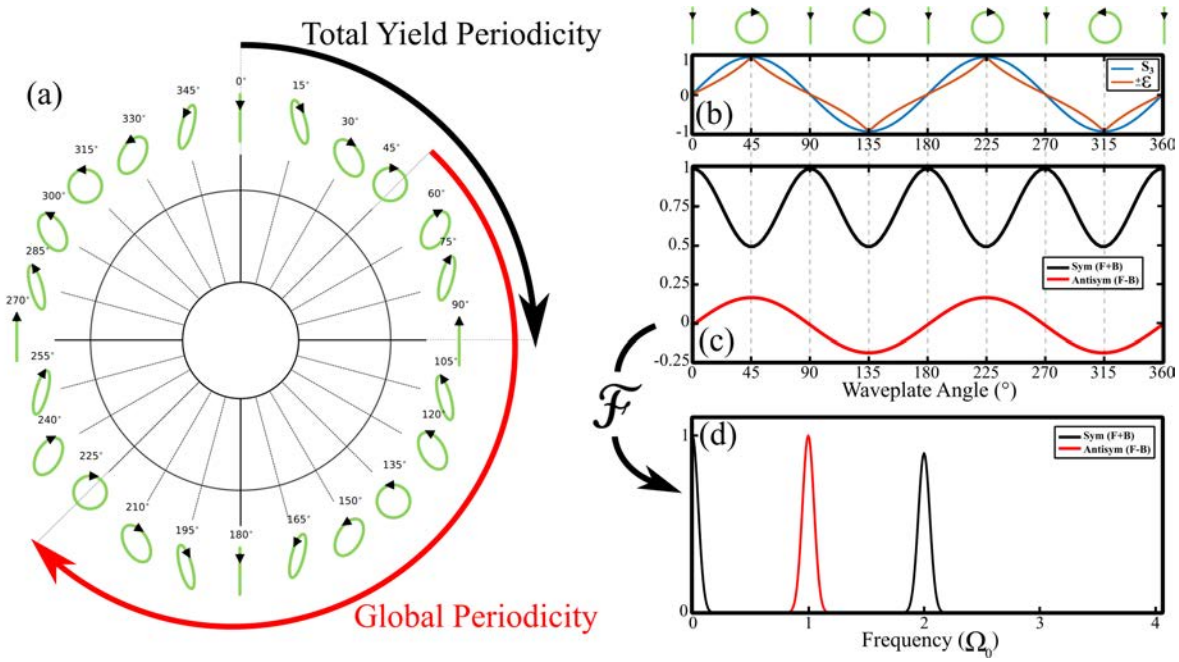


**Figure 3.11** – *Principle of the continuous ellipticity modulation scheme. (a) Laser polarization as a function of the quarter waveplate rotation. (b) Evolution of the Stokes parameter $S_3$ and ellipticity $\epsilon$ of the laser as a function of the waveplate rotation. Note that $\epsilon$, which is by definition a positive quantity, has been modulated by a positive sign for right polarizations and a minus sign for left polarizations for clearer comparison with $S_3$. (c) Schematic evolution of the total signal and the antisymmetric part of the signal of the VMI images, in the case where the dichroic response scales linearly with $S_3$. (d) Corresponding Fourier transform of the periodic symmetric and antisymmetric signal.*

Except for the Belfast's measurements, we used in this experiment the BlastBeat laser system in CELIA which is a Yb-doped fiber laser delivering 50 $W$ of 130 $fs$ pulses at a repetition rate between 166 $kHz$ and 2 $MHz$ (Tangerine SP, Amplitude). Second harmonic generation was performed from the output wavelength 1030 $nm$ to 515 $nm$ with a type-I $\beta$-Barium Borate (BBO) crystal, and isolated from the fundamental frequency with two dichroic mirrors. The quarter-waveplate modulating the polarization was mounted on a fast direct-drive rotation stage capable of rotations up to 720 $°/s$ (RGV100BL, Newport). The acquisition of the VMI images (apparatus

described in Section 2.II) was done using a S-CMOS camera (Orca Flash 4.0, Hamamatsu) without deadtime between images. The camera was also triggered by the rotation so that the ellipticity is calibrated, meaning that the initial phase is known.

The high repetition rate of the laser enabled a camera exposure time of $\tau_{exp} = 50\ ms$. We set the waveplate angular velocity at $\omega_{\lambda/4} = 45\ °/s$, so that the full 180° periodicity (which is the one of the asymmetry) is described in 80 points, which is decent for a Fourier transform, in $T_0 = 4\ s$. As the rotation still goes during the exposure, each image is an average over 2.25°, on which the PEELD does not evolve too much.

### II. 3 Accurate Measurement of the Enantiomeric Excess

We will present in this section the application of the c-PEELD to determine the enantiomeric excess (*ee*) of a pure chemical compound. The signal from the VMI images was numerically integrated to reduce it to the asymmetry factor $G^{raw}(t)$, as defined in Eq. 3.5 for each image. The possible asymmetry artifact induced by the spatial inhomogeneity of the detector gain was corrected by averaging the signal between the opposite ellipticities as :

$$G(t) = \frac{1}{2}(G^{raw}(t) - G^{raw}(t + T_0/2)) \tag{3.6}$$

as $T_0/2$ is the time taken for a 90° rotation of the quarter waveplate. $G(t)$ recorded in the two pure enantiomers of Fenchone is presented in Fig. 3.12 (a). A 2 $MHz$ repetition rate was used with the exposure and rotation parameters indicated above, so that each point is a sum over 100k laser shots. The initial position corresponds to the linear polarization, and the 24 $s$ displayed correspond to 3 full rotations, *i.e.* $6 \cdot T_0$. The sinusoidal shaded area represents the evolution of the total photoelectron yield (or 'total signal'), and shows that it maximizes in linear polarization, every 90° ($T_0/2$). The evolution of the $G(t)$ factor of the (+) and (-)-Fenchone are plotted in red and blue, respectively. It periodically follows the one presented in Fig. 3.8 (a), as the $S_3$ parameter is continuously scanned (*cf* Fig. 3.11). As expected, the asymmetry is clearly inverted between the two enantiomers. The Fourier transform of the total signal and the asymmetry factor $G(t)$ are depicted in Fig. 3.12 (b), respectively in black and red. The $T_0/2$ modulation of the total signal shows an isolated peak at $2\Omega_0$, where $\Omega_0 = \frac{2\pi}{T_0} = 0.25\ Hz$. Other frequencies could appear at $2k\Omega_0$, $k \in \mathbb{N}^*$ (as the total signal has a $T_0/2$ periodicity), corresponding to the non-linearity of the signal variation with the polarization. Note as well that in this Fourier decomposition, a circular dichroism of the ionization yield [Boesl 13] would appear as a $\Omega_0$ component of the in the total signal with a phase depending on the enantiomer.

The Fourier transform of the asymmetry parameter $\mathcal{F}[G(t)] = \mathcal{G}(\Omega)$ (in red) presents a rich structure that can be used as a molecular fingerprint. Indeed, the non-linear dependency of G with respect to $S_3$ (seen in Fig. 3.8) appears as a frequency comb here, and is molecular-sensitive. This aspect will be discussed more in detail at the end of this section. The frequency comb of the Fourier transform of $G(t)$ is made of odd $\Omega_0$ orders $(2k+1)\Omega_0$, $k \in \mathbb{N}^*$. This structure comes from the fact that the dichroic signal has a 180° ($= \Omega_0$) periodicity, but is necessarily symmetric around $|S_3| = 1$ and antisymmetric around $S_3 = 0$, excluding the even orders. This non-overlap between the total and the dichroic frequency components makes the separation very

robust. Typically, if the inhomogeneity correction (Eq. 3.6) is not applied, artifacts will clearly be indicated by odd orders in the total signal spectrum.

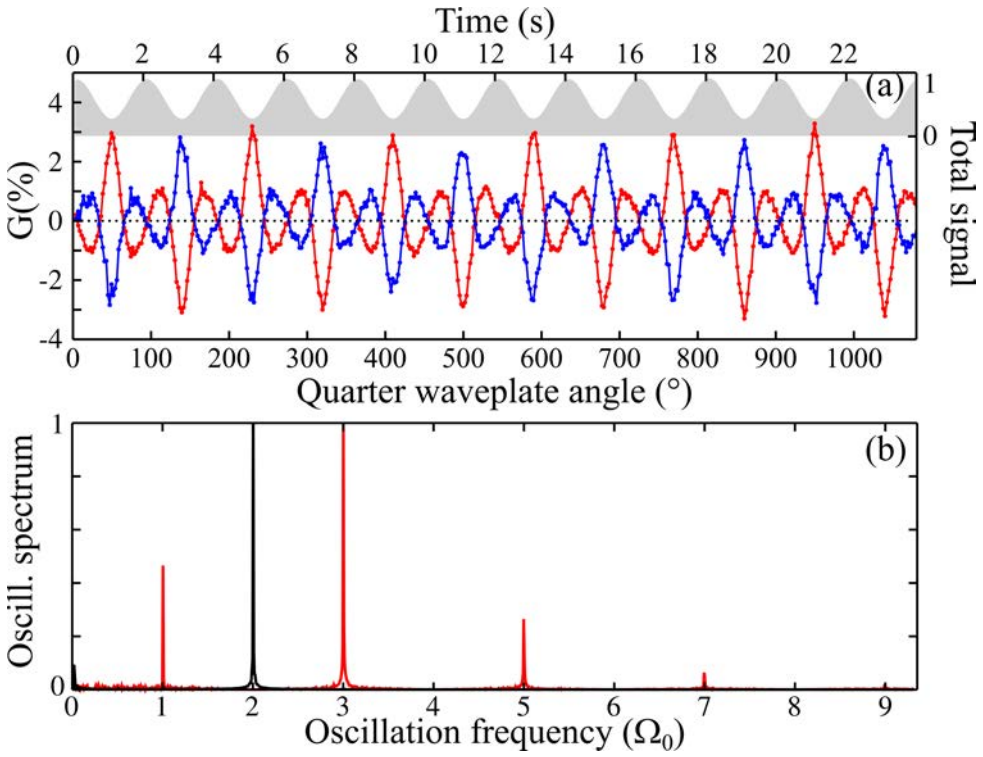


**Figure 3.12** – *(a) Unfiltered temporal evolution of the forward/backward asymmetry G(t) in (+)-Fenchone (red) and (-)-Fenchone (blue) at 5×10$^{12}$ W.cm$^{-2}$ as the ellipticity is continuously scanned by rotating a quarter waveplate. The total photoelectron yield from (+)-Fenchone is depicted in gray. (b) Oscillation spectrum of the forward/backward asymmetry (red) and of the total signal (black) obtained by Fourier transforming the temporal signals. The fundamental frequency is* $\Omega_0 = 0.25$ *Hz.*

The relative amplitudes and phases of the components of $\mathcal{G}((2k+1)\Omega_0)$ are molecular-specific. Additionally, since G is a normalized quantity, their absolute amplitude is only proportional to the enantiomeric excess in the analyzed sample. If we focus on the stronger peak $\mathcal{G}(3\Omega_0)$, which is the less subject to noise, the calibration from a known sample of enantiomeric excess $ee^{ref}$ directly provides :

$$ee = \pm \frac{|\mathcal{G}(3\Omega_0)|}{|\mathcal{G}^{ref}(3\Omega_0)|} \cdot ee^{ref} \tag{3.7}$$

while the $\pm$ sign is given by the 0 or $\pi$ phase of the $3\Omega_0$ component relatively to the reference. We used an enantiopure (+)-Fenchone sample as a reference here (Sigma Aldrich), as it provides the less noisy reference, but in principle the calibration can be done with any known enantiomeric excess $ee^{ref}$. The fact that the $\mathcal{G}(3\Omega_0)$ component dominates the $\mathcal{G}(\Omega_0)$ one indicates that the nonlinearity induced by the anisotropy of excitation is the main driver of the evolution of $G$ with respect to $S_3$ in this case.

This procedure has been tested in several samples of known $ee$, with an acquisition time of 10 minutes each. The first one is (-)-Fenchone (Sigma Aldrich) specified at $84.2\% \pm 4\%$. The two other ones are mixtures of the two commercial enantiomers, determined with the precision

of a microbalance. The results of the measurements are presented in Table 3.1.

| Mixture | Expected *ee* | *ee* measured by c-PEELD |
|---|---|---|
| (−)-Fenchone | $-84.2 \pm 4\%$ * | $-84.0 \pm 0.4\%$ |
| Mix 1 | $63.1 \pm 4\%$ | $62.7 \pm 0.5\%$ |
| Mix 2 | $25.1 \pm 4\%$ | $24.9 \pm 0.4\%$ |

**Table 3.1** – *Measurement of the enantiomeric excess of three mixtures of Fenchone using (+)-Fenchone as a reference with $ee_{ref} = 1$. Each measurement corresponds to a 10 minute acquisition. The error bars of the c-PEELD measurements are 95% confidence intervals. * = values from the supplier (Sigma Aldrich).*

Note that the errorbar of the c-PEELD is much smaller and consistent with the one of the supplier.

**Error Estimation**

Error estimation is crucial in analytical applications. We first assess the statistical error by slicing the 10 minutes measurements in the (+)-Fenchone into slices by applying a Gaussian filter of variable duration $\tau$ FWHM. A statistical analysis is then applied to the enantiomeric excess estimated for each slice. The 95% confidence interval is depicted on Figure 3.13 (a). As one can see, the Fourier transform is not optimally precise if the window is too short and does not cover enough oscillations, providing about 5% precision in 3 s (only 4/3 oscillations in $G(t)$). On the other hand, the errorbar quickly diminishes to its minimum value around $\tau = 30$ $s$. From this point, increasing the number of oscillations is not the bottleneck anymore, yielding a constant $\sim 2\%$ precision. This means that the uncertainty can then only be improved by adding more measurements, by simply repeating the process several times and averaging the results. This procedure has been implemented on a 10 minute measurement. While keeping the total acquisition duration constant (10 min), the number of slices has been increased by decreasing the slice duration $\tau$. The resulting Student's statistical analysis is shown in Figure 3.13 (b), and display a 95% confidence interval kept relatively constant under 0.5% over the whole range. Notably, using a high number of subsets diminishes the error down to 0.3%.

Beyond statistical error, the estimation of the systematic error is also important. Obviously, as the c-PEELD is a method based on the comparison with a reference, the enantiomeric purity of the reference can induce a systematic error, affecting the accuracy of the measurement. Moreover, the measurement of the reference can present an error, but this one can be minimized by affording a long enough measurement. In addition, as the technique relies on a signal modulation, the linearity of the detector has to be verified. In order to estimate it, a 10 minute acquisition in (+)-Fenchone has been recorded while increasing the micro-channel plates voltage by 20 $V$ every 30 s, then decreasing it again (Figure 3.13 (c)). The variation of global signal covered here was about two orders of magnitudes. A Gabor analysis of the signal has been performed using a Gaussian window of 3 s FWHM. It constitutes a way to get the instantaneous variation of $\mathcal{G}(3\Omega_0)$ (more details in the next paragraph). The resulting estimation of the *ee* is shown on panel (d). One can see that the retrieved *ee* is systematically lower than the expected value ($ee = +1$ for (+)-Fenchone) during the first 3 minutes by $\sim 5\%$. Despite being within

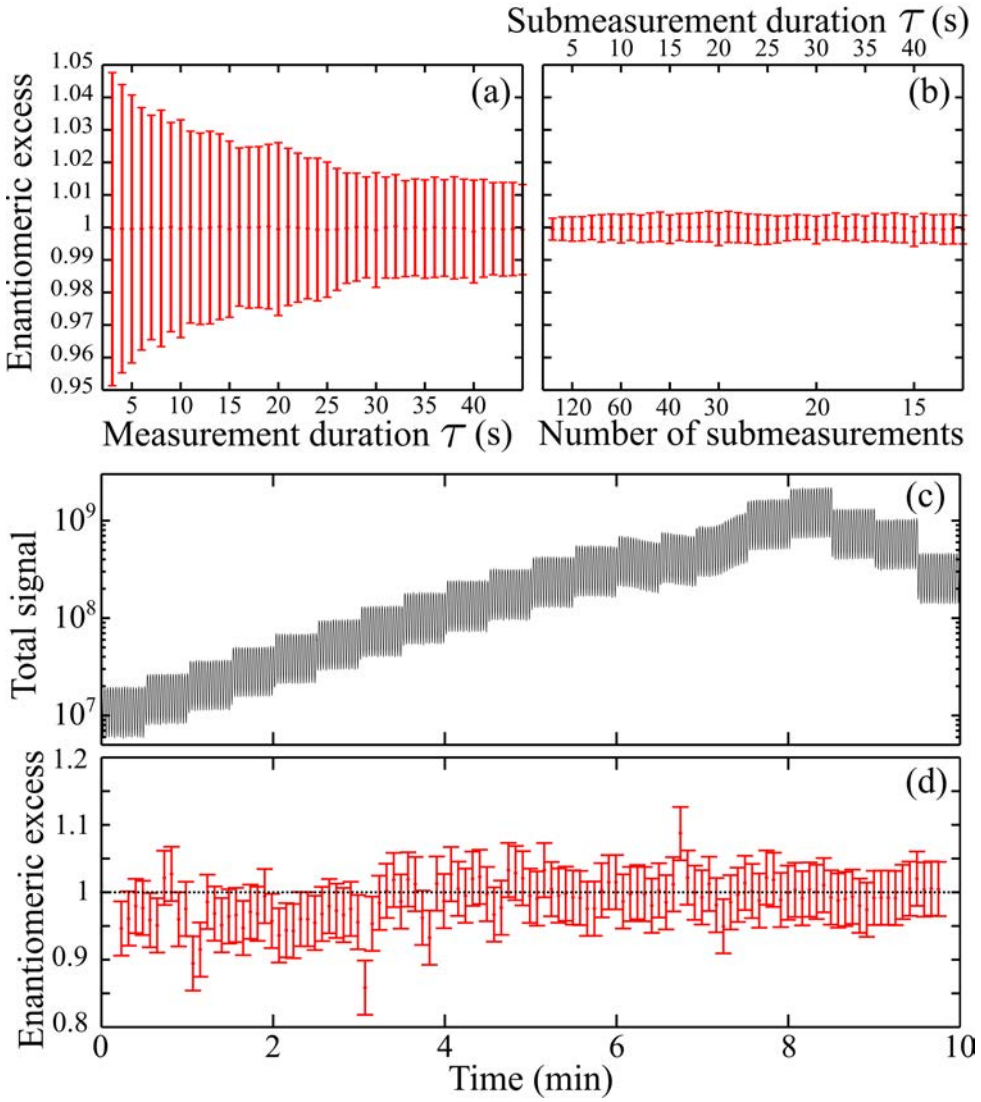


**Figure 3.13** – *Statistical analysis of the enantiomeric excess measurement by PEELD. (a) 95% confidence interval of the enantiomeric excess of a pure (+)-Fenchone sample, as a function of the duration of the measurement. (b) Results of a 10 min ee measurement by statistical analysis of sets of submeasurements, as a function of the number and duration of the submeasurements. (c-d) Total signal and enantiomeric excess measured while increasing the gain of the microchannel plates detector every 30 s.*

the range of the statistical error, this indicates that a new calibration could be useful at low MCP gain. But importantly, the data presented between 3 and 10 minutes demonstrates that the *ee* estimation is robust over an order of magnitude of signal variation. This is significant compared to the sources of fluctuations such the molecular gas jet density or laser power. This last parameter must be stable enough however, since the PEELD can depend on the laser intensity, as shown in Fig. 3.10. This is a considerable advantage of the fiber laser sources, with the drawback of handling adequately the high average power to avoid pointing and beam quality fluctuations, due to thermal effects.

## II. 4 Continuous Measurement of the Enantiomeric Excess

Since c-PEELD technique provides measurements of the enantiomeric excess of a sample within a few seconds, we will demonstrate that it can be used to track it in real-time. In order to mimic the temporal evolution of the *ee* during a chemical reaction, for instance, we connected the tubes containing the pure (+), (-) and the two mixtures of Fenchone determined in Table 3.1 to the gas pipe supplying the VMI jet. We then consecutively opened them while closing the other ones to vary the sample composition. The c-PEELD signal recorded on-the-fly is shown in Figure 3.14. The total signal, plotted in panel (a), presents a quite constant level except when a new tube is open, as the pressure built with the sample evaporation goes back to equilibrium in a few tens of seconds. Nevertheless, we have seen that this does not have consequences on the measured *ee*.

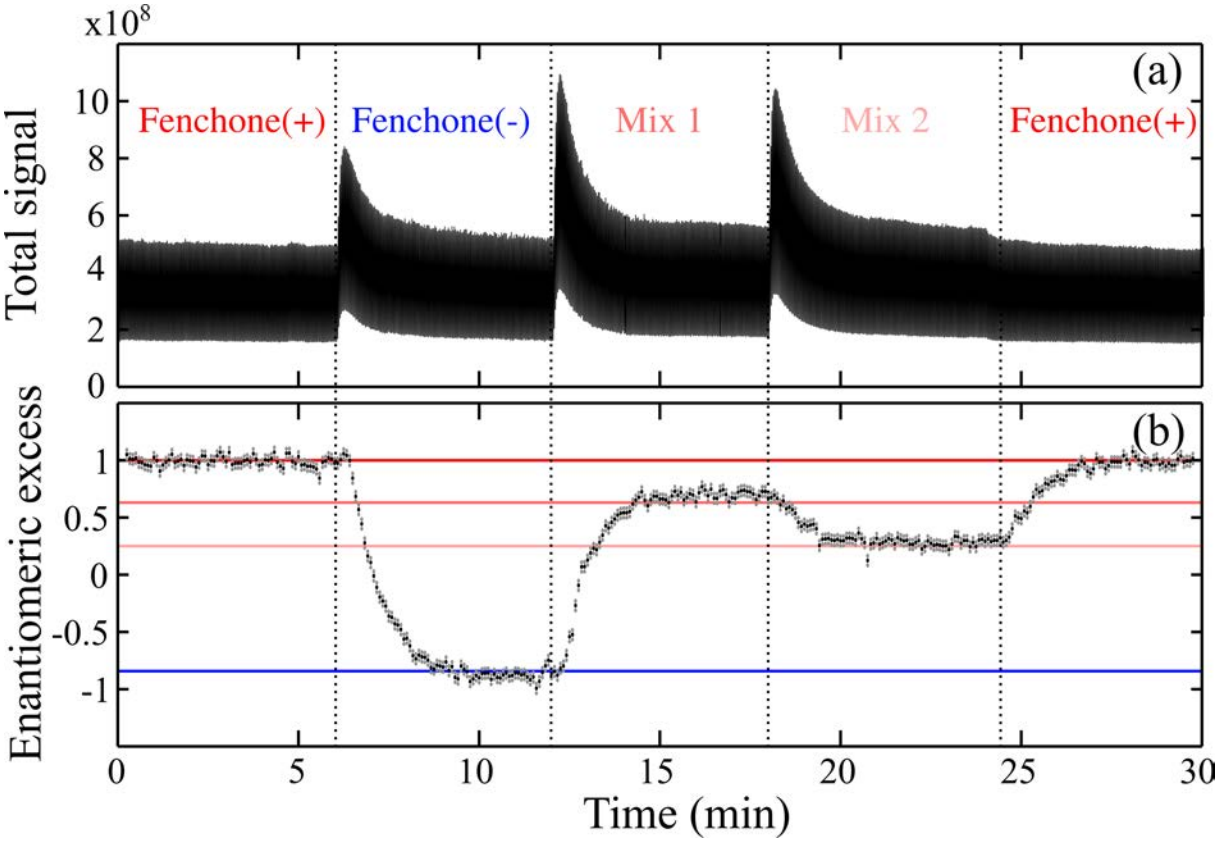


**Figure 3.14** – *Continuous monitoring of enantiomeric excess by c-PEELD. (a) Total photoelectron signal as a function of time, as different samples are successively connected to the jet. (b) Measured enantiomeric excess (black dots) and 95% confidence error bars (gray). The horizontal lines are the theoretical values of the enantiomeric excesses of the different mixtures.*

The Gabor analysis of the asymmetry parameter $G(t)$ has been performed with Gaussian envelopes of 5 s FWHM. This time-frequency analysis consists in multiplying the time-domain signal $G(t)$ with a sliding (Gaussian) window centered on a variable time $\tau$, and perform its Fourier transform :

$$\mathcal{G}(\Omega,\tau) = \int_{-\infty}^{+\infty} G(t) e^{-\frac{(t-\tau)^2}{2\sigma^2}} e^{i\Omega t} dt \tag{3.8}$$

which basically quantifies the spectral components as a function of time. Of course, like any time-frequency analysis, the larger the time resolution, the worse the frequency resolution and *vice versa*. In our case, it means that $\sigma$ is a trade-off between temporal responsiveness and the retrieved *ee* precision. Note that other kernel functions, *i.e.* different than the Gaussian, can be interesting as discussed in [Volpato 19] but less straightforward to interpret. The evolution of the enantiomeric excess and its sign, respectively extracted from the amplitude and phase of $\mathcal{G}(3\Omega_0, \tau)$, are presented on Figure 3.14 (b). Every time the supplying flask is changed, a transient occurring on 2-3 minutes is observed. This corresponds to the inertia of the gas dynamics in the pipe towards the VMI, and particularly of the long 200 $\mu$m-diameter capillary that creates the jet. After this transient, the signal converges to the expected *ee*, depicted with the lines colored lines respectively to the labels in panel (a), within the 0.4% errorbar determined in the previous section for this Gabor window. The slight offset of the measurement compared to the expected value for some mixtures is probably due to a change of laser duration, identified as resulting from the room temperature oscillations in the laboratory with a $\sim$ 20 minute period. This change of pulse duration modifies the intensity of the frequency-doubled beam, and thus the PEELD calibration. This means that further improvement can be done by more efficiently locking the laser parameters, for instance by setting a feedback loop on the 515 nm beam energy. In any case, the compromise between the *ee* precision and the temporal resolution demonstrated in this experiments constitutes a major breakthrough for chiral analysis in the gas phase.

**Alternative Detection Setup**

The results presented so far were obtained using a Velocity Map Imaging device. Although being a quite standard instrument in Physics laboratories, it remains quite expensive and its multidimensional angular resolution of the photoelectron distribution is not fully necessary when the only chiral observable is the asymmetry factor G. For this reason, the group of Jason Greenwood in the Queen's University of Belfast has developed a much more simple device presented in Figure 3.15, designed to directly collect the electrons emitted forward and backward, regardless of their kinetic energy [Miles 17]. They have performed the measurements presented here in Belfast, and sent us the results to integrate them to our analysis.

This device, called CERSEI (Chiral Electron Removal and Separation for Enantiomer Identification), relies on an homogeneous magnetic field ($\sim$ 30 Gauss) generated by two coils collinearly to the laser axis to guide the photoelectrons out of the interaction chamber. Once the forward- and backward-emitted electrons are separated, they are deflected from the laser axis by adding a homogeneous electric field and collected on two separate Channel Electron Multipliers (CEM). The laser pulses used here were 1.8 $\mu J$ of the second harmonic (520 $nm$) from the 300 $fs$ pulses generated at a repetition rate of 1 $MHz$ (Spirit HE, Spectra Physics). A 20 $cm$ focal length lens was used to focus the beam in the effusive gas jet, produced from a capillary, reaching an intensity of $10^{12}$ $W.cm^{-2}$. The rather small chamber was solely pumped by a 200 $L.s^{-1}$ turbomolecular pump to about $10^{-6}$ mbar with the jet and around $10^{-7}$ mbar without. Under these conditions, the data were acquired sequentially for 30 s every 10° of the wave plate angle. The counting rate used here was below 0.1 ionization per short to avoid saturation, but this could be significantly improved by replacing the CEM with MCPs.

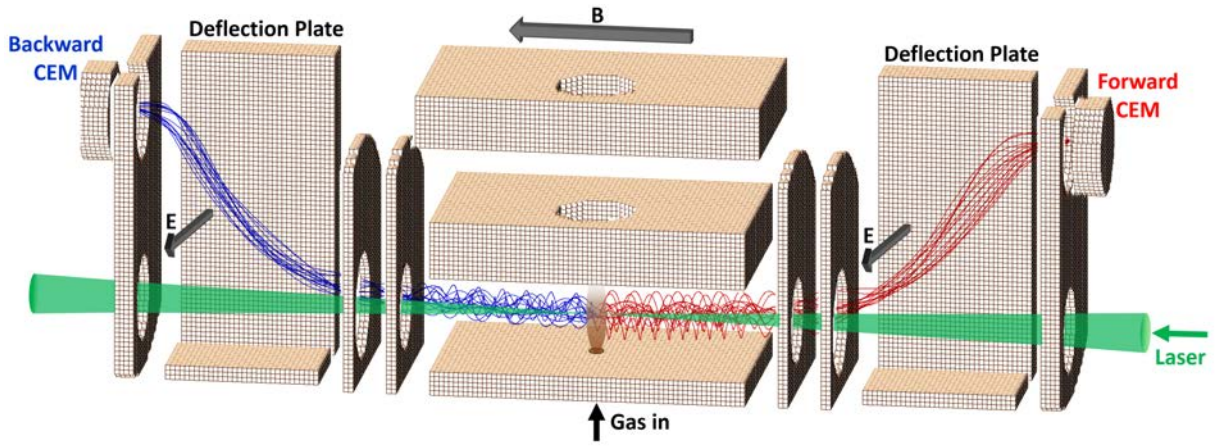


**Figure 3.15** – *Schematic of the Belfast instrument used to directly measure PEELD, detailed in the text. The electrodes and simulated trajectories were produced by SIMION 8.0 charge particle optics software.*

The evolution of G with respect to $S_3$ measured with this device in (+)-Fenchone is shown in Figure 3.16 (a). It behavior is in good agreement with what has been measured in the VMI. An emulation of the c-PEELD technique is shown on panel (b), where the pure (+)-Fenchone (red) is compared to a mixture of $ee = -66\%$ Fenchone (blue). We do observe the sign inversion of the G(t) function along with its amplitude modulation, that provided a measurement of $ee = -63 \pm 5\%$.

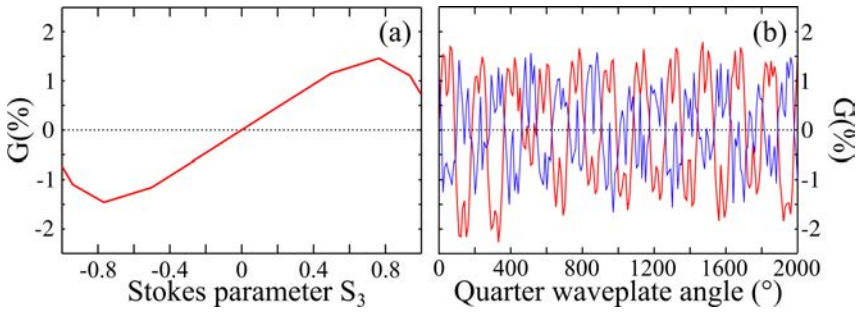


**Figure 3.16** – *Temporal evolution of the forward/backward asymmetry G in (+)-Fenchone (red) and a Fenchone mixture with ee = 63% using 520 nm pulses at ∼ 1×10$^{12}$ W.cm$^{-2}$, as the ellipticity is continuously scanned by rotating a quarter waveplate. These measurements were taken with the CERSEI instrument in Belfast.*

This measurement can readily be improved by using a higher laser intensity that would increase the signal and the nonlinearity of G with respect to $S_3$. But more importantly, this demonstrates the possibility to implement the PEELD and c-PEELD with a very simple and compact instrument.

## II. 5 High-Dimensional Molecular Fingerprint : Multi-Component Analysis

### 2D Fingerprints

As mentioned in the introduction of this section, the enantiomeric analysis of a multi-component mixture can be challenging. For instance, measuring the PECD in coincidence with

the photons has been demonstrated but suffers from an inherent very long acquisition time, and does not resolve isomers. We have also seen in Figure 3.8 that the G factor was very different for (+)-Fenchone and (+)-Camphor, giving a glimpse of its potentiality, but does not differ significantly between (+)-Camphor and (+)-Limonene. However, reducing the dimensionality of the c-PEELD to the simple asymmetry factor G is not the only way to use it for analytical purposes. Conversely here, we propose to capitalize on the multidimensional measurement of the photoelectron distribution to get a highly molecular-specific fingerprint. Despite containing all the information available, the 3D distributions can not be used for real-time monitoring since their acquisition time is too long. A good trade-off consists in using the numerically integrated 1D or the 2D distributions, provided in a few tens of milliseconds by the VMI in our setup.

The molecular fingerprints are generated from both the forward/backward symmetric part (denoted PhotoAngular Distribution, PAD) and antisymmetric part (PEELD) of the signal modulated by the continuous wave plate rotation. They are obtained from the VMI integration $\overline{P}$ along $y$ of the total distribution $P$ as :

$$\overline{P}(p_x, p_z, t) = \int P(p_x, p_y, p_z, t) dp_y \tag{3.9}$$

where $x$ is the axis of the linear laser field and $z$ is the laser propagation axis. The PAD and the chiral-sensitive PEELD evolutions are respectively given by :

$$\overline{P}^{sym}(p_x, p_z, t) = \frac{1}{2}(\overline{P}(p_x, p_z, t) + \overline{P}(p_x, -p_z, t)) \tag{3.10}$$

$$\overline{P}^{anti}(p_x, p_z, t) = \frac{1}{2}(\overline{P}(p_x, p_z, t) - \overline{P}(p_x, -p_z, t)) \tag{3.11}$$

A Fourier transform is performed, similarly to G(t), for each pixel of the detector plane $(x, z)$ to get the oscillation spectra map $\overline{\mathcal{P}}^{sym}(p_x, p_z, \Omega)$ and $\overline{\mathcal{P}}^{anti}(p_x, p_z, \Omega)$. For the same reasons as to 0D $\mathcal{G}(\Omega)$ shown in Figure 3.12, the symmetric and antisymmetric parts present frequencies respectively at $2k\Omega_0$ and $(2k+1)\Omega_0$, $k \in \mathbb{N}^*$. This time, since each pixel do not have necessarily the same oscillation phases, plotting the amplitude map of each frequency is not an adequate representation. Nevertheless, as the symmetric and antisymmetric parts are respectively even and odd with respect to the variation of $S_3$, one can assume that the complete information is respectively contained in the real and imaginary parts if the time zero is defined on the linear polarization. This convenient representation will be used throughout this paragraph. The $(x, z)$ maps of the two first and main peaks $k = \{1, 2\}$ of $\overline{\mathcal{P}}^{sym}(p_x, p_z, 2k\Omega_0)$ and $\overline{\mathcal{P}}^{anti}(p_x, p_z, (2k+1)\Omega_0)$ measured in (+)-Fenchone, (+)-Camphor and (+)-Limonene with $I_{515nm} = 5 \times 10^{12}\ W.cm^{-2}$ are presented in Figure 3.17.

The spectroscopic assignment of the different features observed can be found in the literature cited in the introduction of this chapter. Qualitatively, the important point here is that the signature are very molecular-specific and distinguishable. For example in the $\overline{\mathcal{P}}^{sym}$ maps, the Fenchone distributions (a) are dominated by the outer ring, while the ones of Camphor (b) are more balanced between the outer and the inner features, and the Limonene fingerprint is significantly greater at the center. The $\overline{\mathcal{P}}^{anti}$ pictures are even more clearly distinguishable.

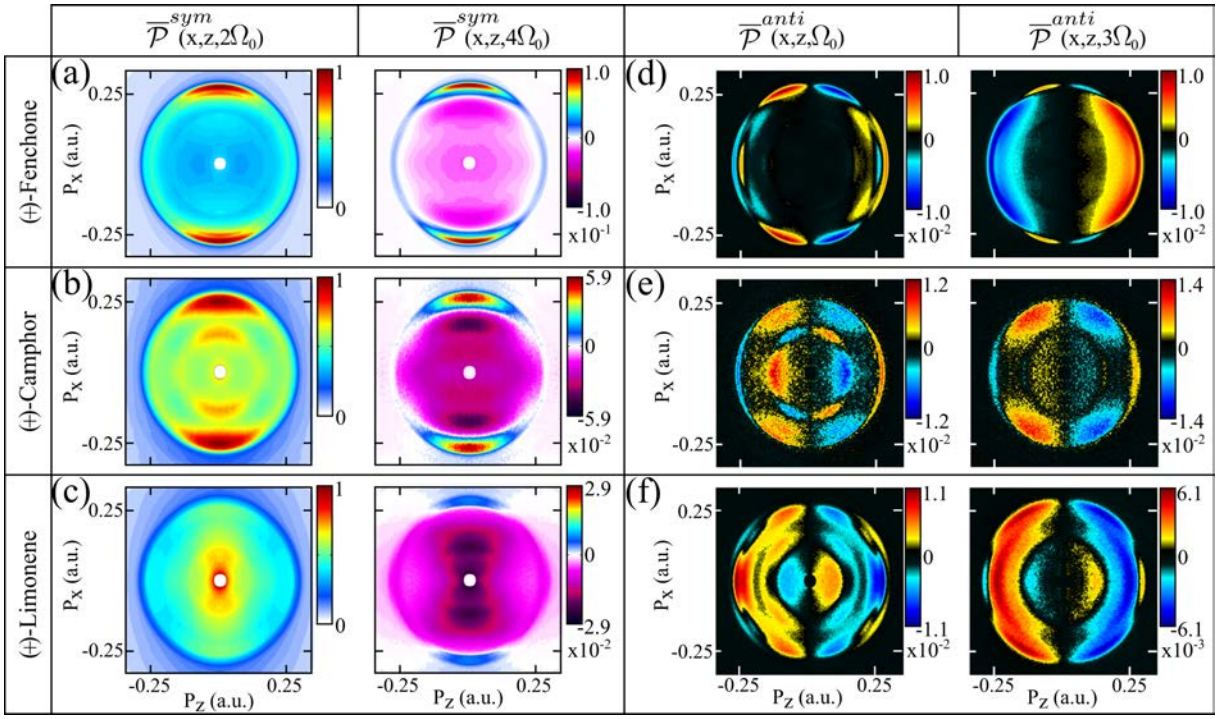


**Figure 3.17** – *Fourier decomposition of the oscillations of the VMI images with ellipticity in (+)-Fenchone (top), (+)-Camphor (mid) and (+)-Limonene (bottom), using 515 nm pulses at 5×10$^{12}$ W.cm$^{-2}$. (a-c) Symmetric components of the image $\overline{\mathcal{P}}^{sym}(p_x, p_z, 2k\Omega_0)$. (d-f) Antisymmetric components of the images $\overline{\mathcal{P}}^{anti}(p_x, p_z, (2k+1)\Omega_0)$. All values are normalized to the maximum of $\overline{\mathcal{P}}^{sym}(p_x, p_z, 2\Omega_0)$. The z axis is the laser propagation direction and the x axis is the main axis of the laser polarization ellipse.*

The $2\Omega_0$ map of $\overline{\mathcal{P}}^{sym}$ dominates the symmetric signal and thus maximizes in linear polarization for all the $(p_x, p_z)$ points. The $4\Omega_0$ component can be more complex since it reflects the non-linearity with respect to $S_3$. However, the negative central part is probably related to the rotation of the field ellipse axis relatively to the projection axis, and is not physically meaningful. The spectral maps of the antisymmetric parts present even richer structures. The sign change of the low energy PEELD can be due to vibrational excitation of the ion, as observed in the PECD, or also to the longer scattering process of the low kinetic energy electrons. Note that two areas of opposite sign in the same half of the detector can cancel out in the integration giving G(t) (or $\mathcal{G}(\Omega)$), reducing its sensitivity. For instance in Fenchone, we understand through these 2D maps why the integrated $\mathcal{G}(3\Omega_0)$ is stronger than $\mathcal{G}(\Omega_0)$, as seen in Fig. 3.12 (b) : the multitude of nodes in the $\overline{\mathcal{P}}^{anti}(p_x, p_z, \Omega_0)$ map reduces significantly its integrated value. In any case, one can see that this enriched 2D fingerprint succeeds in discriminating Camphor and Limonene, which was not the case with the 0D quantity.

**1D Fingerprints**

High-dimensional measurements provides a high fingerprint selectivity, but increases the acquisition time. One can expect the 2D maps shown in Fig. 3.17 to be adapted for highly complex mixtures analysis but in the context of continuous measurements, we found that 1D fingerprints were a good compromise. These latter are generated by numerically integrating the

VMI images along the polarization axis $x$ and keep the laser propagation axis $z$ as the remaining dimension :

$$\overline{\overline{P}}(p_z,t) = \int \overline{P}(p_x,p_z,t)dp_x \tag{3.12}$$

We then performed a Fourier analysis in the same manner as previously to get the reference spectral component $\overline{\overline{\mathcal{P}}}^{sym}(p_z,2k\Omega_0)$ and $\overline{\overline{\mathcal{P}}}^{anti}(p_z,(2k+1)\Omega_0)$ of (+)-Fenchone (compound A) and (+)-Camphor (compound B). The time-resolved composition and $ee$ is then retrieved with a Gabor analysis of the signal from the evolving sample, with a 30 s Gaussian filter. In a general manner, the composition of a mixture of two species A and B is retrieved using the c-PEELD signal as follows. The absolute composition at every time $t$ is determined from the symmetric parts $\overline{\overline{\mathcal{P}}}^{sym}$ by minimizing the function $f$ with a least-square algorithm :

$$\begin{aligned} f = &|\overline{\overline{\mathcal{P}}}^{sym}_{mix}(p_z,2\Omega_0,t) - a(t)\overline{\overline{\mathcal{P}}}^{sym}_{A}(p_z,2\Omega_0) - (1-a(t))\overline{\overline{\mathcal{P}}}^{sym}_{B}(p_z,2\Omega_0)|^2 \\ &+ \alpha_4|\overline{\overline{\mathcal{P}}}^{sym}_{mix}(p_z,4\Omega_0,t) - a(t)\overline{\overline{\mathcal{P}}}^{sym}_{A}(p_z,4\Omega_0) - (1-a(t))\overline{\overline{\mathcal{P}}}^{sym}_{B}(p_z,4\Omega_0)|^2 \\ &+ \alpha_6|\overline{\overline{\mathcal{P}}}^{sym}_{mix}(p_z,6\Omega_0,t) - a(t)\overline{\overline{\mathcal{P}}}^{sym}_{A}(p_z,6\Omega_0) - (1-a(t))\overline{\overline{\mathcal{P}}}^{sym}_{B}(p_z,6\Omega_0)|^2 \\ &+ ... \end{aligned} \tag{3.13}$$

The minimization parameter $a(t)$ and $(1-a(t))$ then gives the relative proportion of signal coming from the species $A$ or $B$ respectively, independently of their $ee$. The conversion into absolute concentration in the sample can be simply done in principle by taking into account the absolute photoionization cross sections and partial pressures of each compound, but is beyond the scope of this study. The $\alpha_{2k}$ coefficients can be used to adjust the weight of the different spectral components, which can be relevant if one or several of them are much more compound-specific than others.

The second step consists in retrieving the respective enantiomeric excess $ee_A$ and $ee_B$ from the antisymmetric components of the c-PEELD $\overline{\overline{\mathcal{P}}}^{anti}$ by minimizing the function g :

$$\begin{aligned} g = &|\overline{\overline{\mathcal{P}}}^{anti}_{mix}(p_z,\Omega_0,t) - a(t)ee_A(t)\overline{\overline{\mathcal{P}}}^{anti}_{A}(p_z,\Omega_0) - (1-a(t))ee_B(t)\overline{\overline{\mathcal{P}}}^{anti}_{B}(p_z,\Omega_0)|^2 \\ &+ \beta_3|\overline{\overline{\mathcal{P}}}^{anti}_{mix}(p_z,3\Omega_0,t) - a(t)ee_A(t)\overline{\overline{\mathcal{P}}}^{anti}_{A}(p_z,3\Omega_0) - (1-a(t))ee_B(t)\overline{\overline{\mathcal{P}}}^{anti}_{B}(p_z,3\Omega_0)|^2 \\ &+ \beta_5|\overline{\overline{\mathcal{P}}}^{anti}_{mix}(p_z,5\Omega_0,t) - a(t)ee_A(t)\overline{\overline{\mathcal{P}}}^{anti}_{A}(p_z,5\Omega_0) - (1-a(t))ee_B(t)\overline{\overline{\mathcal{P}}}^{anti}_{B}(p_z,5\Omega_0)|^2 \\ &+ ... \end{aligned} \tag{3.14}$$

Here the parameters $\beta_{2k+1}$ plays the same role of tunable balancing coefficients. The optimization of $f$ and $g$ can be either done sequentially or globally, but led to the same result in this case.

The calibrations 1D maps of pure (+)-Fenchone (orange) and (+)-Camphor (blue) are depicted on the left panels in Figure 3.18, respectively (b), (c) and (d). The $\overline{\overline{\mathcal{P}}}^{sym}(p_z,2\Omega_0)$ components are sufficient to make the distinction between the two compounds, so all the other $\alpha_{2k}$ were set to zero. On the contrary, one can see that $\overline{\overline{\mathcal{P}}}^{anti}(p_z,3\Omega_0)$ adds a lot of sensitivity

compared to $\overline{\overline{\mathcal{P}}}^{anti}(p_z, \Omega_0)$ to retrieve the respective *ee*. For this reason, we set $\beta_3 = 10$ so that the $3\Omega_0$ weight gets comparable with the $\Omega_0$ component in the minimization, and all other $\beta_{2k+1}$ to zero.

Figure 3.18 shows the tracking of (b) $\overline{\overline{\mathcal{P}}}^{sym}_{mix}(p_z, 2\Omega_0, t)$, (c) $\overline{\overline{\mathcal{P}}}^{anti}_{mix}(p_z, \Omega_0, t)$ and (d) $\overline{\overline{\mathcal{P}}}^{anti}_{mix}(p_z, 3\Omega_0, t)$ of an evolving sample. The absolute composition obtained from $a(t)$ and $(1-a(t))$ is plotted in (e) and the retrieved *ee* of the two species is plotted in (f). The sample evolution sequence started from $t = 0$ to $t \approx 2'30''$ with partially connected flasks of (-)-Fenchone and (-)-Camphor. As one can see in Figure 3.18 (a), the total signal level decreases at first. Panel (e) reveals that it comes from a transient in the signal of Fenchone, while the Camphor one remains stable. At $t \approx 2'30''$, we open more the (-)-Fenchone valve and we slightly close the (-)-Camphor valve. This is clearly detected and visible in (e). Note that meanwhile, the *ee* found remain completely independent on the relative signal level, at $ee_{fenchone} = -82 \pm 5\%$ and $ee_{camphor} = 94 \pm 2\%$ in a 95% confidence interval. At $t = 5'$, the (-)-Fenchone sample was swapped with the (+) enantiomer. Once again, this change is clearly visible, without affecting $ee_{camphor}$, and shows a $\sim 3'$ transient, converging to $ee_{fenchone} = 91 \pm 8\%$ from $t \approx 8'$ to the end. The *ee* found remains stable, even while the partial pressure of Fenchone decreases gradually in time. At $t = 10'$, the (-)-Camphor flask is closed while opening the (+) one. Once again, we keep track of the evolution without affecting the measurement of the other compound.

This experiment thus demonstrates the capacity of the c-PEELD technique to track the absolute and enantiomeric composition of a mixture with a remarkable precision and temporal resolution. The next step in the retrieval of the fast evolution of *ee* is to fit the evolving 2D maps $\overline{\mathcal{P}}(p_x, p_z, \Omega, t)$ instead of the integrated 1D $\overline{\overline{\mathcal{P}}}(p_z, 2\Omega, t)$. The main question is how to be efficient in the fitting procedure to provide the evolution in real time for the users. For this purpose, Antoine Comby and Baptiste Fabre are developing strategies based on neural network optimization.

The fast *ee* tracking technique developed here could be interesting for industrial purposes. At this stage, it can be used for instance for monitoring in live the quality of a product in a production line. Another exciting application would be the resolution of complex unknown samples. Typically, natural extracts, that are sometimes very important for obtaining enantiopure compounds, are often challenging to characterize. Our method could be very competitive in this context, but several challenges remain to be faced. Firstly, a calibration on known pure samples is required, meaning that one needs prior knowledge on the analyzed samples. Secondly, we still have to determine the sensitivity of the detection for species in large minority, and the ability to identify the different molecules in a more complex mixture (more that two species). Finally, we still have to establish whether or not the PEELD effect is universal and applies for a wide spectrum of molecules. These questions are currently being investigated in our group. Of course, the effect lies in the intermediate excited states in the REMPI process. But one could wonder if their sole presence is necessary, or if the effect also depends on their nature. This question will be addressed in the next section.

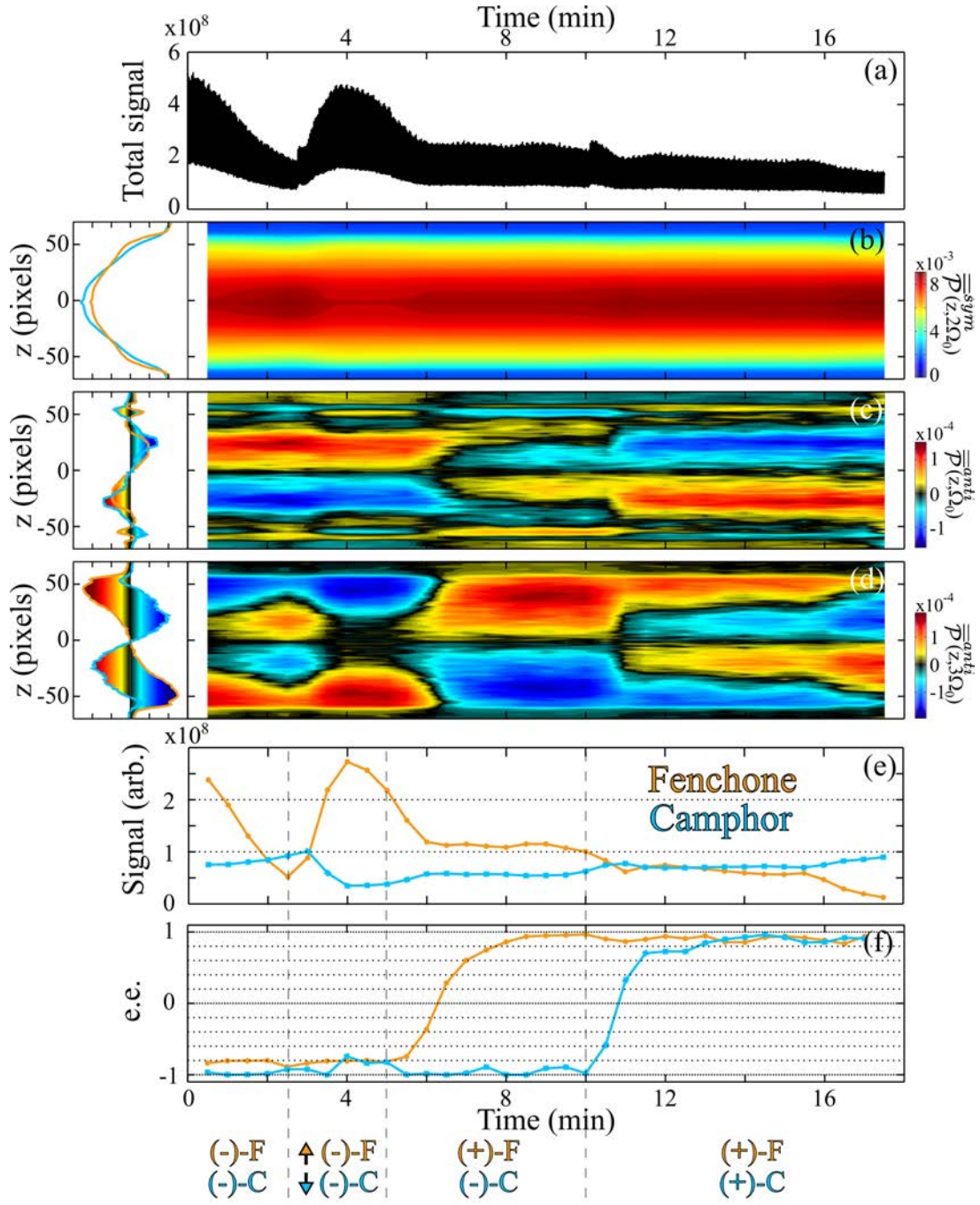


**Figure 3.18** – *Real-time analysis of a dynamical Camphor-Fenchone mixture. The fingerprints* $\overline{\overline{\mathcal{P}}}^{sym}(p_z, 2\Omega_0)$, $\overline{\overline{\mathcal{P}}}^{anti}(p_z, \Omega_0)$ *and* $\overline{\overline{\mathcal{P}}}^{anti}(p_z, 3\Omega_0)$ *from pure (+)-Fenchone (orange) and (+)-Camphor (blue) were recorded using pure samples before the dynamical measurement and are presented in the left column. See the text for the sample evolution sequence. (a) Total signal from the gas mixture during the c-PEELD measurement. (b) Temporal evolution of the 1D symmetric component at* $2\Omega_0$*, extracted from a Gabor analysis with a 30 s window. (c) 1D antisymmetric component at* $\Omega_0$*. (d) 1D antisymmetric component at* $\Omega_0$*. (e) Contribution to the total signal and (f) enantiomeric excess of Fenchone (orange) and Camphor (blue) retrieved by fitting the symmetric and antisymmetric components.*

# III Elliptical Dichroism Studied in the COLTRIMS

We have seen in Section 3.II that the PhotoElectron Elliptical Dichroism (PEELD) effect could enrich the usual PhotoElectron Circular Dichroism (PECD) in the REMPI regime. We have demonstrated that this effect could be used for analytic purposes, in particular yielding enough signal-to-noise ratio to extract the enantiomeric and isomeric content of a sample, either very precisely or in real time. In this context, the velocity map imaging spectrometer (VMI) is the detection instrument of choice, as it can afford a high level of signal. In particular, the complete resolution of the 3D photoelectron angular distribution is not required in this case.

The situation differs if the goal is the complete resolution of the phenomenon, and without such a constrain on the duration of the acquisitions. Firstly, the measurement of the 3D distributions can be either performed using the VMI or the COLTRIMS, and knowing which one is the most suited is not trivial. We will thus compare these two techniques. Secondly, we will compare the response of two closely-structured chiral molecules, Ethyl-Lactate and Methyl-Lactate, to further investigate the mechanism of anisotropy of excitation. Finally, one of the main experimental goal and challenge of this thesis, namely the measurement of dichroic signals in coincidence with different ions an fragments, will be addressed.

## III. 1 Direct COLTRIMS Measurement and VMI Tomography

Two techniques, presented in Chapter 2, are at our disposal to measure arbitrary 3D photoelectron angular distributions.

On the one hand, the tomographic reconstruction dwells on the reconstruction from a set of 2D (VMI) projections, projected along different axis relatively to the laser polarization. The technique benefits from the fast acquisition of each projection, but several are required. The more complex the structure is, the more projections are needed to correctly reconstruct it. Roughly, details that are finer than the angular step between the projections can not be resolved, but additional issues can be encountered. The noise can affect the reconstructed distributions, especially in the fine structures. Moreover, the slow fluctuations of the laser (*e.g.* power and pointing) can slightly change the ionization conditions between the beginning and the end of the measurement, and can affect drastically the reconstruction. The main signal limitation here is the saturation of the detector (in particular the camera) and avoiding the creation of space charge (where too many electrons are produced and repel each other, inducing a distortion of the image). These issues can be tempered by respectively reducing the camera exposure time and increasing the laser repetition rate at constant signal level.

On the other hand, the direct measurement of the distributions using the delay line detector of the COLTRIMS takes a lot of time compared to a VMI image, but is done in one time. If only the electron distributions are needed, the ion detector can be switched off, the coincidence condition is not applied and all the electrons are collected. In this case, the only signal acquisition limitation is the one of the detector. This time, as the MCPs are operated at high gain, the time between two consecutive electrons in each channel can be too short to let the channel fully recover its gain (in typically 1 ms). The other detection limitation can occur if too many electrons are

produced at each laser shot, as the delay lines are not suited for many multi-hit events. This last problem can, again, be limited by increasing the laser repetition rate, and happens well before the space charge encountered in the VMI. At the end, the maximum counting rate is about 100 kHz, but the equivalent quantity is hard to define in the VMI. Technically speaking, the COLTRIMS also uses a reconstruction algorithm to retrieve the full electron distribution, but it is different from the tomographic one. Indeed, it uses only explicit equations from the delay lines timings that do not use any assumption on the signal structure and complexity, but the COLTRIMS also has a given resolution (discussed in the previous chapter). The technique is, however, less sensitive to the laser fluctuations, as they are averaged in the measurement and do not confuse the reconstruction. Finally, the measurement performed with the COLTRIMS can be monitored live, and possibly divided in subsets and corrected relatively to the fluctuations, while the tomography needs the complete set to be recorded in a row.

At the end, the comparison of the direct COLTRIMS measurement and the VMI tomographic reconstruction is not trivial. We will thus assess the respective pros and cons based on two experimental examples where the laser electric field has no cylindrical symmetry.

**Elliptically Polarized Field**

The first case presented is the one of interest in this chapter, namely the ionization of chiral molecules with elliptically polarized light in the multiphoton regime. The photoionization of (+)-Fenchone has been performed at 515 nm for Stokes parameters $S_3 = 1$, 0.9 and 0.6 in the VMI at an intensity of $5 \times 10^{13}$ $W.cm^{-2}$ and the COLTRIMS at $6 \times 10^{13}$ $W.cm^{-2}$. In the VMI measurement, the laser repetition rate was 2 MHz to maximize the signal at a reasonable peak intensity. 36 projections have been recorded by rotating the laser field ellipse by steps of 10 degrees. Each time, a continuous PEELD measurement has been performed by continuously varying the ellipticity and keeping the axis of the electric field ellipse fixed. The symmetric and antisymmetric parts at different $S_3$ values are then reconstructed from the oscillating components, as explained in the previous section. Each projection took 200 s to be recorded, for a total duration of 120 min for the whole measurement. In the COLTRIMS measurement, the laser repetition rate was set to 1 MHz ($S_3$=1), 750 kHz ($S_3$=0.9) and 400 kHz ($S_3$=0.6) to get a fixed 100 kHz of electron counting rate at the same intensity. This time, each of the three distributions at various $S_3$ was recorded independently, at fixed $|S_3|$, where the sign of the ellipticity has been inverted several times to remove the experimental artifacts. For each distribution, 300 M counts have been recorded, for a total duration of 150 min for the whole dataset.

The reconstructed 3D distributions (PES) and the corresponding dichroic signal (PEELD) (forward/backward antisymmetric part along the laser axis) are presented in Fig. 3.19. The first observation is that the global shapes of both the PES and the PEELD show a good agreement between the two methods. Another substantiating information is that the distributions show a cylindrical symmetry when the field is circularly polarized. At this time, these observations constituted the first validation of the COLTRIMS capacity, but also confirmed the foundation of the photoelectron elliptical dichroism effect. A further comparison confirms that only minor details differ, such as the inner part of the PEELD at $S_3 = 0.6$. However, the amplitude of the

dichroic signal is greater in the COLTRIMS measurements. This might be caused to the way the normalization is performed, as the continuous PEELD measurements are normalized respectively to Fourier frequency $\mathcal{G}(2\Omega_0)$ whereas it is done relatively to the pixel with the highest level of signal in the direct COLTRIMS measurement.

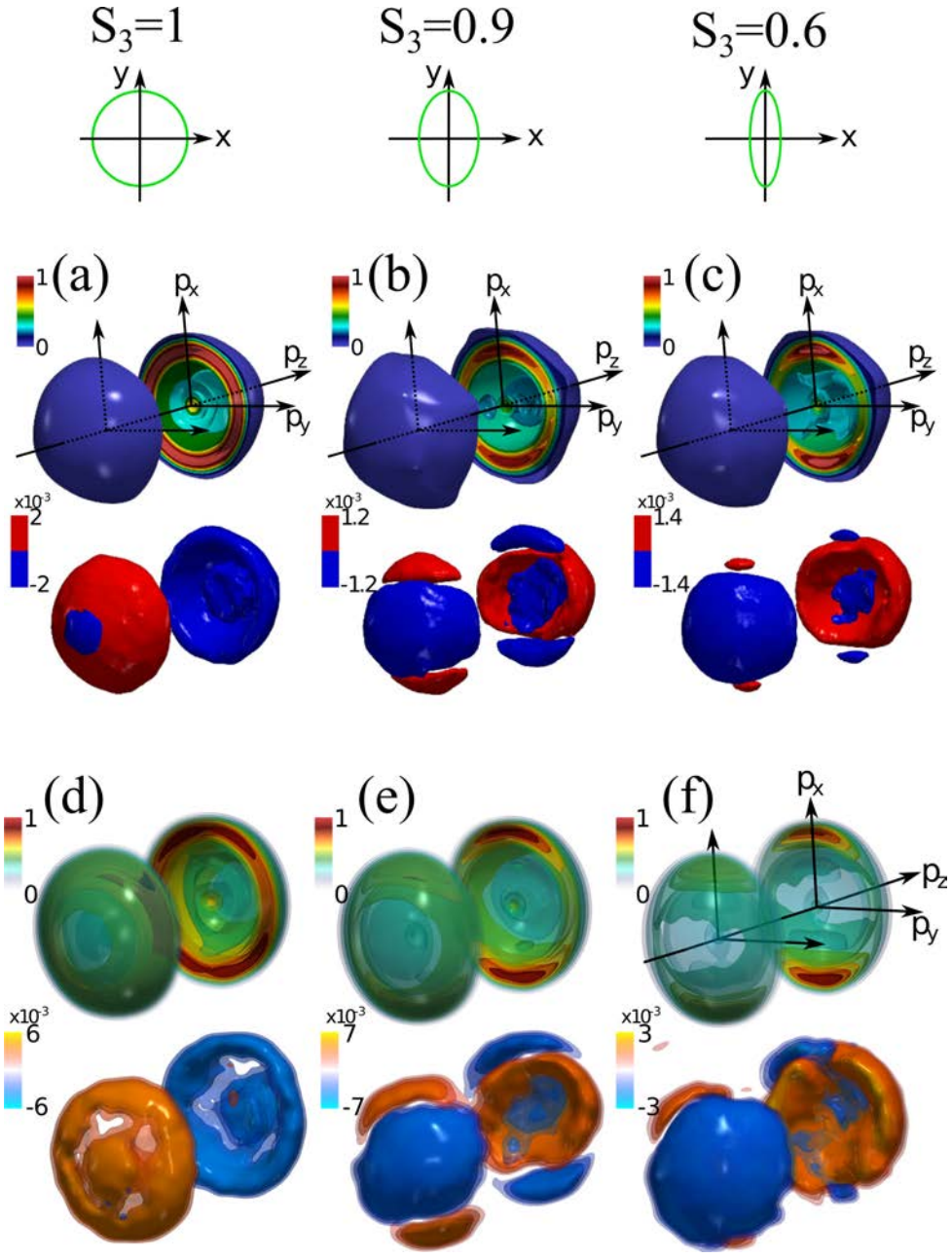


**Figure 3.19** – *Complete photoelectron angular distributions, measured in (+)-Fenchone at 515 nm, retrieved by tomographic reconstruction in the VMI at* $5 \times 10^{13}$ *W.cm*$^{-2}$ *(a-c) and directly measured in the COLTRIMS at* $6 \times 10^{13}$ *W.cm*$^{-2}$ *(d-f). The laser Stokes parameter was* $S_3 = 1$ *in the first column, 0.9 in the second and 0.6 in the third one. In each panel, the normalized total distribution is depicted above and the corresponding dichroic signal (forward/backward antisymmetric along the laser axis) is shown below.*

In this example, the ellipticity of the field breaks the cylindrical symmetry of the distributions and make the 3D reconstruction necessary. The duration of the acquisitions is also

relatively similar, and the tunability of the laser repetition rate is a great asset to maximize the signal in any case. The structures to resolve are not very complex and both methods succeed in measuring them, but this is not always the case.

**Orthogonal Two-Color Field**

This second example is based on the 3D measurement of the ESCARGOT effect, presented in Section 4.III, again in (+)-Fenchone. It is the chirosensitive response obtained in the photoelectron angular distribution of chiral molecules ionized with an orthogonal two-color field, produced by combining beams at 1030 nm and 515 nm, orthogonally and linearly polarized. We will focus on two cases here, where the field follows a "C"-shape and an "8"-shape. The estimated laser conditions used in the VMI were $I_{1030nm} = 1.6 \times 10^{13}$ $W.cm^{-2}$ and $I_{515nm} = 3.4 \times 10^{12}$ $W.cm^{-2}$, at a repetition rate of 750 kHz. 25 projections were recorded at an angular step of 15 degrees, for a acquisition of about 1 min per projection. For each image, the two-color phase was scanned in order to extract the oscillating components, as explained in the corresponding chapter. The whole acquisition thus took 25 min. For the COLTRIMS measurements, the intensities were estimated about $I_{1030nm} = 4.6 \times 10^{12}$ $W.cm^{-2}$ and $I_{515nm} = 2.5 \times 10^{12}$ $W.cm^{-2}$, at a laser repetition rate of 166 kHz, for an electron acquisition rate of about 100 kHz. The continuous variation of the field shape was not possible, so each image was recorded at a fixed two-color phase. The $2\pi$ periodicity of the signal was sampled in 9 steps. At each point, 100 M counts were recorded in about 17 min, for a complete duration of 150 min.

The comparison is presented in Fig. 3.20, where the result of the tomographic reconstruction is depicted in panels (a) and (b) and the COLTRIMS measurement in (c) and (d). The distributions are in qualitative agreement in terms of global shape. In particular, the PES is driven along the 2w axis ($p_y$) depending on the two-color phase, and the dichroic signal appears with the same sign. However, several discrepancies can be pointed out. Firstly, the laser intensity is supposed to be higher in the VMI measurement but the ATI peak, present in the COLTRIMS measurement (like the four corners of a square), does not appear in the VMI. Secondly, the total signal is much more noisy in the VMI, whereas its dichroic part looks smoother than in the direct measurement. Since the 3D structures observed in the COLTRIMS symmetric parts are well reproduced by TDSE calculations, this would indicate that the tomography hardly manage to grasp the fine details in this case. Finally, the amplitude of the dichroic signal is greater in the VMI than in the COLTRIMS, which goes against the observation done in the previous example. This could be explained by a wrong estimation of the intensity, since its magnitude should decrease at stronger fields, or by an overestimation in the reconstruction.

The direct measurement provided by the COLTRIMS appears to be better than the tomographic reconstruction to resolve fine 3D angular structures. Nevertheless, one should keep in mind that this latter has been recorded with 6 times less statistics. On an equal footing, the VMI measurement could thus be done with more signal to get a better signal-to-noise ratio, or with more projections in order to resolve finer structures. We can then expect the performance of the tomography to be closer to the one of the direct measurement.

In term of pure performances, the two methods seem to be relatively similar, at least in

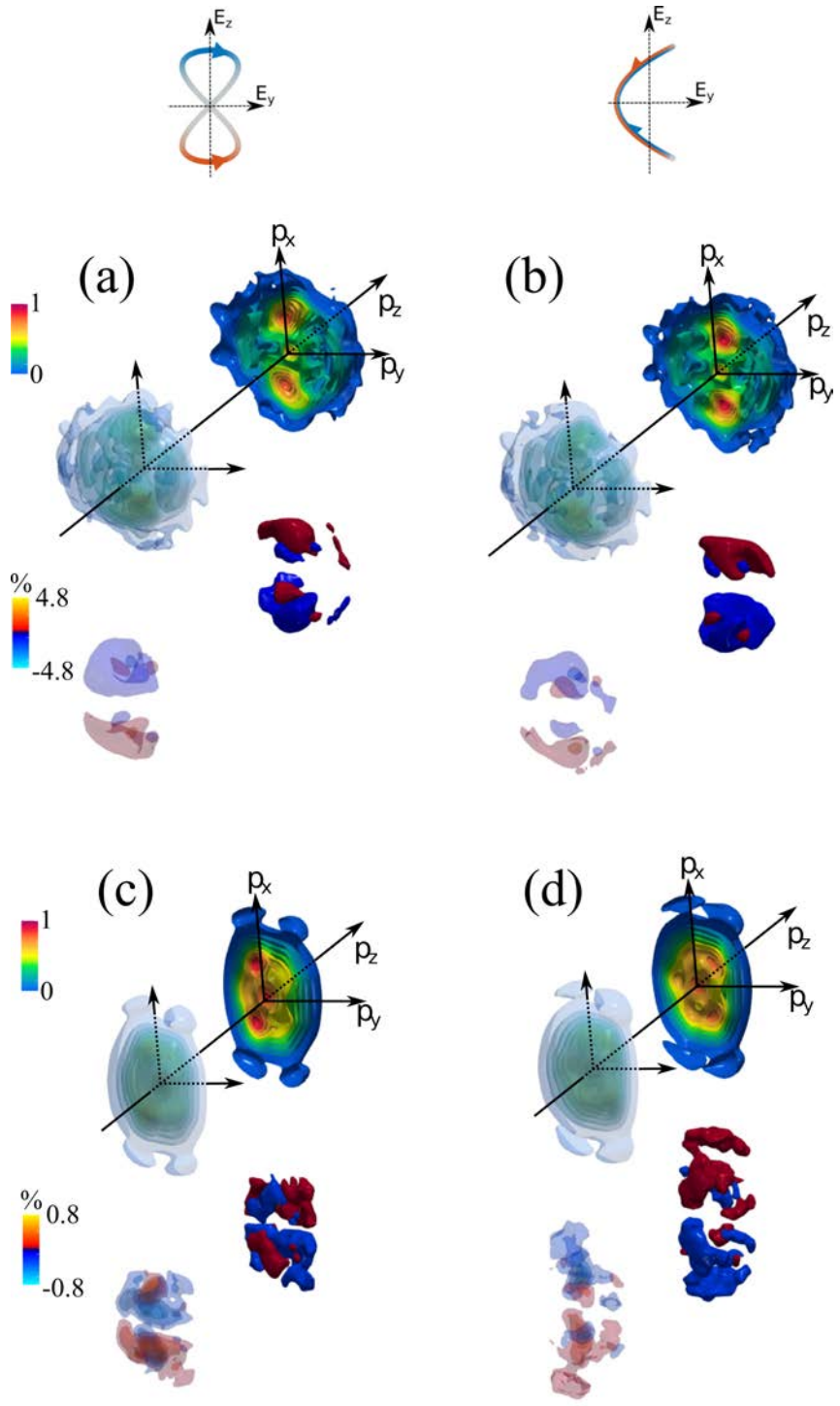


**Figure 3.20** – *Complete photoelectron angular distributions, measured in (+)-Fenchone using orthogonal two-color fields, retrieved by tomographic reconstruction in the VMI(a-b) and directly measured in the COLTRIMS (c-d). The tailored field was "8"-shaped in the left column and "C"-shaped in the right one. In each panel, the normalized total distribution is depicted above and the corresponding dichroic signal (forward/backward antisymmetric along the laser axis) is shown below.*

the same order of magnitude. Yet, what comes out from this comparison is a gap in robustness and ease of implementation. In particular, as the tomographic reconstruction requires an offline analysis, the outcome of an experiment can only be known afterwards. If the result lacks

statistics or angular resolution, which is hard to know in advance, extending the dataset might be difficult. Also, determining if a reconstruction is reliable or not can also be complex without external reference. Conversely, the direct measurement can be monitored online, and if an interesting feature starts to show up, one can just let the acquisition run until the result is satisfactory. Moreover, the algorithm performing the reconstruction of the angular distributions in the COLTRIMS is explicit, and its behavior and reliability can be more easily checked. Finally, the VMI is a rather simple apparatus which is used here in one of its most advanced manner. Contrarily, the capacity of the COLTRIMS is only partially used here, and the goal is of course to go towards its complete use. We will thus dwell on COLTRIMS measurements for the rest of this section.

### III. 2 Elliptical Dichroism in Ethyl- and Methyl-Lactate

Historically, most of the studies on chiral molecules were carried out in our group on Fenchone, and sometimes in one of its isomer, Camphor, or in Limonene, for several reasons. As mentioned in the introduction of this chapter, many pioneering studies on PECD were conducted in these molecules that have become a good benchmark, showing large dichroic response to circular fields. Indeed, terpenes are rigid molecules without distribution of conformers, each of them having a specific PECD. In addition, their study in the gas phase is simplified by their high volatility. Meanwhile, one of the initial aims of this thesis was the investigation of the chiral recognition, which is the ensemble of mechanisms involved in the way chiral molecules interact with each other, for example in enantioselective chemical reactions. In this perspective, the time-resolved photodissociation of heterodimers of chiral molecules can be interesting to give, for instance, a varying chiral response depending on the point at which the dissociation is. For efficiently creating heterodimers, similarly-structured chiral molecules with a high permanent dipole must be used. For this purpose, we decided to investigate Methyl-Lactate and Ethyl-Lactate, that are shown in Fig. 3.21.

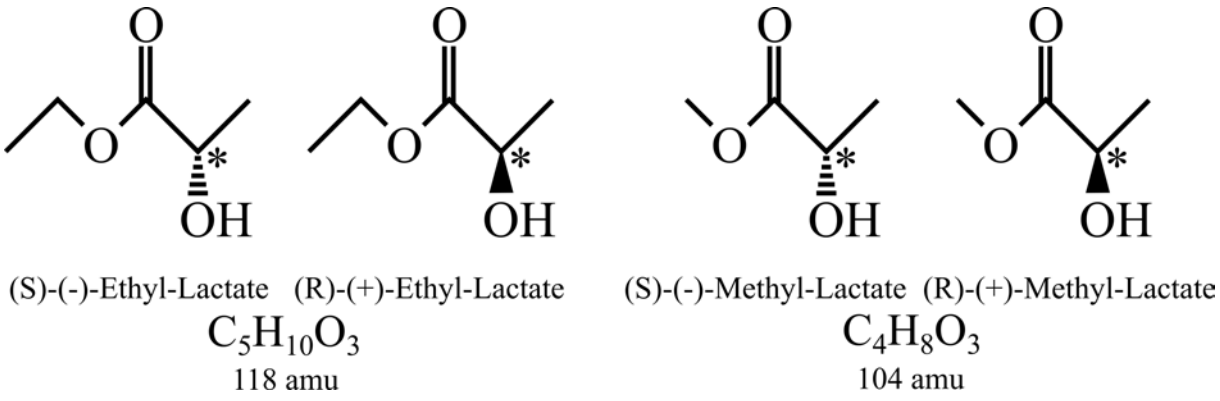


**Figure 3.21** – *Molecular structures of the Ethyl-Lactate and Methyl-Lacate.*

Prior to any time-resolved or PEELD experiment, these new systems must be characterized. This has been done almost from scratch, as the energy levels of these molecules and their REMPI schemes were not found in the literature. We will firstly focus on the photoelectron distributions. The analysis of the mass spectra will be presented in further section of this part.

**Synchrotron Absorption Spetrum**

The first stage of the characterization is the absorption spectrum. Below 6 eV, this was done using different solvents at the Institut des Sciences Moleculaires at the University of Bordeaux, but no absorption bands were found in this UV range. Synchrotron sources are ideal above 6 eV, as their wavelength is precisely tunable and calibrated. We had the chance to obtain absorption spectra recorded and analyzed by Nelson De Oliveira, specialist of the VUV Fourier transform spectroscopy, one of the experimental branch of the DESIRS beamline of the synchrotron SOLEIL, France. The Fourier transform can be performed on this beamline between 5 eV and 40 eV [de Oliveira 09], but our range of interest is up to the ionization threshold of the molecules, which we determined experimentally at 10.29 eV, as will be shown in this section. The absorption spectrum of Ethyl- and Methyl-Lactate at a 1 mbar pressure are presented in Fig. 3.22. The photon energy resolution is 0.45 meV. One can see that the spectrum of the two molecules are very similar, which makes sense given their similar structures. However, small differences can be noticed, caused by the ethyl- or methyl- groups.

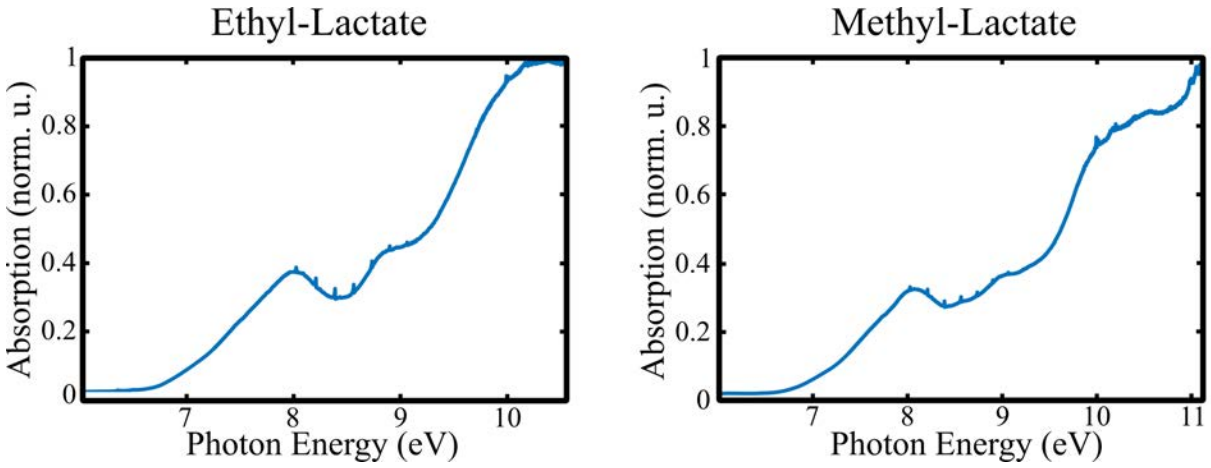


**Figure 3.22** – *One-photon absorption spectrum of Ethyl-Lactate (left) and Methyl-Lactate (right), measured at the DESIRS beamline at the synchrotron SOLEIL.*

Even if these spectra correspond to the one-photon process, and are thus not quantitatively usable as is in multiphoton ionization, they present two major interests. Firstly, they give the position of the broad level manifolds present in the molecules. As these manifolds of molecular excited states always show a high density of states of different symmetries, they are still likely to be involved in any REMPI scheme. Secondly, these spectra are essential for the calibration and the assessment of the reliability of theoretical calculations. This enables, for instance, to check that the calculation basis is large enough to reproduce the high-lying states. Additionally, calculated levels often show a systematic offset, that can thus be corrected. This will be used in further section of this manuscript.

**Power Scaling Law**

Another important step consists in identifying the resonances at play in the multiphoton ionization of the two molecules at the two wavelengths of interest, 515 nm and 343 nm. The

easiest way to determine it experimentally is the variation of the ionization yield $S$ as a function on the laser intensity $I$. In the nonresonant multiphoton regime, is should scale as $S \propto I^n$ where $n$ is the number of photons required for the photoionization. However, if an intermediate resonance is involved in the process, the excitation step can become the bottleneck and drive the yield. As a result, one can fit the scaling law in two ways :

$$\begin{aligned} S &= A \cdot I^{n*} \\ S &= \sum_{m=1}^{n} A_m \cdot I^m \end{aligned} \tag{3.15}$$

where either an effective $n* \in \mathbb{R}^+$ is fitted, or alternatively where the weight of the integer polynomial orders $A_m$ are determined. This procedure is only applicable, of course, below any saturation. We have performed the second type of fit to directly retrieve the relative contributions of the resonances in the REMPI process, on the measurement of the counting rate of photoelectrons in coincidence with the ions. The results are presented in Fig. 3.23. Interestingly, the branching ratio significantly differ between the two molecules. In the 3-photon ionization at 343 nm, the process in Ethyl-Lactate is mostly driven by the excitation at 7.2 eV (95 %), while only 5 % scales as the non-resonant ionization. In contrast, they are more balanced in Methyl-Lactate (respectively 45 % and 55 %). By comparison with the absorption spectrum in Fig. 3.22, the excitation occurs in the tail of the first manifold of states peaking around 8 eV. In the 5-photon ionization by the 515 nm wavelength, resonances at 4.8 eV (70 %) and 7.2 eV (30 %) are dominant in Ethyl-Lactate. In liquid phase, we did not observe any absorption band around 5 eV. Anyway, the density of state at this energy is probably much lower, with a lower oscillator strength, and since this excitation is performed with two photons, this particular level could be less visible at one photon for symmetry reasons. Another explanation would be the saturation of the transitions, leading to an irrelevant scaling, but this is unlikely to be the case at the energy per pulse used, as less than one molecule was ionized per laser shot in average.

In contrast in Methyl-Lactate, the power scaling law indicates the prominence of the intermediates levels at 7.2 eV (75 %) and 9.6 eV (25 %), just below the ionization threshold. These results suggest that even if the two molecular systems only differ by a substituent group, their REMPI processes are strongly dissimilar. They can thus constitute a good benchmark for investigating the role of the intermediate resonances at play in the PEELD effect.

**Photoelectron Spectra**

The photoelectron kinetic energy spectra of Ethyl-Lactate and Methyl-Lactate were recorded at 343 nm and 515 nm, with linearly polarized field. The results are presented in Fig. 3.24.

The spectra of Ethyl- and Methyl-Lactate are qualitatively similar, even if their $I_p$ were found respectively at 10.1 eV and 10.3 eV in coincidence with the parent ion. The ionization energy is reached with a 343 nm wavelength (3.61 eV) in 4-photon absorption at 10.8 eV (up to respectively 0.7 eV and 0.5 eV kinetic energy in EL and ML), or 5-photon at 14.4 eV (up to 4.3

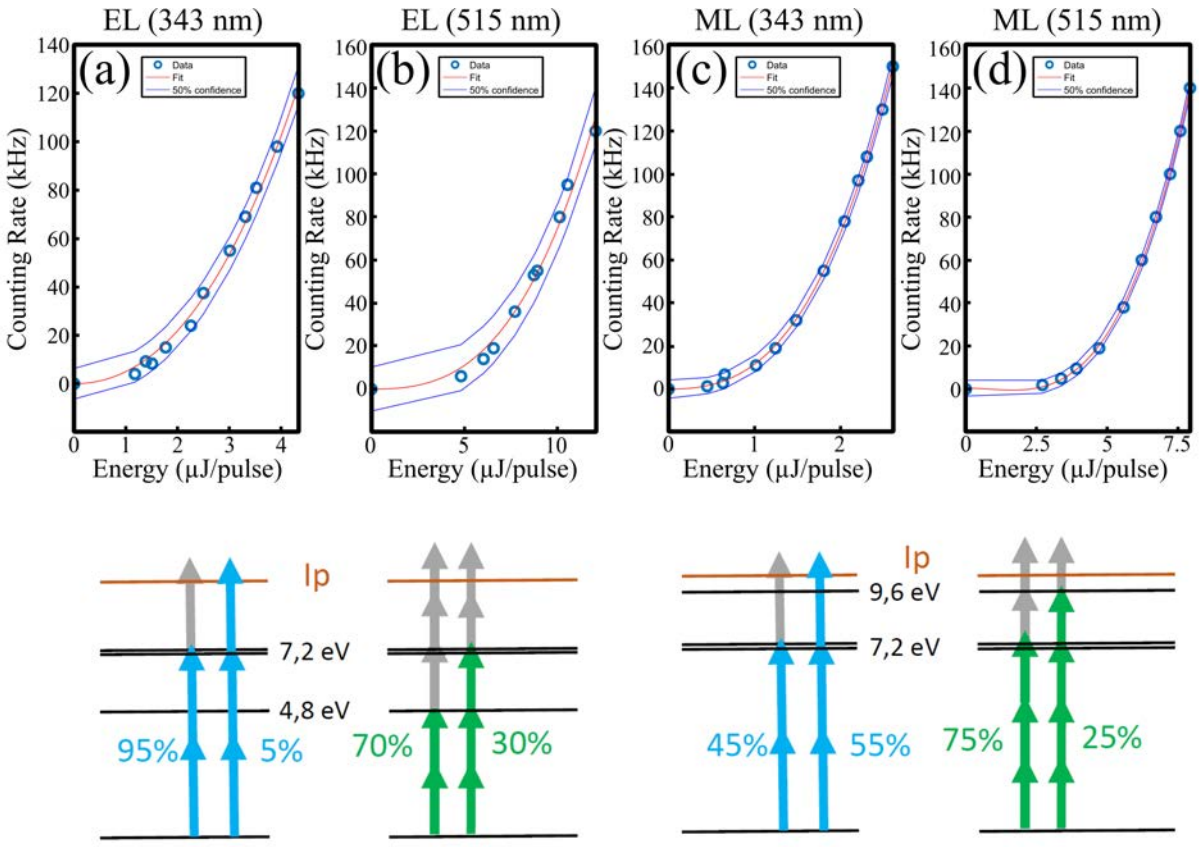


**Figure 3.23** – *Power scaling law of Ethyl-Lactate (EL) at 343 nm (a) and 515 nm (b), and Methyl-Lactate (ML) at 343 nm (c) and 515 nm (d). The experimental data, the fit and the 50 % confidence interval are depicted. The resulting resonant contributions are depicted below. The experiment was performed at a laser repetition rate of 500 kHz.*

eV and 4.1 eV). At 515 nm (2.41 eV), the 5-photon process reaches 12.0 eV (up to 1.9 eV and 1.7 eV of kinetic energy). The first ATI of the 0.8 eV peak is visible at 3.2 eV.

The direct assignment of the spectra is challenging since the system is highly dissociative upon ionization, as we will see in this section. As a result, part of the energy is kept in the ionic system and the photoelectron spectra tend to peak at low kinetic energy. In addition, the peaks are relatively broad, probably due to the resolution of our spectrometer as discussed in the previous chapter. Nevertheless, the study of the angular dependency of the photoelectrons distribution will show interesting results.

**Wavelength- and Molecule- Dependency of the PEELD**

Experimental measurements of the PhotoElectron Elliptical Dichroism has been carried out in the COLTRIMS in both (-)-Ethyl-Lactate and (-)-Methyl-Lactate (carried by 2 bars of $N_2$ as seeded gas), at 343 nm and 515 nm. In each case, distributions were recorded at field ellipticities of 100 % ($|S_3| = 1$), 64 % ($|S_3| = 0.90$) and 36 % ($|S_3| = 0.63$). Each acquisition was performed by periodically rotating a half waveplate in front of a fixed quarter waveplate in order to reverse the sign of the helicity while keeping the axis of the field ellipse fixed. The photoelectron distributions discussed here were not recorded in coincidence with the ions, in

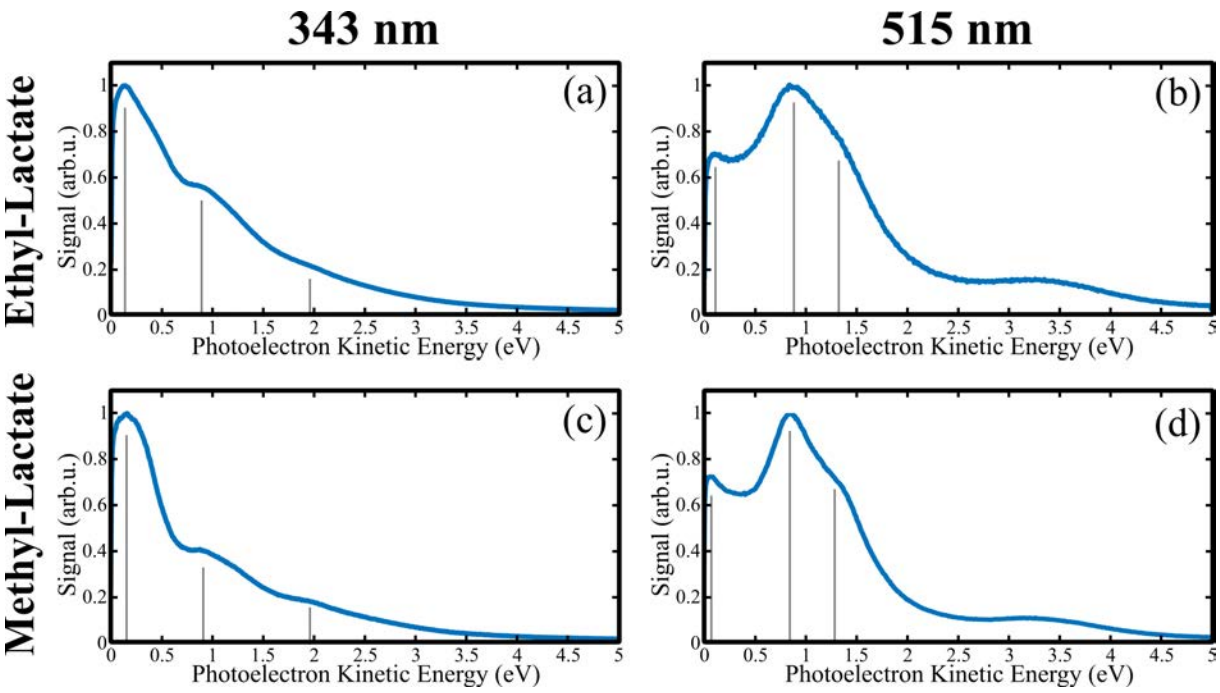


**Figure 3.24** – *Photoelectron kinetic energy spectra of (a) Ethyl-Lactate at 343 nm, (b) Ethyl-Lactate at 515 nm, (c) Methyl-Lactate at 343 nm and (d) Methyl-Lactate at 515 nm, recorded with a linearly polarized field. The conditions were (a) 2 µJ/pulse at a repetition rate of 166 kHz, (b) 6µJ/pulse, 166 kHz, (c) 1.6 µJ/pulse, 166 kHz, (d) 4.3 µJ/pulse, 250 kHz. The chiral molecules were carried by 2 bars of $N_2$ and the nozzle heated at 90°C.*

order to use a high counting rate and get a good statistics rapidly and identify the interesting cases. A summary of the experimental conditions used is given in Table 3.2. The repetition rate of the laser is tuned to maximize the counting rate at a given energy per pulse. Note that the multiphoton ionization efficiency is larger in linear polarization than in circular at a fixed power. This could also have been compensated with the repetition rate, but we preferred to do the measurements in a row for a better comparison.

The photoelectron distributions were fully measured, but representing them in 3D does not necessarily provide the most quantitative comparison. Conversely to the distributions obtained with the previous systems (as in Fig. 3.19), the PES maximizes at zero kinetic energy, which can be related to the dissociative aspect of the ionization, but the PEELD response is spread at higher energy. In the present discussion, we will focus on 2D distributions in the plane containing the main axis of the ellipse (vertical) and the laser propagation axis (horizontal). Compared to the VMI-like projections, we can here select central cuts of the distributions between -$50\times10^{-3}$ and +$50\times10^{-3}$ a.u. (in momentum) to get a better contrast. The results are presented in Fig. 3.25. The columns display, from left to right, the dichroic responses obtained with a field ellipticity of 100%, 64% and 36% and the corresponding cut of the total signal. The sign of the dichroic signal is presented with the same convention as for PECD, *i.e.* for a left rotating field (negative values of $S_3$). The rows (a-e) correspond to the conditions given in Table 3.2. The white circles indicate the main signal peak found in the PES and are reported in the corresponding PEELD distributions. The PES and PEELD are defined here in polar coordinates $(r, \theta)$ where the radius is $r \propto \sqrt{E_{kin}}$ and the angle $\theta$ is defined from the forward direction of the laser

| Molecule | Wavelength (nm) | Energy ($\mu$J/pulse) | Repetition Rate (kHz) | Ellipticity % | Counting Rate (kHz) | Counts (M) |
|---|---|---|---|---|---|---|
| (-)-EL | 343 | 4.3 | 166 | 100 | 93 | 620 |
| | | | | 64 | 97 | 640 |
| | | | | 36 | 105 | 675 |
| (-)-EL | 515 | 15 | 166 | 100 | 70 | 510 |
| | | | | 64 | 80 | 550 |
| | | | | 36 | 110 | 560 |
| (-)-EL | 515 | 9.5 | 900 | 100 | 70 | 400 |
| | | | | 64 | 100 | 610 |
| | | | | 36 | 150 | 665 |
| (-)-ML | 343 | 3.4 | 500 | 100 | 140 | 750 |
| | | | | 64 | 150 | 700 |
| | | | | 36 | 155 | 870 |
| (-)-ML | 515 | 10 | 500 | 100 | 45 | 590 |
| | | | | 64 | 125 | 750 |
| | | | | 36 | 130 | 770 |

**Table 3.2** – *Overview of the experimental conditions used in the measurement of the PEELD in Ethyl- and Methyl-Lactate at 343 nm and 515 nm.*

(horizontal, right). From the raw signal $S_{raw}(r,\theta)$, the PES is obtained with an up/down and left/right symmetrization, to remove the experimental artifacts :

$$\begin{aligned} S_{u/d}(r,\theta) &= \frac{1}{2}\left(S_{raw}(r,\theta) + S_{raw}(r,-\theta)\right) \\ PES(r,\theta) &= \frac{1}{2}\left(S_{u/d}(r,\theta+\pi/2) + S_{u/d}(r,-\theta+\pi/2)\right) \end{aligned} \tag{3.16}$$

and the PEELD is obtained from the left/right antisymmetric part (*i.e.* along the laser axis) of the the up/down symmetric signal $S_{u/d}$, normalized radius by radius relatively to the PES, as :

$$\begin{aligned} PEELD_{unnorm}(r,\theta) &= \frac{1}{2}\left(S_{u/d}(r,\theta+\pi/2) - S_{u/d}(r,-\theta+\pi/2)\right) \\ PEELD(r,\theta) &= 2 \times (PEELD_{unnorm}(r,\theta)/PES(r,\theta)) \end{aligned} \tag{3.17}$$

The order of magnitude of the dichroic signal is in the few percents range. Overall, on the contrary to rigid molecules such as Fenchone or Camphor, Ethyl- and Methyl-Lactate are floppy systems, such that the amplitude of their PECD is relatively smaller. Note that in the presented figure, a threshold has been applied to put at zero the dichroic signal where the total signal is less than 10% of its maximum, since the noise in this region can become dominant.

As one can see in Fig. 3.25, the PEELD measured at 343 nm, in both (-)-Ethyl- and (-)-Methyl-Lactate (rows (a) and (d)) show a typical one-photon behavior (described previously in this chapter). The distributions have a low-order symmetry and the amplitude decreases at lower ellipticity, as expected for a [2+1] ionization (supported by the power law of Fig. 3.23). In

addition, the PEELD amplitude linearly scales with $S_3$, even if only three points are compared here, and the shape of the patterns does not evolve with the ellipticity. These features suggest that the anisotropy breaking in the photoelectron elliptical dichroism plays a minor role in these cases. The effects of anisotropy of excitation are not visible, and the process is certainly driven by the last photon absorbed from the intermediate resonance.

In Ethyl-Lactate at 515 nm (rows (b) and (c)), the dichroic observable seems to be more typical of a REMPI scheme. Contributions of higher-orders Legendre polynomials are visible, with a sign flip around the laser axis. Again, the amplitude slightly decreases at low ellipticity but the pattern remains largely unaffected. Several features appear at different energies, slightly above and below the white ring depicted, but also at very low energy. When reducing the intensity (from (b) to (c)), the relative contribution of the inner features increases. We will investigate these energy structures in further detail in the next section, but in any case the PEELD effect remains weak here. These observations are consistent with the REMPI scheme found in Fig. 3.23 (b). Since the anisotropy breaking does not seem to take place here, the presence of the high-orders of polynomials simply comes from the fact that several photons are involved in the ionization step.

These situations contrast with the observations made in (-)-Methyl-Lactate at 515 nm (e). Similarly to the Ethyl-Lactate, several energy structures appear in the dichroic signal, yet with a less visible contribution of high-order symmetries. This goes along with the corresponding REMPI scheme found with the power scaling law, where less photons are involved in the ionization step. Conversely to the other cases, the amplitude of the forward/backward antisymmetric part is not maximized in circular polarization, which is a typical sign of the PEELD effect, as pointed out in the previous section of this chapter. In addition, one can note the evolution of the pattern with the field ellipticity. In particular, the features above the 0.8 eV circle change sign near the horizontal axis and at the center and is very similar to what has been noticed in Fenchone, Camphor and Limonene in Fig. 3.7. Meanwhile, the low kinetic energy feature move from a multiphoton (presence of $b_3$) to a single photon (only $b_1$) aspect when reducing $\epsilon$.

This comparison points out that the anisotropy of excitation yielding the PEELD effect is not systematic. One has to keep in mind that the PECD is a quantity that is averaged over randomly aligned samples, and that the contribution of all the orientations can greatly vary. The photoexcitation process can preferentially select the molecules for which the transition dipole is in the polarization plane with circular polarizations, along the polarization axis with linear polarizations, or in between depending on the field ellipticity. In some cases, the dichroic response of the molecules in a plane are very similar than along an axis, in such a way that the response do not vary from the linear ellipticity dependency. In some other cases, the preferential excitation is very noticeable in the signal. From the example given here, it does not seem like some general rule can be easily drawn, from the molecular structure, the number of states or the number of photons involved. Unfortunately, this can set a limitation to the enrichment of the PEELD response compared to the PECD in some cases, and the evolution of the PECD depending on the molecular orientation is not trivial to predict theoretically. Also, when several excited states come into play in the REMPI, some of them can evolve while others do not. We will see in the next section that an additional effect can also come into play.

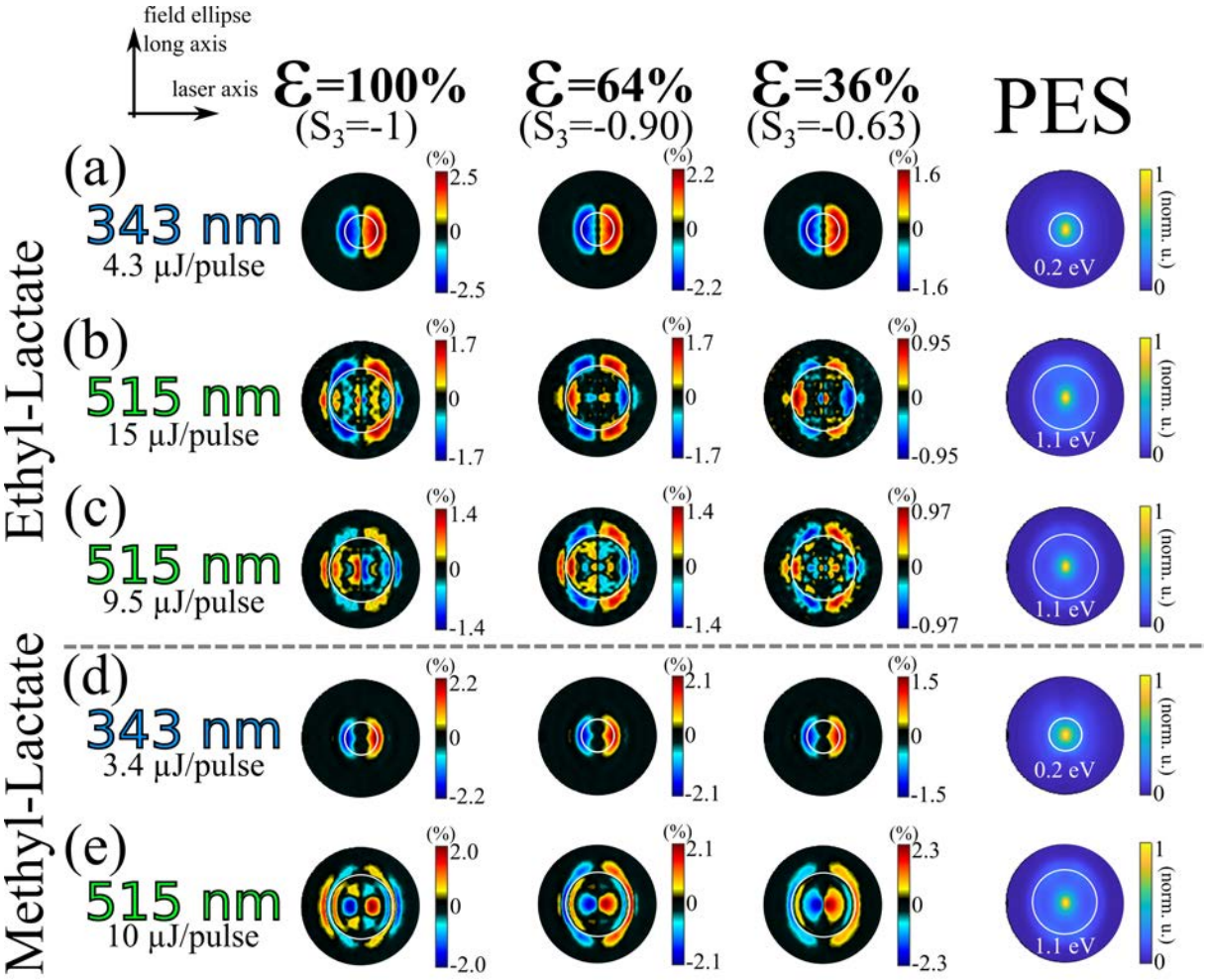


**Figure 3.25** – *Central cuts of the photoelectron angular distributions of the total signal (far right) and the corresponding dichroic parts for field ellipticites of 100%, 64% and 36% (from left to right). The measurements were performed in (-)-Ethyl-Lactate at 343 nm (a) and 515 nm (b-c), and in (-)-Methyl-Lactate at 343 nm (d) and 515 nm (e) in the conditions indicated in Table 3.2. The vertical axis corresponds to the main field ellipse axis and the horizontal one to the laser propagation axis (from left to right). The cuts were obtained by integrating over ± 0.05 a.u. (momentum) along the small ellipse axis, centered around zero. The white circles indicate the main peak in the PES and are reported in the corresponding rows. The sign of the dichroic signal is presented with the same convention as for PECD, i.e. for a left rotating field (negative values of $S_3$).*

## III. 3 Coincidence Measurement : Dependency to the Fragmentation

The main appeal of the COLTRIMS is of course its coincidence capacity. It is also challenging in term of acquisition time, and renders a systematic study difficult. We will thus focus here on the photoionization process of the (-)-Methyl-Lactate at a 515 nm wavelength as this case displays a noticeable PEELD effect. The acquisition of the angular distributions at three field ellipticities presented in Fig. 3.25 (e) took about 6 hours (at one compound and one wavelength), at an electron counting rate of the order of 100 kHz. As discussed in the previous chapter, the counting rate when the coincidence is needed is in the 10-15 kHz range (for a laser repetition rate of typically 166 kHz) due to some limitations, and only a fraction of this can be used because,

among others, of the detection efficiency. Furthermore, since the contributions of the different ionic species can be more or less prominent in the mass spectrum, the effective counting rate of each species of interest can be very low.

Not all the observables take the same amount of data to be satisfactorily resolved. The 1D quantities, such as the photoion mass spectrum and the photoelectron kinetic energy distribution can usually be determined in a few minutes. The VMI-like 2D projections of the electron take more statistics (typically ten times more), and the complete 3D distributions needs another order of magnitude of duration. The challenge comes when one wants to obtain the dichroic signals, that are of the order of a few percents of the total signal, and when ions in minority are studied, each of these conditions adding an additional temporal order of magnitude. We will see in this part a preliminary study in coincidence to define the current capacities.

**Fragment-Dependent PECD**

Upon ionization, molecules can fragment into different ionic species depending on several factors. Firstly, the fragmentation depends on the molecular orbital ionized. This can be qualitatively understood for the localized orbitals [Backx 75, Tan 78], as removing an electron from a bonding orbital can weaken the bond. However in general, several fragmentation pathways can happen with different branching ratios, increasing the complexity and rendering a one-to-one assignment difficult. Secondly, the cation can be left in an excited state upon ionization, some of these states being unstable (dissociative). In REMPI processes, the dissociation can even happen from the excited states if they lie above the dissociative limit, and thus depend on these excited states. Finally, since all these parameters depend on the molecular orientation relatively to the laser field, the fragmentation can also depend on this parameter.

As already discussed in this chapter, the PECD also depends on all these factors. The consequences on the PECD and its link with the fragmentation channel can thus be of high interest. For instance, can we assign the ionized orbitals in a molecular system that is highly dissociative upon ionization as the Methyl-Lactate? Does the dissociative nature of this ionization prohibits the appearance of a PECD? The first fragmentation channels of the ionisation continuum are often correlated to the appearance of excited states of the cation. This correlation have been used for instance in CRATI (channel-resolved ATI) to reveal the energy shift induced by a strong field [Boguslavskiy 12]. This has also been used in single-photon PECD to disentangle the contributions from different orbitals ionized [Garcia 14]. However, systems for which the fragmentation diagrams are pure enough to directly assign the features are rare, and the situation is more complex in most cases. Nevertheless, we will use this approach in the context of multiphoton PEELD.

The photoelectron circular dichroism (PECD) is known to be potentially correlated to the fragmentation pathway. In the one-photon ionization regime in Methyl-Oxyrane, the PECD can vary depending on the molecular orbital ionized, as well as the fragmentation [Garcia 13, Garcia 14] as discussed just above. In the strong field ionization regime, again in Methyl-Oxyrane, a dependency has also been found [Fehre 19], even if the electrons are mostly ionized from the HOMO in this regime. It has been interpreted as an alignment effect,

as both the PECD [Tia 17] and the fragmentation [Litvinyuk 03, Hansen 12] are sensitive to it. In this case since the initial orbital is fixed, the alignment effect involves preferential transitions to excited states. In the multiphoton regime, two studies (respectively in Camphor and Limonene) showed that the kinetic energy spectra and their angular dependency were not sensitive to the correlated ion [Lehmann 13, Rafiee Fanood 16]. This was interpreted as typical of the post-ionization fragmentation, meaning for instance in the second reference that the photoelectrons were emitted at 3 photons and the fourth photon was used to dissociate the ion (post-ionization absorption). Another study demonstrated that in Methyl-Oxyrane, the electron kinetic energy distribution shows a different amplitude of the PES depending on the fragment. This modulates the amplitude of the final PECD figure, but the sign of the PECD at a given energy was not affected by itself [Rafiee Fanood 14].

At 12.0 eV, reached by 5-photon ionization at 515 nm, Methyl-Lactate shows already a rich fragmentation behavior, as shown in Fig. 3.26 (a). Unfortunately, the ionization continuum with the energy of appearance of the fragments have not been studied with a tunable VUV source. The relative contributions will be presented in Table 3.3 and the assignment of the mass spectrum, as well as the fragmentation mechanisms will be discussed in the next section. We will here concentrate on the three main fragments, detected in a broad peak around 31-32 amu, a narrow one at 32 amu and the dominant, broad one at 45 amu. The width of the features correspond to the recoil acquired during the fragmentation process. An unfragmented ion is very narrow while the fragments are typically much broader. The distributions of photoelectrons depicted in Fig. 3.26 (b) and (c) are obtained by filtering the corresponding ion masses. Note that the broad peak around 31-32 amu is only selected on the left side of the 32 amu narrow signal here. The row (b) shows the central cuts of the total distributions in the plane containing the laser axis, normalized relatively to the signal without coincidence (right). The row (c) depicts the corresponding dichroic signal obtained in circular polarization, of the order of 2% relatively to their respective PES. These images were reconstructed from a total of 680 Mcounts recorded at 11 kHz, for an acquisition duration of about 17 hours, split between two days. The laser repetition rate used was 166 kHz, at an intensity $I_{515nm} = 17$ $\mu$J/pulse. Methyl-Lactate was carried by 1 bar of helium, and the jet nozzle was heated at 110°C. Note that the statistics without coincidence is not only the sum of all the coincidences, but also accounts for the electron counted without ions.

All the PES associated with the different fragments show a component at zero kinetic energy, which can be related to the dissociation, but they also present different signal distributions at higher kinetic energies. This will also be detailed later in this section. Let us, for now, concentrate on the dichroic response measured, Fig. 3.26 (c). On one hand, the PECD obtained from the sum of the signal over all the species (right) is clearly comparable to the one presented in Fig. 3.25 (e). In addition, the PECD associated with the dominant mass at 45 amu (70% of the signal) looks very similar to the one without coincidence, which makes sense. On the other hand, the signal from the less abundant species clearly suffers from the lack of statistics. The PECD in coincidence with the 32 amu fragment could suggest that the very different PES indeed induces a change in the PECD, similarly to what was found in [Rafiee Fanood 14]. In

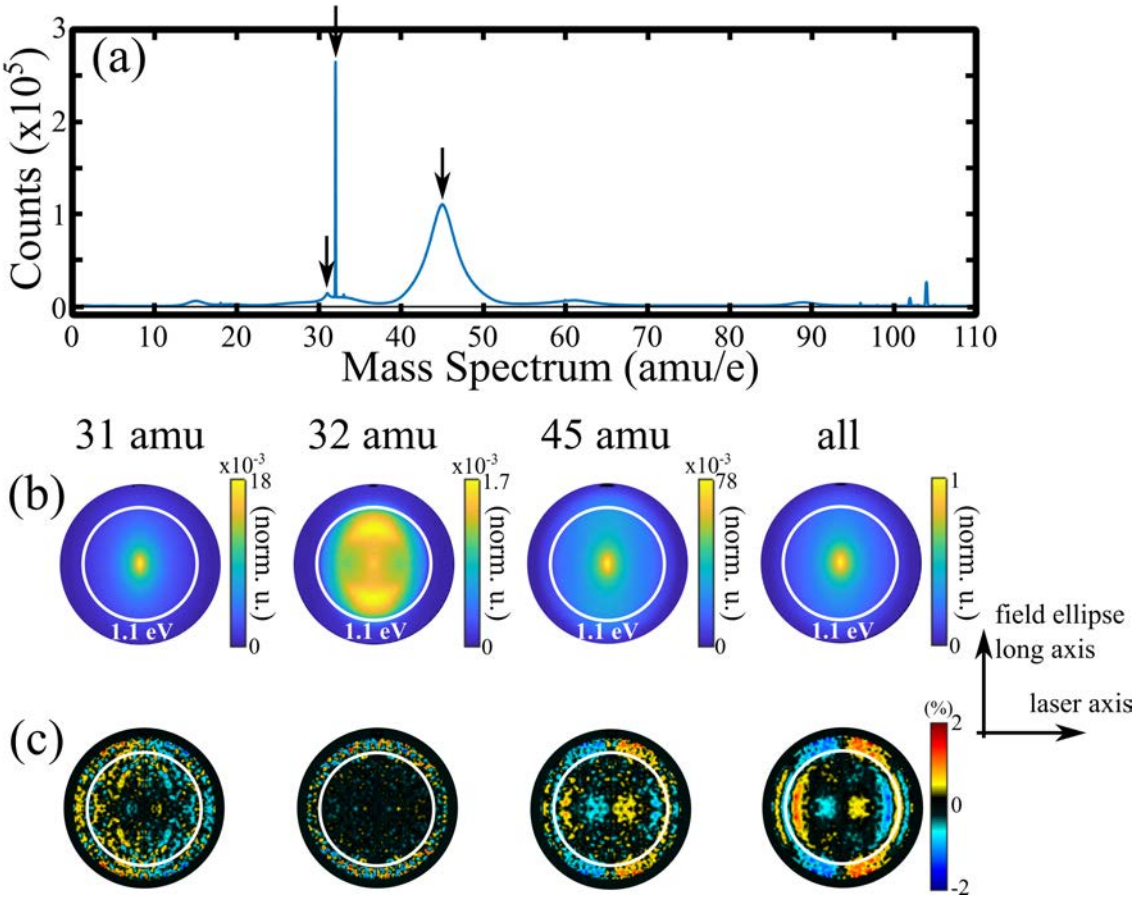


**Figure 3.26** – *Photoelectron and photoion coincidence measurement in (-)-Methyl-Lactate obtained with a 515 nm wavelength, at $I_{515nm}$ = 17 $\mu J$/pulse and a laser repetition rate of 166 kHz. (a) Mass spectrum, where the parent unfragmented ion is visible at 104 amu. Methyl-Lactate was carried by 1 bar of helium, and the jet nozzle was heated at 110°C. b) Central cuts of the photoelectron distributions in coincidence with the ion masses at 31 amu, 32 amu and 45 amu indicated by the arrow in (a), and the total counts without condition on the ions. The vertical axis is the main axis of the field ellipse and the horizontal is the laser axis. (c) Corresponding forward/backward antisymmetric signal, normalized energy by energy, obtained using circular polarization.*

particular, the prominence of the outer ring compared to the inner feature changes their relative contributions in the PECD. Interestingly in the distribution associated with the mass 31 amu, the dichroic signature would indicate globally an opposite sign compared to the unfiltered one, but more signal would be required to confirm this statement.

The capacity to acquire PECD and PEELD in coincidence is thus technically feasible and demonstrated here. Generally speaking, based on the Fig. 3.25 and 3.26, we can assume that about 750 M electron counts are necessary to get a good statistics in 2D projections or cuts. With the current limitations, this takes about 2 hours of acquisition without coincidence and 20 hours with the coincidence condition. These numbers are of course multiplied for fragments in minority, which means having a stable acquisition during a few days, and this number can be multiplied if the study requires several points, for instance in ellipticity for the PEELD or in delay for time-resolved pump-probe experiments. For this purpose, work is currently in progress to implement further active stabilizations to the laser source, automatic safety measures and

remote control and monitoring of the experiment to leave it run continuously over days. We also aim at increasing the acquisition rate, by moving from a window to continuous coincidence assignment scheme.

**Kinetic Energy Distributions**

Even if the measurement of the dichroic signal directly in coincidence with the ionic species would require an additional experiment, further information can already be found in the analysis of the kinetic energy distributions. A radial cut in the PECD figure along the laser propagation axis (forward), without coincidence filter, is depicted in Fig. 3.27 (a). The features of alternating sign are located at 0.1 eV, 0.7 eV, 1.1 eV and 1.45 eV. From the comparison with the Fig. 3.25 (e), the ellipticity dependent-feature is mostly visible in the outer rings. Its origin can be investigated by comparing it to the distributions of the total signal in coincidence obtained in circular polarization, that are shown in Fig. 3.27 (b).

Firstly, it is interesting to note that the distributions greatly differ between the species. The electrons in coincidence with the unfragmented ion (104 amu) have the highest kinetic energy since no energy is taken by the fragmentation. Using this particular signal is a good way to determine the vertical $I_p$ of the molecule, estimated at 10.29 eV here. The distributions associated with the fragments are made of three peaks in variable proportion, appearing at 0.1 eV, 0.8 eV and 1.3 eV. These peaks can be associated to different photofragmentation channels, and their relative ratio in the signal in coincidence with each fragment as well as the ratio between the fragments can give access to the different branching ratios. This gives the perspective to not only study the dependency of the PECD or PEELD to the final fragment, but more specifically to the fragmentation pathway.

Secondly, except for the lowest energy peak, the location of the PECD is shifted compared to the PES, and the sign flips occur around the PES maxima. This effect is also quite typical of many other systems, but a competition can take place here between the dichroic signal from the PES lines at 0.8 eV and 1.3 eV as they are close enough, and this is where the PEELD effect is located in Fig. 3.25 (e). The coincidence capacity gives again some interesting information. Even if the contribution of the 45 amu fragment is dominant, the other ones are not negligible in the signal without coincidence. However, the electrons at a kinetic energy of about 1.5 eV, where the PEELD is located, mainly originate from the 45 amu fragment.

The same distributions as a function of the associated ion, obtained in linear polarization is presented in Fig. 3.27 (c). Two major differences appear. The first one is that the high energy shoulder at 1.3 eV in the total signal and only in the dominant 45 amu fragment has largely decreased in proportion. We have measured that the transition appears continuously and smoothly as a function of the field ellipticity (not shown here). The PEELD effect could thus be caused either by an actual change of the dichroic response, or by a variation of the relative contribution of two overlapping ionization channels, leading both to the mass 45 amu. The second interesting difference in circular polarization is in the relative ratio of the total signal between the different fragments, indicated by the scaling factors in the figure. The PEELD could then be potentially linked to a variation in the relative proportions of the ion yields as a function of the ellipticity.

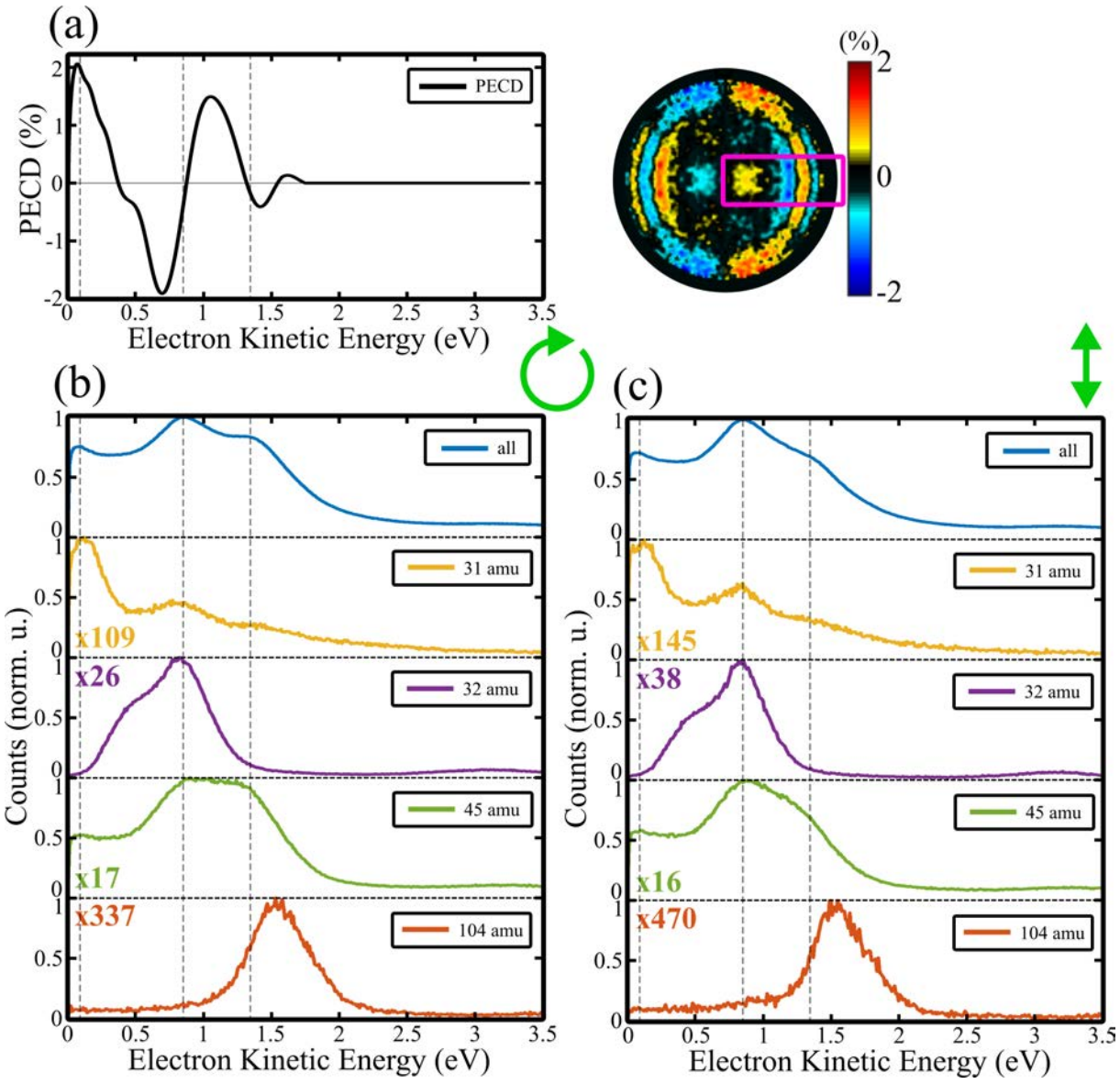


**Figure 3.27** – *(a) Radial cut forward along the laser axis in the PECD figure obtained without coincidence filter in (-)-Methyl-Lactate ionized at 515 nm. (b) Angularly integrated kinetic energy spectrum of the total photoelectron signal without coincidence and in coincidence with the fragments at 31 amu, 32 amu, 45 amu, the parent ion at 104 amu, obtained with a circular light polarization. The scaling factor are indicated in each panel. (c) Same as (b), obtained with a linearly polarized field.*

This latter effect can also be monitored in the ellipticity-dependent mass spectrum. The effect if small and hard to read directly on the mass spectrum. In particular, the normalization can be either performed relatively to the integrated spectrum or to the maximum. Neither cases are fully satisfactory, and artifacts related to the exact acquisition rate (replica) can affect the result. Let us then simply mention that the ratio between the amplitudes of the 32 amu and 45 amu peaks can vary by 75% depending on the light ellipticity, where the 32 amu fragment is relatively maximized in linear polarization. Interestingly, the results suggest that the dependency does not linearly scale with $S_3$. However, the results analyzed so far are not reliable enough and one must stay cautious with them. If this variation was to be confirmed, it

could be related to the PEELD, since in particular the 32 amu and 45 amu masses take part in the photoelectron features in the 0.8-1.5 eV range.

The dependency to the field ellipticity of the electron kinetic energy spectrum (and possibly of the mass spectrum) can be interpreted as a variation of the ionization and fragmentation pathways. While the anisotropy of excitation in a randomly aligned sample can occur within a single pathway, the ionization of Methyl-Lactate at 515 nm turns out to show a particularly rich behavior as several processes are at play. The effect observed in the fragmentation can be caused by two things, as referenced above in this section. The first one is a dependency of the ionic state to the ellipticity, meaning that the weight of different molecular orbitals involved can vary. In this case, one can expect the transition dipoles to the excited states to be affected. The second one would be a direct orientation effect, since the fragmentation is sensitive to it, even from a single orbital, at least in the strong field regime [Fehre 19]. In both cases, this would be linked to the anisotropy of excitation at the origin of the PEELD.

Note that we have planed to investigate if the photoelectron distributions were sensitive to the associated fragment momentum. For instance in the dominant 45 amu mass, the large TOF distribution corresponds to the recoil of the fragments upon fragmentation. A decent statistics should be achievable even for subsets of the mass distribution, and this might unravel additional information about the anisotropy of the process.

### III. 4 Fragmentation Mechanisms

In order to more precisely determine the molecular effects involved in the present system, it can be interesting to assign the features presented so far, in particular the different fragments. The comparison between Methyl- and Ethyl-Lactate helps doing so. Fig. 3.28. shows the two mass spectrum obtained in the photoionization of these two species with a circularly polarized 515 nm field.

A summary of the main masses detected in Methyl-Lactate is given in Table 3.3. Note that a few false masses can appear (not highlighted in red), because of the laser shot replica discussed in the previous chapter. The Methyl-Lactate mass spectrum presented in Fig. 3.26 (a) will be used as a reference in the table, since this was the one corresponding to the coincidence measurements. Fig. 3.28 is just used for comparison between Methyl- and Ethyl-Lactate and fragment assignment, since they were not recorded in exactly the same jet conditions. A very small pollution of water is neglected, as well as the peaks corresponding to the $^{13}C$ isotopes.

| Mass (amu) | 15 | 19 | 31-32 | 32 | 45 | 61 | 89 | 96 | 102 | 104 |
|---|---|---|---|---|---|---|---|---|---|---|
| Peak Area (norm.) | 3% | / | 14% | 3% | 70% | 5% | 2% | 0.05% | 0.2% | 0.5% |

**Table 3.3** – *Area of the ionic species in the Methyl-Lactate mass spectrum of reference shown in 3.26 (a), ionized at 515 nm at an energy of 17 $\mu J$/pulse and a repetition rate of 166 kHz, in circular polarization. The target was carried by 1 bar of helium, and the nozzle was heated at 110°C. This corresponds to the measurements performed in coincidence presented.*

The fragmentation of Methyl-Lactate can be compared to a study found in the literature that determined several plausible fragmentation mechanism by electron impact [Tajima 95],

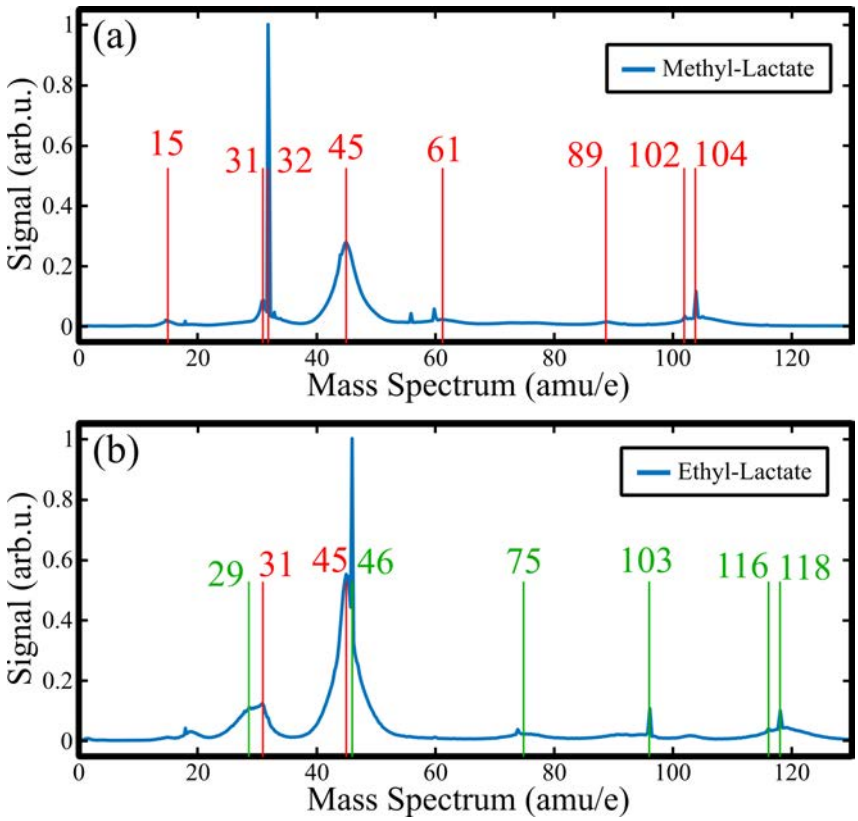


**Figure 3.28** – *Mass spectrum of (a) Methyl-Lactate and (b) Ethyl-Lactate, ionized with a circularly polarized 515 nm field. The laser conditions were (a) 10 µJ/pulse and 166 kHz repetition rate and (b) 4.2 µJ/pulse, 500 kHz. In both cases, the chiral molecules were carried by 2 bars of $N_2$, and the nozzle heated at 90°C. The masses found in ML (a) in the reference spectrum (3.26 (a)) are highlighted in red, and the other ones are false masses caused by the replica, or water (18 amu). The masses that also appear in EL (b) are in red, while the ones that are shifted relatively to ML are indicated in green.*

adapted in Fig. 3.29. The masses of the fragments measured in our case in Methyl-Lactate (in red in Fig. 3.28 (a)) are highlighted in bold. They were also found in Ethyl-Lactate (in red in Fig. 3.28 (b)), except for the shifted masses indicated by the mark 'EL' (in green in Fig. 3.28 (b)). The fragments at 19 amu, 45 amu and 89 amu are relatively simple to explain, while the one at 61 amu comes from a so-called McLaffertie rearrangement. This assignment is confirmed by the fact that the 61 amu mass appear at 75 amu in Ethyl-Lactate. The 32 amu mass corresponds to the detachment of the methanol group, since this peak is shifted to 46 amu in Ethyl-Lactate. The 31 amu mass probably comes from the deprotonation of the methanol group, while the 15 amu fragment is probably $CH_3^+$ and the one at 102 amu subsequent to a deprotonation of the parent molecule (104 amu) (respectively at 116 amu and 118 amu in Ethyl-Lactate). The only unexplained signal is at 96 amu but is only found in very small quantity. Interestingly, some fragments conserve the chirality of the parent molecule while others do not. This brings the perspective to carry out time-resolved pump-probe experiments, where the loss or the modification of the chirality would be tracked during the fragmentation process using a circular or elliptical probe pulse. Note that the degeneracy of the mass associated with some fragments, in particular at 15 amu and 89 amu, can be lifted by comparing the mass spectra with

the one of Ethyl-Lactate, even if the branching ratios are not necessarily equals. The 89 amu peak is completely shifted to 103 amu, meaning that the second mechanism in Fig. 3.29 would dominate over the first one. Nevertheless, the 15 amu peak does not appear in the Ethyl-Lactate mass spectrum but species are found at 29, indicating that the first mechanism actually appear but is likely to leave the charge on the ethyl or methyl fragment.

Note that complementary measurements of the Methyl-Lactate mass spectrum, performed on another beamline at other wavelengths, will be presented in the next section, in Fig. 3.38.

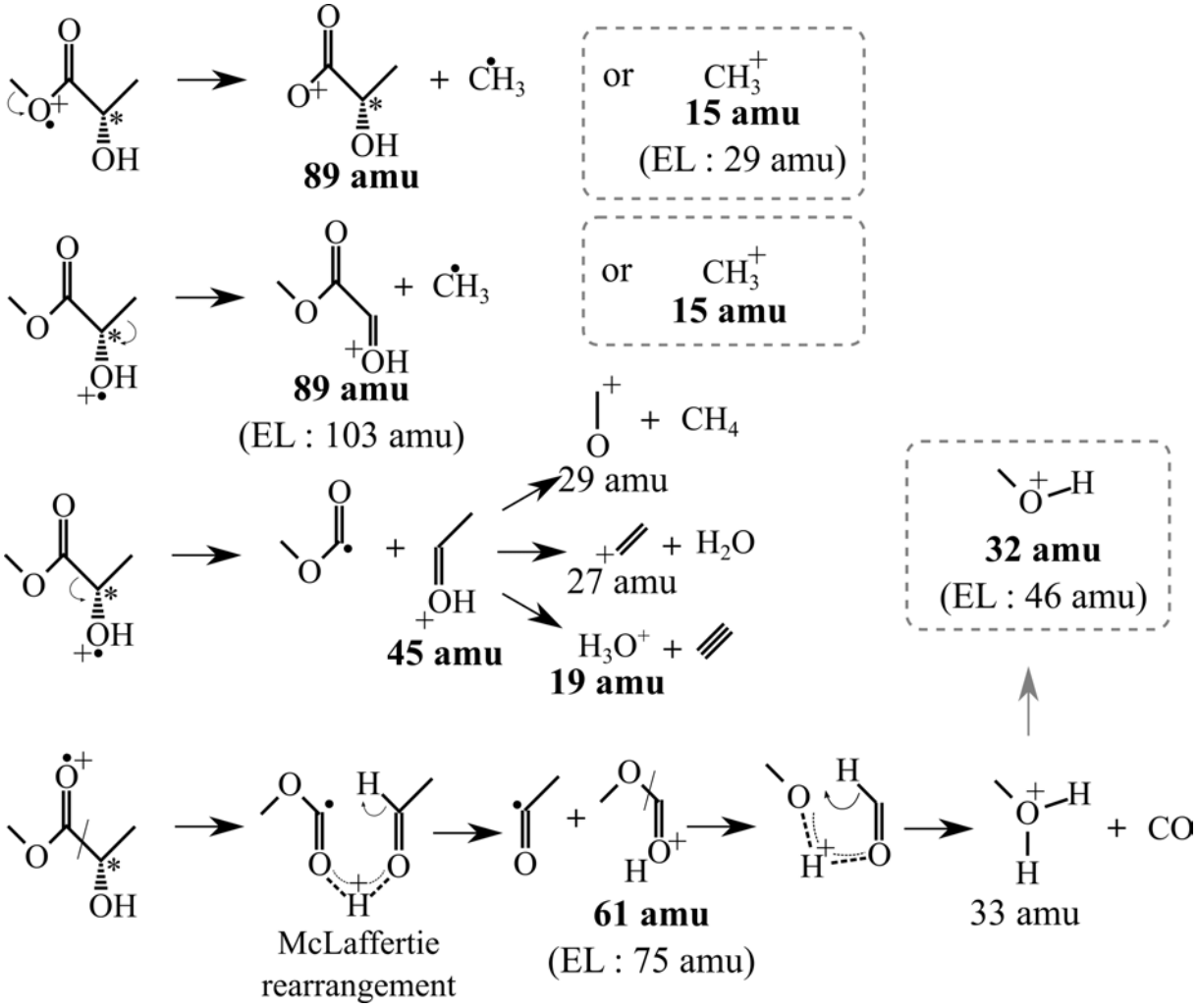


**Figure 3.29** – *Plausible fragmentation mechanisms of the Methyl-Lactate, adapted from [Tajima 95]. The masses indicated in bold are the one observed in our conditions. The mass shifts that are visible by replacing the methyl by an ethyl group (in Ethyl-Lactate, EL) are indicated.*

The fragmentation mechanisms in the ion continuum can be of great interest since they give a hint into the localization, or the orbital from which the photoelectron has been ionized. This can be compared, in particular, to theoretical calculations, as we will see in the following part.

### III. 5 TDDFT Calculations

In this context, the energy diagram of the molecule is also a central information. We had the chance to get it calculated by Nadia Ben Amor and Marie-Catherine Heitz from the Laboratoire de Chimie et Physique Quantique (Toulouse, France), and Bernard Pons from our group. The task is quite challenging in this molecule, especially since a good description of the Rydberg states requires many states in the basis to grasp the proper electronic overview in the 7-9 eV range, *i.e.* 3-1 eV below the $I_p$. Moreover this molecule does not have a high degree of symmetry, and the *ab initio* calculations are challenging in their assignment. Different levels of calculation have been compared, depending on the compromise between the number of and the precision on each one required. So far, the best results have been obtained using Time-Dependent Density Functional Theory (TDDFT), using the CAM-B3LYP functional, and two basis can be used depending on the needs. The first one is the Aug-cc-pVTZ, where the triple zeta provides a good description at a high computational cost. As a consequence, this basis is used to finely describe the excitations up to a certain energy, and the transitions beyond this point are missing. Up to 57 excited states can be calculated within a decent time (of the order of a few days or weeks) here. This means that the high-lying Rydberg states are partially missing. To overcome this issue, an alternative consists in using a Dunning-Hay VDZPD basis (valence double zeta, polarization and diffuse orbitals) for each atom, with a double basis of Rydberg 2s-2p-2d states and a f function centered on the center of mass of the cation. This choice is made in order to reduce the computational cost while still having a basis that should be suited for the remote Rydberg states, as up to 100 levels are calculated with this basis. The diagram of the calculated excited states obtained with the two basis is depicted in the upper panel of Fig. 3.30, where the $y$ axis is the one-photon oscillator strength. In the lower panel, the levels are convoluted with a Gaussian function of width 0.2 eV to reproduce the broadening of the lines. The one-photon absorption spectrum measured with the synchrotron source is also depicted for comparison and calibration of a small energy offset, which is typical in DFT calculation.

One can see from the figure that the triple zeta calculations are in remarkably good agreement with the synchrotron reference. In particular, the three main peaks are quantitatively reproduced. However, an additional peak is found a 6.9 eV and some levels are obviously lacking above 10 eV. The results from the double zeta also looks in good agreement at high energy, but do not match below 8.5 eV. Nevertheless, they reproduce more accurately the high-energy end of the spectrum.

The TDDFT calculations also provide the structures of the excited states at play in the different REMPI schemes, and in particular the nature of the transition and the localization of the wavefunction [Harvey 14, Derbali 19]. To illustrate the idea, the isodensity surfaces of the electron density of the HOMO, HOMO-1 and HOMO-2 are depicted in Fig. 3.31. The orbital energies calculated are respectively -9.43 eV, -9.98 eV and -10.69 eV. The vertical ionization potential, obtained from the energy difference between the neutral and cationic fundamental states at the equilibrium geometry of the neutral, were calculated for the HOMO at 10.51 eV and the HOMO-1 at 10.67 eV, in relatively good agreement with the 10.29 eV measured experimentally. This study is still in progress, but we aims at establishing the correlation between

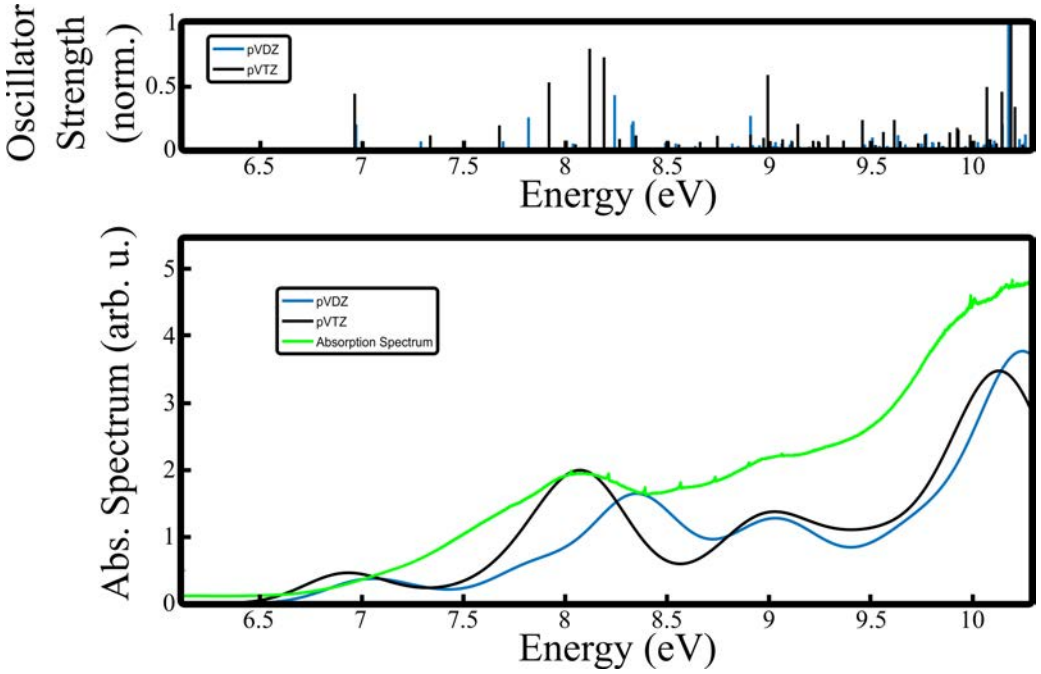


**Figure 3.30** – *(Upper panel) Diagram of the excited states of Methyl-Lactate obtained with TDDFT calculations up to the ionization threshold at 10.29 eV, where the y axis is the one-photon oscillator strength. The blue lines are obtained with the double zeta basis and the black lines with the triple zeta basis. (Lower panel) Convolution of the levels calculated with a Gaussian of width 0.2 eV. The one-photon absorption spectrum measured with a synchrotron source is also depicted for comparison. Note that the double zeta curve is shifted by +50 meV and the one of the triple zeta by -50 meV to match the synchrotron calibration at best.*

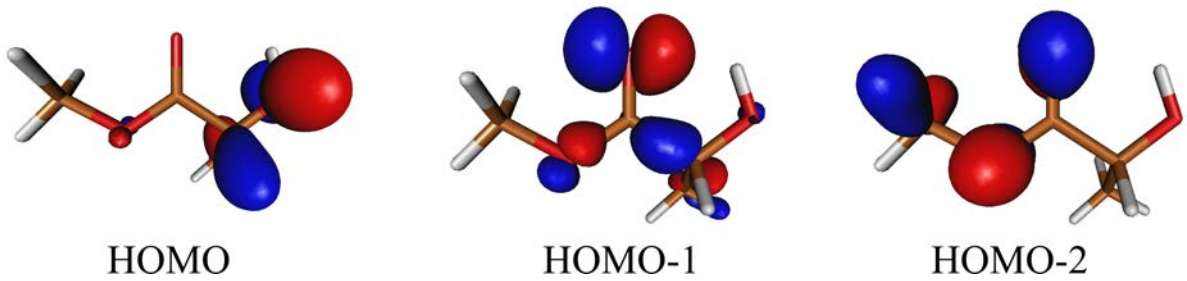


**Figure 3.31** – *Isodensity surfaces of the electron density of the HOMO, HOMO-1 and HOMO-2, calculated using TDDFT in Methyl-Lactate.*

fragmentation mechanisms to the excitation. For instance, the charge creation on the -OH group at the origin of the 89 amu, 45 amu and 19 amu fragments (second and third rows in Fig. 3.29) are likely to originate from the ionization of the HOMO. Conversely, the first row yielding a 89 amu mass would be more related to the HOMO-2. In the same fashion, the ionization of the carbonyl oxygen and the bond breaking that initiate the McLaffertie rearrangement (last row) would be due to the electron removal in the HOMO-1. This is a simplistic vision, and the transitions often involve several states in various proportion, but this information could be potentially accessible from the inversion of the branching ratios detected in photoelectron kinetic energy spectrum in coincidence with the fragments.

We will see in the next section that these calculations are also at the basis of cutting-edge

modeling of the time-resolved response of the excited wavepacket.

### III. 6 Perspectives

The COLTRIMS device coupled with the table-top high repetition rate source has been developed in order to go beyond the limitations of the VMI spectrometer. The elements presented in this section were the first implementation of the COLTRIMS that had an interest beyond purely technical purposes, and used both the photoelectron 3D angular resolution and the coincidence capacity. We have demonstrated that although the full capacities are not yet available at the same time, each of them individually works, and the objective to combine them seems at reach. At the moment, one can already state that the underlying molecular effects involved in the photoelectron elliptical dichroism leave traces in both the photoelectron and the photoion signals, even if this study is still under progress. In this perspective, new molecular systems have been characterized from scratch and showed interesting effects.

The initial goal was the time-resolved study of the dissociation of heterodimers of chiral species. In addition to the challenging acquisition time that it will require, we did not manage to produce a significant dimer signal so far, and this can be due to two reasons. The first one is that the molecular jet conditions were not suited for their production. The second possibility is that we actually produced dimers, but the high disposition of the system to fragment breaks almost all of them before detection at the total energy investigated. The main solution would be to get a tunable UV source to reach a total energy lying above the $I_p$ of the complex but below the $I_p$ of the respective fragments. This dissociation is however not necessarily prohibitive, and we have planned to try with smoother ionization conditions, for example in single-photon processes from the HHG source. From the presented study, it also turns out that the concept could be transposed to the fragmentation of the monomer into chiral of achiral fragments. The easiest way would be to perform the ionization on some neutral fragment, if the fragmentation can occur from a pump pulse below ionization threshold. Conversely, double ionization schemes could also be of interest, but more challenging.

## IV Time-Resolved PhotoElectron Circular Dichroism

The resonance-enhanced multiphoton ionization of molecules presented in this chapter is particularly suited for time-resolved studies. In particular, the electronic dynamics of the excited intermediate states can be investigated by the well-known pump-probe scheme, where the excitation and the ionization steps are decoupled and performed by different laser pulses.

**Circular Pump - Linear Probe : TR-PXECD**

On the one hand, one can use a circularly polarized pump photon and a linear probe. The dichroic effect involved is the photoexcitation-induced photoelectron circular dichroism (PXECD), as already mentioned in the introduction of this chapter, and depicted in Fig. 3.4. In this study [Beaulieu 18b], our group has shown that in the [1+1'] ionization of Fenchone and Camphor with a pump around 200 nm and a 405 nm probe, the dynamical evolution of the

dichroic part of the signal could give informations complementary to the PES. Fig. 3.32 shows the total signal (zeroth order), first order $b_1$ and third order $b_3$ coefficients of the decomposition of the angular distributions on a basis of Legendre polynomials, for (+)-Fenchone excited at 201 nm and (+)-Camphor excited at 202 nm and 200 nm, as a function of the pump-probe delay and the photoelectron energy. Note that the definition of the decomposition is given in Eq. 3.1 and that the aspect of the first and third orders are displayed in Fig. 3.2 (b). In Fenchone (left column), the exponential decrease of the PES, fitted with a time constant of 3.3 ps, simply describes the vibronic relaxation of the excited states towards lower states. Conversely, the dynamics of the dichroic signal occurs over a few hundreds of femtoseconds, and reveals the decoherence of the excited wavepacket. In addition, $b_1$ shows a smooth decay in the low energy region while an oscillatory behavior is found in the higher energies. The opposite can be found in the $b_3$. This time-dependent and electron-energy-dependent behavior has been attributed to be characteristic of internal vibrational torsional motion and may indicate the change of the chiral structure of the molecule induced by such motion. In Camphor (center and right columns), the PES dynamics is quite similar, while the one of the PXECD is drastically shorter despite a similar Rydberg state lifetime. This shows that this latter effect is very sensitive to the exact structure of the molecule. Finally, varying the excitation wavelength from 202 nm to 200 nm also modifies the dichroic dynamics, showing that this observable is very sensitive, in this example to the vibrational excitation. Further discussion can be found in the paper. Broadly speaking, this example illustrates the enhanced sensitivity provided by the angle-resolved photoelectron spectra, in particular in the dichroic response in chiral molecules.

**Linear Pump - Circular Probe : Excited-State TR-PECD**

On the other hand, the pump pulse can remain linear, and thus not induce any dichroic interaction. The excited wavepacket can then be ionized using a circularly polarized probe, in order to isolate the PECD from the excited state. This type of study has already been performed in our group [Comby 16], again without my personal contribution, in a similar [1+1'] scheme in Fenchone. The linearly polarized pump centered around 201 nm (6.17 eV) performed the excitation to the 3s Rydberg state while the circular probe at 403 nm performed the ionization with a single photon, as schematized in Fig. 3.33 (a). Firstly, the pump pulse can not initiate any dichroic interaction here, yet a significant PECD has been measured. This showed that PECD can originate from such a loosely bounded state, whose electronic density is depicted in the figure. In particular, it is very similar in sign and amplitude to the one from the one-photon ionization from the HOMO using VUV photons [Nahon 16]. Secondly, the evolution of both the PES and PECD could be tracked independently and occurred typically over a few ps, as shown in Fig. 3.33 (b).

Even if the distribution does not have a cylindrical symmetry, indicated by the tilde over the quantities, the decomposition on a basis of Legendre polynomials has been performed to quantitatively monitor the pump-probe delay dependency. Their temporal evolution is depicted in Fig. 3.34 (a) and (b), and the time constants extracted from the exponential fits are given in the panel (c). Interestingly, not all the coefficients show the same dynamics. Simply put, the 3.28 ps decay of the total ionization yield ($\widetilde{B}_0$) reflects the lifetime of the 3s Rydberg state

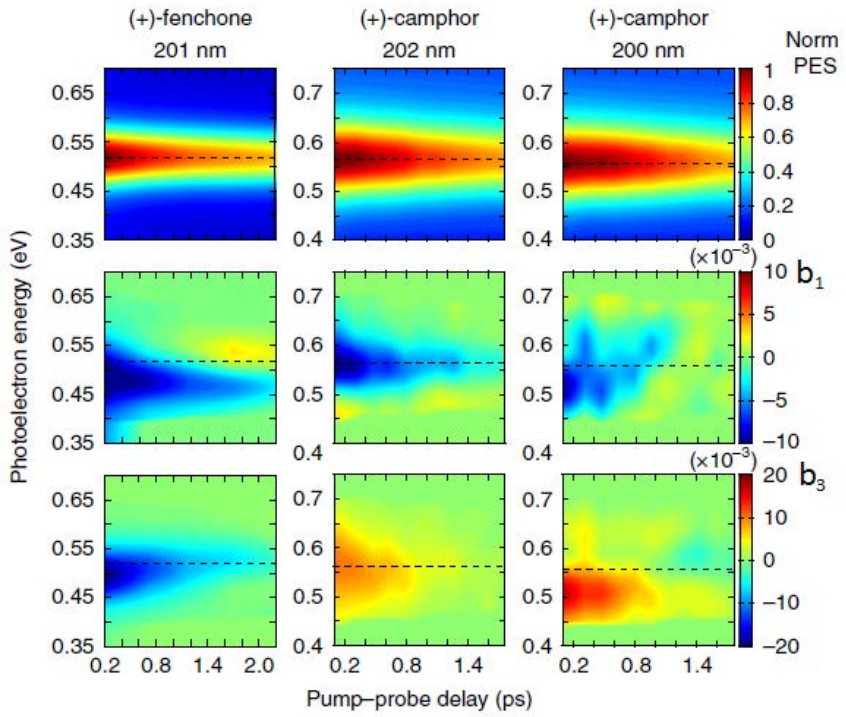


**Figure 3.32** – *Evolution of the PES and PXECD Legendre coefficients as a function of the pump–probe delay and the photoelectron kinetic energy, in (+)-Fenchone with a 201 nm pump, and in (+)-Camphor with a 202 nm pump or with a 200 nm pump. The black dotted lines represent the kinetic energy of the photoelectron corresponding to the maximum of PES. The decay times of the main PES component are 3.28±0.05 and 2.36±0.07 ps for Fenchone and Camphor, respectively. Extracted from [Beaulieu 18b].*

and its decay through internal conversion processes to lower valence states. The evolution of $\widetilde{b}_1$ is driven by the Rydberg-continuum transition dipole, while $\widetilde{b}_2$ and $\widetilde{b}_3$ are sensitive to the anisotropy of excitation induced by the linearly polarized pump. The faster decay time of these latter has been interpreted as a signature of the loss of anisotropy due to the rotational motion of the molecules [Blokhin 03], and supported by calculations.

Finally, a 400 fs transient can be noticed on the rising edge of $\widetilde{b}_1$. It has been interpreted as a signature of the intramolecular vibrational relaxation. In the early stage after the excitation, the redistribution of the population into the vibrational states of the 3s Rydberg state, each of them potentially having a different dichroic response, would blur the averaged signal and lead to this decrease. As only some of them can relax efficiently, the recovery of the $\widetilde{b}_1$ amplitude corresponds to the survival of a few states only with a high sensitivity to the overall chirality of the molecule.

**Temporal Resolution**

The two studies presented above were carried out with the Ti:Sa laser source Aurore at CELIA operating at 1 kHz, and the detector used was the VMI presented in the previous chapter. The pulse duration was of the order of 75 fs, enabling a sub-100 fs dynamical resolution. This was enough for the processes described, but remains restrictive for faster processes. Indeed, since PECD is a powerful and sensitive probe of molecular chirality, we anticipate the ultrafast

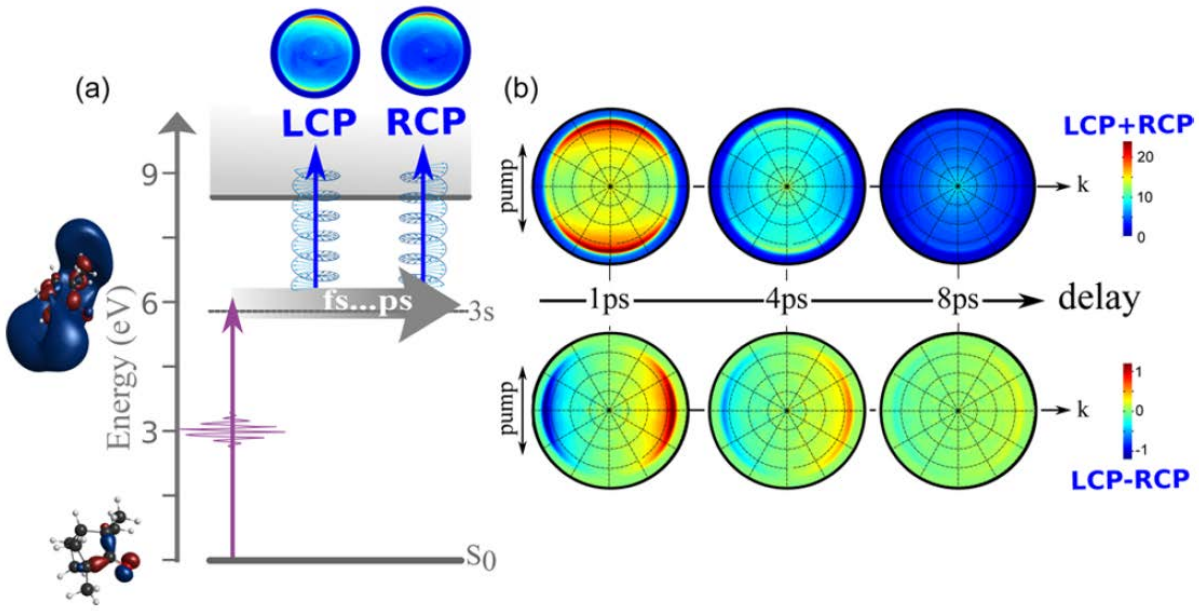


**Figure 3.33** – *(a) Schematic of the excitation scheme used to measure time-resolved PECD from the 3s Rydberg state of Fenchone. The HOMO and the 3s orbitals are drawn to illustrate the difference in the initial wave function of the outgoing electron. (b) The photoelectron images recorded in (-)-Fenchone. Each probe helicity are subtracted one from the other to extract the unnormalized odd Legendre polynomial coefficients, while the sum of these images provides the photoelectron spectrum (PES). Extracted from [Comby 16].*

resolution of chiral dynamics to bring additional informations at the few femtosecond timescale, which remains unexplored so far. Our new fiber laser system does not help in this way, since its pulse duration is even longer, about 135 fs. For this reason, we found interesting to initiate a collaboration with a group disposing of a much shorter source. This section presents the preliminary results obtained from an experiment I performed with Vincent Wanie, Erik Månsson and Andrea Trabattoni, directed by Francesca Calegari at the Deutsches Elektronen-Synchrotron (DESY) in Hamburg, Germany.

## IV. 1 Few-Optical Cycle UV-IR Beamline

### Overview of the Beamline

The beamline in Hamburg at which the Time-Resolved PECD experiment was conducted has been newly built and specifically designed for few-femtoseconds and attosecond experiments, and is described in [Galli 19]. The commercial source (Coherent) is a Ti:Sa laser delivering 20 fs pulses at 800 nm, at a repetition rate of 1 kHz and an energy of 10 mJ/pulse after a double stage amplification. It is also CEP-stable. The pulses are compressed in a 1 meter-long hollow-core fiber postcompression stage, filled with argon ($\sim$ 0.15 mbar). The spectrum can be broaden up to 500-1000 nm, for a duration of 4-5 fs at an energy of 2.5 mJ/pulse (from 6 mJ/pulse). The beam is then sent under vacuum for the rest of the beamline in order to remain optimally compressed. This defines a high standard in terms of automation and remote control of the setup. The beam can then be split into three arms. In the first one, it is kept as is, while the second one can be used to perform high-order harmonics generation in the XUV range. Noticeably, the last

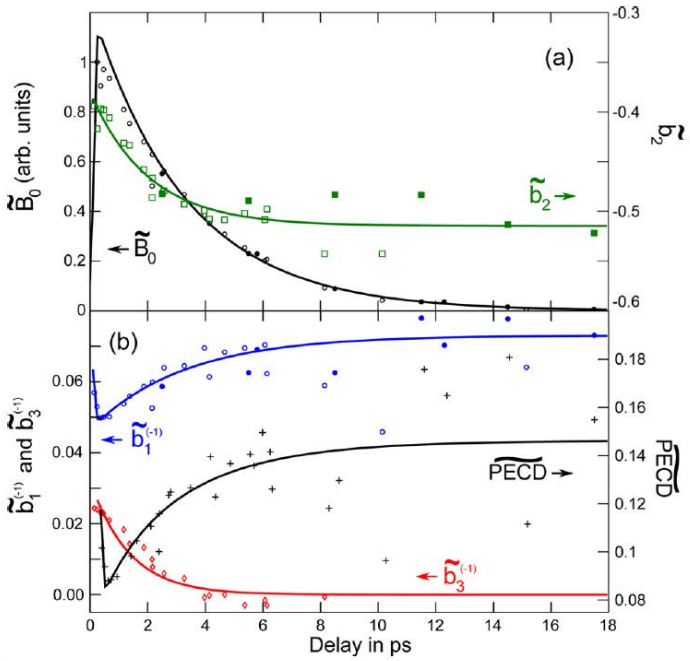


(c)

| observable | time constant (ps) | converging value of the $\tilde{b}_i^{(-1)}$ fit at long delay |
|---|---|---|
| $\tilde{B}_0$ | 3.28 ± 0.05 | 0 |
| $\tilde{b}_1^{(-1)}$ | 3.25 ± 0.5 | 0.073 ± 0.017 |
| $\tilde{b}_2$ | 2.0 ± 0.3 | – |
| $\tilde{b}_3^{(-1)}$ | 1.4 ± 0.3 | 0 |

[a]The uncertainties correspond to 50% confidence bounds.

**Figure 3.34** – *Temporal evolution of the Legendre polynomials coefficients extracted from the measurement on (−)-Fenchone (empty markers) and (+)-Fenchone (filled markers, with a sign inversion). (a) Even orders, corresponding to the PES. (b) Odd orders, corresponding to the PECD. Note that when the population in the 3s state starts to be less than 10% (delay ≥ 7 ps), the normalization by a small $\tilde{B}_0$ increases the dispersion of the normalized coefficients. (c) Table of the time constants extracted from the exponential fit of the coefficients evolution. Adapted from [Comby 16].*

arm is used to perform third harmonic generation in rare gas (argon here, at 1 bar) in a glass cell. The material of the cell has been chosen for its high ablation threshold. It is placed in a differential pumping stage, so that the residual pressure in the rest of the beamline remains low, and the gas can be collected and reused. This THG stage has been designed in order to keep the duration very short and avoid propagation through a dense medium. As a result, the 266 nm pulses produced can have a duration in the sub-2 fs range (2-3 optical cycles). The energy in optimal conditions is about 215 nJ/pulse at the source and 150 nJ/pulse on target. The arms are then recombined in a slightly non-collinear geometry in the detection apparatus to perform pump-probe experiments. This latter consists in a VMI for the electrons, while the other side is made of a deflectron in order to measure the ion mass spectrum with a high resolution $\frac{\Delta m}{m}$ for heavy masses. Note that their VMI has a more complex field geometry than ours, especially because it must be adapted to the drilled repeller plate used for the ion detection. The photoelectron/photoion detector has been designed to perform covariance measurements, even if this capacity has not been fully implemented yet. An XUV spectrometer is also placed

at the end of the beamline for high-order harmonics spectroscopy experiments. A scheme of the setup is presented in Fig. 3.35. Note that the system is also designed for a high stability, in particular relatively to the vibrations and the delay drift.

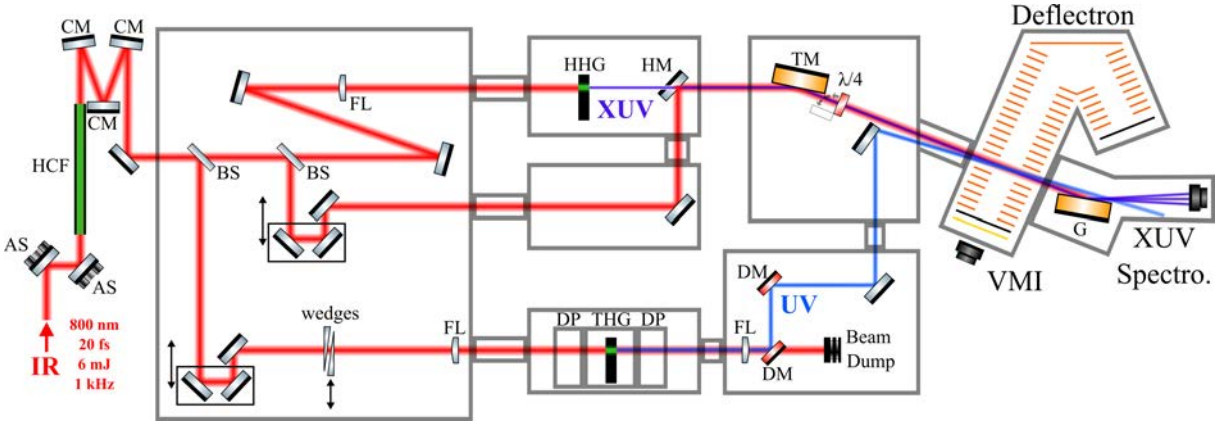


**Figure 3.35** – *Simplified scheme of the ultrashort IR-UV-XUV beamline used in our collaboration in Hamburg. AS = active stabilization, HCF = hollow-core fiber, CM = chirped mirror, BS = beamsplitter, FL = focusing lens, TM = toroidal mirror, DP = differential pumping, DM = dichroic mirror, G = grating.*

Originally, this beamline has been developed in order to provide multiple pump-probe schemes in the IR, UV and XUV range. The main novelty lies in the generation of the few-optical cycle UV wavelength, which is of particular interest for the study of biologically-relevant molecules as many of them present excited states in this range. While pulse duration should enable the resolution of ultrafast processes, such as charge migration, the repetition rate prevents the coincidence measurement. This typically illustrates the compromises that have to be made in the current state of the laser science and technology, and in this case the covariance measurements was preferred. This beamline is thus very complementary to the one developed at CELIA in Bordeaux.

**Experimental Scheme and Characterization of the Pulses**

The third harmonics generated is centered at 260 nm and, given its bandwidth, overlaps spectrally with the fourth harmonics of our ytterbium laser at 257 nm. In this sense, an excitation of a molecular system with a two-photon transition of the THG (centered at 9.3 eV) would end in the same energy region as a four-photon absorption of the 515 nm photons (9.6 eV), with a broader spectral bandwidth. We have thus chosen Methyl-Lactate as a chiral target, since this energy lies in the Rydberg states manifold just below the ionization threshold, as characterized in the previous section. In addition, this can potentially provide a point of comparison between different REMPI schemes with different wavelengths and bandwidths but similar central energy, which is inaccessible in Bordeaux so far as the fourth harmonic of the 1030 nm still remains challenging to couple in the COLTRIMS.

We then use a [2+1'] REMPI scheme with wavelengths respectively centered at 260 nm and 700 nm, as schematized in Fig. 3.36 (a). Problematically for PECD studies, the frequency conversion process in the THG is only efficient in linear polarization because of the central

symmetry of the medium. Moreover, with such a duration, we could not insert a quarter waveplate in the UV beam. The only arm for which the polarization can be modulated is thus the infrared one. In this case, the dispersion induced by the waveplate is pre-compensated in the chirped mirrors of the postcompression, which is not possible in the UV arm since this would decrease the THG efficiency.

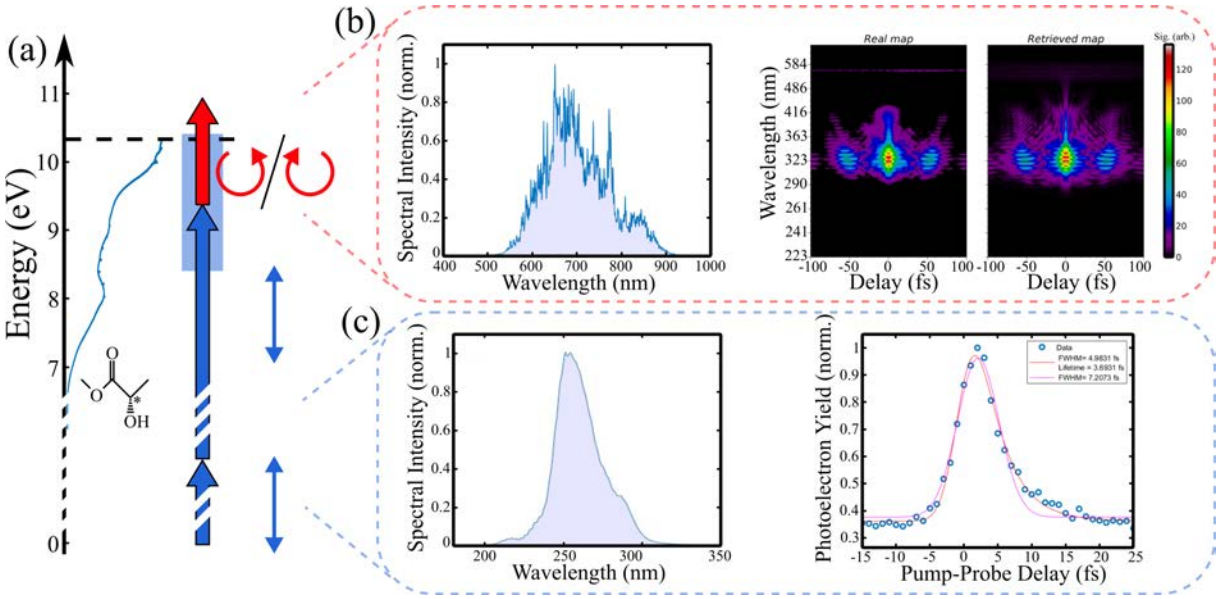


**Figure 3.36** – *(a) Pump-probe scheme used in the TR-PECD experiment, in Methyl-Lacate. The absorption spectrum is depicted along the energy axis, and the blue shaded area represents the two-photon spectral width of the pump only. We see that some photoelectron background can be expected at low kinetic energy from the pump alone. (b) Characterization of the probe pulse centered at 700 nm, with the spectrum (left) and its SHG-FROG trace (right), retrieving a duration of 5.7 fs FWHM. (c) Characterization of the pump pulse, with the spectrum (left) and the cross-correlation trace recorded by photoionization of krypton. Its fit yields a 9.5-13 fs UV pulse duration.*

The spectra of the 700 nm and 260 nm beams is presented in the panels (b) and (c) of Fig. 3.36, as well as the corresponding pulse duration measurement. In the first case, it has been directly retrieved using a SHG-FROG device. The duration of the pump has been estimated from a cross-correlation ionization trace with the probe pulse in krypton, where the trace has been fitted with a function :

$$Ae^{\frac{-(t-t_0)^2}{2\sigma^2}} + B\left[1 + erf(\frac{t-t_0}{\sqrt{2}\sigma} - \frac{\sigma}{\sqrt{2}\tau})\right] e^{\frac{-(t-t_0)}{\tau}} + y_0 \tag{3.18}$$

where the first term accounts for the pulses durations and the second for potentially excited states of krypton, of lifetime $\tau$. From the number of photons involved $n_{IR} = 3$ and $n_{UV} = 2$, the measurement of $\sigma$ from the cross correlation and the knowledge of the duration of the IR pulse $\sigma_{IR}$, one can retrieve the UV duration $\sigma_{UV}$ with :

$$\sigma^2 = \sqrt{\frac{\sigma_{IR}^2}{n_{IR}} + \frac{\sigma_{UV}^2}{n_{UV}}} \tag{3.19}$$

At the end, the IR pulse FWHM is estimated to be 5.7 fs (for a Fourier limited duration

of 4.3 fs), with small pre- or post-pulses at 50 fs from the center (as visible in the FROG trace in Fig. 3.36 (b), with an amplitude of about 30%), that are relatively far enough to not play a role in the dynamics. The UV duration has been determined to be reasonably in the 9.5-13 fs range in our conditions, probably due to the fact that the conditions in which the conversion efficiency is the best are not necessarily exactly the one giving the shortest duration on target. In the [2+1'] scheme used, we can reasonably assume a sub-10 fs dynamical resolution.

The spectral support of the short pulses (9.4±1.0 eV for the excitation and 1.8±0.4 eV for the ionization) can be in fact problematic for the energy resolution of the processes. In particular, the tail of the UV spectrum can directly ionize the Methyl-Lactate ($I_p$ = 10.3 eV) without probe, inducing a background at low photoelectron kinetic energy. Moreover, a lot of states can be excited, inducing a complex dynamics. Finally, the bandwidth of the probe can also blur the resolution in the kinetic energy spectrum, and yield broad features instead of clearly defined ones.

## IV. 2 Characterization and Analysis of the Measurements

A pump-probe experiment is always more challenging than with a single-pulse, and one must maximize the part of the signal that actually comes from the desired REMPI scheme. In our case, the edge of the pump spectrum could directly ionize the molecule, leaving a constant background in the low photoelectron kinetic energy region. This part can be removed in the analysis, but it constituted a limitation of the dynamical range of the detector in order to avoid saturation by the localized background. Accounting in addition for the repetition rate of 1 kHz, the signal-to-noise ratio was a central concern in the experiment. A common way to improve it is to simply repeat the measurements several times $N$ and average the data, for a signal-to-noise ratio increasing as $\propto \sqrt{N}$. This can not be done infinitely, however, as the laser stability becomes an issue at some point. The analysis of the experimental data must then be performed carefully in order to assess the credibility of the observations, as proposed in this part.

**Pump-Probe Signal**

The best pump-probe conditions were found in an empirical manner, as the estimation of the pump intensity is quite hard because of the weak average power. The UV intensity was simply maximized (while keeping a stable spectrum), as we were not able to produce three-photon features from the pump only anyway. When doing this, the zero kinetic energy features indicated a decent two-photon excitation. The intensity of the probe pulse was more tricky to set, as we wanted a good pump-probe signal but avoid multiphoton absorption from the excited states a much as possible. We have thus performed a power scaling law to identify the regimes at reach. The data is fitted with a function $y = y_0 + Ax^n$ where $y_0$, $A$ and $n$ are adjusted, and the results are presented in Fig. 3.37. The fit performed up to high power presented in panel (a) shows a strong nonlinear evolution $n = 4.1$. This indicates the prevalence of the non-resonant [1+4'] process here. However, when focusing only on the low powers (panel (b)), the scaling $n = 1.6$ is much closer to the linear behavior expected for the desired [2+1'] scheme,

yet with the presence of the [2+2']. Even if the results presented are integrated over the whole photoelectron kinetic energy spectrum and could be energetically selected, the bandwidth of the pulses prevents from a complete disentanglement of the [2+1'] and [2+2'] processes. This issue will be discussed further in this section. Interestingly, in the case where the pump and probe do not overlap temporally (panel (c)), the non-resonant processes are eliminated and the yield scales with $n = 1.1$. This indeed indicates that part of the signal comes from cross-correlation effects while a non-negligible part comes from the actual [2+1'] pump-probe scheme we are interested in. Note that the [2+2'] process is not uninteresting by itself, but the features overlap renders the assignment of the processes more difficult.

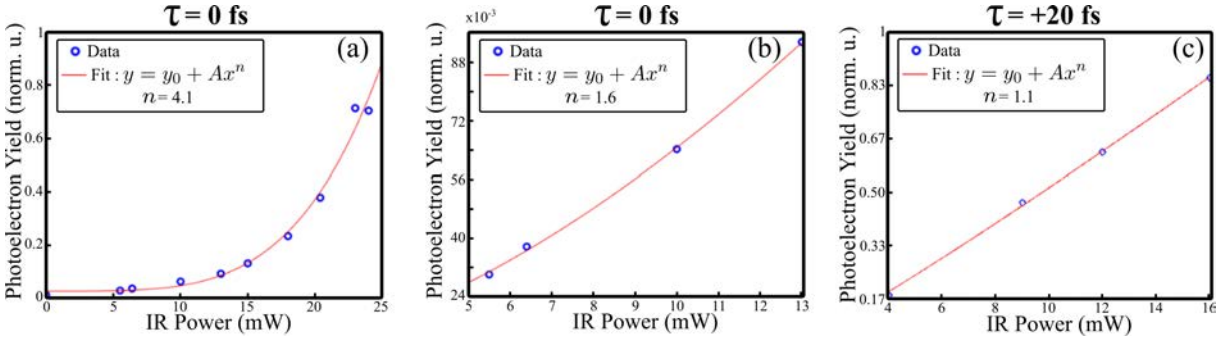


**Figure 3.37** – *Power scaling law of the IR probe in the 260 nm + 700 nm REMPI of Methyl-Lactate. (a) At pump-probe overlap on a wide power range, (b) At pump-probe overlap, at low power, (c) At pump probe delay of +20 fs, at low power.*

We thus chose the optimal IR power as 8 mW, corresponding to a 8 $\mu$J/pulse energy and a $1.9\times10^{12}$ W.cm$^{-2}$ power on target.

**Kinetic Energy Distribution and Mass Spectrum**

The mass spectrum obtained in Methyl-Lactate with a zero delay between the pump and the probe is presented in Fig. 3.38, and is compared to the one obtained in Bordeaux at 515 nm. Note that the jet conditions are completely different, but no dimers were found in any case. As will be discussed later, the pump-probe contrast is close to x2 in the Hamburg measurements. This means that about half of the ion signal comes from the ionization from the tail of the pump spectrum for a total energy of about 10.3 eV, and half of it from the [2+1'] process, for a total energy brought to the system centered around 11.3 eV. In comparison, the 5-photon absorption at 515 nm was at 12.0 eV.

Interestingly, most of the masses are common to the two cases, as indicated in green (15 amu, 18 amu, 19 amu, 33 amu, 45 amu, 61 amu, 76 amu, 89 amu, 102 amu and 104 amu for the parent molecule). These peaks have mostly been already discussed in the previous Section 3.III. This confirms that Methyl-Lactate is highly dissociative upon ionization. Two processes overlap in the Hamburg measurements, but importantly, the mass spectrum recorded with the pump alone is exactly the same. This indicates that the appearance of these fragments indeed occurs below the ionization threshold at 10.3 eV. This is confirmed by the fact that only a small fraction of the masses detected here are at 104 amu, *i.e.* the parent ion. In addition, half of the signal also comes from the [2+1'] REMPI and no additional fragments can be observed with the

probe at a total energy centered at 11.3 eV.

Contrarily, the peaks at 31 amu and 32 amu visible at 515 nm (in blue) do not appear in the Hamburg measurements, meaning that these fragments appear between 11.3 eV and 12.0 eV. Note that the two unassigned peaks at 56 amu and 59 amu on the blue curve do not appear in the reference spectra of Methyl-Lactate used in coincidence.

Interestingly, the mass resolution of the deflectron is greater than the one of the COLTRIMS, and enables to unveil small peaks, indicated in red (27 amu, 29 amu, 43 amu, 44 amu, 59 amu). They have probably not enough statistics to be studied in coincidence anyway, but this remains interesting since this is the first mass spectrum comparison in Methyl-Lactate. Note that the peaks measured by the deflectron are slightly asymmetric, so there is no species for instance at 46 amu.

We will not discuss the pump-probe delay dependency of the mass spectra extensively in this manuscript, as the analysis is not complete yet. Let us simply mention that the total photoion yield follows the one of the photoelectrons, and that the mass-dependent signal level is very small and is hardly reliable. We will thus focus on the photoelectron distributions for the rest of this section.

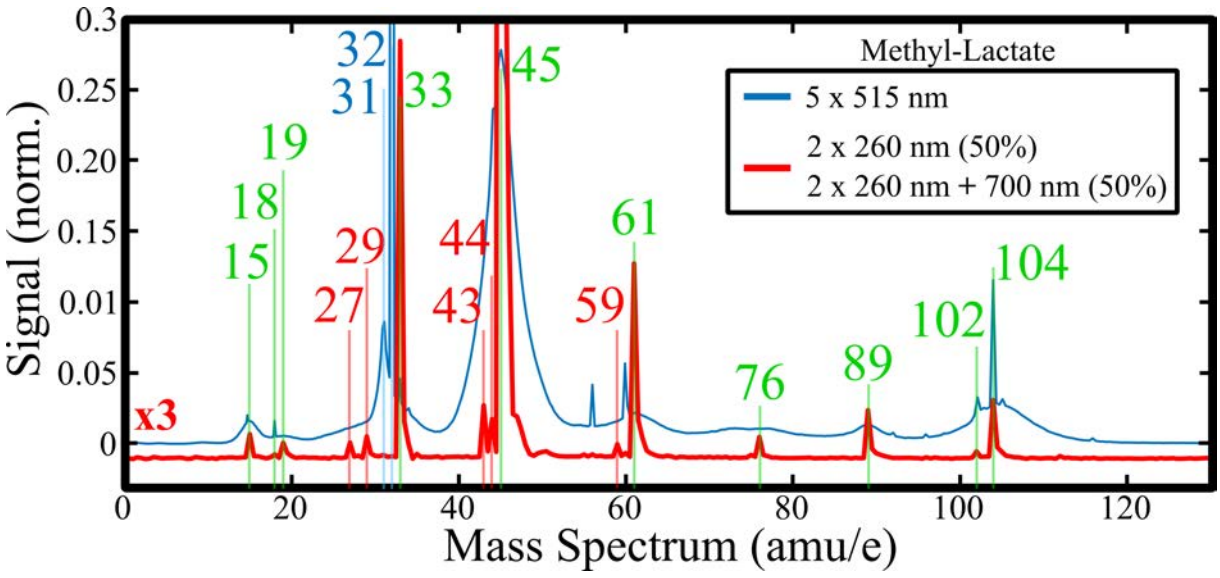


**Figure 3.38** – *Mass spectrum of Methyl-Lactate obtained in Hamburg at 260 nm + 700 nm (red) and in Bordeaux at 515 nm (blue). In the first case, 50% of the signal comes from the 2-photon ionization from the pump for a total energy around 10.3 eV, and 50% from the [2+1'] REMPI centered at 11.3 eV. In the second case, the ionization is performed with 5 photons, at 12.0 eV. The masses that match are indicated in green, the ones specific to the ionization at 12.0 eV in blue and the ones resolved only in Hamburg in red. Note that the mass resolution of the deflectron is greater than the one of the COLTRIMS. The maximum of the two curves are normalized to 1, and zoomed in the 0-0.3 region. The red curve is also multiplied by a factor of x3 and a -0.01 offset is applied to improve visibility.*

The corresponding photoelectron kinetic energy spectrum obtained in Methyl-Lactate with a zero delay between the pump and the probe is depicted in Fig. 3.39 (a). It is very monotonous and no peaks are visibly present. This illustrates the spectroscopic challenge of using such short pulses, as already discussed. The strong signal around zero kinetic energy comes from the

ionization from the probe alone. Additionally, most of the signal is within 1 eV. This is in good agreement with the [2+1'] process, where 11.3 eV are brought in a system with an ionization threshold of 10.3 eV, and its monotonic decrease is typical of a dissociative ionization.

**First Tests and Raw PECD**

The present experiment was the first real one on the new beamline in Hamburg, and thus involved an important work of characterization. Firstly, we had to make sure that the monotonic photoelectron kinetic energy distributions did not come from a issue with the VMI. The comparison between the VMI photoelectron distributions obtained using short pulses and 20 fs-long pulses that did not undergo the postcompression, in Fenchone and using the IR only at a high intensity to generate ATI peaks is presented in Fig. 3.39 (b) and (c). The ATI peaks are clearly defined with the long pulses, and the resolution of the VMI is thus not an issue. Note that the long pulses can be used for calibration and comparison of the PECD from a reference (not shown here). The broad features visible in the PECD measured with the short pulses can thus not be directly assigned, but ranges of kinetic energy can be defined. From this point, the results presented in the rest of the section were obtained with the short pulses.

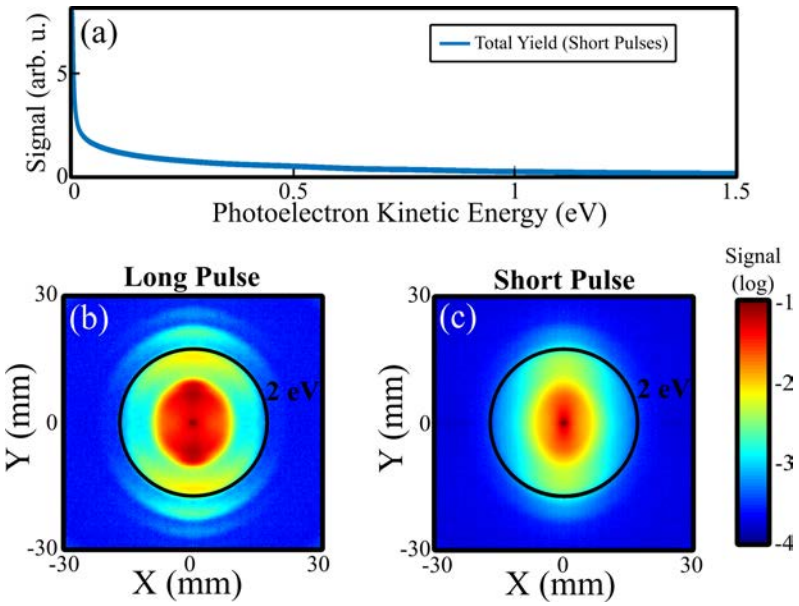


**Figure 3.39** – *(a) Photoelectron kinetic energy distribution acquired in Methyl-Lactate using short pulses, at the pump-probe overlap in the conditions indicated above. (b) VMI projections of the photoelectron distributions obtained in Fenchone using the IR pulses only, showing several ATI peaks. The left panel shows the case obtained with pulses of 20 fs (narrow spectrum, no postcompression) and the right one with 5.6 fs pulses. The IR power is 2.5 W for the long pulses and 1.6 W for the short ones, because of the losses in the postcompression. All the other parameters are the same.*

Secondly, we had to make sure that the PECD images obtained did not present experimental artifacts. In particular, we have noticed that the complex field configuration of this VMI induced a high sensitivity to the centering of the interaction volume in the spectrometer, which is not supposed to be the case in a simple VMI. The distortion induced could create a false PECD signal of several tens of percents and completely cover the actual dichoic signal. We could fully solve this issue by precisely positioning the VMI (with a precision of the order of 1 mm) with

respect to the laser focii by monitoring the symmetry of the distributions obtained in rare gas. Once this issue was fixed, the second milestone consisted in verifying that the PECD measured in Methyl-Lactate reverses with the enantiomer handedness, shown in Fig. 3.40. The PECD in this figure is calculated from the raw distributions, without performing the projection on a Legendre polynomial basis. It is obtained from the difference of the raw distributions obtained with a right circular polarization and a left circular polarization, forward/backward antisymmetrized. It is also normalized relatively to the PES pixel by pixel, and a threshold of 1.5% is used to cut the PECD that comes from a too weak PES. The results appears quite noisy and not structured, but the sign flip between the two enantiomers is clearly visible. In addition, the amplitude of the PECD found in the two cases is about 2.2-2.4%. Note the presence of a reproducible evolution of the central feature with the pump-probe delay, indicating a probable dynamics accessible.

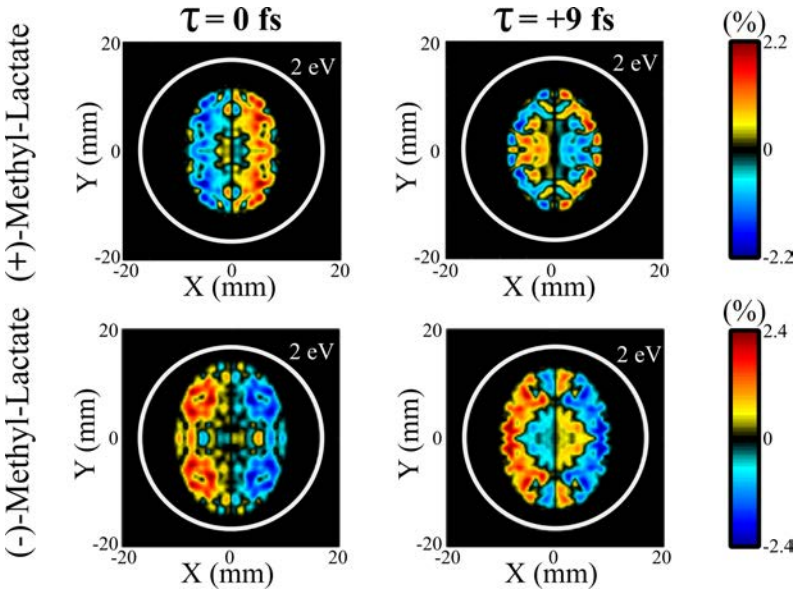


**Figure 3.40** – *Raw PECD figures measured in (+)- (upper row) and (-)-Methyl-Lactate (lower row), at a pump-probe delay $\tau$ of 0 fs (left column) and +9 fs (right column). The PECD is normalized here pixel by pixel to the PES and is cut at 1.5% of the PES. The horizontal axis is the laser propagation axis and the vertical one corresponds to the pump polarization.*

In order to more quantitatively describe the evolution of the PECD with respect to the pump-probe delay, further analysis of the raw PES and PECD distributions was performed, as we will see in the next paragraph.

**Analysis Scheme and Statistical Error**

For a given dataset acquired, the delays are scanned 22 times (denoted cycles here, 11 in the forward delay direction and 11 backwards) in order to enhance the signal-to-noise ratio. Instead of directly averaging them, we have chosen to perform a Student's statistical analysis in order to quantify the credibility of the observations, in which the level of noise was significant. For a quantitative analysis, the photoelectron angular distribution at each delay for each cycle undergo a projection on a basis of Legendre polynomials using the pBASEX algorithm discussed in the previous chapter. For this, the VMI projections are converted into polar coordinates and

the angular distribution of each momentum (or energy) radius is fitted by Legendre polynomials, up to the fourth order. The momentum range used was from 0.02 a.u. (5 meV) to 0.44 a.u. (2.6 eV) by steps of 5 $\times 10^{-3}$ a.u., and the convergence of the fit with respect to the number of polynomial orders has been checked. At this point, the data is relatively noisy and a slight 2D Gaussian filter is applied along the delay and energy dimensions ($\sigma = 1$ pixel in energy and time). This is justified by the fact that narrow energy structures should not appear because of the spectral width as mentioned above, and that features appearing at the scale of the delay steps can not be resolved anyway. A variable number of cycles (1 to 22) are then grouped into subsets of data (respectively 22 to 1), on which the statistical analysis is performed.

Similarly to what has been already presented in this chapter in Fig. 3.13, this procedure enables one to determine if the statistical error of the final averaged curve is the best with many noisy measurements of a few cleaner measurements (for a given total number of cycles), and determines the final best confidence interval. The evolution of the final error of the coefficient of the Legendre polynomials orders $b_0$, $2b_1/b_0$, $0.5b_3/b_0$ and the MPPECD $(2b_1 - 0.5b_3)/b_0$ as a function of the number of cycles in a subgroup (for a total of 22 cycles) is presented in Fig. 3.41. The Student's statistics used to obtain these curves can be understood as, on the one hand, the confidence decreases if too few subgroups are averaged and, on the other hand, if each subgroup is too noisy. It appears clear from it that the best statistical uncertainty is obtained by grouping the cycles 4-by-4 or 5-by-5 in 5 subgroups. Note that the error on $b_0$ (a) suffers less from the division into many subgroups as its signal-to-noise ratio is much higher than for the other parameters. Furthermore, this implies that the normalized quantities are not too much affected by the noise of the denominator. This procedure is used for the rest of the presented results to evaluate the errorbars of the observables $b_0$, $b_1$ and $b_2$.

## IV. 3 Experimental Results

### First Observations

The evolution of the measured $b_0$ and $b_1/b_0$ as a function of the pump probe delay, integrated over the kinetic energy, is presented in Fig. 3.42. The delay is scanned here from -20 fs to 61 fs with steps of 3 fs. The total yield ($b_0$, in panel (a)) shows a clear pump-probe signal with a contrast of x2, where the baseline is due to the tail of the pump spectrum (the probe can not ionize by itself). The rising edge is about 20 fs-long and after the pump-probe overlap, the signal decreases more slowly, with a time parameter of the order of several tens of femtoseconds. Clearly, we see here that the lifetime of the excited states of Methyl-Lactate around 9.3 eV is very short. In addition to this, an oscillatory component in the falling edge can be noticed and is relatively safely above the errorbars. This type of pump-probe signal is typical of cases where the pump performs the excitation and the probe ionizes the excited states whose lifetime is visible in the decay here.

The first order of the Legendre polynomials (panel (b)) also presents a rich behavior. At large negative delays (-20 fs), the PECD found is close to zero. This makes sense, as the pump is linearly polarized. Around the temporal overlap, the PECD increases to about +1%. After this transient, the dichroic signal changes sign to maximize about -1% around +20 fs.

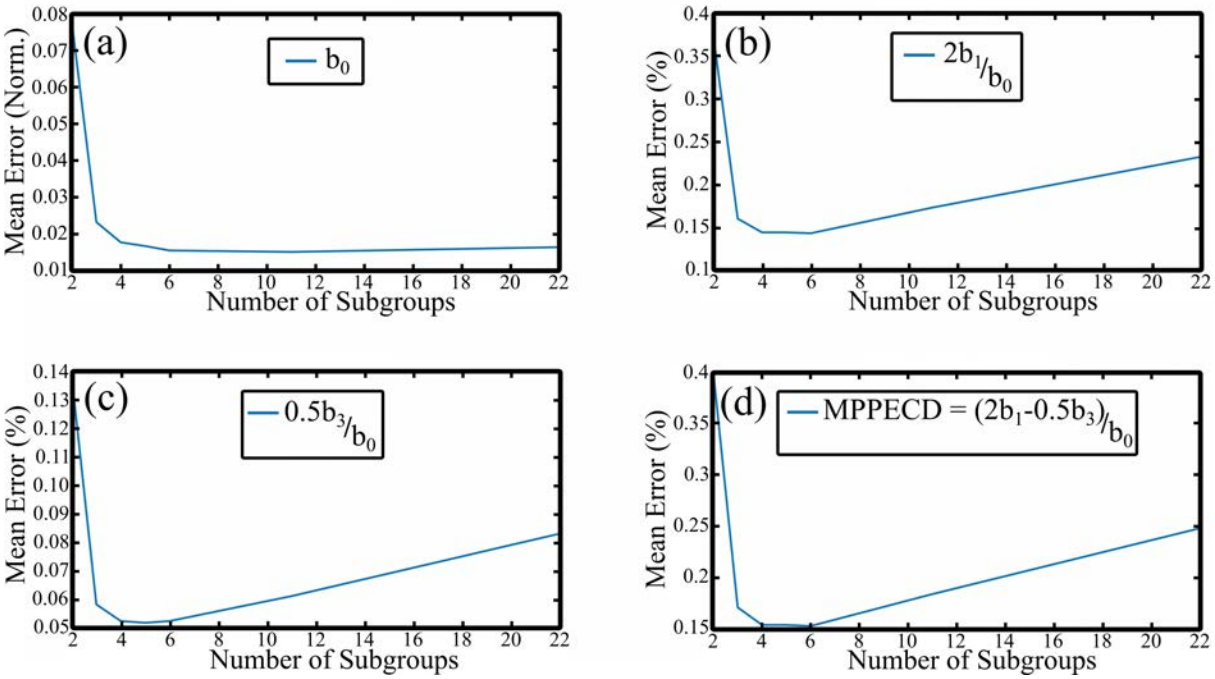


**Figure 3.41** – *Evolution of the final error of the coefficient of the Legendre polynomials orders $b_0$ (a), $2b_1/b_0$ (b), $0.5b_3/b_0$ (c) and the MPPECD $(2b_1 - 0.5b_3)/b_0$ (d) as a function of the number of cycles in a subgroup (for a total of 22 cycles). The errors here are averaged over the energy and the delays and calculated relatively to the final average of all the subgroups. Note that the percents in the panels (b), (c) and (d) are expressed relatively to $b_0$.*

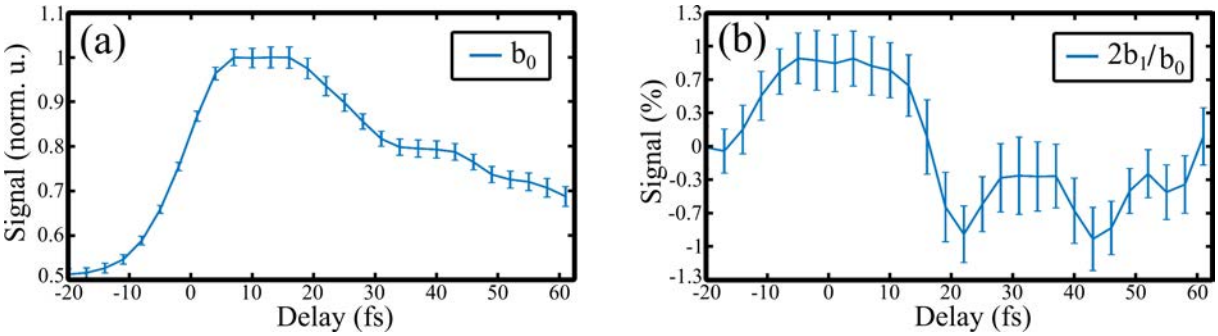


**Figure 3.42** – *Evolution of the kinetic energy-integrated $b_0$ and $b_1/b_0$ as a function of the pump probe delay. The errorbars indicated are estimated from the statistical analysis.*

Interestingly, $b_1$ also shows an oscillatory component from this point to the end of the scan at +61 fs. Importantly, these oscillations appear reasonably beyond the uncertainty.

### Fit and Extraction of the Components

Beyond the qualitative description of the features observed in both $b_0$ and $b_1$, a fitting procedure is performed to extract them more quantitatively. The fit function is the same as the one used in the cross-correlation measurement :

$$Ae^{\frac{-(t-t_0)^2}{2\sigma^2}} + B\left[1 + erf(\frac{t-t_0}{\sqrt{2}\sigma} - \frac{\sigma}{\sqrt{2}\tau})\right] e^{\frac{-(t-t_0)}{\tau}} + y_0 \tag{3.20}$$

and contains two terms. The first one is a Gaussian, describing the cross-correlation effects, *i.e.* possible non-resonant effects, of width $\sigma$. The second one, described by the error function (erf) and the exponential term accounts for the pump-probe signal from the excited states, with a lifetime $\tau$. It originates from the convolution of the Gaussian pulse profile (for the instantaneous probability of excitation) with the exponential decay of the states. The fit is performed to optimize the amplitudes $A$ and $B$, the baseline $y_0$, the width of the cross-correlation $\sigma$ and the decay $\tau$, and such for each polynomial order. The result is depicted in Fig. 3.43, for $b_0$ (a), $2b_1/b_0$ (b), $b_2$ (c) and the MPPECD (d). This latter is defined in Eq. 3.2 in the introduction of this chapter, and quantifies the number of electrons emitted forward compared to backward, normalized by the total yield.

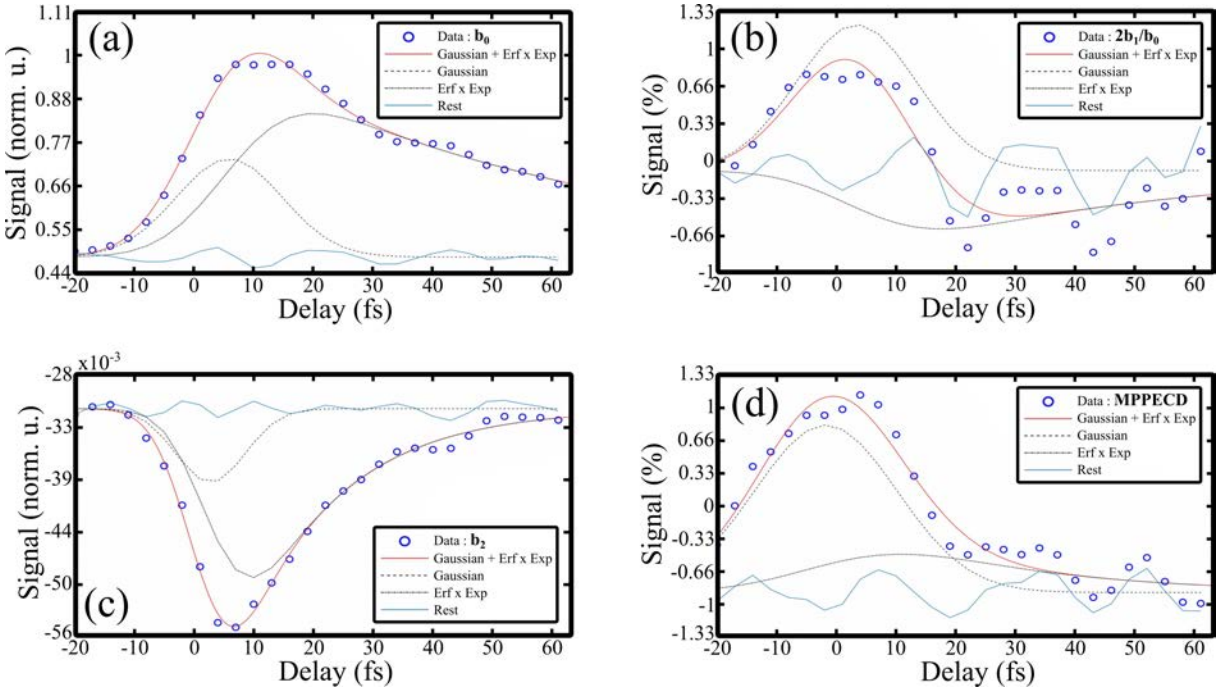


**Figure 3.43** – *Fit of the energy-integrated Legendre polynomials coefficients $b_0$ (a), $2b_1/b_0$ (b), $b_2$ (c) and the TRPECD (d), with the function of Eq. 3.18. In each panel, the data is indicated with the blue circles, the complete fit with the red line, the two terms in the fit are depicted in dotted line for information and the rest, in light blue, is the difference between the the experimental data and the fit. The normalization is performed relatively to the maximum value of $b_0$ in (a) and (c) and relatively to $b_0$ at each point in (b) and (d).*

In all the cases, the non-oscillatory components of the curves are nicely fitted by the function. The oscillatory part is isolated by subtracting the fit to the experimental data. The 0 fs reference of the delays is just an experimental approximation here. The fitted parameters are summarized in the Table 3.4. Note that the fit of the MPPECD suggests an irrelevant negative baseline, and one should be cautious with it.

We have not completely concluded the interpretation of these results so far, but several observations can be made. The narrower distribution found in $b_2$ (panel (c)) compared to $b_0$ (panel (a)) reflects the nonlinearity of the anisotropy of excitation. Alternatively, this could also be explained by the presence of higher nonlinear non-resonant processes at the temporal overlap. Also, the shorter decay parameter could be a sign of the loss of anisotropy. In any

| | $y_0$ (arb.u.) | A (arb.u.) | B (arb.u.) | $t_0$ (fs) | $\sigma$ (fs) | $\tau$ (fs) |
|---|---|---|---|---|---|---|
| $b_0$ | 875 ±18 | 451 ±47 | 455 ±31 | 5.9 ±0.7 | 8.9 ±0.5 | 58 ±6.0 |
| $2b_1/b_0$ | -0.5 ±1.5 | 7.8 ±1.8 | -2.4 ±1.9 | 3.4 ±1.9 | 10.1 ±2.1 | 45 ±63 |
| $b_2$ | -56 ±0.6 | -14 ±7.4 | -31 ±5.2 | 2.8 ±1.3 | 5.8 ±0.6 | 17 ±1.4 |
| MPPECD | -5.7 ±4.1 | 10 ±6 | 3 ±8 | -2.2 ±1.7 | 12.0 ±3.3 | 29 ±113 |

**Table 3.4** – *Overview of the parameters retrieved in the evolution of $b_0$, $2b_1/b_0$, $b_2$ and the $MPPECD = (2b_1 - 0.5b_3)/b_0$, fitted by the Eq. 3.20, as shown in Fig. 3.43. The errors given are the one sigma, i.e. 63% confidence.*

case, the fits present significant resonant and a non-resonant components. We have, in addition, measured that this latter increases in proportion at higher intensities, which is in agreement with the [1+4'] process suggested by the power scaling law at high intensity at the overlap. In the moderate field conditions used here, the relative contributions are balanced, and give a hint on the evolution found in $b_1$ (panel (b)). Indeed, the strong positive sign found at the temporal overlap can be associated with these non-resonant transitions, while the dichroic signal from the excited states, with a negative sign, prevails after the cross-correlation. The decay of the $b_1$ is also fitted as shorter than the one of the $b_0$ and could also indicate some underlying process.

One of the main interest of the procedure is, of course, the extraction of the oscillatory component, displayed in Fig. 3.44. We will focus on the $b_0$ and $b_1/b_0$ orders, but the results are qualitatively similar for $b_2$ and the MPPECD (repectively following $b_0$ and $b_1$). The two components oscillate with a $\approx$ 22 fs period. Its amplitude could follow the part of the fit corresponding to the resonant features, *i.e.* maximizing around 20-30 fs. The two curves oscillate almost perfectly in phase opposition, but importantly, the mirroring is not perfect, in such a way that a normalization artifact is unlikely to be at the origin of the $b_1/b_0$ oscillation. To the best of our knowledge, the observation of such femtosecond oscillations in the PECD has not been reported so far and their potential origin will be discussed in the next section.

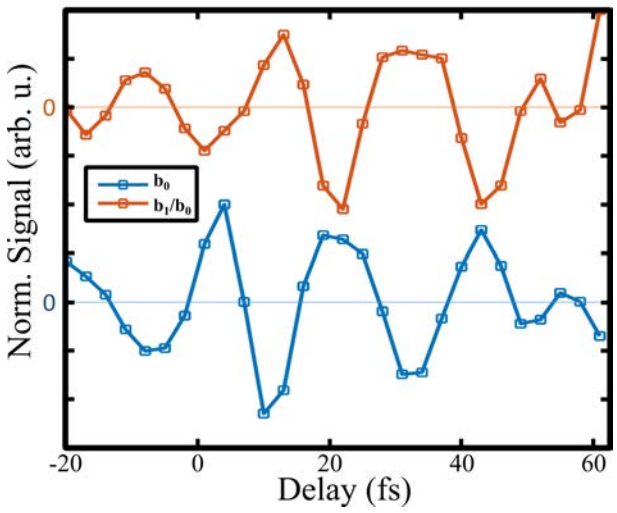


**Figure 3.44** – *Oscillatory components of $b_0$ and $b_1/b_0$, extracted from the fit presented in Fig. 3.43. The two curves are normalized and shifted vertically for a clearer comparison.*

**Kinetic Energy Dependency**

The results presented so far are averaged over the whole 0.05-2.6 eV kinetic energy range. As the PECD is known to be sensitive to the intermediate excited state, its resolution in energy would be of high interest. While the spectral ∼2 eV bandwith of the pump creates a wide wavepacket over the excited states, the ∼ 0.8 eV bandwidth of the probe broadens the features in the photoelectron spectrum. The photoelectron kinetic energy spectrum is thus completely unstructured. However, the different components of the spectrum can still preferentially originate from different states, located one probe photon below in energy. We will thus see in this paragraph a preliminary energy resolution of the PECD. As previously mentioned, the noise level in the experiment prevents from a fine energy resolution, and the spectrum can only be integrated over wide radius ranges. The delay-averaged photoelectron kinetic energy spectrum is presented in Fig. 3.45 (a), and is split into three areas of relatively similar integrated level of signal. The corresponding temporal evolution of the $b_0$ and $b_1/b_0$ parameters, for energies of 0-75 meV, 75-210 meV and 210-750 meV are depicted respectively in panel (b), (c) and (d). At first sight, it appears that the evolution in the 0-75 meV range mostly follows the one of the full radius-integrated quantities in Fig. 3.44, as expected since it is the largest contribution. The polynomial coefficients follow the same trend in the 210-750 meV region, namely presenting oscillations of about 22 fs in phase opposition. Surprisingly, the evolution in the 75-210 meV differs from the others. While the $b_1$ remains almost identical, the $b_1/b_0$ component oscillates this time in phase. Note that the effect does not come from a simple sign inversion, from an offset of the fitted baseline for example, but seems to be actual. Overall, the oscillation period remains similar. Interestingly enough, this observation suggests that the time-resolved measurement of the PECD yielded in chiral molecules at this timescale provides additional information compared to the time-resolved PES.

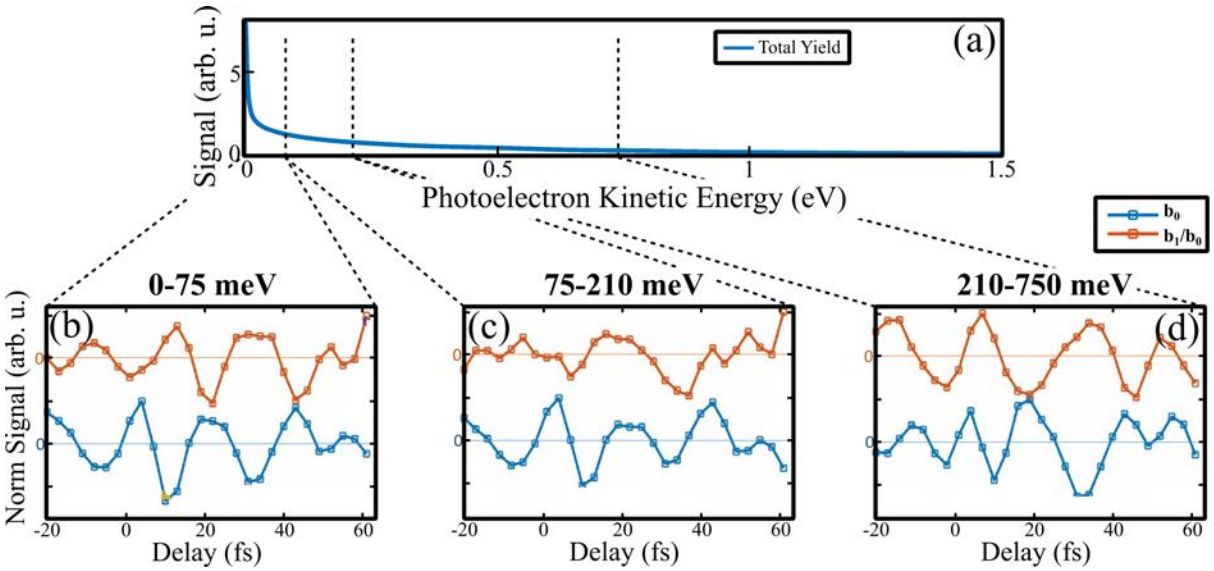


**Figure 3.45** – *(a) Delay-integrated photoelectron kinetic energy spectrum, obtained using short pulses. The corresponding temporal evolution of the $b_0$ and $b_1/b_0$ parameters, for energies of 0-75 meV, 75-210 meV and 210-750 meV is depicted respectively in panel (b), (c) and (d). In each panel, the two curves are normalized and shifted vertically for a clearer comparison.*

The choice of the energy ranges used is not completely fixed yet. The example taken here simply aims a showing that the relative phase of the oscillations between the different Legendre polynomials can be evolving along the kinetic energies. The substantial singularity of the intermediate energies is however relatively robust. This is also related to the question of the statistical error. The assessment of the errorbar is indeed crucial to determine what radial selection is affordable.

In the perspective of identifying the excited state involved, understanding the processes at play and determining relevant kinetic energy integration ranges, theoretical support can be of high interest.

### IV. 4 Interpretation and Theoretical Modeling

While the interpretation of the fitted curves in term of resonant and non-resonant contributions is relatively clear, the origin of the oscillations is more intricate. We have been investigating two interpretations so far. On the one hand, the $\sim$ 22 fs period could be associated with the C=O vibration. Its appearance in the PECD is plausible, since this observable is very sensitive to the molecular potential, but in this case its effect on the $b_0$ is not obvious. Generally, small changes in the molecular structure should not affect the total yield significantly, except in specific cases such as the presence of a shape resonance [Piancastelli 99]. This case would be very interesting and fortunate, yet quite unlikely to apply. On the other hand, the oscillatory behavior could be explained straightforwardly by quantum beats between several electronic excited states, whose energy difference would match 22 fs ($\approx$ 200 meV). This type of effect is quite clear in the case of simple systems where only a few states are involved, but in such a molecule, the density of state is quite large and the oscillations are likely to be blurred. In order to answer this question, advanced theoretical modeling is currently being developed by Nadia Ben Amor and Marie-Catherine Heitz from the Laboratoire de Chimie et Physique Quantique (Toulouse, France) and Bernard Pons from our group. The TDDFT calculations presented at the end of the previous section are used here in particular to obtain the two-photon excitation cross-section of the excited states. In the present case, the description of the Rydberg states is important and the double zeta basis is used. The cross-section can then be convoluted with the two-photon spectral intensity of the pump to obtain quantitatively the excited wavepacket. This procedure is depicted in Fig. 3.46 (a), and the resulting wavepacket is show in panel (b). In this latter plot, the transitions from a dominant HOMO character are depicted in red, with a dominant HOMO-1 character in green, and the transitions without a dominant character in black circles. It is interesting to note that except for a few points, most of the significant levels above 9.4 eV have a dominant HOMO-1 character while the one below this value are mostly HOMO. This is typically a criterion on which a relevant energy selection on the experimental kinetic energy spectrum could be defined. As always in a molecular system, many states are at play, yet the $\sim$ 200 meV difference could be associated with the dominant levels around 9.33 eV and 9.49 eV, or between 9.41 eV and 9.61 eV.

In order to go beyond these initial guesses, the theoreticians are currently working on developing and implementing a model fully grasping the pump-probe dynamics. To that end,

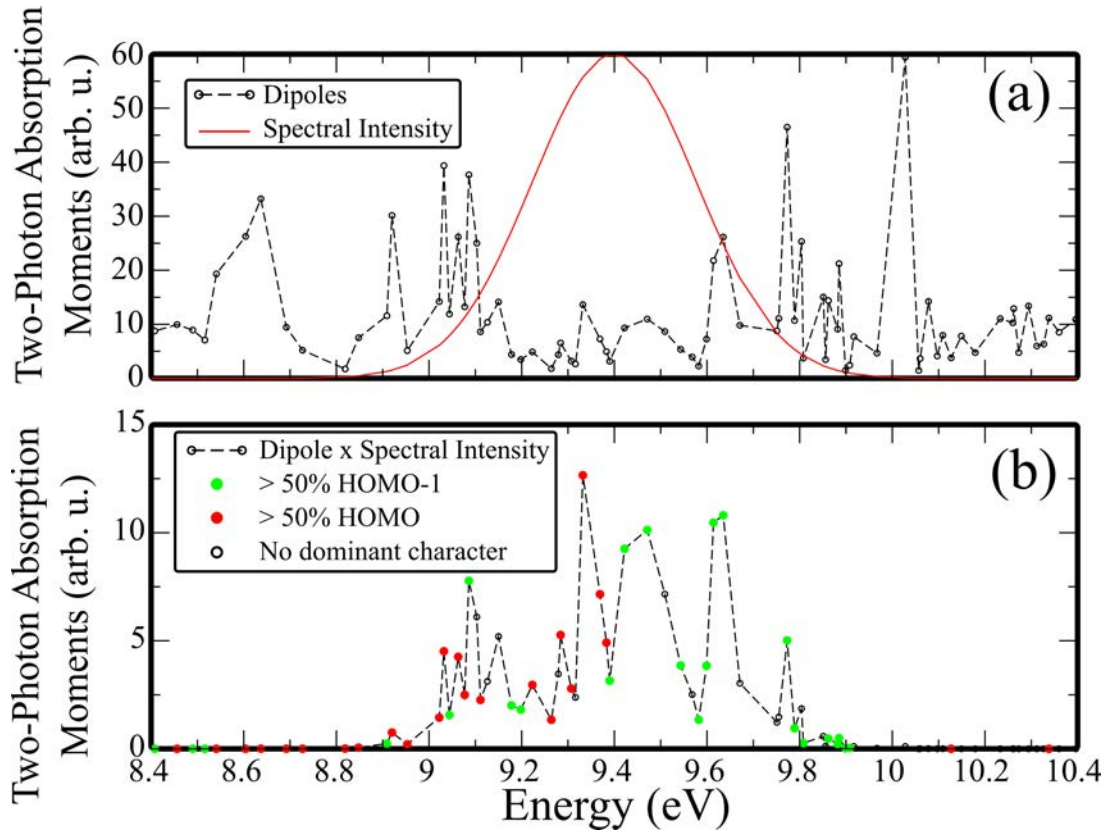


**Figure 3.46** – *Modeling of the excited wavepacket created in the Methyl-Lactate, computed by TDDFT. (a) Two-photon excitation cross-section of the excited states in the region of interest. The spectral intensity of the pump is depicted in red. (b) Convolution of the cross-section with the spectral intensity. The transitions from a dominant HOMO character are depicted in red, with a dominant HOMO-1 character in green, and more mixed transitions in black circles.*

the ionization from the excited wavepacket is described with a semi-analytic expression (Fermi's golden rule) of the transition to molecular scattering states. This remains in the single active electron approximation with a fixed molecular geometry. More details can be found in the PhD thesis of Alex Clergerie. Simply, this type of calculations should provide quantitatively the time-dependent, angularly resolved photoelectron distribution and will account for the electronic beatings. If the vibrational dynamics happened to be involved, this calculation could be repeated for several molecular geometry.

# V Conclusion and Perspectives

Several milestones have been presented in this chapter, based on the high sensitivity of photoelectron circular dichroism in Resonance-Enhanced Multiphoton Ionization.

Firstly, the high-repetition rate beamline has been implemented with the VMI in order to get a cutting-edge signal-to-noise ratio. The use of a lock-in ellipticity modulation scheme provides an enrichment of the dichroic response of chiral molecules, and has been implemented for continuous isomeric and enantiomeric content monitoring. We believe that the state-of-the-art performances obtained can be used beyond the scope of an academic laboratory. In this

perspective, Antoine Comby, a former PhD student of the group, has started a spin-off project and has been designing and building a commercial-grade system aiming at providing continuous enantiomeric excess measurement, with a compact fiber laser source and integrated VMI.

Secondly, the broad characterizations from scratch of two chiral systems, Ethyl- and Methyl-Lactate, have been presented. This enables us to extend the scope of REMPI chiral studies to new systems, whose strong fragmentation could reveal interesting characteristics. Furthermore, these molecules should efficiently form dimers (permanent dipole of 3.48 D for Ethyl-Lactate, 3.23 D for Methyl-Lactate, calculated with DFT). They are thus systems of choice for the investigation of the mechanisms involved in the chiral recognition process. Preliminary results have been obtained with the new photoelectron-photoion coincidence detection device, and give a hint of the wide variety of the observables provided. In particular, the most complete yet challenging experiments, namely time-resolved PECD measurements in coincidence, seem at reach and various setup improvements to reach this level have been discussed.

In the meantime, the characteristics of our setup have been complemented by using an external ultrashort IR-UV source to perform pump-probe resolution of the chiral dynamics at an unprecedented timescale. It appears that PECD is indeed able to reveal processes of the order of tens of femtoseconds, and its interpretation in terms of underlying chiral dynamics is still under investigation.

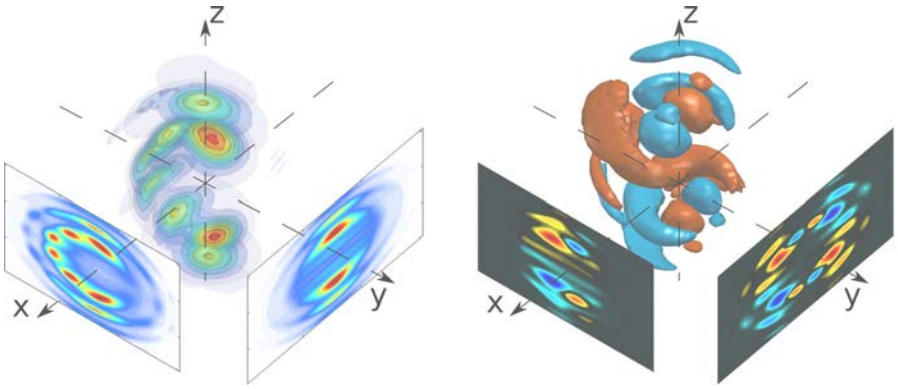


# Chapter 4

# Strong Field Regime

## . 1 Context

We have seen in the general introduction of this thesis that PECD was originally observed and described in the single-photon ionization regime, already bringing a strong chiral sensitivity to many molecular aspects : orbital ionized, vibrational level, isomerism, conformerism, etc. The multiphoton regime has then been developed in Chapter 3, and presents wide perspectives. In particular in resonance-enhanced multiphoton ionization, the excitation of intermediate bound states has great implications in the PECD observed and provides an additional sensitivity. As we have seen, their effects can be isolated by decoupling the excitation and the ionization steps. This is also of high interest as it brings the possibility of time-resolved pump-probe experiments. Nevertheless, the complexity of the PECD signal, originating from its wide spectrum of sensitivity, increases in the multiphoton regime.

If the field intensity is further increased, one can reach the strong field ionization regime. One might expect that in this case the observable is all the more complex. Oppositely, it turns out that one can reach a semi-classical regime where the interaction is significantly simplified. Furthermore, the ionization is largely reduced to the sole HOMO. We will see in the introduction of this chapter that many interesting manipulations can be performed in this regime, such as attosecond metrology or electron trajectories control. However, structural effects are usually negligible in strong field conditions. Can molecular chirality be encoded in such a regime? Can we use the broad toolbox provided by strong field interaction to resolve chirality at an unprecedented timescale?

## . 2 From the Perturbative Description

The entire physical description of the phenomena presented so far in this manuscript relies on a critical hypothesis : it stands only if the interaction force of the electronic system with the laser field is small compared to the molecular interactions. Namely, the field is perturbative. Quantum-mechanically speaking, the electronic Hamiltonian can be written :

$$\hat{\mathcal{H}} = \hat{\mathcal{H}}_0 + \hat{\mathcal{V}}(t) \tag{4.1}$$

where $\hat{\mathcal{H}}_0$ is the field-free (unperturbed) Hamiltonian and $\hat{\mathcal{V}}$ is the perturbation. We assume here that the eigenstates and eigenvalues of $\hat{\mathcal{H}}_0$ are known. In our case, as the laser wavelength that we use is always much larger than the size of a molecule (respectively hundreds of nanometers compared to hundreds of picometers), one can apply the electric dipole approximation, writing :

$$\hat{\mathcal{V}}(t) = \hat{\mathcal{V}}_0 cos(\omega t) \tag{4.2}$$

where $\omega$ is the angular frequency of the laser field. Assuming $\hat{\mathcal{V}}_0 \ll \hat{\mathcal{H}}_0$, one can apply the time-dependent perturbation theory (see [Cohen-Tannoudji 77] Chap. XIII for a comprehensive description of the method). In this description, the field slightly affects the energy of the eigenstates of $\hat{\mathcal{H}}_0$ (Stark-shift), and most importantly, it induces couplings between them. These two quantities can be calculated at different order of the perturbation and a general formula can be derived, yielding the well-know Fermi's golden rule. The transition probability from an initial state $|\varphi_i\rangle$ to a final state $|\varphi_f\rangle$ can be written at the first order as :

$$\Gamma^{(1)}_{i\to f} \propto |\langle\varphi_f|\hat{\mathcal{V}}_0|\varphi_i\rangle|^2 \delta(E_f - E_i - \hbar\omega) \tag{4.3}$$

This formula can be generalized at any order $n \in \mathbb{N}^*$ as :

$$\begin{aligned}\Gamma^{(n)}_{i\to f} \propto \sum_{k_1,\dots,k_{n-1}} & |\langle\varphi_f|\hat{\mathcal{V}}_0|\varphi_{k_1}\rangle\langle\varphi_{k_1}|\hat{\mathcal{V}}_0|\varphi_{k_2}\rangle \dots \langle\varphi_{k_{n-2}}|\hat{\mathcal{V}}_0|\varphi_{k_{n-1}}\rangle\langle\varphi_{k_{n-1}}|\hat{\mathcal{V}}_0|\varphi_i\rangle|^2 \\ & \times \delta(E_f - E_{k_1} - \hbar\omega)\delta(E_{k_1} - E_{k_2} - \hbar\omega)\dots\delta(E_{k_{n-1}} - E_i - \hbar\omega)\end{aligned} \tag{4.4}$$

where $k_1, k_2 \dots k_{n-2}, k_{n-1} \dots$ are all the possible intermediate (real or virtual) states.

The order in the perturbative development, *i.e.* the number of $\langle\varphi|\hat{\mathcal{V}}_0|\varphi\rangle$ terms in Eq. (4.4) corresponds to the number of photons involved in the transition. This result contains very fundamental properties : the field couples states separated by $\hbar\omega$ with each other, the electron density can "jump" several times with multiphoton processes though intermediate states, and so on. Also, as $\hat{\mathcal{V}}_0$ scales linearly with the electric field, a n-photon process efficiency scales as $\Gamma^{(n)} \propto E_0^{2n} \propto I^n$ with $E_0$ the electric field amplitude and $I$ the laser intensity. Interestingly, the notion of photon clearly appears here even though the field is not explicitly quantified.
This description does not stand anymore if $\hat{\mathcal{V}}_0 \lesssim \hat{\mathcal{H}}_0$, as the effect of the field becomes comparable with that of the molecular potential. The energy levels are strongly modified, and not even well-defined anymore. We will see in this chapter how deeply this affects the understanding of the underlying physics, and how complementary the nonperturbative regime can be in terms of insight provided.

To give an order of magnitude of the interactions, the electric field felt by an electron on the Bohr orbit is about 5 $\times 10^{11}$ $V.m^{-1}$ (= 1 a.u.). This field corresponds, for an electromagnetic wave, to an energy flux of 3.5 $\times 10^{16}$ $W.cm^{-2}$. However, this constitute an upper bound for

valence electrons, and strong field effects can arise at a fraction of this intensity.

# I Introduction of the Strong Field Regime

## I. 1 Strong Field Approximation (SFA)

With the advent of ultrashort pulsed laser has come the ability to generate extremely high field intensities, way above $10^{14}$ $W.cm^{-2}$. Around this value, the perturbative description begins to fail and the potential energy surface on which the electron density evolves becomes drastically affected. In one dimension $x$, the field term $\hat{\mathcal{V}}(t)$ in Eq. (4.1) can be written as :

$$\hat{\mathcal{V}}(t) = \hat{\mathcal{V}}_0 cos(\omega t) = V_0 \hat{X} cos(\omega t) \tag{4.5}$$

with $\hat{X}$ the position operator. This simply describes a linear function added to the potential, alternatively modulated in time. The simple case of a 1D Coulombian atomic potential affected by this field term is depicted in Fig. 4.1.

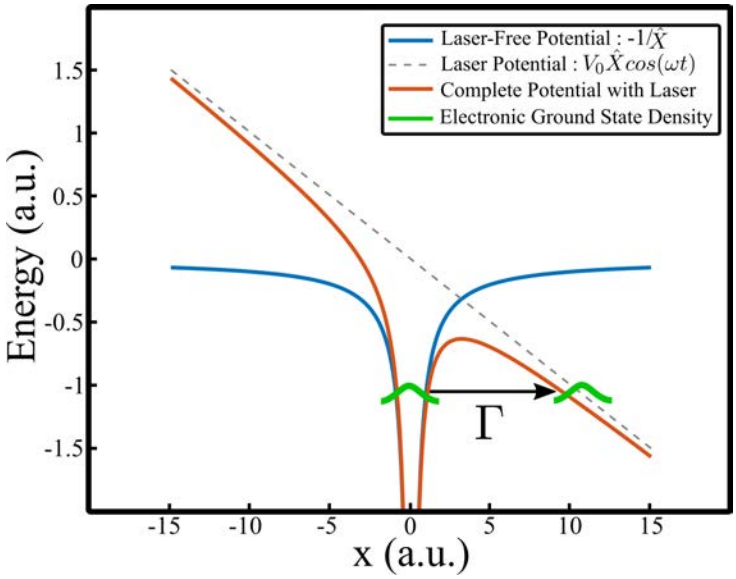


**Figure 4.1** – *One dimensional view of the bending of a Coulomb potential by a strong laser field.*

A comprehensive model, the Strong Field Approximation (SFA), starts here by considering that only the ground state of the molecular (or atomic) potential is taken into account (namely the HOMO). Secondly, one can consider that the potential is bent enough so that the electronic density can tunnel out of the well at a rate $\Gamma$, expressed in atomic units for simplicity :

$$\Gamma = \Gamma_0 e^{\frac{-2(2I_p)^{3/2}}{3|E_0|}} \tag{4.6}$$

with $I_p$ the ionization threshold of the ground state, $E_0$ the electric field amplitude and $\Gamma_0$ a pre-factor that depends on the molecular structure [Haessler 11]. Because of this exponential decrease of the tunneling rate with the ionization potential, the ionization is largely dominated by the highest occupied orbital. Developed initially in the 1960's by Keldysh [Keldysh 65,

Perelomov 66], this description is valid providing the field does not evolve too quickly compared to the electronic density, *i.e.* the tunneling process remains adiabatic. An important indicator of the adiabaticity is the well-known Keldysh parameter $\gamma$, which compares the tunneling time with the laser frequency. Note that the concept of tunneling time is slightly tricky : it is defined relatively to a classical particle even if the tunneling process is intrinsically quantum, and puzzling quantities, such as imaginary times, can arise. The Keldysh parameter $\gamma$ is defined as :

$$\gamma = \omega \frac{\sqrt{2m_e I_p}}{eE_0} \tag{4.7}$$

and gives a qualitative estimation of the tunneling regime. The aforementioned quasi-static condition is valid if $\gamma \ll 1$, *i.e.* for high field intensities and low field frequencies. On the other hand, if $\gamma \gg 1$, the perturbative description previously mentioned prevails. The transition between these two clearly-defined regimes around $\gamma \simeq 1$ can be more subtle as we will see at the end of this chapter. Note also that if the field is strong enough to completely erase the barrier, the tunneling description does not stand, but this case (the barrier suppression ionization) is of limited interest in this manuscript.

The tunneled-out electronic wavefunction then evolves under the influence of the electric field, and the SFA neglects the influence of the ionic atomic or molecular potential on this evolution. In a first approximation, the electron dynamics can be treated classically by integrating the classical equations of motion, correctly reproducing some observed features. In the SFA model itself, the propagation in the continuum of an electron that tunneled out at a time $t_i$ can be expressed in terms of semi-classical action :

$$S(\vec{p}, t_i, t) = -\int_{t_i}^{t} [\frac{(\vec{p} + \vec{A}(t'))^2}{2} + I_p] dt' \tag{4.8}$$

where $\vec{A} = -\int_{-\infty}^{t} \vec{E}(t')dt'$ is the vector potential of the electromagnetic field. The solutions can be found by solving the saddle-point equation :

$$\frac{\partial S}{\partial t} = \frac{(\vec{p} + \vec{A}(t))^2}{2} + I_p = 0 \tag{4.9}$$

Within this description of the light-matter interaction, the atomic or molecular potential only influences the tunneling rate $\Gamma_0$ through the ionization potential $I_p$. In spite of its simplicity, this model has been remarkably successful in describing important features of strong-field physics. We will illustrate this by a few examples in this introduction.

## I. 2 Variety of Processes

What happens to the electrons driven by the laser field after the tunnel ionization? Several types of processes can follow, depending on the exact field configuration and the ionization time within the optical cycle, as depicted in Fig. 4.2. Firstly, the photoelectrons can simply directly leave the vicinity of the ionic core (b), namely the direct trajectories, which dominate the ionization in the rising edge of the electric field. These electrons can also undergo additional acceleration

by the field, leading to the above-threshold ionization (ATI). This can also be understood as an absorption of photons above the threshold. Even if the field is not quantified here, the additional kinetic energy is an integer value of $\hbar\omega$. In any case, several trajectories, ionized at different times within an optical cycle, can end up with the same final momenta . As a result, trajectories can interfere and yield an interference pattern. This can reveal information about the relative phase accumulated by the trajectories, and is referred to as photoelectron interferometry.

Secondly, if the electrons are tunneled out in the falling edge of the laser electric field, their initial acceleration can be compensated by the electric field at the following half-optical cycle, whose force points towards the opposite direction. As a result, the electrons can go back to the ionic core, and induce rescattering processes. The trajectories can then keep the same direction (forward recattering, as depicted in (c)) or 'bounce back' on the core (backward rescattering , (d)), and lead to more complex interference patterns. For instance, elastic rescattering is used in photoelectron holography and laser-induced electron diffraction. These effects are of particular interest, since they can reveal some of the ion's structural information. Inelastic rescattering, where part of the photoelectron energy is given back to the ion, underlies for instance nonsequential double ionization processes.

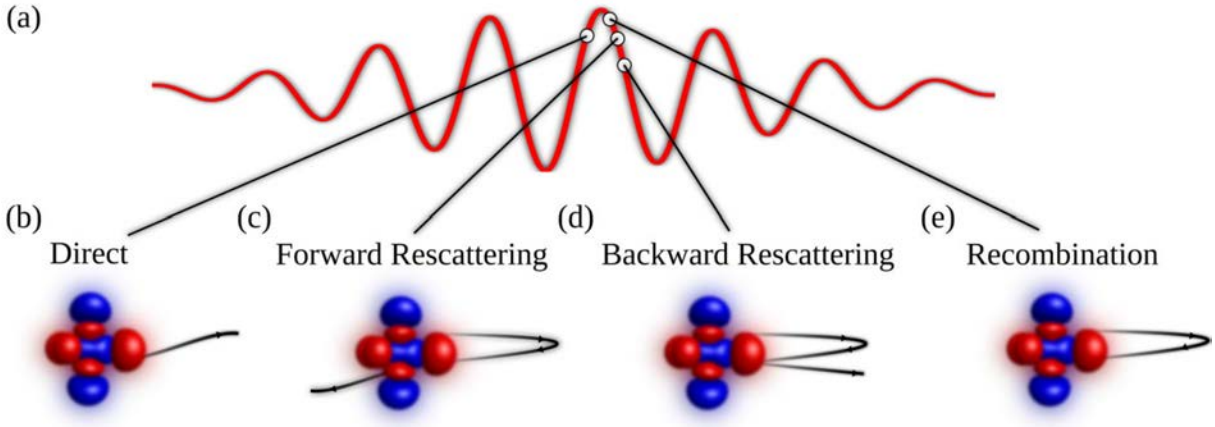


**Figure 4.2** – *Schematic of few different processes that can occur after the removal of an electron through strong-field ionization. (a) Gaussian-shaped few-cycle electric field. The white dot represents the time at which the electron is emitted in the continuum. (b) The electrons that are born in the continuum just before the maximum of the field are directly accelerated away from the ionic core. The ATI spectra arise from this type of trajectories. (c) The electrons which are born significantly after the maximum of the electric field can experience forward rescattering. (d) the electrons which are born later after the maximum of the electric field can experience backward rescattering. (e) The electrons which are born just after the maximum of the electric field can experience radiative recombination. Note that more complicated trajectories have been ignored here, such as multiple rescattering trajectories. Reproduced from the PhD thesis of Samuel Beaulieu.*

Finally, the trajectories that can come back close to the ionic core and overlap spatially with the initial wavefunction can sustain radiative recombination (Fig. 4.2 (e)). In this case, the kinetic energy accumulated by the electron is converted into the emission of high-energy photons, and is commonly known as high-order harmonics generation (HHG).

These effects can be fostered or tempered relatively to each other with the field conditions but are usually closely linked and intricate. A few examples of processes we are interested in in

this thesis are further detailed in this introduction.

## I. 3 High-order Harmonics Generation (HHG)

One of the great successes of the strong field physics has been the ability to produce high-order harmonics of a laser field. As more extensively discussed in Section 2.I, the generated radiation has very interesting properties. Firstly, it is a coherent source of photons in the energy range from the XUV to the X-ray domains. Secondly, HHG can be used to obtain extremely short pulses, at an unprecedented duration down to a few dozens of attoseconds, and is thus of particular interest for pump-probe time-resolved experiments. Thirdly, the process is very sensitive to the generation medium, and can be used to directly probe the latter.

We will see in this section how the mechanism of the high-order harmonics generation can be described in a typical strong-field framework.

**The High-order Harmonics Generation Process**

The theoretical description widely used today to understand the HHG process is based on the three-step model [Corkum 93, Schafer 93], as schematized in Fig. 4.3 (a). (1) The laser field bends the atomic or molecular potential so that part of the ground state wavefunction can tunnel out in the continuum in one direction. This must be done in a controlled manner so that this process occurs efficiently but not all the density must be ionized. This is typically the case with intensities about $10^{14}\ W.cm^{-2} = 2.8 \times 10^{-3}\ a.u.$, where $E_0 = 53 \times 10^{-3}\ a.u.$ and $I_p$ are comparable in Eq. (4.6) (typically $I_p \approx 10\ eV = 370 \times 10^{-3}\ a.u.$). (2) The outgoing wavepacket is driven and accelerated in the continuum by the field. As this latter oscillates in time, it changes sign half an optical cycle after the tunneling. The wavepacket is thus driven back towards the ionic core. (3) The electron wavepacket can radiatively recombine from the continuum to the ground state, yielding the emission of a high-energy photon.

This model can seem simplistic, but it is surprisingly efficient at describing many properties of the HHG :

i) The process is periodic in time as it is repeated every half-optical cycle. This manifests itself as a comb-like emission spectrum in the energy domain, and can be understood as spectral interference (Fig. 4.3 (b)). Only odd harmonics of the driving field show up as the process is repeated twice per optical cycle. This somehow re-introduces the notion of photon quantification. Note that even harmonics can be generated by breaking the temporal symmetry of the process, for example by adding the second harmonic of the driving field [Mauritsson 09].

ii) Electrons in the continuum accumulate kinetic energy before recombining. This can be calculated classically using the so-called Simpleman model [Corkum 93, Schafer 93]. The classical equations of motion are just integrated for the ejected electrons, starting with zero velocity. Important features then appear. The maximum kinetic energy that can be gained by an electron in the continuum determines the position of the cut-off of the harmonic spectrum. Furthermore, two distinct electron trajectories, with different ionization and recombination times, lead to the same final kinetic energy, *i.e.* to the same emitted photon energy (see Fig. 4.3 (c)). These two

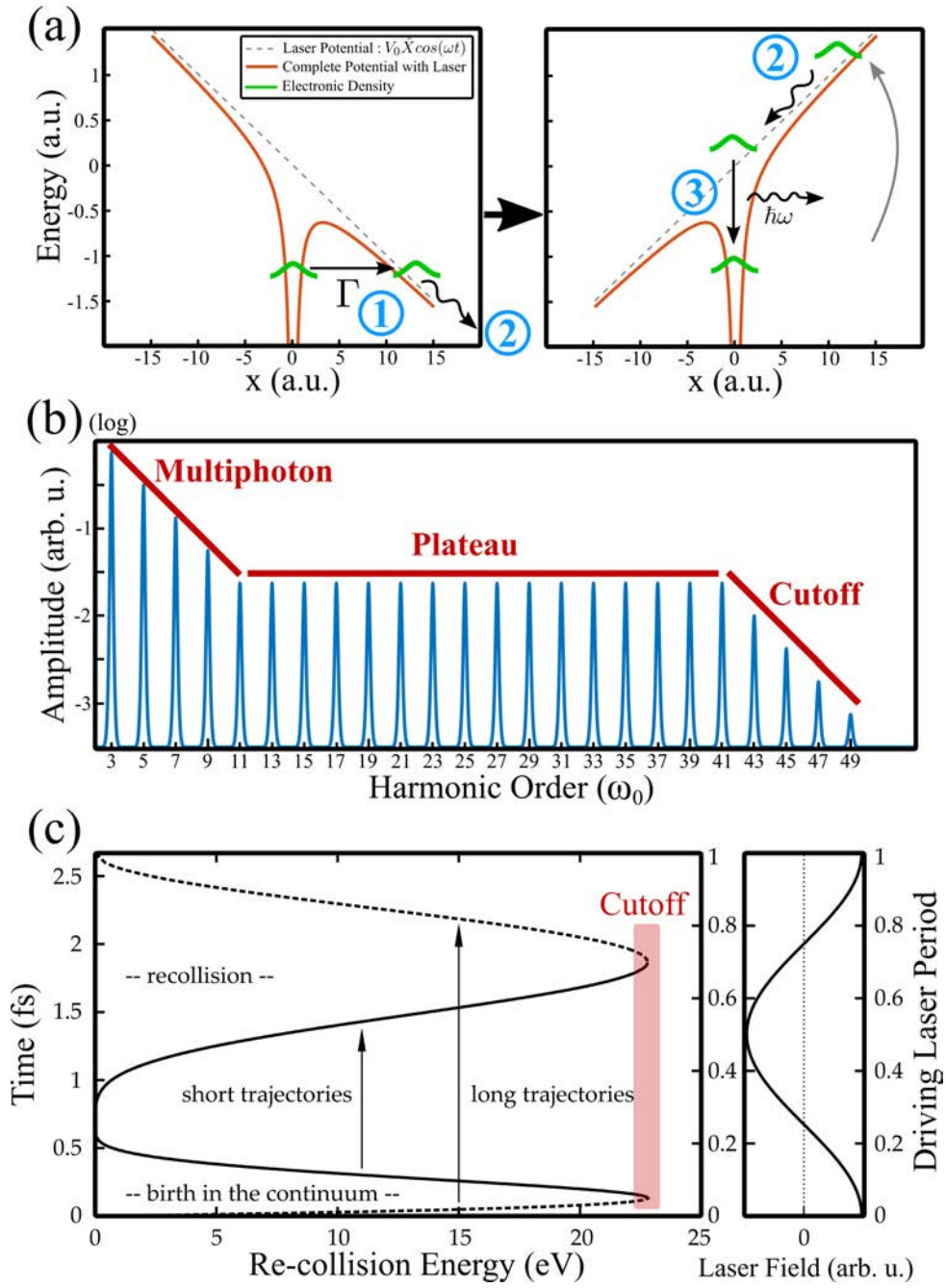


**Figure 4.3** – *(a) Three-step model of the high-order harmonics generation process. (b) Typical HHG spectrum. (c) Reproduced from [Haessler 11]. Left panel : classical calculation of ionization and recollision times as a function of the electron recollision energy, for an 800 nm laser and an intensity of* $I = 1.4 \times 10^{14}$ *W.cm*$^{-2}$*. The electric field of the driving laser has a cosine time-dependence, i.e. time zero marks the field maximum. Full and dashed lines mark the short and long trajectories, respectively. Right panel: driving laser field on same time axis.*

trajectories, referred to as short and long trajectories, can be distinguished in experiments, typically by their different divergence [Catoire 16]. A major improvement to this model, initiated in by Lewenstein *et al.* in 1994 [Lewenstein 94], consists in considering the quantum aspect of the electron dynamics by calculating the action integral of Eq. (4.8). Surprisingly, this does not significantly deviate from the classical calculation, validating the qualitative aspects of the

latter, but provides of course finer description of the quantum effect, such as the trajectories interferences. Right from the classical model, the spectral cut-off of the emission appears around $I_p + 3.17U_p$, where $U_p = \frac{e^2 < \vec{E}^2 >}{2m_e\omega^2}$ is the ponderomotive energy, corresponding to the mean kinetic energy of the electrons in the electric field. This is of crucial interest for generating high energy photons, as one should thus induce the highest possible $U_p$ for this purpose. However, one should still keep in mind that this can also influence the ionization rate and the Keldysh parameter.

iii) The emission results from the recombination of a wavepacket with its own source. As a result, the emitted radiation conserves the coherence of the driving field. The coherence of the process is highlighted and exploited for example in interferometric techniques, such as the RABBITT (Reconstruction of Attosecond Burst By Interference of Two-photon Transitions) [Véniard 96]. For doing this, sidebands of the harmonics generated by a field with the same frequency as the driving field are created in a photoelectron spectrum where two quantum path can interfere. This gives access to the relative phase between the harmonics. The spatial coherence can also be used for instance in two-sources interferometry [Smirnova 09].

iv) Temporally, the launching of the trajectories does not spread uniformly across the driving laser pulse. Indeed, the ionization maximizes around the high field intensities. As a result, the emission of a given harmonic is confined around the corresponding trajectories recombination. Since the driving field is periodic, the harmonic emission is also periodic, and forms a train of pulses, emitted every half optical cycle. Being temporally confined within half an optical cycle, each pulse has a duration in the sub-femtosecond, or attosecond range. Furthermore, the trajectories corresponding to different emission wavelengths do not recombine at the same time. As a results, the attosecond emission is chirped, alternatively positively and negatively along every driving half optical cycle (Fig. 4.4). As the process efficiency is also modulated with the driving field, the HHG emission temporally appears as a train of attosecond pulses [Paul 01, Mairesse 03]. Recent techniques can be implemented to reduce this train to a single, isolated attosecond pulse. For example, as a strong field is required here, one can use few-cycles laser pulse to confine the generation to a single half-optical cycle [Hentschel 01], namely amplitude gating. Another way around can be found by noticing that, as the wavepacket must be driven back to the ionic core, the process declines drastically with the driving field ellipticity [Chang 04, Strelkov 04]. By combining two delayed, counter-rotating circular polarization, a field can be obtained with only half an optical cycle being linear. This polarization gating confines the HHG to a single attosecond pulse. Even more efficient combinations of gating, such as double-optical gating, have been developed since then [Chang 07]. Note also that for the isolated attosecond pulse to be as short as possible, the intrinsic chirp between the harmonics needs to be compensated, for instance by inserting metallic foils to compress the pulse down to 53 as [Li 17].

v) The efficiency of the whole process in inherently low, up to the $10^{-5}$ range in the best cases [Comby 20a]. Studies converged to an efficiency scaling as $\lambda^{4-8}$ [Tate 07, Shiner 09, Comby 20a]. Three factors determine the global efficiency. Firstly, the ionization rate must be maintained at a reasonable level to avoid complete ionization of the system. Secondly, due to its quantum nature, the propagating wavepacket always spreads perpendicularly to the laser field. As a result, a significant fraction of the accelerated electrons never overlaps spatially with the ground

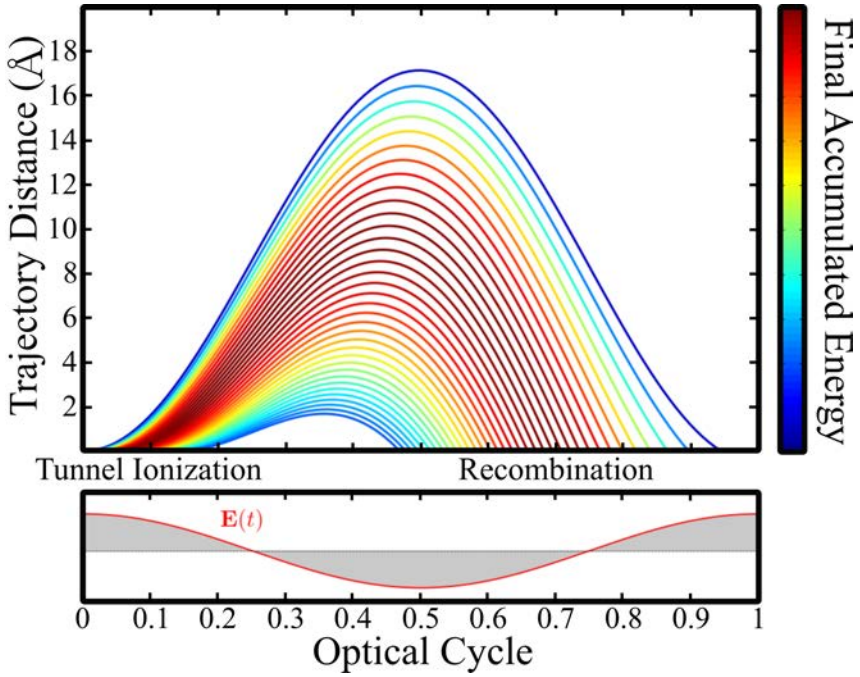


**Figure 4.4** – *Electron trajectories, for a 800 nm field at* $I = 1 \times 10^{14}$ $W.cm^{-2}$. *The color represents the final accumulated kinetic energy, i.e. the HHG photon energy. Reproduced from the PhD thesis of Julien Higuet.*

state. Thirdly, the recombination efficiency, which is linked to the transition dipole between the ground state and the continuum, is by itself limited. This dipole is the complex conjugate of the one-photon ionization dipole, and is known to decrease drastically with the photoelectron kinetic energy. Note that it also encodes the spatial information of the source, for instance the symmetry of the orbitals, the geometry of a molecular system etc., and is the term of interest in high-order harmonics spectroscopy.

This description at the atomic or molecular scale misses an essential point : the macroscopic response. The process always occurs coherently between many centers in the gas target, driven by the same laser field. All the single-center responses must thus constructively add up along the interaction volume for the process to be efficient. This primarily leads to the collimation of the HHG emission along the laser field, but it is also of crucial interest for the conversion efficiency of the process. Indeed, for it to be maximized, one should consider the so-called phase-matching conditions [Gaarde 08] : the dispersion of the HHG along the target must be controlled. Also, re-absorption of the HHG must be kept low [Constant 99]. This typically implies avoiding too much ionization and avoiding too high gas density. This is of course in contradiction with the initial proclivity to use higher intensity and higher gas density to increase the efficiency. It means that the process is fundamentally limited as a compromise must be found. At the end, the length-density product of the generating media is the relevant parameter to consider [Rothhardt 14, Comby 18].

As we now understand, the high-order harmonics generation process has strong-field specific characteristics. Several parameters are to be considered simultaneously to optimize the process, depending on the goal. In any case, the process can be kept efficient by scaling the

experiment while keeping some parameters constant [Heyl 16]. High-enough HHG intensity to induce non-linear processes has recently become available [Takahashi 13, Senfftleben 20], using long focal length. Long wavelengths can be used to generate photons at very high frequency, up to the $keV$ range [Popmintchev 12]. On the one hand, if only a high average photon flux is required, high-repetition rate sources have been shown to be of great interest [Klas 16]. Our group recently reached the $mW$ range at 18 $eV$ at a repetition rate of 166 $kHz$ [Comby 19]. Other very good results have also been obtained with a different technology, generating the harmonics in a cavity [Porat 18b]. HHG has been widely used as a secondary radiation source in the XUV and x-ray domain, but it can also be used to resolve the dynamics in the generating medium itself, as we will see in the next paragraph.

**High Harmonic Spectroscopy**

As we have seen in Section 2.I, the high-order harmonic generation process has been widely used as a secondary radiation source in the XUV and x-ray domain. We will see here that it can also be used to self-probe the generating medium itself. On the one hand, one can use HHG in such a way by manipulating the generating medium. For instance, the process is sensitive to many molecular effects, such as molecular alignment [Kanai 05], vibrational wavepacket [Lein 05, Baker 06, Miller 16], and vibronic excitation [Ferré 15a], among others. The excited wavepacket can be used to perform tomographic reconstruction of the molecular orbitals [Itatani 04, Haessler 10, Vozzi 11, Peng 19].

An alternative approach also exists. As we have seen above, HHG can be understood with a simple, yet efficient three-step model. From this model, it appears clear that the electron trajectories can also be manipulated with more complex field configurations. This is typically achieved by using two-color fields that are harmonic to each other, such as a fundamental field and its second harmonic. For instance, adding a second perpendicular generation field can enhance the control on the trajectories of the scattering electrons and modulate the recollision angle, which can help decoupling nuclear and electronic degrees of freedom [Ferré 16]. This configuration can also be used to allow or forbid the recombination of chosen trajectories, *i.e.* harmonics, and reveal the exit time of the electrons [Shafir 12] (see Fig. 4.5 (a)). Even more complex vectorial fields can be employed, such as counter-rotating bicircular bichromatic driving fields (see Fig. 4.5 (b) and (c)). These latter enable for an effective return of the wavepacket in the vicinity of the ionic core despite rotating [Fleischer 14, Kfir 16]. We will see that the manipulation of the electron trajectories in this same fashion can also be of high interest in photoelectron spectroscopy, and will be at the core of this chapter.

## I. 4 Strong Field Photoelectron Spectroscopy

We have seen in the previous section that the photons emitted during strong field processes can be used as an observable. However, the electrons tunneled out of the atomic or molecular potential do not necessarily recombine, and are actually very often emitted. The perspective of collecting and measuring them is exciting, in order to get a complementary insight in the

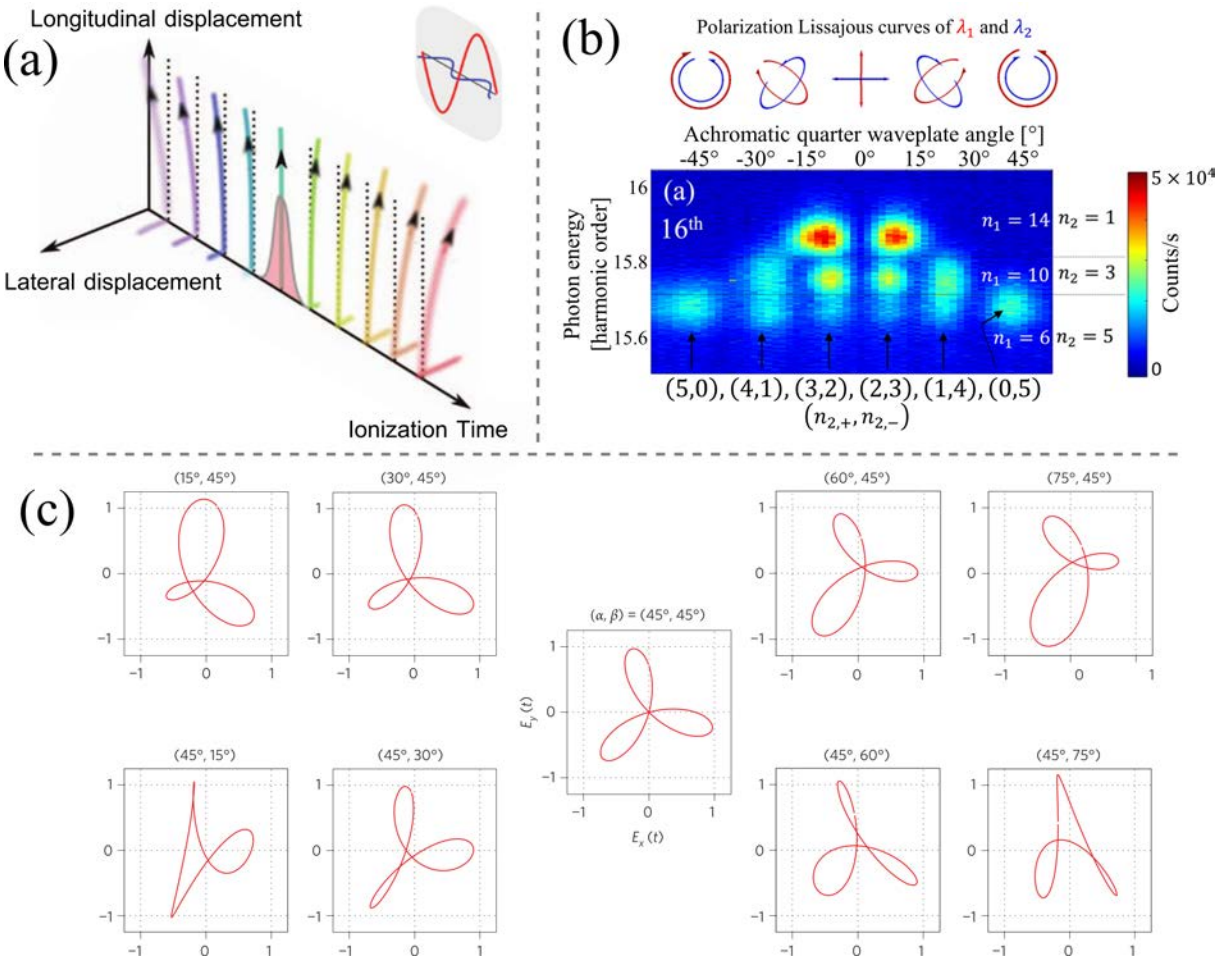


**Figure 4.5** – *(a) Principle of the displacement gate, with two linearly polarized fields : one which is strong (red) and the other one which is orthogonally polarized, weaker in intensity and modulated twice as fast (second harmonic, blue). The orthogonal field forbids or allows the recombination depending on the trajectory, i.e. the harmonic order. Adapted from [Shafir 12]. (b) HHG spectrum of the 16th harmonics of a two-color field, as a function of the driving fields polarizations. The slight wavelength incommensurate ratio $\lambda_2 = 0.51\lambda_1$ enables to distinguish energetically the different photon combinations leading to this harmonic order, as indicated on the right. The different angular momentum combinations allowed are scanned with the fields ellipticities, as indicated below. Extracted from [Kfir 16]. (c) Exotic laser fields that can be obtained experimentally, providing a control on the electron trajectories. Reproduced from [Fleischer 14].*

electronic attosecond dynamics. In a first place neglecting the interaction of the tunneled out electron with the ionic potential, the classical kinematic momentum $\vec{p} = m\vec{v}$ of an electron freely oscillating in a field is $\vec{p}(t) = \vec{p}(t') - \vec{A}(t') + \vec{A}(t)$ for any times $t$ and $t'$. This ensures the conservation of the canonical momentum of the photoelectrons $\vec{p} - \vec{A} = \vec{C}^t$ at all time in the scattering. Assuming that the electrons have zero kinetic energy right after being tunneled out (at $t_i$), this imposes the final momentum $\vec{p}_f$ when the laser field has passed ($\vec{A}_f = \vec{0}$) to be :

$$\vec{p}_f = -\vec{A}(t_i) \tag{4.10}$$

This directly links the detected photoelectron momentum distribution with the vector potential of the field at the ionization time, and obviously the ionization time itself, and can be

used in various ways. We will thoroughly use this property in this manuscript. For now, let us simply describe the shape of the distributions that can be observed.

**Photoelectron Interferometry**

The most simple scheme is performed by ionizing targets with a single linearly polarized strong laser field. In this case, several distinct ionization times can correspond to the same final momentum, but their phases accumulated during the scattering process differ. As a result, interferences can appear, and are commonly referred to as photoelectron interferometric patterns.

We invite the reader unfamiliar with photoelectron interferometry to check the Simpolator [Lein : Simpolator 0] to get a didactic feeling of the different patterns. This tool enables one to visualize the different trajectories contributions, depending on their ionization times (which quarter-optical cycle) and their type (direct or rescattered). An illustration of the different interference patterns is proposed in Fig. 4.6, calculated for a single 800 nm field at 2 $\times 10^{14}$ $W.cm^{-2}$, linearly horizontally polarized. The trajectories included are indicated in the lower caption of each panel. Let us define the time zero at a positive maximum of the field. The direct trajectories launched during the first quarter-optical cycle are shown in (a). They all end up with a positive momentum along the laser axis $p_z$ because the vector potential is negative during this part of the cycle ($-\vec{A}$ is depicted in red dotted line in the caption), with a certain transverse distribution along $p_y$ (and $p_x$, not calculated here). The photoelectron momentum cutoff appears around $2U_p$ (in our case $U_p = 0.44$ a.u., for a cutoff in momentum at 1.3 a.u.). Interestingly, the photoelectrons tunneling out during the second quarter-optical cycle (b) appear with the same final momentum distribution on the same half of the detector. As a result, including the direct trajectories of both the first and second quarters leads to an interference pattern on one half of the detector (c), called intracycle interferences. This pattern will be discussed more extensively in the next paragraph.

The direct trajectories from the two subsequent quarters will have an exactly symmetric behavior on the negative $p_z$ part of the final momentum. Including all the direct trajectories from a complete optical cycle thus lead to the figure shown in Fig. 4.6 (d). Importantly, photoelectrons tunneling out during consecutive optical cycles can also overlap and interfere. For instance, the pattern obtained from the first quarter of two consecutive optical cycles of shown in panel (e). This concentric ring pattern, or intercycle interferences, corresponds to the ATI rings. By taking into account all the direct trajectories of two optical cycles, the final distribution (f) is simply obtained by overlapping the intracycle (d) and intercycle (e) patterns.

Finally, everything can become significantly more complex if the rescattered trajectories are taken into account. The rescattered trajectories from the first optical quarter are depicted in (g). This time, their final momentum distributions spread much more and on both sides. In here, the direct trajectory can be seen as a phase reference that can be used to access the phase accumulated during the rescattering process. For instance, their interference with the direct trajectories from the same quarter cycle is shown in panel (h). Panel (i) shows the photoelectron momentum distribution obtained by taking into account all the direct and rescattered trajectories from two full optical cycles. The interferences might appear very intricate. However, the pattern of the direct trajectories (shown in (f)) globally dominates in

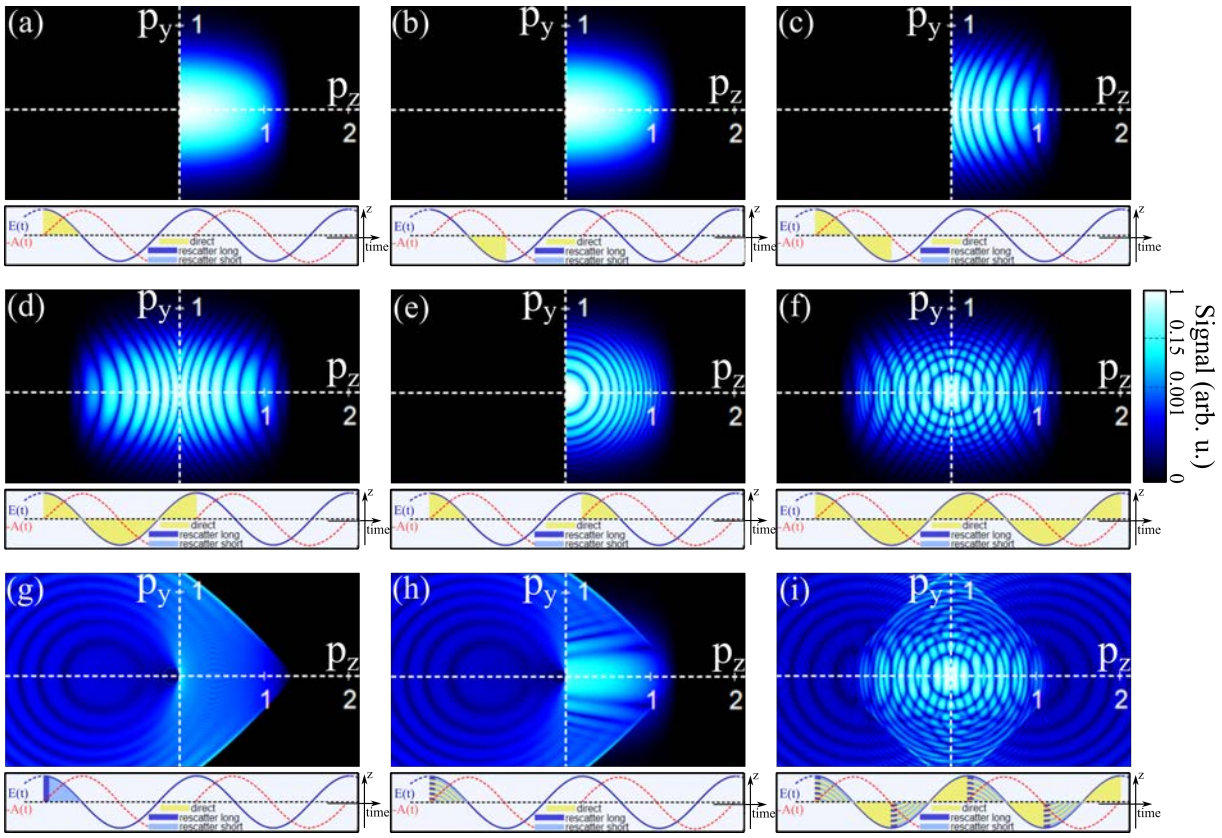


**Figure 4.6** – *Photoelectron distributions for ionization times in different quarter-optical cycles and different types of trajectories, calculated with the Simpolator [Lein : Simpolator 0]. Laser is linearly polarized here along the z axis. The simulations are performed at 800 nm and 2* $\times 10^{14}$ *W.cm*$^{-2}$*. (a) Direct trajectories from the first quarter. (b) Direct trajectories from the second quarter, ending in the same half of the detector. (c) Interference pattern obtained by including the direct trajectories from the first and second quarter-optical cycles, namely intracycle interferences. (d) Pattern obtained with all the direct trajectories of a single optical cycle. (e) Interference pattern obtained from the overlap of the first quarters of two consecutive optical cycles, namely intercycle interferences or ATI. (f) Distribution obtained from all the direct trajectories over two optical cycles, which is a combination of the intercycle and intracycle intereferences. (g) Rescattered trajectories from the first quarter. (h) Interferences between the direct and rescattered trajectories from the first quarter. (i) Complete pattern obtained with all the trajectories in two optical cycles.*

the low momentum values, at least at the field intensity used.

**Advanced Patterns**

Other more complicated patterns can be found in the literature. One can cite the *spider* (see Fig. 4.7 (1-a)), identified as interference between two forward-scattered electrons from the same cycle [Huismans 11, Hickstein 12] or the *fishbone*, from direct and backscattered trajectories [Bian 12, Li 15, Haertelt 16]. Rescattered electrons are of course very sensitive to the ionic core and more advanced theoretical tools start to be necessary to correctly reproduce their behavior, among which can be cited Coulomb-corrected SFA (CCSFA) where the Coulomb potential of the ion is perturbatively taken into account in the SFA action. Many other advanced methods have recently flourished, grasping for instance the physics of the *fan* structure, involving intermediate bound states [Rudenko 04, Maharjan 06]. These advances are

comprehensively summarized in [Faria 20].

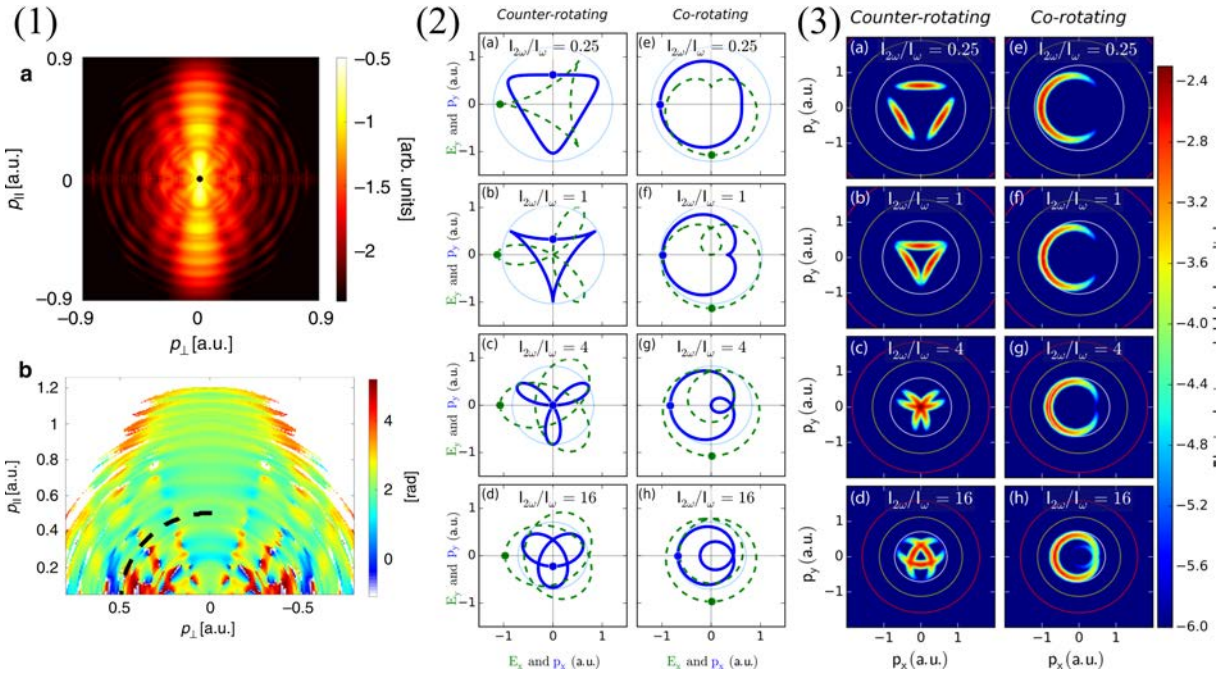


**Figure 4.7** – *(1) Two-color photoelectron interferometry. The spider pattern (a) can be modulated by the second weak, collinear field. The phase of the resulting oscillation (b) is used to reveal attosecond ionization times differences. Reproduced from [Porat 18a]. (2) Co-rotating and counter-rotating bicircular bichromatic electric fields (green dashed lines) for different field ratios, and the corresponding vector potentials (solid blue lines). (3) Corresponding calculated photoelectron momentum distributions in the polarization plane, where the trajectories are driven by the tailored vector potential. (2) and (3) are adapted from [Mancuso 16].*

The resolution of the complex interference patterns can be challenging, in particular experimentally since they always overlap. Recent progresses in photoelectron interferometry have emerged with the use of more subtle field configurations. For instance, adding a weak, second harmonic along the driving field can affect the tunnel barrier, modulating the spider structures (see Fig. 4.7 (1-b)) and revealing differences in ionization times of the order of tens of attoseconds [Porat 18a]. A linear second harmonic field can also be added orthogonally in order to streak the distribution depending on their ionization times. This gives the possibility to relieve the degeneracy between some trajectories [Zhang 14a, Richter 15], identify for instance different types of trajectories [Li 15, Li 16, Richter 16] and unraveling fundamental properties of the tunnel ionization [Han 17]. Similarly to HHG, more exotic laser fields can be employed to manipulate the photoelectron trajectories [Mancuso 16] as shown in Fig. 4.7 (2) and (3) with circularly polarized fields where the two main parameters are the relative helicities and field ratio. For example, counter-rotating two-color fields can be used, where the vector potential follows a clover shape. Cusp-like distributions of photoelectrons along the laser propagation axis, revealing the Coulomb focusing contribution [Dimitriou 04], can be detected, in opposition with the Gaussian-distributed direct trajectories [Eckart 18]. This effect comes from the electrostatic field created by the ionic core, acting as a lens on the scattering trajectories, and

will be discussed more extensively in this chapter.

**Direct Trajectories**

We will be, in this manuscript, mainly interested in the most simple interferometric patterns originating from the direct scattering trajectories, isolated in Fig. 4.8 (a). As we have seen, these trajectories dominate at moderate field intensity. Let us describe them more quantitatively here. They can be expressed from the SFA analytically [Maxwell 17], and split into intercycle and intracycle interferences, as already discussed. Similarly to the harmonic comb generated in HHG mentioned in the previous section, this intercycle interference (paths 1 and 1' in Fig. 4.8 (a)) arises as modulations in the frequency domain, here corresponding to the kinetic energy of the photoelectrons. As a result, constructive interferences in the distribution occurs at :

$$E_{kin} = \frac{p_x^2 + p_y^2 + p_z^2}{2} = n\omega - I_p - U_p \tag{4.11}$$

for $n \in \mathbb{N}^*$, $n\omega - I_p - U_p > 0$. This corresponds to the well-know Above-Threshold Ionization (ATI) rings, that can also be understood as an electronic density ionized from the absorption of $n$ photons, depicted in Fig. 4.8 (b). In this figure, the white rings indicate the solutions of Eq. 4.11.

The second family, intracycle, arises from the interference between electrons born within the same optical cycle (for instance paths 1 and 2 in Fig. 4.8 (a)). [Maxwell 17] proposed to split them in two types, A and B, respectively within a half optical cycle and between two consecutive halves optical cycles. Similarly, their analytical expression can be derived, for an electric field along $z$, as :

$$\left(p_z - \frac{4\sqrt{U_p}}{\pi}\right)^2 + p_x^2 + p_y^2 = 2n\omega - 2I_p - 2U_p + \left(\frac{4\sqrt{U_p}}{\pi}\right)^2 \tag{4.12}$$

where $n \in \mathbb{N}^*$, $2n\omega - 2I_p - 2U_p + (4\sqrt(U_p)/\pi)^2 > 0$. One again, the patterns appears as a concentric ring pattern, but this time off-centered by $4\sqrt(U_p)/\pi$, as seen on Fig. 4.8 (c). The white dotted circles highlight the solutions of Eq. 4.12, and are a good approximation with the calculated distributions (full circles) along the $p_z$ axis corresponding to the laser polarization. Calculation gives the possibility to isolate each of these patterns, but of course the "actual" physical distribution is obtained by overlapping them, as presented in panel (d).

These patterns are relatively simple and well understood. Can we use them to reveal information about molecular chirality in the strong field interaction regime? Can we use the sub-optical cycle sensitivity to the photoelectron interferometry to get access to chiral information at an attosecond timescale? Can the description in terms of photoelectron trajectories be used to understand how chirality is encoded into the photoelectrons individually?

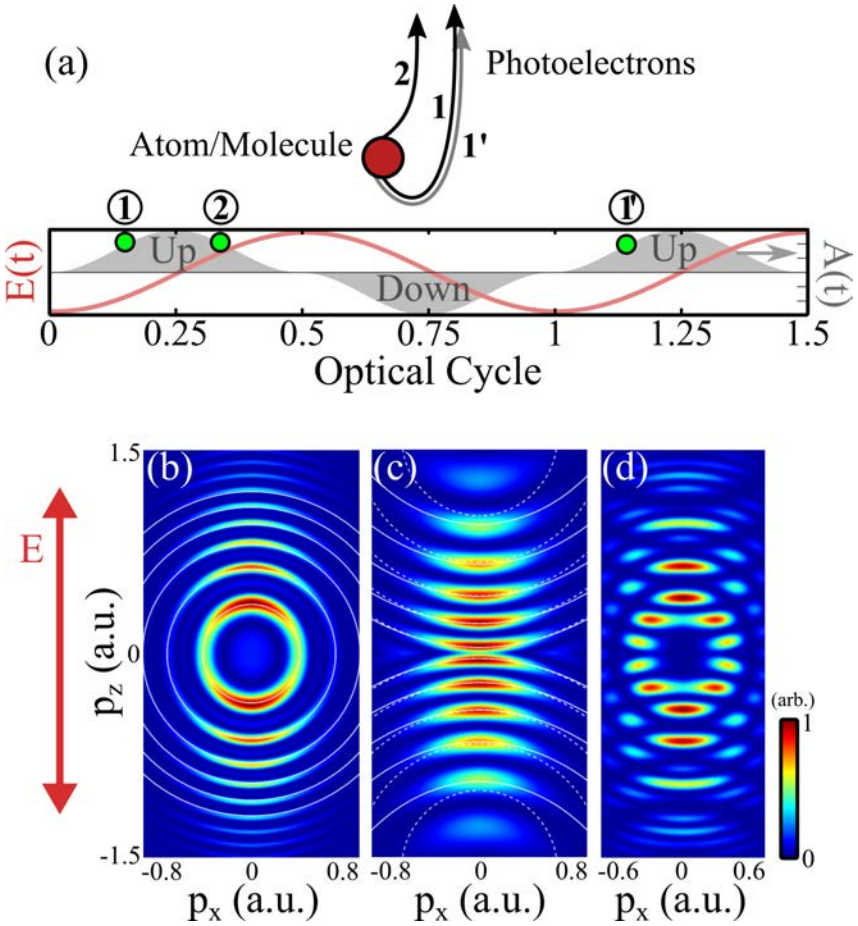


**Figure 4.8** – *(a) Scheme of the direct photoelectron trajectories with the same final momentum, ionized at different times. The ionization time of the three trajectory examples, with a final momentum upwards, are reported on the temporal panel. The interference can occur between two optical cycles (e.g. between trajectories 1 and 1'), yielding the ATI pattern presented in (b). It can also originate from ionization times within half an optical cycle (1 and 2), yielding the pattern on (c). The white lines in (b) and (c) correspond respectively to the solutions of the analytical expression 4.11 and 4.12. The combination of the two effects gives the modulation shown in (d). (b,c,d) are adapted from [Maxwell 17].*

## I. 5 Chirality in the Strong Field Regime

The details of the molecular potential are neglected in the strong field approximation. However, as we have seen in the examples above, the potential can play a significant role in the strong field physics, raising numerous questions. Are strong field processes sensitive to molecular chirality? Does the asymmetric interaction of the electrons with the chiral potential and chiral field reveal the same information as the non-chiral part of the interaction? Can sub-cycle tailored laser fields be used to probe molecular chirality?

High harmonics generation in chiral molecules has been proved to be sensitive to the chirality of the target, through laser-induced magnetic transitions in the ion, occurring between ionization and recombination [Cireasa 15]. However, the HHG process loses its efficiency as the ellipticity increases because the electron can hardly be driven back to the ionic core. HHG is thus not possible with circularly polarized light. To circumvent that issue, advanced field shapes can

be used, offering both a rotation of the electric field and the possibility to produce recolliding electron trajectories [Kfir 15, Fleischer 14, Neufeld 18]. The chiral effect remains weak, but this scheme was recently used for time-resolved studies of the chiral response using transient HHG gratings [Baykusheva 19]. The main limitation of these chiral HHG experiments is that they rely on magnetic dipole interactions. Very recently, innovative schemes have been proposed to design high-harmonic generation experiments that would be chiral-sensitive in the electric dipole approximation [Ayuso 19, Neufeld 19], by relying on complex 3D driving laser fields. One of these schemes is currently being implemented in our team by Sandra Beauvarlet.

Within this thesis, we have focused on using PhotoElectron Circular Dichroism as an electric-dipole sensitive observable of molecular chirality. As we have seen, PECD is well-suited in the single-photon and multiphoton regime. We have mentioned in the introduction of this thesis that PECD had been shown to persist in the tunnel ionization regime in a measurement performed in Fenchone, providing a rather uniform, low PECD signal over a broad electron kinetic energy range [Beaulieu 16b, Beaulieu 16a]. The existence of PECD is not allowed within the strong field approximation, as shown in [Dreissigacker 14]. However, Classical Trajectory Monte-Carlo (CTMC) simulations performed in our group showed that the emergence of strong field PECD could be understood semi-classically. The trajectories of electrons scattering in a chiral molecular potential under the influence of a circularly polarized laser field were calculated and averaged over molecular orientations. The resulting photoelectron angular distributions showed a forward-backward asymmetry, even in a strong laser field, as depicted in Fig. 4.9.

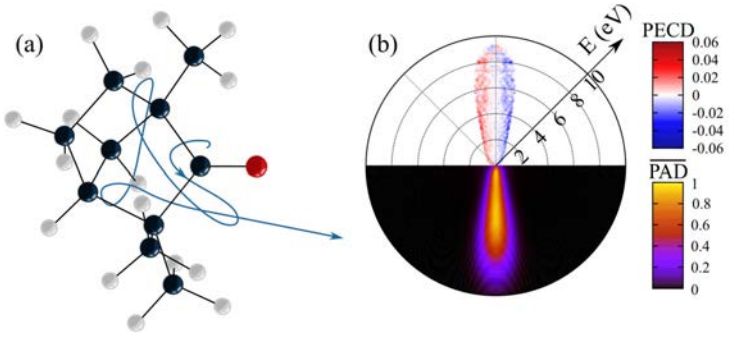


**Figure 4.9** – *(a) Typical ionizing CTMC electron trajectory in fenchone embedded in a circularly polarized laser pulse at a 800 nm wavelength and $I = 10^{14}$ $W.cm^{-2}$. (b) PAD (bottom half) and PECD (top half) from CTMC calculations in the tunneling ionization regimes. The light propagation axis is horizontal and the radius extends up to 10 eV. Reproduced from [Beaulieu 16a].*

The possibility to measure PECD in strong fields opens many perspectives of transferring the tools used to manipulate and measure the underlying attosecond dynamics. A first step in this direction was taken with the measurement of the attosecond dynamics of chiral photoionization [Beaulieu 17]. In this study, a self-referenced attosecond photoelectron interferometric measurement has been performed to measure the temporal profile of the forward and backward electron wavepackets with a few-attoseconds resolution. An angle-dependent delay has been measured between the electrons ejected forward and backward, which reaches 24 attoseconds. Furthermore, the temporal shape of the electron wavepacket has also been reconstructed from autoionizing states.

Within this thesis, we have taken a step forward by using tailored laser fields to address fundamental questions : Does the instantaneous rotation of the field matter in chiral light-matter interaction? Is PECD a quantity that builds up over the optical cycles or, conversely, does it reflect an instantaneous interaction with the field? What is the timescale of the chiral response in the electron ejection? Is tunnel ionization sensitive to the chirality of the molecular potential?

# II Enantioselective Sub-Cycle Antisymmetric Response Gated by electric-field rOTation (ESCARGOT)

The first investigation of sub-optical cycle chiral photoionization was performed in collaboration with Shaked Rozen and Nirit Dudovich from the Weizmann Institute of Science (Israel), and published in Physical Review X [Rozen 19].

Dichroic effects arise from the asymmetric interplay between a chiral potential and a chiral field. Chiroptical processes generally rely on the use of circularly polarized radiation. We have seen in Section 3.II that using elliptical polarizations could significantly enrich the chiral photoionization phenomenon in the resonance-enhanced multiphoton regime. Here, we aim at using more complex fields, resulting from the combination of multiple laser pulses with different frequencies and polarizations. The very definition of the polarization state of such field raises a challenge. Polarization is usually defined as a constant quantity in time. To take into account the slow variations of the polarization, on can define the *instantaneous ellipticity* of a light pulse as [Boge 14] :

$$\epsilon(t) = tan\left[\frac{1}{2}arcsin\left(\frac{2E_z(t)E_y(t)sin(\phi_{zy})}{E_z^2(t)+E_y^2(t)}\right)\right] \tag{4.13}$$

where $\vec{u}_z$ and $\vec{u}_y$ are the two components of the polarization plane and $\phi_{zy}$ is their relative phase. This quantity $\epsilon(t)$ reflects the temporal evolution of the ellipticity. To describe more complex electric fields, a new quantity can be introduced. Lipkin defined a quantity in the 1960's, the "zilch" [Lipkin 64], later renamed *optical chirality* in the 2010's [Tang 10]. The optical chirality $C$ is given by :

$$C = \frac{\epsilon_0}{2}\vec{E}\cdot\vec{\nabla}\times\vec{E} + \frac{1}{2\mu_0}\vec{B}\cdot\vec{\nabla}\times\vec{B} \tag{4.14}$$

and is a geometric picture that quantifies the chirality of any arbitrary shape of electric field. Interestingly enough, this idea has been used to shape fields with greater optical chirality than circular polarization [Tang 11].

By neglecting the transverse derivatives and assuming that the field has a slowly varying envelope, in such a way that the remaining $x$ derivatives (along the propagation axis) can be replaced by temporal derivatives, the geometric definition of the optical chirality given in Eq. (4.14) can be transformed into a temporal quantity [Neufeld 18] that we will call *instantaneous chirality IC* throughout the manuscript. As the electric dipole approximation prevails over the other contributions and describes PECD, the magnetic field can be neglected, leading to :

$$IC(t) = \frac{\epsilon_0}{2c_0}[E_z(t)\partial_t E_y(t) - E_y(t)\partial_t E_z(t)] \tag{4.15}$$

where $c_0$ is the speed of light. We assume here that the field propagates along the $\vec{u}_x$ axis. The instantaneous chirality quantifies the rotational velocity of the electromagnetic field. We will use it normalized relatively to a right circular polarization, meaning that $|IC| = 1$ corresponds to an evolution of the field $\partial\vec{E}/\partial t$ orthogonal to the field $\vec{E}$, with a positive (respectively negative) sign for clockwise (anticlockwise) rotations, from the target point of view.

We will see in this chapter how these instantaneous quantities become relevant with tailored laser fields and how we can use them to monitor the chiral dynamics of the photoelectrons at a sub-optical cycle timescale.

## II. 1 Orthogonal Bilinear Bichromatic Field

Orthogonal Bilinear Bichromatic electric fields can be easily generated by combining two linearly, orthogonally polarized pulses with respective frequencies $\omega$ and $2\omega$. It can can be expressed, assuming the fundamental frequency is along $\vec{u}_z$ and its second harmonic along $\vec{u}_y$, as :

$$\vec{E}(t) = E_0[cos(\omega t)\vec{u_z} + rcos(2\omega t + \varphi_{\omega/2\omega})\vec{u_y}] \tag{4.16}$$

where $r = E_{2\omega}/E_\omega$ is the field ratio and $\varphi_{\omega/2\omega}$ is the relative phase between them. The parameter $\varphi_{\omega/2\omega}$ has a great impact on the field shape, depicted in Fig. 4.10 (a). It can range from a "C"- ($\varphi_{\omega/2\omega} = \{0, \pi\}$) to an "8"-shape ($\varphi_{\omega/2\omega} = \{\pi/2, 3\pi/2\}$), through some less symmetric "bent-8"-shape (e.g. $\varphi_{\omega/2\omega} = 3\pi/4$). This OTC (orthogonal two-color) field is of great interest in our case as its instantaneous chirality alternates sign within one optical cycle (define as the $\omega$ frequency cycle), as the colorscale in Fig. 4.10 (a) indicates. Fig. 4.10 (b-c) respectively show the evolution of the instantaneous ellipticity and the instantaneous chirality over the laser period depending on $\varphi_{\omega/2\omega}$, as defined in Eq. (4.13) and (4.15).

Noticeably, the $\epsilon(t)$ or $IC$ are not equal to zero most of the time but as they change sign, these quantities integrated over a laser cycle vanish to zero. One can thus wonder : can we induce and detect a dichroic response when ionizing a chiral molecule with such a field? In other words, the question is to know whether the instantaneous or the average chirality of the field matter in chiroptical processes.

**Semi-classical Picture**

Following the semi-classical interpretation of the PECD mentioned in (I. 5), one can qualitatively think about two limit cases, summarized in Fig. 4.11 with the point of view of a typical velocity map imaging PECD experiment. The characteristic time $\tau$ it takes for the ejected electron to scatter into the chiral molecular potential under the influence of the chiral field while escaping will be the relevant factor here. On one hand, if $\tau \gg 2\pi/\omega$ ($\sim 3.4$ fs in our experiment), the dynamics will be alternatively driven by positive and negative IC, resulting in no dichroic effect in average. On the other hand, if $\tau \lesssim 2\pi/\omega$, one can expect some dichroic signal to survive.

In the VMI configuration proposed, the photoelectron distribution is projected on the de-

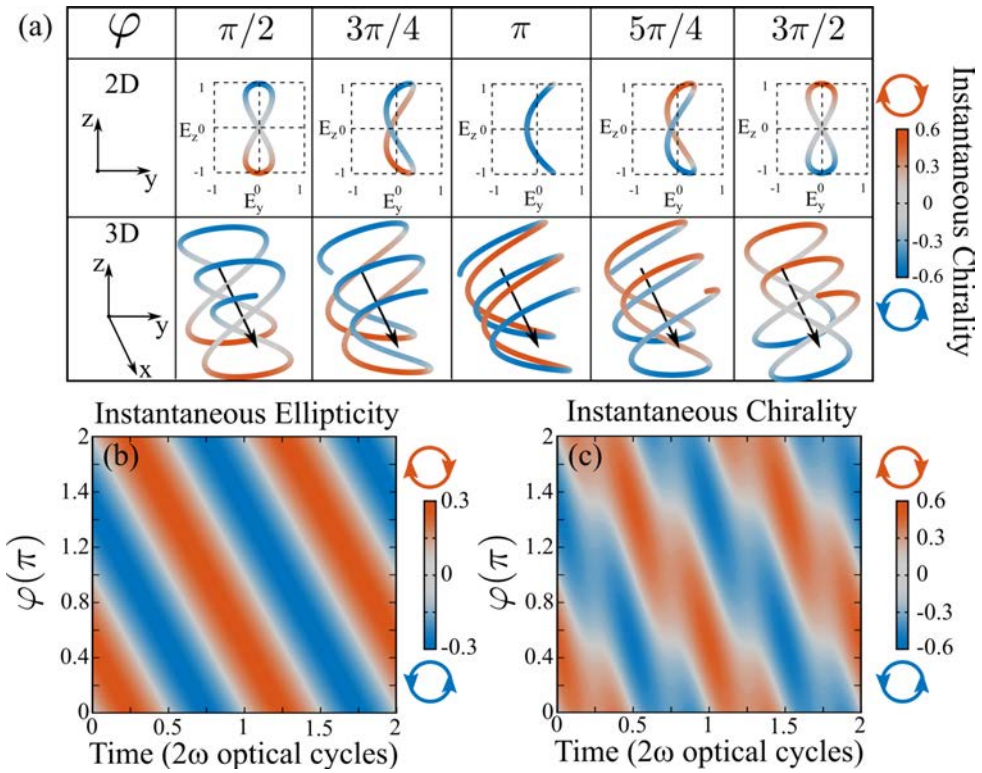


**Figure 4.10** – *Schematic description of the sub-cycle instantaneous ellipticity and optical chirality of the pulse. (a) 2D and 3D representations of the shape of a composite electric field obtained by combining a fundamental component at $\omega$ polarized along $z$ and a $2\omega$ component along $y$, with 10% intensity ratio, for different relative phases $\varphi_{\omega/2\omega}$ between the two components. The color indicates the instantaneous chirality at each instant in the cycle. Note that in 2D representation of the 0 and $\pi$ phases, we can only see the first half cycle of the laser field. The second half cycle is not visible since it traces exactly the same route as the first half, only in the reverse direction, which causes the chirality of the second half to be opposite. (b) Instantaneous ellipticity (defined in Eq. 4.13) and (c) Instantaneous chirality (Eq. 4.15) of the tailored field along a laser optical cycle, as a function of $\varphi_{\omega/2\omega}$.*

tector, resolving the $\vec{u}_x$ and $\vec{u}_z$ dimensions, respectively being the laser propagation axis and the $\omega$ field axis. The key ingredient here is the fact that in the strong field regime, the relationship between the final momentum of the photoelectron and the vector potential at the ionization time given in Eq. (4.10) imposes the upper half of the distribution to come from one half-optical cycle and the lower half of the distribution to come from the other half cycle. The observable of interest is the part of the distribution antisymmetric along the propagation axis, as we look for the chirosensitive part of the signal, but also antisymmetric along the $\omega$ polarization axis, as the instantaneous chirality of the field is inverted between the upper and the lower halves along this axis. We named this effect Enantioselective Sub-Cycle Antisymmetric Response Gated by electric-field rOTation (ESCARGOT, "snail" in French). Note that it is not properly speaking a dichroic effect, since it does not result from the subtraction of two opposite field helicities. Interestingly, in parallel to our study, a similar effect has been predicted to occur in the few photon ionization regime [Demekhin 18], with a different interpretation involving quantum path interferences in a coherent control fashion.

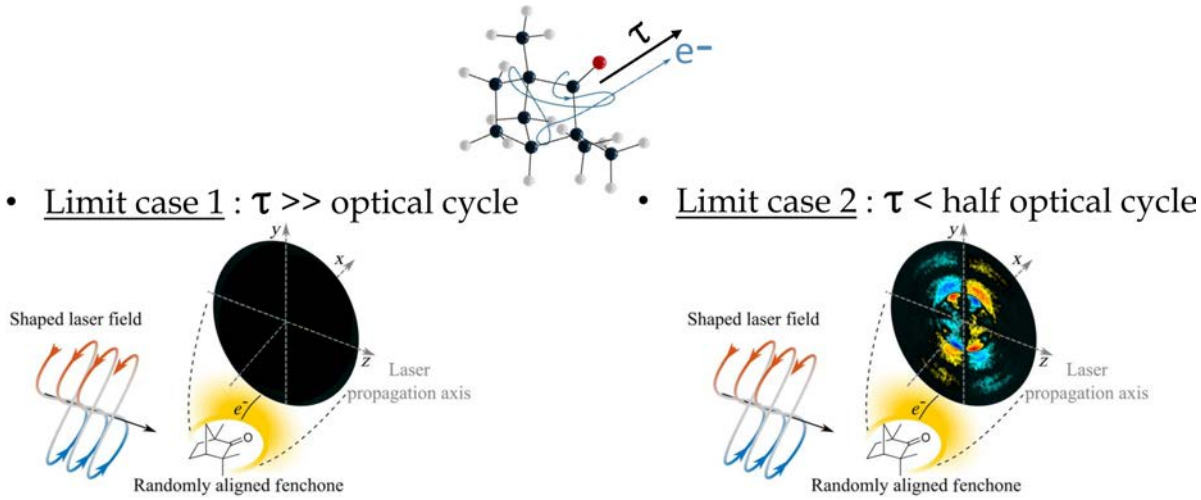


**Figure 4.11** – *Scheme of the two limit cases presented in the text. (left) If the photoelectron scatters in the chiral potential under the influence of the tailored field for a duration much greater than the optical cycle, the instantaneous chirality of field should cancel out. (right) If this duration is smaller than half an optical cycle, one can expect a non-vanishing imprinting of the instantaneous chirality in the photoelectron angular distribution.*

## II. 2 Velocity Map Imaging Experiment

### Experimental Setup

Photoionization of (+)-Fenchone and (+)-Camphor molecules has been conducted in a VMI using a single arm of the Blast Beat fiber laser system at CELIA, described in Section 2.I of this manuscript. The 50 W output of one amplifier, delivering 130 fs pulses at 1030 nm ($\omega$ in this case) at a repetition rate of 750 kHz, was split into two arms in a Mach-Zehnder interferometer using a half-waveplate combined with a polarizing beamsplitter to control the field ratio $r$ in Eq. (4.16), as presented in Fig. 4.12. The first arm remained at the fundamental frequency, while the second one was frequency-doubled in a 1 mm thick type-I beta barium borate (BBO) crystal to generate the second harmonic ($2\omega = 515\ nm$). The polarization axis of the second harmonic was rotated using a half-waveplate to be into the orthogonal two-color field configuration. The arms were recombined using a dichroic mirror, while the relative delay was coarsely controlled with a pair of mirrors on a translation stage and finely adjusted by a pair of fused silica wedges in the 1030 nm arm. A 1 mm calcite plate was put in the recombined beam to ensure a perfect cross-polarization. Indeed, small imperfections in the orthogonality could induce experimental artifacts, in particular the $2\omega$ components along the $\omega$ axis could modulate the tunneling rate. The birefringent character of the calcite plate enables to temporally separate the main (perfectly orthogonal) component of the $2\omega$ field from its collinear imperfections. As a result, this latter is temporally shifted away from the strong laser pulse, and is not intense enough anymore to induce any effect by itself. Finally, a $f = 30\ cm$ lens was used to focus the two-color pulses in the VMI. The chromatism of the lens was compensated by using a slightly detuned telescope in the $\omega$ arm to ensure the overlap of the $\omega$ and $2\omega$ focii.

Usually in attosecond physics, a very high level mechanical stability of the setup must be reached. In particular, vibrations must be avoided. We have dealt with this issue, but

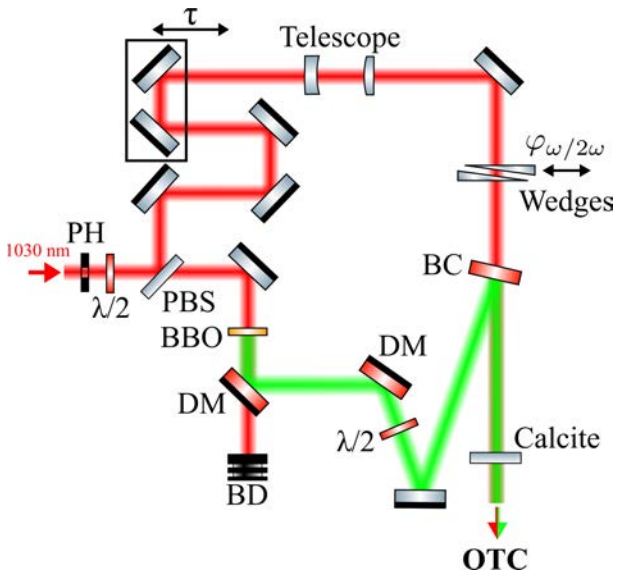


**Figure 4.12** – *Scheme of the optical setup used to generate the orthogonal two-color (OTC) field. PH = pinhole, λ/2 = half waveplate, PBS = polarizing beamsplitter, BBO = beta-barium borate crystal, DM = dichroic mirror, BD = beam dump, BC = beam combiner.*

non-negligible thermal drifts could not be avoided. Indeed, despite enabling for very short acquisitions, the high-repetition rate source suffers from a high average power and deleterious thermal effects. As a result, we have noticed that the two-color phase could evolve within the acquisition time. In order to overcome this issue, a Fourier filter procedure was employed to isolate the relevant signal. The two-color delay was continuously scanned with the wedges in the fundamental arm over 270 fs, corresponding to a $\sim 980\ rad$ ($\approx 80$ times $\omega$) scan in $\varphi_{\omega/2\omega}$. They were moved with a motorized stage at a speed of 16 $\mu m/s$. With a wedge angle $\theta = 2.9°$ and an optical index of $n_{SiO_2,1030nm} = 1.4627$, an optical cycle is scanned in 48 $\mu m$, so the whole scan duration was $\sim 240\ s$. The VMI camera exposure time was 50 ms, for a total of $\sim 5000$ images, meaning an optical cycle was resolved in about 60 points. The thermal drifts were completely filtered-out by the procedure described in the next paragraph since they do not match any of the frequencies of interest.

An alternative setup using an active two-color phase stabilization is presented in Section 4.III, in the case the detection system requires more acquisition time.

**Fourier Filter Analysis**

The periodic modulation of the up/down and forward/backward antisymmetrized part of the signal was isolated, for each pixel, at twice the fundamental frequency, in the same fashion as the PEELD experiment presented in Section 3.II. This enabled us to reconstruct the ES-CARGOT signal at every two-color phase $\varphi_{\omega/2\omega}$ by applying an inverse Fourier transform on the filtered component. This procedure reveals the quite weak relevant quantity, whose order of magnitude is about 1%, and get over the experimental imperfections in the measurement. This issue is usually solved in PECD experiments by doing a differential measurement between left and right circular polarization, but using a Fourier analysis provides a much more reliable way to do in our tailored field configuration. The absolute phase is not directly accessible with

the optical setup used. However, it can be retrieved in the Fourier analysis : the ionization probability also oscillates with $\varphi_{\omega/2\omega}$, and we assumed that it maximizes when the electric field maximizes (at 0, $\pi$...). This yields a $4\omega$ oscillating component in the total signal, as shown in Fig. 4.13, which is used as a reference for the $2\omega$ oscillation of the antisymmetric image. This method of absolute phase calibration is nevertheless not fully trustworthy. It turns out that we have noticed afterwards that this was not fully accurate at all intensities. We will not extensively discuss this aspect in this section since it does not affect the interpretations presented. A more reliable absolute phase calibration will be provided in the next section, using the complete 3D measurements of the photoelectron angular distributions, which are not accessed here.

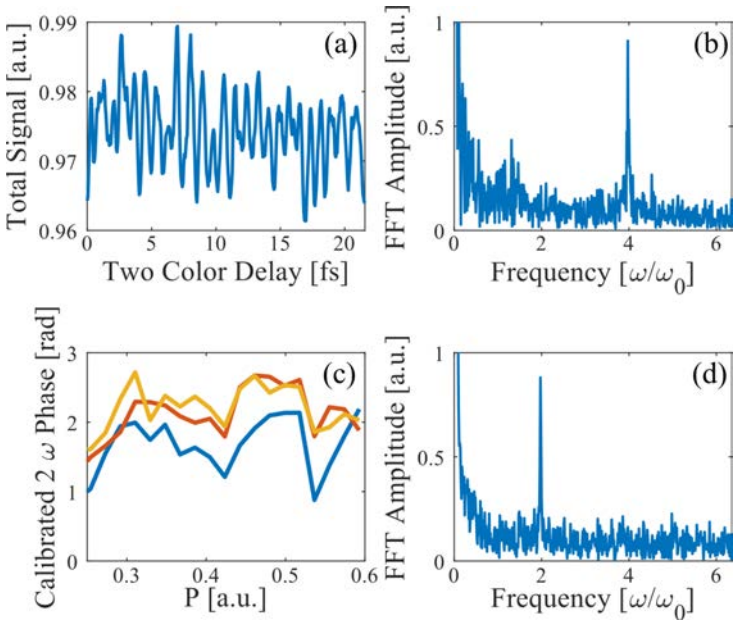


**Figure 4.13** – *Calibration of the two-color phase using $4\omega$ oscillations. (a) Total photoelectron yield of a typical (+)-Fenchone scan as a function of two-color delay, normalized to the maximal total signal in the scan. (b) Fourier transform amplitude of the signal in (a), in units of the fundamental frequency $\omega_0 = 291$ THz, the frequency of the 1030 nm field, showing a clear peak at the $4\omega$ frequency. (c) The phase of the antisymmetric signal as function of momentum P, for three (+)-Fenchone scans. The phases were extracted by averaging over all the pixels with the same total signal momentum in one quarter of the detector, for each image in the scan, and calculating the Fourier transform of the time evolution of this averaged signal. Then the phase of the $2\omega$ Fourier component was extracted, and calibrated according to the $4\omega$ oscillation phase of the total signal. The calibration is tested only for momentum higher than 0.25 a.u. since one can see in Fig. 4.14 in lower momenta, the asymmetric signal changes sign many times within each quarter of the detector, and therefore averaging over each quarter is meaningless. (d) An example for the Fourier transform amplitude of the antisymmetric signal for momentum 0.4 a.u., in units of $\omega_0$.*

Note that a $\pi$ uncertainty remains on $\varphi_{\omega/2\omega}$, simply corresponding to a sign change of the instantaneous chirality, meaning that we only access here the shape of the field and not which way it is rotating. This only yields a sign uncertainty in the chiral signal, which is not such a relevant feature. Again, the method presented in the next section enables to lift off this ambiguity.

**Experimental Results**

Fig. 4.14 shows the ESCARGOT measurement performed in (+)-Fenchone at $I_\omega = 2 \times 10^{13}$ $W.cm^{-2}$ and $7 \times 10^{13}$ $W.cm^{-2}$, and in (+)-Camphor at $3 \times 10^{13}$ $W.cm^{-2}$, respectively in the first, second and third row. The intensity ratio was kept at $I_{2\omega}/I_\omega = 0.1$, corresponding to a field ratio of $r = 0.3$. Note that the electric field shape is included in each caption, but the polarization plane is not the one detected in this VMI configuration, the laser propagation axis being the horizontal axis here. The left column depicts the total distribution, while the other ones show the ESCARGOT signal for $\varphi_{\omega/2\omega} = \{0, \pi/4, \pi/2, 3\pi/4, \pi\}$. The rest of the range between $\pi$ and $2\pi$ is just the same panel with an opposite sign. One can observe in panel (a) and (m) that the total distributions at low intensities show characteristic energy structures. The rings up to 0.2 a.u. correspond to the ionization of different orbitals in a 8-photon absorption scheme of the dominating fundamental $\omega$ field, for both Fenchone and Camphor. In Fenchone, the first ATI of the dominant component around 0.15 a.u. is visible at 0.35 a.u., a well as a very weak second ATI around 0.45 a.u.. In Camphor, the dominant feature appears around 0.1 a.u., and the corresponding ATI appear around 0.3 and 0.4 a.u.. This is a typical behavior of the strong field regime, which is close to be reached here : since the tunnel ionization drastically decreases with the energy of the orbital ionized, most of the signal originates from the HOMO. On the other hand, the distribution at higher intensity (g) goes towards a well-established strong field regime : it is much more continuous because of the broadening induced by the ponderomotive shift, the energy of the ATI cutoff increases and the distribution gets narrower along the vertical axis (the $\omega$ polarization axis).

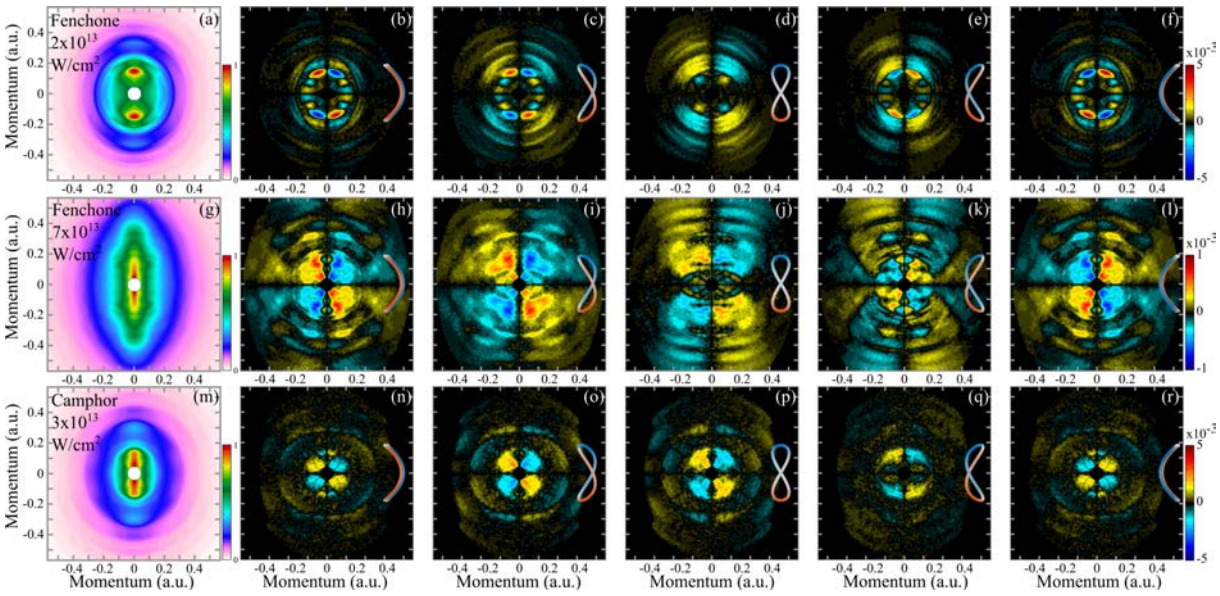


**Figure 4.14** – *Experimental data from the Fourier analysis of the VMI images. (a,g,m) Normalized projections in the VMI plane of the the photoelectron angular distribution for (a) (+)-Fenchone with a fundamental field of 2 $\times 10^{13}$ $W.cm^{-2}$ (g) (+)-Fenchone at 7 $\times 10^{13}$ $W.cm^{-2}$ and (m) (+)-Camphor at 3 $\times 10^{13}$ $W.cm^{-2}$. (b-f),(h-l),(n-r) Evolution of the ESCARGOT signal as a function of the relative phase $\varphi_{\omega/2\omega}$ between the two components of the ionizing field ($\varphi_{\omega/2\omega}$ = 0, $\pi/4$, $\pi/2$, $3\pi/4$ and $\pi$ from left to right). The shape of the two-color field, colored according to the instantaneous chirality, is shown next to each image. The ESCARGOT signal is normalized to the maximum of the photoelectron spectrum in (a,g,m). The data is presented after up-down antisymmetrization.*

The first and main feature of these results is of course the presence of a forward/backward

asymmetric ESCARGOT signal in the order of $0.1 - 0.5\%$ of the total signal, with an up/down sign inversion expected from the change of instantaneous chirality along the optical cycle. This confirms experimentally that the dynamics of the photoelectron in the vicinity of the chiral potential occurs at the sub-optical cycle scale, *i.e.* in the sub-3.4 $fs$ range. Noticeably, this occurs at all two-color phases, even for the "C"-shaped OTC field. Secondly, one can see that the distributions are strongly dependent on $\varphi_{\omega/2\omega}$, and can range at low intensity in (+)-Fenchone (b-f) from a quite continuous fourfold pattern like in Fig. 4.14 (d) to a much more structured pattern involving sign change between electrons with the same kinetic energy (e.g. (b)). Interestingly, at higher intensity (h-l), the structure becomes less dependent to the two-color phase and only shows a global sign change between (j) and (k). This behavior is also reproduced in (+)-Camphor, an isomer of Fenchone, at lower intensity (n-r) between panels (q) and (r). By comparing the results obtained in Fenchone and Camphor at low intensity (first and third rows), it appears that the distribution at this intensity range depends strongly on the molecular potential. Moreover, the amplitude of the ESCARGOT signal decreases at higher intensity. Qualitatively, this can be understood as the molecular potential plays a less important role towards strong field regime.

At first sight, one could expect that the electric field configuration used in (c) and (e) should give the same ESCARGOT signal, since the fields shapes are just mirror imaged along a dimension which is summed in the VMI projections. This is not the case at all, and reflects the dynamical origin of the ESCARGOT signal : while the shape of the fields are indeed mirrored, the rotation of the field vector along these shapes is inverted. This can be visualized with the colorscale of the field shape in the caption of each panel, as a positive instantaneous chirality (in red) corresponds to a clockwise rotation and a negative IC (in blue) corresponds to a anti-clockwise rotation. This means that not only the shape, but also the dynamical evolution of the optical cycle matters here.

Another dynamical aspect of the process lies in the fact that a significant amplitude of ESCARGOT signal can be measured at every two-color phase. Demekhin *et. al.* claimed that this was not possible, for a purely geometric argument [Demekhin 18] : in particular with a "C"-shaped field ($\varphi_{\omega/2\omega} = 0$ or $\pi$), the instantaneous chirality of the clockwise and anticlockwise components should cancel out. We thus see here that not only the geometric, but also the dynamical aspects of the driving field play a role. This latter breaks the perfect reversal between the two components and as a result, one of them can overcome the other. A further discussion will be proposed later in this manuscript.

**Robustness and Validity of the Measurements**

The error margin of the measurement has been estimated by splitting the 270 fs scan in 10 scans of 27 fs each. The 95% confidence interval has been calculated by statistical analysis (such as detailed in Section 3.II). This yielded a maximum $0.5 \pm 0.1\%$ dichroic signal for Fenchone at low intensity, while it reaches a lower value of $0.10 \pm 0.03\%$ at high intensity. The ESCARGOT signal is thus decently above the errorbar.

A common practice in chiroptical measurements consists in comparing the signal obtained

from opposite enantiomers. Unfortunately, this procedure is not possible here, because of the absolute sign ambiguity in the instantaneous chirality of the laser field. To circumvent this issue, we performed the ESCARGOT measurements in a racemic mixture of Fenchone, which contains both enantiomers in equal proportions. The results are presented in Fig. 4.15, and compared to those obtained in a pure enantiomer, with the same colorscale. The signal in the racemic mixture completely vanishes in the low intensity case, validating the chiral sensitivity of the measurement. At high intensity, a non-zero ESCARGOT signal is detected, showing sharp structures. This signal originates from artifacts in the photoelectron imaging. It is however clearly lower and more localized than the signal obtained in the pure enantiomer, ensuring that the ESCARGOT signal in (+)-Fenchone is also genuine at high intensity.

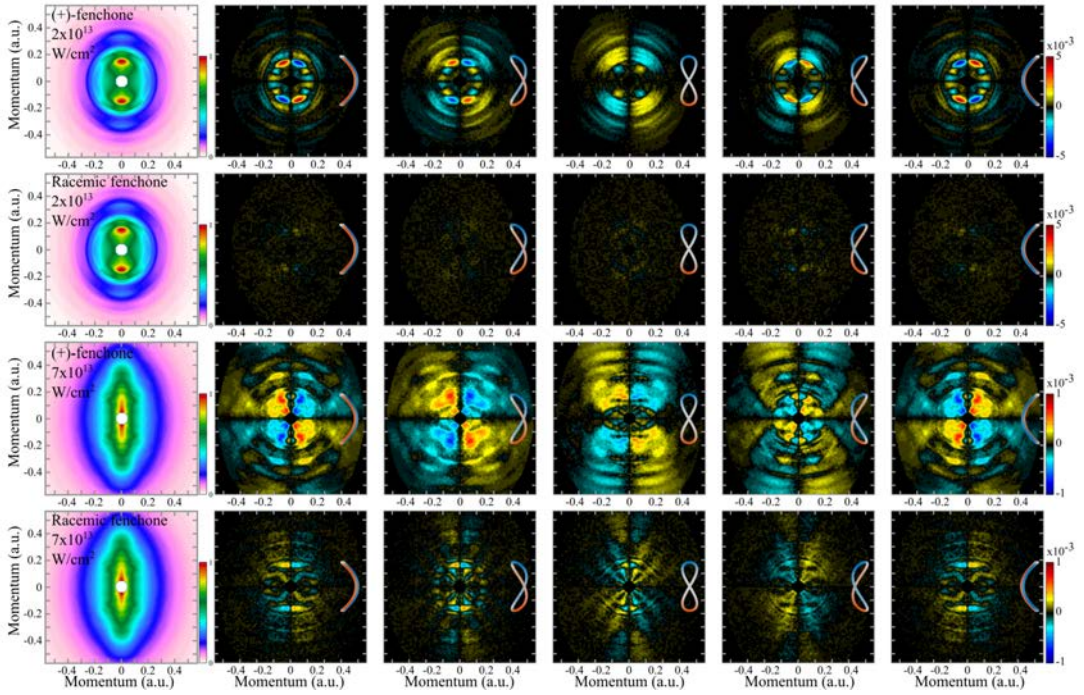


**Figure 4.15** – *Comparison of the ESCARGOT signal obtained in (+)-Fenchone (first and third rows) and a racemic mixture (second and forth rows), at* $2 \times 10^{13}$ *W.cm*$^{-2}$ *and* $7 \times 10^{13}$ *W.cm*$^{-2}$.

Data presented up to now were up/down antisymmetrized, to follow the expected symmetry of the ESCARGOT signal. The results obtained without the antisymmetrization procedure are shown in Fig. 4.16. These raw results are mostly up/down antisymmetric, which justifies the numerical antisymmetrization of the ESCARGOT.

In order to confirm and get a better insight of the features shown by the experimental results, we will compare them to numerical simulation.

## II. 3 Numerical Time-Dependent Schrödinger Equation Resolution

The following modeling has been mainly performed by Bernard Pons from our group. Time-Dependent Schrödinger Equation (TDSE) calculations consists in numerically propagating the wavefunction with a discrete iteration timestep, on a discrete spatial grid. In principle, it does not neglect any effect (such as the influence of the potential), works at any regime and is only

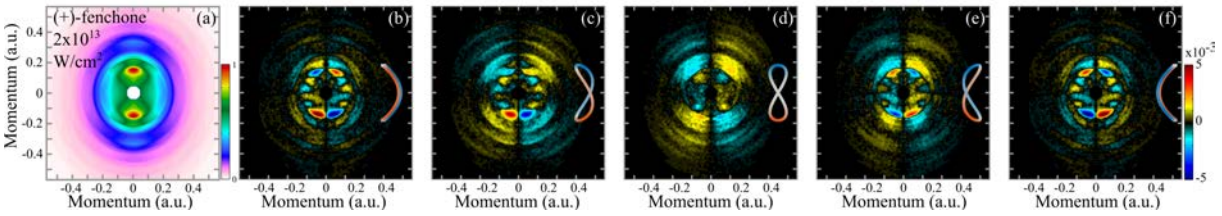


**Figure 4.16** – *Experimental data without up-down antisymmetrization. (a) Normalized projection in the $(x, z)$ plane of the the photoelectron angular distribution for (+)-Fenchone with a fundamental field of 2 $\times 10^{13}$ $W.cm^{-2}$. (b-f) Evolution of the ESCARGOT signal as a function of the relative phase $\varphi_{\omega/2\omega}$ between the two components of the ionizing field. The shape of the two-color field, colored according to the instantaneous chirality, is shown next to each image. The ESCARGOT signal is normalized to the maximum of the photoelectron spectrum in (a).*

limited by the numerical precision of the grid. However, as this type of calculation can become extremely demanding in processing power, the grid can not be arbitrarily large and arbitrarily finely discretized, and numerical tricks are often required (see paragraph below for more details). The calculations presented here have been performed in a toy-model chiral molecule, where the nuclei are frozen in a chiral geometry , as it is the simplest chiral potential that can be engineered. This system, also known as Bernardine (in honor of its creator Pr. Bernard Pons) is built with four nuclei located at $\vec{R}_0 = \vec{0}$, $\vec{R}_1 = \vec{x}$, $\vec{R}_2 = 2\vec{y}$ and $\vec{R}_3 = 3\vec{z}$, in atomic units, with respective charges $Z_0 = -1.9$ $a.u.$ and $Z_{1-3} = 0.9$ $a.u.$. The field-free Hamiltonian that will apply to the single-electron wavefunction is then $\mathcal{H}_0 = -\frac{1}{2}\nabla^2 - \sum_{i=0}^{3} \frac{Z_i}{|\vec{r}-\vec{R}_i|}$ where $\vec{r}$ is the position of the electron. The calculation then consists in numerically solving the Schrödinger equation :

$$\left(-i\frac{\partial}{\partial_t} + \mathcal{H}_0 + \mathcal{V}(\vec{r}, t)\right)\Psi(\vec{R}, \vec{r}, t) = 0 \tag{4.17}$$

where $\mathcal{V}$ is the oscillating field potential in the electric dipole approximation as written in Eq. (4.5). The goal of using such a simple toy-model molecule is of course not to grasp the fine structures of the molecular potential but to see what general features can be identified. It has been designed here so that its fundamental state, depicted in Fig. 4.17, has an ionization potential $I_p = 8.98$ $eV$, in the range of the ones of Fenchone and Camphor. Note that the standard one-photon PECD in this toy-model molecule is about 2% with circularly polarized field.

**Numerical Results**

The calculated 3D photoelectron distributions have been integrated along the $2\omega$ polarization axis to be comparable with the 2D VMI projection. The calculations, performed for three intensities $I_\omega = 5 \times 10^{12}$ $W.cm^{-2}$, $2 \times 10^{13}$ $W.cm^{-2}$ and $5 \times 10^{13}$ $W.cm^{-2}$ with an field intensity ratio of $I_{2\omega}/I_\omega = 0.1$ are presented in Fig. 4.18 in the same way as the experimental results. One can see in the total signal distribution (a,g,m) that the intensities used here cover the transition between the multiphoton and the strong field regime, with many ATI rings.

The calculations also display a remarkable ESCARGOT signal, for all two-color phases. Interestingly, some remarkable elements found in the experiment are nicely reproduced here. At low intensity, the sign modulations along the low-energy ring (e.g. with the "C"-shaped laser

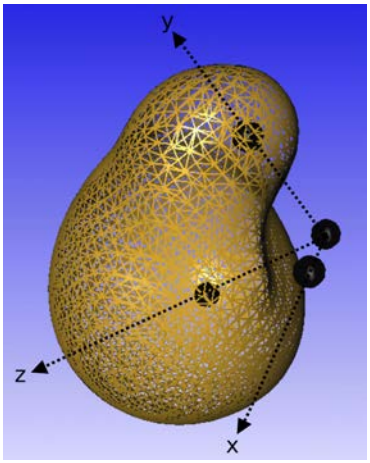


**Figure 4.17** – *Skeleton and isosurface representation of the fundamental state of the toy model chiral molecule employed in the TDSE calculations.*

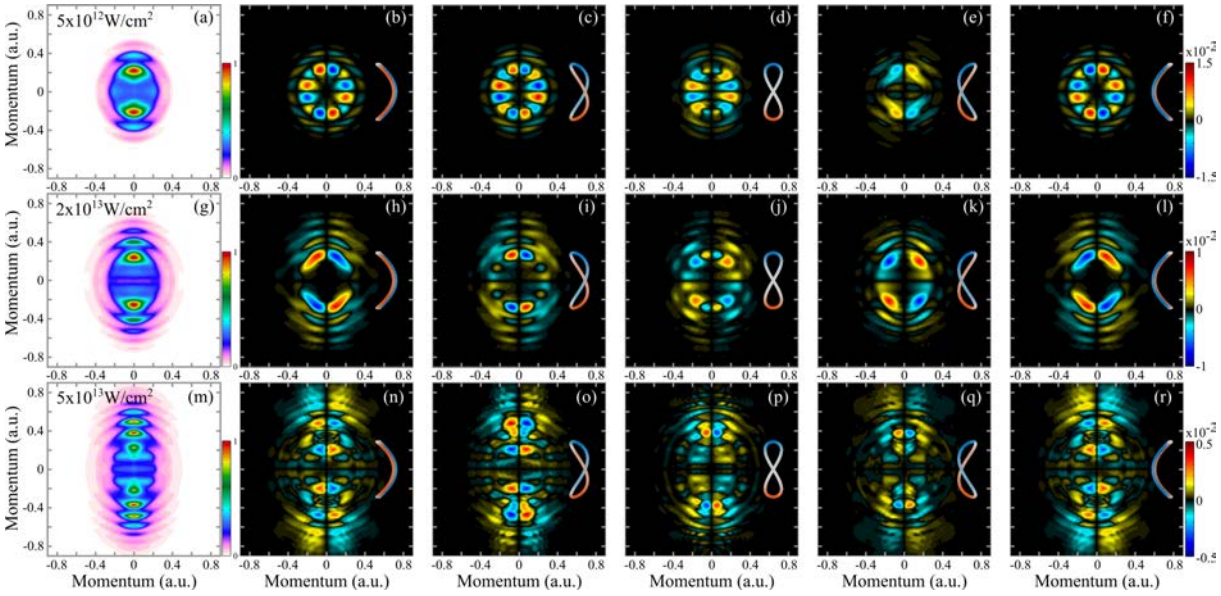


**Figure 4.18** – *TDSE calculations of photoionization of a toy model chiral molecule by the tailored orthogonal two-color field. (a,g,m) Projections in the $(x, z)$ plane of the symmetric part of the photoelectron spectrum, at $5 \times 10^{12}$ $W.cm^{-2}$ (a), $2 \times 10^{13}$ $W.cm^{-2}$ (g) and $5 \times 10^{13}$ $W.cm^{-2}$ (m) . (b-f),(h-l),(n-r) Corresponding projections of the ESCARGOT signal, defined as the antisymmetric part of the photoelectron distribution with respect to the propagation axis $z$ and fundamental laser polarization axis $x$. The relative phase between the two components of the laser field are $\varphi_{\omega/2\omega} = 0$, $\pi/4$, $\pi/2$, $3\pi/4$ and $\pi$ from left to right. The shape of the two-color field, colored according to the instantaneous chirality, is shown next to each calculation.*

field in (b)) also disappear for a different two-color phase (e). While increasing the intensity to the intermediate value (second row), one can see that these modulations tend to reduce as the field becomes more prominent compared to the molecular potential. The amplitude of the asymmetric part of the signal also diminishes with intensity, (respectively from 1.5% to 1.0% to 0.5%) in a way that when the strong field regime is well established (third row), the signal coming from the ATI rings dominates and the distribution sharpens along the field axis. In-depth comparison will be detailed in further section.

**Method of the Calculation**

Details about the calculation itself can be found in [Rozen 19]. One way to perform the spatial discretization for the TDSE calculations is to define a cartesian grid on which each unit is affected by the surrounding ones at each timestep, using a numerical propagator function derived from the analytical Schrödinger equation. An alternative, used here, consists in expressing the wavefunctions spatially on a basis of physically meaningful functions. The basis of functions used are the $j_l(k_l r)\mathcal{Y}_{lm}^{sin,cos}(\Omega_r)$ with $0 \leq l \leq l_{max}$ and $-l \leq m \leq l$, where $l$ and $m$ are the angular and magnetic quantum numbers respectively. $\mathcal{Y}_{lm}^{sin,cos}$ are sine and cosine real spherical harmonics, describing the angular dependency, and $j_l(k_l r)$ are spherical Bessel functions, describing the radial part of the functions. As the basis is necessarily finite, the parameters were bounded to $r_{max} = 200\ a.u.$, $l_{max} = 10$ and $k_{max} = 7\ a.u.$. It is important in this situation to verify whether the results are affected by these boundaries or not. Indeed, if the grid is too small, *i.e.* a non-negligible electronic density reaches the boundaries within the temporal range of the calculation, the end of the grid (a purely numerical limitation) will act as a "wall" on which the wavefunction can bounce back. To make sure this is not the case, a convergence check was performed, which consists in doing the calculation on a larger grid and see if it influences the results. This is especially sensitive at high intensity, as the wavefunction can be excited to high $l$ (this is the mathematical equivalent of saying that the distribution get peaked along the field) and that large $r$ can be reached because of the numerous ATI peaks. The convergence check in $l$ is presented in Fig. 4.19, where the same calculations using $l_{max} = 10$ and $l_{max} = 14$ are depicted. The total signals (a) and (c) can not be distinguished from each other, while the ESCARGOT signal (b) and (d) is also in good agreement. The only noticeable difference in the high momentum values along the vertical ($\omega$ polarization) axis, but is not significant. This type of comparison can be done for all the parameters, but typical signs can also indicate a convergence issue. In particular, the wave structures at the high momentum values along the vertical axis are typical of a reflection of the wavefunction on the boundaries of the spatial box. Since these effects remain localized on the outer features and do not affect the results qualitatively, especially at lower intensities, we assumed that the convergence is verified.

Moreover, as the ESCARGOT signal comes from a randomly oriented target, the calculation must be performed and summed over many molecular orientations. Once again, only a discrete set of orientation can be calculated. In our case, an angular Euler spacing of $\Delta\alpha = \Delta\beta = \Delta\gamma = \pi/4$ was used, corresponding to a total of 256 orientations. This convergence has also been verified, as displayed in Fig. 4.20.

The calculation is also necessarily discretized and limited in the time domain. This is the reason why the fundamental frequency used here was 800 $nm$, with the second harmonic field at 400 $nm$. Compared to the 1030-515 nm used in the experiment, this represents a reduction of about 30% of the laser period, reducing the cost of the calculations. In order to keep the computational load affordable, the calculation has been performed over four optical cycles, corresponding to $\sim 11\ fs$. The envelope of the pulse was designed to be a linear rising slope during the first cycle, flat during the two central cycles and a falling linear slope for the last cycle. The main effect of using such a short pulse appears as a carrier-envelope phase (CEP)

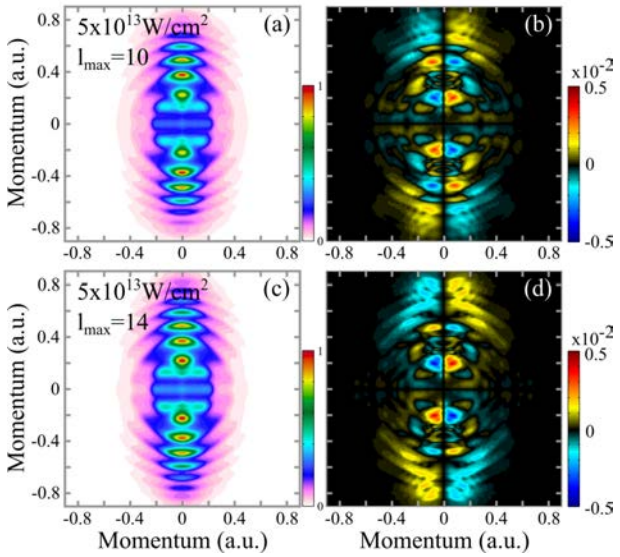


**Figure 4.19** – *Convergence check with respect to the maximum angular momentum included in the TDSE calculations : Symmetric (a) and antisymmetric (b) parts of the photoelectron momentum distribution obtained with $l_{max} = 10$. (c) and (d) are the counterparts of (a) and (b), respectively, obtained with $l_{max} = 14$. All other TDSE parameters are the same in both calculations: $r_{max} = 200$ a.u., $k_{max} = 7$ a.u.,$\Delta\alpha = \Delta\beta = \Delta\gamma = \pi/4$ with a two-color phase of $\varphi_{\omega/2\omega} = 0$.*

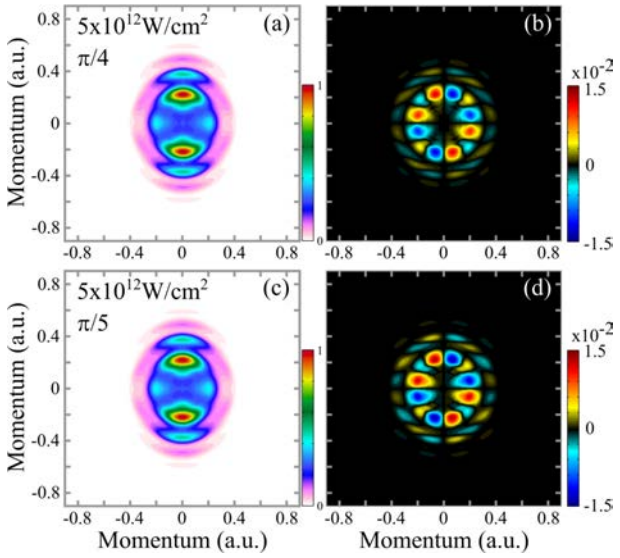


**Figure 4.20** – *Convergence check with respect to the number of random molecular orientations included in the TDSE calculations : Symmetric (a) and antisymmetric (b) parts of the photoelectron momentum distribution obtained with an angular Euler spacing $\Delta\alpha = \Delta\beta = \Delta\gamma = \pi/4$. (c) and (d) are the counterparts respectively of (a) and (b), obtained with $\Delta\alpha = \Delta\beta = \Delta\gamma = \pi/5$. All other TDSE parameters are the same in both calculations: $r_{max} = 200$ a.u., $l_{mac} = 10$ and $k_{max} = 7$ a.u., with two-color phase of $\varphi_{\omega/2\omega} = 0$.*

dependency, *i.e.* the relative phase between the electric field oscillation and its envelope. Indeed, depending on the CEP, the symmetry of the field and the asymmetry of the ESCARGOT signal along the $\omega$ axis can be broken, as shown in Fig. 4.21. The upper panels of this figure represent the electric fields for CEP values of 0, $\pi/2$ and $\pi$, depicted for a two-color phase $\varphi_{\omega/2\omega} = 0$ for clarity. The worst CEP effect in the photoelectron distributions calculated was found at

$\varphi_{\omega/2\omega} = 3\pi/4$, and is depicted on the lower panels for a CEP of 0 (a), $\pi/2$ (b) and $\pi$ (c). However, the effect can be canceled by antisymmetrizing the distribution along the fundamental field axis. The ESCARGOT signal becomes independent of the CEP, as shown in panels (d), (e) and (f). Note that in the experiment, as the laser pulse duration was much longer, this effect was completely negligible and this operation was performed to get rid of the experimental artifacts.

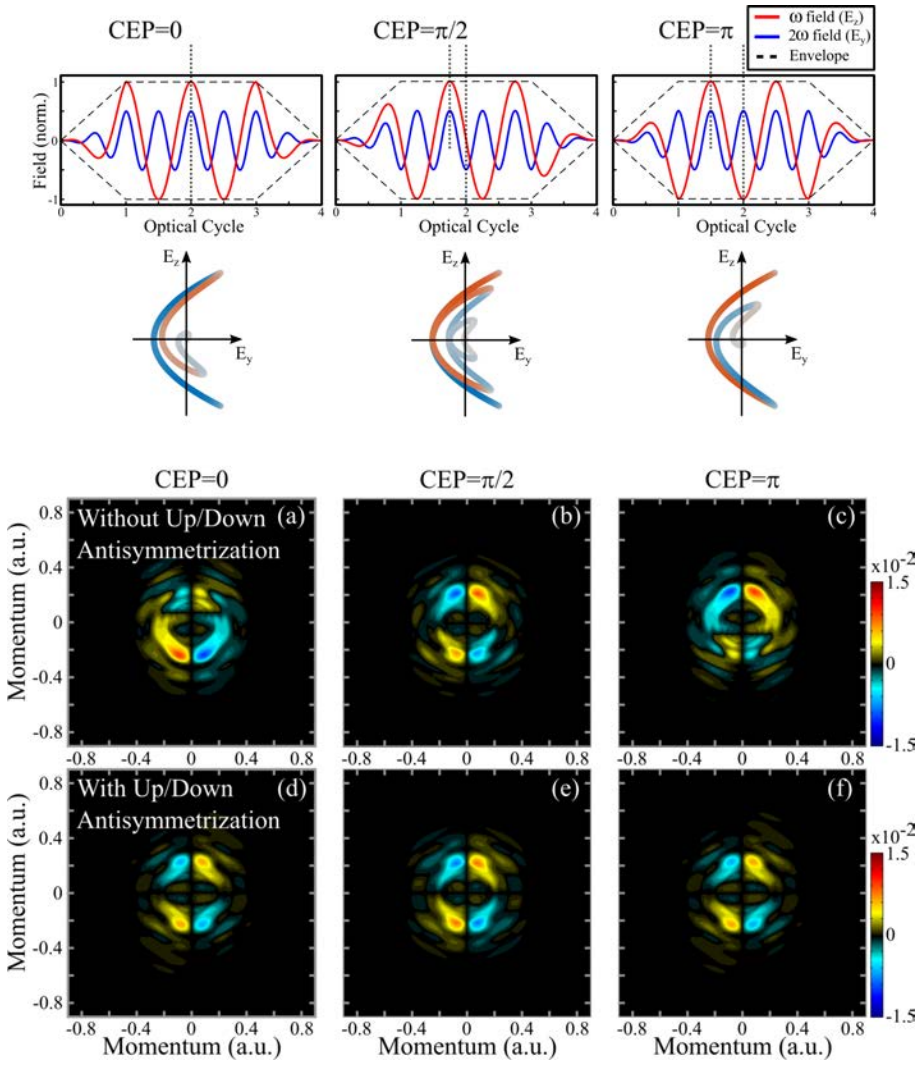


**Figure 4.21** – *(Upper panels) Visualization of the CEP on the shape of the orthogonal two-color electric field, for CEP phases of 0, $\pi/2$ and $\pi$, depicted for a two-color phase $\varphi_{\omega/2\omega} = 0$ for clarity. (Lower panels) Influence of the carrier-envelop phase $\phi_{CEP}$ in the TDSE calculations at 5 $\times 10^{12}$ W.cm$^{-2}$ and for a two-color phase $\varphi_{\omega/2\omega} = 3\pi/4$. (a-c) Projections of the ESCARGOT signal, defined as the antisymmetric part of the photoelectron distribution with respect to the propagation axis $x$. (d-f) Corresponding signal, antisymmetrized along the fundamental laser polarization axis $z$. The carrier-envelop phase is $\phi_{CEP} = 0$ in (a,c), $\phi_{CEP} = \pi/2$ in (b,e), and $\phi_{CEP} = \pi$ in (c,f).*

## II. 4 Interpretation in Terms of Electron Trajectories

Both experiment and TDSE simulations show characteristic features that have to be understood. To do so, a simple model based on a typical strong field picture has been developed. It consists

in calculating the classical trajectories, starting with zero momentum at the exit of the tunnel barrier, under the influence of the OTC field only. The influence of the ionic core is neglected in the calculation of the trajectories, but it is of course of crucial importance for the chiral response. This aspect is artificially added to the model by considering an effective asymmetric interaction between the chiral potential and the chiral field. More precisely, this means weighting every trajectory calculated by the instantaneous chirality of the field while the electron is within a certain range. Here we model this range with a Gaussian function with a FWHM of $r_0 = 1$ $nm$ centered at zero. In other words, the asymmetric interaction fades out with the distance, and the integrated value of the IC along each trajectory reflects the ESCARGOT signal. This model is very qualitative, and we developed it in 1D along the $\omega$ polarization axis as this field dominates the dynamics of the photoelectrons ($I_{2\omega}/I_\omega = 0.1$ throughout this study).

Results are shown in Fig. 4.22 for photoelectrons ionized during an optical cycle. The red line in the first panel (a) depicts the $\omega$ electric field and the shaded area corresponds to the final kinetic energy of the electrons along this field axis, born at the corresponding time. The final kinetic energy is maximized for the electrons born when the field is minimal and *vice-versa*. They end up in the negative $z$ range when they are emitted in a falling slope of the field and in the positive $z$ range if emitted in a rising slope. A few typical electron trajectories are shown in (b) and (c), respectively in the cases $\varphi_{\omega/2\omega} = \pi/2$ and 0. Note that only the IC differs from between these two panels. The value of the instantaneous chirality is encoded in the color of the lines.

As the kinetic energy curves in (b) show, two electron trajectories lead to the same final energy on each side (up and down) of the detector : $e_1$ and $e_2$ for the lower part and $e_3$ and $e_4$ for the upper part. The instantaneous chiralities experienced by the electrons 1 and 2 are exactly opposite at their time of birth. However, the chiral response is not expected to be instantaneous, but to be accumulated during the departure of the electrons from the region of influence of the ionic potential, typically 1 nm from the core. In the case of the "8"-shaped electric field (b), trajectory $e_2$ (born at $t_i = 0.3T_0$ where $T_0 = 3.44$ fs corresponding to 1030 nm) escapes the core quite rapidly and experiences only a given sign of IC in the vicinity of the core. Electrons $e_1$, born at $t_i = 0.2T_0$, sees a small opposite IC for a short time until $0.25T_0$ (hardly visible in the color scale), but is mostly affected by the negative IC for the rest of its trajectory. This means that these two trajectories, both ending on the lower part, will have a very similar integrated IC, yielding one given sign of ESCARGOT signal. A symmetric situation is found $0.5T_0$ ($\sim 1.7$ fs) later with electrons $e_4$ and $e_5$, that will be imprinted with the opposite chirality and will end up on the other side. This entanglement between $p_z$ and the IC sign explains the up/down antisymmetry of the ESCARGOT. This picture is slightly more complex for low kinetic energy electrons such as $e_3$, as they spend more time in the vicinity of the core and get alternatively affected by opposite IC. This could induce a drop in the signal for the trajectories ending with low momentum along z, that we can observe in the experiment (Fig. 4.14 (j)) and in the calculations as we go towards the strong field regime (Fig. 4.18 second and third row).

The situation is slightly different with the "C"-shaped electric field (Fig. 4.22 (c)). Both $e_1$ and $e_2$ experience a sign change of the chirality of the field during their escape. This can mitigate the accumulated value but except for very specific kinetic energy electrons at specific two-color

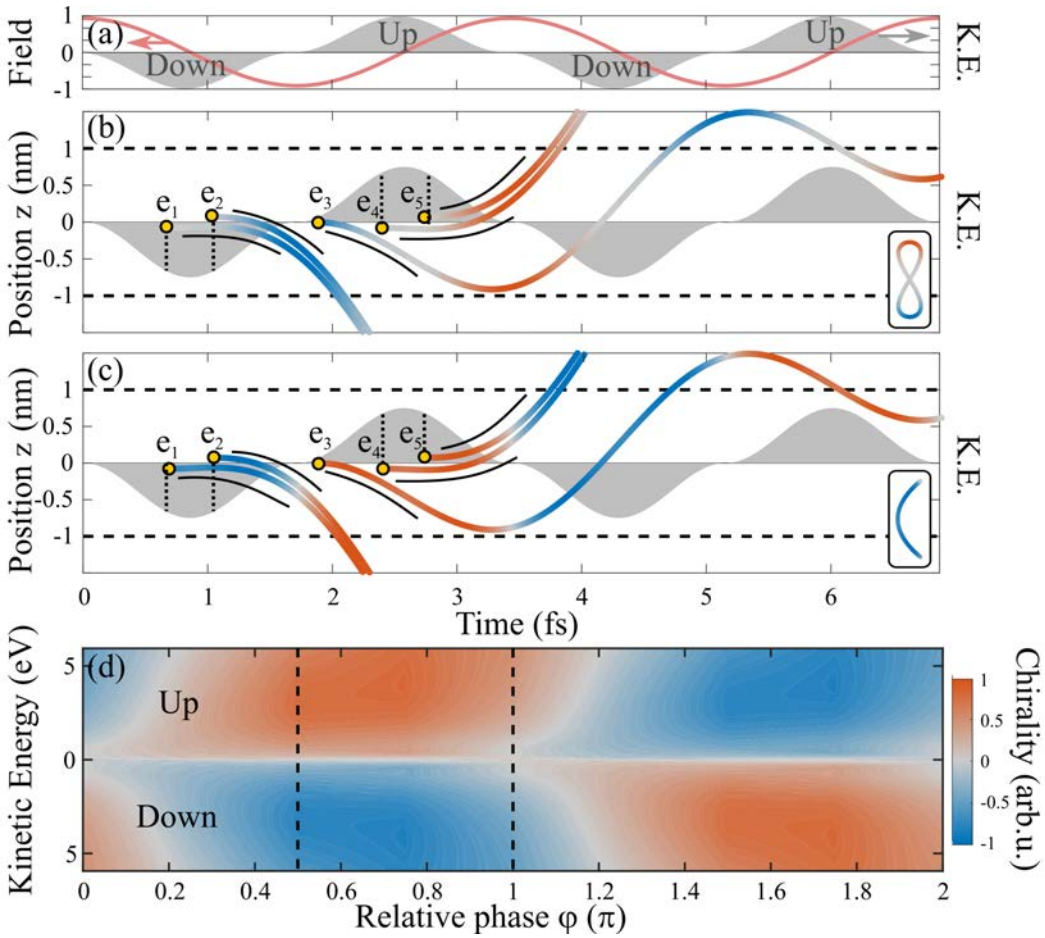


**Figure 4.22** – *Sub-cycle control over the instantaneous chirality of the field. (a) Oscillation of the fundamental electric field (red) and final kinetic energy of the electrons as a function of their ionization time (gray). The kinetic energy is plotted as a positive value for electrons with an upwards final velocity and as negative for electrons with a final downwards velocity, in order to differentiate between electrons reaching each half of the detector. (b-c) Two pairs of electron trajectories ($e_{1,2}$ and $e_{4,5}$), each pair leading to the same final kinetic energy, and a trajectory of a low energy electron ($e_3$). The trajectories are plotted for $\varphi_{\omega/2\omega} = \pi/2$ (b) and $\varphi_{\omega/2\omega} = \pi$ (c). The colormap depicts the instantaneous chirality of the field. (d) Instantaneous chirality integrated over the time duration in which each electron is closer than 1 nm to the molecular core, as a function of the two-color phase and final kinetic energy of the electron. The quantity is averaged over the trajectories contributing to each final photoelectron kinetic energy.*

phases, it remains not equal to zero. The rest of the predictions made for the "8"-shaped field remains valid.

The value of the instantaneous chirality integrated over a 1 $nm$ gaussian range experienced by photoelectrons within 5 $eV$ kinetic energy as function of the two-color phase is shown on Fig. 4.22 (d). The quantity displayed is averaged over the trajectories contributing to each final photoelectron kinetic energy, in order to mimic the final signal. The two cases presented above correspond to the dashed lines. Overall, the model emphasizes the sensitivity of the ESCARGOT signal to the electron trajectories in the vicinity of the chiral potential, under the influence of the chiral field.

### II. 5 Discussion and Perspective

We have seen that in the strong field regime, the trajectories of the photoelectrons were driven by the laser electric field and vector potential. Tailored fields can be generated to finely drive the dynamics of the photoelectrons at the attosecond and molecular level. In the domain of molecular chirality, this study demonstrates experimentally and theoretically that the concept of instantaneous rotation, or instantaneous chirality of the field can be relevant for chiroptical measurements. Indeed, beyond the cycle-averaged definition of the polarization of light, sub-optical cycle instantaneous chirality can be imprinted to the dynamics of the electrons emitted from a chiral molecule, yielding an asymmetric signal typical of the dichroic interaction at the basis of the PhotoElectron Circular Dichroism. We have seen that in the case of bilinear bichromatic fields that this response can be observed at any two-color phase, from the multiphoton to the strong field regime. When going toward strong fields, the signal becomes less complex and less prominent as the field starts to overcome the chiral molecular potential. A strong field picture of classical electron trajectories helps understanding the qualitative features of the ESCARGOT signal, such as antisymmetry along the $\omega$ axis, sensitivity to the two-color phase and globally grasps the dynamical buildup of the process.

However, beyond this qualitative description, several features remain unclear. Firstly, fine details of the molecular potential can drastically affect the interaction, as we see from the comparison between two isomers, Fenchone and Camphor (Fig. 4.14). Secondly, structures in the ESCARGOT patterns such as sign inversion or modulations of the signal along a radius of constant kinetic energy (especially at low kinetic energy) are measured and calculated. One can suspect quantum interference to be at the origin of this. Indeed, as we have seen, several electron trajectories born at different times, that have experienced different instantaneous chirality, can end up with the same final momentum. This is known to produce interference patterns, as we have seen in previous section with photoelectron interferometry. Although this effect should arise in the polarization plane, which is not accessed here, this might be revealed in a Velocity Map Imaging configuration by the asymmetry of the interaction, along the laser propagation axis $x$. This perspective gives strong motivations for extending this study with a device capable of 3D photoelectron angular distribution measurement, such as a COLTRIMS, as we will see in the next section.

## III Three-Dimensional Chiral Photoelectron Interferometry

The study presented in this chapter has also been carried out in collaboration with Shaked Rozen and Nirit Dudovich from the Weizmann Institute of Science, Israel. It is currently in preparation for publication.

### III. 1 Mapping of the Vector Potential

As mentioned in the introduction of this chapter, orthogonal bilinear bichromatic (or orthogonal two-color, OTC) fields have already been proved to be interesting in the strong field ionization of achiral targets [Zhang 14a, Richter 15, Richter 16]. In a the Strong Field Approximation (SFA)

presented in the introduction of this chapter, the conservation of the canonical momentum can be derived and a simple mapping relates the final photoelectron momentum $\vec{p}_f$ with the vector potential at the ionization time $\vec{A}(t_i)$, where $\vec{E} = -\frac{\partial \vec{A}}{\partial t}$, as :

$$\vec{p}_f = -\vec{A}(t_i) \tag{4.18}$$

with a certain distribution. The relevant quantity here is thus not the electric field but its corresponding vector potential. The qualitative principle of the photoelectron interferometry is depicted in Fig. 4.23 (1). The two limit shapes of the orthogonal bilinear bichromatic field are displayed here. In panel (1-a), the "8"-shaped electric field has a corresponding "C"-shaped vector potential, and in (1-b) the "C"-shaped electric field has an "8"-shaped vector potential. Note that the colorbars used for both the field and the vector potential correspond to the instantaneous chirality of the field, and can be used to visualize the temporal mapping. In each case, the projection of the photoelectron distribution in the polarization plane calculated with the SFA model is presented, and several features stand out.

Firstly, the photoelectrons can be ionized at different times within the optical cycle, and the tunneling rate given in Eq. 4.6 associates the high probability to the maxima of the field, depicted in full arrows in the figure. Conversely, the low probabilities are shown in dotted arrows and originate from low field amplitudes. As a consequence, the majority of the signal yielded appears in the low kinetic energy region. Note that the concentric ring pattern originates from the repetition of the optical cycle over time, and corresponds to the Above-Threshold Ionization (ATI) peaks. Secondly, the $2\omega$ component of the field (along $y$) clearly distorts the vector potential, either in a "C"- or "8"-shaped depending on the two-color phase (respectively $\varphi_{\omega/2\omega} = -\pi/2$ and $\varphi_{\omega/2\omega} = 0$). This clearly affects the distribution and dresses the trajectories along the $y$ axis, creating a strong asymmetry in panel (1-a) which follows $-\vec{A}$ while leaving the pattern symmetric in (1-b).

The distortion of the vector potential can be used to control the photoelectron trajectories. The photoelectron angular distributions experimentally obtained in argon in [Richter 15] for the single-color and the two-color cases are compared in Fig. 4.23 (2-a) and (2-b). They firstly show that the photoelectron trajectories can indeed be dressed by the second harmonic field, in particular toward one half of the detector. Furthermore, with the "C"-shaped vector potential used here, two photoelectron trajectories tunneled out at different times within the optical cycle (either during the clockwise or the anticlockwise half-cycles) can end up with the same momentum. As a result, a strong modulation is visible across the whole distribution, corresponding to the intracycle interferences described in the introduction of this chapter. The authors have also shown that this modulation could be controlled with the two-color phase, as displayed in the panels (3). Depending on the shape of the vector potential, photoelectron trajectories can indeed either end up in one or the other half of the detector, when inverting the "C" shape. Additionally, tailoring an "8"-shaped vector potential spatially splits the two solutions. As a result, the interferences vanish.

The orthogonal two-color field is thus very interesting for controlling and disentangling

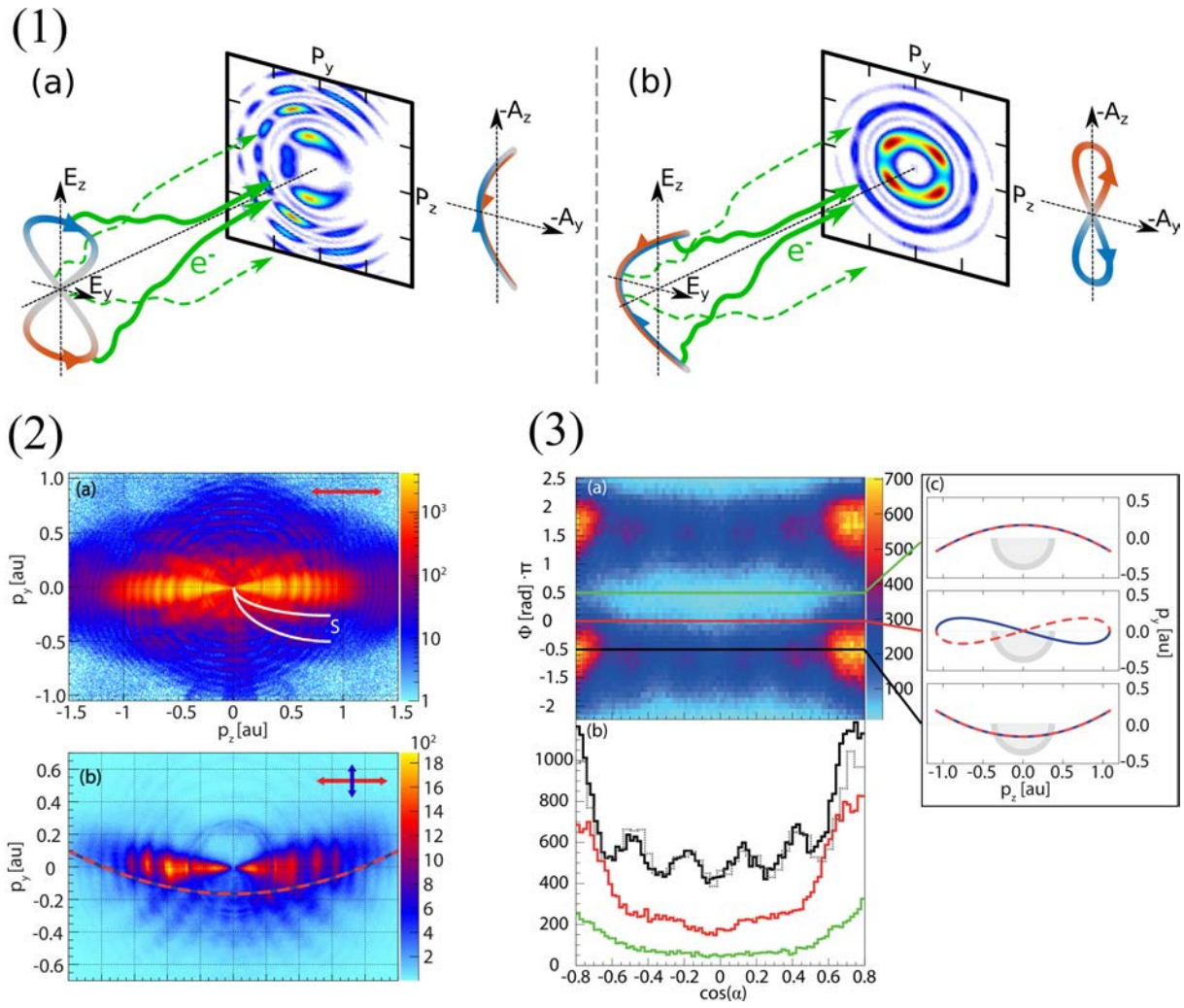


**Figure 4.23** – *(1) Schematic representation of the photoelectron interferometry using a tailored field. The mapping of the final photoelectron momentum is given by the vector potential at the ionization time. High ionization probabilities are depicted with the full green arrows while the low probabilities are shown with dotted arrows. (1-a) "8"-shaped electric field, with a corresponding "C"-shaped vector potential. (1-b) "C"-shaped electric field, with a corresponding "8"-shaped vector potential. The colors used for both the field and the vector potential correspond to the instantaneous chirality of the field, and can be used to visualize the temporal mapping. (2) Photoelectron distributions obtained in argon with* $I_{780nm} = 1.4 \times 10^{14}$ $W.cm^{-2}$ *(2-a) and with an additional orthogonal second harmonic with an intensity ratio of* $I_{390nm}/I_{780nm} = 0.09$ *and a "C"-shaped vector potential (2-b). The orientation of the fields are depicted in each panel and the vector potential is indicated by the dashed line. (3) Evolution of the interferences on one half of the detector as a function of the two-color phase. (3-a) Dependence of the spatially-integrated pattern with the two-color phase and* $p_z/p_{total}$*. (3-b) Lineouts of the photoelectron signal for different two-color phases. The corresponding shape of the vector potential is depicted in (3-c). (2) and (3) are adapted from [Richter 15].*

the different contributions of the photoelectron trajectories. The patterns obtained reveal the phase of the emitted photoelectron wavepacket. This phase can be related to two terms : the initial phase and the phase individually accumulated during the scattering, and such for each interfering trajectory. In [Han 17], it has been demonstrated that these controlled interference patterns can reveal the sub-barrier phase acquired by the wavepackets upon tunneling. These studies were performed in achiral targets, so the instantaneous chirality of the

field was not playing a role. Can we use this interferometric scheme to access these quantities that were missing in the ESCARGOT study? Can we expect such quantities to be affected by the chiral nature of the interaction? Can different trajectory reveal different aspects of this interaction? The distinction of the trajectories is particularly hard in the VMI projections, and the resolution is obtained here in the polarization plane of the laser field. Does the resolution of this third dimension explain the origin of the VMI projections presented in the previous study?

The interferences we will be interested in correspond to the direct trajectories [Li 16, Maxwell 17] discussed in the introduction of the chapter, and their pattern in the one-color case has been given in Eq. 4.12. Qualitatively, we do not expect the second harmonic field to drastically modify the pattern itself, since the fundamental field still is dominant and the mapping still scans the projection plane up and down along an optical cycle. We rather expect modulations of its amplitude according to the overlap of the trajectories, as just explained, and potentially of its phase depending on the different effects at play.

## III. 2 Chirality in the Photoelectron Interferometry : TDSE Support

**Three-Dimensional Picture**

On the one hand, the photoelectron interferometry is accessible in the polarization plane and the mapping associated enables the sub-optical cycle assignment of the ionization time. On the other hand, the dichroic signal in which the chiral interaction between the chiral potential and the instantaneous chirality of the field is encoded along the laser propagation axis. The complete 3D resolution of the photoelectron distributions is thus necessary, in order to combine these two aspects of the strong field ionization by the tailored laser field.

The distributions have been calculated by numerically solving the Time-Dependent Schrödinger Equation (TDSE) in a toy-model chiral molecule. The method is presented in the previous section. The results obtained at a field intensity of $I_{800nm} = 2 \times 10^{13}\ W.cm^{-2}$ and $I_{400nm} = 2 \times 10^{12}\ W.cm^{-2}$, for a two-color phase $\varphi_{\omega/2\omega} = -\pi/2$ ("8"-shaped electric field and "C"-shaped vector potential) are presented in Fig. 4.24. Isosurfaces of the symmetric part of the distribution (along the laser propagation axis) are depicted in the panel (a). Note that only an up/down symmetrization (along the $\omega$ axis $z$) of the signal is performed here in order to cancel the CEP artifact of the calculations, as already discussed. Its projection in the polarization plane is highlighted in panel (b). In this plane, the distribution clearly follows the "C"-shape of the vector potential. In addition, the interference pattern associated with the direct trajectories is evident. Thus, even though TDSE does not provide a direct way to investigate the details of the electron trajectories, their signature remains clear in the signal. A striking difference can be noted in the projection of the distribution along the $2\omega$ axis, in panel (c). This projection plane corresponds to the one accessible in a standard VMI configuration, as presented in the previous section. This projection appears hardly affected by the dressing field compared to the one-color case, and the ATI rings are the only clear structure. This indicates that the weaker second harmonic field indeed only dresses the photoelectron trajectories along its axis.

The situation greatly differs in the ESCARGOT part of the signal, depicted in panel (d).

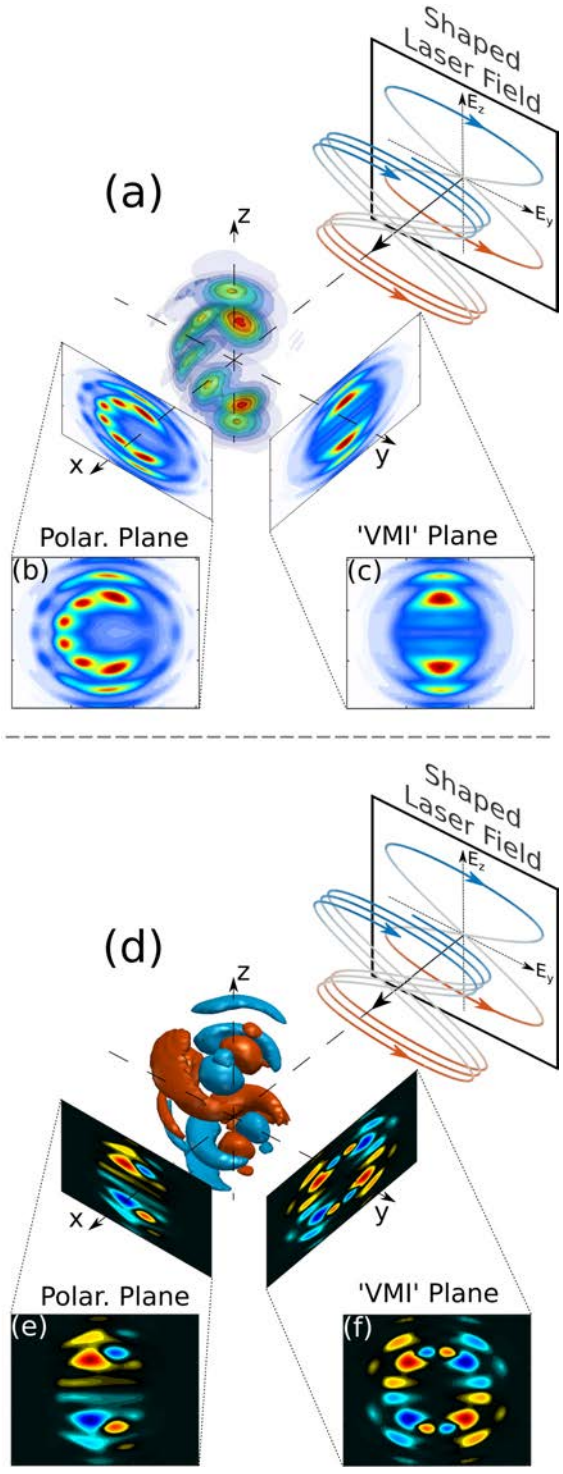


**Figure 4.24** – *Isosurface representation of the complete (a) and chirosensitive part (d) of the 3D photoelectron momentum distributions calculated by TDSE resolution on a toy model chiral molecule. The x,y and z axis are respectively the laser propagation axis, the 2ω polarization axis and the ω polarization axis. The calculations were done with* $\varphi_{\omega/2\omega} = -\pi/2$, $I_{800nm} = 2 \times 10^{13}$ $W.cm^{-2}$ *and* $I_{400nm} = 2 \times 10^{12}$ $W.cm^{-2}$. *Panels (b) and (e) highlight the respective projections in the polarization plane from the target point of view. Panels (c) and (f) show the projections along the 2ω polarization axis, denoted 'VMI' plane here. (d) results from the integration over the positive* $p_x$ *half of the distribution and the other panels from the integration over the whole respective axis.*

It is obtained by taking the forward/backward antisymmetric part (along the laser propagation axis $x$) of the raw results. As expected, an additional up/down antisymmetry along the $\omega$ axis $z$ is visible, and originates from the mirror symmetry of the field (and vector potential) along this axis. Small imperfections of this up/down sign inversion (CEP artifacts) are canceled by forcing the antisymmetry. The projection in the polarization plane of the ESCARGOT signal, performed over the forward half (target point of view) is presented in panel (e). Qualitatively, this projection follows the modulations of the total signal visible in (b), with a relatively low amplitude along the $2\omega$ (horizontal) axis and a strong amplitude along the $\omega$ (vertical) axis. Interestingly, in addition to the up/down antisymmetry, a sign flip between different fringes of the pattern is visible at the tips of the "C" shape. Finally, the dressing of the second harmonic also induces an asymmetry of the dichroic signal along the $2\omega$ axis. These informations were not accessible in the previous VMI experiment as this axis was integrated. The corresponding projection is shown in panel (f). The most striking feature is that conversely to the total distribution, the VMI projection of the forward/backward antisymmetric signal appears strongly modulated by the trajectories interference. This suggests that the interferometric pattern, originally only visible in the polarization plane, is encoded and revealed along the laser propagation axis by the asymmetric interaction of the field with a chiral potential. The chirosensitive ESCARGOT signal thus adds an important observable to investigate complex photoelectron scattering processes in polyatomic molecules, if these latter are chiral.

**Complementarity of the Observables**

Let us focus here on a simple example to illustrate the complementarity of the observables. With a "C"-shaped vector potential ($\varphi_{\omega/2\omega} = -\pi/2$), a given set of final photoelectron momentum in the polarization plane $(p_y, p_z)$ can be associated with two distinct trajectories, or two ionization times within an optical cycle, depicted by the red and blue points in Fig. 4.25 (a). The location of their contribution in the total and dichroic part of the signal in the projection is depicted in panels (b) and (c), respectively. Scanning the location along the vector potential scans the ionization time difference, and thus the difference of accumulated phase between the trajectories, giving rise to the interference pattern.

In this configuration, the instantaneous chirality of the electric field (IC, defined in Eq. 4.15) at the ionization times of the two interfering photoelectron trajectories is exactly opposite. This statement remains valid at any place of the plane. The origin of the two trajectories within the optical cycle of the laser field is depicted in panel (d). If the chirosensitive signal was only originating from the initial instantaneous response at the time of ionization, the contributions of the two trajectories would cancel out and the chiral signal would globally vanish. However, in the semi-classical interpretation of the PECD in the strong field regime, depicted in panel (e), the photoelectron driven by the field takes a certain time $\tau$ to escape the chiral molecular potential. As simplistically modeled in Fig. 4.22, the instantaneous chirality of the field is thus not only imprinted to the electron at its ionization time but also during its scattering in the vicinity of the ionic core. In Fig. 4.25 (d), even if the two trajectories have an opposite instantaneous chirality at the origin, they have the same positive gradient of IC in such a way that the subsequent IC is maximized in the positive values in the first case while it tends to

lower negative values in the second. Consequently, the chiral signal from the first trajectory prevails in the final observable.

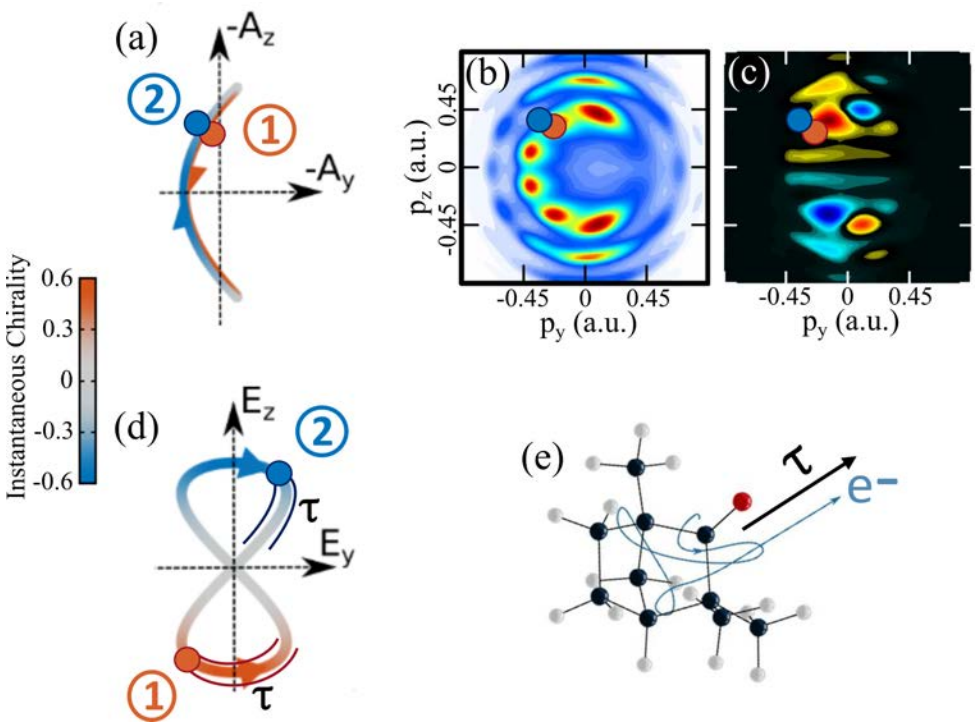


**Figure 4.25** – *Location of an arbitrary set of two photoelectron trajectories associated with the same final momentum $p_y, p_z$ in the polarization plane, in the case of $\varphi_{\omega/2\omega} = -\pi/2$. (a) "C"shaped vector potential. (b) Projection of the photoelectrons in the polarization plane, calculated using TDSE in the same conditions as the Fig. 4.24. (c) Corresponding dichroic signal. (d) "8"-shaped electric field. The origin of the same trajectories in the optical cycle are displayed, and the subsequent instantaneous chirality during a time $\tau$ is highlighted in the two cases. The arrows indicate the direction of rotation. (e) Schematic representation of a photoelectron trajectory scattering in the chiral molecular potential under the influence of a chiral field during a certain duration $\tau$.*

This constitutes a significant observation for the interpretation of chiral scattering processes and PECD in general. On one side, it draws the link between the chirality experienced individually by the trajectories and the final dichroic signal. On the other side, this suggests that such a dichroic effect can give further and complementary insight compared to achiral photoelectron interferometry. Indeed, while the mapping of the vector potential only gives information about the ionization time in a first approximation, the chiral interaction adds a perspective into the dynamics of the scattering, namely after the ionization.

**Evolution with the Two-Color Phase**

As already presented in Fig. 4.10, the shape of the electric field can be tailored from a "C" to an "8" or any intermediate form, by controlling the two-color phase $\varphi_{\omega/2\omega}$. The corresponding vector potential is of course affected, and the distribution evolves with it. The projections of the 3D TDSE calculations in the polarization plane using $I_{800nm} = 2 \times 10^{13}$ $W.cm^{-2}$ and $I_{400nm} = 2 \times 10^{12}$ $W.cm^{-2}$ are shown in Fig. 4.26, for $\varphi_{\omega/2\omega} = -\pi/2$ (a,f), $-\pi/4$ (b,g), 0 (c,h), $+\pi/4$ (d,i) and $+\pi/2$ (e,j). The corresponding fields and vector potentials are indicated above with the

target point of view, and the colorbar corresponds to the field instantaneous chirality.

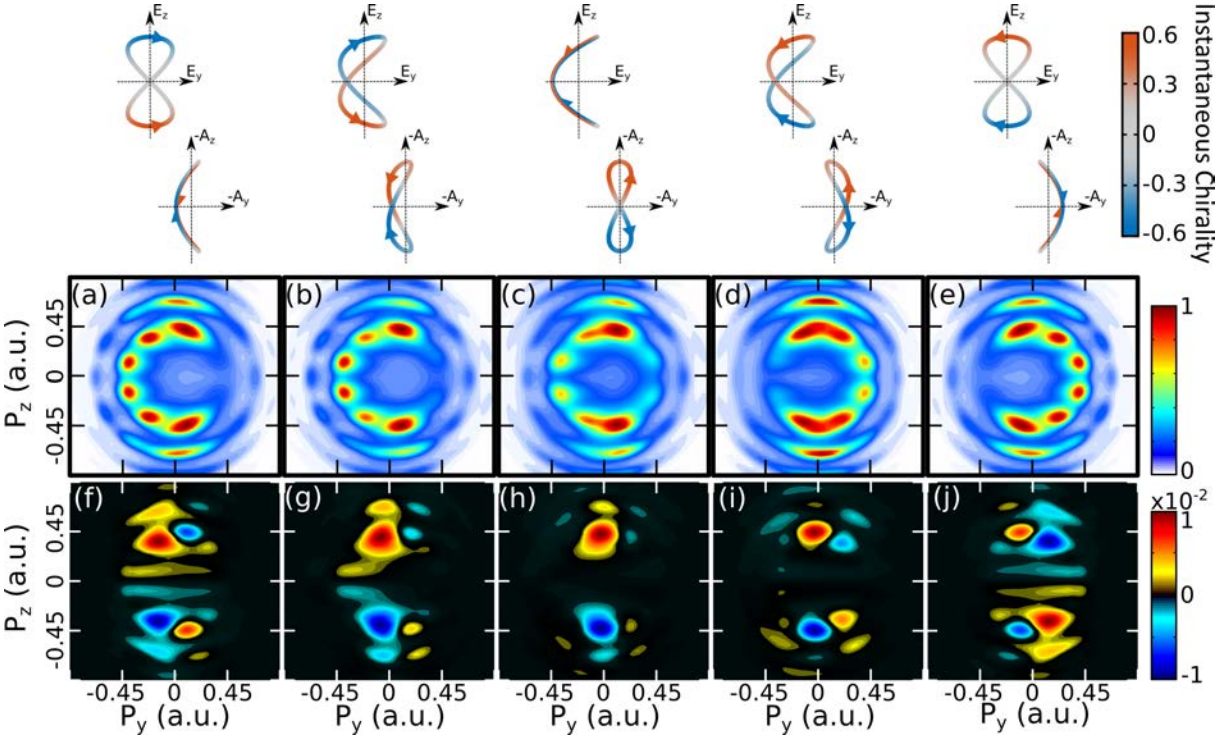


**Figure 4.26** – *2D projections, from the target point of view, of the total (a-e) and forward/backward antisymmetric part (f-j) of the 3D photoelectrons angular distribution from TDSE calculation on a toy model chiral molecule. Columns : $\varphi_{\omega/2\omega} = -\pi/2$ (a,f), $-\pi/4$ (b,g), 0 (c,h), $+\pi/4$ (d,i) and $+\pi/2$ (e,j)) with respect to Eq. 4.16. The total signals are integrated along the whole distributions while the antisymmetric parts are along the forward half. The fields used were $I_{800nm} = 2 \times 10^{13}$ $W.cm^{-2}$ and $I_{400nm} = 2 \times 10^{12}$ $W.cm^{-2}$.*

The TDSE calculations at this moderate intensity nicely display the dressing effect of the $2\omega$ field, where the total distributions (a-e)continuously follow the mapping of the vector potential from the "C" to the inverted "C" shape. The contrast of the interference fringes also appear very contrasted in these two cases. The amplitude of the modulations is weaker with the "8"-shaped vector potential, as fewer trajectories overlap. The chirosensitive responses (f-j) reach 1% of the total signal, and also follow the shape and modulations of driven by the mapping of the photoelectron distribution. Furthermore, the modulation of the two-color phase not only influences the final distribution but also the instantaneous chirality of the field in the early times of the scattering. A first approach to understand the structures of the ESCARGOT signal can consist in extending the reasoning presented just above in Fig. 4.25. At $\varphi_{\omega/2\omega} = -\pi/2$ or $+\pi/2$ (Fig. 4.26 (f,j)), several trajectories imprinted with an opposite sign of IC can overlap at the same location. The balance between the respective chirosensitive signals evolves along the "C" shape and could yield the sign flip observed. Contrarily, the upper (or lower) half of the distribution obtained with the "8"-shaped vector potential (h) are mainly driven by a given sign of IC. As a result, the ESCARGOT signal is dominated by this given IC.

The resulting structures are thus constituted over several overlapping effects. The next section will focus on the experimental measurements of the complete 3D distributions. In order to describe them more quantitatively, and in particular the effect of the sub-optical cycle chirality

of the field, another section will present a second modeling based on SFA.

## III. 3 Experimental Measurements

### Experimental Setup

The description of the setup used to generate the bilinear bichromatic field can be found in the previous chapter, and adapted in the present case in Fig. 4.27. The intensities were tuned to 9.5 W at 1030 nm ($\omega$) with 0.8 W of 515 nm ($2\omega$), with orthogonal linear polarizations, at a laser repetition rate of 166 kHz. A sub-cycle stabilization was actively performed using a piezoelectric stage. The feedback loop was locked on a photodiode monitoring fringes between 1030 nm beams from the two arms picked up from the recombination dichroic mirror, while most of the power was reflected or transmitted for the collinear recombination. The relative sub-optical cycle phase was finely tuned using a pair of fused silica wedges placed after the recombination. A telescope with x3 magnification and a f=60 cm effective focal length was used to focalize the two collinear beams. A slightly detuned telescope was placed in the $\omega$ arm to compensate the chromatic aberration of the lenses so that the focii of the $\omega$ and $2\omega$ beams overlap in the detector.

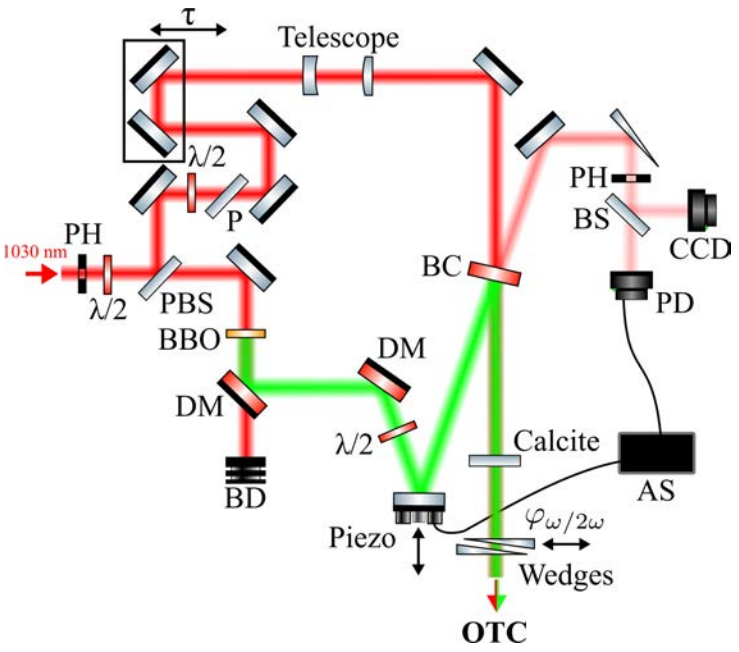


**Figure 4.27** – *Scheme of the optical setup used to generate the orthogonal two-color (OTC) field. PH = pinhole, λ/2 = half waveplate, PBD = polzarizing beamsplitter, P = polarizer, BBO = beta-barium borate crystal, DM = dichroic mirror, BD = beam dump, BC = beam combiner, PD = photodiode, AS = active delay stabilization.*

The signal has been measured using the COLTRIMS apparatus described in Sections 2.III-2.IV. The shaped laser beam was focused under vacuum on a supersonic molecular jet made by injecting 2 bars of carrier gas ($N_2$) in a heated bubbler of (+)-Fenchone ($\geq$98 % purity, Sigma Aldrich) and carried by gradually heated pipes, to avoid condensation, to the nozzle. The photoelectrons produced were carried on the detector using an homogeneous electric field (8.2 V.cm$^{-1}$ over 29.1 cm) and confined with a magnetic field (8.25 Gauss) from the main Helmholtz coils. The geomagnetic field was compensated using smaller transverse coils. The experiment

does not directly capitalize on the coincidence capacity of the COLTRIMS, as the ion side has been used only for alignment and characterization purposes. The so-called coincidence condition, imposing much less than one ionization per laser shot to avoid fake coincidence, is relaxed here. The only count rate limitation was the dynamical response of the MCPs and delay lines, enabling a 3D reconstruction in affordable times. The event counting rate was about 100 kHz and 100M counts were recorded for each phase.

Contrary to the VMI detection, the acquisition takes much more time and the Fourier filtering can not be performed. A direct measurement of the signal for selected two-color phases has thus been preferred. The $2\pi$ periodicity of the signal was sampled in 9 steps, spaced by $\pi/4$. The acquisition at each point took about 17 min, for a complete duration of 150 min. In the experiment, the absolute two-color phase can not be accessed directly, and only the relative phase is stabilized and scanned. The phase calibration has been achieved by comparing the asymmetry induced along the $2\omega$ field axis in the complete distributions. This $p_y$ axis was not resolved in the VMI measurements and must provide the phase without the modulo $\pi$ uncertainty left in the Fourier analysis used in the previous study. Note that the projections along the $2\omega$ axis (not depicted here) are in good agreement with the VMI measurements, but indicate that the previous calibration using the oscillation of the total photoelectron yield might not be accurate at low intensity.

**Results**

The projections of the 3D photoelectron momentum distributions measured experimentally are presented in Fig. 4.28 in a similar way than the TDSE results. The field intensities ($I_{1030nm} = 4.6 \times 10^{12}\ W.cm^{-2}$ and $I_{515nm} = 2.5 \times 10^{12}\ W.cm^{-2}$) are relatively low compared to the calculations but the longer wavelength partially attenuates the difference in the ionization regime. Measurements were also performed at higher intensity but a damage on the detector prevents us from correctly isolating the dichroic signal, unfortunately. Nevertheless, the data presented here can be compared with the theory.

The projections of the total distributions displayed in panels (a) to (e) indeed follow the shape of the vector potential. In particular the center of mass of the distribution in the polarization plane clearly moves from left to right here. The interferences are also less contrasted than in the calculation since the detection setup and phase stabilization have a given resolution. With the fields and wavelength used and the approximate formula of the pattern given in Eq. 4.12, one can expect the fringe spacing to be greater than in the TDSE calculations (shown in Fig. 4.26). With this in mind, the observed pattern seems plausible.

The projections of the forward/backward antisymmetric parts of the signal reach here 0.3 % in amplitude (while it was about 1% in the TDSE). Their evolution also seems similar to the TDSE calculations, in particular their continuous evolution from $-\pi/2$ to $+\pi/2$ with a global sign flip appearing at $+\pi/4$. The images obtained with the "C"-shaped vector potential also display a sign change at the tips of the C, and the one associated with the "8"-shaped vector potential has a dominant contribution. Note that photoelectrons are detected in the low kinetic energy region, which is not the case in the calculation. As these trajectories are likely to spend more time in the vicinity of the potential, we do not expect this part of the signal

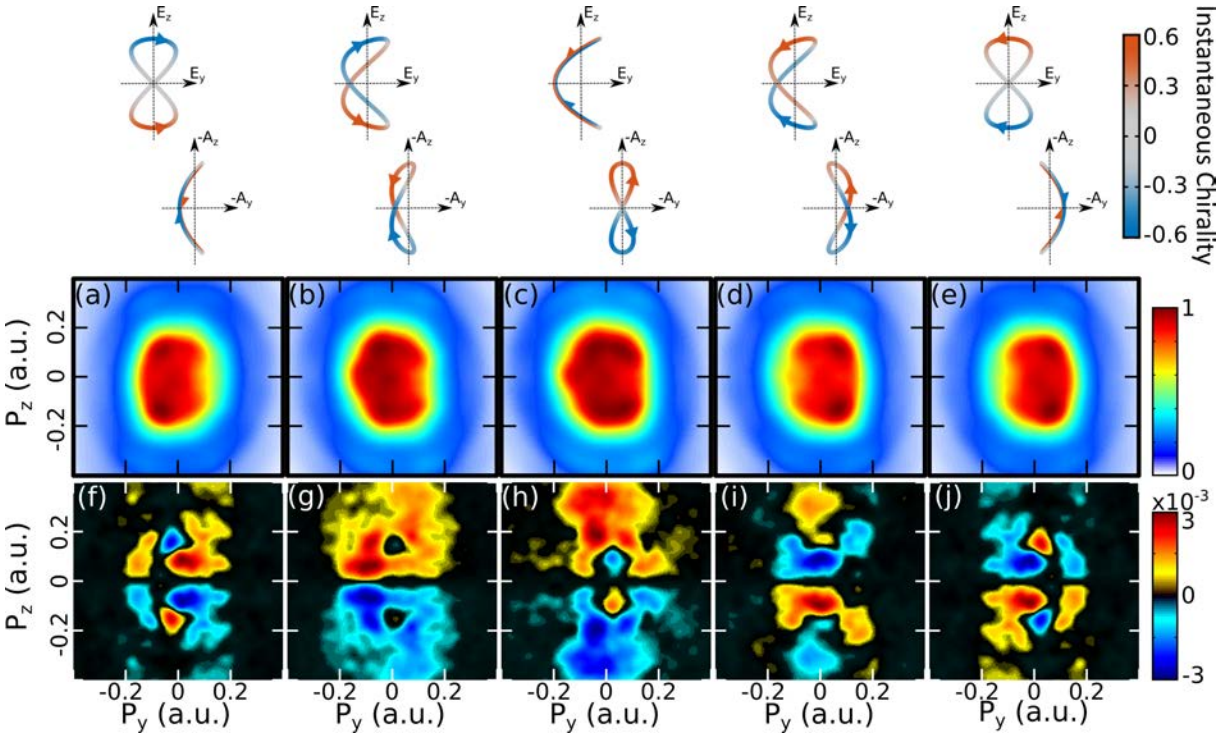


**Figure 4.28** – *2D projections, from the target point of view, of the total (a-e) and forward/backward antisymmetric part (f-j) of the 3D photoelectrons momentum distributions experimentally measured in the COLTRIMS in (+)-Fenchone, for two-color phases $\varphi_{\omega/2\omega} = -\pi/2$ (a,f), $-\pi/4$ (b,g), 0 (c,h), $+\pi/4$ (d,i) and $+\pi/2$ (e,j)) with respect to Eq. 4.16. The total signals are integrated along the whole $p_x$ while the antisymmetric parts are along the forward half. The field intensity was estimated at $I_{1030nm} = 4.6 \times 10^{12}$ $W.cm^{-2}$ and $I_{515nm} = 2.5 \times 10^{12}$ $W.cm^{-2}$.*

to be comparable with the TDSE. Some quantitative discrepancies can be obviously pointed out, but the calculations and the experiment are not done in the same system and a perfect match would be surprising. Still, the experiment globally confirms that the dichroic response can be tailored with the electric field in the polarization plane. The relatively good qualitative agreement suggests that the process is not so much driven by the fine details of the molecular potential, but rather by the instantaneous chirality of the field.

### III. 4 Explicit Description of the Trajectories : SFA Calculations

The TDSE calculations provide a quantitative simulation of the photoionization with a few assumptions (in particular without conditions on the ionization regime or on the interaction with the potential) and constitutes a reliable point of comparison. However, it does not provide a intuitive picture in term of photoelectron trajectories, which is at the root of our interpretation. For this purpose, the SFA model presented in the introduction of this chapter is more suited and associates explicitly ionization time with final momentum. Nevertheless, its main downside is the complete omission of the interaction between the electron and the ionic core during the scattering process. This constitutes an issue in some cases already presented, but specifically in our case, this means that the chiral interaction can not be described as is. For this reason, we propose the following phenomenological add-on to the SFA model. Note

that most of the SFA calculations were performed by Shaked Rozen.

**Identification of the Trajectories**

The standard calculation of the photoelectron ejection is firstly performed using the Eq. 4.9. The final 2D distributions $a(\vec{p}, t_0)$ in the polarization plane $\vec{p} = (p_y, p_z)$ are thus expressed from the action integral $S(\vec{p}, t_0)$ defined in Eq. 4.8, where $t_0$ is the ionization time, as :

$$a(\vec{p}, t_0) = |\sum_{traj} e^{iS(\vec{p},t_0)}|^2 \tag{4.19}$$

The calculation is performed over three optical cycles and the signal is obtained by coherently summing over the continuum of trajectories. The result is presented in Fig. 4.29 (a) in the case of a "C"-shaped vector potential, but the following reasoning stands for all phases. While two solutions per set $(p_y, p_z)$ per optical cycle are obtained in the one-color case, four distinct ones are found with the orthogonal bilinear bichromatic field. They can be split in four families that are depicted in Fig. 4.29 (b) to (e). The radial modulation comes from the repetition of the ionization at each optical cycle. It can be interesting in addition to represent the map of the ionization time within an optical cycle for each family, as a function of the final photoelectron momentum (panels (f-i)). The colorscale of these panels indicates the ionization time $t_0$ of the solutions, with a threshold at 20% of the signal. The radial modulations were suppressed here for visibility by selecting the trajectories within a single cycle. Fortunately, the first two families dominate the signal for most of the final momenta, in such a way that we can still consider the interference of the direct trajectories as a two-source inteferometry. If this was not the case, the fringes would have been much more complex to interpret straightforwardly. The optical cycle is indicated on the vector potential depicted and starts from the upper tip. The family 1 (panel (b)) originates from the first half optical cycle, when the vector potential rotates anticlockwise. Its upper half is emitted during the first quarter of the optical cycle, and the lower part during the second quarter. The situation is symmetric for the family 2, which corresponds to the photoelectrons ionized during the second half of the optical cycle, when the vector potential rotates clockwise.

Several types of interference can thus be distinguished. The first one results from two photoelectrons originating from two consecutive quarter cycles (for example 0.25-0.5 $T_0$ and 0.5-0.75 $T_0$, or -0.25-0 $T_0$ and $0 - 0.25T_0$, where $T_0$ is the fundamental optical period). The second type comes from electron from the same optical cycle but not from consecutive quarters (for instance 0-0.25 $T_0$ and 0.75-1 $T_0$). These two types are commonly refereed to as intracycle interferences, and their pattern can be derived analytically in the one-color case as presented in Eq. 4.12 [Maxwell 17]. In addition, intercycle inteferences can arise from trajectories ionized at different optical cycles (such as -0.25-0 and 0.75-1 $T_0$) and correspond to the ATI concentric rings, given in Eq. 4.11. The final signal (in panel (a)) is thus simply a product of all these patterns.

**Embedding the Chiral Interaction in SFA**

In order to introduce chirality in the SFA signal, we implement a phenomenological pertur-

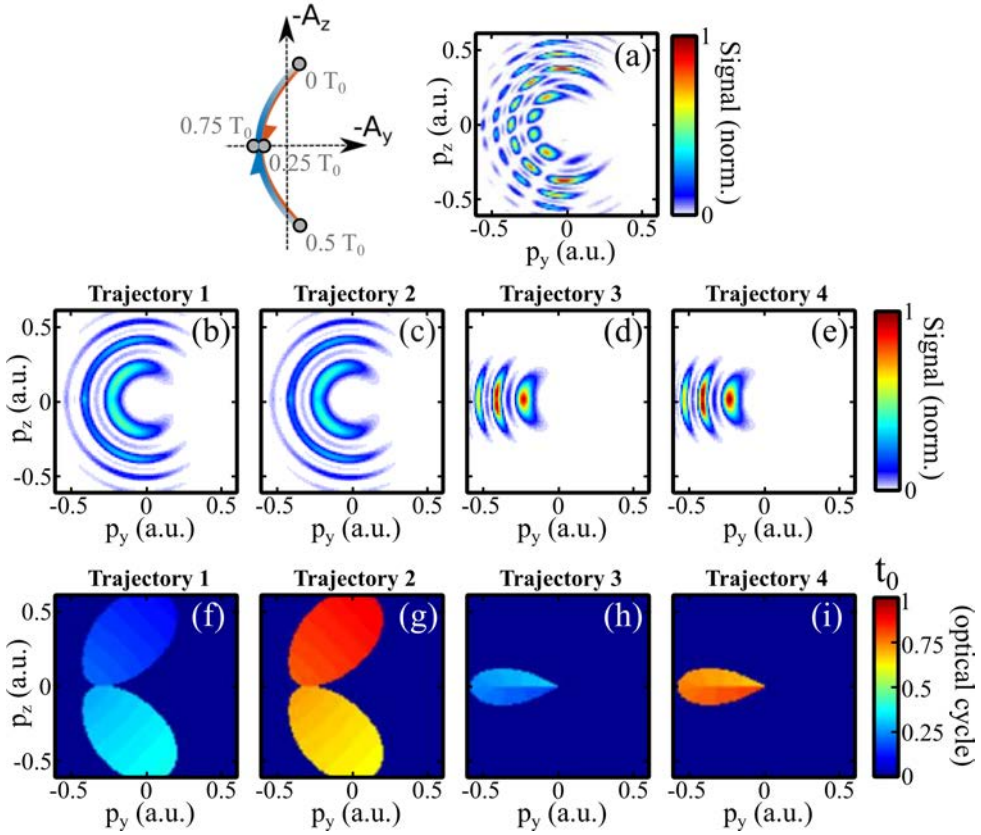


**Figure 4.29** – *Decomposition of the solutions of the SFA in the polarization plane in trajectories, in the case where the vector potential is "C"-shaped. (a) Total distribution obtained by coherently summing all the contributions. (b-e) Four distinct types of solutions found at each optical cycle. The radial modulation comes from the repetition of the ionization at each optical cycle. (f-i) Map of the ionization time within an optical cycle for each family, as a function of the final photoelectron momentum. The colorbar indicates the ionization time, with a threshold at 20% of the single-cycle signal, i.e. without radial modulations, for clarity. The quarter optical cycles are depicted on the vector potential above.*

bation of the solutions found. This is based on a simple assumption, which consists in considering that the chiral interaction can have two effects on the complex photoelectron signal : a phase and/or an amplitude modulation. The PECD originates from a phase difference between the scattering partial waves [Powis 08] (see Fig. 4.30 (a)). In a typical PECD experiment, only the amplitude asymmetry of the photoelectron wavepacket can be accessed, through the detection of the number of electrons ejected forward and backward. Phase-resolved chiral photoionization has recently revealed that the forward and backward wavepackets also carry chirosensitive phase shifts [Beaulieu 17]. In the SFA picture, each trajectory results from a set of interfering partial waves (see Fig. 4.30 (b)). The chiroptical interaction thus modulates both the amplitude and phase of each trajectory. Comparing the interference patterns produced by these trajectories in the forward and backward hemispheres thus directly gives access to the chiral-induced phase shift between the two trajectories.

To phenomenologically introduce the chiral-induced phase and amplitude modulations, we propose to express the forward/backward antisymmetric signal in the polarization plane as :

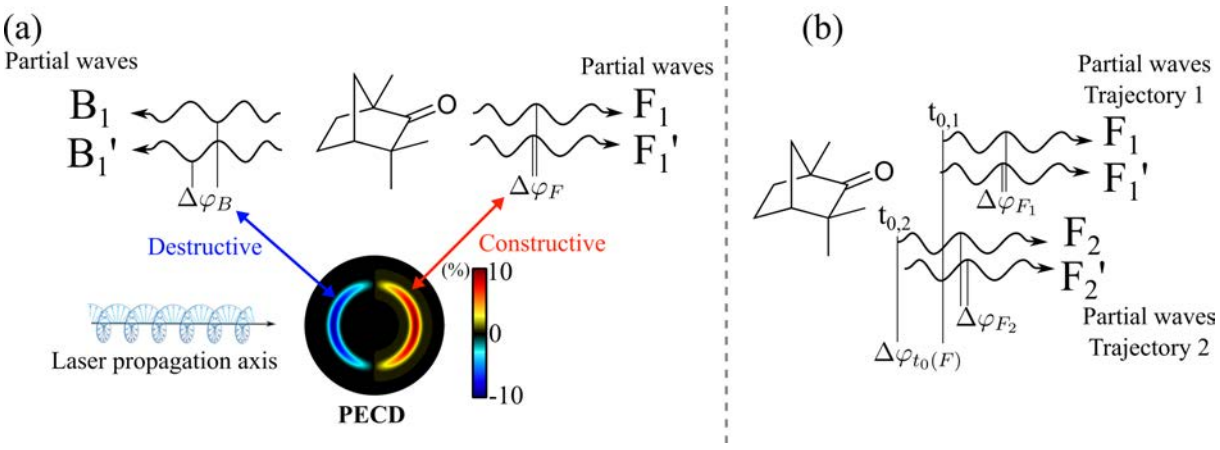


**Figure 4.30** – *Origin of the PECD in term of partial waves forward/backward phase offset induced by the chirality. (a) A phase difference $\Delta\varphi_F$ or $\Delta\varphi_B$ between the partial waves results in a the variation of the angular yield, namely PECD. (b) In the case where several trajectories interfere, the phase between the partial waves in each trajectory $\Delta\varphi_{F_1}$ and $\Delta\varphi_{F_2}$ induces the amplitude modulation. The phase between the partial waves among the trajectories due to the ionization time offset $\Delta\varphi_{t_0(F)}$ induces the term denoted as "phase effect" in the text. Note that this latter can also be affected by the relative phase between the partials waves $\Delta\varphi_{F_1}$ and $\Delta\varphi_{F_2}$. The backward part was omitted here for clarity.*

$$a_{F/B}(\vec{p}, t_0) = |\sum_{traj} e^{i(S(\vec{p},t_0)+\delta)}(1+\delta')|^2 - |\sum_{traj} e^{i(S(\vec{p},t_0)-\delta)}(1-\delta')|^2 \tag{4.20}$$

where

$$\begin{aligned} \delta &= \alpha \int_{t_0}^{+\infty} IC(t)R(t_0 - t)dt \\ \delta' &= \beta \int_{t_0}^{+\infty} IC(t)R(t_0 - t)dt \end{aligned} \tag{4.21}$$

are respectively the phase and amplitude perturbations for each trajectory ionized at $t_0$, induced by its interaction with the subsequent instantaneous chirality of the field $IC(t)$ and the chiral ionic potential, that has a certain range $R$. This range is actually expressed in space, and we presently use a simple Gaussian function to describe it :

$$R(t_0 - t) = e^{-\frac{r(t-t_0)^2}{2r_0^2}} \tag{4.22}$$

where $r(t - t_0)$ is the distance from the ionic center to the electron at a time $t - t_0$ and $r_0$ is a range parameter. In this model, $\alpha$ and $\beta$ are respectively quantifying the phase and amplitude perturbations of the action. This model is pretty simplistic and does not aim at precisely grasping the details of the chiral interaction. However, it has the advantage of explicitly describing the different terms in a phenomenological manner. Three parameters are adjusted in order to reproduce the chiral-sensitive signal, namely the amplitude ($\beta$), the phase ($\alpha$) and the range ($r_0$). Their respective effects can be decomposed in distinct features, as presented in Fig.

4.31.

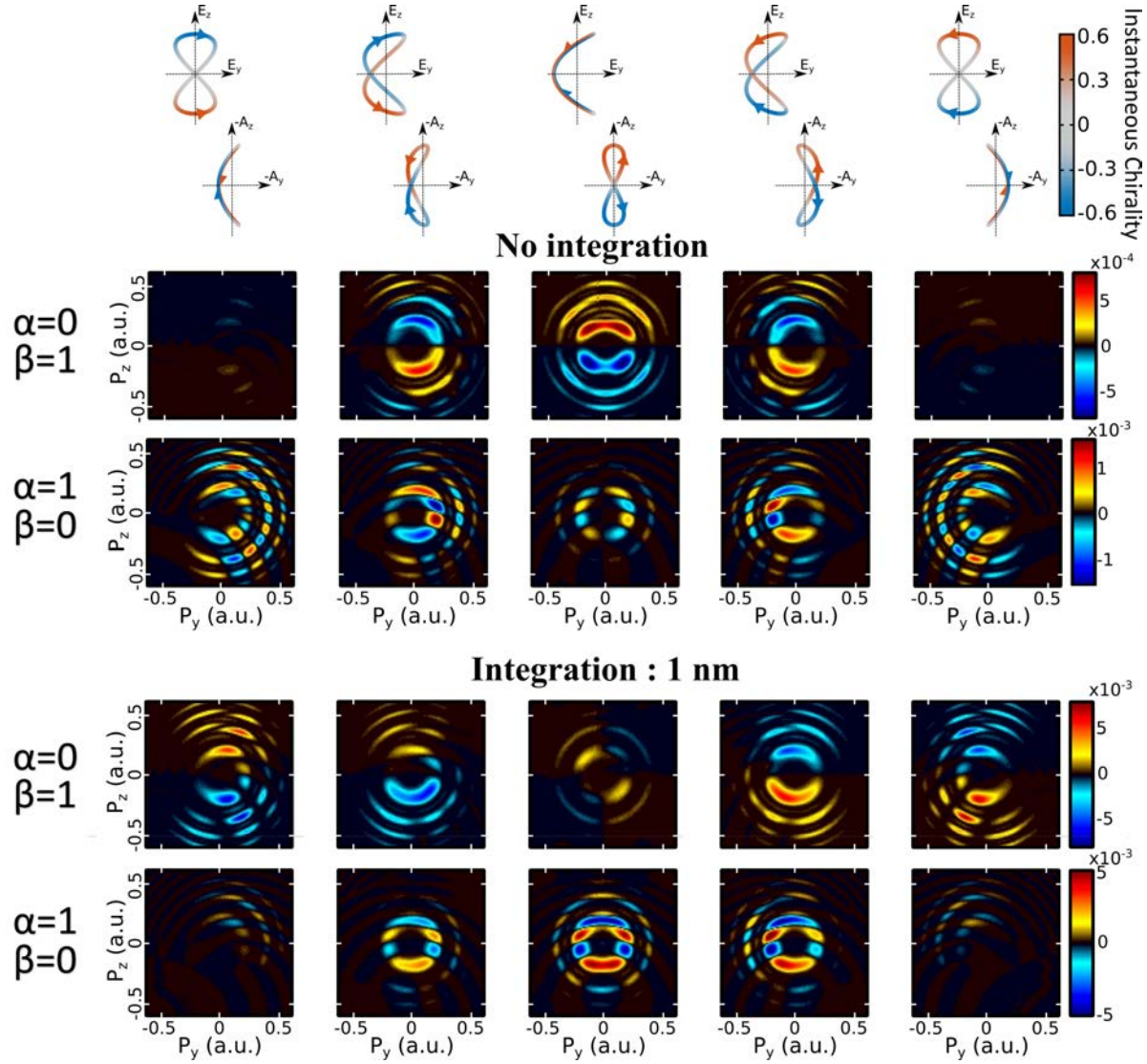


**Figure 4.31** – *Effect of the phase ($\alpha$), the amplitude ($\beta$) and the integration range $r_0$ in the dichroic signal obtained in the polarization plane with the simple chirality-embedded SFA model presented in the text. The columns correspond to the field and vector potential depicted above, and the field conditions used were $I_{800nm} = 2 \times 10^{13}$ $W.cm^{-2}$ and $I_{400nm} = 2 \times 10^{12}$ $W.cm^{-2}$. 'No integration' refers to the case where we only take into account the IC at the exit time $IC(t_0)$, by using $R = \delta(r)$.*

Let us first consider the case where the chiral response is supposed to be instantaneous ('no integration'). When the vector potential is "C"-shaped, a pure amplitude chiral response leads to no ESCARGOT signal. This is due to the fact that the two families of trajectories ending up in the same place of the detector have experienced opposite instantaneous chiralities. The difference in amplitude then cancel out each other, leading to a zero net asymmetry. On the other hand, an instantaneous phase response can lead to a significant ESCARGOT signal. Indeed, the phase difference between the interfering trajectories is cumulative since it represents opposite forward/backward pattern offsets. Even small shifts can be magnified in the forward/backward difference. Conversely with an "8"-shaped vector potential, the amplitude effects of each half of the detector add up and yield a strong ESCARGOT signal, while the chiral phase difference

tends to reduce. The different patterns are also very distinguishable, and such for any two-color phase. The amplitude effect ($\beta = 1$) tends to yield a homogeneous ESCARGOT response over the upper and lower halves of the distributions, while the phase effect ($\alpha = 1$) always induces a strongly oscillating pattern at twice the frequency of the total signal.

The modulation of the magnitude of the different effects with the two-color phase is almost opposite when a 1 nm integration range is applied. In any case, the phase- and amplitude-related ESCARGOT signals do not maximize at the same two-color phase, regardless of the integration. The optimization of the parameters is thus based on three observables, to be compared with the TDSE and experimental results. The first one is the relative steadiness of the dichroic signal amplitude with $\varphi_{\omega/2\omega}$. The second one is the qualitative structure of the signal, in particular the sign flip a certain phases. Finally, the global amplitude is taken into account. A more quantitative manner to determine the parameters is still being investigated, but the results obtained so far can be a good basis of discussion.

The patterns resulting from the SFA calculations are very different from those observed in the TDSE, in which the forward/backward asymmetry is mainly localized around the vertical direction, *i.e.* around the polarization axis of the fundamental laser. This is due to the fact that one key element is missing from out interpretation : Coulomb focusing, which will be now discussed.

## III. 5 Coulomb Focusing and Yukawa Screened Potential

**Discrepancy Between TDSE and SFA**

The photoelectron distributions obtained from the TDSE (Fig. 4.26) and the SFA model (Fig. 4.31) show a puzzling discrepancy. While the total signal is homogeneously distributed along the "C" shape of the vector potential and the chiral parts prominently appear along the vertical ($\omega$) axis in the TDSE case, they are both dominant along the horizontal ($2\omega$) axis in the SFA. We were initially suspecting an issue in the theoretical descriptions, but very recent developments indicate that it might actually be meaningful.

The SFA model is relatively simple and neglects the interaction of the photoelectron and the ionic core during the scattering process. Still, a smoking-gun trace of the influence of this latter has been experimentally detected in the orthogonal bilinear bichromatic field configuration [Richter 16]. In this study, performed at $I_{780nm} = 1.4 \times 10^{14}\ W.cm^{-2}$ and $I_{390nm} = 1.3 \times 10^{13}\ W.cm^{-2}$, two distinct features in the photoelectron signal in the polarization plane have been identified, as shown in Fig. 4.32 (a-c). The first one corresponds to the features described so far, which follow the dressing of the vector potential. The authors called it the "streakable" part, as the $2\omega$ polarization acts as a streaking field (isolated in Fig. 4.32 (b)). In addition to this, an "unstreakable" component can be noticed. Interestingly, the unstreakable part completely vanishes if the Coulomb interaction is removed from calculations. It thus corresponds to the trajectories that have undergone Coulomb focusing from the ionic core, meaning that the electrons that have spent enough time in the vicinity of the cation have been attracted to it and their momentum ends up being affected. This effect was already known

for leaving typical traces, for example, by turning Gaussian distributions into cusp-like profiles in the photoelectron distributions along the laser axis. This has been demonstrated with linear one-color fields [Dimitriou 04] and counter-rotating circularly polarized two-color fields [Eckart 18]. In the present case of an orthogonal bilinear bichromatic field, the focusing effect almost completely cancels the dressing effect of the second harmonic in the polarization plane and the corresponding trajectories end up along the $p_y = 0$ axis, regardless of the two-color phase.

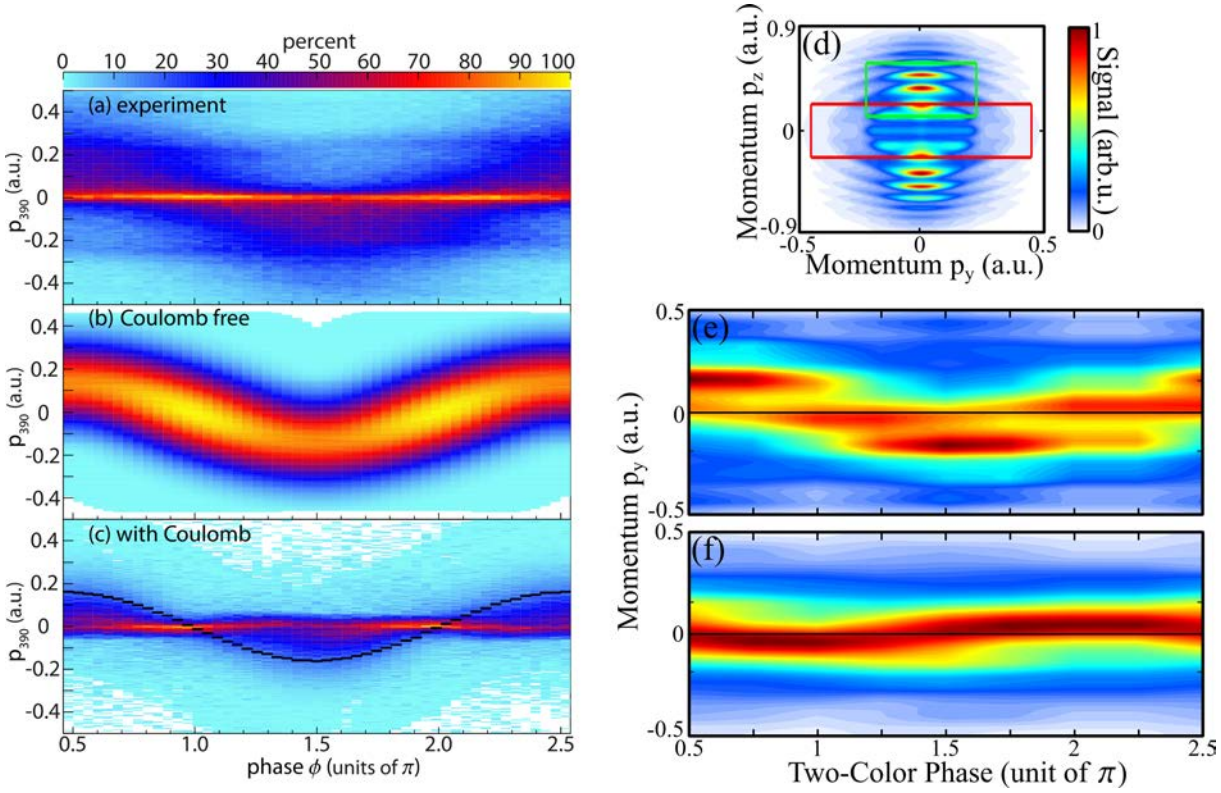


**Figure 4.32** – *(a-c) Adapted from [Richter 16] : evolution of the photoelectron distribution produced with an orthogonal two-color field along the 2ω axis as a function of the two-color phase. (a) Experimental distributions measured in argon at at* $I_{780nm} = 1.4 \times 10^{14}$ *W.cm*$^{-2}$ *and* $I_{390nm} = 1.3 \times 10^{13}$ *W.cm*$^{-2}$*. (b) CTMC simulations neglecting the Coulomb potential. (c) CTMC simulations including the Coulomb potential. (d-f) TDSE calculations from our team at* $I_{800nm} = 5 \times 10^{13}$ *W.cm*$^{-2}$ *and* $I_{400nm} = 5 \times 10^{12}$ *W.cm*$^{-2}$*. (d) Photoelectron momentum distribution in the polarization plane of the laser, integrated over* $p_x$*, where the ω field is along the z axis and the 2ω field along the y axis. (e) Evolution along the 2ω axis of the central part of the distribution (red box in (d)), as a function of the two-color phase. (f) Same as (e), for the ATI peaks (green box in (d)). Note that the phase units of π are defined relatively to the fundamental field.*

**TDSE at High Field Intensity**

The discrepancy between our SFA and TDSE results might also be due to the low intensity used in the calculations ($I_{800nm} = 2 \times 10^{13}$ *W.cm*$^{-2}$ and $I_{400nm} = 2 \times 10^{12}$ *W.cm*$^{-2}$). Indeed, the strong field approximation is well-suited to describe the processes occurring at high intensity. We thus increased the intensity to $I_{800nm} = 5 \times 10^{13}$ *W.cm*$^{-2}$ and $I_{400nm} = 5 \times 10^{12}$ *W.cm*$^{-2}$. The results of the TDSE calculations are compared to the ones of [Richter 16] in Fig. 4.32 (d-f). The simulated 3D photoelectron distribution were integrated over two different regions. The

evolution of the central part (red box in (d)) along the $2\omega$ axis as a function of the two-color phase is shown in panel (e), while the one of the high energy features (green box in (d)) are depicted in (f). Interestingly, these two components show a completely different behavior. The central part seems to follow the curve of the "streakable part", *i.e.* the vector potential, meaning that this part of the signal could be associated with direct trajectories. Conversely, the ATI peaks oscillate much less with the dressing of the vector potential (and even in opposition to it). They could then be associated with the Coulomb-focused trajectories.

In order to see how these different types of photoelectron trajectories are affected by the dressing of the $2\omega$ field, the projection in the polarization plane of the total distributions and their respective forward/backward antisymmetric parts are presented in Fig. 4.33 for different phases. Comparatively to the calculations at lower fields, the higher field conditions directly impact the distributions, in particular several ATI peaks are visible in the total signal (a-e). It appears clear from the evolution of the complete distributions that the central part (first ring) is shaped and dressed by the vector potential, smoothly evolving here from the "C" (a) to the inverted "C" shape (e). This is another way to visualize the fact that this part of the signal is "streakable". Oppositely, the signal along the vertical axis is almost unaffected by the two-color phase. As just mentioned, this could be the signature of Coulomb-focused trajectories.

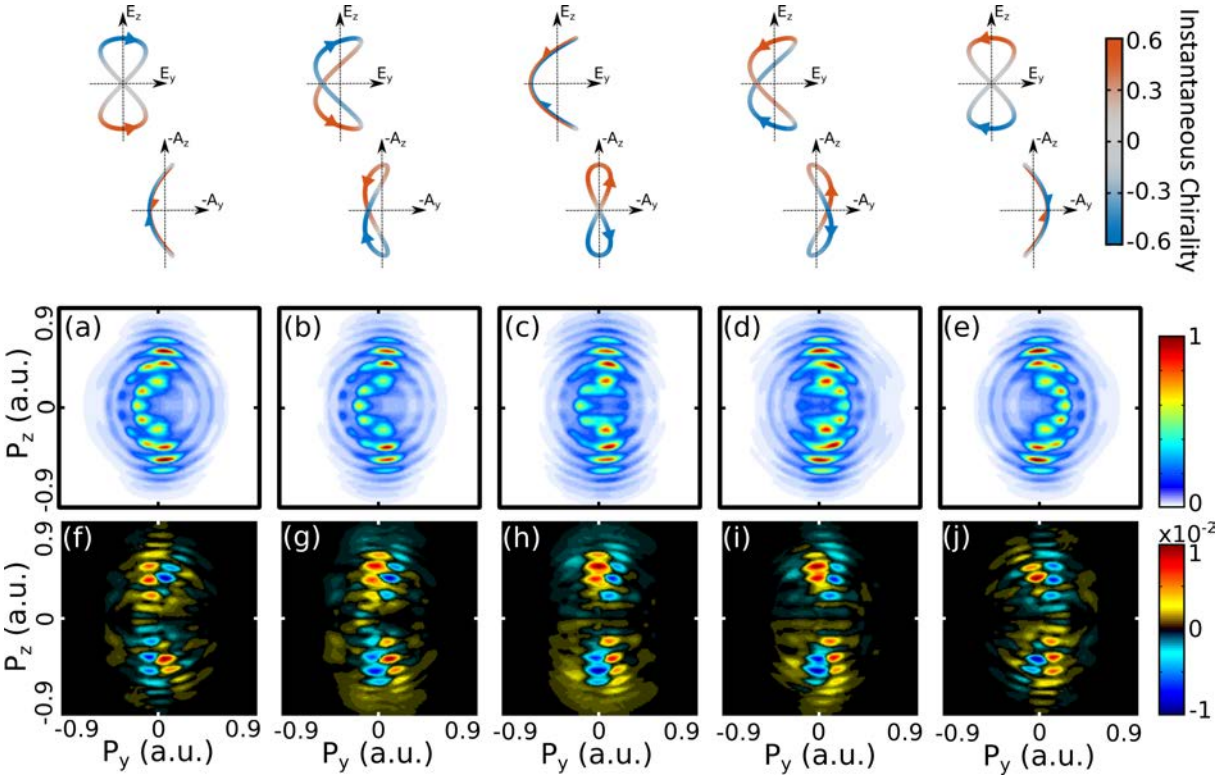


**Figure 4.33** – *2D projections, from the target point of view, of the total (a-e) and forward/backward antisymmetric part (f-j) of the 3D photoelectrons angular distribution from TDSE calculation on a toy model chiral molecule. Columns : $\varphi_{\omega/2\omega} = -\pi/2$ (a,f), $-\pi/4$ (b,g), 0 (c,h), $+\pi/4$ (d,i) and $+\pi/2$ (e,j)) with respect to Eq. 4.16. The total signals are integrated along the whole distributions while the antisymmetric parts are along the forward half. The fields used were $I_{800nm} = 5 \times 10^{13}$ $W.cm^{-2}$ and $I_{400nm} = 5 \times 10^{12}$ $W.cm^{-2}$.*

Such features could be of high interest in this study. As these trajectories do not interact with the ionic potential in the same way (they spend more time in its vicinity), one can expect them to be differently imprinted with the chirality of the potential. A particularly interesting behavior, displayed in the present case, is that the ESCARGOT signal is indeed mainly located along the vertical axis on the ATI signal (f-j). One can have the following interpretation. In this regime, the amplitude of the ESCARGOT signal typically decreases since the molecular potential is less prominent compared to the field [Beaulieu 16a]. The direct trajectories are thus less imprinted with the chiral interaction. Conversely, the Coulomb-focused trajectories recover part of this sensitivity. Determining the qualitative influence of the ionic potential on the 3D photoelectron angular distributions produced by a tailored laser field is not an easy task. The interpretation can be simplified by taking a different look at the results, within the framework of the attoclock technique.

**Origin of the ESCARGOT Signal**

The attoclock effect is described in the introduction of the next section. Simply put, when performing ionization with a short circularly or elliptically polarized pulse, the ionization can be confined to the peak of the field. Since the field rotates, any angular offset of the distribution compared to the vector potential can be read as a temporal offset, called attoclock delay, as shown in Fig. 4.34 (a). Interestingly, the attoclock idea can also be implemented with more exotic fields [Han 18]. In our case, the rotation of the field (and vector potential) is inverted between the upper and lower halves (see panel (b)). As a result, the angular offset is opposite between these two halves.

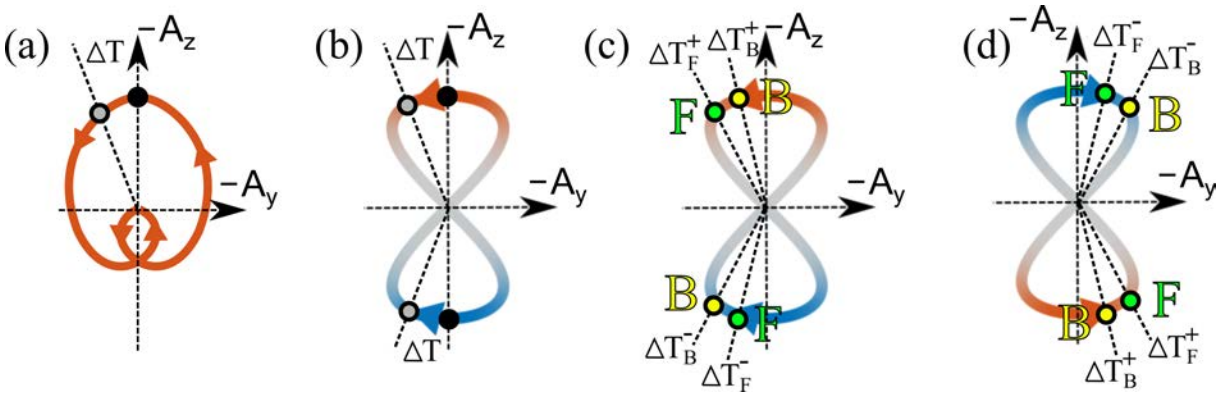


**Figure 4.34** – *(a) Principle of the attoclock effect on a circularly polarized short pulse. The tunneling is confined at the peak (black) dot. Since the vector potential rotates, an angular offset of the distribution (grey dot) can be read as a delay in the ionization $\Delta T$. (b) Same principle applied with the orthogonal two-color field with $\varphi_{\omega/2\omega} = 0$, for an achiral target. (c) Same as (b), with a chiral target. The chiral interaction can induce a chiral attoclock effect, meaning that the delay can be slightly different for the photoelectrons emitted forward ($\Delta T_F^{\pm}$) and backward ($\Delta T_B^{\pm}$), depending on the instantaneous chirality of the field (±). The example is depicted for $\Delta T_F^+ > \Delta T_B^+$ (positive values of instantaneous chirality (+), in red). Since it is a dichroic effect, it reverses with the IC. This leads to the up/down asymmetry of the ESCARGOT signal. (d) Same as (c), with $\varphi_{\omega/2\omega} = \pi$. The instantaneous chirality of the field is reversed here. However, this also means that the rotation is mirrored compared to (c), in such a way that the relative position between the forward and backward parts of the signal is the same as in (c).*

We propose here to extent the concept to chiral interaction, which consists in assuming that the attoclock delay $\Delta T$ could be slightly different between the forward and the backward parts of the photoelectron distribution. Since it is a dichroic effect, the effect would reverse if the sign of the field instantaneous chirality is inverted. The consequences on the dichroic signal is qualitatively depicted in Fig. 4.34 (c). Let us assume for instance that $\Delta T_F^+ > \Delta T_B^+$ (with a positive sign of IC). In this example ($\varphi_{\omega/2\omega} = 0$), this means that the forward signal will be located on the left of the backward signal on the upper half. The effect is of course mirrored on the lower half, since the IC is inverted. This can be compared to the case of $\varphi_{\omega/2\omega} = \pi$, depicted in the panel (d). The instantaneous chirality of the field is reversed here. However, this also means that the rotation is mirrored compared to (c), in such a way that the relative position between the forward and backward parts of the signal is the same as in (c) (*i.e.* forward signal on the left of the backward signal in the upper half in our example). Since the chirosensitive signal adds up regardless of the sign of the instantaneous chirality of the field, this means that this effect remains qualitatively identical for all two-color phases, and in particular even for the "C"-shaped vector potential. This reproduces the behavior observed in the unstreakable part of the ESCARGOT signal calculated with TDSE at high intensity (Fig. 4.33 (f-j)). Surprisingly, this means that the ESCARGOT signal does not sustain a simple sign flip when inverting the field chirality. The only way to invert the sign of the features is to swap the enantiomer handedness. The 3D ESCARGOT signal is thus singularly defined by the absolute set of field and enantiomer (oppositely to PECD, where for instance, the signal from a (+) enantiomer and RCP can not be distinguished from the one of the (-) one with a LCP). Note that monitoring only the projection along the $2\omega$ axis removes this resolution, in such a way that the VMI projections of the ESCARGOT signal does simply flip sign while inverting the IC, as we have seen in the previous section.

The SFA model presented above predicts interferometric effects to be involved in the ESCARGOT signal. However, they are covered by the Coulomb-focusing effect that refocuses all the patterns along the $\omega$ axis. Can we still access the ionization phases? For this purpose, it is possible to remove the effect of the Coulomb potential in the calculations. Instead of performing them with a standard Coulomb potential ($V(r) = -1/r$), a screened Yukawa potential has been used here. This latter aims at mimicking the Coulomb potential at short distances but cuts its long-range tail, expressed by adding a $e^{-(r-r_0)}$ cutoff term. The complete study is still being carried out, but the first results are promising. The comparison between the TDSE calculations using a Coulomb or a Yukawa potential, at $I_{800nm} = 5 \times 10^{13}$ $W.cm^{-2}$ and $I_{400nm} = 5 \times 10^{12}$ $W.cm^{-2}$ and for the "8"-shaped vector potential ($\varphi_{\omega/2\omega} = 0$) is given in Fig. 4.35. The first striking result is that the features associated with the Coulomb-focused trajectories (along the vertical axis in (a)) completely disappear with the Yukawa potential (b), confirming the initial assignment. Furthermore, the ESCARGOT signal in this region also cancels (d), indicating that the latter indeed originates from long range effects. Conversely, the central features associated with the direct trajectories remains significant in the complete distribution (b), which is in good agreement with our interpretation.

Nevertheless, the Coulomb focusing can not be completely switched off with the Yukawa

potential. Since the corresponding features lie along the $\omega$ polarization axis, it is possible to avoid their residual contribution by looking away from the polarization plane. The result is depicted in Fig. 4.35, for $\varphi_{\omega/2\omega} = 0$ (e) and $\pi/2$ (f), for the ESCARGOT signal integrated between $p_x$ = [0.18 - 0.27] a.u. along the laser propagation axis. The patterns obtained look very modulated in this case. They can be compared to SFA calculations performed with a chiral phase effect only ($\alpha = 0.01$ and $\beta = 0$ in Eq. 4.21), and with a very short integration time of the instantaneous chirality of 50 as, shown in panels (g) and (h). We see that the patterns are in good qualitative agreement. We have not concluded on this particular comparison yet, but this already strongly suggests that the chiral phase effects indeed play a role in the direct photoelectron trajectories. Furthermore, the very short integration time required to reproduce the features at both two-color phases indicates that the effect corresponds to a chiral phase imposed at the onset of the wavepacket, *i.e.* the tunnel ionization.

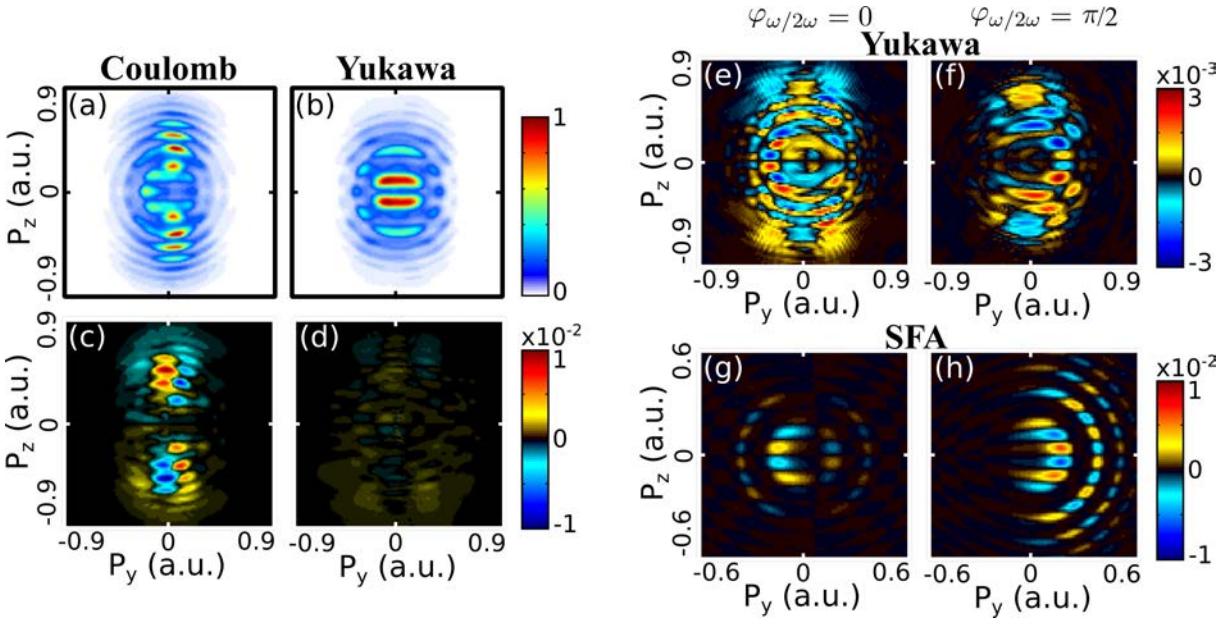


**Figure 4.35** – *(a-d) 2D projections in the polarization plane calculated by TDSE at $I_{800nm} = 5 \times 10^{13}$ $W.cm^{-2}$ and $I_{400nm} = 5 \times 10^{12}$ $W.cm^{-2}$ and for the "8"-shaped vector potential ($\varphi_{\omega/2\omega} = 0$). The total distributions (upper panels) and ESCARGOT parts (lower panels) are presented, for Coulomb (a,c) and Yukawa screened potential (b,d). (c) and (d) are displayed with the same colorbar for comparison. (e-f) Slice of the ESCARGOT signal obtained with the Yukawa potential in TDSE in the field polarization plane $(p_y, p_z)$, integrated away from the center between 0.18 a.u. and 0.27 a.u. in $p_x$, the laser propagation axis. (e) and (f) correspond respectively to the two-color phases $\varphi_{\omega/2\omega} = 0$ and $\pi/2$. (g-h) ESCARGOT signal from the extended SFA model presented in the text, performed with a chiral phase effect only ($\alpha = 0.01$, $\beta = 0$), and with an integration of the instantaneous chirality of 50 as, in the same field conditions, for two-color phases of $\varphi_{\omega/2\omega} = 0$ (g) and $\pi/2$ (h).*

Finally, this is to be compared to the experimental ESCARGOT measurements, shown in Fig. 4.28. Even if is was performed in moderate field conditions, the features corresponding to the chiral attoclock seems to be distinguishable. It is not evident, however, to know if the absence of fast modulations are related to the resolution of the COLTRIMS, or the longer wavelength used for instance. As we see, the complete distribution is itself less modulated. In any case,

it would be interesting to reproduce the measurements in stronger field conditions. It might enable to measure the tunneling phase shifts, if we manage to isolate the interference structures from the Coulomb-focused features. In the meantime, we have used another way to tackle the question of the sensitivity of the tunnel-ionization to chirality. For this, we have used the chiral attoclock with a different field configuration, as we will see in the last section.

### III. 6 Perspectives

The high density of information contained in the 3D photoelectron momentum distribution leads to many results in the presented study. We have demonstrated that the combination of the photoelectron interferometry with the sub-optical cycle gating of the instantaneous chirality of the laser field shows substantial increase of the information provided individually by each technique. In particular, the chiral interaction adds dynamical informations to the vector potential mapping, and inversely the mapping relates the PECD to the interaction individually experienced by the photoelectron trajectories. Beyond the experimental feasibility, the complementarity of the TDSE in terms of completeness and the SFA in terms of explicit trajectory description is shown. Recent developments indicate that different types of trajectories can be identified depending on the field condition used. While they have already been investigated using the interferometry, the chirality adds a fundamental insight into the picture. The nature of the interaction at the origin of this photoelectron dichroism can be finally unraveled by using a screened Yukawa potential in the modeling. The final investigations and structuration of the concepts presented are still being carried out, but will undoubtedly be of high interest.

We will see in the next section that these concepts are not specific to the orthogonal two-color fields and can be tackled from another point of view with different shapes of tailored laser fields.

## IV Chiral Attoclock

As seen throughout this chapter, tailored laser fields can be extensively used in the strong field regime to unravel the different processes at play. In this last section, we will briefly describe a study conducted in our group, where counter-rotating bicircular bichromatic (CBCBC) fields have been employed in the strong field ionization of chiral molecules. The discussion will remain concise since I have not personally participated in the experiment and the calculations. Yet, I got involved in the analysis and the discussions, and the outcomes give a particularly relevant perspective in this chapter. The results are currently under reviewing for publication.

**The Attoclock Principle**

When performing strong field ionization with a short circularly or elliptically polarized pulse, the ionization can be confined to the peak of the field because of the exponential ionization rate (given in Eq. 4.6). And as the field rotates, any angular offset of the distribution compared to the vector potential can be understood as a temporal offset, called attoclock [Eckle 08, Torlina 15]. It gives a dynamical resolution at the attosecond timescale without using typical pump-probe

schemes and is of particular interest for investigating fundamental questions such as tunneling time. Indeed, even if simple models and experiments assume that the time it takes for the electron to "go through" the tunnel is equal to zero, the veracity of this assumption remains uncertain. Some studies concluded to a finite time [Pfeiffer 12, Landsman 14, Camus 17]. However, some other claim that it could be due to other effects [Kheifets 20], such as the Wigner time-delay, corresponding to a phase offset of a wavefunction escaping a potential compared to the free wave. In addition, non-zero momentum at the exit of the tunnel barrier has also been proposed [Camus 17]. In fact, the same result can be either interpreted as resulting from zero tunneling delay and zero longitudinal momentum [Ni 18], or from nonzero value of both these quantities whose effects cancel out each other [Han 19, Kheifets 20]. Interestingly, the attoclock idea can also be implemented with more exotic field configurations [Han 18].

Can the very high sensitivity of the attoclock be used to retrieve the interplay between the field and the chiral molecular potential? In particular, can it be affected, similarly to PECD, differently for the photoelectron emitted forward and backward? Can different types of photoelectron trajectories be affected differently depending on their interplay with the chiral ionic core?

### IV. 1 Counter-Rotating Bicircular Bichromatic Field

The combination of two counter-rotating laser circularly polarized laser fields at $\omega$ and $2\omega$ yields a threefold field shape. The field amplitude ratio changes the shape, in between a triangle and a clover, as depicted in Fig. 4.36 (a) for $E_{\omega/}/E_{2\omega} = 2$ (left), 1 (center) and 0.5 (right). The two-color phase does not determine the shape, but only induces a global rotation. Conversely to the orthogonal bilinear bichromatic field, the "leaves" are identical and the final distribution has the same threefold symmetry, without inversion of the chiral response.

The 3D photoelectron momentum distribution from such a field has been measured experimentally using the tomographic reconstruction of VMI images. For each distribution, 31 projections have been recorded, each of them accumulated over $10^4$ laser shots (10 seconds at a repetition rate of 1 kHz, on the Ti:Sa source Aurore at CELIA). The results obtained in (+)-Camphor and (+)-Fenchone are depicted in Fig. 4.36 (2). The complete distributions (a) and (c) reflect the threefold symmetry of the field and several ATI are visible. Interestingly, since the field has a non-zero instantaneous chirality, a chiral-sensitive signal can be isolated by selecting the forward/backward antisymmetric part along the laser propagation axis (b) and (d).

### IV. 2 Families of Trajectories

Once again, the distributions obtained can be understood with the semi-classical framework in terms of photoelectron trajectories. In this study, Classical Trajectory Monte Carlo (CTMC) calculations have been performed in order to get an intuitive picture. This method consists in classically propagating statistical ensembles of electronic trajectories, under the molecular potential and laser field. $10^7$ non-interacting trajectories have been propagated in the phase space, and the ionized ones can be selected and analyzed individually. The electrons can be considered as freed when they escape the sphere of radius 5 a.u. . Slices of the 3D distribution

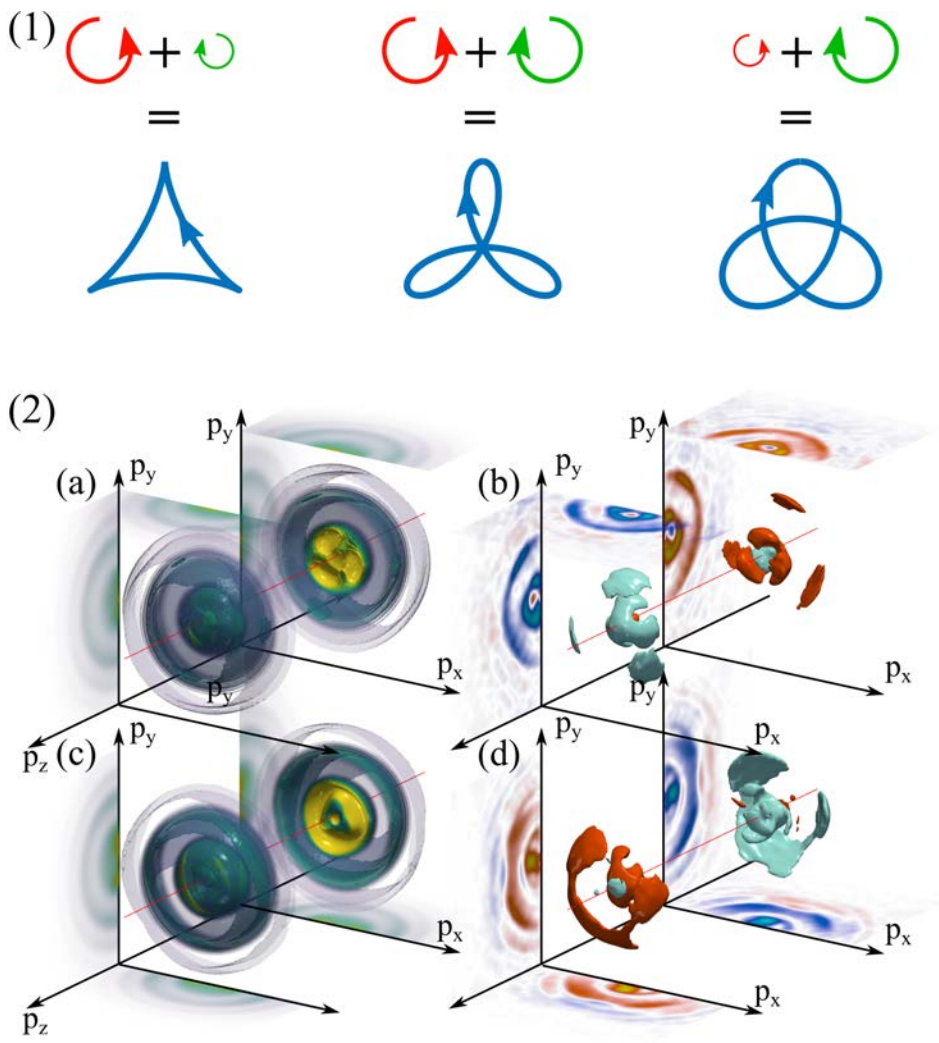


**Figure 4.36** – *(1) Threefold clover shape of the counter-rotating bicircular bichromatic laser field, for a field ratio $E_{\omega}/E_{2\omega} = 2$ (left), 1 (center) and 0.5 (right). (2) Experimental measurements, using tomographic reconstruction of VMI projections, of the 3D photoelectron angular distribution (a,c) and forward/backward asymmetry (b,d) obtained by photoionizing (+)-Camphor (a,b) and (+)-Fenchone (c,d) by a CBCBC field with $I_{800nm} = I_{400nm} = 8 \times 10^{12}$ $W.cm^{-2}$. The laser propagates along the z axis.*

calculated in an atomic target are presented is given in Fig. 4.37 (a). The mapping of the final momentum given by the vector potential at the ionization time $\vec{p}_f = -\vec{A}(t_i)$ still holds in principle and explains the threefold shape of the distributions. Nevertheless, it appears here that the slice of the distribution in the polarization plane has more of a fan shape, while it resembles a clover then an inverted fan when looking towards the high values of $|p_z|$ (along the laser axis).

It turns out that this evolution can be explained by the interplay between different types of trajectories. Two families have been identified, and are compared in the Fig. 4.37. Family 1, in blue, is made of the photoelectrons emitted during approximately the first half of each "leaf" (0-650 as), and are positively chirped (low energies first), as visible in panel (b). The second family depicted in red exits the atom during the next half (695-950 as), is more confined temporally and is negatively chirped. Their ionization dynamics also differ. Initially bounded in the 2.5 a.u. sphere in their classical ground state, the electrons of family 1 escape the 5 a.u.

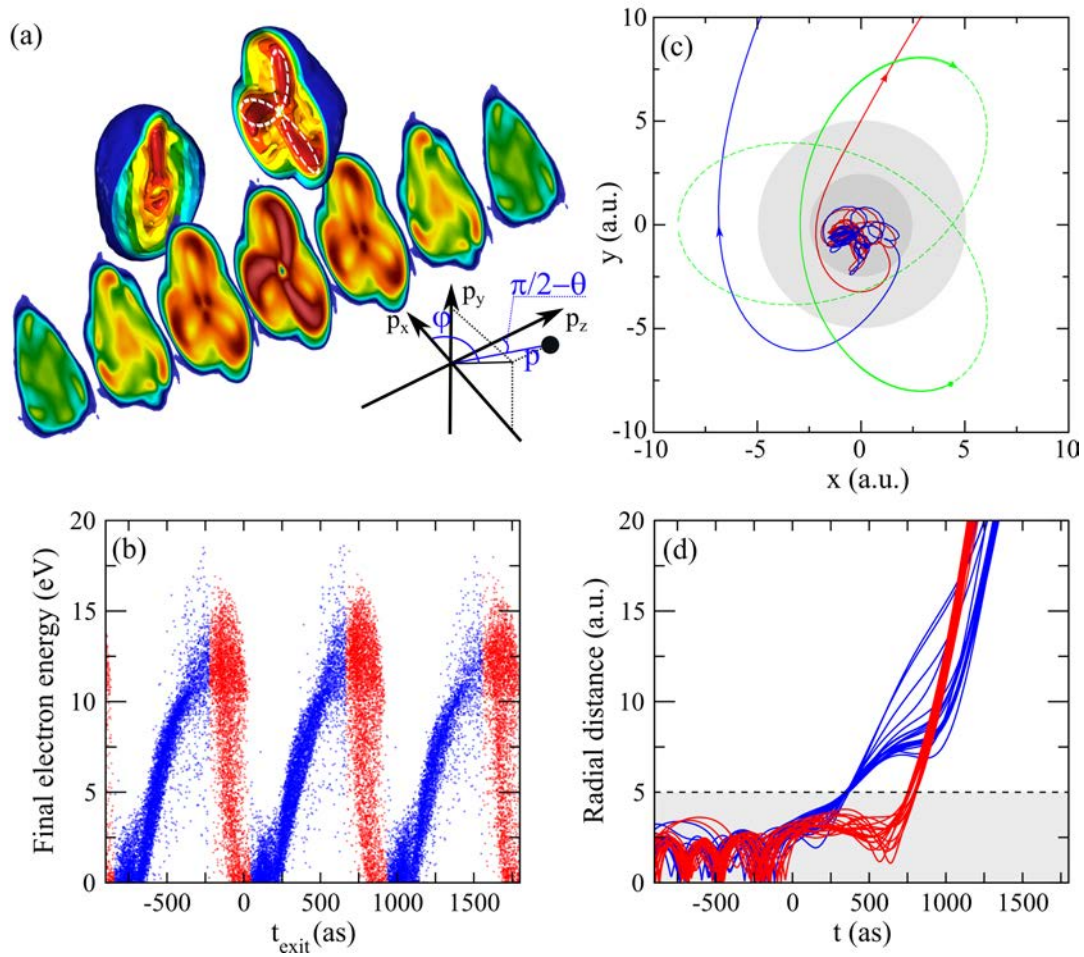


**Figure 4.37** – *CTMC simulations of atomic photoionization by a CBCBC field at $\hbar\omega = 1.55$ eV, $I_\omega = 1.6 \times 10^{14}$ W.cm$^{-2}$ and $r = I_{2\omega}/I_\omega = 4$. (a) 3D electron momentum distribution, and cuts parallel to the laser polarization plane. The dotted white line corresponds to the shape of $-\vec{A}(t)$, where $\vec{A}(t)$ is vector potential associated to the CBCBC field. (b) Final energy of the freed electrons as a function of the time at which they exit the atom, discriminating the direct (blue) and delayed (red) families, that are repeated within each leaf of the vector potential clover. (c) Average trajectories of direct (blue) and delayed (red) electrons leaving their initial confinement region (dark shaded area) and the atom (light shaded area) within one leaf of $\vec{A}(t)$. The dashed green line is $-\vec{E}(t)$, where $\vec{E}(t)$ is the CBCBC field, the arrow corresponding to the release time interval of the electrons. (d) Temporal evolution of the radial distance from the origin for direct (blue) and delayed (red) electrons ending up with 6.8 eV kinetic energy.*

radius relatively quick upon excitation (c). Conversely the electrons from family 2 spend more time in the vicinity of the potential before escaping it. Panel (d) shows the temporal evolution of the radius of the photoelectrons as a function of time, for trajectories ending at 6.8 eV. The first bunch escapes the atom around 360 as, while the second one remains within $\sim 4$ a.u. for about 600 as before being ionized.

This soft rescattering experienced by the second family of electron trajectories prior to the ionization induces a broadening of the momentum distribution along the laser axis, compared to the first family. As a result, while the first family dominates the signal in the polarization plane, the second one gradually overcomes as $|p_z|$ increases. This statement is corroborated by

quantum calculations, and remains valid at lower intensities and different field ratios.

**Trajectory-Sensitive Attoclock**

In the SFA framework, the tunnel ionization is instantaneous and the photoelectron exits with no momentum, and the final momentum is directly given by the vector potential. However, as mentioned in the introduction of the chapter, these hypothesis are not necessarily always valid and deviations from this model have been reported. In addition, these effects can not really be distinguished from each other experimentally and the interpretation depends on the point of view. In any case, the attoclock technique is particularly suited to investigate these questions, where an angular offset of the distribution can be read as a delay.

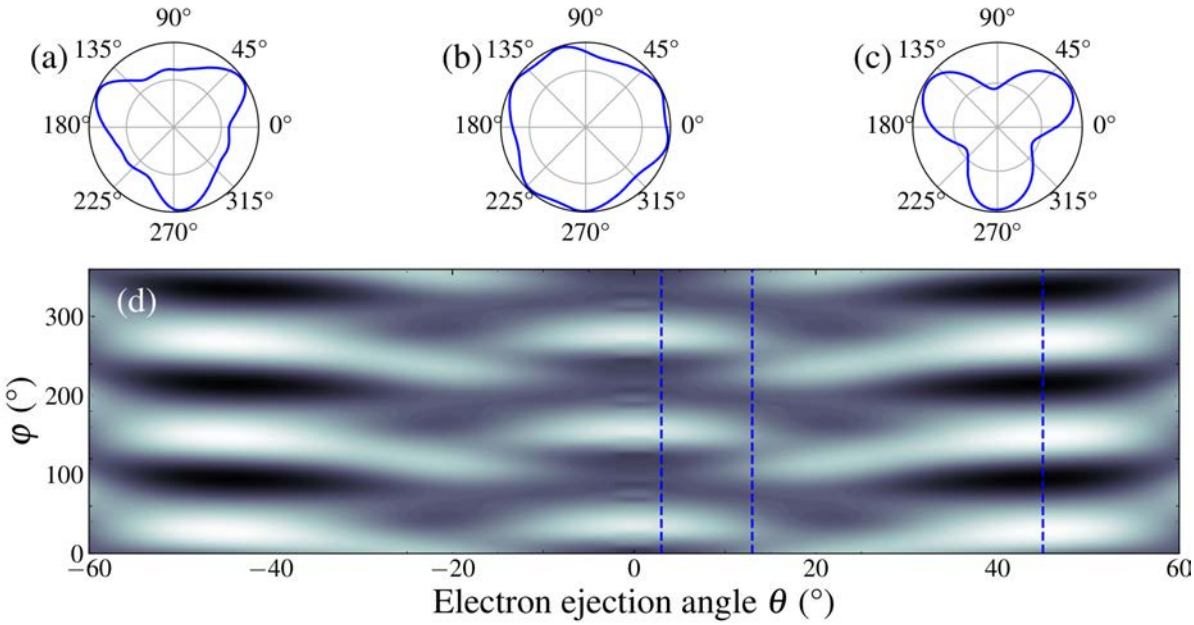


**Figure 4.38** – *Photoionization of argon atoms by a 800-400 nm CBCBC field at* $I_\omega = 1.4 \times 10^{14}$ $W.cm^{-2}$ *and* $r = I_{2\omega}/I_\omega \approx 1$. *(a-c) Attoclock polar plots of the signal of the first ATI peak at 1.3 eV, for electrons ejected at* $\theta = 3°$ *(a),* $\theta = 13°$ *(b), and* $\theta = 45°$ *(c). (d) Photoelectron signal as function of the electron ejection angle* $\theta$ *and streaking angle* $\varphi$. *The signal is normalized at each* $\theta$ *by its* $\varphi$*-averaged value. The blue vertical lines correspond to the slices shown in (a-c).*

The experimental measurement of the photoelectron produced with a CBCBC field in argon at $I_\omega = 1.4 \times 10^{14}$ $W.cm^{-2}$ and $r = I_{2\omega}/I_\omega \approx 1$ is presented in Fig. 4.38. The evolution of the distribution as a function of the streaking angle $\varphi$ and the ejection angle $\theta$ (see Fig. 4.37 (a) for the parametrization) is shown in Fig. 4.38. It appears that the clover-shaped distribution is found in the polarization plane (low $\theta$ values) (a). While increasing $\theta$, six peaks appear (b) and beyond $\sim 35°$, only three remain (c). This confirms the features identified in the CTMC calculations, as the two families of trajectories appear distinctively here at low and high $\theta$, and overlap and interfere at intermediate values. Interestingly, the evolution of the attoclock as a function of the ejection angle $\theta$ can be clearly read here, and evolves from one family to the

other (panel (d)).

## IV. 3 Sensitivity to Chirality

**Experimental Measurements**

The forward/backward asymmetry (FBA) in the distribution measured in chiral molecules presented in Fig. 4.36 will not be discussed extensively here. Let us simply mention that the interference between the different families of trajectories enhances the contrast of the dichroic response at the location where they overlap. The field parameters can then be tuned to balance the relative contributions of the families. The FBA can be maximized beyond 100 % (the normalization used enables a maximum of 200 %), due to destructive interferences between the families backward but not forward. This high value is obtained at an intensity where the strong field ionization regime is not well established. In order to discuss the sensitivity of the attoclock effect to chirality, we will thus use higher intensities.

The evolution of the streaking angle $\varphi$ with the ejection angle $\theta$ recorded in (+)-Camphor and (+)-Fenchone at $I_\omega = 5 \times 10^{13}$ $W.cm^{-2}$ and $r = I_{2\omega}/I_\omega \approx 0.1$ is presented in Fig. 4.39, respectively (a) and (b). The signal is normalized at each $\theta$ by its $\varphi$-averaged value to increase visibility. Similarly to the argon measurements, the threefold pattern is clearly visible here and shifts according to the ejection angle, *i.e.* to the dominating family of trajectories. The streaking phase of the angular oscillation $\varphi_0(\theta)$ is extracted by Fourier analysis and highlighted in the upper panels. The difference between the phase measured forward (positive $\theta$) and backward (negative $\theta$) is calculated and converted into attoseconds, from the knowledge of the laser wavelength. The chiral attoclock is depicted in the middle row, while the forward/backward asymmetry is presented on the lower one.

In both chiral molecules, the chiral attoclock effect is weak at low values of $\theta$. This means that the attoclock effect of the photoelectron trajectories belonging to the family 1 are hardly affected by the chirality of the potential. Interestingly, in the region where the family 2 become comparable in amplitude with the first one (around $\pm$ 40°), the chiral attoclock suddenly increases up to dozens of attoseconds, indicating that the second family is much more sensitive to this effect. This effect remains similar on the higher ATI peaks, where the effect become even more located at the transition. Note that the effect is similar, yet distinguishable in the two system presented. This suggests that the fine details of the molecular potential play a role here. Finally, note that a significant forward/backward asymmetry can be seen (lower row) for all trajectories, even if the values obtained for the direct electrons are generally lower than for the delayed electrons, especially in Fenchone.

**Short- and Long-Range Effects**

Time-Dependent Schrödinger Equation (TDSE) calculations have been performed with the CBCBC field, in a toy-model chiral molecule similarly to what have been already presented in this chapter. Briefly, they nicely reproduce the features described so far, in particular the different families of trajectories and the attoclock effect. In the perspective of unraveling the contribution of the short- and long-range effects of the potential, the comparison between the

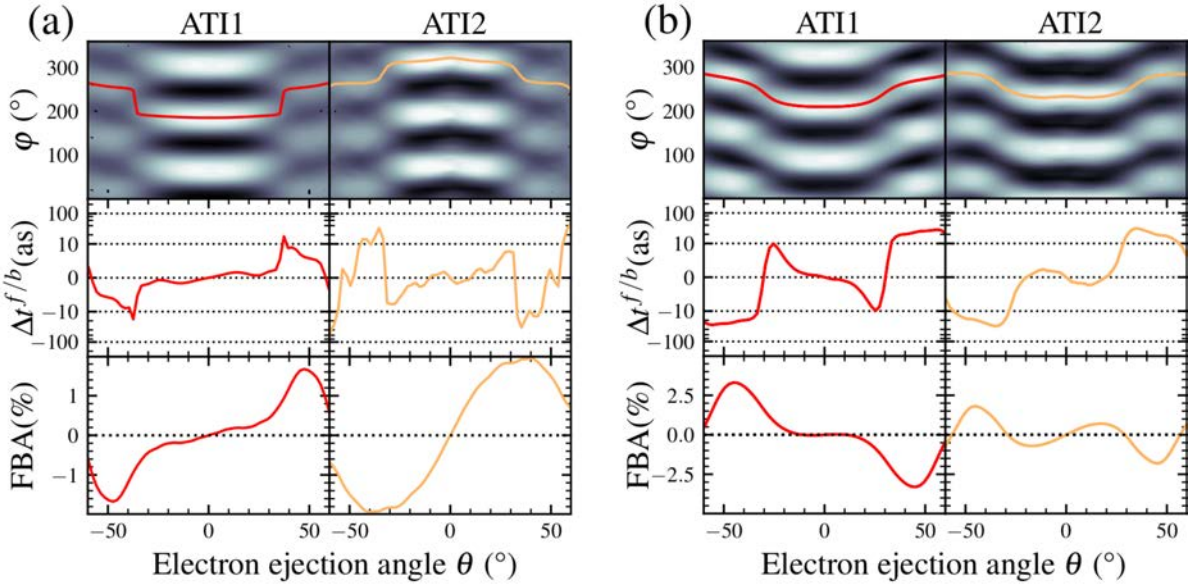


**Figure 4.39** – *Attoclock measurements in (+)-Camphor (a) and (+)-Fenchone (b) at* $I_\omega = 5 \times 10^{13}$ $W.cm^{-2}$ *and* $r = I_{2\omega}/I_\omega \approx 0.1$ *and right circular polarization of the fundamental. Top row : Photoelectron signal of the two first ATI peaks as a function of the electron ejection angle* $\theta$ *and streaking angle* $\varphi$*. The signal is normalized at each* $\theta$ *by its* $\varphi$*-averaged value. The lines represent the streaking phase* $\varphi_0(\theta)$ *extracted by Fourier analysis. Middle row : Differential attoclock delay* $\Delta t^{f/b}(\theta)$ *between electrons ejected forward and backward. The scale is linear between -10 as and +10 as, and logarithmic beyond. Bottom row : Forward/Backward asymmetry (FBA).*

Coulomb and screened Yukawa potentials has been performed. Noticeably, the jump in of the streaking phase between the two families of trajectories is still visible with the screened potential, indicating that both families still exist. Importantly, the chiral attoclock and forward/backward asymmetry remain visible for the second family. This corroborates the vision given by the CTMC calculations in Fig. 4.37, namely that the delayed photoelectrons are imprinted by the chirality of the potential while they spend hundreds of attoseconds in its vicinity. Conversely, the chiral attoclock effect almost completely vanishes for the direct trajectories. This shows that these photoelectrons are affected by the chirality of the potential at long ranges, which is consistent with previous studies [Torlina 15, Sainadh 19]. Notably, the forward/backward asymmetry remains significant for the direct trajectories. This means that in this case, this very simple observable can have a superior sensitivity to the molecular potential. This is due to the quantum nature of the photoionization process, which encodes the subtle influence of scattering phase-shifts in the photoelectron circular dichroism [Powis 08].

## IV. 4 Discussion

The present study show both theoretically and experimentally that the chiral potential can play a significant role in strong field ionization. Its effect emerges not only in the forward/backward asymmetry of the signal similarly to PECD, but also here in the angular streaking performed by the CBCBC field. This contradicts the picture of adiabatic tunneling, where the photoelectrons instantaneously tunnel out of the potential barrier at a large enough distance to scatter almost

only under the influence of the field. From the parameters used here, the Keldysh parameter is indeed about 1.5, meaning that the tunneling regime is rather non-adiabatic. The consequences are typically transverse momentum shift at the tunnel exit, a delayed appearance in the continuum, or an increase of electron energy leading to a shift of the tunneling exit distance towards the ionic core [Klaiber 15].

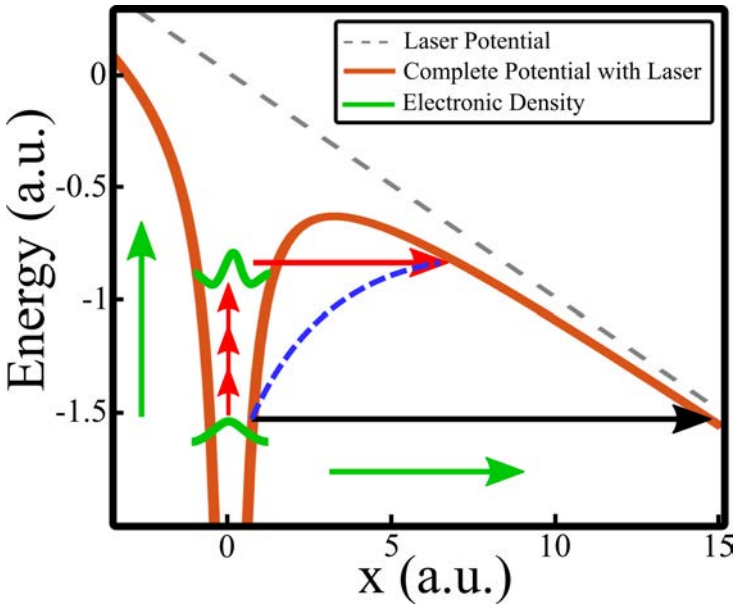


**Figure 4.40** – *Illustration of the under-the-barrier motion of the electron during the tunneling process. The adiabatic picture is represented by the black arrow. The non-adiabatic picture is depicted by the blue dotted line. The non-adiabatic process can be described as an excitation followed by an adiabatic ionization (red arrows). The tunneling and multiphoton ionization channels are represented by respectively the horizontal and vertical green arrows. Inspired from [Klaiber 15].*

The latter effect is particularly crucial in the case of chiral interaction, since the closer the electrons emerge from the core, the stronger the influence of the chiral ionic potential will be. The non-adiabatic tunneling regime can be decomposed into two steps. The electron gets excited in a first place, and then tunnels out adiabatically from the excited states [Klaiber 15, Ni 18]. This vision is close to the one presented here with the semi-classical analysis of the delayed family of photoelectrons, and is corroborated with quantum calculations (not shown here).

The presented work demonstrates that the short range potential can strongly influence the electron wavepacket before it gets tunneled out, which is unveiled here by the asymmetric part of the interaction. It could explain the reminiscence of PECD even close to the adiabatic tunneling regime [Beaulieu 16a]. Additionally, evidences also indicate a vanishing influence of these short range effects on the outcome of the attoclock measurements.

# V Conclusion and Perspectives

We have seen in this chapter that the strong field ionization regime was providing a particularly rich insight into the molecular chirality. Indeed, the semi-classical picture in terms of photoelectron trajectories enables us to rationalize the chirality experienced individually by the

photoelectrons. Their interference is a central observable here, and provide a very sensitive probe. In particular, tailored laser fields allow for their fine control and can be used in different configurations, to reveal complementary points of views on the same global process. The sub-optical nature of the chiral interaction of the photoelectron driven by the field under the influence of the molecular potential opens a broad doorway to dynamics occurring at a timescale hardly accessible in a pump-probe scheme. Beyond this, the spatio-temporal mapping of the final momenta unveils the different interactions that the scattering electrons underwent. Not only this gives a deeper understanding of the processes at the origin of the photoelectron circular dichroism. The use of the chirality turns out to particularly enrich the observables already widely used in the strong field Physics community. Paradoxically, the complexification of the light-matter interaction scheme (using polyatomic molecules and complex field shapes) leads to the simplification of the interpretation. Indeed, the forward/backward asymmetries in the angular distribution isolates specifically the crossed interaction with the field and the potential.

# Chapter 5

# General Conclusion and Perspectives

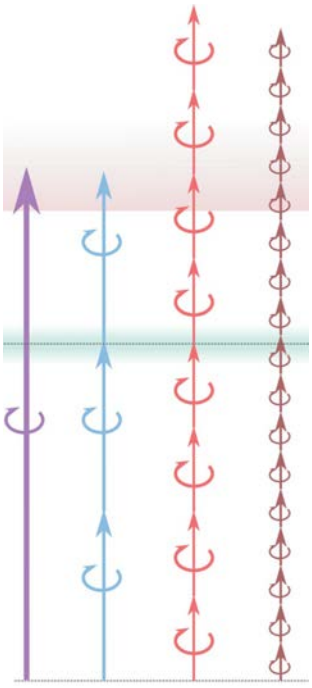

We will here briefly summarize the results presented throughout this manuscript and discuss the perspectives of improvements and future studies.

## Experimental Developments

The development of a high repetition rate laser beamline based on a commercial-grade fiber laser technology has been presented. It shows great advantages in terms of day-to-day ease of use, and enables one to carry out molecular physics experiments with an unprecedented acquisition time. A broad range of light-matter interaction regimes can be reached : the fundamental near-infrared wavelength can be used in strong field interaction or sustain frequency conversion to perform multiphoton ionization. We have seen that XUV photons could also be produced by (cascaded) high-order harmonics generation. The fluxes obtained with this technique are highly competitive compared to the other technologies currently available. In order to use it in our field of interest, the monochromatization and production of circularly or elliptically polarized harmonics have been discussed. An optical parametric amplification stage has also been presented. The wavelength tunability is indeed a great asset, in particular so that the photon energy matches certain resonant processes. We are currently examining the possibilities to implement it permanently to our setup.

This technology also has drawbacks, which we have dealt with. Firstly, the high repetition rate goes along with a high average power which has to be handled to avoid in particular thermal drifts. We have seen that they could cause trouble during experiments, but could be circumvented by using lock-in detection schemes. We also foresee to implement further active stabilizations to the beamline so that it can be used in a more reliable manner. In a similar fashion, we have seen that a sub-optical cycle delay stabilization has also been achieved in an interferometer to generate tailored laser fields. Secondly, the duration of the pulses provided are relatively long, compared to other laser technologies. Hollow-core capillary postcompression has been employed to reduce it. While we are still working on implementing it on a daily

basis, other recent technologies such as multipath cells [Lavenu 18] or solitonic compression [Travers 19] are being considered.

The tunability of the repetition rate offers an important degree of freedom for the investigation of molecular processes : the pulse energy can be kept constant while the signal level is maximized. With this high repetition rate source, photoionization experiments were carried out in our velocity map imaging spectrometer with an unprecedented statistics acquisition. This allows either to monitor much finer effects, or to investigate additional degrees of freedom by increasing the dimensionality of the measurement.

It also breaks an important limitation of table-top sources : coincidence measurements, which set a limitation in terms of events per shot. A significant part of this thesis was dedicated to building, implementing, characterizing and optimizing a photoelectron/photoion coincidence spectrometer (COLTRIMS). Despite being a relatively mature technique, this constitutes a new field of expertise in our laboratory. Even if the unmounted apparatus and acquisition software were acquired from a company, the development of the device remains challenging. In particular, continuous progress has been made for the optimization of its counting rate, which is the cornerstone of advanced experiments. Several perspectives to further improve it are still being investigated, and especially reconsidering the numerical coincidence acquisition and tagging.

Coincidence detection requires long acquisitions. For this purpose, the stabilization of the beamline mentioned just above, as well as its automation and remote control are crucial.

## Multiphoton Regime

### PEELD

Photoelectron circuclar dichroism (PECD) is a powerful observable of molecular chirality, which has multiple sensitivities. We have here investigated the role of the anisotropy of excitation that can take place in resonance-enhanced multiphoton ionization or chiral organic compounds. In particular, they can be revealed by the non-trivial dependency of the asymmetries in the photoelectron angular distributions to the laser field ellipticity, in simple one-color experiments (photoelectron elliptical dichroism, or PEELD). We have seen that the informations encoded are highly enantiomer- and molecular-specific, and can be used for analytical purposes. Combined with the high repetition rate source, a technique of measurement of the enantiomeric excess of a sample has been developed. It presents highly competitive performances, either in terms of accuracy or in terms of reactivity, enabling for continuous monitoring. Furthermore, the ellipticity-dependent distributions can constitute molecular fingerprints, and be used to track the composition of multicomponent mixtures. A spin-off project has been initiated to implement the process at an industrial-grade level. In this context, the systematic investigation of the robustness of the measurement is crucial. In particular, the generalization of the observations to a wide range of chiral compounds is important, as well as its repeatability in various laser conditions.

Generally speaking, the multiphoton regime enables a great variety of configurations. The first PEELD results obtained with the tunable wavelength source are under analysis. Fig. 5.1 shows the primary results. It shows the interesting potential of selecting the different excitations, as well as non-trivial behavior such as the sign flip of $b_1$ or $b_3$ around 2 eV depending on the laser wavelength and ellipticity.

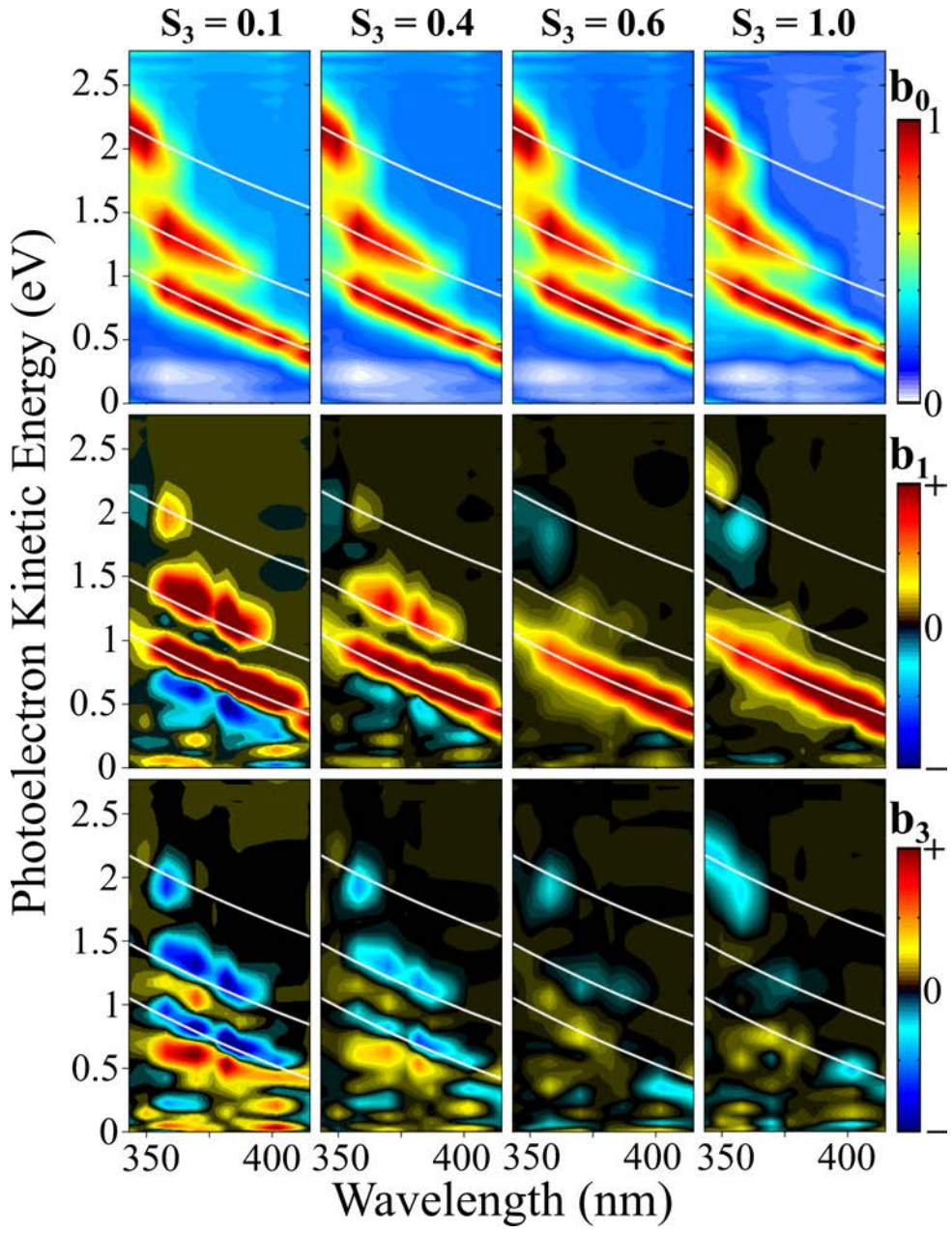


**Figure 5.1** – *Photoelectron elliptical dichroism with a tunable wavelength source. The columns correspond to Stokes parameters $S_3$ = 0.1, 0.4, 0.6 and 1.0, from left to right. (Top row) Photoelecron kinetic energy spectra ($b_0$) as a function of the laser wavelength. The white lines indicate the ionization from the 3s, 3p and $\pi^*$ excited states. (Middle row) Corresponding first order of Lengendre polynomials $b_1$. (Bottom row) Corresponding $b_3$.*

Furthermore, the investigation of the PEELD effect as a function of the pulse duration and

spectrum width, using the postcompression, has been initiated.

## Time-Resolved Chiral Dynamics

### Few-femtosecond photorelaxation of (M)Ethyl-Lactate

A time-resolved PECD experiment has been performed on an external ultrashort UV-IR beamline in a VMI. This constitutes the first investigation of the process at the few-femtosecond timescale. The first conclusions indicate that interesting dynamics can be revealed at this timescale. The broad spectral support of the short pulses can however mix different processes and theoretical modeling is currently being performed to clarify the interpretation.

The developments carried out in this thesis open the way to perform time-resolved pump-probe measurements, enabled by resonance-enhanced multiphoton ionization, in coincidence experiments. In this fashion, one could for instance use a pump pulse to initiate the breaking of a chiral molecule into achiral fragments. A circular probe could then reveal molecular chirality at various delays, *i.e.* different stages of the fragmentation.

### Light-Induced Chirality

A collaboration with Jason Greenwood and Caiomhe Bond has also taken place to study transient chirality : in molecules such as Stilbene or Azobenzene, sterical hindrance can strain the molecule into a chiral isomer. We hoped that the photoisomerization induced by a circular pump could have preferentially induced the transient formation of a given enantiomer, which would have been tracked by a circular probe. Unfortunately, the effect is expected to be very weak (magnetic dipole effect) in such a way that we have not managed to identify it experimentally so far.

### Towards Time-Resolved Chiral Recognition

Two chiral molecules that have a good tendency to form dimers, Ethyl- and Methyl-Lactate, have been characterized in the perspective of investigating the dynamics of the chiral recognition processes. It turns out that their particularly rich fragmentation can also be a good support in this context. The investigation of the fragment-dependent photoelectron distributions has been presented, and preliminary results indicate that they can be used to disentangle different contributions in the photofragmentation and photoionization processes, which is the goal of using coincidence detection here. The opening toward fragment-resolved PECD measurements is clear, and recent improvements of the beamline should undoubtedly enable us to reach this milestone.

Apart from this, double ionization experiments would be of high interest to investigate for instance PECD in cationic species. Yet, the process is usually minority and remains technically challenging in coincidence detection. Finally, XUV-VIS pump-probe experiments would also constitute a very good support. The ionization could for instance be induced by the XUV photons and dressed by the visible ones, or conversely. For this purpose, the coherent combination of our two amplifiers and the complete stabilization of the beamline are crucial.

## Strong Field Regime

We have seen that investigating molecular chirality by using the tools of the strong field interaction regime can bring interesting insights into both domains. On the one hand, the semi-classical interpretation of photoionization in terms of electron trajectories enables to describe the chirality experienced individually by the photoelectrons. On the other hand, chirosensitive effects add a dynamical observable of the effect of the molecular potential. Despite the fact that this latter is neglected in a first approximation in strong fields, it indeed plays an important role in photoionization. By introducing chirality in this context, the effect of the molecular potential can be isolated by monitoring specifically the forward/backward antisymmetric part of the photoelectron angular distributions.

The sensitivity of the photoelectron trajectories to the vectorial properties of the laser field has been investigated using two types of tailored field : orthogonal bilinear bichromatic and counter-rotating bicircular bichromatic fields. The first configuration has been used to show that chirosensitive processes could be induced by the instantaneous chirality of the electric field at the sub-optical timescale. This constitutes an important observation, since it opens the investigation of chirality to an unprecedented timescale of processes. Beyond this, the shape of the electric field has been used to manipulate the different photoelectron trajectories as well as their experienced chirality. The interference pattern observed is a very sensitive observable, and can be controlled in order to reveal different interactions affecting different trajectories. By combining experimental measurements and several types of theoretical models, we have seen that some trajectories can directly escape the molecular potential while some other spend more time in its vicinity. As a result, they end up being affected differently by its chirality.

Depending on the field configuration, complementary observations can be made. We have in particular isolated chiral phase effects and chiral attoclock effects. These quantities are typically used to reveal very fine strong field effects at the attosecond timescale : the tunneling phase, the scattering of the wavepacket, the rescattering onto the ionic core, and other processes related to the diabaticity of the process, such as the initial velocity, the tunneling time and distance, the interplay with intermediate bound states and so on. These effects are often intricate and hard to distinguish, in such a way that the interpretations can be sometimes controversial and disputed. Adding chirality can offer a new angle of view into these processes, which are of fundamental interest.

Furthermore, photoionization is not the only process of interest in strong field physics. The manipulation of the field chirality and the electron trajectories could also be related for instance to the high-order harmonics generation process. Again, this could be used either to access further information about the generating medium, or to control the properties of the emitted radiation.

## Conclusion

The work described in this manuscript has covered a broad spectral range of ionizing sources, from the IR to the XUV, associated with different ionization mechanisms, from tunnel ionization to single-photon absorption. In the view of this diversity, can we draw conclusions on the ideal

light source, regime, and observable to investigate ultrafast chirality?

**XUV/Single-Photon Ionization** : In this regime, PECD has the great advantage of being a universal probe and offering a broad range of sensitivities. Furthermore, its theoretical description, based on the perturbative approach, starts to be quantitative and enables one to isolate each of these sensitivities. Nevertheless, the production of circularly polarized ultrashort XUV pulses remains experimentally challenging. The single-photon ionization also often opens many photoionization channels, whose contributions overlap in the photoelectron spectra. This issue worsens with the broad bandwidth supporting ultrashort pulses. Good perspectives are provided by photoelectron-photoion coincidence spectroscopy, which enables partial deciphering of the spectra in this sense.

**REMPI** : Resonance-enhanced multiphoton ionization is much easier to perform experimentally speaking. The signal yielded is strong, and very fast acquisitions can be performed, for instance using VMI. It is more selective in the ionization channels than single-photon processes, and tends to present less congested photoelectron spectra. The strong influence of the intermediate resonances can be interesting, but significantly complicate its description. Still, theory starts to be semi-quantitative [Goetz 17, Demekhin 18, Goetz 19]. Experimentally, the PEELD effect can be used to increase the dimensionality of the measurement, and COLTRIMS can help identifying orientation dependency.

**Strong Fields** : This framework presents an intrinsic attosecond resolution, and allows for a simplified semi-classical description. It has a high versatility in terms of trajectory manipulation. In addition, single (or few) ionization channels/orbitals are naturally selected by tunnel ionization. However, the probe can significantly perturb the system. A quantitative description for real systems is thus difficult. Interestingly, advanced optical schemes can be applied to isolate background-free signatures of the chiral potential. Moreover, this can be investigated using Coulomb-corrected theoretical strong-field approaches.

PECD is thus an observable of choice of molecular chirality, as it is strong, relatively easy to access, highly versatile and allows for multiple angles of view. These studies are conducted in the gas phase and present the advantage of being carried out in isolated systems, where hopefully all the processes can be grasped explicitly. With the recent technological advances, in particular in liquid jet techniques for photoelectron ultrafast spectroscopy [Jordan 20], I look forward to the extension of PECD towards the world of liquid phase. I believe that the ultrafast resolution of the chiral interactions occurring in this phase could be of high interest for the understanding of many chemical processes, involved in particular in living systems.

| | **Beamline** | **VMI** | **COLTRIMS** |
|---|---|---|---|
| **Experimental Developments** (Ch. 2) | *Short Pulses : Ultrafast Dynamics*<br><br>*Improved Stability : Pump-Probe Coincidence* | *TR-XUV PECD*<br><br>*PEELD : Reliability and Compacity for Industrial Applications* | *Double skimmer : Clusters and XUV*<br><br>*Continuous Assignment Coincidences : High Acquisition Rate* |
| **Multiphoton** (Ch. 3) | *UV REMPI Schemes* | *Spectroscopy : Resonances*<br><br>*TR-PEELD* | *Clusters*<br><br>*Chiral Recognition* |
| **Strong Field** (Ch. 4) | *3D Vectorial Fields*<br><br>*Passive Sub-Cycle Stability* | *Nonadiabatic Tunneling* | *Strong-Field PECD/Fragmentation* |

**Figure 5.2** – *Table summarizing some perspectives presented in this thesis manuscript.*

# Bibliography


[Ashfold 06] M. N. R. Ashfold, N. H. Nahler, A. J. Orr-Ewing, O. P. J. Vieuxmaire, R. L. Toomes, T. N. Kitsopoulos, I. A. Garcia, D. A. Chestakov, S.-M. Wu & D. H. Parker. *Imaging the dynamics of gas phase reactions.* Phys. Chem. Chem. Phys., **8**, 1, pages 26–53, (2006). [Cited on page 66.]

[Ayuso 19] D. Ayuso, O. Neufeld, A. F. Ordonez, P. Decleva, G. Lerner, O. Cohen, M. Ivanov & O. Smirnova. *Synthetic chiral light for efficient control of chiral light–matter interaction.* Nature Photonics, **13**, 12, pages 866–871, (2019). [Cited on pages 128 and 209.]

[Backx 75] C. Backx & M. J. V. d. Wiel. *Electron-ion coincidence measurements of $CH_4$.* Journal of Physics B: Atomic and Molecular Physics, **8**, 18, pages 3020–3033, (1975). [Cited on page 162.]

[Baker 06] S. Baker, J. S. Robinson, C. A. Haworth, H. Teng, R. A. Smith, C. C. Chirila, M. Lein, J. W. G. Tisch & J. P. Marangos. *Probing Proton Dynamics in Molecules on an Attosecond Time Scale.* Science, **312**, 5772, pages 424–427, (2006). [Cited on pages 54 and 202.]

[Barreau 18] L. Barreau, K. Veyrinas, V. Gruson, S. J. Weber, T. Auguste, J.-F. Hergott, F. Lepetit, B. Carré, J.-C. Houver, D. Dowek & P. Salières. *Evidence of depolarization and ellipticity of high harmonics driven by ultrashort bichromatic circularly polarized fields.* Nature Communications, **9**, 4727, (2018). [Cited on page 59.]

[Barreau 20] L. Barreau, A. D. Ross, S. Garg, P. M. Kraus, D. M. Neumark & S. R. Leone. *Efficient table-top dual-wavelength beamline for ultrafast transient absorption spectroscopy in the soft X-ray region.* Scientific Reports, **10**, 5773, (2020). [Cited on pages 53 and 54.]

[Batista Jr. 15] J. M. Batista Jr., E. W. Blanch & V. d. S. Bolzani. *Recent advances in the use of vibrational chiroptical spectroscopic methods for stereochemical characterization of natural products.* Natural Product Reports, **32**, 9, pages 1280–1302, (2015). [Cited on page 127.]

[Baykusheva 19] D. Baykusheva, D. Zindel, V. Svoboda, E. Bommeli, M. Ochsner, A. Tehlar & H. J. Wörner. *Real-time probing of chirality during a chem-*

*ical reaction.* Proceedings of the National Academy of Sciences, **116**, 48, pages 23923–23929, (2019). [Cited on pages 128 and 209.]

[Beaulieu 16a] S. Beaulieu, A. Ferré, R. Géneaux, R. Canonge, D. Descamps, B. Fabre, N. Fedorov, F. Légaré, S. Petit, T. Ruchon, V. Blanchet, Y. Mairesse & B. Pons. *Universality of photoelectron circular dichroism in the photoionization of chiral molecules.* New Journal of Physics, **18**, 10, page 102002, (2016). [Cited on pages 41, 42, 121, 209, 244, and 254.]

[Beaulieu 16b] S. Beaulieu, A. Comby, B. Fabre, D. Descamps, A. Ferré, G. Garcia, R. Géneaux, F. Légaré, L. Nahon, S. Petit, T. Ruchon, B. Pons, V. Blanchet & Y. Mairesse. *Probing ultrafast dynamics of chiral molecules using time-resolved photoelectron circular dichroism.* Faraday Discussions, **194**, pages 325–348, (2016). [Cited on pages 119, 121, and 209.]

[Beaulieu 17] S. Beaulieu, A. Comby, A. Clergerie, J. Caillat, D. Descamps, N. Dudovich, B. Fabre, R. Géneaux, F. Légaré, S. Petit, B. Pons, G. Porat, T. Ruchon, R. Taïeb, V. Blanchet & Y. Mairesse. *Attosecond-resolved photoionization of chiral molecules.* Science, **358**, pages 1288—1294, (2017). [Cited on pages 209 and 238.]

[Beaulieu 18a] S. Beaulieu, A. Comby, D. Descamps, B. Fabre, G. A. Garcia, R. Géneaux, A. G. Harvey, F. Légaré, Z. Mašín, L. Nahon, A. F. Ordonez, S. Petit, B. Pons, Y. Mairesse, O. Smirnova & V. Blanchet. *Photoexcitation circular dichroism in chiral molecules.* Nature Physics, **14**, 5, pages 484–489, (2018). [Cited on pages 121, 123, and 124.]

[Beaulieu 18b] S. Beaulieu, A. Comby, D. Descamps, S. Petit, F. Légaré, B. Fabre, V. Blanchet & Y. Mairesse. *Multiphoton photoelectron circular dichroism of limonene with independent polarization state control of the bound-bound and bound-continuum transitions.* The Journal of Chemical Physics, **149**, 13, page 134301, (2018). [Cited on pages 124, 125, 126, 172, and 174.]

[Berthod 06] A. Berthod. *Chiral recognition mechanisms.* Analytical Chemistry, **78**, 7, pages 2093–2099, (2006). [Cited on pages 30 and 31.]

[Bian 12] X.-B. Bian & A. D. Bandrauk. *Attosecond Time-Resolved Imaging of Molecular Structure by Photoelectron Holography.* Physical Review Letters, **108**, 263003, (2012). [Cited on page 205.]

[Billaud 12] P. Billaud, M. Géléoc, Y. J. Picard, K. Veyrinas, J. F. Hergott, S. Marggi Poullain, P. Breger, T. Ruchon, M. Roulliay, F. Delmotte, F. Lepetit, A. Huetz, B. Carré & D. Dowek. *Molecular frame photoemission in dissociative ionization of $H_2$ and $D_2$ induced by high harmonic generation femtosecond XUV pulses.* Journal of Physics B: Atomic,

Molecular and Optical Physics, **45**, 194013, (2012). [Cited on pages 43 and 44.]

[Blokhin 03] A. P. Blokhin, M. F. Gelin, E. V. Khoroshilov, I. V. Kryukov & A. V. Sharkov. *Dynamics of optically induced anisotropy in an ensemble of asymmetric top molecules in the gas phase.* Optics and Spectroscopy, **95**, 3, pages 346–352, (2003). [Cited on page 174.]

[Boesl 13] U. Boesl, A. Bornschlegl, C. Logé & K. Titze. *Resonance-enhanced multiphoton ionization with circularly polarized light: chiral carbonyls.* Analytical and Bioanalytical Chemistry, **405**, pages 6913–6924, (2013). [Cited on page 137.]

[Boge 14] R. Boge, S. Heuser, M. Sabbar, M. Lucchini, L. Gallmann, C. Cirelli & U. Keller. *Revealing the time-dependent polarization of ultrashort pulses with sub-cycle resolution.* Optics Express, **22**, 22, page 26967, (2014). [Cited on page 210.]

[Boguslavskiy 12] A. E. Boguslavskiy, J. Mikosch, A. Gijsbertsen, M. Spanner, S. Patchkovskii, N. Gador, M. J. J. Vrakking & A. Stolow. *The Multielectron Ionization Dynamics Underlying Attosecond Strong-Field Spectroscopies.* Science, **335**, 6074, pages 1336–1340, (2012). [Cited on page 162.]

[Bordas 96] C. Bordas, F. Paulig, H. Helm & D. L. Huestis. *Photoelectron imaging spectrometry: Principle and inversion method.* Review of Scientific Instruments, **67**, 6, pages 2257–2268, (1996). [Cited on page 66.]

[Bourgalais 20] J. Bourgalais, N. Carrasco, L. Vettier, T. Gautier, V. Blanchet, S. Petit, D. Descamps, N. Fedorov, R. Delos & J. Gaudin. *On an EUV Atmospheric Simulation Chamber to Study the Photochemical Processes of Titan's Atmosphere.* Scientific Reports, **10**, 10009, (2020). [Cited on page 58.]

[Böwering 01] N. Böwering, T. Lischke, B. Schmidtke, N. Müller, T. Khalil & U. Heinzmann. *Asymmetry in Photoelectron Emission from Chiral Molecules Induced by Circularly Polarized Light.* Physical Review Letters, **86**, 7, pages 1187–1190, (2001). [Cited on page 34.]

[Calegari 16] F. Calegari, A. Trabattoni, A. Palacios, D. Ayuso, M. C. Castrovilli, J. B. Greenwood, P. Decleva, F. Martín & M. Nisoli. *Charge migration induced by attosecond pulses in bio-relevant molecules.* Journal of Physics B: Atomic, Molecular and Optical Physics, **49**, 142001, (2016). [Cited on page 54.]

[Camus 17] N. Camus, E. Yakaboylu, L. Fechner, M. Klaiber, M. Laux, Y. Mi, K. Z. Hatsagortsyan, T. Pfeifer, C. H. Keitel & R. Moshammer. *Experimental*

*Evidence for Quantum Tunneling Time.* Physical Review Letters, **119**, 023201, (2017). [Cited on page 248.]

[Catoire 16] F. Catoire, A. Ferré, O. Hort, A. Dubrouil, L. Quintard, D. Descamps, S. Petit, F. Burgy, E. Mével, Y. Mairesse & E. Constant. *Complex structure of spatially resolved high-order-harmonic spectra.* Physical Review A, **94**, 063401, (2016). [Cited on page 199.]

[Chandler 87] D. W. Chandler & P. L. Houston. *Two-dimensional imaging of state-selected photodissociation products detected by multiphoton ionization.* The Journal of Chemical Physics, **87**, 2, pages 1445–1447, (1987). [Cited on page 66.]

[Chang 04] Z. Chang. *Single attosecond pulse and XUV supercontinuum in the high-order harmonic plateau.* Physical Review A, **70**, 043802, (2004). [Cited on page 200.]

[Chang 07] Z. Chang. *Controlling attosecond pulse generation with a double optical gating.* Physical Review A, **76**, 051403(R), (2007). [Cited on page 200.]

[Chen 10] M.-C. Chen, P. Arpin, T. Popmintchev, M. Gerrity, B. Zhang, M. Seaberg, D. Popmintchev, M. M. Murnane & H. C. Kapteyn. *Bright, Coherent, Ultrafast Soft X-Ray Harmonics Spanning the Water Window from a Tabletop Light Source.* Physical Review Letters, **105**, 173901, (2010). [Cited on page 53.]

[Cireasa 15] R. Cireasa, A. E. Boguslavskiy, B. Pons, M. C. H. Wong, D. Descamps, S. Petit, H. Ruf, N. Thiré, A. Ferré, J. Suarez, J. Higuet, B. E. Schmidt, A. F. Alharbi, F. Légaré, V. Blanchet, B. Fabre, S. Patchkovskii, O. Smirnova, Y. Mairesse & V. R. Bhardwaj. *Probing molecular chirality on a sub-femtosecond timescale.* Nature Physics, **11**, 8, pages 654–658, (2015). [Cited on pages 128 and 208.]

[Cohen-Tannoudji 77] C. Cohen-Tannoudji, B. Diu & F. Laloë. Quantum mechanics, volume 2. Hermann and John Wiley and Sons, Inc., (1977). [Cited on page 194.]

[Comby 16] A. Comby, S. Beaulieu, M. Boggio-Pasqua, D. Descamps, F. Légaré, L. Nahon, S. Petit, B. Pons, B. Fabre, Y. Mairesse & V. Blanchet. *Relaxation Dynamics in Photoexcited Chiral Molecules Studied by Time-Resolved Photoelectron Circular Dichroism: Toward Chiral Femtochemistry.* The Journal of Physical Chemistry Letters, **7**, 22, pages 4514–4519, (2016). [Cited on pages 41, 173, 175, and 176.]

[Comby 18] A. Comby, S. Beaulieu, E. Constant, D. Descamps & Y. Mairesse. *Absolute gas density profiling in high-order harmonic generation.* Optics Express, **26**, 15, page 6001, (2018). [Cited on pages 55 and 201.]

[Comby 19] A. Comby, D. Descamps, S. Beauvarlet, A. Gonzalez, F. Guichard, S. Petit, Y. Zaouter & Y. Mairesse. *Cascaded harmonic generation from a fiber laser: a milliwatt XUV source.* Optics Express, **27**, 15, page 20383, (2019). [Cited on pages 55, 56, 57, and 202.]

[Comby 20a] A. Comby, E. Bloch, S. Beauvarlet, D. Rajak, S. Beaulieu, D. Descamps, A. Gonzalez, F. Guichard, S. Petit, Y. Zaouter, V. Blanchet & M. Y. *Bright, polarization-tunable high repetition rate extreme ultraviolet beamline for coincidence electron-ion imaging.* arXiv:2006.06297, (2020). [Cited on pages 49, 55, 58, 59, and 200.]

[Comby 20b] A. Comby, C. M. Bond, E. Bloch, D. Descamps, B. Fabre, S. Petit, Y. Mairesse, J. B. Greenwood & V. Blanchet. *Using photoelectron elliptical dichroism (PEELD) to determine real-time variation of enantiomeric excess.* Chirality, 1–9, (2020). [Cited on page 121.]

[Constant 99] E. Constant, D. Garzella, P. Breger, E. Mével, C. Dorrer, C. Le Blanc, F. Salin & P. Agostini. *Optimizing High Harmonic Generation in Absorbing Gases: Model and Experiment.* Physical Review Letters, **82**, 8, pages 1668–1671, (1999). [Cited on page 201.]

[Corkum 93] P. B. Corkum. *Plasma perspective on strong field multiphoton ionization.* Physical Review Letters, **71**, 13, pages 1994–1997, (1993). [Cited on page 198.]

[Cousin 17] S. L. Cousin, N. Di Palo, B. Buades, S. M. Teichmann, M. Reduzzi, M. Devetta, A. Kheifets, G. Sansone & J. Biegert. *Attosecond Streaking in the Water Window: A New Regime of Attosecond Pulse Characterization.* Physical Review X, **7**, 041030, (2017). [Cited on page 53.]

[Dasch 92] C. J. Dasch. *One-dimensional tomography: a comparison of Abel, onion-peeling, and filtered backprojection methods.* Applied Optics, **31**, 8, page 1146, (1992). [Cited on page 69.]

[de Oliveira 09] N. de Oliveira, D. Joyeux, D. Phalippou, J. C. Rodier, F. Polack, M. Vervloet & L. Nahon. *A Fourier transform spectrometer without a beam splitter for the vacuum ultraviolet range: From the optical design to the first UV spectrum.* Review of Scientific Instruments, **80**, 043101, (2009). [Cited on page 155.]

[Demekhin 18] P. V. Demekhin, A. N. Artemyev, A. Kastner & T. Baumert. *Photoelectron Circular Dichroism with Two Overlapping Laser Pulses of Carrier Frequencies $\omega$ and $2\omega$ Linearly Polarized in Two Mutually Orthogonal Directions.* Physical Review Letters, **121**, 253201, (2018). [Cited on pages 121, 126, 212, 217, and 262.]

[Derbali 19] I. Derbali, H. R. Hrodmarsson, Z. Gouid, M. Schwell, M.-C. Gazeau, J.-C. Guillemin, M. Hochlaf, M. E. Alikhani & E.-L. Zins. *Photoionization and dissociative photoionization of propynal in the gas phase: theory and experiment.* Physical Chemistry Chemical Physics, **21**, 26, pages 14053–14062, (2019). [Cited on page 170.]

[Dimitriou 04] K. I. Dimitriou, D. G. Arbó, S. Yoshida, E. Persson & J. Burgdörfer. *Origin of the double-peak structure in the momentum distribution of ionization of hydrogen atoms driven by strong laser fields.* Physical Review A, **70**, 061401(R), (2004). [Cited on pages 206 and 242.]

[Dörner 00] R. Dörner, V. Mergel, O. Jagutzki, L. Spielberger, J. Ullrich, R. Moshammer & H. Schmidt-Böcking. *Cold Target Recoil Ion Momentum Spectroscopy: a 'momentum microscope' to view atomic collision dynamics.* Physics Reports, **330**, 2-3, pages 95–192, (2000). [Cited on page 73.]

[Dowek 07] D. Dowek, M. Lebech, J. Houver & R. Lucchese. *Circular dichroism in molecular frame photoemission.* Molecular Physics, **105**, 11-12, pages 1757–1768, (2007). [Cited on page 39.]

[Dowek 09] D. Dowek, A. Haouas, R. Guillemin, C. Elkharrat, J.-C. Houver, W. B. Li, F. Catoire, L. Journel, M. Simon & R. R. Lucchese. *Recoil frame photoemission in inner-shell photoionization of small polyatomic molecules.* The European Physical Journal Special Topics, **169**, 1, pages 85–93, (2009). [Cited on page 43.]

[Dreissigacker 14] I. Dreissigacker & M. Lein. *Photoelectron circular dichroism of chiral molecules studied with a continuum-state-corrected strong-field approximation.* Physical Review A, **89**, 053406, (2014). [Cited on page 209.]

[Dribinski 02] V. Dribinski, A. Ossadtchi, V. A. Mandelshtam & H. Reisler. *Reconstruction of Abel-transformable images: The Gaussian basis-set expansion Abel transform method.* Review of Scientific Instruments, **73**, 7, pages 2634–2642, (2002). [Cited on page 70.]

[Dubietis 17] A. Dubietis, G. Tamošauskas, R. Šuminas, V. Jukna & A. Couairon. *Ultrafast supercontinuum generation in bulk condensed media (Invited Review).* arXiv:1706.04356 [physics], (2017). [Cited on page 61.]

[Eckart 16] S. Eckart, M. Richter, M. Kunitski, A. Hartung, J. Rist, K. Henrichs, N. Schlott, H. Kang, T. Bauer, H. Sann, L. Schmidt, M. Schöffler, T. Jahnke & R. Dörner. *Nonsequential Double Ionization by Counter-rotating Circularly Polarized Two-Color Laser Fields.* Physical Review Letters, **117**, 133202, (2016). [Cited on page 44.]

[Eckart 18] S. Eckart, M. Kunitski, M. Richter, A. Hartung, J. Rist, F. Trinter, K. Fehre, N. Schlott, K. Henrichs, L. P. H. Schmidt, T. Jahnke, M. Schöffler, K. Liu, I. Barth, J. Kaushal, F. Morales, M. Ivanov, O. Smirnova & R. Dörner. *Ultrafast preparation and detection of ring currents in single atoms.* Nature Physics, **14**, pages 701–704, (2018). [Cited on pages 206 and 242.]

[Eckle 08] P. Eckle, M. Smolarski, P. Schlup, J. Biegert, A. Staudte, M. Schöffler, H. G. Muller, R. Dörner & U. Keller. *Attosecond angular streaking.* Nature Physics, **4**, pages 565–570, (2008). [Cited on page 247.]

[Eppink 97] A. T. J. B. Eppink & D. H. Parker. *Velocity map imaging of ions and electrons using electrostatic lenses: Application in photoelectron and photofragment ion imaging of molecular oxygen.* Review of Scientific Instruments, **68**, 9, pages 3477–3484, (1997). [Cited on page 66.]

[Evans 12] A. C. Evans, C. Meinert, C. Giri, F. Goesmann & U. J. Meierhenrich. *Chirality, photochemistry and the detection of amino acids in interstellar ice analogues and comets.* Chemical Society Reviews, **41**, 16, page 5447, (2012). [Cited on page 27.]

[Faria 20] C. F. d. M. Faria & A. S. Maxwell. *It is all about phases: ultrafast holographic photoelectron imaging.* Reports on Progress in Physics, **83**, 3, page 034401, (2020). arXiv: 1906.11781. [Cited on page 206.]

[Fehre 19] K. Fehre, S. Eckart, M. Kunitski, C. Janke, D. Trabert, J. Rist, M. Weller, A. Hartung, L. P. H. Schmidt, T. Jahnke, R. Dörner & M. Schöffler. *Link between Photoelectron Circular Dichroism and Fragmentation Channel in Strong Field Ionization.* The Journal of Physical Chemistry A, **123**, 30, pages 6491–6495, (2019). [Cited on pages 45, 162, and 167.]

[Ferray 88] M. Ferray, A. L'Huillier, X. F. Li, L. A. Lompre, G. Mainfray & C. Manus. *Multiple-harmonic conversion of 1064 nm radiation in rare gases.* Journal of Physics B: Atomic, Molecular and Optical Physics, **21**, 3, pages L31–L35, (1988). [Cited on pages 53 and 54.]

[Ferré 15a] A. Ferré, A. E. Boguslavskiy, M. Dagan, V. Blanchet, B. D. Bruner, F. Burgy, A. Camper, D. Descamps, B. Fabre, N. Fedorov, J. Gaudin, G. Geoffroy, J. Mikosch, S. Patchkovskii, S. Petit, T. Ruchon, H. Soifer, D. Staedter, I. Wilkinson, A. Stolow, N. Dudovich & Y. Mairesse. *Multichannel electronic and vibrational dynamics in polyatomic resonant high-order harmonic generation.* Nature Communications, **6**, 5952, (2015). [Cited on page 202.]

[Ferré 15b] A. Ferré, C. Handschin, M. Dumergue, F. Burgy, A. Comby, D. Descamps, B. Fabre, G. A. Garcia, R. Géneaux, L. Merceron, E. Mével, L. Nahon,

S. Petit, B. Pons, D. Staedter, S. Weber, T. Ruchon, V. Blanchet & Y. Mairesse. *A table-top ultrashort light source in the extreme ultraviolet for circular dichroism experiments.* Nature Photonics, **9**, pages 93–98, (2015). [Cited on pages 39 and 59.]

[Ferré 16] A. Ferré, H. Soifer, O. Pedatzur, C. Bourassin-Bouchet, B. Bruner, R. Canonge, F. Catoire, D. Descamps, B. Fabre, E. Mével, S. Petit, N. Dudovich & Y. Mairesse. *Two-Dimensional Frequency Resolved Opto-molecular Gating of High-Order Harmonic Generation.* Physical Review Letters, **116**, 053002, (2016). [Cited on page 202.]

[Fleischer 14] A. Fleischer, O. Kfir, T. Diskin, P. Sidorenko & O. Cohen. *Spin angular momentum and tunable polarization in high-harmonic generation.* Nature Photonics, **8**, 7, pages 543–549, (2014). [Cited on pages 59, 202, 203, and 209.]

[Gaarde 08] M. B. Gaarde, J. L. Tate & K. J. Schafer. *Macroscopic aspects of attosecond pulse generation.* Journal of Physics B: Atomic, Molecular and Optical Physics, **41**, 13, page 132001, (2008). [Cited on page 201.]

[Galli 19] M. Galli, V. Wanie, D. P. Lopes, E. P. Må nsson, A. Trabattoni, L. Colaizzi, K. Saraswathula, A. Cartella, F. Frassetto, L. Poletto, F. Légaré, S. Stagira, M. Nisoli, R. Martínez Vázquez, R. Osellame & F. Calegari. *Generation of deep ultraviolet sub-2-fs pulses.* Optics Letters, **44**, 6, page 1308, (2019). [Cited on page 175.]

[Ganjitabar 18] H. Ganjitabar, R. Hadidi, G. A. Garcia, L. Nahon & I. Powis. *Vibrationally-resolved photoelectron spectroscopy and photoelectron circular dichroism of bicyclic monoterpene enantiomers.* Journal of Molecular Spectroscopy, **353**, pages 11–19, (2018). [Cited on pages 39 and 120.]

[Ganjitabar 20] H. Ganjitabar, G. A. Garcia, L. Nahon & I. Powis. *Decoupling vibration and electron energy dependencies in the photoelectron circular dichroism of a terpene, 3-carene.* The Journal of Chemical Physics, **153**, 3, page 034302, (2020). [Cited on pages 37, 39, and 120.]

[Garcia 04] G. A. Garcia, L. Nahon & I. Powis. *Two-dimensional charged particle image inversion using a polar basis function expansion.* Review of Scientific Instruments, **75**, 11, pages 4989–4996, (2004). [Cited on pages 35 and 70.]

[Garcia 13] G. A. Garcia, L. Nahon, S. Daly & I. Powis. *Vibrationally induced inversion of photoelectron forward-backward asymmetry in chiral molecule photoionization by circularly polarized light.* Nature Communications, **4**, 2132, (2013). [Cited on pages 38, 120, and 162.]

[Garcia 14] G. A. Garcia, H. Dossmann, L. Nahon, S. Daly & I. Powis. *Photoelectron circular dichroism and spectroscopy of trifluoromethyl- and methyl-oxirane: a comparative study.* Physical Chemistry Chemical Physics, **16**, page 16214, (2014). [Cited on pages 37, 45, and 162.]

[Gardner 17] D. F. Gardner, M. Tanksalvala, E. R. Shanblatt, X. Zhang, B. R. Galloway, C. L. Porter, R. Karl Jr, C. Bevis, D. E. Adams, H. C. Kapteyn, M. M. Murnane & G. F. Mancini. *Subwavelength coherent imaging of periodic samples using a 13.5 nm tabletop high-harmonic light source.* Nature Photonics, **11**, pages 259–263, (2017). [Cited on page 53.]

[Gaumnitz 17] T. Gaumnitz, A. Jain, Y. Pertot, M. Huppert, I. Jordan, F. Ardana-Lamas & H. J. Wörner. *Streaking of 43-attosecond soft-X-ray pulses generated by a passively CEP-stable mid-infrared driver.* Optics Express, **25**, 22, page 27506, (2017). [Cited on page 53.]

[Gethyn Timothy 16] J. Gethyn Timothy. *Review of multianode microchannel array detector systems.* Journal of Astronomical Telescopes, Instruments, and Systems, **2**, 030901, (2016). [Cited on page 77.]

[Goetz 17] R. E. Goetz, T. A. Isaev, B. Nikoobakht, R. Berger & C. P. Koch. *Theoretical description of circular dichroism in photoelectron angular distributions of randomly oriented chiral molecules after multi-photon photoionization.* The Journal of Chemical Physics, **146**, 2, page 024306, (2017). [Cited on pages 121, 124, and 262.]

[Goetz 19] R. E. Goetz, C. P. Koch & L. Greenman. *Quantum Control of Photoelectron Circular Dichroism.* Physical Review Letters, **122**, 1, (2019). [Cited on pages 121, 126, and 262.]

[Goulielmakis 10] E. Goulielmakis, Z.-H. Loh, A. Wirth, R. Santra, N. Rohringer, V. S. Yakovlev, S. Zherebtsov, T. Pfeifer, A. M. Azzeer, M. F. Kling, S. R. Leone & F. Krausz. *Real-time observation of valence electron motion.* Nature, **466**, pages 739–743, (2010). [Cited on page 54.]

[Guo 04] C. Guo, R. D. Shah, R. K. Dukor, X. Cao, T. B. Freedman & L. A. Nafie. *Determination of Enantiomeric Excess in Samples of Chiral Molecules Using Fourier Transform Vibrational Circular Dichroism Spectroscopy: Simulation of Real-Time Reaction Monitoring.* Analytical Chemistry, **76**, 23, pages 6956–6966, (2004). [Cited on page 128.]

[Hadidi 18] R. Hadidi, D. K. Bozanic, G. A. Garcia & L. Nahon. *Electron asymmetries in the photoionization of chiral molecules: possible astrophysical implications.* Advances in Physics: X, **3**, 1, page 1477530, (2018). [Cited on pages 26, 39, and 127.]

[Haertelt 16] M. Haertelt, X.-B. Bian, M. Spanner, A. Staudte & P. B. Corkum. *Probing Molecular Dynamics by Laser-Induced Backscattering Holography.* Physical Review Letters, **116**, 133001, (2016). [Cited on page 205.]

[Haessler 10] S. Haessler, J. Caillat, W. Boutu, C. Giovanetti-Teixeira, T. Ruchon, T. Auguste, Z. Diveki, P. Breger, A. Maquet, B. Carré, R. Taïeb & P. Salières. *Attosecond imaging of molecular electronic wavepackets.* Nature Physics, **6**, 3, pages 200–206, (2010). [Cited on page 202.]

[Haessler 11] S. Haessler, J. Caillat & P. Salières. *Self-probing of molecules with high harmonic generation.* Journal of Physics B: Atomic, Molecular and Optical Physics, **44**, 20, page 203001, (2011). [Cited on pages 195 and 199.]

[Han 17] M. Han, P. Ge, Y. Shao, M.-M. Liu, Y. Deng, C. Wu, Q. Gong & Y. Liu. *Revealing the Sub-Barrier Phase using a Spatiotemporal Interferometer with Orthogonal Two-Color Laser Fields of Comparable Intensity.* Physical Review Letters, **119**, 073201, (2017). [Cited on pages 206 and 228.]

[Han 18] M. Han, P. Ge, Y. Shao, Q. Gong & Y. Liu. *Attoclock Photoelectron Interferometry with Two-Color Corotating Circular Fields to Probe the Phase and the Amplitude of Emitting Wave Packets.* Physical Review Letters, **120**, 073202, (2018). [Cited on pages 244 and 248.]

[Han 19] M. Han, P. Ge, Y. Fang, X. Yu, Z. Guo, X. Ma, Y. Deng, Q. Gong & Y. Liu. *Unifying Tunneling Pictures of Strong-Field Ionization with an Improved Attoclock.* Physical Review Letters, **123**, 073201, (2019). [Cited on page 248.]

[Hansen 12] J. L. Hansen, L. Holmegaard, J. H. Nielsen, H. Stapelfeldt, D. Dimitrovski & L. B. Madsen. *Orientation-dependent ionization yields from strong-field ionization of fixed-in-space linear and asymmetric top molecules.* Journal of Physics B: Atomic, Molecular and Optical Physics, **45**, 1, page 015101, (2012). [Cited on page 163.]

[Hartmann 19] G. Hartmann, M. Ilchen, P. Schmidt, C. Küstner-Wetekam, C. Ozga, F. Scholz, J. Buck, F. Trinter, J. Viefhaus, A. Ehresmann, M. Schöffler, A. Knie & P. Demekhin. *Recovery of High-Energy Photoelectron Circular Dichroism through Fano Interference.* Physical Review Letters, **123**, 043202, (2019). [Cited on page 37.]

[Harvey 14] J. Harvey, R. P. Tuckett & A. Bodi. *Shining new light on the multifaceted dissociative photoionisation dynamics of $CCl_4$.* Phys. Chem. Chem. Phys., **16**, 38, pages 20492–20499, (2014). [Cited on page 170.]

[Hädrich 16] S. Hädrich, M. Kienel, M. Müller, A. Klenke, J. Rothhardt, R. Klas, T. Gottschall, T. Eidam, A. Drozdy, P. Jójárt, Z. Várallyay, E. Cormier,

K. Osvay, A. Tünnermann & J. Limpert. *Energetic sub-2-cycle laser with 216 W average power.* Optics Letters, **41**, 18, page 4332, (2016). [Cited on page 60.]

[Heck 95] A. J. R. Heck & D. W. Chandler. *Imaging Techniques for the Study of Chemical Reaction Dynamics.* Annual Review of Physical Chemistry, **46**, 335–72, (1995). [Cited on page 69.]

[Helm 93] H. Helm, N. Bjerre, M. J. Dyer, D. L. Huestis & M. Saeed. *Images of photoelectrons formed in intense laser fields.* Physical Review Letters, **70**, 21, pages 3221–3224, (1993). [Cited on page 66.]

[Hemmers 04] O. Hemmers, R. Guillemin & D. Lindle. *Nondipole effects in soft X-ray photoemission.* Radiation Physics and Chemistry, **70**, pages 123–147, (2004). [Cited on page 33.]

[Hentschel 01] M. Hentschel, R. Kienberger, C. Spielmann, G. A. Reider, N. Milosevic, T. Brabec, P. Corkum, U. Heinzmann, D. M. & F. Krausz. *Attosecond metrology.* Nature, **414**, pages 509–513, (2001). [Cited on pages 53 and 200.]

[Hergenhahn 04] U. Hergenhahn, E. E. Rennie, O. Kugeler, S. Marburger, T. Lischke, I. Powis & G. Garcia. *Photoelectron circular dichroism in core level ionization of randomly oriented pure enantiomers of the chiral molecule camphor.* The Journal of Chemical Physics, **120**, 10, pages 4553–4556, (2004). [Cited on page 35.]

[Hergott 02] J.-F. Hergott, M. Kovacev, H. Merdji, C. Hubert, Y. Mairesse, E. Jean, P. Breger, P. Agostini, B. Carré & P. Salières. *Extreme-ultraviolet high-order harmonic pulses in the microjoule range.* Physical Review A, **66**, 021801(R), (2002). [Cited on page 54.]

[Heyl 16] C. M. Heyl, H. Coudert-Alteirac, M. Miranda, M. Louisy, K. Kovacs, V. Tosa, E. Balogh, K. Varjú, A. L´ Huillier, A. Couairon & C. L. Arnold. *Scale-invariant nonlinear optics in gases.* Optica, **3**, 1, page 75, (2016). [Cited on page 202.]

[Hickstein 12] D. D. Hickstein, P. Ranitovic, S. Witte, X.-M. Tong, Y. Huismans, P. Arpin, X. Zhou, K. E. Keister, C. W. Hogle, B. Zhang, C. Ding, P. Johnsson, N. Toshima, M. J. J. Vrakking, M. M. Murnane & H. C. Kapteyn. *Direct Visualization of Laser-Driven Electron Multiple Scattering and Tunneling Distance in Strong-Field Ionization.* Physical Review Letters, **109**, 073004, (2012). [Cited on page 205.]

[Huismans 11] Y. Huismans, A. Rouzee, A. Gijsbertsen, J. H. Jungmann, A. S. Smolkowska, P. S. W. M. Logman, F. Lepine, C. Cauchy, S. Zamith,

T. Marchenko, J. M. Bakker, G. Berden, B. Redlich, A. F. G. van der Meer, H. G. Muller, W. Vermin, K. J. Schafer, M. Spanner, M. Y. Ivanov, O. Smirnova, D. Bauer, S. V. Popruzhenko & M. J. J. Vrakking. *Time-Resolved Holography with Photoelectrons.* Science, **331**, 6013, pages 61–64, (2011). [Cited on page 205.]

[Inokuma 13] Y. Inokuma, S. Yoshioka, J. Ariyoshi, T. Arai, Y. Hitora, K. Takada, S. Matsunaga, K. Rissanen & M. Fujita. *X-ray analysis on the nanogram to microgram scale using porous complexes.* Nature, **495**, 7442, pages 461–466, (2013). [Cited on page 127.]

[Itatani 04] J. Itatani, J. Levesque, D. Zeidler, H. Niikura, H. Pépin, J. C. Kieffer, P. B. Corkum & D. M. Villeneuve. *Tomographic imaging of molecular orbitals.* Nature, **432**, 7019, pages 867–871, (2004). [Cited on page 202.]

[Itatani 05] J. Itatani, D. Zeidler, J. Levesque, M. Spanner, D. M. Villeneuve & P. B. Corkum. *Controlling High Harmonic Generation with Molecular Wave Packets.* Physical Review Letters, **94**, 123902, (2005). [Cited on page 54.]

[Jagutzki 02] O. Jagutzki, V. Mergel, K. Ullmann-Pfleger, L. Spielberger, U. Spillmann, R. Dörner & H. Schmidt-Böcking. *A broad-application microchannel-plate detector system for advanced particle or photon detection tasks: large area imaging, precise multi-hit timing information and high detection rate.* Nuclear Instruments and Methods in Physics Research Section A: Accelerators, Spectrometers, Detectors and Associated Equipment, **477**, 1-3, pages 244–249, (2002). [Cited on page 75.]

[Jahnke 04] T. Jahnke, T. Weber, T. Osipov, A. Landers, O. Jagutzki, L. Schmidt, C. Cocke, M. Prior, H. Schmidt-Böcking & R. Dörner. *Multicoincidence studies of photo and Auger electrons from fixed-in-space molecules using the COLTRIMS technique.* Journal of Electron Spectroscopy and Related Phenomena, **141**, 2-3, pages 229–238, (2004). [Cited on page 43.]

[Johnson 18] A. S. Johnson, D. R. Austin, D. A. Wood, C. Brahms, A. Gregory, K. B. Holzner, S. Jarosch, E. W. Larsen, S. Parker, C. S. Strüber, P. Ye, J. W. G. Tisch & J. P. Marangos. *High-flux soft x-ray harmonic generation from ionization-shaped few-cycle laser pulses.* Science Advances, **4**, eaar3761, (2018). [Cited on page 53.]

[Jordan 20] I. Jordan, M. Huppert, D. Rattenbacher, M. Peper, D. Jelovina, C. Perry, A. von Conta, A. Schild & H. J. Wörner. *Attosecond spectroscopy of liquid water.* Science, 369, pages 974–979, (2020). [Cited on page 262.]

[Jorissen 02] A. Jorissen & C. Cerf. *Asymmetric Photoreactions as the Origin of Biomolecular Homochirality: A Critical Review.* Origins of Life and Evolution of the Biosphere, **32**, pages 129–142, (2002). [Cited on page 27.]

[Kanai 05] T. Kanai, S. Minemoto & H. Sakai. *Quantum interference during high-order harmonic generation from aligned molecules.* Nature, **435**, 7041, pages 470–474, (2005). [Cited on page 202.]

[Kastner 16] A. Kastner, C. Lux, T. Ring, S. Züllighoven, C. Sarpe, A. Senftleben & T. Baumert. *Enantiomeric Excess Sensitivity to Below One Percent by Using Femtosecond Photoelectron Circular Dichroism.* ChemPhysChem, **17**, 8, pages 1119–1122, (2016). [Cited on pages 41 and 129.]

[Kastner 17] A. Kastner, T. Ring, B. C. Krüger, G. B. Park, T. Schäfer, A. Senftleben & T. Baumert. *Intermediate state dependence of the photoelectron circular dichroism of fenchone observed via femtosecond resonance-enhanced multi-photon ionization.* The Journal of Chemical Physics, **147**, 1, page 013926, (2017). [Cited on pages 41, 64, 121, and 122.]

[Kastner 19] A. Kastner, T. Ring, H. Braun, A. Senftleben & T. Baumert. *Observation of Photoelectron Circular Dichroism Using a Nanosecond Laser.* ChemPhysChem, **20**, pages 1416–1419, (2019). [Cited on page 121.]

[Kastner 20] A. Kastner, G. Koumarianou, P. Glodic, P. C. Samartzis, N. Ladda, S. T. Ranecky, T. Ring, S. Vasudevan, C. Witte, H. Braun, H.-G. Lee, A. Senftleben, R. Berger, G. B. Park, T. Schäfer & T. Baumert. *High-resolution resonance-enhanced multiphoton photoelectron circular dichroism.* Physical Chemistry Chemical Physics, **22**, 14, pages 7404–7411, (2020). [Cited on pages 61 and 121.]

[Keldysh 65] L. V. Keldysh. *Ionization in the field of a strong electromagnetic wave.* Soviet Physics, Journal of Experimental and Theoretical Physics, **47**, pages 1945–1957, (1965). [Cited on page 196.]

[Keller 03] U. Keller. *Recent developments in compact ultrafast lasers.* Nature, **424**, 6950, pages 831–838, (2003). [Cited on page 48.]

[Kfir 15] O. Kfir, P. Grychtol, E. Turgut, R. Knut, D. Zusin, D. Popmintchev, T. Popmintchev, H. Nembach, J. M. Shaw, A. Fleischer, H. Kapteyn, M. Murnane & O. Cohen. *Generation of bright phase-matched circularly-polarized extreme ultraviolet high harmonics.* Nature Photonics, **9**, 2, pages 99–105, (2015). [Cited on pages 59 and 209.]

[Kfir 16] O. Kfir, E. Bordo, G. Ilan Haham, O. Lahav, A. Fleischer & O. Cohen. *In-line production of a bi-circular field for generation of helically polarized high-order harmonics.* Applied Physics Letters, **108**, 21, page 211106, (2016). [Cited on pages 59, 202, and 203.]

[Kheifets 20] A. S. Kheifets. *The attoclock and the tunnelling time debate.* Journal of Physics B: Atomic, Molecular and Optical Physics, **53**, 7, page 072001, (2020). arXiv: 1910.08891. [Cited on page 248.]

[Klaiber 15] M. Klaiber, K. Z. Hatsagortsyan & C. H. Keitel. *Tunneling Dynamics in Multiphoton Ionization and Attoclock Calibration.* Physical Review Letters, **114**, 083001, (2015). [Cited on page 254.]

[Klas 16] R. Klas, S. Demmler, M. Tschernajew, S. Hädrich, Y. Shamir, A. Tünnermann, J. Rothhardt & J. Limpert. *Table-top milliwatt-class extreme ultraviolet high harmonic light source.* Optica, **3**, 11, page 1167, (2016). [Cited on pages 56 and 202.]

[Koide 91] T. Koide, T. Shidara, M. Yuri, N. Kandaka & H. Fukutani. *Production and direct measurement of circularly polarized vacuum-ultraviolet light with multireflection optics.* Applied Physics Letters, **58**, 23, pages 2592–2594, (1991). [Cited on page 59.]

[Krausz 09] F. Krausz & M. Ivanov. *Attosecond physics.* Reviews of Modern Physics, **81**, 1, pages 163–234, (2009). [Cited on page 54.]

[Landsman 14] A. S. Landsman, M. Weger, J. Maurer, R. Boge, A. Ludwig, S. Heuser, C. Cirelli, L. Gallmann & U. Keller. *Ultrafast resolution of tunneling delay time.* Optica, **1**, 5, page 343, (2014). [Cited on page 248.]

[Lavenu 17] L. Lavenu, M. Natile, F. Guichard, Y. Zaouter, M. Hanna, E. Mottay & P. Georges. *High-energy few-cycle Yb-doped fiber amplifier source based on a single nonlinear compression stage.* Optics Express, **25**, 7, page 7530, (2017). [Cited on page 60.]

[Lavenu 18] L. Lavenu, M. Natile, F. Guichard, Y. Zaouter, X. Delen, M. Hanna, E. Mottay & P. Georges. *Nonlinear pulse compression based on a gas-filled multipass cell.* Optics Letters, **43**, 10, page 2252, (2018). [Cited on pages 60 and 258.]

[Lehmann 13] C. S. Lehmann, N. B. Ram, I. Powis & M. H. M. Janssen. *Imaging photoelectron circular dichroism of chiral molecules by femtosecond multiphoton coincidence detection.* The Journal of Chemical Physics, **139**, 23, page 234307, (2013). [Cited on pages 40, 45, 120, 121, and 163.]

[Lein : Simpolator 0] M. Lein : Simpolator. *https://lein.itp.uni-hannover.de/simpolator.html*, (0). [Cited on pages 204 and 205.]

[Lein 05] M. Lein. *Attosecond Probing of Vibrational Dynamics with High-Harmonic Generation.* Physical Review Letters, **94**, 053004, (2005). [Cited on page 202.]

[Lépine 14] F. Lépine, M. Y. Ivanov & M. J. J. Vrakking. *Attosecond molecular dynamics: fact or fiction?* Nature Photonics, **8**, 3, pages 195–204, (2014). [Cited on page 54.]

[Lewenstein 94] M. Lewenstein, P. Balcou, M. Y. Ivanov, A. L'Huillier & P. B. Corkum. *Theory of high-harmonic generation by low-frequency laser fields.* Physical Review A, **49**, 3, pages 2117–2132, (1994). [Cited on page 199.]

[L'Huillier 03] A. L'Huillier, D. Descamps, A. Johansson, J. Norin, J. Mauritsson & C.-G. Wahlstrom. *Applications of high-order harmonics.* The European Physical Journal D - Atomic, Molecular and Optical Physics, **26**, 1, pages 91–98, (2003). [Cited on page 54.]

[Li 15] M. Li, X. Sun, X. Xie, Y. Shao, Y. Deng, C. Wu, Q. Gong & Y. Liu. *Revealing backward rescattering photoelectron interference of molecules in strong infrared laser fields.* Scientific Reports, **5**, 8519, (2015). [Cited on pages 205 and 206.]

[Li 16] Y. Li, Y. Zhou, M. He, M. Li & P. Lu. *Identifying backward-rescattering photoelectron hologram with orthogonal two-color laser fields.* Optics Express, **24**, 21, page 23697, (2016). [Cited on pages 206 and 229.]

[Li 17] J. Li, X. Ren, Y. Yin, K. Zhao, A. Chew, Y. Cheng, E. Cunningham, Y. Wang, S. Hu, Y. Wu, M. Chini & Z. Chang. *53-attosecond X-ray pulses reach the carbon K-edge.* Nature Communications, **8**, 186, (2017). [Cited on pages 53 and 200.]

[Lipkin 64] D. M. Lipkin. *Existence of a New Conservation Law in Electromagnetic Theory.* Journal of Mathematical Physics, **5**, 5, pages 696–700, (1964). [Cited on page 210.]

[Litvinyuk 03] I. V. Litvinyuk, K. F. Lee, P. W. Dooley, D. M. Rayner, D. M. Villeneuve & P. B. Corkum. *Alignment-Dependent Strong Field Ionization of Molecules.* Physical Review Letters, **90**, 23, page 233003, (2003). [Cited on page 163.]

[Lux 12] C. Lux, M. Wollenhaupt, T. Bolze, Q. Liang, J. Köhler, C. Sarpe & T. Baumert. *Circular Dichroism in the Photoelectron Angular Distributions of Camphor and Fenchone from Multiphoton Ionization with Femtosecond Laser Pulses.* Angewandte Chemie International Edition, **51**, 20, pages 5001–5005, (2012). [Cited on pages 40, 41, and 120.]

[Lux 15] C. Lux, M. Wollenhaupt, C. Sarpe & T. Baumert. *Photoelectron Circular Dichroism of Bicyclic Ketones from Multiphoton Ionization with Femtosecond Laser Pulses.* ChemPhysChem, **16**, 1, pages 115–137, (2015). [Cited on pages 41, 121, 126, 127, and 133.]

[Maharjan 06] C. M. Maharjan, A. S. Alnaser, I. Litvinyuk, P. Ranitovic & C. L. Cocke. *Wavelength dependence of momentum-space images of low-energy electrons generated by short intense laser pulses at high intensities.* Journal

of Physics B: Atomic, Molecular and Optical Physics, **39**, 8, pages 1955–1964, (2006). [Cited on page 205.]

[Mairesse 03] Y. Mairesse, A. de Bohan, L. J. Frasinski, H. Merdji, L. C. Dinu, P. Monchicourt, P. Breger, M. Kovacˇev, R. Taïeb, B. Carré, H. G. Muller, P. Agostini & P. Saliè res. *Attosecond Synchronization of High-Harmonic Soft X-rays.* Science, **302**, 5650, pages 1540–1543, (2003). [Cited on page 200.]

[Mancuso 16] C. A. Mancuso, D. D. Hickstein, K. M. Dorney, J. L. Ellis, E. Hasović, R. Knut, P. Grychtol, C. Gentry, M. Gopalakrishnan, D. Zusin, F. J. Dollar, X.-M. Tong, D. B. Milošević, W. Becker, H. C. Kapteyn & M. M. Murnane. *Controlling electron-ion rescattering in two-color circularly polarized femtosecond laser fields.* Physical Review A, **93**, 053406, (2016). [Cited on page 206.]

[Manzhos 03] S. Manzhos & H.-P. Loock. *Photofragment image analysis using the Onion-Peeling Algorithm.* Computer Physics Communications, **154**, 1, pages 76–87, (2003). [Cited on page 69.]

[Marangos 16] J. P. Marangos. *Development of high harmonic generation spectroscopy of organic molecules and biomolecules.* Journal of Physics B: Atomic, Molecular and Optical Physics, **49**, 13, page 132001, (2016). [Cited on page 54.]

[Mauritsson 09] J. Mauritsson, J. M. Dahlström, E. Mansten & T. Fordell. *Sub-cycle control of attosecond pulse generation using two-colour laser fields.* Journal of Physics B: Atomic, Molecular and Optical Physics, **42**, 13, page 134003, (2009). [Cited on page 198.]

[Maxwell 17] A. S. Maxwell, A. Al-Jawahiry, T. Das & C. F. d. M. Faria. *Coulomb-corrected quantum interference in above-threshold ionization: Working towards multitrajectory electron holography.* Physical Review A, **96**, 023420, (2017). [Cited on pages 207, 208, 229, and 237.]

[McPherson 87] A. McPherson, G. Gibson, H. Jara, U. Johann, T. S. Luk, I. A. McIntyre, K. Boyer & C. K. Rhodes. *Studies of multiphoton production of vacuum-ultraviolet radiation in the rare gases.* Journal of the Optical Society of America B, **4**, 2, pages 595–601, (1987). [Cited on pages 53 and 54.]

[Meckel 08] M. Meckel, D. Comtois, D. Zeidler, A. Staudte, D. Pavicic, H. C. Bandulet, H. Pepin, J. C. Kieffer, R. Dorner, D. M. Villeneuve & P. B. Corkum. *Laser-Induced Electron Tunneling and Diffraction.* Science, **320**, 5882, pages 1478–1482, (2008). [Cited on pages 43 and 44.]

[Menssen 16] A. Menssen, C. S. Trevisan, M. S. Schöffler, T. Jahnke, I. Bocharova, F. Sturm, N. Gehrken, B. Gaire, H. Gassert, S. Zeller, J. Voigtsberger, A. Kuhlins, F. Trinter, A. Gatton, J. Sartor, D. Reedy, C. Nook, B. Berry, M. Zohrabi, A. Kalinin, I. Ben-Itzhak, A. Belkacem, R. Dörner, T. Weber, A. L. Landers, T. N. Rescigno, C. W. McCurdy & J. B. Williams. *Molecular frame photoelectron angular distributions for core ionization of ethane, carbon tetrafluoride and 1,1-difluoroethylene.* Journal of Physics B: Atomic, Molecular and Optical Physics, **49**, 5, page 055203, (2016). [Cited on page 43.]

[Miles 17] J. Miles, D. Fernandes, A. Young, C. Bond, S. Crane, O. Ghafur, D. Townsend, J. Sá & J. Greenwood. *A new technique for probing chirality via photoelectron circular dichroism.* Analytica Chimica Acta, **984**, pages 134–139, (2017). [Cited on pages 41, 126, 127, 129, 133, and 142.]

[Miller 16] M. R. Miller, A. Jaroń-Becker & A. Becker. *High-harmonic spectroscopy of laser-driven nonadiabatic electron dynamics in the hydrogen molecular ion.* Physical Review A, **93**, 013406, (2016). [Cited on page 202.]

[Miron 08] C. Miron, P. Morin, D. Céolin, L. Journel & M. Simon. *Multipathway dissociation dynamics of core-excited methyl chloride probed by high resolution electron spectroscopy and Auger-electron–ion coincidences.* The Journal of Chemical Physics, **128**, 15, page 154314, (2008). [Cited on page 43.]

[Moshammer 94] R. Moshammer, J. Ullrich, M. Unverzagt, W. Schmidt, P. Jardin, R. E. Olson, R. Mann, R. Dörner, V. Mergel, U. Buck & H. Schmidt-Böcking. *Low-Energy Electrons and Their Dynamical Correlation with Recoil Ions for Single Ionization of Helium by Fast, Heavy-Ion Impact.* Physical Review Letters, **73**, 25, pages 3371–3374, (1994). [Cited on page 73.]

[Moshammer 96] R. Moshammer, M. Unverzagt, W. Schmitt, J. Ullrich & H. Schmidt-Böcking. *A 4pi recoil-ion electron momentum analyzer: a high-resolution "microscope" for the investigation of the dynamics of atomic, molecular and nuclear reactions.* Nuclear Instruments and Methods in Physics Research Section B: Beam Interactions with Materials and Atoms, **108**, 4, pages 425–445, (1996). [Cited on page 73.]

[Mower 18] M. P. Mower & D. G. Blackmond. *In-Situ Monitoring of Enantiomeric Excess During a Catalytic Kinetic Resolution.* ACS Catalysis, **8**, 7, pages 5977–5982, (2018). [Cited on page 128.]

[Nahon 04] L. Nahon & C. Alcaraz. *SU5: a calibrated variable-polarization synchrotron radiation beam line in the vacuum-ultraviolet range.* Applied Optics, **43**, 5, page 1024, (2004). [Cited on page 59.]

[Nahon 06] L. Nahon, G. A. Garcia, C. J. Harding, E. Mikajlo & I. Powis. *Determination of chiral asymmetries in the valence photoionization of camphor enantiomers by photoelectron imaging using tunable circularly polarized light.* The Journal of Chemical Physics, **125**, 11, page 114309, (2006). [Cited on pages 35, 36, 120, and 126.]

[Nahon 16] L. Nahon, L. Nag, G. A. Garcia, I. Myrgorodska, U. Meierhenrich, S. Beaulieu, V. Wanie, V. Blanchet, R. Géneaux & I. Powis. *Determination of accurate electron chiral asymmetries in fenchone and camphor in the VUV range: sensitivity to isomerism and enantiomeric purity.* Physical Chemistry Chemical Physics, **18**, 18, pages 12696–12706, (2016). [Cited on pages 35, 37, 120, 129, and 173.]

[Nayak 18] A. Nayak, I. Orfanos, I. Makos, M. Dumergue, S. Kühn, E. Skantzakis, B. Bodi, K. Varju, C. Kalpouzos, H. I. B. Banks, A. Emmanouilidou, D. Charalambidis & P. Tzallas. *Multiple ionization of argon via multi-XUV-photon absorption induced by 20-GW high-order harmonic laser pulses.* Physical Review A, **98**, 023426, (2018). [Cited on page 54.]

[Neufeld 18] O. Neufeld & O. Cohen. *Optical Chirality in Nonlinear Optics: Application to High Harmonic Generation.* Physical Review Letters, **120**, 133206, (2018). [Cited on pages 209 and 210.]

[Neufeld 19] O. Neufeld, D. Ayuso, P. Decleva, M. Y. Ivanov, O. Smirnova & O. Cohen. *Ultrasensitive Chiral Spectroscopy by Dynamical Symmetry Breaking in High Harmonic Generation.* Physical Review X, **9**, 031002, (2019). [Cited on page 209.]

[Ni 18] H. Ni, U. Saalmann & J.-M. Rost. *Tunneling exit characteristics from classical backpropagation of an ionized electron wave packet.* Physical Review A, **97**, 013426, (2018). [Cited on pages 248 and 254.]

[Nisoli 96] M. Nisoli, S. De Silvestri & O. Svelto. *Generation of high energy 10 fs pulses by a new pulse compression technique.* Applied Physics Letters, **68**, 20, pages 2793–2795, (1996). [Cited on page 60.]

[Nisoli 17] M. Nisoli, P. Decleva, F. Calegari, A. Palacios & F. Martín. *Attosecond Electron Dynamics in Molecules.* Chemical Reviews, **117**, 16, pages 10760–10825, (2017). [Cited on page 54.]

[Oberheide 97] J. Oberheide, P. Wilhelms & M. Zimmer. *New results on the absolute ion detection efficiencies of a microchannel plate.* Measurement Science and Technology, **8**, 4, pages 351–354, (1997). [Cited on page 81.]

[Oppermann 19] M. Oppermann, B. Bauer, T. Rossi, F. Zinna, J. Helbing, J. Lacour & M. Chergui. *Ultrafast broadband circular dichroism in the deep ultraviolet.* Optica, **6**, 1, page 56, (2019). [Cited on page 33.]

[Osborn 16] D. L. Osborn, C. C. Hayden, P. Hemberger, A. Bodi, K. Voronova & B. Sztáray. *Breaking through the false coincidence barrier in electron–ion coincidence experiments.* The Journal of Chemical Physics, **145**, 16, page 164202, (2016). [Cited on page 96.]

[Pasteur 48] L. Pasteur. *Recherches sur les relations qui peuvent exister entre la forme cristalline, la composition chimique et le sens de la polarisation rotatoire.* Annales de Chimie et de Physique, **24**, 3, pages 442–459, (1848). [Cited on page 28.]

[Patterson 13a] D. Patterson & J. M. Doyle. *Sensitive Chiral Analysis via Microwave Three-Wave Mixing.* Physical Review Letters, **111**, 023008, (2013). [Cited on page 128.]

[Patterson 13b] D. Patterson, M. Schnell & J. M. Doyle. *Enantiomer-specific detection of chiral molecules via microwave spectroscopy.* Nature, **497**, 7450, pages 475–477, (2013). [Cited on page 128.]

[Paul 01] P. M. Paul, E. S. Toma, P. Breger, G. Mullot, F. Augé, P. Balcou, H. G. Muller & P. Agostini. *Observation of a Train of Attosecond Pulses from High Harmonic Generation.* Science, **292**, 5522, pages 1689–1692, (2001). [Cited on pages 53 and 200.]

[Peng 19] P. Peng, C. Marceau & D. M. Villeneuve. *Attosecond imaging of molecules using high harmonic spectroscopy.* Nature Reviews Physics, **1**, 2, pages 144–155, (2019). [Cited on page 202.]

[Perelomov 66] A. M. Perelomov, V. S. Popov & M. V. Terent'Ev. *Ionization of Atoms in an Alternating Electric Field.* Soviet Physics, Journal of Experimental and Theoretical Physics, **23**, 5, pages 1393–1409, (1966). [Cited on page 196.]

[Pertot 17] Y. Pertot, C. Schmidt, M. Matthews, A. Chauvet, M. Huppert, V. Svoboda, A. von Conta, A. Tehlar, D. Baykusheva, J.-P. Wolf & H. J. Wörner. *Time-resolved x-ray absorption spectroscopy with a water window high-harmonic source.* Science, **355**, pages 264–267, (2017). [Cited on page 54.]

[Pfeiffer 12] A. N. Pfeiffer, C. Cirelli, M. Smolarski, D. Dimitrovski, M. Abu-samha, L. B. Madsen & U. Keller. *Attoclock reveals natural coordinates of the laser-induced tunnelling current flow in atoms.* Nature Physics, **8**, 1, pages 76–80, (2012). [Cited on page 248.]

[Piancastelli 99] M. Piancastelli. *The neverending story of shape resonances.* Journal of Electron Spectroscopy and Related Phenomena, **100**, 1-3, pages 167–190, (1999). [Cited on pages 39 and 189.]

[Pitzer 13] M. Pitzer, M. Kunitski, A. S. Johnson, T. Jahnke, H. Sann, F. Sturm, L. P. H. Schmidt, H. Schmidt-Bocking, R. Dorner, J. Stohner, J. Kiedrowski, M. Reggelin, S. Marquardt, A. Schiesser, R. Berger & M. S. Schoffler. *Direct Determination of Absolute Molecular Stereochemistry in Gas Phase by Coulomb Explosion Imaging.* Science, **341**, 6150, pages 1096–1100, (2013). [Cited on pages 43, 127, and 128.]

[Popmintchev 12] T. Popmintchev, M.-C. Chen, D. Popmintchev, P. Arpin, S. Brown, S. Alisauskas, G. Andriukaitis, T. Balciunas, O. D. Mucke, A. Pugzlys, A. Baltuska, B. Shim, S. E. Schrauth, A. Gaeta, C. Hernandez-Garcia, L. Plaja, A. Becker, A. Jaron-Becker, M. M. Murnane & H. C. Kapteyn. *Bright Coherent Ultrahigh Harmonics in the keV X-ray Regime from Mid-Infrared Femtosecond Lasers.* Science, **336**, 6086, pages 1287–1291, (2012). [Cited on pages 53 and 202.]

[Porat 18a] G. Porat, G. Alon, S. Rozen, O. Pedatzur, M. Krüger, D. Azoury, A. Natan, G. Orenstein, B. D. Bruner, M. J. J. Vrakking & N. Dudovich. *Attosecond time-resolved photoelectron holography.* Nature Communications, **9**, 2805, (2018). [Cited on page 206.]

[Porat 18b] G. Porat, C. M. Heyl, S. B. Schoun, C. Benko, N. Dörre, K. L. Corwin & J. Ye. *Phase-matched extreme-ultraviolet frequency-comb generation.* Nature Photonics, **12**, 7, pages 387–391, (2018). [Cited on pages 56 and 202.]

[Powis 00] I. Powis. *Photoelectron circular dichroism of the randomly oriented chiral molecules glyceraldehyde and lactic acid.* The Journal of Chemical Physics, **112**, 1, pages 301–310, (2000). [Cited on page 34.]

[Powis 08] I. Powis, C. J. Harding, G. A. Garcia & L. Nahon. *A Valence Photoelectron Imaging Investigation of Chiral Asymmetry in the Photoionization of Fenchone and Camphor.* ChemPhysChem, **9**, 3, pages 475–483, (2008). [Cited on pages 34, 37, 120, 238, and 253.]

[Powis 14] I. Powis. *Communication: The influence of vibrational parity in chiral photoionization dynamics.* The Journal of Chemical Physics, **140**, 11, page 111103, (2014). [Cited on page 38.]

[Rafiee Fanood 14] M. M. Rafiee Fanood, I. Powis & M. H. M. Janssen. *Chiral Asymmetry in the Multiphoton Ionization of Methyloxirane Using Femtosecond Electron–Ion Coincidence Imaging.* The Journal of Physical Chemistry A, **118**, 49, pages 11541–11546, (2014). [Cited on pages 41, 45, and 163.]

[Rafiee Fanood 15] M. M. Rafiee Fanood, N. B. Ram, C. S. Lehmann, I. Powis & M. H. M. Janssen. *Enantiomer-specific analysis of multi-component mixtures by correlated electron imaging–ion mass spectrometry.* Nature Communications, **6**, 7511, (2015). [Cited on pages 41, 121, 122, and 129.]

[Rafiee Fanood 16] M. M. Rafiee Fanood, M. H. M. Janssen & I. Powis. *Wavelength dependent photoelectron circular dichroism of limonene studied by femtosecond multiphoton laser ionization and electron-ion coincidence imaging.* The Journal of Chemical Physics, **145**, 12, page 124320, (2016). [Cited on page 163.]

[Reid 12] K. L. Reid. *Photoelectron angular distributions: developments in applications to isolated molecular systems.* Molecular Physics, **110**, 3, pages 131–147, (2012). [Cited on page 122.]

[Ren 18] X. Ren, J. Li, Y. Yin, K. Zhao, A. Chew, Y. Wang, S. Hu, Y. Cheng, E. Cunningham, Y. Wu, M. Chini & Z. Chang. *Attosecond light sources in the water window.* Journal of Optics, **20**, 2, page 023001, (2018). [Cited on pages 53 and 54.]

[Richter 15] M. Richter, M. Kunitski, M. Schöffler, T. Jahnke, L. P. Schmidt, M. Li, Y. Liu & R. Dörner. *Streaking Temporal Double-Slit Interference by an Orthogonal Two-Color Laser Field.* Physical Review Letters, **114**, 143001, (2015). [Cited on pages 206, 226, 227, and 228.]

[Richter 16] M. Richter, M. Kunitski, M. Schöffler, T. Jahnke, L. P. H. Schmidt & R. Dörner. *Ionization in orthogonal two-color laser fields: Origin and phase dependences of trajectory-resolved Coulomb effects.* Physical Review A, **94**, 033416, (2016). [Cited on pages 206, 226, 241, and 242.]

[Ritchie 76] B. Ritchie. *Theory of the angular distribution of photoelectrons ejected from optically active molecules and molecular negative ions.* Physical Review A, **13**, 4, pages 1411–1415, (1976). [Cited on page 34.]

[Rothhardt 14] J. Rothhardt, M. Krebs, S. Hädrich, S. Demmler, J. Limpert & A. Tünnermann. *Absorption-limited and phase-matched high harmonic generation in the tight focusing regime.* New Journal of Physics, **16**, 3, page 033022, (2014). [Cited on page 201.]

[Rozen 19] S. Rozen, A. Comby, E. Bloch, S. Beauvarlet, D. Descamps, B. Fabre, S. Petit, V. Blanchet, B. Pons, N. Dudovich & Y. Mairesse. *Controlling Subcycle Optical Chirality in the Photoionization of Chiral Molecules.* Physical Review X, **9**, 031004, (2019). [Cited on pages 210 and 221.]

[Rudenko 04] A. Rudenko, K. Zrost, C. D. Schröter, V. L. B. d. Jesus, B. Feuerstein, R. Moshammer & J. Ullrich. *Resonant structures in the low-energy electron continuum for single ionization of atoms in the tunnelling regime.* Journal of Physics B: Atomic, Molecular and Optical Physics, **37**, 24, pages L407–L413, (2004). [Cited on page 205.]

[Sainadh 19] U. S. Sainadh, H. Xu, X. Wang, A. Atia-Tul-Noor, W. C. Wallace, N. Douguet, A. Bray, I. Ivanov, K. Bartschat, A. Kheifets, R. T. Sang & I. V. Litvinyuk. *Attosecond angular streaking and tunnelling time in atomic hydrogen.* Nature, **568**, 7750, pages 75–77, (2019). [Cited on page 253.]

[Sann 16] H. Sann, T. Havermeier, C. Müller, H.-K. Kim, F. Trinter, M. Waitz, J. Voigtsberger, F. Sturm, T. Bauer, R. Wallauer, D. Schneider, M. Weller, C. Goihl, J. Tross, K. Cole, J. Wu, M. Schöffler, H. Schmidt-Böcking, T. Jahnke, M. Simon & R. Dörner. *Imaging the Temporal Evolution of Molecular Orbitals during Ultrafast Dissociation.* Physical Review Letters, **117**, 243002, (2016). [Cited on page 44.]

[Schafer 93] K. J. Schafer, B. Yang, L. F. DiMauro & K. C. Kulander. *Above threshold ionization beyond the high harmonic cutoff.* Physical Review Letters, **70**, 11, pages 1599–1602, (1993). [Cited on page 198.]

[Schäfers 99] F. Schäfers, H.-C. Mertins, A. Gaupp, W. Gudat, M. Mertin, I. Packe, F. Schmolla, S. Di Fonzo, G. Soullié, W. Jark, R. Walker, X. Le Cann, R. Nyholm & M. Eriksson. *Soft-x-ray polarimeter with multilayer optics: complete analysis of the polarization state of light.* Applied Optics, **38**, 19, page 4074, (1999). [Cited on page 59.]

[Scharge 07] T. Scharge, C. Cézard, P. Zielke, A. Schütz, C. Emmeluth & M. A. Suhm. *A peptide co-solvent under scrutiny: self-aggregation of 2,2,2-trifluoroethanol.* Physical Chemistry Chemical Physics, **9**, 32, page 4472, (2007). [Cited on page 31.]

[Scoles 88] G. Scoles. Atomic and molecular beam methods, volume 1. Oxford University Press, (1988). [Cited on page 85.]

[Scuderi 11] D. Scuderi, K. Le Barbu-Debus & A. Zehnacker. *The role of weak hydrogen bonds in chiral recognition.* Physical Chemistry Chemical Physics, **13**, 40, page 17916, (2011). [Cited on page 30.]

[Senfftleben 20] B. Senfftleben, M. Kretschmar, A. Hoffmann, M. Sauppe, J. Tümmler, I. Will, T. Nagy, M. J. J. Vrakking, D. Rupp & B. Schütte. *Highly non-linear ionization of atoms induced by intense high-harmonic pulses.* Journal of Physics: Photonics, **2**, 3, page 034001, (2020). [Cited on pages 54 and 202.]

[Shafir 12] D. Shafir, H. Soifer, B. D. Bruner, M. Dagan, Y. Mairesse, S. Patchkovskii, M. Y. Ivanov, O. Smirnova & N. Dudovich. *Resolving the time when an electron exits a tunnelling barrier.* Nature, **485**, 7398, pages 343–346, (2012). [Cited on pages 202 and 203.]

[Shiner 09] A. D. Shiner, C. Trallero-Herrero, N. Kajumba, H.-C. Bandulet, D. Comtois, F. Légaré, M. Giguère, J.-C. Kieffer, P. B. Corkum & D. M. Villeneuve. *Wavelength Scaling of High Harmonic Generation Efficiency.* Physical Review Letters, **103**, 073902, (2009). [Cited on page 200.]

[Shubert 14] V. A. Shubert, D. Schmitz, D. Patterson, J. M. Doyle & M. Schnell. *Identifying Enantiomers in Mixtures of Chiral Molecules with Broadband Microwave Spectroscopy.* Angewandte Chemie International Edition, **53**, 4, pages 1152–1155, (2014). [Cited on page 128.]

[Smeenk 09] C. Smeenk, L. Arissian, A. Staudte, D. M. Villeneuve & P. B. Corkum. *Momentum space tomographic imaging of photoelectrons.* Journal of Physics B: Atomic, Molecular and Optical Physics, **42**, 18, page 185402, (2009). [Cited on page 71.]

[Smirnova 09] O. Smirnova, Y. Mairesse, S. Patchkovskii, N. Dudovich, D. Villeneuve, P. Corkum & M. Y. Ivanov. *High harmonic interferometry of multi-electron dynamics in molecules.* Nature, **460**, 7258, pages 972–977, (2009). [Cited on page 200.]

[Soai 00] K. Soai, T. Shibata & I. Sato. *Enantioselective Automultiplication of Chiral Molecules by Asymmetric Autocatalysis.* Accounts of Chemical Research, **33**, 6, pages 382–390, (2000). [Cited on page 27.]

[Stener 04] M. Stener, G. Fronzoni, D. Di Tommaso & P. Decleva. *Density functional study on the circular dichroism of photoelectron angular distribution from chiral derivatives of oxirane.* Journal of Chemical Physics, **120**, 7, pages 3284–3296, (2004). [Cited on page 35.]

[Strelkov 04] V. Strelkov, A. Zair, O. Tcherbakoff, R. Lopez-Martens, E. Cormier, E. Mével & E. Constant. *Generation of attosecond pulses with ellipticity-modulated fundamental.* Applied Physics B: Lasers and Optics, **78**, 7-8, pages 879–884, (2004). [Cited on page 200.]

[Sturm 17] F. P. Sturm, X. M. Tong, A. Palacios, T. W. Wright, I. Zalyubovskaya, D. Ray, N. Shivaram, F. Martín, A. Belkacem, P. Ranitovic & T. Weber. *Mapping and controlling ultrafast dynamics of highly excited H 2 molecules by VUV-IR pump-probe schemes.* Physical Review A, **95**, 012501, (2017). [Cited on page 43.]

[Tajima 95] S. Tajima, Y. Nagai, O. Sekiguchi, M. Fujishige & N. Uchida. *Fragmentation of the metastable molecular ion of methyl lactate: The formation of oxygen-protonated methanol [CH3OH2]+ involving double hydrogen atom transfers.* Journal of the American Society for Mass Spectrometry, **6**, 3, pages 202–206, (1995). [Cited on pages 167 and 169.]

[Takahashi 02] E. Takahashi, Y. Nabekawa & K. Midorikawa. *Generation of 10-mJ coherent extreme-ultraviolet light by use of high-order harmonics.* Optics Letters, **27**, 21, pages 1920–1922, (2002). [Cited on page 54.]

[Takahashi 13] E. J. Takahashi, P. Lan, O. D. Mücke, Y. Nabekawa & K. Midorikawa. *Attosecond nonlinear optics using gigawatt-scale isolated attosecond pulses.* Nature Communications, **4**, 2691, (2013). [Cited on pages 54 and 202.]

[Tan 78] K. H. Tan, C. E. Brion, P. E. van der Leeuv & M. J. van der Wiel. *Absolute oscillator strengths (10-60 eV) for the photoabsorption, photoionisation and fragmentation of $H_2O$.* Chemical Physics, **29**, pages 299–309, (1978). [Cited on page 162.]

[Tang 10] Y. Tang & A. E. Cohen. *Optical Chirality and Its Interaction with Matter.* Physical Review Letters, **104**, 163901, (2010). [Cited on page 210.]

[Tang 11] Y. Tang & A. E. Cohen. *Enhanced Enantioselectivity in Excitation of Chiral Molecules by Superchiral Light.* Science, **332**, 6027, pages 333–336, (2011). [Cited on page 210.]

[Tao 16] Z. Tao, C. Chen, T. Szilvási, M. Keller, M. Mavrikakis, H. Kapteyn & M. Murnane. *Direct time-domain observation of attosecond final-state lifetimes in photoemission from solids.* Science, **353**, 6294, pages 62–67, (2016). [Cited on page 54.]

[Tate 07] J. Tate, T. Auguste, H. G. Muller, P. Salières, P. Agostini & L. F. DiMauro. *Scaling of Wave-Packet Dynamics in an Intense Midinfrared Field.* Physical Review Letters, **98**, 013901, (2007). [Cited on page 200.]

[Tia 17] M. Tia, M. Pitzer, G. Kastirke, J. Gatzke, H.-K. Kim, F. Trinter, J. Rist, A. Hartung, D. Trabert, J. Siebert, K. Henrichs, J. Becht, S. Zeller, H. Gassert, F. Wiegandt, R. Wallauer, A. Kuhlins, C. Schober, T. Bauer, N. Wechselberger, P. Burzynski, J. Neff, M. Weller, D. Metz, M. Kircher, M. Waitz, J. B. Williams, L. P. H. Schmidt, A. D. Müller, A. Knie, A. Hans, L. Ben Ltaief, A. Ehresmann, R. Berger, H. Fukuzawa, K. Ueda, H. Schmidt-Böcking, R. Dörner, T. Jahnke, P. V. Demekhin & M. Schöffler. *Observation of Enhanced Chiral Asymmetries in the Inner-Shell Photoionization of Uniaxially Oriented Methyloxirane Enantiomers.* The Journal of Physical Chemistry Letters, **8**, 13, pages 2780–2786, (2017). [Cited on pages 39, 40, 120, 123, and 163.]

[Torlina 15] L. Torlina, F. Morales, J. Kaushal, I. Ivanov, A. Kheifets, A. Zielinski, A. Scrinzi, H. G. Muller, S. Sukiasyan, M. Ivanov & O. Smirnova. *Interpreting attoclock measurements of tunnelling times.* Nature Physics, **11**, 6, pages 503–508, (2015). [Cited on pages 247 and 253.]

[Travers 19] J. C. Travers, T. F. Grigorova, C. Brahms & F. Belli. *High-energy pulse self-compression and ultraviolet generation through soliton dynamics in hollow capillary fibres.* Nature Photonics, **13**, 8, pages 547–554, (2019). [Cited on pages 60 and 258.]

[Trinter 13] F. Trinter, J. B. Williams, M. Weller, M. Waitz, M. Pitzer, J. Voigtsberger, C. Schober, G. Kastirke, C. Müller, C. Goihl, P. Burzynski, F. Wiegandt, T. Bauer, R. Wallauer, H. Sann, A. Kalinin, L. P. H. Schmidt, M. Schöffler, N. Sisourat & T. Jahnke. *Evolution of Interatomic Coulombic Decay in the Time Domain.* Physical Review Letters, **111**, 093401, (2013). [Cited on page 44.]

[Turchini 04] S. Turchini, N. Zema, G. Contini, G. Alberti, M. Alagia, S. Stranges, G. Fronzoni, M. Stener, P. Decleva & T. Prosperi. *Circular dichroism in photoelectron spectroscopy of free chiral molecules: Experiment and theory on methyl-oxirane.* Physical Review A, **70**, 014502, (2004). [Cited on pages 35 and 120.]

[Turchini 09] S. Turchini, D. Catone, G. Contini, N. Zema, S. Irrera, M. Stener, D. Di Tommaso, P. Decleva & T. Prosperi. *Conformational Effects in Photoelectron Circular Dichroism of Alaninol.* ChemPhysChem, **10**, 11, pages 1839–1846, (2009). [Cited on pages 35 and 120.]

[Turchini 13] S. Turchini, D. Catone, N. Zema, G. Contini, T. Prosperi, P. Decleva, M. Stener, F. Rondino, S. Piccirillo, K. C. Prince & M. Speranza. *Conformational Sensitivity in Photoelectron Circular Dichroism of 3-Methylcyclopentanone.* ChemPhysChem, **14**, 8, pages 1723–1732, (2013). [Cited on pages 35, 38, 120, and 121.]

[Tzallas 03] P. Tzallas, D. Charalambidis, N. A. Papadogiannis, K. Witte & G. D. Tsakiris. *Direct observation of attosecond light bunching.* Nature, **426**, 6964, pages 267–271, (2003). [Cited on page 54.]

[Ullrich 87] J. Ullrich & H. Schmidt-Böcking. *Time-of-flight spectrometer for the determination of microradian projectile scattering angles in atomic collisions.* Physics Letters A, **125**, 4, pages 193–196, (1987). [Cited on page 73.]

[Ullrich 88] J. Ullrich, M. Horbatsch, V. Dangendorf, S. Kelbch & H. Schmidt-Bocking. *Scattering-angle-dependent multiple ionisation cross sections in high-energy heavy-ion-atom collisions.* Journal of Physics B: Atomic, Molecular and Optical Physics, **21**, 4, pages 611–624, (1988). [Cited on page 73.]

[Ullrich 95] J. Ullrich, R. Moshammer, M. Unverzagt, W. Schmidt, P. Jardin, R. Dörner, V. Merge & H. Schmidt-Böking. *Ionization collision dynamics*

*in 3.6 MeV/u $Ni^{24+}$ on He encounters.* Nuclear Instruments and Methods in Physics Research B, **98**, pages 375–379, (1995). [Cited on page 73.]

[Ullrich 03] J. Ullrich, R. Moshammer, A. Dorn, R. Dörner, L. P. H. Schmidt & H. Schmidt-Böcking. *Recoil-ion and electron momentum spectroscopy: reaction-microscopes.* Reports on Progress in Physics, **66**, 9, pages 1463–1545, (2003). [Cited on page 73.]

[Véniard 96] V. Véniard, R. Taïeb & A. Maquet. *Phase dependence of (N+1)-color (N>1) IR-UV photoionization of atoms with higher harmonics.* Physical Review A, **54**, 1, pages 721–728, (1996). [Cited on page 200.]

[Vetter 97] W. Vetter & V. Schurig. *Enantioselective determination of chiral organochlorine compounds in biota by gas chromatography on modified cyclodextrins.* Journal of Chromatography A, **774**, 1-2, pages 143–175, (1997). [Cited on page 127.]

[Veyrinas 13] K. Veyrinas, C. Elkharrat, S. Marggi Poullain, N. Saquet, D. Dowek, R. R. Lucchese, G. A. Garcia & L. Nahon. *Complete determination of the state of elliptically polarized light by electron-ion vector correlations.* Physical Review A, **88**, 063411, (2013). [Cited on page 59.]

[Volpato 19] A. Volpato & E. Collini. *Optimization and selection of time-frequency transforms for wave-packet analysis in ultrafast spectroscopy.* Optics Express, **27**, 3, page 2975, (2019). [Cited on page 142.]

[Vozzi 11] C. Vozzi, M. Negro, F. Calegari, G. Sansone, M. Nisoli, S. De Silvestri & S. Stagira. *Generalized molecular orbital tomography.* Nature Physics, **7**, 10, pages 822–826, (2011). [Cited on page 202.]

[Warrick 17] E. R. Warrick, J. E. Bækhøj, W. Cao, A. P. Fidler, F. Jensen, L. B. Madsen, S. R. Leone & D. M. Neumark. *Attosecond transient absorption spectroscopy of molecular nitrogen: Vibrational coherences in the $b'^1\Sigma_u^+$ state.* Chemical Physics Letters, **683**, pages 408–415, (2017). [Cited on page 54.]

[Westphal 89] C. Westphal, J. Bansmann, M. Getzlaff & G. Schönhense. *Circular Dichroism in the Angular Distribution of Photoelectrons from Oriented CO Molecules.* Physical Reveiw Letters, **63**, 2, pages 151–154, (1989). [Cited on page 39.]

[Whitaker 03] B. Whitaker. Imaging in molecular dynamics : technology and applications. Cambridge University Press, (2003). [Cited on page 66.]

[Wiley 55] W. C. Wiley & I. H. McLaren. *Time-of-Flight Mass Spectrometer with Improved Resolution.* Review of Scientific Instruments, **26**, 12, pages 1150–1157, (1955). [Cited on page 66.]

[Wollenhaupt 09] M. Wollenhaupt, M. Krug, J. Köhler, T. Bayer, C. Sarpe-Tudoran & T. Baumert. *Three-dimensional tomographic reconstruction of ultrashort free electron wave packets.* Applied Physics B, **95**, 4, pages 647–651, (2009). [Cited on page 71.]

[Zehnacker 08] A. Zehnacker & M. Suhm. *Chirality Recognition between Neutral Molecules in the Gas Phase.* Angewandte Chemie International Edition, **47**, 37, pages 6970–6992, (2008). [Cited on pages 30 and 31.]

[Zhang 14a] L. Zhang, X. Xie, S. Roither, D. Kartashov, Y. Wang, C. Wang, M. Schöffler, D. Shafir, P. B. Corkum, A. Baltuška, I. Ivanov, A. Kheifets, X. Liu, A. Staudte & M. Kitzler. *Laser-sub-cycle two-dimensional electron-momentum mapping using orthogonal two-color fields.* Physical Review A, **90**, 061401(R), (2014). [Cited on pages 206 and 226.]

[Zhang 14b] L. Zhang, X. Xie, S. Roither, Y. Zhou, P. Lu, D. Kartashov, M. Schöffler, D. Shafir, P. B. Corkum, A. Baltuška, A. Staudte & M. Kitzler. *Subcycle Control of Electron-Electron Correlation in Double Ionization.* Physical Review Letters, **112**, 193002, (2014). [Cited on page 43.]

[Zhao 20] X. Zhao, S.-J. Wang, W.-W. Yu, H. Wei, C. Wei, B. Wang, J. Chen & C. D. Lin. *Metrology of Time-Domain Soft X-Ray Attosecond Pulses and Reevaluation of Pulse Durations of Three Recent Experiments.* Physical Review Applied, **13**, 034043, (2020). [Cited on page 53.]

## Étude des dynamiques chirales femtosecondes et attosecondes par imagerie de vecteur vitesse et spectroscopie de photoelectrons et photoions en coïncidence

**Résumé :** L'absence de symétrie miroir dans la structure d'une molécule, ou chiralité, est d'importance fondamentale dans de nombreux domaines, de la biologie à la chimie, la synthèse de médicaments ou encore la physique. Elle est étudiée ici à son échelle de temps naturelle, de la femtoseconde ($10^{-15}$ s) à l'attoseconde ($10^{-18}$ s), en utilisant des impulsions laser ultrabrèves. Quand une molécule chirale est ionisée par un champ laser polarisé circulairement, de fortes asymétries chirosensitives peuvent apparaître dans la distribution angulaire de photoélectrons, à savoir le dichroïsme circulaire de photoelectrons.

Nous verrons comment une source laser à haute cadence de nouvelle génération peut être utilisée avec un spectromètre imageur de vecteur vitesse ou un spectromètre de photoélectrons-photoions en coïncidence pour accéder à ces asymétries. L'intéraction lumière-matière sera explorée dans deux régimes. D'une part, l'ionisation multiphotonique montre une grande sensibilité moléculaire. Des champs polarisés elliptiquement seront en particuler utilisés pour étudier les mécanismes d'anisotropie d'excitation. Des processus dépendants de la fragmentation seront résolus avec la détection en coïncidence, et nous accèderons à des dynamiques femtoseconde avec des schémas pompe-sonde résolus en temps. D'autre part, l'ionisation en champs forts nous fait disposer d'un cadre semi-classique simplifié. Il sera utilisé pour décoder l'intéraction lumière-matière à l'échelle d'une fraction de cycle optique, à l'origine des processus chiroptiques, en utilisant des champs laser vectoriels complexes. Cela nous permettra de comprendre comment les trajectoires individuelles de photoélectrons sont imprégnées par la chiralité, tout en enrichissant la boîte à outils des champs forts d'une observable hautement sensible.

*Mots-clés : Chiralité - Laser à haute cadence - Spectroscopie de coïncidence - Dichroisme circulaire de photoelectrons - Dynamiques Femtoseconde et Attoseconde*

## Femtosecond and attosecond chiral dynamics investigated by velocity map imaging and photoelectron photoion coincidence spectroscopy

**Abstract :** The absence of mirror symmetry in the structure of a molecule, or chirality, is of fundamental importance in a broad range of fields, from biology, chemistry, drug synthesis, and physics. It is investigated here at its natural timescale, from femtosecond ($10^{-15}$ s) to attosecond ($10^{-18}$ s), by the use of ultrashort laser pulses. When a chiral molecule is ionized by a circularly polarized laser field, strong chirosensitive asymmetries can appear in the photoelectron angular distribution, namely photoelectron circular dichroism.

We will see here how new generation high repetition rate laser beamline can be employed with a velocity map imaging spectrometer or a photoelectron-photoion coincidence spectrometer in order to access these asymmetries. The light-matter interaction will be investigated in two regimes. One the one hand, multiphoton ionization shows a high molecular sensitivity. Elliptically polarized fields will be used in particular to study the mechanisms of anisotropy of excitation. Fragmentation-dependent processes will be resolved with the coincidence detection, and femtosecond dynamics will be accessed by using time-resolved pump-probe schemes. On the other hand, strong field ionization provides a simplified semi-classical framework. It will be used to unravel the sub-optical cycle light-matter interaction at the origin of chiroptical processes by the use of tailored vectorial laser fields. This will enable us to understand how the individual photoelectron trajectories are imprinted with chirality, while enriching the strong-field toolbox with a highly sensitive observable.

*Key-words : Chirality - High repetition rate laser - Coincidence spectroscopy - Photoelectron circular dichroism - Femtosecond and Attosecond Dyncamics*